ORNL-5059
NRC-1, NRC-5

Test of 6-Inch-Thick Pressure Vessels. Series 2: Intermediate Test Vessels V-3, V-4, and V-6

R. H. Bryan
J. G. Merkle
M. N. Raftenberg
G. C. Robinson
J. E. Smith

OAK RIDGE NATIONAL LABORATORY
OPERATED BY UNION CARBIDE CORPORATION • FOR THE U.S. ATOMIC ENERGY COMMISSION

BLANK PAGE

Printed in the United States of America. Available from
National Technical Information Service
U.S. Department of Commerce
5285 Port Royal Road, Springfield, Virginia 22161
Price: Printed Copy $7.60; Microfiche $2.25

ORNL-5059
NRC-1, NRC-5

Contract No. W-7405-eng-26

REACTOR DIVISION

TEST OF 6-INCH-THICK PRESSURE VESSELS. SERIES 2: INTERMEDIATE TEST VESSELS V-3, V-4, and V-6

R. H. Bryan M. N. Raftenberg
J. G. Merkle G. C. Robinson
J. E. Smith

Work funded by the Nuclear Regulatory Commission
under Interagency Agreement 40-495-75

NOVEMBER 1975

OAK RIDGE NATIONAL LABORATORY
Oak Ridge, Tennessee 37830
operated by
UNION CARBIDE CORPORATION
for the
ENERGY RESEARCH AND DEVELOPMENT ADMINISTRATION

CONTENTS

BLANK PAGE

FOREWORD

The work reported here was performed mostly at Oak Ridge National Laboratory (ORNL) under sponsorship of the U.S. Nuclear Regulatory Commission's (NRC) Heavy-Section Steel Technology (HSST) Program, which is directed by ORNL. The program is conducted as part of the ORNL Pressure Vessel Technology Program, of which G. D. Whitman is manager. The manager for the NRC is E. K. Lynn.

This report is designated Heavy-Section Steel Technology Program Technical Report No. 37. Prior reports in this series are listed below.

1. S. Yukawa, *Evaluation of Periodic Proof Testing and Warm Prestressing Procedures for Nuclear Reactor Vessels*, HSSTP-TR-1, General Electric Company, Schenectady, N.Y. (July 1, 1969).

2. L. W. Loechel, *The Effect of Section Size on the Transition Temperature in Steel*, MCR-69-189, Martin Marietta Corporation, Denver, Colo. (Nov. 20, 1969).

3. P. N. Randall, *Gross Strain Measure of Fracture Toughness of Steels*, HSSTP-TR-3, TRW Systems Group, Redondo Beach, Calif. (Nov. 1, 1969).

4. C. Visser, S. E. Gabrielse, and W. VanBuren, *A Two-Dimensional Elastic-Plastic Analysis of Fracture Test Specimens*, WCAP-7368, Westinghouse Electric Corporation, PWR Systems Division, Pittsburgh, Pa. (October 1969).

5. T. R. Mager, F. O. Thomas, and W. S. Hazelton, *Evaluation by Linear Elastic Fracture Mechanics of Radiation Damage to Pressure Vessel Steels*, WCAP-7328 (Rev.), Westinghouse Electric Corporation, PWR Systems Division, Pittsburgh, Pa. (October 1969).

6. W. O. Shabbits, W. H. Pryle, and E. T. Wessel, *Heavy Section Fracture Toughness Properties of A 533 Grade B Class 1 Steel Plate and Submerged Arc Weldment*, WCAP-7414, Westinghouse Electric Corporation, PWR Systems Division, Pittsburgh, Pa. (December 1969).

7. F. J. Loss, *Dynamic Tear Test Investigations of the Fracture Toughness of Thick-Section Steel*, NRL-7056, U.S. Naval Research Laboratory, Washington, D.C. (May 14, 1970).

8. P. B. Crosley and E. J. Ripling, *Crack Arrest Fracture Toughness of A 533 Grade B Class 1 Pressure Vessel Steel*, HSSTP-TR-8, Materials Research Laboratory, Inc., Glenwood, Ill. (March 1970).

9. T. R. Mager, *Post-Irradiation Testing of 2 T Compact Tension Specimens*, WCAP-7561, Westinghouse Electric Corporation, PWR Systems Division, Pittsburgh, Pa. (August 1970).

10. T. R. Mager, *Fracture Toughness Characterization Study of A 533, Grade B, Class 1 Steel*, WCAP-7578, Westinghouse Electric Corporation, PWR Systems Division, Pittsburgh, Pa. (October 1970).

11. T. R. Mager, *Notch Preparation in Compact Tension Specimens*, WCAP-7579, Westinghouse Electric Corporation, PWR Systems Division, Pittsburgh Pa. (November 1970).

12. N. Levy and P. V. Marcal, *Three-Dimensional Elastic-Plastic Stress and Strain Analysis for Fracture Mechanics, Phase I: Simple Flawed Specimens*, HSSTP-TR-12, Brown University, Providence, R.I. (December 1970).

13. W. O. Shabbits, *Dynamic Fracture Toughness Properties of Heavy Section A 533 Grade B, Class 1 Steel Plate*, WCAP-7623, Westinghouse Electric Corporation, PWR Systems Division, Pittsburgh, Pa. (December 1970).

14. P. N. Randall, *Gross Strain Crack Tolerance of A 533-B Steel*, HSSTP-TR-14, TRW Systems Group, Redondo Beach, Calif. (May 1, 1971).

15. H. T. Corten and R. H. Sailors, *Relationship Between Material Fracture Toughness Using Fracture Mechanics and Transition Temperature Tests*, T&AM Report 346, University of Illinois, Urbana, Ill. (Aug. 1, 1971).

16. T. R. Mager and V. J. McLoughlin. *The Effect of an Environment of High Temperature Primary Grade Nuclear Reactor Water and the Fatigue Crack Growth Characteristics of A 533 Grade B Class 1 Plate and Weldment Material.* WCAP-7776. Westinghouse Electric Corporation. PWR Systems Division. Pittsburgh. Pa. (October 1971).

17. N. Levy and P. V. Marcal. *Three-Dimensional Elastic-Plastic Stress and Strain Analysis for Fracture Mechanics. Phase II. Improved Modeling.* HSSTP-TR-17. Brown University. Providence. R.I. (November 1971).

18. S. C. Grigory. *Six-Inch-Thick Flawed Tensile Tests. First Technical Summary Report. Longitudinal Specimens 1 through 7.* HSSTP-TR-18. Southwest Research Institute. San Antonio. Tex. (June 1972).

19. P. N. Randall. *Effects of Strain Gradients on the Gross Strain Crack Tolerance of A 533-B Steel.* HSSTP-TR-19. TRW Systems Group. Redondo Beach. Calif. (May 1. 1972).

20. S. C. Grigory. *Tests of Six-Inch-Thick Flawed Tensile Specimens. Second Technical Summary Report. Transverse Specimens Numbers 8 through 10. Welded Specimens Numbers 11 through 13.* HSSTP-TR-20. Southwest Research Institute. San Antonio. Tex. (June 1972).

21. L. A. James and J. A. Williams. *Heavy Section Steel Technology Program Technical Report No. 21. The Effect of Temperature and Neutron Irradiation Upon the Fatigue-Crack Propagation Behavior of ASTM A533. Grade B. Class 1 Steel.* HEDL-TME-72-132. Hanford Engineering Development Laboratory. Richlan l. Wash. (September 1972).

22. S. C. Grigory. *Tests of Six-Inch-Thick Flawed Tensile Specimens. Third Technical Summary Report. Longitudinal Specimens Numbers 14 through 16. Unflawed Specimen Number 17.* HSSTP-TR-22. Southwest Research Institute. San Antonio. Tex. (October 1972).

23. S. C. Grigory. *Tests of Six-Inch-Thick Flawed Tensile Specimens. Fourth Technical Summary Report. Tests of One-Inch-Thick Flawed Tensile Specimens for Size Effect Evaluation.* HSSTP-TR-23. Southwest Research Institute. San Antonio. Tex. (June 1973).

24. S. P. Ying and S. C. Grigory. *Tests of Six-Inch-Thick Tensile Specimens. Fifth Technical Summary Report. Acoustic Emission Monitoring of One-Inch and Six-Inch-Thick Tensile Specimens.* HSSTP-TR-24. Southwest Research Institute. San Antonio. Tex. (November 1972).

25. R. W. Derby et al.. *Test of 6-Inch-Thick Pressure Vessels. Series 1: Intermediate Test Vessels V-1 and V-2.* ORNL-4895 (February 1974).

26. W. J. Stelzman and R. G. Berggren. *Radiation Strengthening and Embrittlement in Heavy Section Plates and Welds.* ORNL-4871 (June 1973).

27. P. B. Crosley and E. J. Ripling. *Crack Arrest in an Increasing K-Field.* HSSTP-TR-27. Materials Research Laboratory. Glenwood. Ill. (January 1973).

28. P. V. Marcal. P. M. Stuart. and R. S. Bettes. *Elastic-Plastic Behavior of a Longitudinal Semi-Elliptical Crack in a Thick Pressure Vessel.* Brown University. Providence. R.I. (June 1973).

29. W. J. Stelzman. Characterization of HSST Plate 02 (in preparation).

30. D. A. Canonico. Characterization of Heavy Section Weldments in Pressure Vessel Steels (in preparation).

31. J. A. Williams. *The Irradiation and Temperature Dependence of Tensile and Fracture Properties of ASTM A533. Grade B. Class 1 Steel Plate and Weldment.* HEDL-TME 73-75. Hanford Engineering Development Laboratory. Richland. Wash. (August 1973).

32. J. M. Steichen and J. A. Williams. *High Strain Rate Tensile Properties of Irradiated ASTM A533 Grade B Class 1 Pressure Vessel Steel.* Hanford Engineering Development Laboratory. Richland. Wash. (July 1973).

33. P. C. Riccardella and J. L. Swedlow, *A Combined Analytical-Experimental Fracture Study*, WCAP-8224, Westinghouse Electric Corporation, PWR Systems Division, Pittsburgh, Pa. (October 1973).

34. R. J. Podlasek and R. J. Eiber, *Final Report on Investigation of Mode III Crack Extension in Reactor Piping*, Battelle Columbus Laboratories, Columbus, Ohio (May 1974).

35. T. R. Mager et al., *Interim Report on the Effect of Low Frequencies on the Fatigue Crack Growth Characteristics of A533 Grade B Class 1 Plate in an Environment of High-Temperature Primary Grade Nuclear Reactor Water*, WCAP-8256, Westinghouse Electric Corporation, Pittsburgh, Pa. (December 1973).

36. J. A. Williams, *The Irradiated Fracture Toughness of ASTM A533, Grade B, Class 1 Steel Measured with a Four Inch Thick Compact Tension Specimen*, HEDL-TME 75-10, Hanford Engineering Development Laboratory, Richland, Wash. (January 1975).

Copies of these reports may be obtained from Laboratory Records Department, Oak Ridge National Laboratory, P.O. Box X, Oak Ridge, Tenn. 37830.

TEST OF 6-INCH-THICK PRESSURE VESSELS, SERIES 2: INTERMEDIATE TEST VESSELS V-3, V-4, AND V-6

R. H. Bryan M. N. Raffenberg
J. G. Merkle G. C. Robinson
J. F. Smith

ABSTRACT

The second series of intermediate vessel tests were crack initiation fracture tests of 6-in.-thick 39-in.-OD steel vessels with sharp surface flaws approximately 2½ in. deep by 8 in. long in the longitudinal weld seams of the test cylinders. Fracture was initiated by means of hydraulic pressurization. One vessel was tested at each of three temperatures: 75, 130, and 190°F. Pretest analyses were made to predict the failure pressures and strains. Fracture toughness data obtained by equivalent-energy analysis of precracked Charpy-V tests and compact-tension specimen tests were used in the fracture analyses. The vessels behaved generally as had been expected. Posttest fracture analyses were also performed for each vessel. This report also includes detailed discussions of the fracture analysis methods developed in support of the vessel tests described.

I. INTRODUCTION

The electric power industry, especially in the United States, has rapidly adopted nuclear power reactors for routine commercial production of electrical energy. During the 1960–1970 decade, boiling-water reactor (BWR) and pressurized-water reactor (PWR) nuclear generating stations became economically competitive with large nonnuclear energy plants. Consequently, the proportion of bulk electrical energy generated by these two types of nuclear reactors has grown from practically zero in 1960 to about 10% of the total capacity in 1975. At the same time, the predominant capacities of nuclear power plants increased so that most of the cumulative nuclear capacity consists of plants rated at about 1100 MW(e).

This higher capacity has been attained partly by improvements in the performance of fuel elements, but the principal contribution to increased generating capacity is the use of reactor cores and associated structures of greater physical dimensions. The demand for larger pressure vessels to contain the water-cooled nuclear reactor cores developed as industrial capacity to produce the vessels materialized. The large reactor vessels must have thicker walls than the vessels of the smaller, earlier power reactors operating at about the same pressure. At present, a PWR vessel for a 1100-MW(e) plant is about 15 ft in diameter with a wall thickness of 8.5 in. Design pressures of PWRs are generally about 2500 psig, and normal operating temperatures are about 550°F; BWR vessels operate at about the same temperature but are designed for lower pressure, namely 1250 psig. BWR vessels for 1100-MW(e) plants are about 20 ft in diameter, but by virtue of the lower pressure the wall thickness need not be as great as in PWRs.

The Heavy-Section Steel Technology (HSST) Program was instituted under the sponsorship of the Atomic Energy Commission* in order to pursue more vigorously industry-sponsored investigations of thick-section vessels for water-cooled nuclear reactor service. The program has generated data related to the technology of thick-section components of reactor pressure vessels, particularly with respect to the influence of flaws on the serviceability of vessels. The program has developed data on the characteristics of plates, weldments, and forgings in terms of mechanical properties, toughness, inherent flaws, and

*Now sponsored by U.S. Nuclear Regulatory Commission.

BLANK PAGE

homogeneity. A major concern of the program is the practicability of accurately estimating the effects of flaws on the service life and strength of structures.

Methods of analysis as well as experimental bases for fracture evaluations of structures are being developed. Flawed specimens have been tested for a wide variety of conditions in terms of specimen size and configuration, loading, and temperature. As a result, considerable insight has been gained with regard to interpretation of test results and to application of results of tests on small specimens to large structures.

One can have confidence in fracture analysis only in proportion to the degree to which the theoretical methods used in such analysis have been confirmed by tests of, or experience with, structures of appropriate dimensions and loading conditions. Accordingly, the HSST program includes simulated service tests, of which the intermediate vessel tests are a part.

The aim of simulated service testing is to provide, through a series of experiments, a connection between behavior of structures observed in a laboratory environment and the behavior of full-size components under the wide variety of conditions that constitute the real operating environment. The main effort of this task is to determine, if not already known, which factors or conditions are important and then to carry out tests with the particular combinations of conditions that will contribute significant information on behavior of structures in service. Factors of concern include material properties; flaw location, orientation, shape, size and sharpness; and loading and environmental conditions. If expense, resources, safety, and time were of no importance, the significance of these factors could be studied under actual service conditions imposed on vessels in a large number of experiments with vessels as large as, or larger than, reactor pressure vessels. Since such an approach is completely impractical, each factor is studied separately or in combination with others on as simple a scale as practicable.

The objective of each simulated service test is to determine the ability of analytical methods to predict actual fracture behavior of a flawed structure under known conditions of material properties and loading. In the planned progression of such tests, analytical methods are confirmed, improved, or their limitations revealed. The testing of intermediate vessels in conjunction with tests of flawed tensile specimens of similar material and flawed models of the intermediate vessels permits consideration of many variables. Thus the intermediate vessel tests are a part of a structural test program which covers ranges of flaw size, section thickness, temperature, and stress state. The effects of differences in transverse restraint, toughness, plastic strain, biaxiality, and stress concentration can be observed and analyzed.

The original objectives emphasized in the simulated service task were (1) to demonstrate capability to predict the "vessel transition temperature" for a selected crack configuration using the material of interest (ASTM A533, grade B, class 1 plate; ASTM A508, class 2 forging); (2) to demonstrate, for the materials of interest, capability to predict various combinations of load (pressure), temperature, and crack configuration in full-thickness walls (6 in. or more) that will not cause fracture, and, finally, a combination that will cause fracture for both frangible and tough fracture conditions.

The intermediate vessel tests have been subdivided into four series:

1. flaws in cylindrical vessels, A508, class 2 forging steel — two vessels;
2. flaws in cylindrical vessels with longitudinal weld seams, A508, class 2 forging steel, submerged-arc welds — three vessels;
3. flaws in cylindrical vessels with longitudinal weld seams, A533, grade B, class 1 plate steel, submerged-arc welds — two vessels;
4. cylindrical vessels with radially attached nozzels, vessels of A508, class 2 forging steel and A533, grade B, class 1 plate steel; nozzle of A508, class 2 forging steel — three vessels.

The report[1] on the first series contains a comprehensive description of the pertinent factors considered in the design of the vessels and construction of the test facility and those leading to the tests of series 1, as well as a documentation of test results and fracture predictions. Emphasis is placed on providing the test results in such a manner that they form a resource for any investigators interested in the problem of fracture. This report describes the three tests in series 2 and documents comprehensive information on the characteristics of the vessels, material properties, conditions of testing, and results so as to facilitate further analysis. The report also describes the use of fracture toughness measurements based upon equivalent-energy concepts. These measurements and the investigations of crack growth by tests of both large tensile specimens and model vessels provided the bases for analytical predictions of rupture conditions.

The test sections of the five vessels of the first two series had identical cylindrical geometry. In the second series, however, the sharpened flaws were prepared in longitudinal weld seams; two vessels also had flaws located in base metal, but in every case ultimate rupture occurred at a weld-metal flaw. One vessel in each series was tested in the temperature range in which static fracture toughness is in sharp transition. In these two tests, linear elastic fracture mechanics based upon strain reasonably describes the observed results, although it is evident that variability in toughness of the weld metal introduces an uncertainty in prediction of rupture. One other test in each series was performed at static upper-shelf temperatures, and similar results were observed in weld and base metal. The third vessel in series 2 was tested at a higher temperature, at which both dynamic and static fracture toughnesses are on the upper shelf. All vessels tested at upper-shelf temperatures demonstrated that the initiation of fracture corresponds to the attainment of plastic instability in the neighborhood of the flaw.

2. DESCRIPTION OF VESSELS

Design and Procurement

Vessels V-3, V-4, and V-6 constitute the second series of vessels under task K of the HSST program.[1] This series was planned to investigate the effect of flaws of various sizes located in weld seams of cylindrical vessels and tested under transitional and tough modes of failure.

Figure 2.1 shows a partial cross section of the vessels: the cylindrical section is the test piece. Base material for all of the shell components is ASTM A508, class 2 forging. In addition to the circumferential

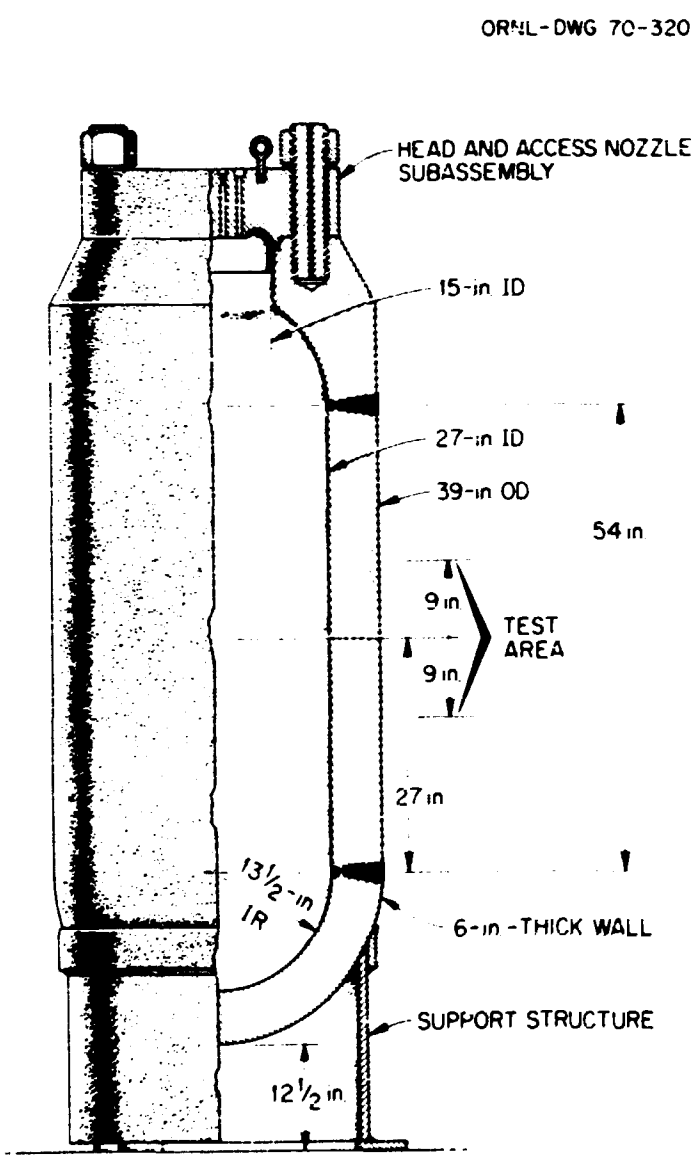

Fig. 2.1. HSST intermediate vessel.

submerged-arc welds shown in Fig. 2.1, a single longitudinal submerged-arc weld was placed in the cylindrical shells of vessels V-3 and V-4 as shown in Fig. 2.2a. A similar longitudinal submerged-arc weld was placed in the cylindrical shell of vessel V-6, after which the shell was partitioned and the resulting two cylindrical parts rotated 180° with respect to each other and rewelded with a circumferential submerged-arc weld as shown in Fig. 2.2b. This feature permitted the investigation of flaws placed at weld intersections (Fig. 2.2b). The joint configuration of the longitudinal and circumferential submerged-arc welds are shown respectively in Figs. 2.3a and 2.3b. Repair welding was accomplished by using a shielded-metal-arc procedure which was qualified with the joint configuration shown in Fig. 2.3c.

In addition to the provision for typical reactor pressure vessel longitudinal and circumferential weld seams, the vessel configuration shown in Fig. 2.1 was influenced by (1) the necessity for a thickness approximately that of light-water reactor vessels, (2) a reasonable assurance that components other than the part being tested would not fail prior to the test part, and (3) the requirement that the vessels be reasonably economical and procurable by lump sum bidding. The design and procurement activities to achieve these objectives for all the intermediate vessels are described in Ref. 1; the principal features are summarized here.

Vessels V-3, V-4, and V-6 were procured by competitive bidding; the award for the vessels was made to Taylor Forge Division, Gulf and Western Products Company on Dec. 23, 1968. Under the provisions of the contract, Taylor Forge's design of the head closure was verified by an analysis performed by Teledyne Materials Research Company according to requirements of the 1968 edition of Section III of the ASME Pressure Vessel Code and according to special requirements of the procurement specifications.[1] By these requirements the head closure was overdesigned in comparison to the cylindrical shell component, thereby giving greater assurance that flaws artificially introduced into the cylinder test area (see Fig. 2.1) would control vessel failure.

The cylindrical shells of vessels V-3, V-4, and V-6 were forged from a single piece forging from two heats, National Forge 3V928 and 1V3828. Mechanical properties of these shells following initial heat treatment were atypical of A508, class 2 materials. Following a study of the effects of retempering,[1] a reheat treatment produced typical mechanical and toughness properties as given in Table 2.1.

Mechanical properties were obtained from all-weld tensile specimens from the ¼ T location of the weld qualification pieces of vessels V-3, V-4, and V-6. Charpy V-notch tests were made at +10°F on full-size specimens from the same weld qualification pieces. Taylor Forge qualified three procedures: WP-379 for longitudinal submerged-arc weld seams; WP-380 for circumferential submerged-arc weld seams; and WP-381 for shielded-metal-arc welds. The results of these specimen tests are shown in Table 2.2.

Radiographic inspection of the longitudinal weld seam of vessels V-4 and V-6 showed that the welds were unacceptable and required repairing. Accordingly, the joint design for the longitudinal seams is somewhat at variance with (larger than) that shown in Fig. 2.3a. It should be noted that no subsequent repairs were necessary to either of the longitudinal seams after the defective welds were cut out and rewelded.

Considerable difficulty was encountered in obtaining acceptable circumferential welds. The hemispherical head-to-shell seam of vessel V-6 was the only weld that did not require repairs. In some cases, four repair attempts were necessary before the welds were acceptable.

In a few cases, the weld defects were found by radiographic inspection, but in most cases the welds failed to meet the ultrasonic inspection requirements. Each of the welds was inspected ultrasonically in accordance with the technique defined in Paragraph N-625 of the 1968 edition of Section III, ASME Nuclear Code. The Taylor Forge test procedure specifies that all shear-wave indications producing signals

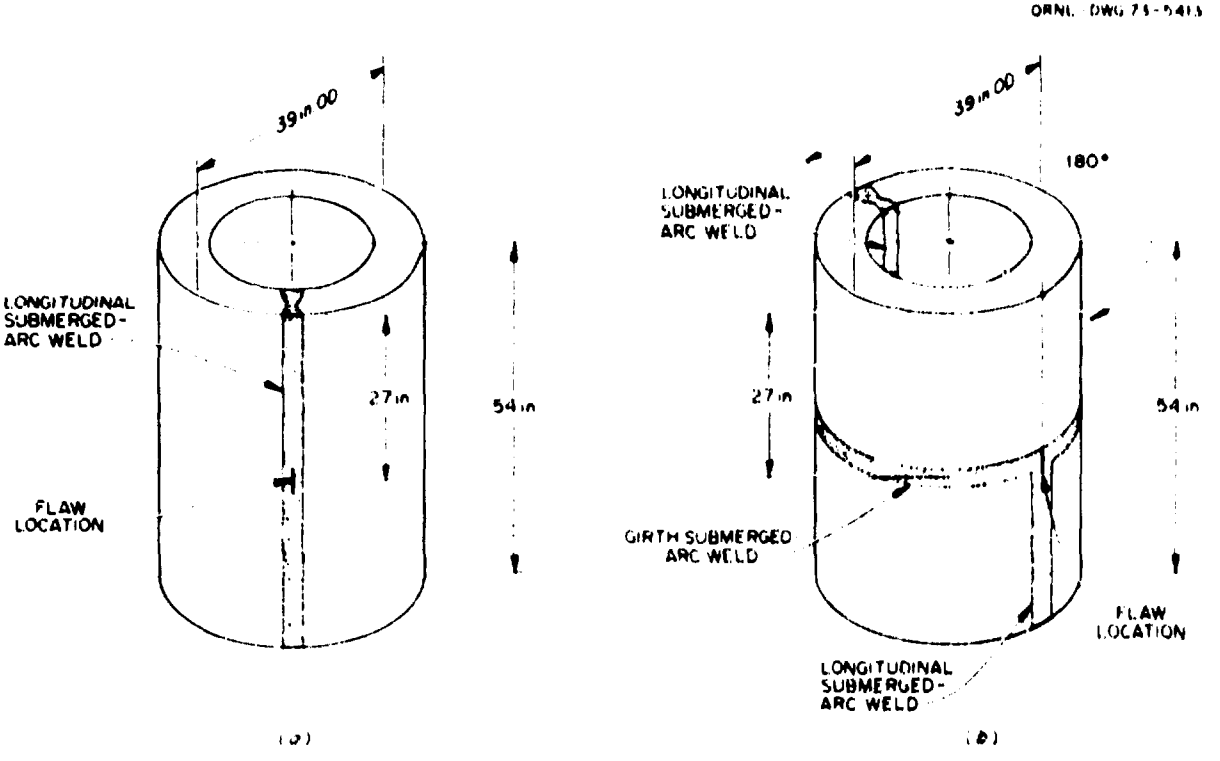

Fig. 2.2. Weld orientation for flaw location. (a) Vessels 3 and 4; (b) vessel 6.

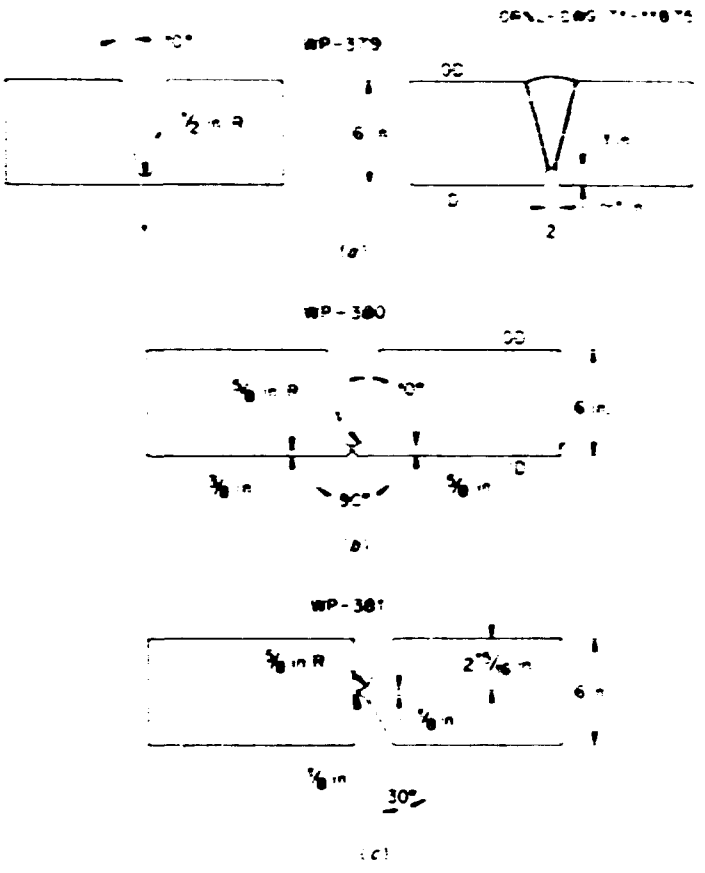

Fig. 2.3. Joint preparations for Taylor Forge welding procedures.

Table 2.1. Test results after retempering at 1320°F

Vessel No.	Ultimate tensile strength (ksi)	Yield strength (ksi)	Reduction in area (%)	Elongation (%)	C_v at +10°F (ft-lb)	Percent shear	Lateral expansion
V-3	91.5	72	69.9	27	66	43	0.060
					40	35	0.039
					33	33	0.031
	92.25	71.5	71	27	62.5	42	0.055
					79	47	0.067
					55.5	37	0.049
V-4	91.25	71.5	68.4	26	86.5	45	0.073
					61.5	43	0.057
					70.5	41	0.060
	91.75	71.5	70.4	26.5	66.5	41	0.059
					69.5	34	0.054
					58.5	32	0.050
V-6	92	71.5	71.2	27	71	45	0.060
					53.5	34	0.047
					72	40	0.064
	91.25	67.5	68.8	25	51	40	0.044
					55.5	31	0.046
					57	34	0.049

Table 2.2. Tensile and impact properties of weld qualification pieces of vessels V-3, V-4, and V-6

Location[a]	Ultimate tensile strength (ksi)	Yield strength (ksi)	Reduction in area (%)	Elongation (%)	C_v at +10 F (ft-lb)	Percent ductile fracture	Lateral expansion (mils)
WP-379							
Weld, ¼ T	85	71.5	62.5	28			
Base metal, ¼ T					36-40-45	30-40-40	25-28-34
HAZ, ¼ T					43-47-49	50-50-50	34-41-38
Weld, ½ T					90-96-97	80-80-80	66-57-70
Weld, 1/16 in. from bottom surface					77-84-74	80-95-80	53-53-52
WP-380							
Weld, ¼ T	81.5	69.4	64.9	28			
Base metal, ¼ T					37-55-60	20-25-25	29-41-46
HAZ, ¼ T					48-57-62	40-40-50	40-45-49
Weld, ½ T					87-92-92	90-80-80	66-63-68
Weld, 1/16 in. from top surface					84-91-95	80-80-80	66-73-74
WP-381							
Weld, ¼ T	95.3	84.8	70.8	29			
Base metal, ¼ T					78-78-68	40-40-40	56-56-51
HAZ, ¼ T					86-96-128	60-60-90	62-75-64
Weld, ½ T					75-73-85	70-70-80	60-57-65
Weld, 1/16 in. from bottom surface					76-72-79	80-80-80	65-62-61

[a] ¼ T, etc. means ¼ thickness from top surface.

equal to the height of the distance amplitude correction (DAC) curves or straight beam indications causing 100% loss of back-surface reflection are rejectable. The reference blocks used for instrument calibration is shown in Fig. 2.4. All the rejectable indications were found by shear-wave inspection, most of them near the ¼ T level.

Vessel V-4 contained the fewest repairs of the three vessels and was free of "rejectable" indications on final inspection. After as many as four repair attempts on the circumferential seams of V-6, rejectable ultrasonic indications were still being found (one each in the top and middle girth seams). In consideration of the fact that further repairs could be more detrimental than helpful and to expedite delivery, it was decided to accept V-6 with these imperfections.

As noted previously, most of the defects found by ultrasonic inspection were not detectable by radiography. However, Taylor Forge reported that in observing the grinding in some of the repair areas they could actually see the defects as they were uncovered. They reported that the defects appeared to be small, very tight "stringer-like" inclusions usually ½ to ¾ in. long and ⅛ to ¼ in. high. In all cases, porosity was observed immediately before grinding into a "stringer."

Each vessel successfully withstood a hydrostatic pressure test of 12,500 psi on completion of final postweld heat treatment (PWHT). Following ultrasonic inspection, the welds of each vessel were inspected with magnetic particles on both the outer and the inner surfaces. The vessels were then helium leak tested

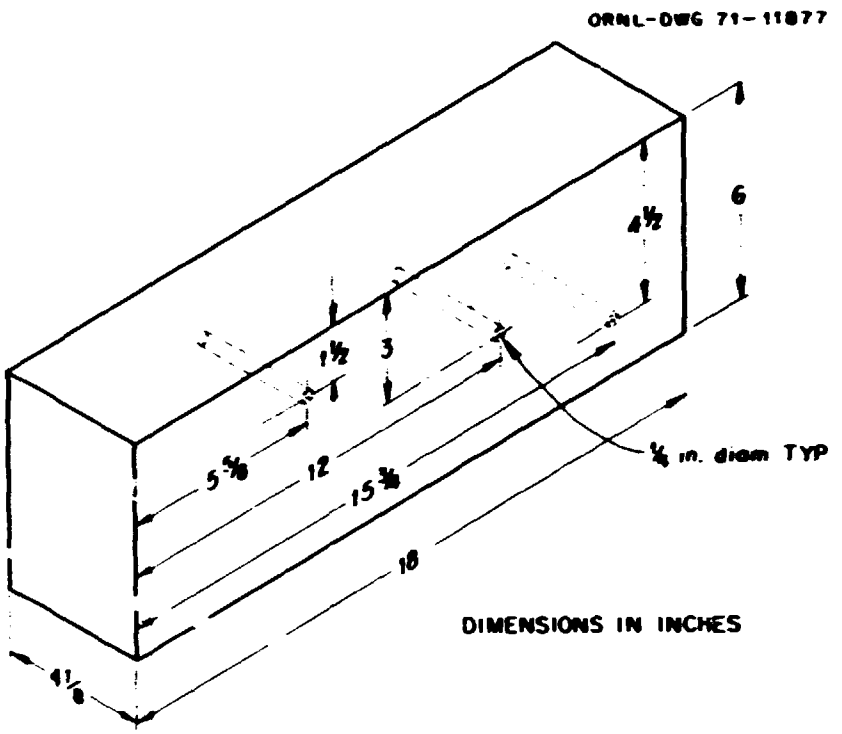

Fig. 2.4. Ultrasonic reference standard.

by pressurizing with a mixture of helium and nitrogen. In each case the leak rate was less than the minimum requirement of 5.8×10^{-5} std cc/sec.

A detailed listing[2] of the mill properties and mill analyses as well as fabrication histories are presented by Childress in a summary fabrication report for the first six vessels, V-1 through V-6.

Flaw Preparation

The artificial flaws were machined into vessels V-3, V-4, and V-6 and sharpened by fatigue by means of the hydraulic pulsing technique originally developed by Abbatiello and Derby[3] for the notch sharpening of the large tensile specimens and then successfully adapted to the flawing of vessels V-1 and V-2.[1] Also, the shear wave ultrasonic technique developed by Baker and Klindt[1] for monitoring the fatigue crack growth on vessels V-1 and V-2 was similarly used in the monitoring of flaw growth of vessels V-3, V-4, and V-6.

Observed and predicted flaw sizes using this ultrasonic technique compared favorably on the first series of vessels.[1] On the second series of vessels an attempt was made to improve and to simplify the procedure by using the amplitude of the reflected pulse from a "standard" flaw as a base for measuring crack growth. It was believed that this simple "go-no-go" standard would be an adequate indication for the monitoring of the fatiguing operation and would eliminate the need for continuous surveillance. The typical hardware setup used for fatiguing and monitoring the crack growth for all outside flaws of the second series of vessels is shown in Fig. 2.5. This figure shows the seal block held against a 2½-in.-wide × 16-in.-long machined flat on the vessel by the tensioning hand-jacking studs loading arrangement and sealed by an O-ring in an oblong configuration around the crack. The pressure intensifier driven by plant air at approximately 100 psig

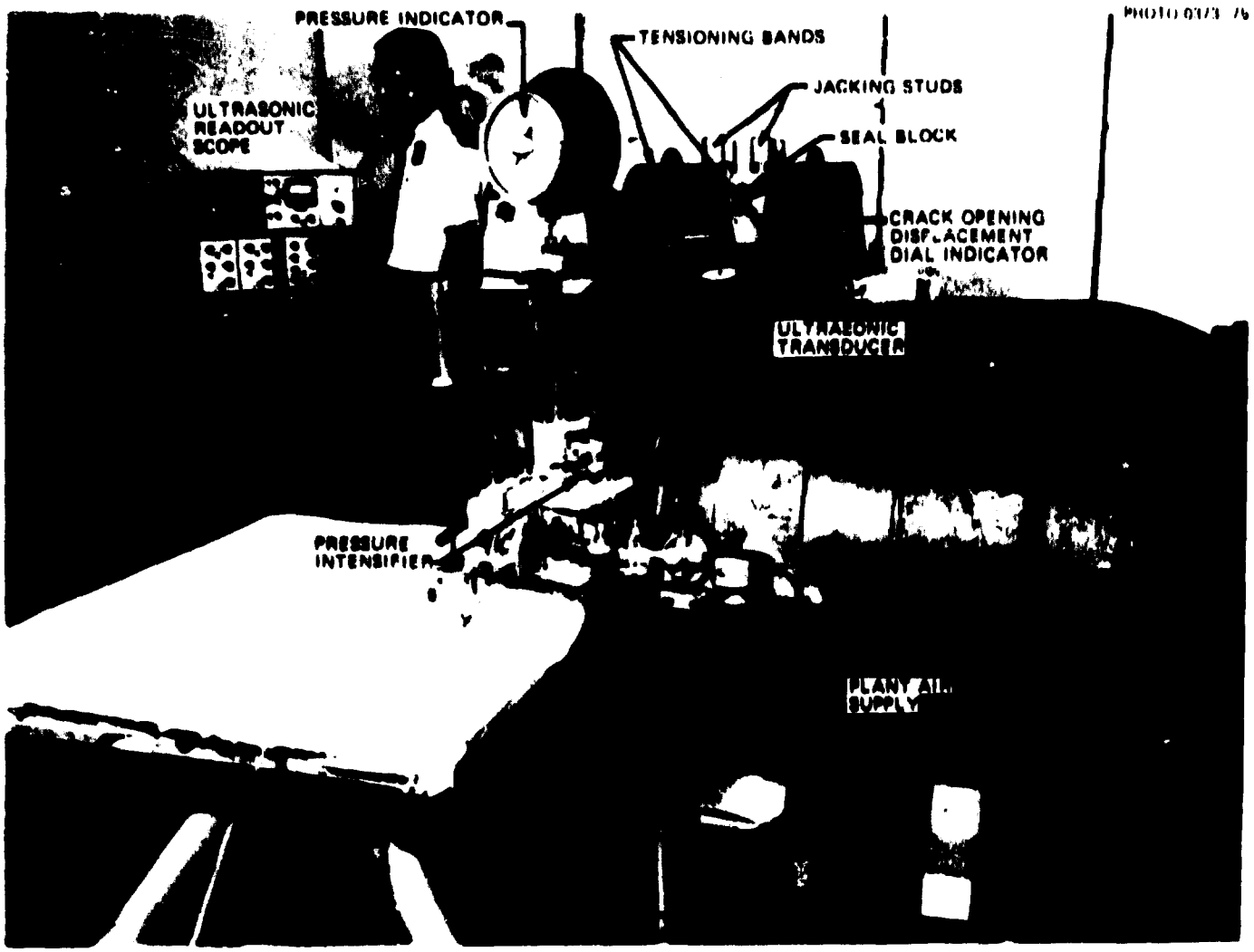

Fig. 2.5. Setup for monitoring crack growth on a vessel.

provided a single pressure pulse, at low cycling pressures, for each stroke of the intensifier piston. The pressure on the discharge of the intensifier was controlled by manually valving tubing volumes in or out as desired for startup and for compensating for crack growth. A "pump and dump" arrangement[4] was required to achieve high cycling pressures, in which case a cycle consisted of four pump strokes.

An ultrasonic transducer was placed on the outside surface abreast the flaw to monitor flaw growth. The transducer was adapted for the shear wave mode of transmission and could be precisely maneuvered for measurement as the crack grew. Crack opening displacement (COD) was measured on some of the flaws by utilizing a dial indicator to measure the spread of pins located 1 in. on either side of the flaw at a distance of $3/4$ in. above the flat on the vessel.

The procedure for growing an interior flaw on vessel V-6 presented considerable mechanical, safety, welding, detection, and pumping problems. Mockups were built and employed to test weld boss configurations, weld attachments, and ultrasonic depth testing techniques and to develop operational and test procedure standards for the work. Figure 2.6 shows the type of weld block and weld configuration used to fatigue flaw C of vessel V-6. A number of precautions were incorporated into the welding operation to assure safety.

Vessel entry by a welder required him to be fully clothed with a heat-resistant, flameproof suit and attached wristlets as shown in Fig. 2.7. Welder qualification certifications were held to demonstrate that all

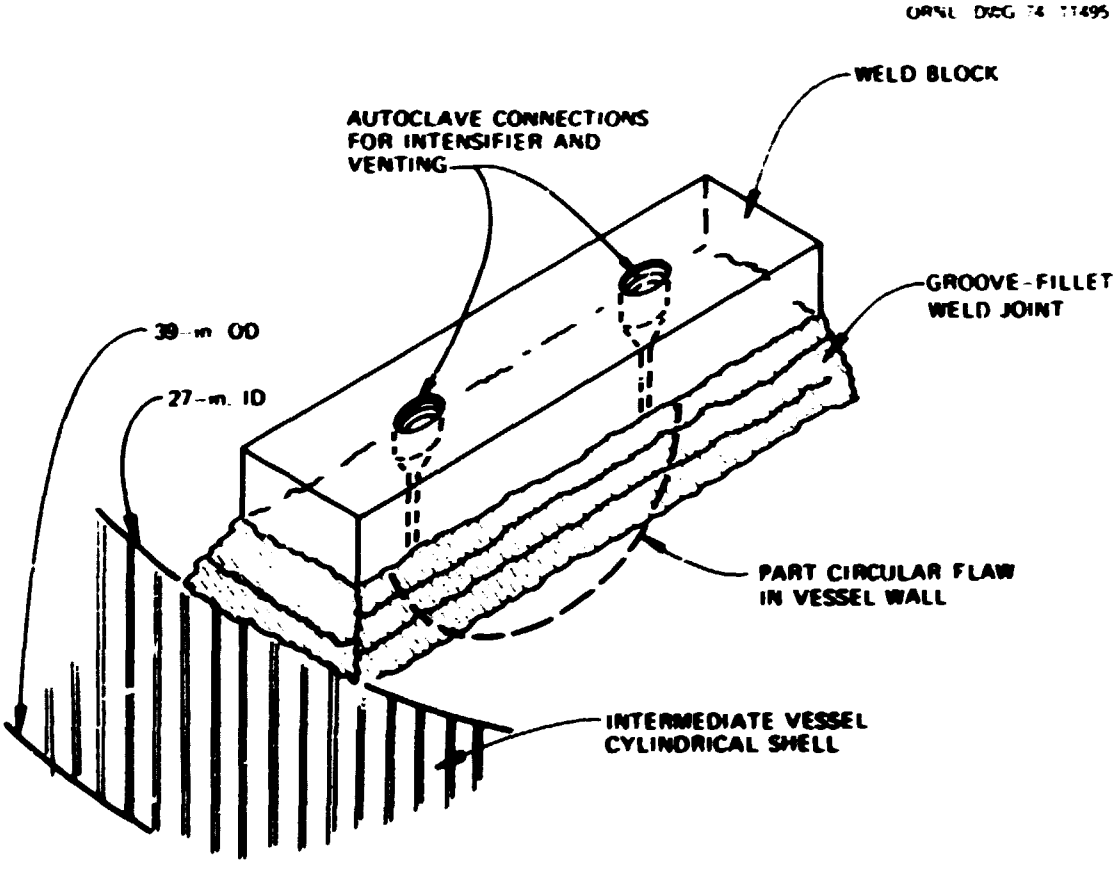

Fig. 2.6. Schematic of weld block used in fatiguing flaw C of intermediate vessel V-6.

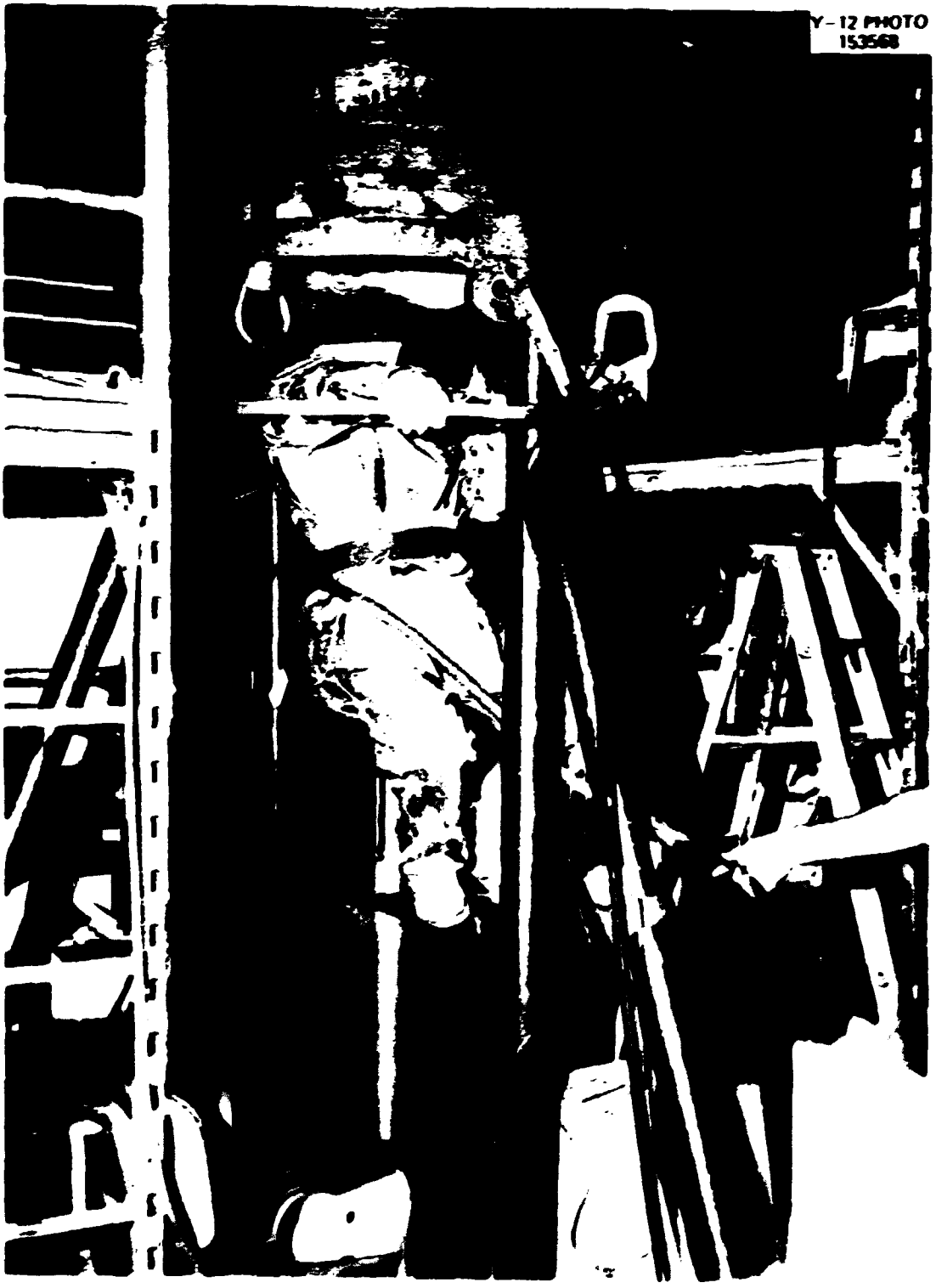

Fig. 2.7. Welder entering a typical intermediate test vessel (V-5).

requisite welding operations could be performed. The special precautions included: the elimination of any electrical shock hazards from the vessel, the supporting structure, and the protective clothing; dual cooling air supplies to the "air conditioned" protective clothing; two-way phone communications; continuous monitoring by personnel stationed there specifically for that purpose; protected insulated nylon rope for wristlets to retain the welder's hands vertically upward to permit assisted evacuation, if required; nonhazardous internal tank lighting; and controlled air circulation in the vessel to prevent asphyxiation.

Local preheating of the boss and the adjacent walls controlled boss and wall temperatures for the boss weld-on process within 350 to 550°F. Manual torch flame heating of the vessel exterior was used along with an insulation blanket liner within the vessel. The preheat was controlled and monitored via thermocouples. Postweld heat was maintained for 2 hr and gradually tapered down thereafter. An E 8018 filler rod was used for the root pass, which was made by gas-tungsten arc. The vessel was allowed to cool down for liquid dye-penetrant testing of the root pass before proceeding with renewed preheat, other gas-tungsten arc passes, and finally manual metal arc passes with E 8010 weld wire specially procured for this purpose. Interpass temperature was controlled to 500°F. The completed weld was again dye-penetrant checked.

After pressure cycling was complete, the weld block pad was scarfed from the vessel interior using oxyacetylene torch gouging. The flame-cut surface was kept a minimum of $\frac{1}{8}$ in. from the inside surface of the vessel. The remainder of the protruding metal was then removed by hand grinding to 250 in. rms minimum to have the finished surface conform within $\frac{1}{16}$ in. of true position of the inside surface.

Table 2.3 lists the data logged during the course of fatiguing each of the flaws. Although it was hoped that the COD measurement could provide an empirical basis for estimating flaw depth, the data obtained were of limited use because of malfunctions from friction and jamming of COD device parts. The ultrasonic measurement of the pretest flaw depth was therefore used as the basis for controlling the fatiguing operation.

Figures 2.8 to 2.10 show the locations, as-built machined dimensions, as-built fatigue crack dimensions of the flaws, and materials in which flaws resided for vessels V-3, V-4, and V-6, respectively. Figures 2.11 to 2.13 show impressions of the machined and fatigue-cracked profiles as determined after vessel failure for vessels V-3, V-4, and V-6, respectively. The deviations from the ideal geometry of a part-circular crack and the significant difference in behavior between fatiguing of base metal and weld metal are noteworthy observations shown by these figures.

Table 2.4 is a comparison of the estimated flaw dimensions based upon ultrasonics and surface indication with the actual flaw dimensions determined after failure. The significant departure from the target depth of 2.5 in. for vessels V-3 and V-4 and the lack of good correspondence between the estimated and actual flaw dimensions led to the conclusion that the standardized ultrasonic procedure was inadequate. Subsequently, on vessel V-6 more attention was paid to the character of the reflected ultrasonic pulses with respect to the motion of the crystal and with respect to the characteristics of the material in which the crack resided. Consequently, the estimates of flaw dimensions on vessel V-6 were significantly improved, but additional improvement was desired to increase the accuracy of pretest failure calculations.

Since the shear wave mode ultrasonic technique proved to be inadequate, Kinzdt and Baker investigated the application of signal modification in the base-line noise ahead of the reflected pulse from the flaw as a means of monitoring crack growth. Investigative mockup experiments proved sufficiently encouraging to incorporate this new approach in the monitoring of flaws B and C of vessel V-6 (see Table 2.3). The approach appeared to have sufficient merit to continue its development for future vessel testing.

Table 2.3. Flaw growth log for intermediate vessels V-3, V-4, and V-6

Vessel and flaw designation	Machined flaw size[a] (in.) a	2b	Peak pressure at indicated number of cycles (psig)	Number of cycles accumulated	Crack opening displacement (in.) Pressure gage On	Off[b]	Ultrasonic technique	Depth estimate by ultrasonics (in.)	Comments
V-3	1.84	7.85	15,000	0	0.0045				
			15,000	1,410	0.0055	0.0055			
			16,000	3,190	0.0048	0.0056			
			16,000	4,083		0.0056			
			16,000	4,302		0.0056			
			16,500	8,500					Cycle counter malfunction basis of cooling rate
			16,500	48,950	0.0035	0.004			
			16,500	50,000	0.0036				
			16,500	52,847					
			15,000	87,574			Shear wave	2.55	Dial indicator malfunction flaw growth of 0.20 in. machined flaw
V-4									
A	1.96	7 7/8	15,000	0		0.0038			
			15,000	27,063		0.0046			
			11,500	58,096					
				66,731			Shear wave	2.60	Flaw growth of 0.11 and ends of machined flaw
B	1.98	8.05	14,500	0	0.0006	0.0006			
			14,500	2,150					Dial indicator malfunction
			16,000	24,000	0.0018	0.0026			
			15,000	36,850	0.0018	0.0016			Dial indicator malfunction
			14,000	45,200	0.0015	0.0022			
			11,000	66,500	0.0012	0.0021			
				106,000			Shear wave	2.60	
V-6									
A	1.25	5.08		0					
				24,[illegible]					Malfunction caused shutd manually, functioned n
				51,867			Shear wave	1.87 ± 0.02	
B	1.31	5.19		0					
			14,500	58,764			Shear wave	1.73 ± 0.02	Liquid dye-penetrant co ultrasonic technique b noise monitoring durin confirmed the depth
C	1.21	5.30	28,000	0			Base-line noise monitoring		
				29,000				1.26	
				49,000				1.69	
				63,164				1.77 ± 0.02	

[a]See Figs. 2.6 to 2.8 for location and dimensions. The symbol a is flaw depth and 2b is flaw length.

[b]Due to volume increase with pressure gage valved into system, the pressure and consequently the COD decreas

BLANK PAGE

Flaw growth log for intermediate vessels V-3, V-5, and V-6

Crack opening displacement		Ultrasonic technique	Depth estimate by ultrasonics (in.)	Comments
Pressure gage				
On	Off[b]			
0.0045				
0.0045	0.0055			
0.0048	0.0056			
	0.0056			
	0.0056			
				Cycle counter malfunction, cycles estimated on basis of cycling rate
0.0035	0.004			
0.0036				
		Shear wave	2.55	Dial indicator malfunction at end of cycling; flaw growth of 0.20 in. visible on ends of machined flaw
	0.0038			
	0.0046			
		Shear wave	2.60	Flaw growth of 0.11 and 0.16 in. visible on ends of machined flaw
0.0006	0.0006			
				Dial indicator malfunction
0.0018	0.0026			
0.0018	0.0016			Dial indicator malfunction
0.0015	0.0022			
0.0012	0.0021			
		Shear wave	2.60	
				Malfunction caused shutdown of pump; restarted manually, functioned normally thereafter
		Shear wave	1.87 ± 0.02	
		Shear wave	1.73 ± 0.02	Liquid dye-penetrant confirmed crack. New ultrasonic technique being developed; base-line noise monitoring during 3342 additional cycles confirmed the depth
		Base-line noise monitoring		
			1.26	
			1.69	
			1.77 ± 0.02	

nd dimensions. The symbol a is flaw depth and 2b is flaw length.

e gage valved into system, the pressure and consequently the COD decrease.

2

ORNL DWG 75-3162

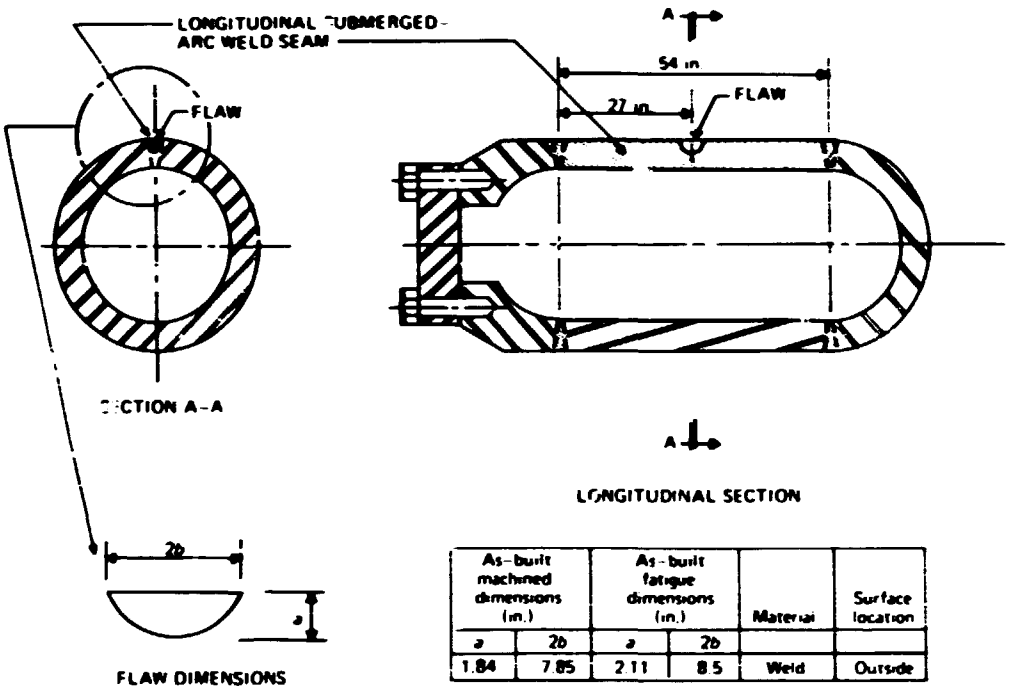

As-built machined dimensions (in.)		As-built fatigue dimensions (in.)		Material	Surface location
a	2b	a	2b		
1.84	7.85	2.11	8.5	Weld	Outside

Fig. 2.8. Sketch showing flaw locations and as-built flaw size for intermediate test vessel V-3.

ORNL-DWG 75-3161R

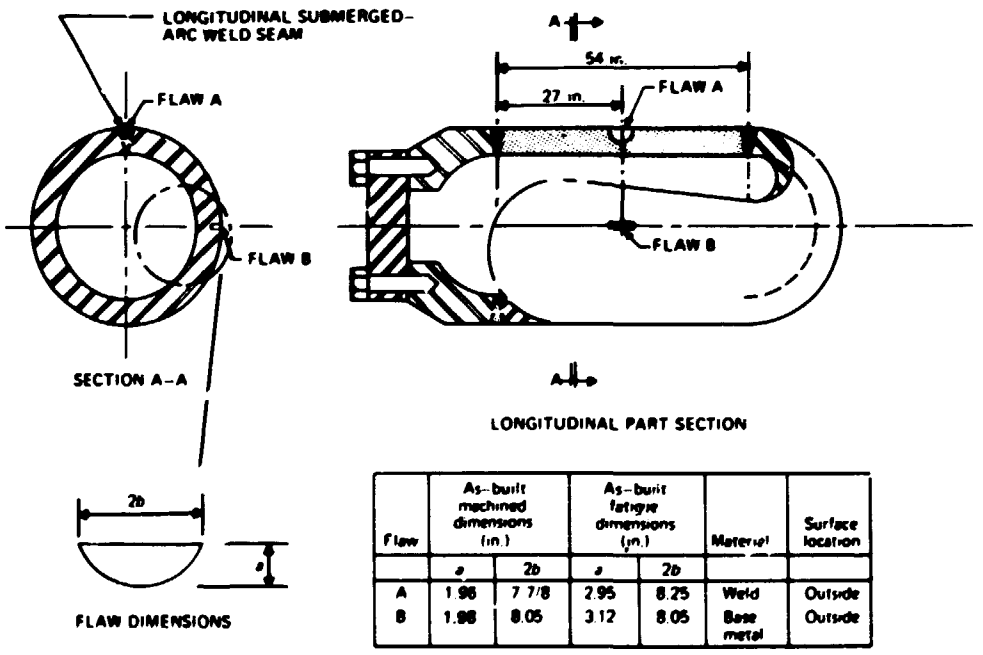

Flaw	As-built machined dimensions (in.)		As-built fatigue dimensions (in.)		Material	Surface location
	a	2b	a	2b		
A	1.96	7 7/8	2.95	8.25	Weld	Outside
B	1.88	8.05	3.12	8.05	Base metal	Outside

Fig. 2.9. Sketch showing flaw locations and as-built flaw size for intermediate test vessel V-4.

ORNL DWG 74 5352R

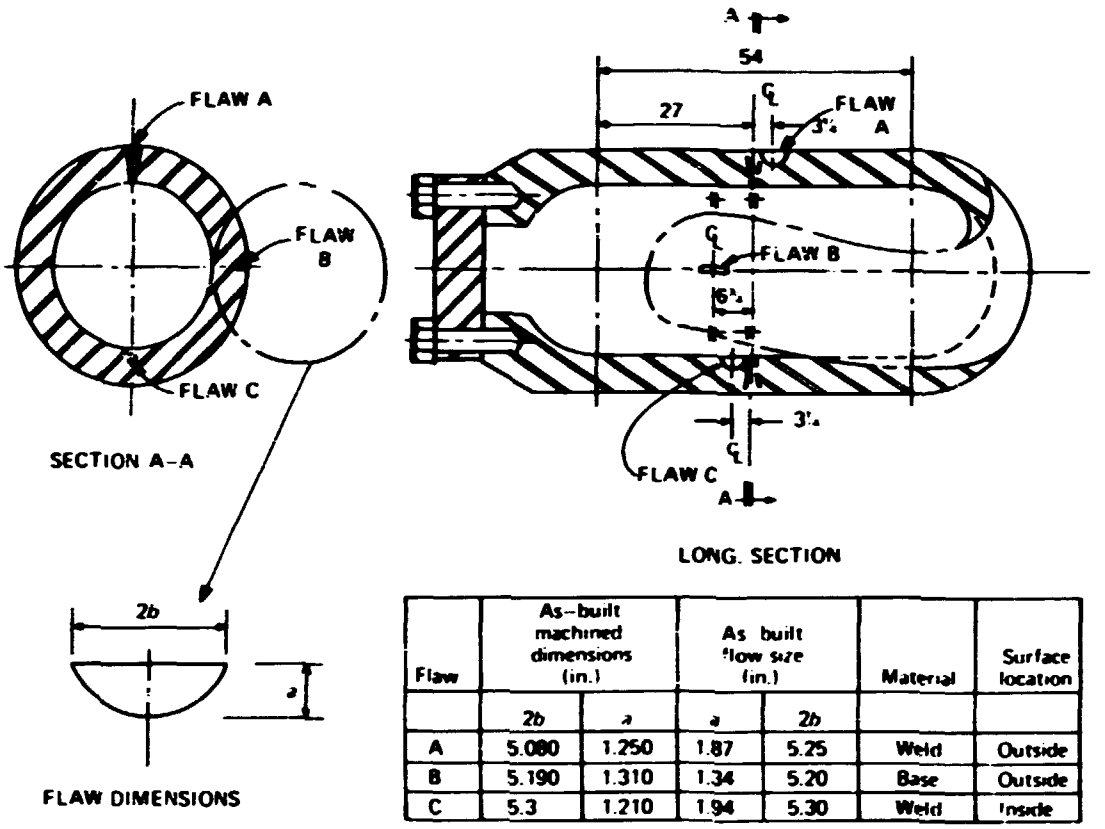

Flaw	As-built machined dimensions (in.)		As built flaw size (in.)		Material	Surface location
	2b	a	a	2b		
A	5.080	1.250	1.87	5.25	Weld	Outside
B	5.190	1.310	1.34	5.20	Base	Outside
C	5.3	1.210	1.94	5.30	Weld	Inside

Fig. 2.10. Sketch showing flaw locations and as-built flaw size for intermediate test vessel V-6.

ORNL DWG 74-11814

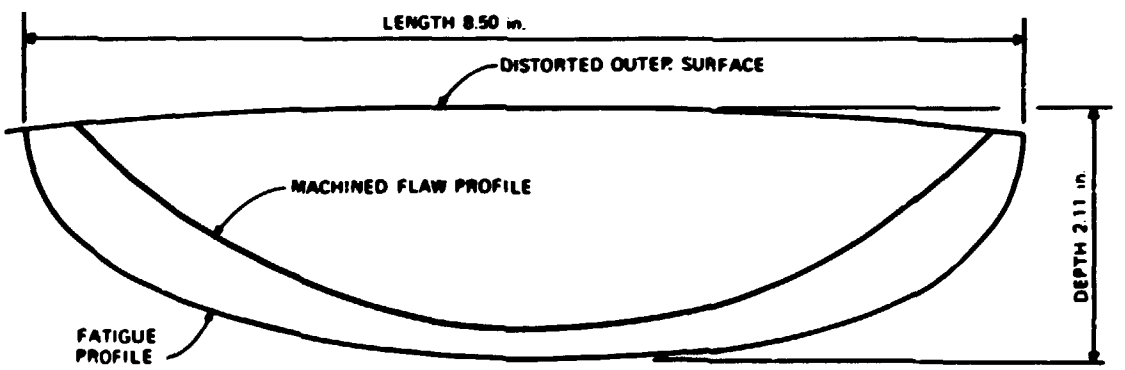

Fig. 2.11. Intermediate vessel V-3 flaw profile determined after vessel failure.

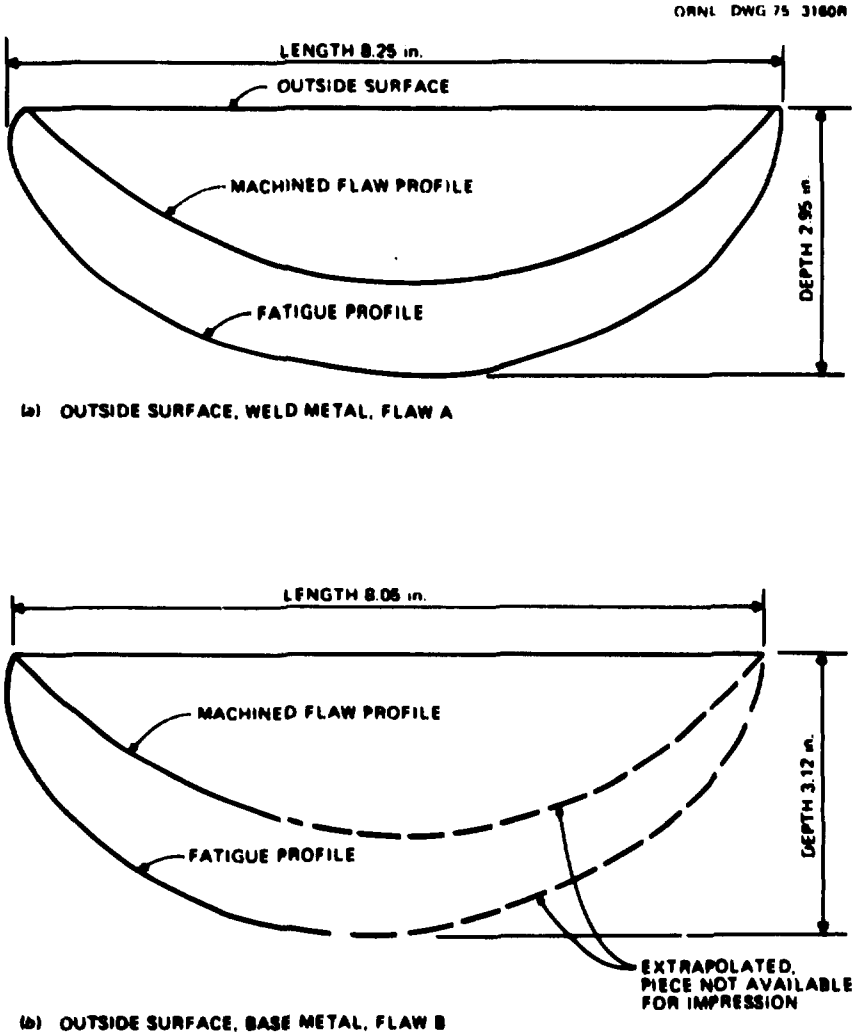

Fig. 2.12. Intermediate vessel V-4 flaw profiles determined after vessel failure.

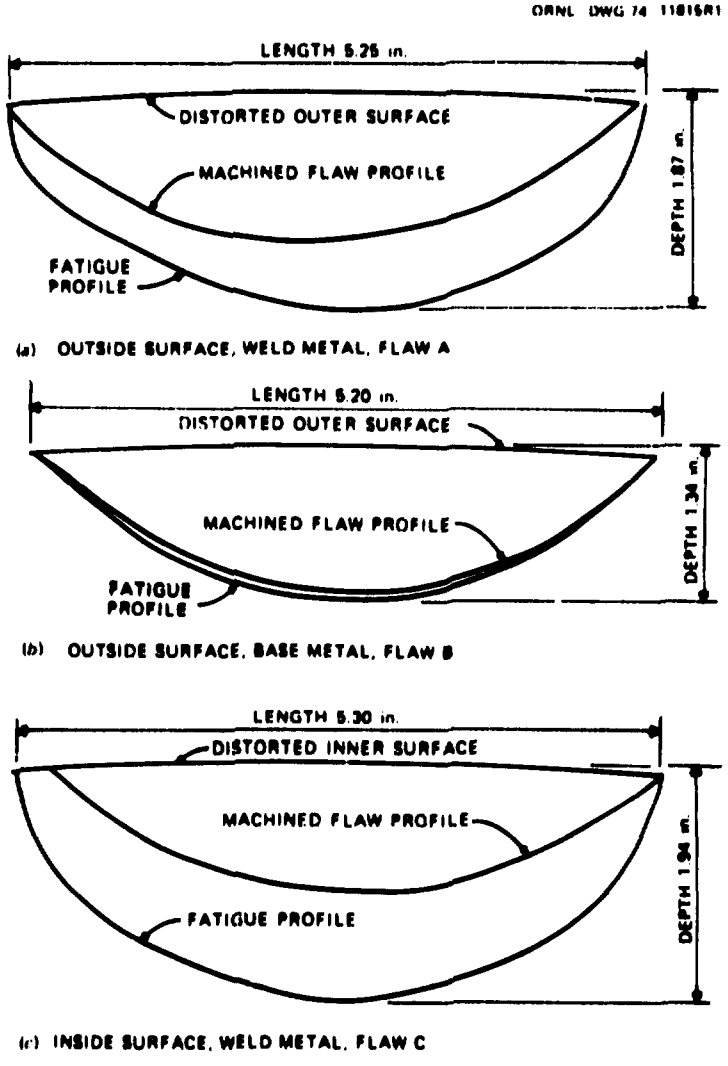

Fig. 2.13. Intermediate vessel V-6 flaw profiles determined after vessel failure.

Table 2.4. Comparison of estimated and actual flaw sizes[a] in vessel V-6 (see Figs. 2.6 to 2.8)

Vessel	Flaw	Flaw location	Estimated flaw size (in.)		Actual flaw size (in.)	
			a	2b	a	2b
V-3		Outside surface, weld metal	2.55	8.25	2.11	8.5
V-4	A	Outside surface, weld metal	2.60	8.25	2.95	8.25
	B	Outside surface, base metal	2.67	8.05	3.12	8.05
V-6	A	Outside surface, weld metal	1.87	5.08	1.87	5.25
	B	Outside surface, base metal	1.73	5.19	1.38	5.20
	C	Inside surface, weld metal	1.77	5.3	1.94	5.36

[a] The symbol a is flaw depth and 2b is flaw length.

Materials Characterization

Prolongations of intermediate vessels V-3, V-4, and V-6 were studied by Stelzman[5,6] to obtain tensile, Charpy-V impact, and static lower-bound fracture toughness data. Similarly, the prolongations were studied by Mager et al. of Westinghouse Electric Corp.[7,8] to obtain static fracture toughness data. These data were used to set the fracture criteria and to predict failure as was done for vessels V-1 and V-2 prior to rupturing the vessel.

Tensile and Charpy V-notch specimens were located in the material of interest (material in which the flaws resided, weld material, and base material) typically as shown in Fig. 2.14. Compact-tension specimens were located in the prolongations as shown in Figs. 2.15 to 2.18. Complete tabulations of tensile, Charpy-V impact and fracture toughness data are given in Appendix A.

Tensile properties

The tensile specimen results were obtained from circumferentially (C) oriented 0.178-in.-gage-diam tensile specimens at a strain rate of 0.016 min^{-1}. Yield and ultimate stress results from V-4 base metal at 75°F were identical to those of the V-1 base metal,[1] both in magnitude and in variation through the vessel wall. Tensile results from the weld metal indicated a somewhat different through-the-wall distribution from the base metal. Figure 2.19 shows strength values obtained from V-3 weld metal. The outer portion of the weld was deposited first and the inner portion last. The region where the inner and outer weld passes abutted was determined by surface etching a cross section of the weld to bring out the weld passes. This region is noted in Fig. 2.19. It is evident that the strength values from the outer half of the weld are considerably lower than the base metal values whereas the strength values from the inner half of the weld are comparable with the base metal results. It was initially thought that the repairs to the weld may have been responsible for this difference, but the room-temperature tensile results from V-4 weld metal (Fig. 2.20) show the same type of behavior. Figure 2.21 shows the tensile results from C-oriented subsized

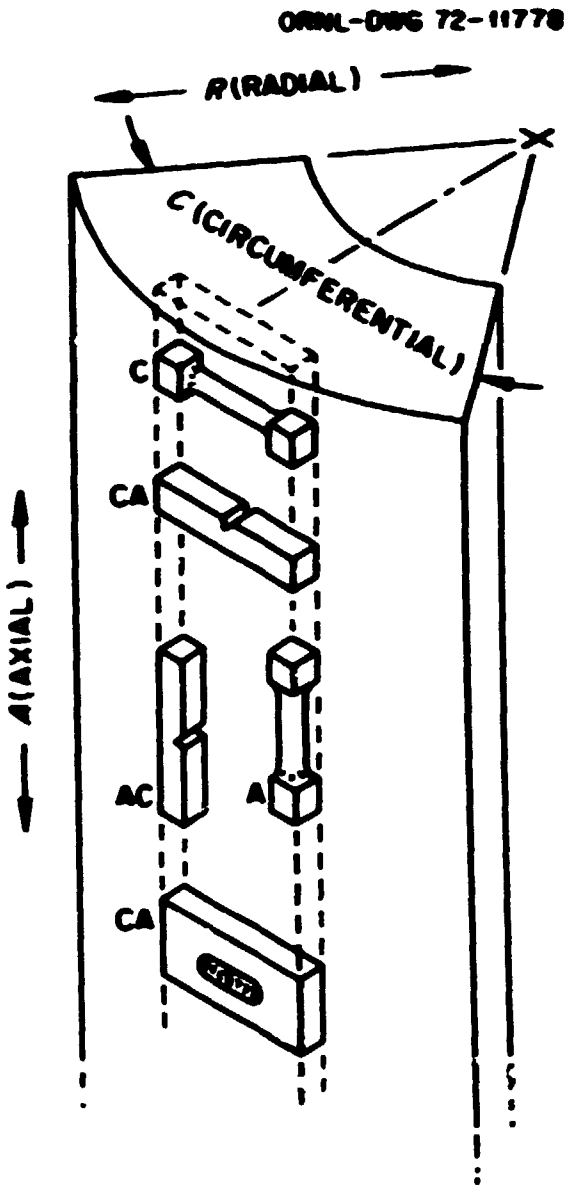

Fig. 2.14. Specimen orientation notation for HSST intermediate vessel materials showing tensile, Charpy V-notch, and drop-weight specimens.

specimens of both submerged-arc weld metal and base metal taken from the V-6 prolongation. The strength distributions through the thickness of the weld and base metals are similar to those for V-4. A comparison of yield and ultimate strengths for V-4 at 74°F and V-6 at 300°F indicates that the weld strength values show little difference and that the V-6 base metal values are about 8% lower due to the higher test temperature. The region where the inner and outer weld passes abut has been indicated in Fig. 2.21 to locate and orient the strength discontinuity. Similar discontinuities were noted in V-3 and V-4 welds. The increase in strengths near this zone is attributed to an increase in the carbon content of the weld deposit from the base metal ligament used as backup for the root pass of the submerged-arc weld. A detailed chemical

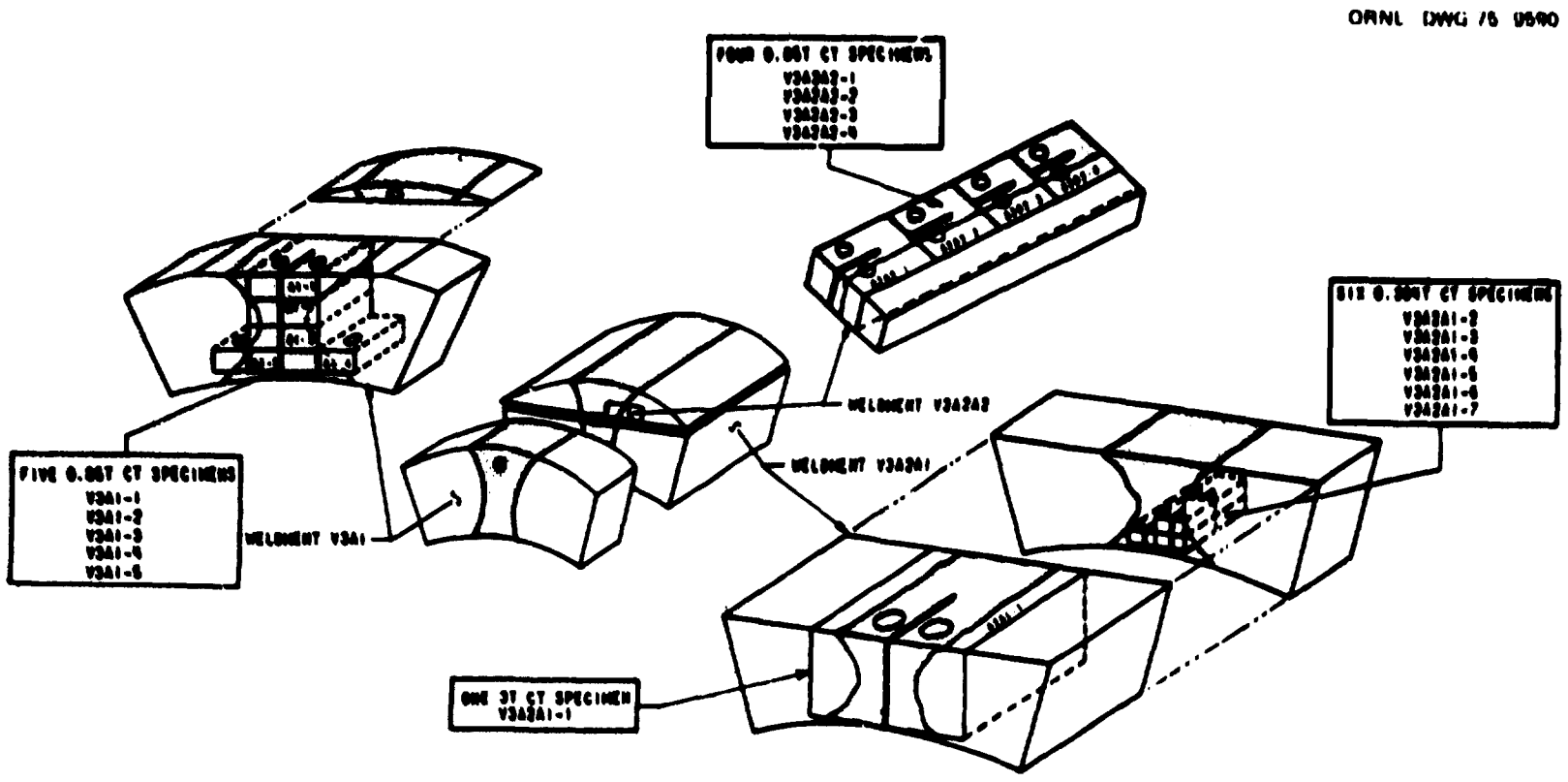

Fig. 2.15. Machining of fracture toughness specimens from HSST intermediate pressure vessel V-3 weldment.

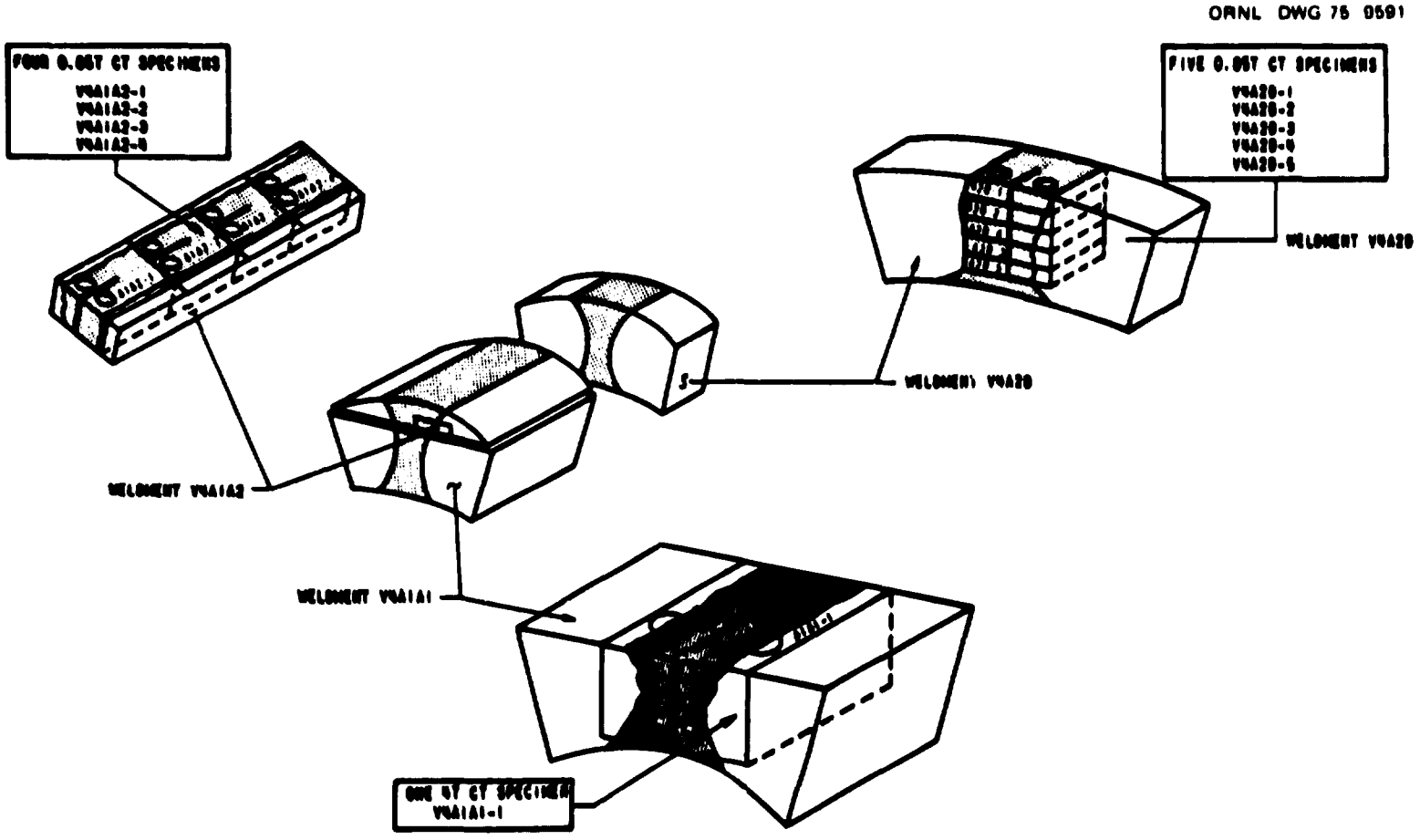

Fig. 2.16. Machining of fracture toughness specimens from INEL intermediate pressure vessel V-9 weldment.

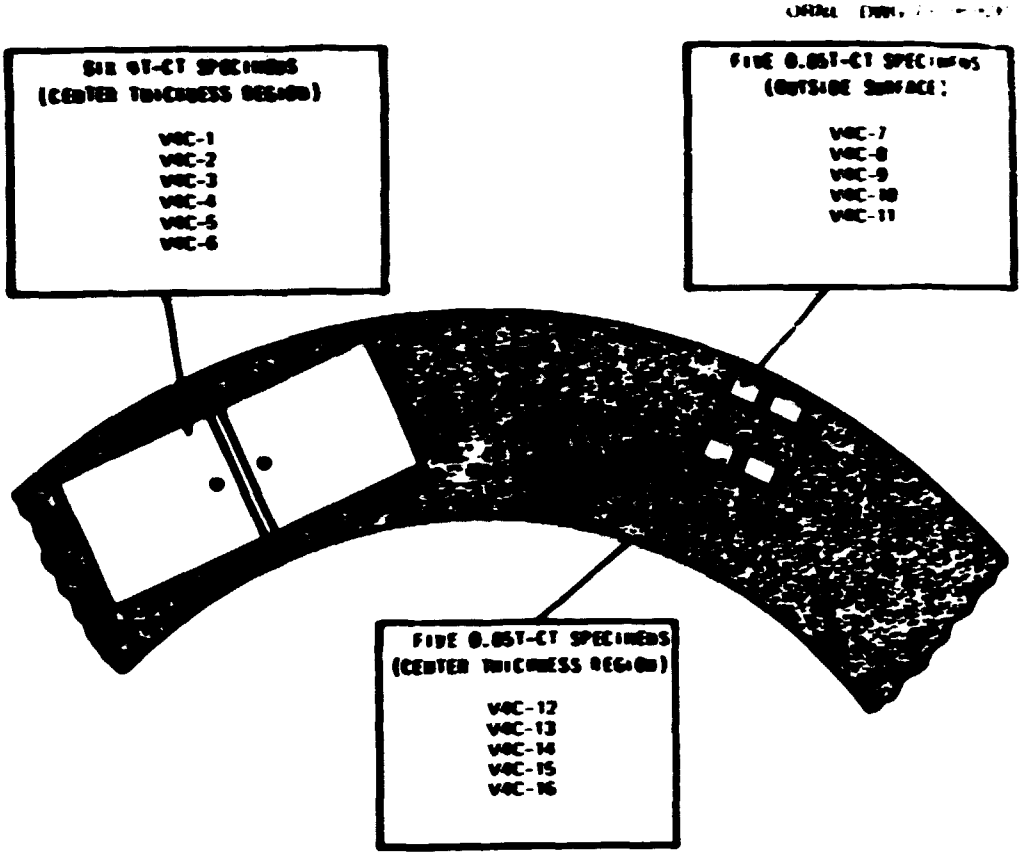

Fig. 2.17. Machining of fracture toughness specimens for ... HSST intermediate pressure vessel V-6 base metal.

analysis and hardness test in a similar region in an identical weld (HSST 51B) by Canonico[7] support this explanation. The changes in the reductions in area and elongations in this zone are not as dramatic and tend to be obscured by the scatter of the data.

Charpy V-notch impact data

Standard Charpy V-notch impact data obtained from ¾T CA-oriented specimens from V-6 base metal, shown in Fig. 2.22, agree with those obtained from ¾T and ⅝T specimens of the same orientation from V-1 base metal when the normal scatter expected of Charpy energy data is considered.[1] Figure 2.23 shows the fracture energy vs test temperature for WL-oriented specimens from the submerged-arc weld in the prolongation of vessel V-6. Because of the limited amount of material for specimens, no Charpy V-notch impact data were obtained on vessels V-3 and V-6. Instead, the V-6 data shown in Figs. 2.22 and 2.23 were compared with the vendor data on vessels V-3, V-4, and V-6 reported earlier in this chapter.

Fracture toughness

Static lower-bound fracture toughness data, K_{Ia}, from CA-oriented precracked Charpy V-notch specimens were obtained by Stelzman for the three vessels at a bending rate of 2.1 in./min. Results from

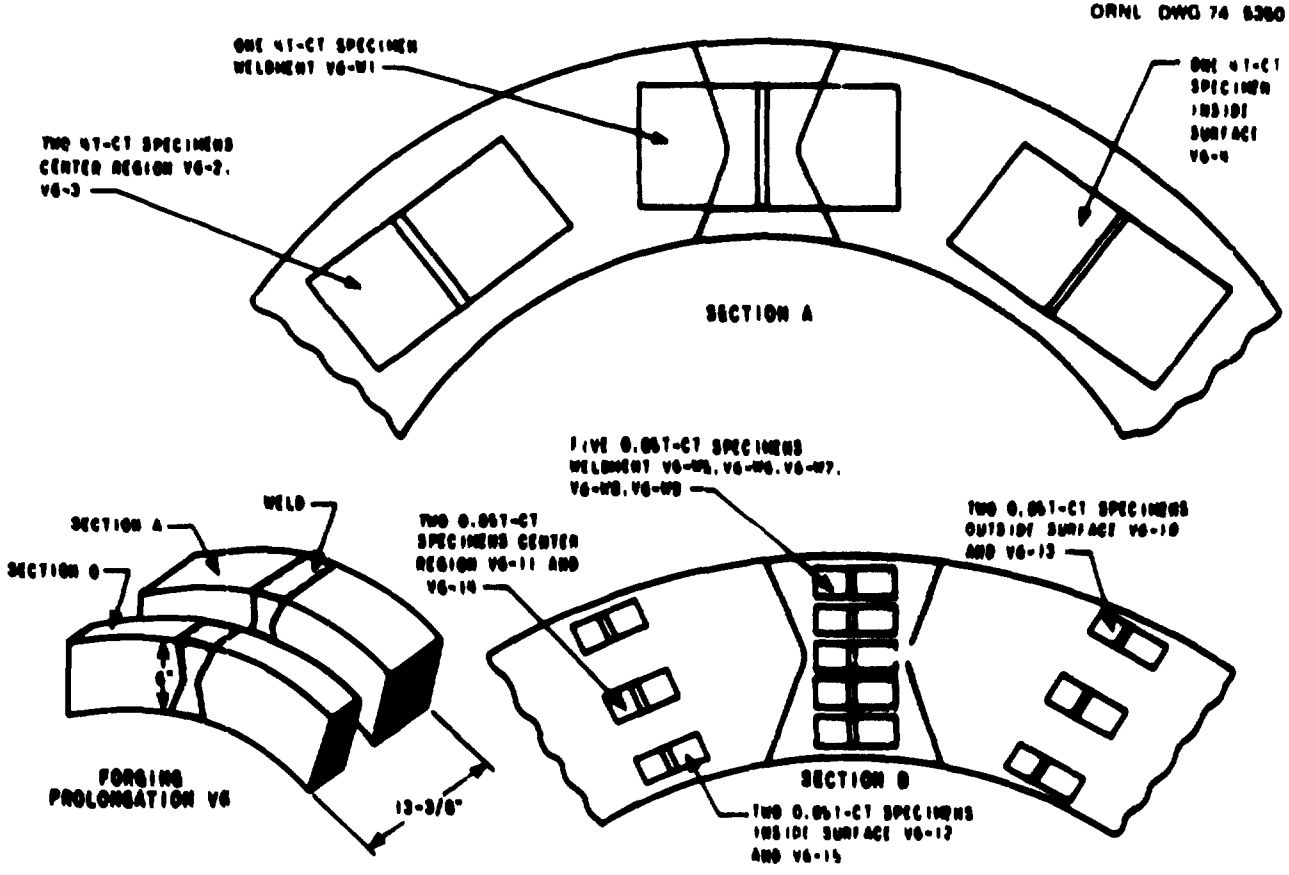

Fig. 2.18. Machining of fracture toughness specimens from HSST vessel V-6 prolongation.

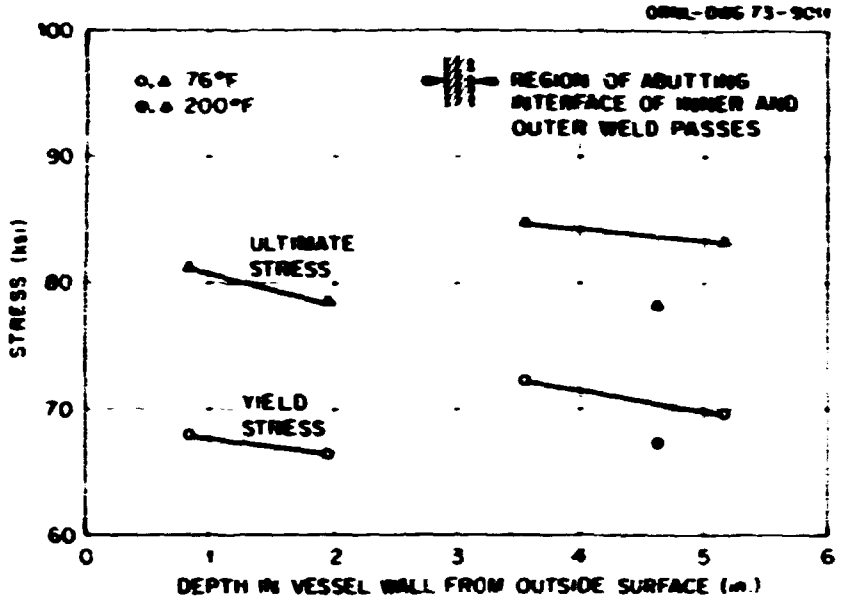

Fig. 2.19. Tensile properties obtained from intermediate vessel V-3 using C-oriented subsized tensile specimens from a 6-in.-thick weld in ASTM A508 class 2 forging steel.

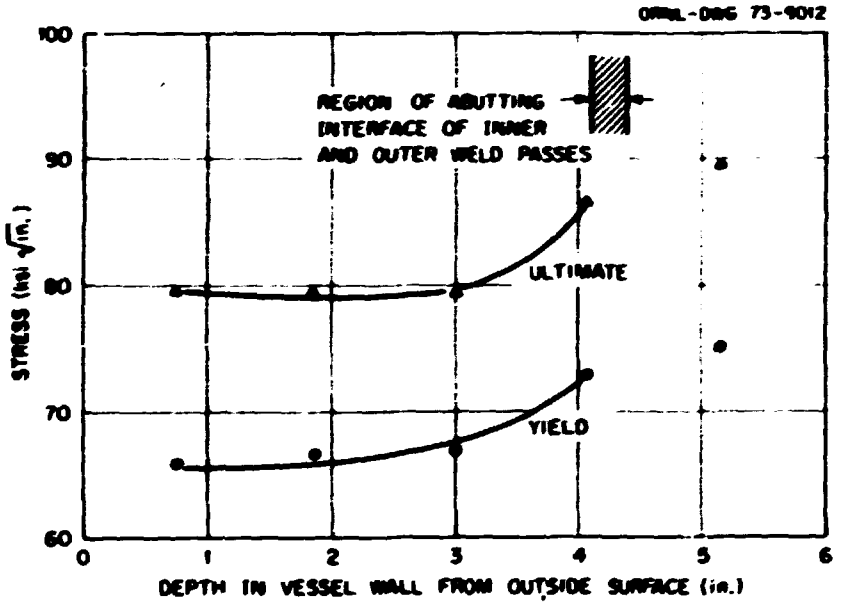

Fig. 2.20. Tensile properties obtained from intermediate vessel V-4 using C-oriented subsized tensile specimens from a 6-in.-thick weld in ASTM A508 class 2 forging steel.

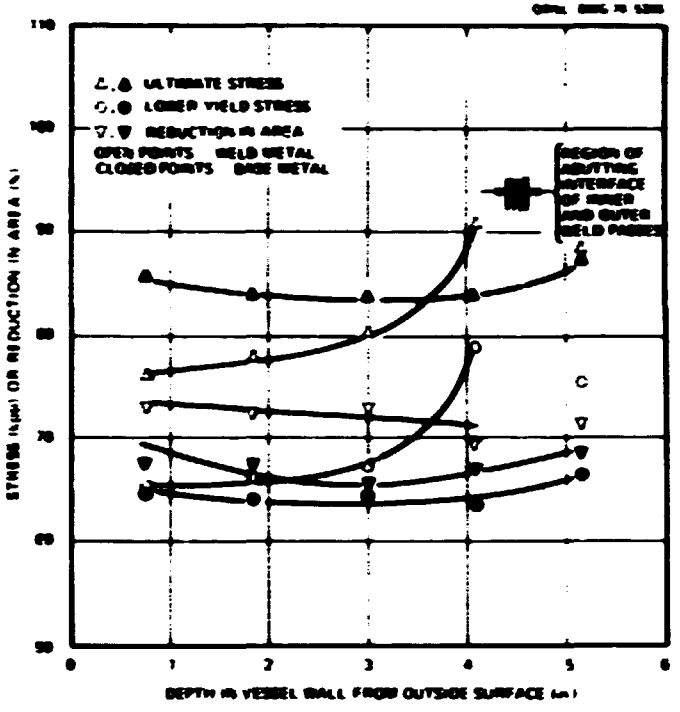

Fig. 2.21. Tensile properties of intermediate vessel V-6 at 200°F using C-oriented subsized tensile specimens from 6-in.-thick weld and base metal of ASTM A508 class 2 forging steel at a strain rate of 0.016 min^{-1}.

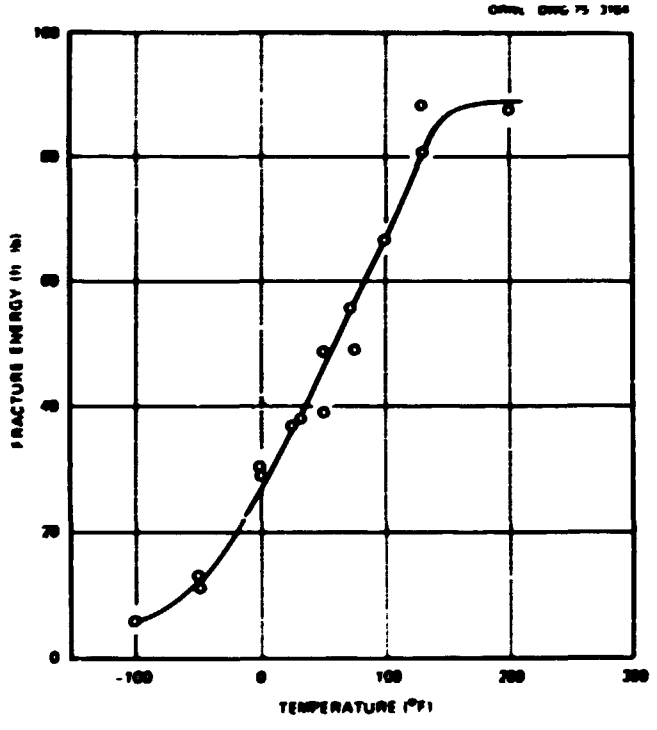

Fig. 2.22. Charpy V-notch impact results from intermediate vessel V-4, ¼ thickness level, CA orientation, 6-in.-thick ASTM A508 class 2 forging steel.

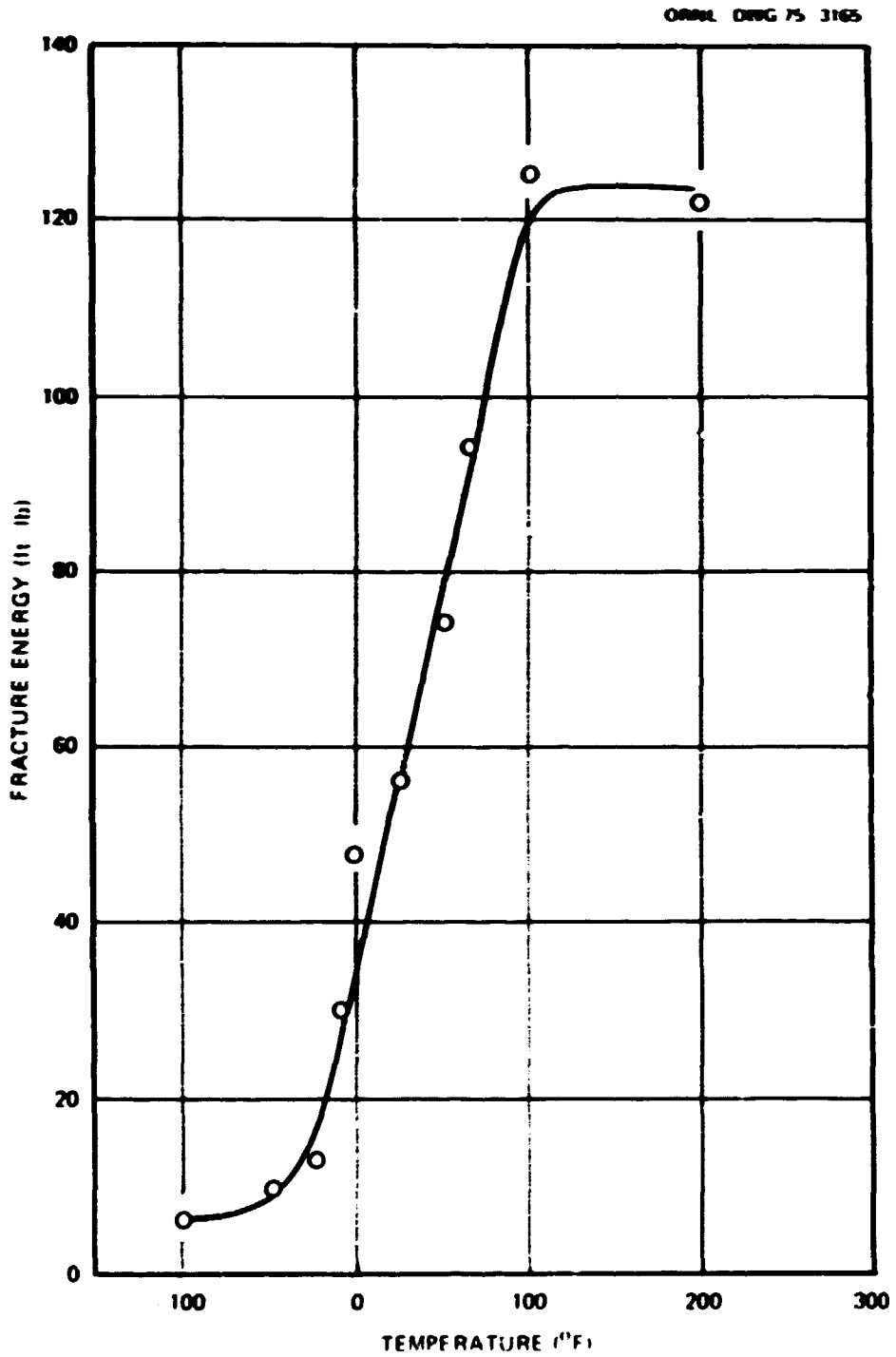

Fig. 2.23. Charpy V-notch impact results from intermediate vessel V-4, WL orientation, 6-in.-thick submerged-arc weld in ASTM A508 class 2 forging steel.

the base metal of V-4 and V-6 are shown in Figs. 2.24 and 2.25, and the results from V-3, V-4, and V-6 weld metal are shown in Figs. 2.26 to 2.29. In some instances a minimum of specimens were available for test, and in others a particular temperature or depth range was chosen for principal investigation. Mager et al.* obtained fracture toughness data from the base metal of prolongations of vessels V-4 and V-6 and from the weld metal of prolongations of vessels V-3, V-4, and V-6. Their base metal data for vessel V-4 are given in Fig. 2.30, and their weld metal data for vessels V-3 and V-4 are given in Figs. 2.31 and 2.32. All the specimens (both those of Stelzman and Mager et al.) were fatigue precracked according to the methods specified in Ref. 10. All lower-bound fracture toughness results were interpreted by means of the equivalent-energy concept.[11-14]

Stelzman's measurements of $K_{Ic,d}$ for V-4 base metal, shown in Fig. 2.24, indicate the same fracture toughness variations with temperature as the V-1 and V-2 data (Fig. 4.11, Ref. 1). Likewise, his data for V-6, shown in Fig. 2.25, do not differ significantly from those of V-4. A comparison of through-the-thickness welds indicates that slightly higher $K_{Ic,d}$ values occur at the outer surface.

The variation of $K_{Ic,d}$ with temperature and depth for submerged-arc weld metal obtained by Stelzman from V-3, V-4, and V-6 is shown in Figs. 2.26 to 2.29. The data at −50°F in Fig. 2.26 suggests that V-3 may have higher toughness values at lower temperatures than V-4; however, additional $K_{Ic,d}$ data from V-4 (Fig. 2.27) at −50°F could result in both welds exhibiting a similar behavior, that is, a decrease in $K_{Ic,d}$ below 32°F and the same toughness plateau above 32°F. Figure 2.28 shows the V-4 data from Fig. 2.27 plotted to show the through-the-weld variations of $K_{Ic,d}$ at several temperatures. The toughness values are fairly constant through the weld between 0 and 200°F, and insufficient data below 0°F bar any conclusion other than $K_{Ic,d}$ values are lower. Also, a decrease in toughness near the interface between the inner and outer welds is indicated. Higher $K_{Ic,d}$ values near the surfaces of the weld were not in evidence. The static fracture toughness data for the V-6 weld metal from CA-oriented precracked Charpy V-notch specimens are shown in Fig. 2.29. The upper shelf is adequately defined at approximately 145 ksi $\sqrt{in.}$, which is slightly lower than the V-3 and V-4 levels. A study of through-the-thickness welds showed that $K_{Ic,d}$ was about 10 ksi $\sqrt{in.}$ higher for the central ($^1/_3$ to $^2/_3$T) region at test temperature levels of 74, 150, and 200°F. At 0 and −50°F, $K_{Ic,d}$ decreased considerably in the region of inner and outer weld pass abutment.

Although the data from the tests by Mager et al. are comparable with data previously obtained for steels of this type, there are some differences. The tests on vessel V-4 indicate that the toughness of the weldment material is less than that of the base metal, while the converse has generally been true in the past. Comparison of the weldment data for vessels V-3 and V-4 with the base metal data[1] for vessels V-1 and V-2 indicates significantly more scatter in weldment than in base metal. The toughness of the weldment material from vessel V-6 is comparable to data obtained in the past and is considerably higher than that in vessel V-3. The fracture toughness through the thickness (inside surface, mid-thickness, and outside surface) of vessel V-6 indicates that the material appears to be homogeneous at 200°F.

Investigations of Heat-Affected Zone (HAZ)

A weld segment from the prolongation of HSST intermediate test vessel V-4 was metallographically examined by the Staatliche Materialprufungsanstalt (MPA) in Stuttgart, by Westinghouse Research Laboratories in Europe (WRLE), and by ORNL. A large number of weldments of 22 Ni Mo Cr 37 steel (German designation for a steel similar in composition to ASTM A508 class 2) were also examined by MPA to attempt to establish qualification standards for the German Reactor Safety Board to impose on nuclear

*Work performed by Westinghouse Electric Corporation for the HSST Program under Union Carbide Corporation Nuclear Division Subcontract No. 3196.

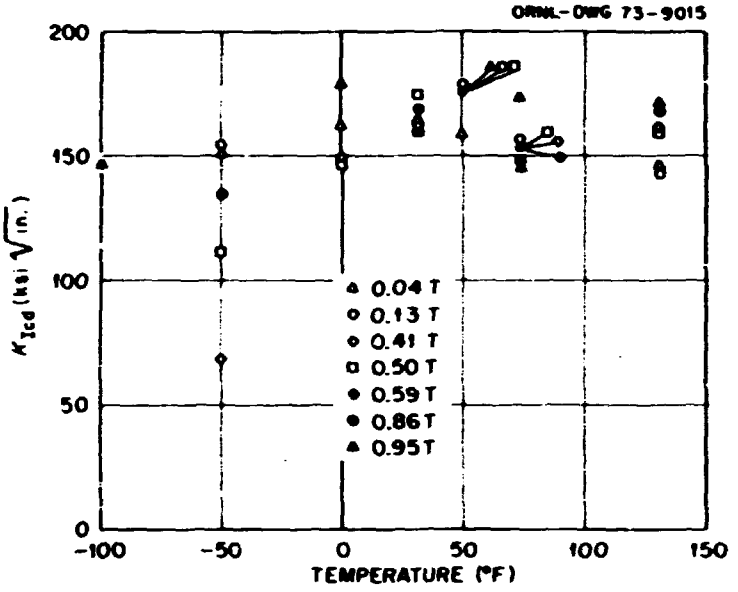

Fig. 2.24. Lower-bound fracture toughness values obtained from intermediate vessel V-4 using CA-oriented precracked Charpy-V specimens from 6-in.-thick ASTM A508 class 2 forging steel.

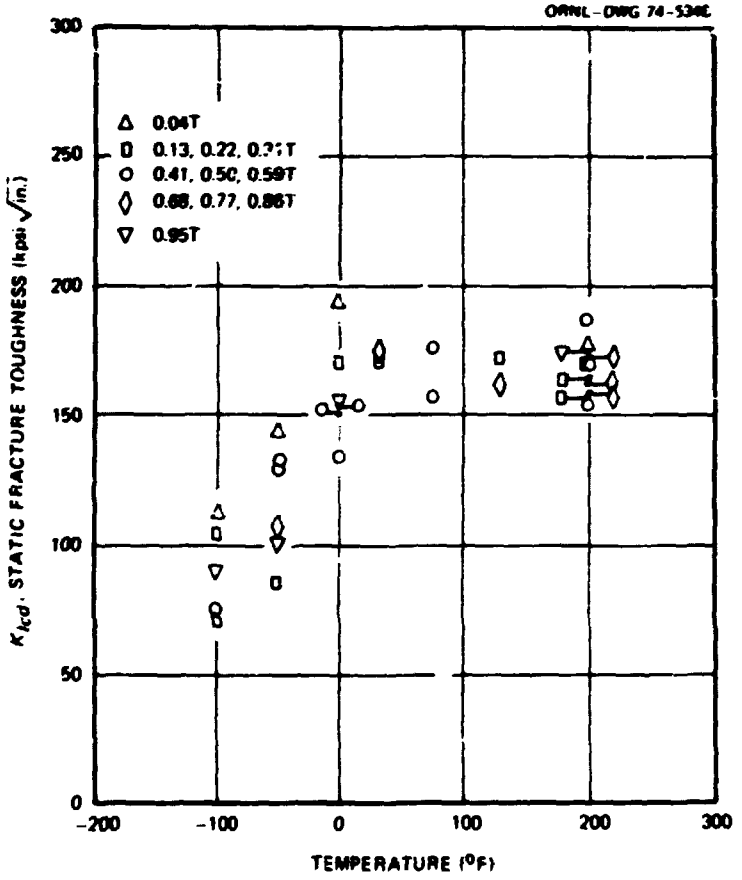

Fig. 2.25. Lower-bound fracture toughness values obtained from intermediate vessel V-6 using CA-oriented precracked Charpy V-notch specimens from 6-in.-thick ASTM A508 class 2 forging steel.

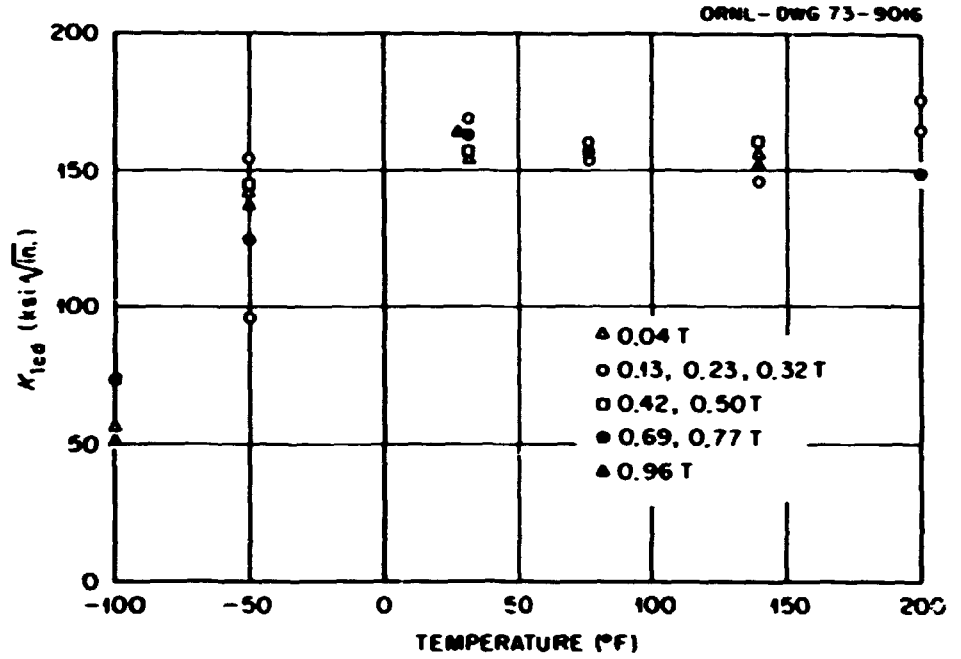

Fig. 2.26. Lower-bound fracture toughness values obtained from intermediate vessel V-3 using CA-oriented precracked Charpy-V specimens from a 6-in.-thick weld in ASTM A508 class 2 forging steel.

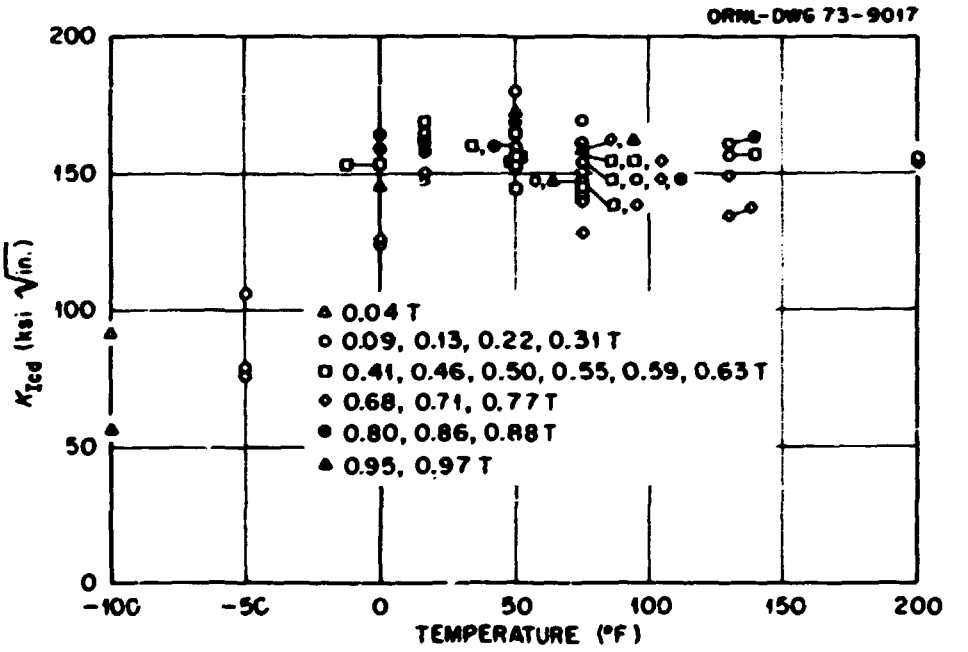

Fig. 2.27. Lower-bound fracture toughness values obtained from intermediate vessel V-4 using CA-oriented precracked Charpy-V specimens from a 6-in.-thick weld in ASTM A508 class 2 forging steel.

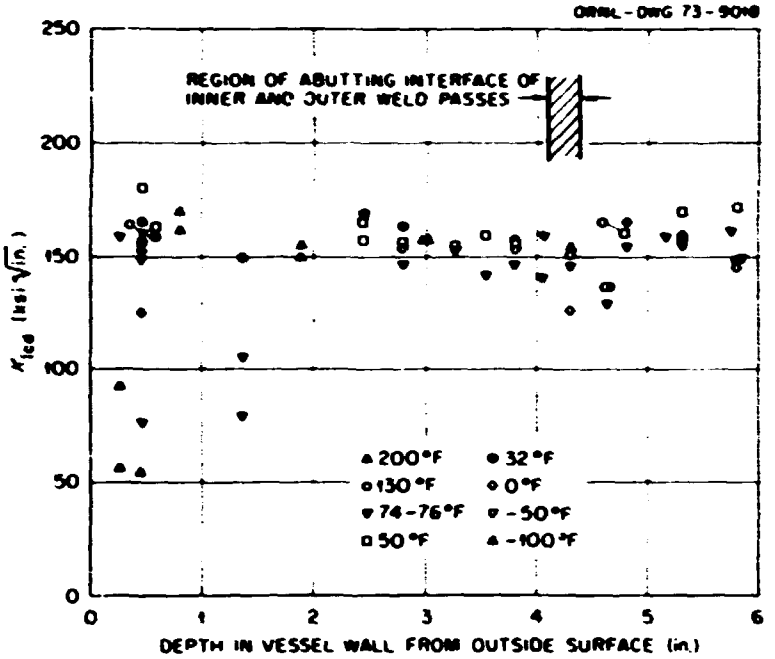

Fig. 2.28. *Lower-bound fracture toughness values obtained from intermediate vessel V-4 using CA-oriented precracked* Charpy-V specimens from a 6-in.-thick weld in ASTM A508 class 2 forging steel.

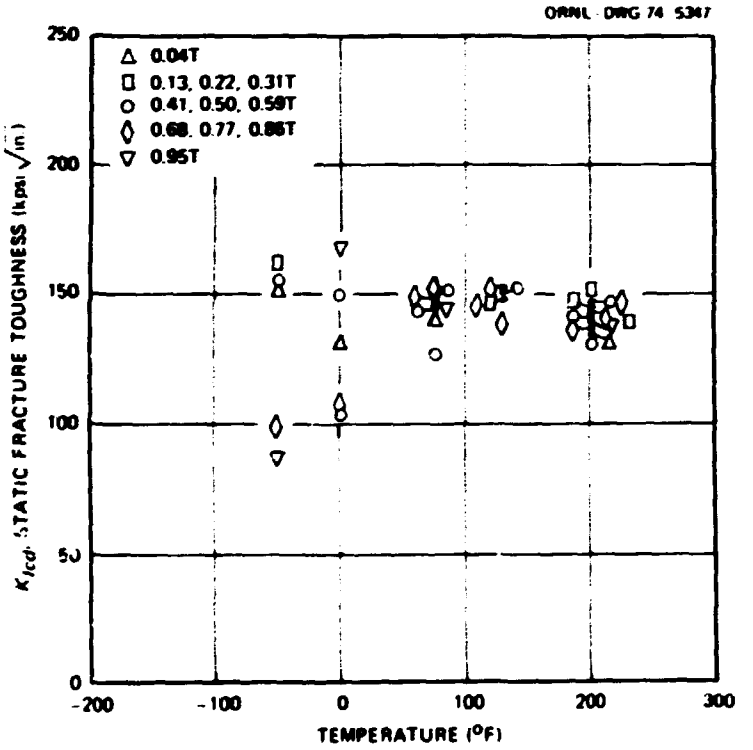

Fig. 2.29. Lower-bound fracture toughness values obtained from intermediate vessel V-6 using CA-oriented precracked Charpy V-notch specimens from a weld in 6-in.-thick ASTM A508 class 2 forging steel.

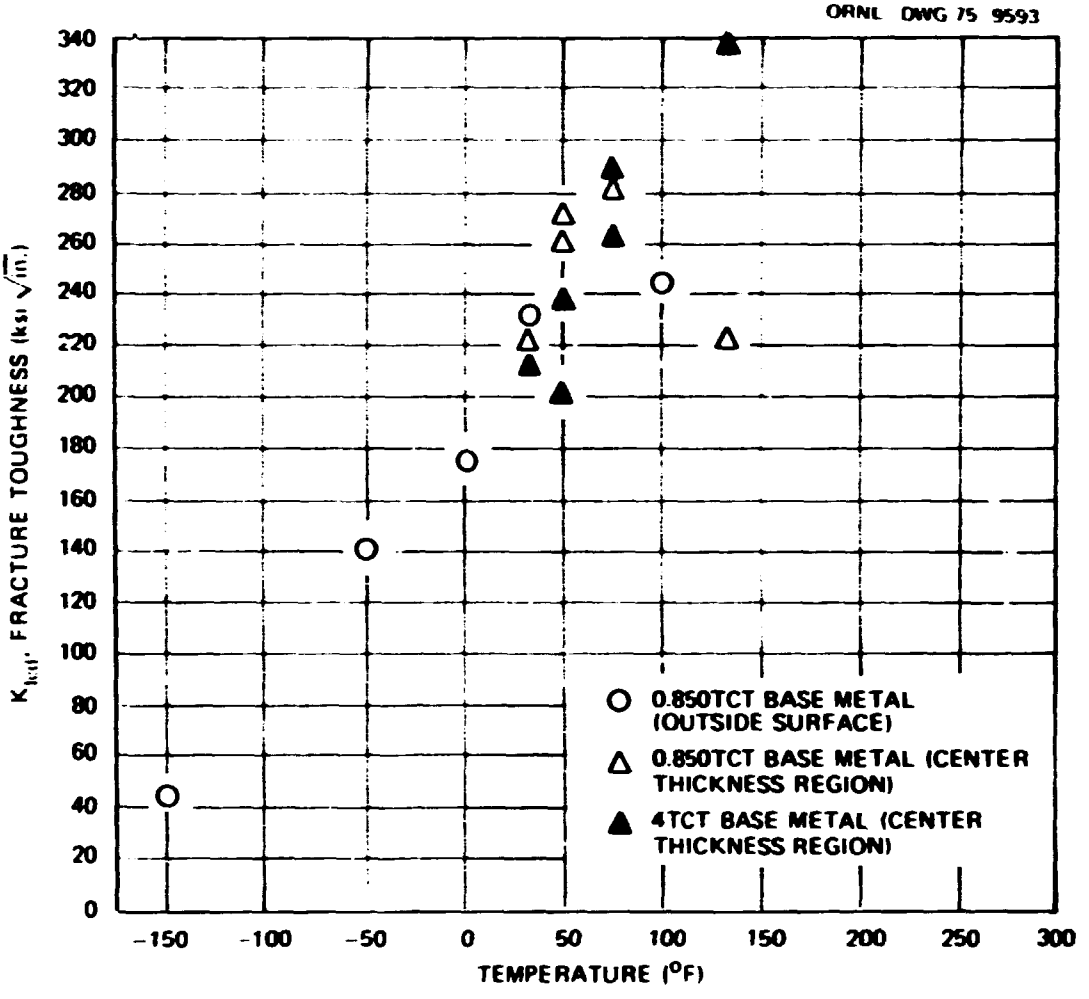

Fig. 2.30. Fracture toughness data for HSST intermediate pressure vessel V-4 base metal.

pressure vessel vendors. The thrust of the MPA studies has been primarily on forging materials, in particular, 22 Ni–Mo–Cr 37 steel; plate materials of interest, particularly ASTM A533, grade B, class 1, have shown no sensitivity toward cracking and are not being studied. Consequently, the MPA characterization has consisted of metallographic examination of HAZ specimens subjected to various thermomechanical treatments. Because of the high Nakamura number (empirical number indicating the relative susceptibility to cracking) of the HSST vessel forging material, the MPA were interested in examining a weld segment from the prolongation of vessel V-4 and obtained the material from WRLE. They found extensive cracks and decohesions in the heat-affected zone of the segment. A similar study by Canonico[15] of a weldment segment from vessel V-3 gave no indication of cracking.

The segment of the prolongation studied by MPA and WRLE included weld metal and base metal. The MPA sectioned the weldment along a plane that was roughly parallel to the weld seam. An 80 × 80 × 20 mm specimen was produced with the large face extending approximately in the thickness direction of the plate. This surface was successively polished and examined metallographically to reveal a number of layers

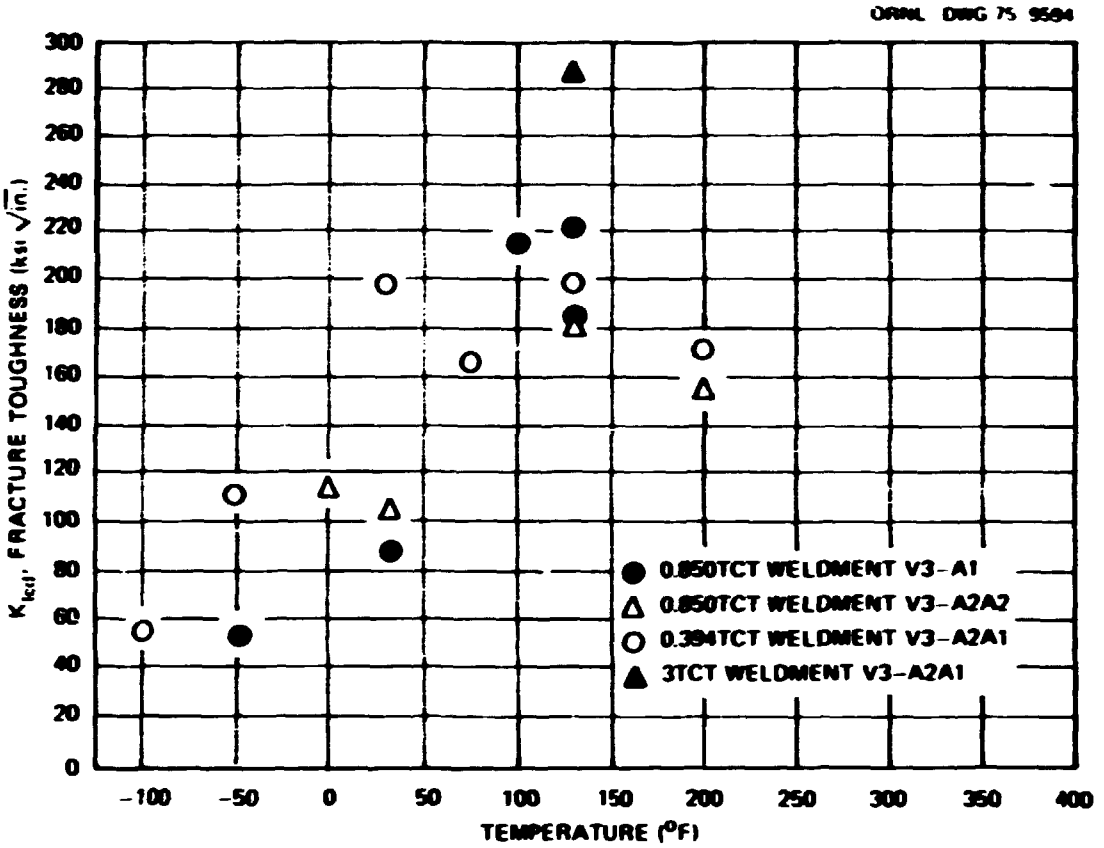

Fig. 2.31. Fracture toughness data for HSST intermediate pressure vessel V-3 weldment material.

through the thickness. The thickness of the specimen included all the HAZ and some of the weld metal. Cracks up to 5 mm long and decohesions of grain boundaries, both perpendicular to the welding direction, were found in the HAZ. As previously noted, chemical analysis showed the HAZ material to have a composition indicative of crack sensitivity in welding. The grain size in this zone was also extremely coarse, near ASTM No. 1.

In a similar examination of a part of the weld segment by WRLE, no indications of cracks or decohesions were found initially, even after bending the specimens. Another portion of the weld segment, near the root of the weld, was examined metallographically after the MPA observations were reported. Hot cracks (parallel to the direction of the weld) up to 4 mm long and some grain boundary decohesions were observed.

Metallographic examination at ORNL of broken Charpy V-notch specimens from the root of the weld in the prolongation of V-4 revealed a few grain boundary decohesions. A magnification of 100 to 1000X was required to ascertain that the indications were indeed decohesions.

The results of these three investigations of the V-4 prolongation material have been discussed among the original investigators. The long cracks perpendicular to the weld found by MPA are much longer than any they observed in their study of qualification weldments of 22 Ni Mo Cr 37 steel produced in Germany. Cracks of that orientation were not found by the other investigators. It was generally recognized that the

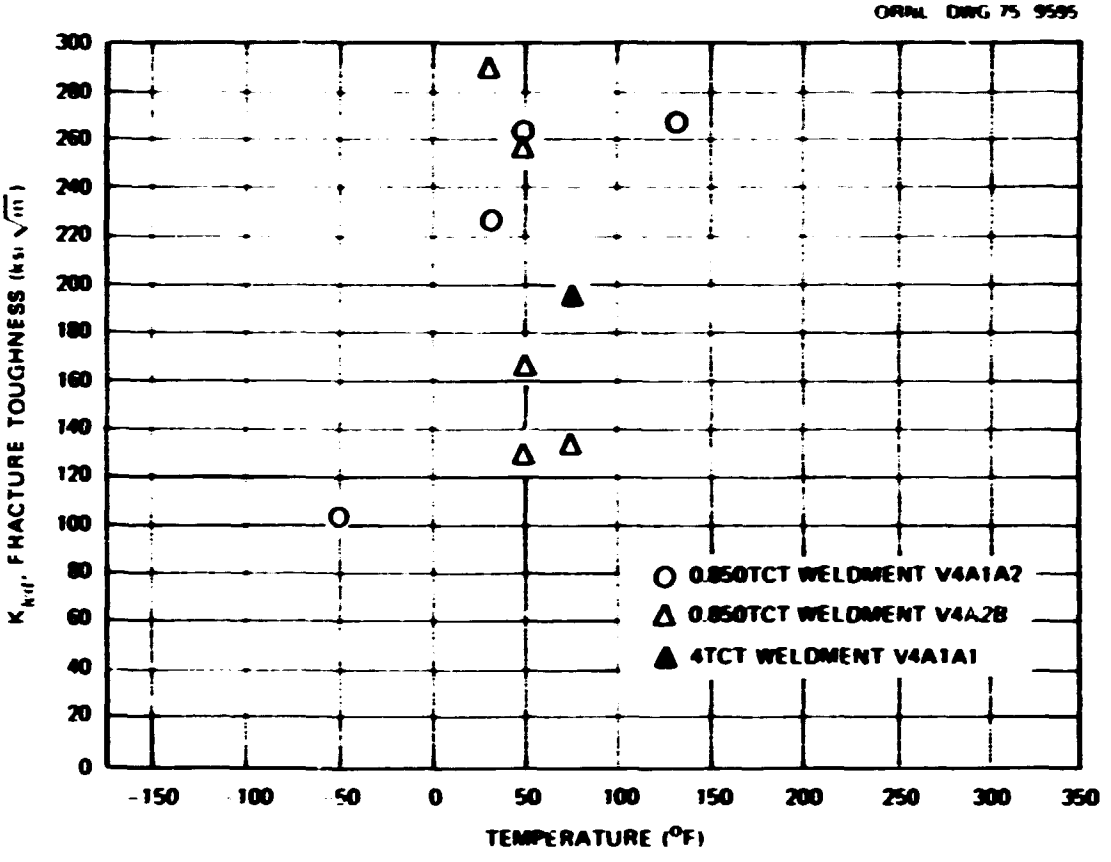

Fig. 2.32. Fracture toughness data for HSST intermediate pressure vessel V-4 weldment material.

chemical composition of V-4 being near the upper limit allowed for ASTM A508 class 2 forgings makes this particular piece of material more prone to cracking in the heat-affected zone than similar material of nominal composition. MPA is conducting further tests of the HSST material to determine creep behavior at stress-relief temperatures; ORNL also plans further investigation of properties of material in heat-affected zones.

3. TEST FACILITY DESIGN AND PERFORMANCE

Test Facility

The test site for this series of intermediate vessel tests was the same as that used for vessels V-1 and V-2; the criteria for site selection and design along with a detailed description of the facility are given in Ref. 1. The test site is located at an old power plant adjacent to the Oak Ridge Gaseous Diffusion Plant (ORGDP) where the vessel is pressurized to failure in a concrete bunkered cell which was converted from an old steam turbine foundation. A sectional view of the test pit is shown in Fig. 3.1, and a typical overhead view of a test vessel in the pit is shown in Fig. 3.2.

The test facility is capable of controlled temperatures from 50 to 350°F and pressurization output to 50,000 psi. Figure 3.3 shows a schematic flow diagram of the facility.

Instrumentation of Vessels

The vessels were instrumented with Chromel-Alumel thermocouples on each test vessel to determine the adequacy of the prescribed test conditions in the regions of interest. From 10 to 16 sensors were used, depending on the number of flaws in the test piece. The locations of thermocouples on vessel V-4 are shown in Fig. 3.4 as a typical layout. Multipoint Brown (Honeywell) recorders were used to record temperatures.

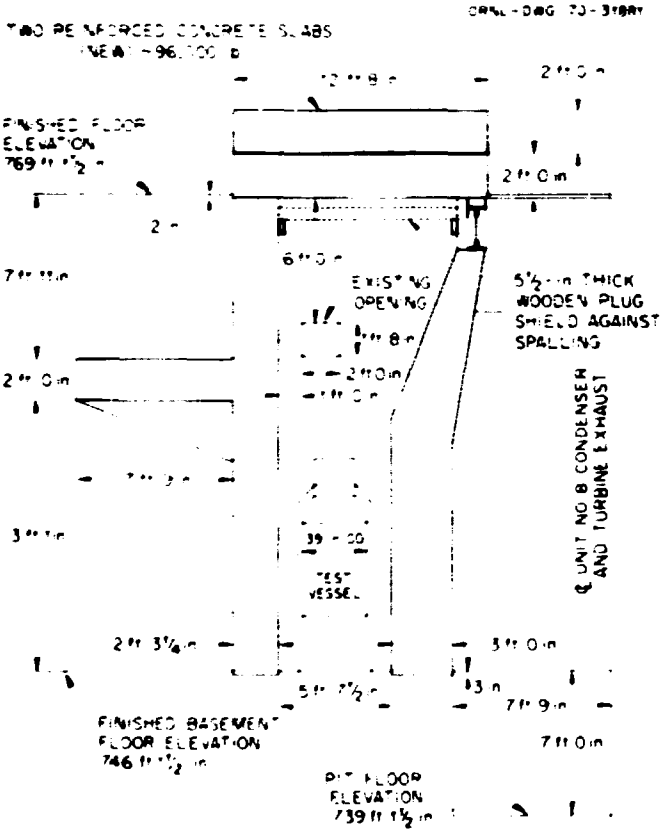

Fig. 3.1. Sectional view of intermediate vessel test pit.

Fig. 3.2. View of test pit from turbine room floor with a typical vessel and associated equipment in place.

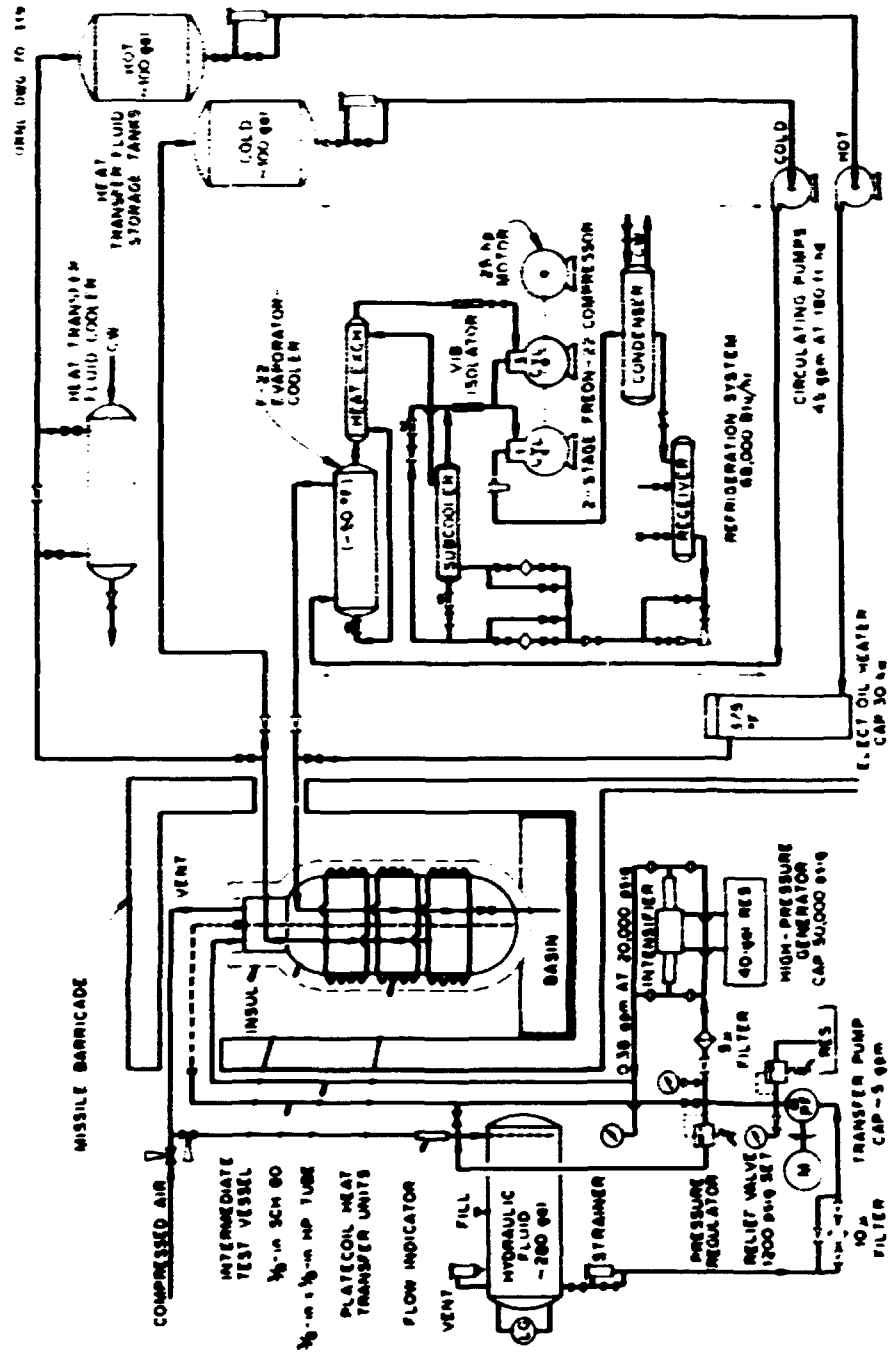

Fig. 3.3. Schematic flow diagram of intermediate vessel test facility.

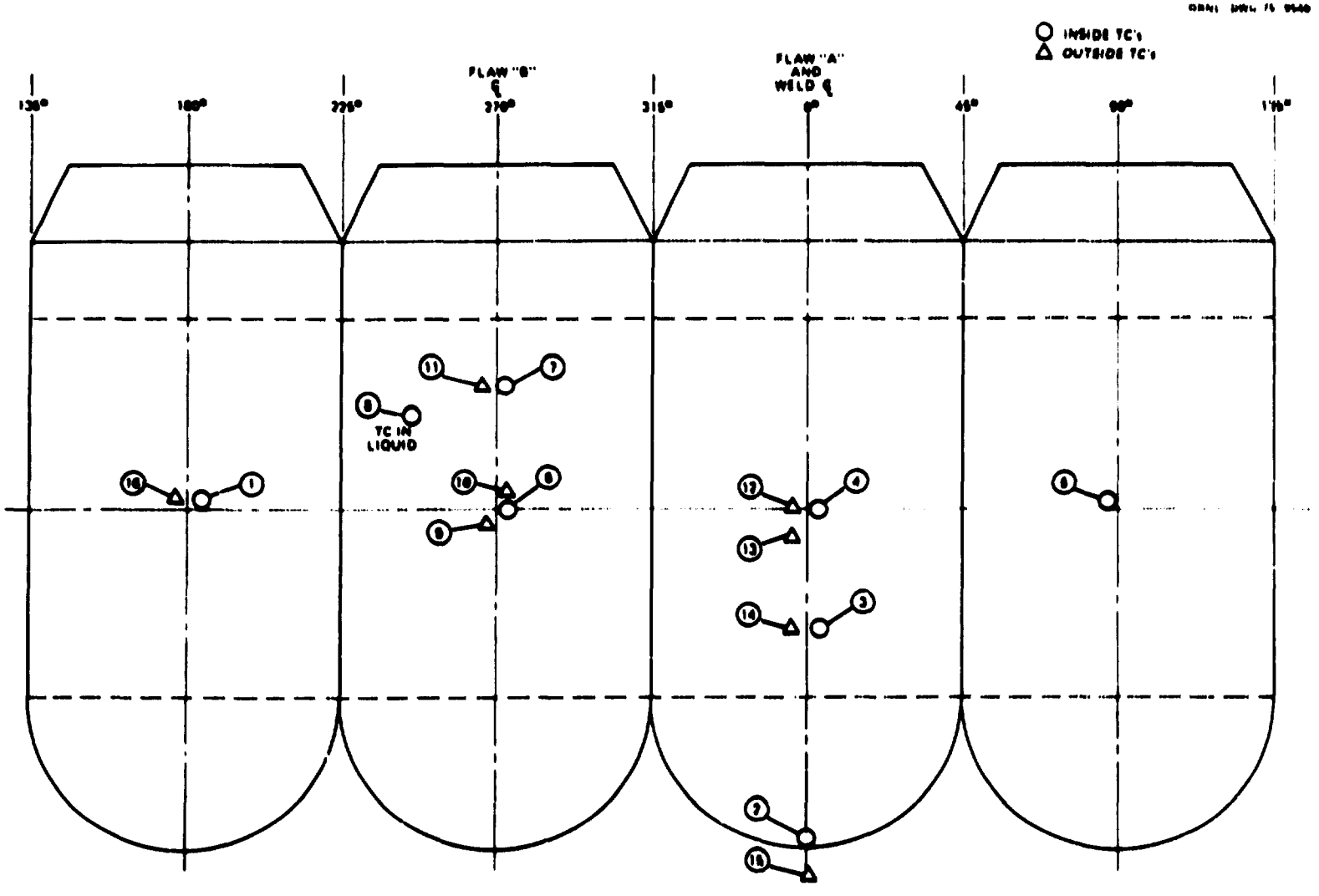

Fig. 3.4. Location of thermocouples on intermediate test vessel V-4, as viewed from outside.

The inner and outer surfaces of the test vessels were instrumented with 60 to 100 strain gages. Locations of these gages for the three vessels are shown in Figs. 3.5 through 3.10. The gages on vessels V-3 and V-4 and the outer surface gages on V-6 were installed according to the procedure[1] used in the testing of V-1 and V-2. The inside surface gage installation procedure for V-6 was modified, as discussed later in this chapter. A Datum System 70 computer-controlled data-acquisition system and portable BLH strain indicators were used to record the strain data. A complete tabulation of strains is given in Appendix B.

The crack-opening displacements (CODs) for outside surface flaws were measured as follows. A dial indicator mounted on a short post adjacent to the flaw was positioned to measure the motion of another post on the opposite side of the flaw. Two approaches were used to record the readings on the dial. The camera of a closed-circuit television set was focused on the notch and the dial. As the pressure was increased, personnel in the control room could watch the notch open and at the same time record the readings on the dial indicator. As a backup for the TV camera, a solenoid-controlled 35-mm still camera was also focused on the notch and dial. A digital counter was mounted near the notch. Whenever a photograph was taken by pushing a button in the control room, the operator also recorded the photograph number and the pressure in the vessel. The COD devices were developed by A. A. Abbatiello, ORNL.

In addition to the dial indicator measurements for the cracks in V-4, linear displacement transducers were used to obtain COD measurements. Self-oscillating and demodulating direct-current differential transformers (DCDTs) were installed to evaluate their performance for future tests. The COD data shown later in this chapter were from the DCDTs, and the results were satisfactory.

A special clip gage with strain gages was developed and calibrated for measurement of inside surface crack-opening displacements. The strain gages were installed using the same procedures as used for other interior strain measurements. The arrangement and concept of the COD clip gage is shown in Fig. 3.11.

Two completely independent systems were used to monitor pressure. The most straightforward method was to use another closed-circuit TV set to follow a conventional Bourdon pressure gage mounted near the high-pressure pump. This approach was basically a redundancy for a more precise system that consisted of a commercially available load cell, a signal-conditioning and excitation unit, and an L&N recorder. After having been calibrated at a standards laboratory, this device was accurate to ±250 psi in 30,000 psi.

Vessels V-3, V-4, and V-6 were monitored by acoustic emission specialists from Westinghouse who brought their own equipment to the test site and installed it themselves. This work is described in detail later in this chapter.

Scanning closed-circuit television systems were also utilized for general surveillance of the test pit and pressurization equipment. For exterior flaws a video tape recorder was utilized for recording a view of the crack behavior up to and during failure.

Test Procedures

Vessel preparation

Each test vessel is flawed and instrumented at the Y-12 facilities of the Reactor Division as described in Ref. 1. The vessel is then transported to the test site and placed in the test cell. The heating-cooling plate coils are installed, the instrumentation lead wires to the control room are connected, and insulation is applied to the vessel. It is then ready to be filled with demineralized water, followed by connection of the pressurization lines. During the filling operation and while the vessel is being brought to the test temperature, installation of television, acoustic emission, and ultrasonic monitoring equipment is completed. After final checks on all recording equipment, the vessel is ready for pressurization.

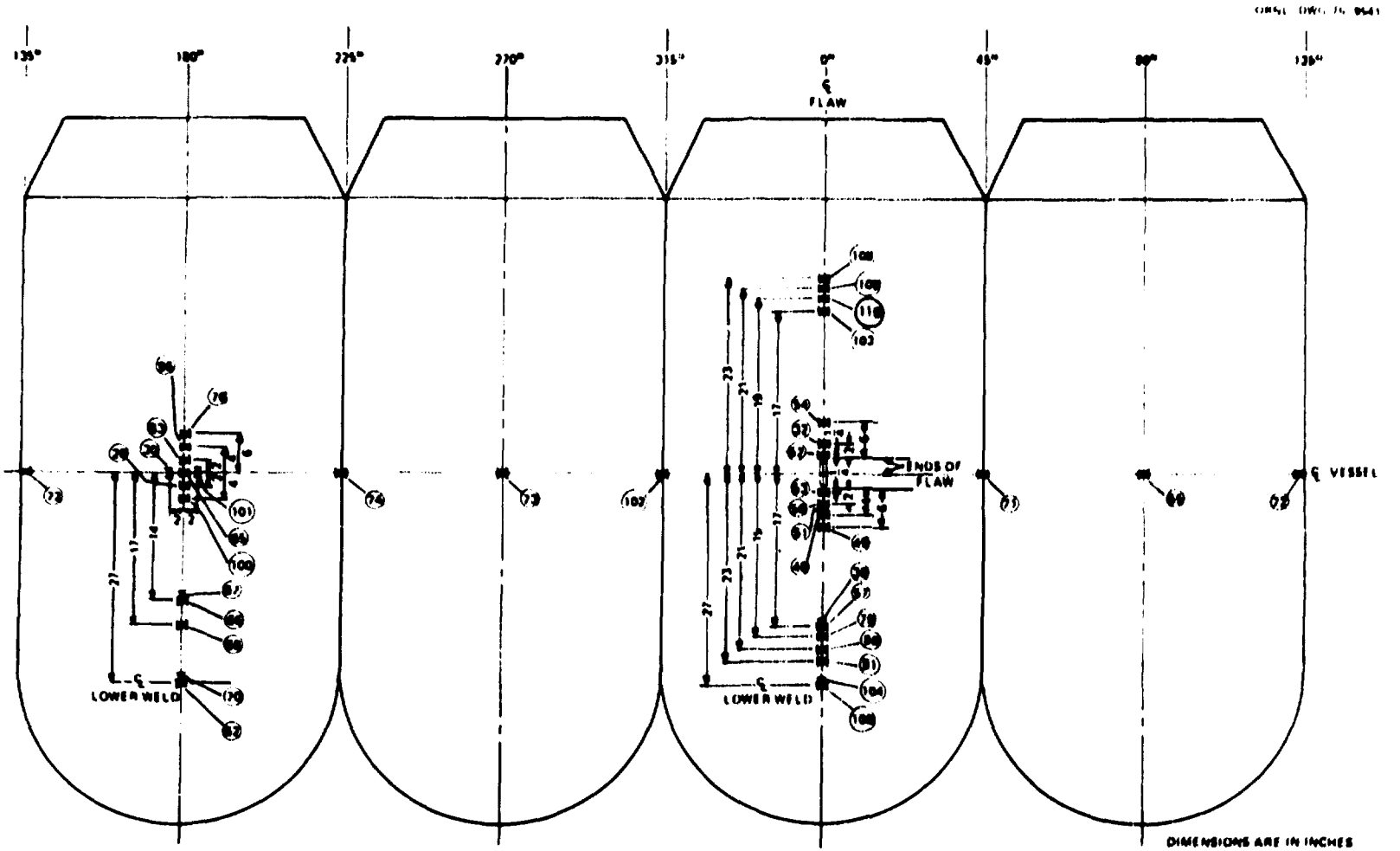

Fig. 3.5. Location of strain gages on outer surface of intermediate test vessel V-3, as viewed from outside. Numbers shown are channel and wire numbers for gages monitored by computer and BLH strain indicators respectively.

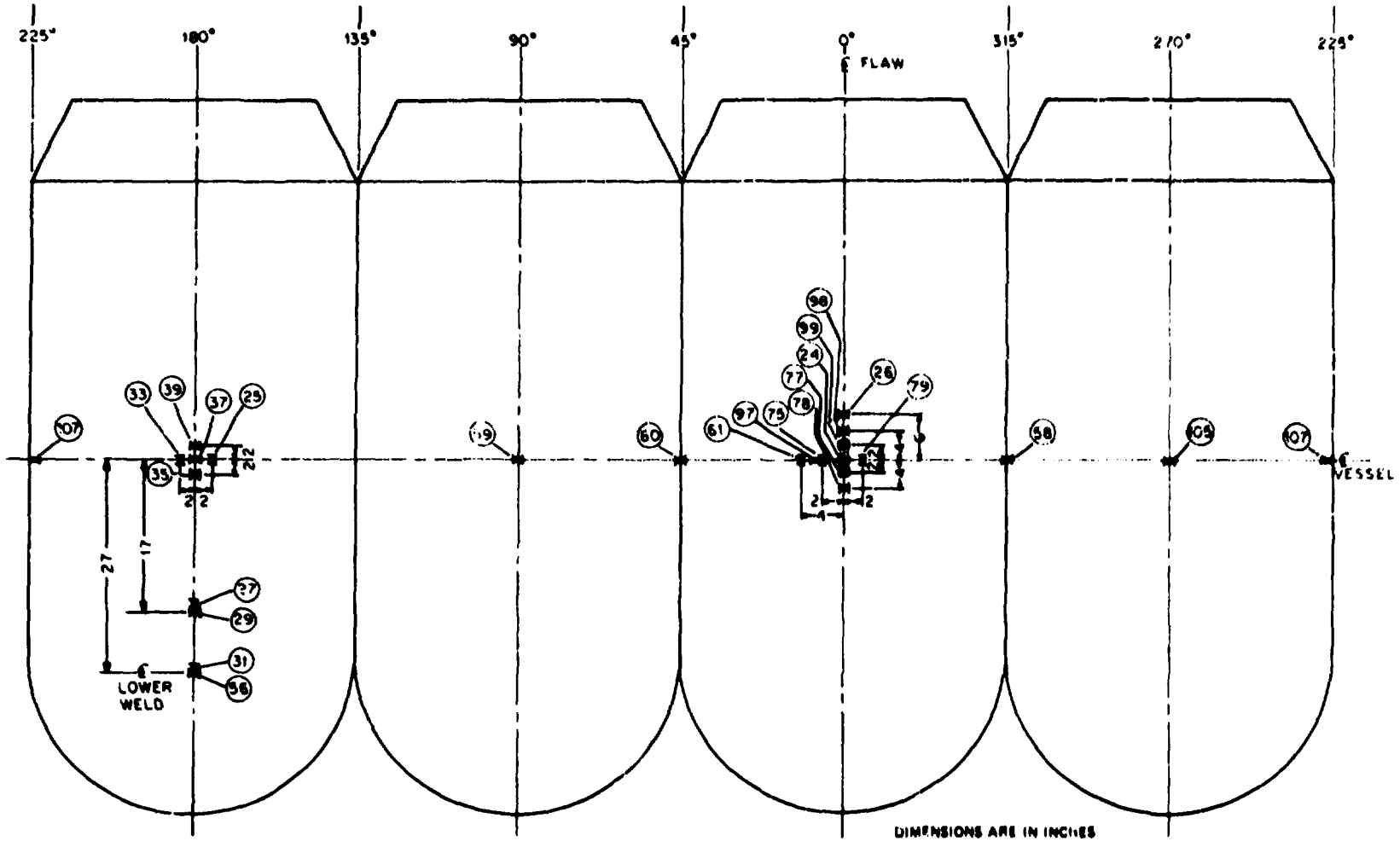

Fig. 3.6. Location of strain gages on inner surface of intermediate test vessel V-3, as viewed from inside. Numbers shown are channel and wire numbers for gages monitored by computer and BLH strain indicators respectively.

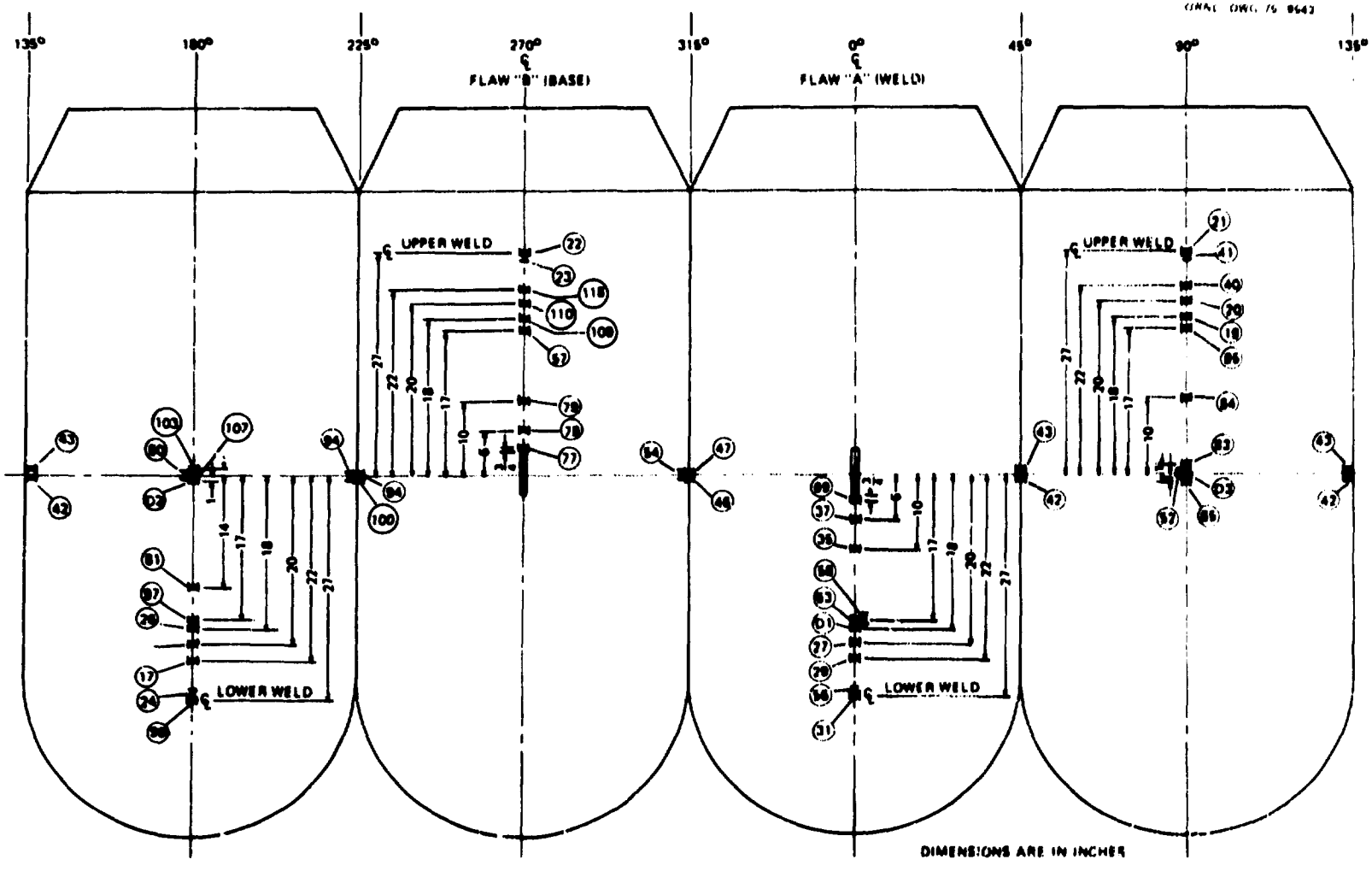

Fig. 3.7. Location of strain gages on outer surface of intermediate test vessel V-4, as viewed from outside. Numbers shown are channel and wire numbers for gages monitored by computer and BLH strain indicators respectively.

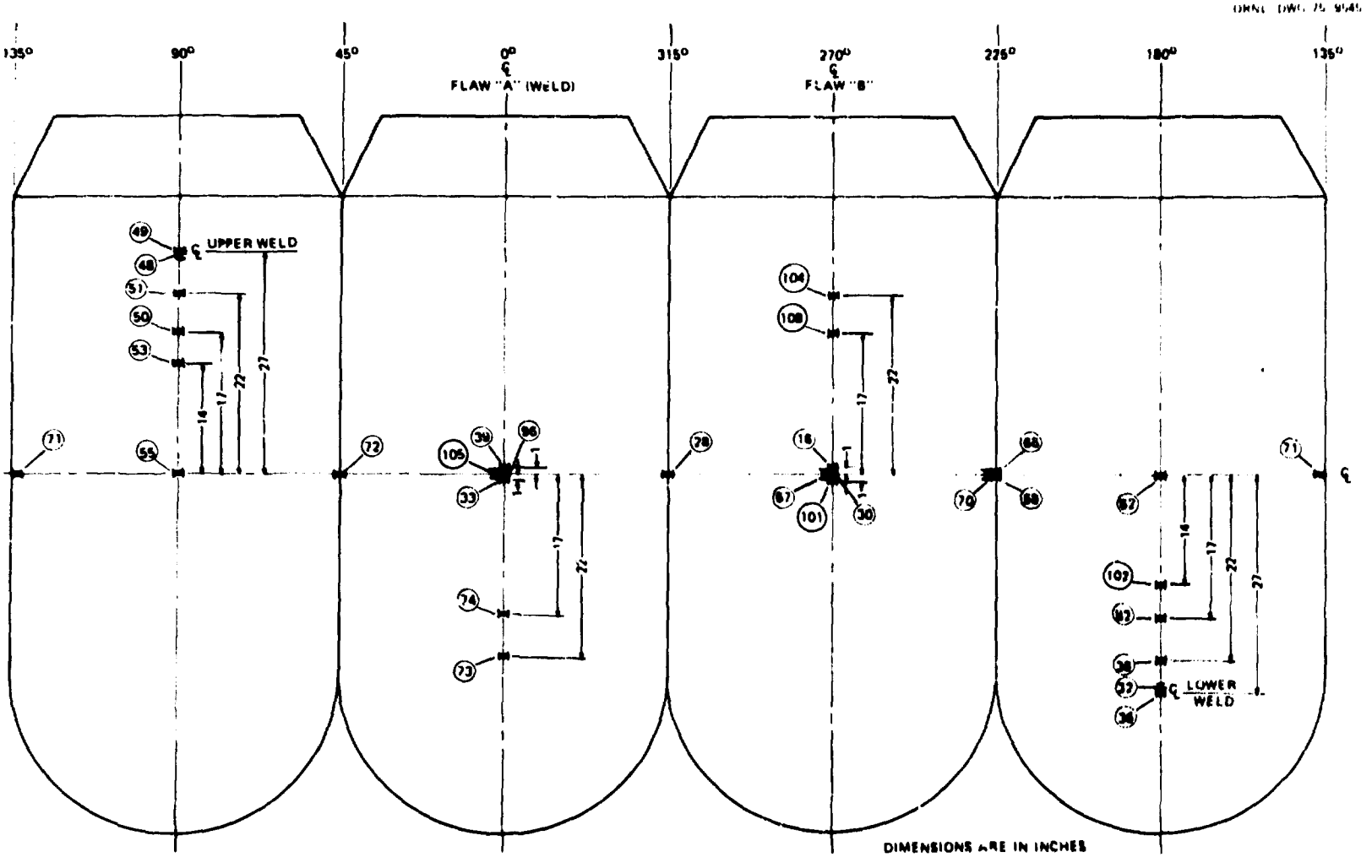

Fig. 3.8. Location of strain gages on inner surface of intermediate test vessel V-4, as viewed from inside. Numbers shown are channel and wire numbers for gages monitored by computer and BLH strain indicators respectively.

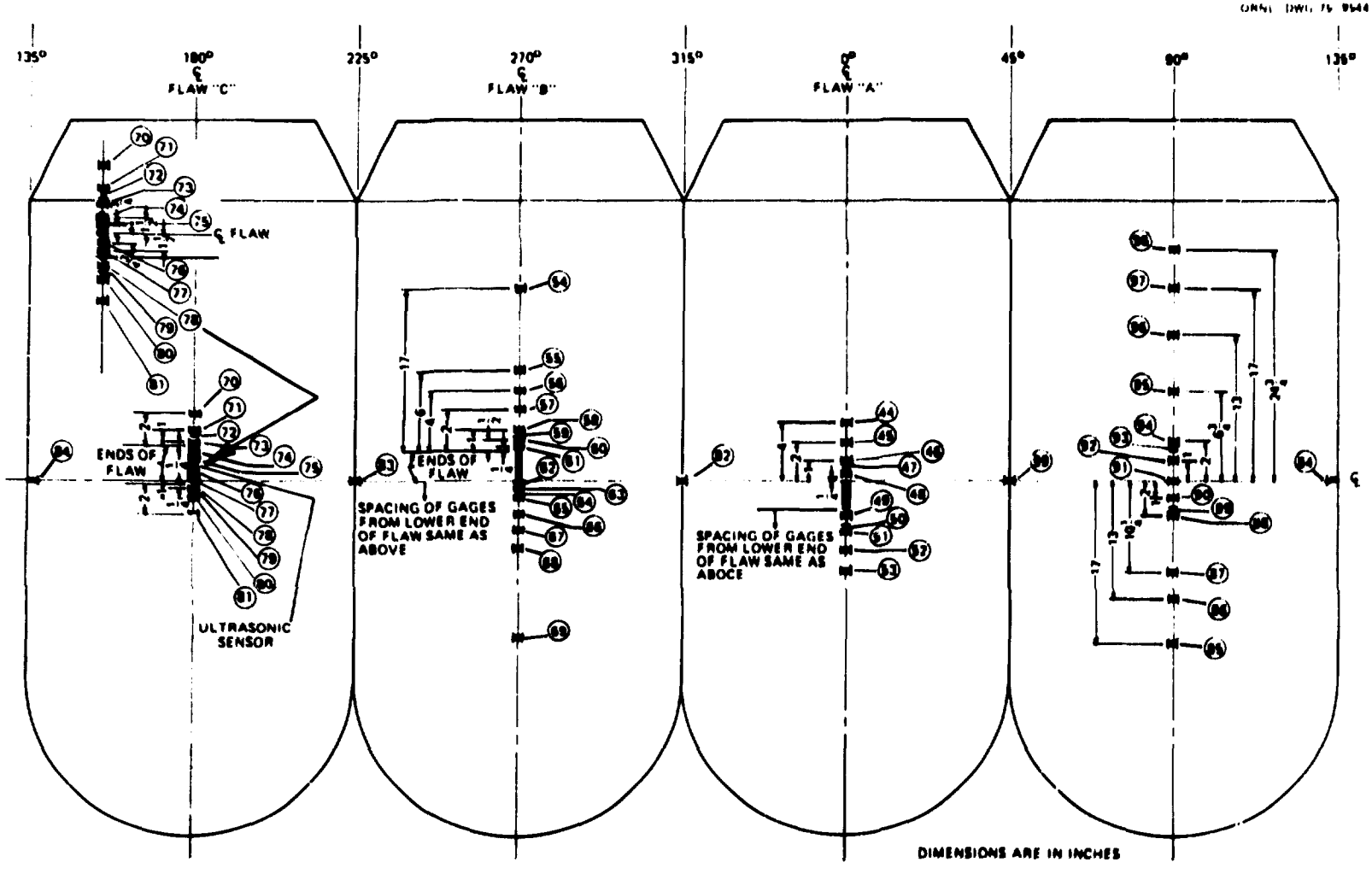

Fig. 3.9. Location of strain gages on outer surface of intermediate test vessel V-6, as viewed from outside. Numbers shown are channel and wire numbers for gages monitored by computer and BLH strain indicators respectively.

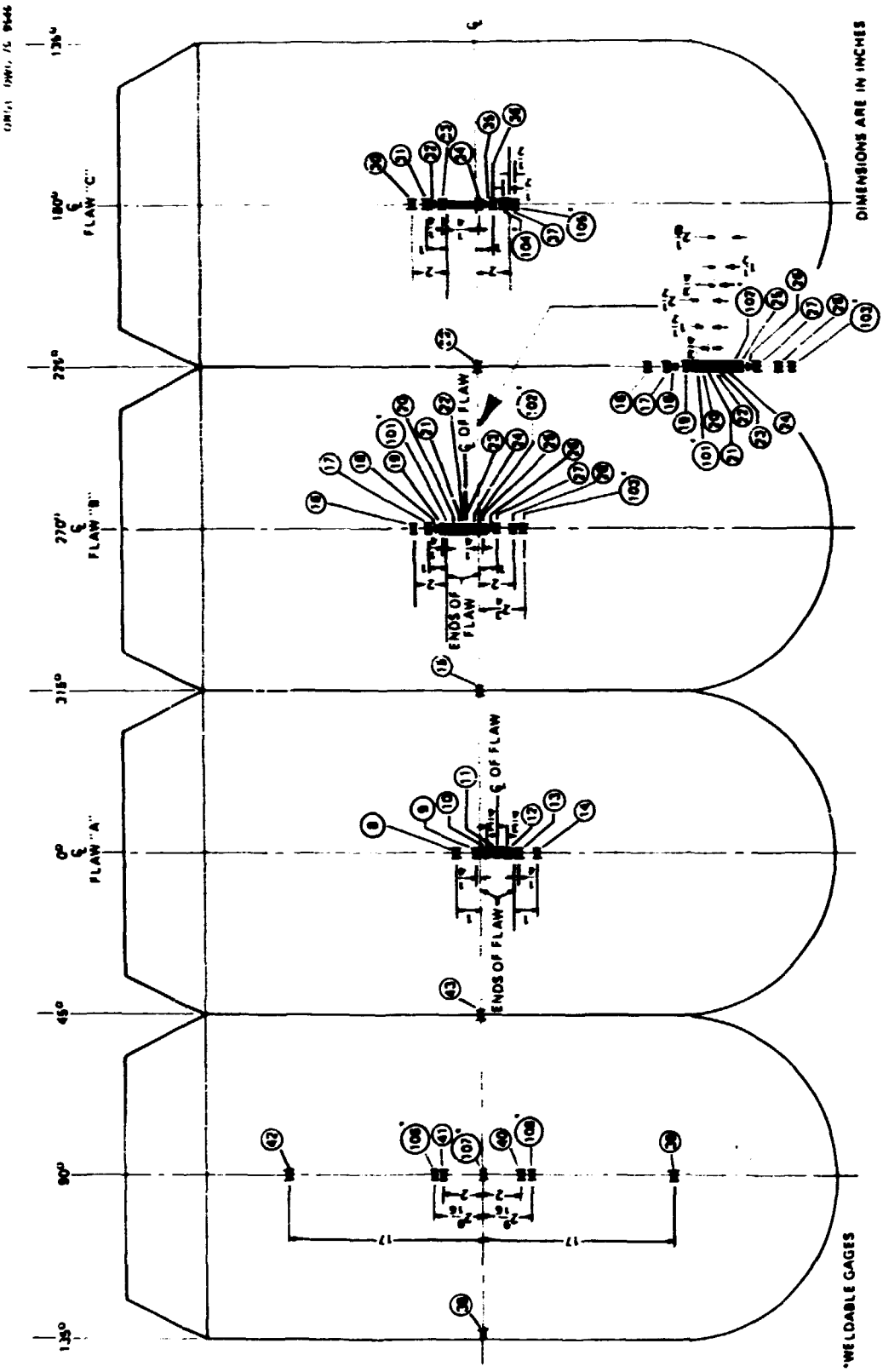

Fig. 3.10. Location of strain gages on inner surface of intermediate test vessel V-6, as viewed from inside. Numbers shown are channel and wire numbers for gages monitored by computer and BLH strain indicators respectively.

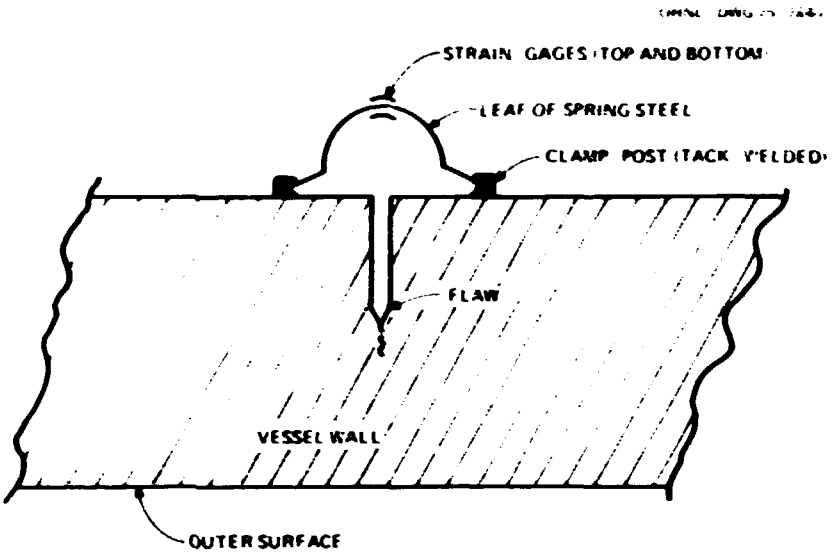

Fig. 3.11. Design concept of COD clip gage for inside crack-opening displacement measurement.

Pressure testing to failure

An initial zero data run is recorded, and pressurization begins. Periodic hold times are scheduled during which a complete set of data is recorded. These pressurization steps usually occur in increments of 4000 psi until 20,000 psi is reached; at that time, smaller increments in pressure are chosen until localized yielding is observed. The pressurization steps are then determined by strain level and observed behavior until failure occurs. As the vessel yields, more than one set of data may be taken during a hold period as the pressure drops off. Also, a previously achieved pressure level may be repeated until strain hardening causes the vessel to become stable at that pressure. The pressure-vs-time records of vessels V-3, V-4, and V-6 are presented in Figs. 3.12 to 3.14 respectively. After failure of the vessel, a final set of data from surviving instrumentation is recorded. The data and actual flaw configurations are examined and evaluated following the test.

Test Results

Test results from V-3, V-4, V-6 are shown in Table 3.1, along with a similar summary of V-1 and V-2 test results.

Intermediate vessel V-3

Figures 3.15 to 3.18 show COD data and representative strain-vs-pressure curves. Strain data germane to the discussion of test results are presented elsewhere in this report, and complete strain data for all three vessels are presented in Appendix B. Figure 3.19 shows vessel V-3 after failure and before removal operations; a closeup of the failure area after cleaning the vessel is depicted in Fig. 3.20. The flaw is clearly evident, the dark area being the machined notch and the somewhat lighter strip below showing the extent of fatigue sharpening. Localized barreling can also be distinguished.

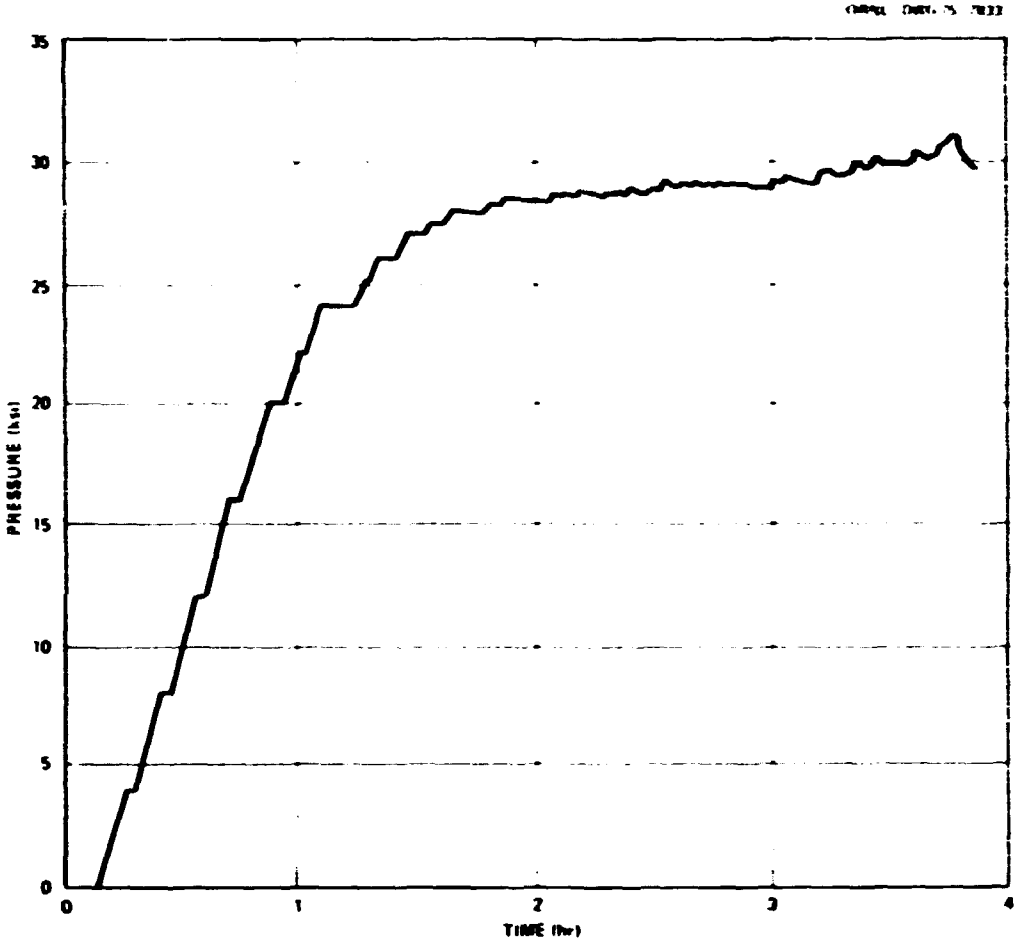

Fig. 3.12. Pressure vs time – intermediate vessel test V-3.

Table 3.1. Summary of test results from five 6-in.-thick intermediate test vessels

Vessel No.	Test temperature (°F)	Flaw dimensions (in.)		Flaw location[a]	Fracture pressure (ksi)	Nominal fracture strain (%)[b]
		Depth	Length			
V-1	130	2.56	8.25	Base metal (o)	28.8	0.92
V-2	32	2.53	8.30	Base metal (o)	27.9	0.19
V-3	130	2.11	8.50	Weld metal (o)	31.0	1.47
V-4[c]	75	2.95	8.25	Weld metal (o)[d]	26.5	0.17
	75	3.12	8.05	Base metal (o)	26.5	0.17
V-6[e]	190	1.87	5.25	Weld metal (o)[d]	31.9	2.0
	190	1.34	5.20	Base metal (o)	31.9	2.0
	190	1.94	5.30	Weld metal (i)	31.9	2.0

[a]Letter o = outside surface; i = inside surface.
[b]Outside circumferential strain on center line of vessel remote from flaw.
[c]Contained two flaws.
[d]Flaw where fracture occurred.
[e]Contained three flaws.

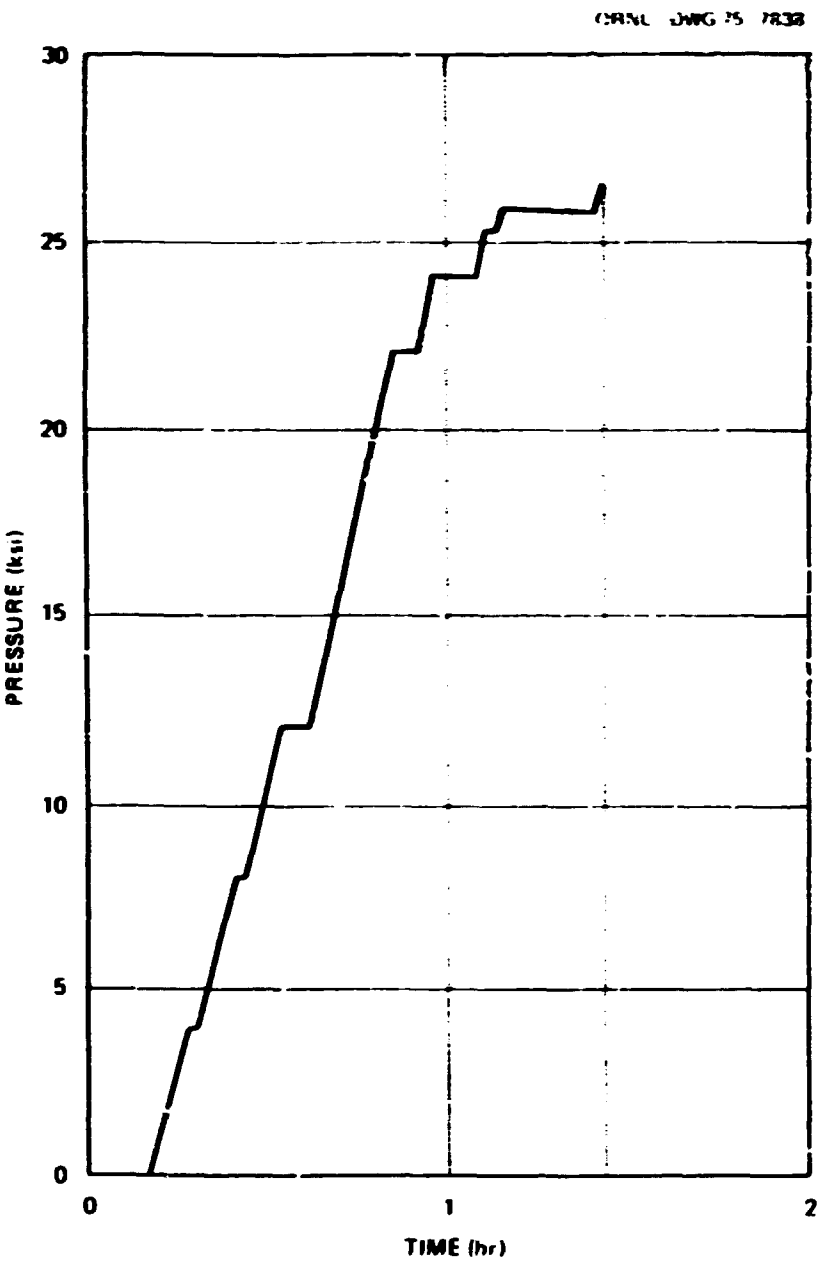

Fig. 3.13. Pressure vs time – intermediate vessel test V-4.

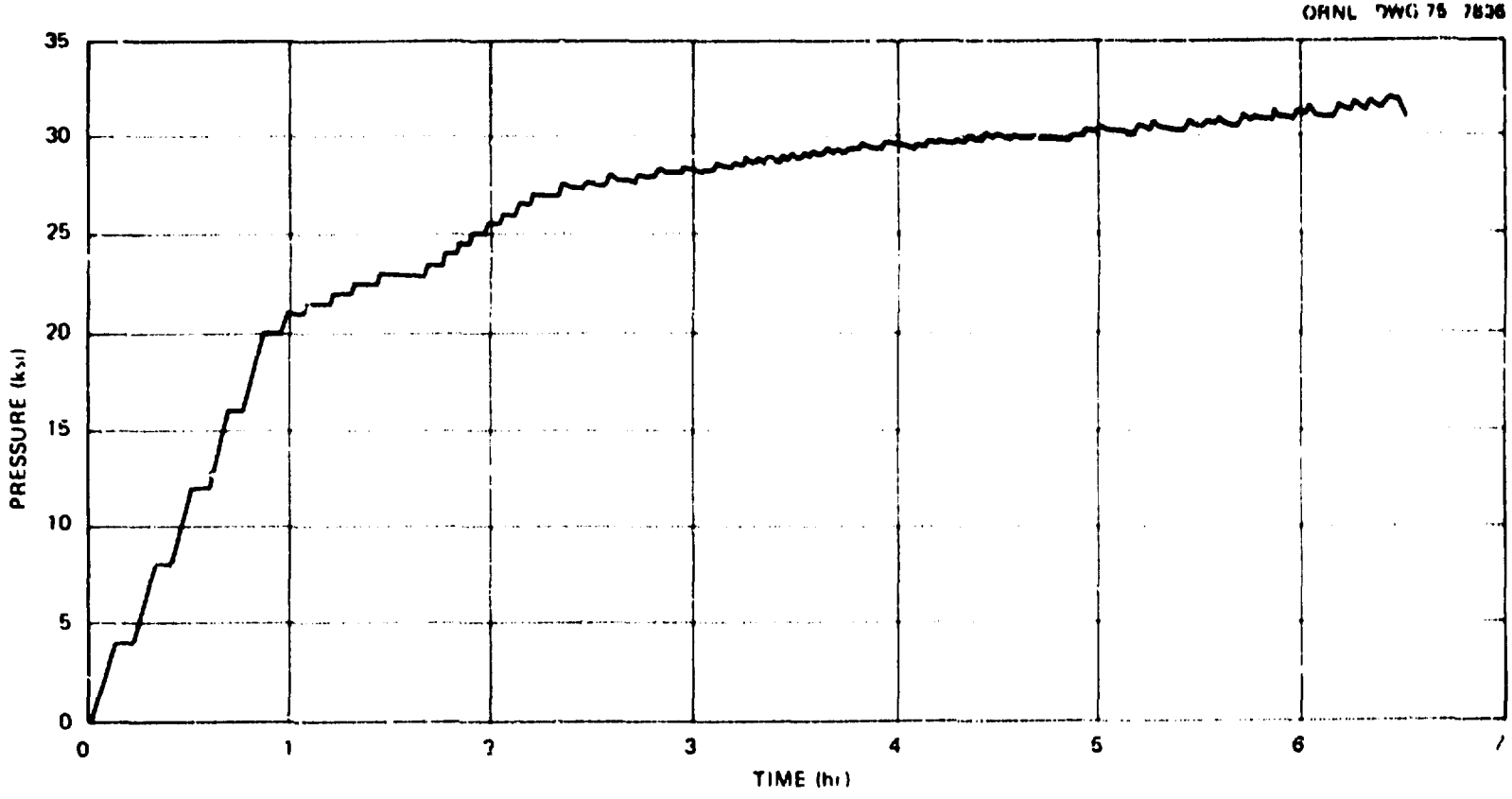

Fig. 3.14. Pressure vs time – intermediate vessel test V-6.

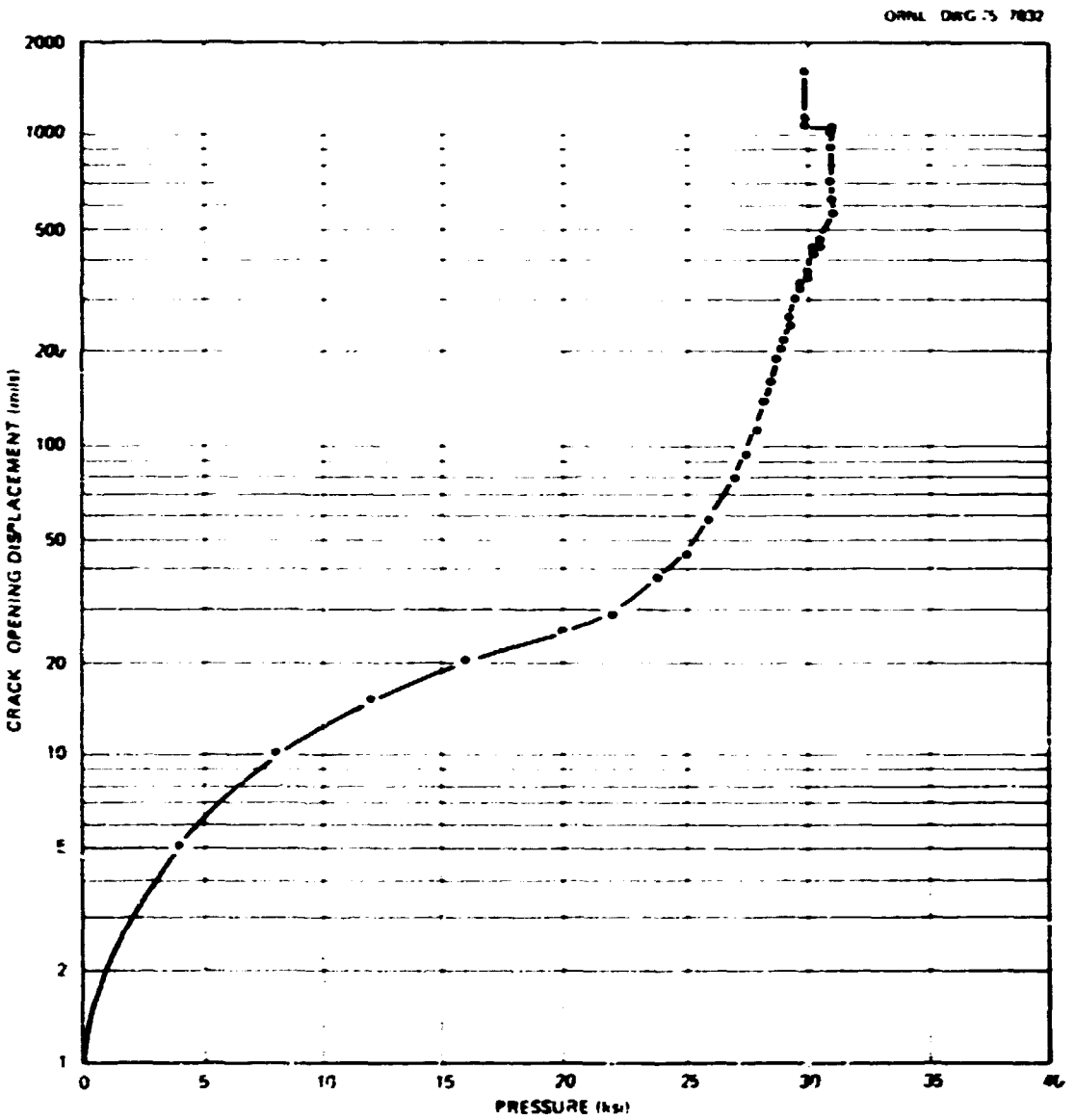

Fig. 3.15. Pressure vs COD – intermediate vessel test V-3.

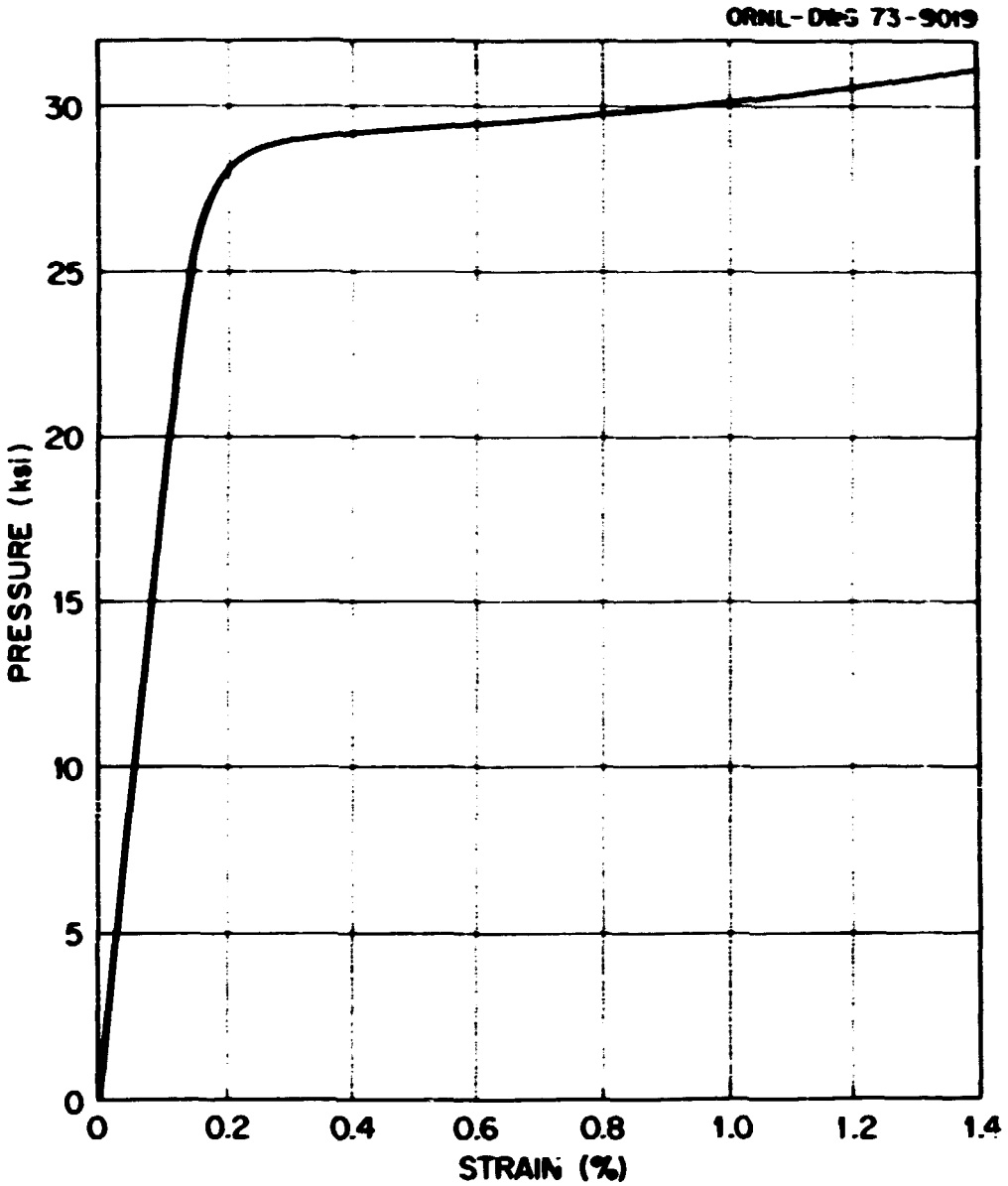

Fig. 3.16. Pressure vs outside surface strain, 180° from flaw – intermediate vessel test V-3.

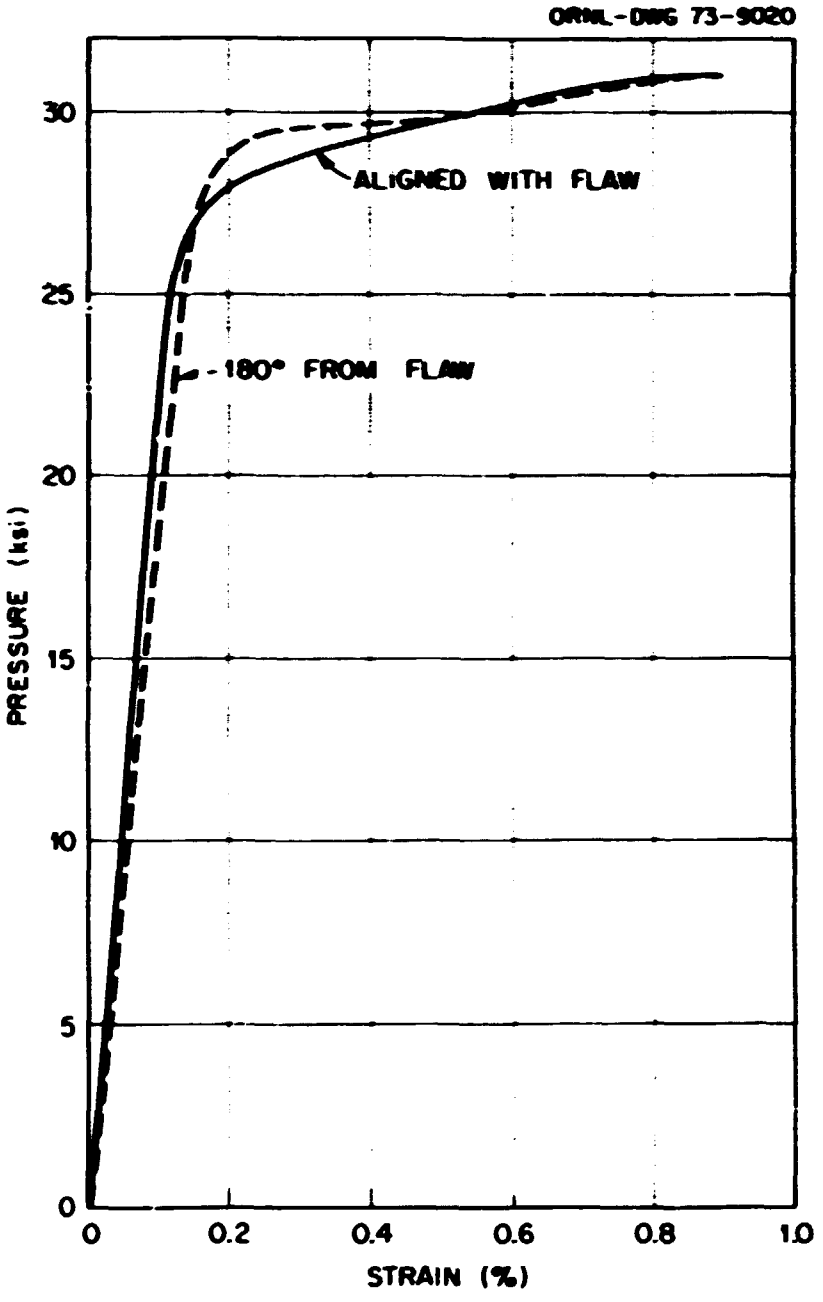

Fig. 3.17. Comparison between pressure vs outside surface circumferential strain curves 17 in. from center line of vessel, one located 180° from flaw in base metal and one aligned with flaw in weld metal – intermediate vessel test V-3.

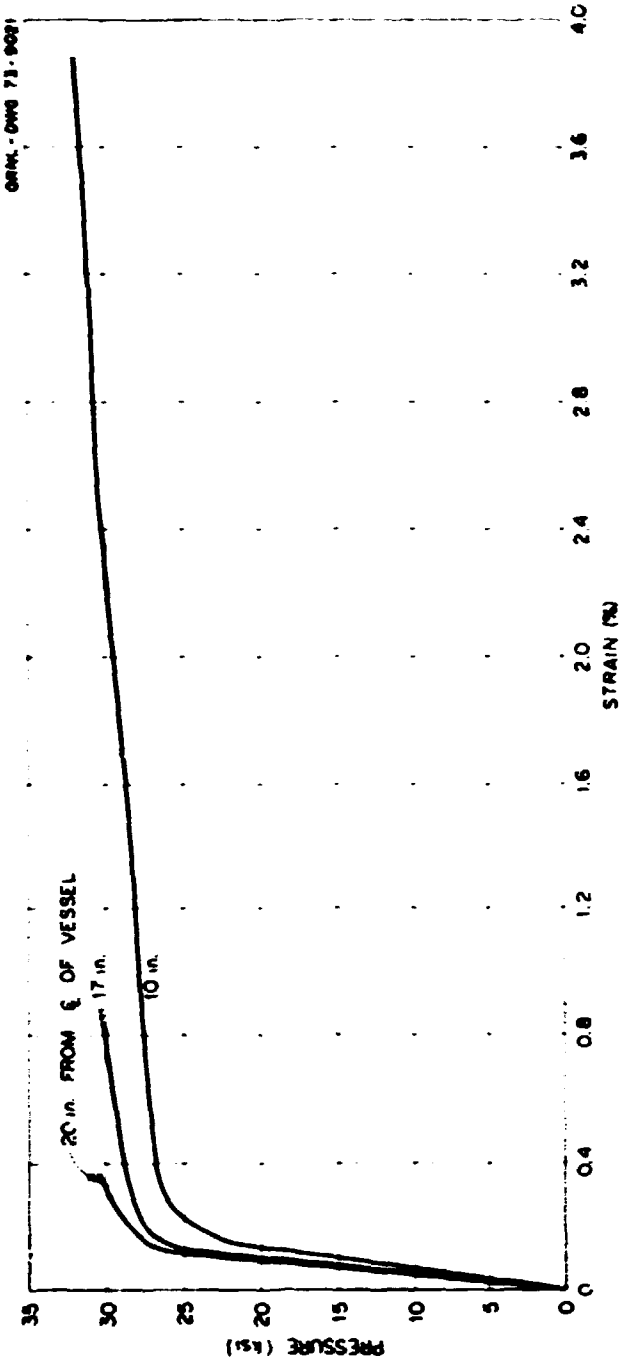

Fig. 3.18. Pressure vs outside surface strain (circumferential) plots at various locations in weld seam aligned with flaw — intermediate vessel test V-3.

ORGDP PHOTO
72-2270

Fig. 3.19. View of intermediate test vessel V-3 in test cell after failure test.

Fig. 3.20. Closeup of crack in intermediate test vessel V-3 after failure.

Intermediate vessel V-4

Figures 3.21 to 3.24 present COD data and representative strain-vs-pressure curves. Figure 3.25 is a closeup of the flaw that caused failure (weld metal). A similarity of fracture behavior can be seen in Fig. 3.26, where a small model of the same material and test conditions is compared with the intermediate vessel.

Intermediate vessel V-6

COD data and representative strain-vs-pressure curves are given in Figs. 3.27 to 3.30. Figure 3.31 shows the outside surface flaws of V-6 while it was still in the test cell. The weld metal flaw at which failure

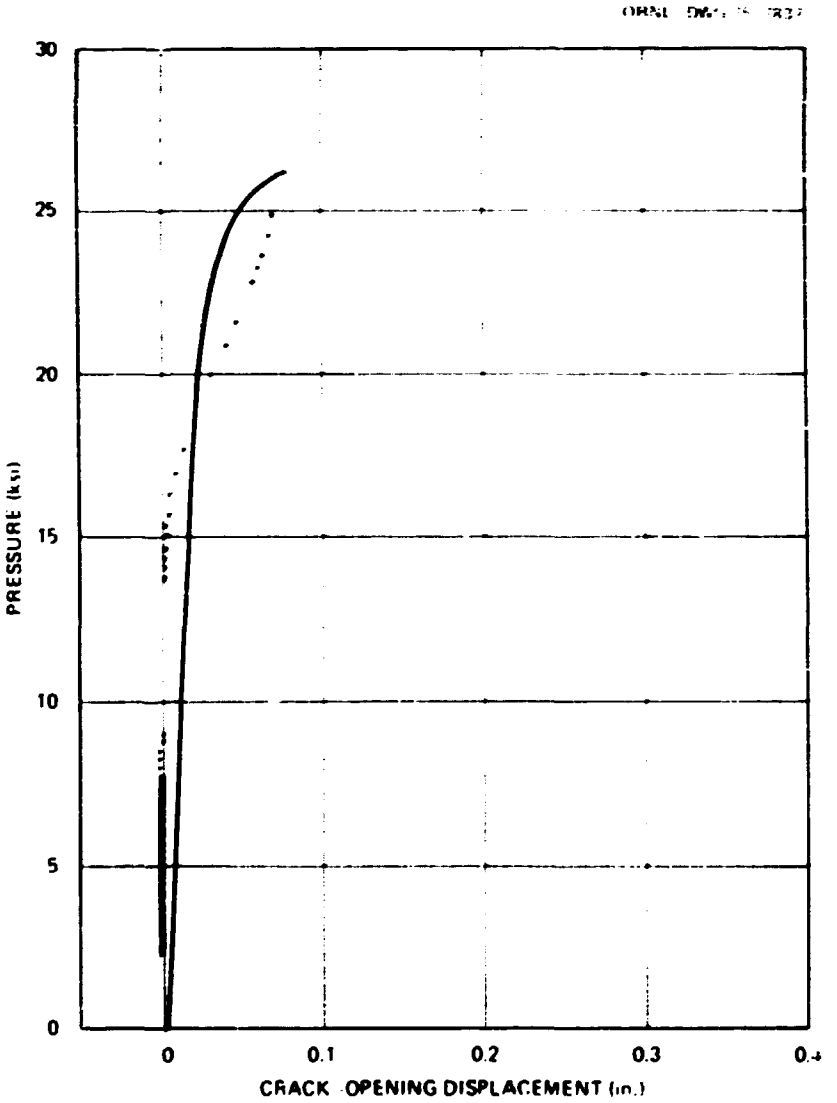

Fig. 3.21. Pressure vs COD (weld metal flaw) – intermediate test vessel V-4.

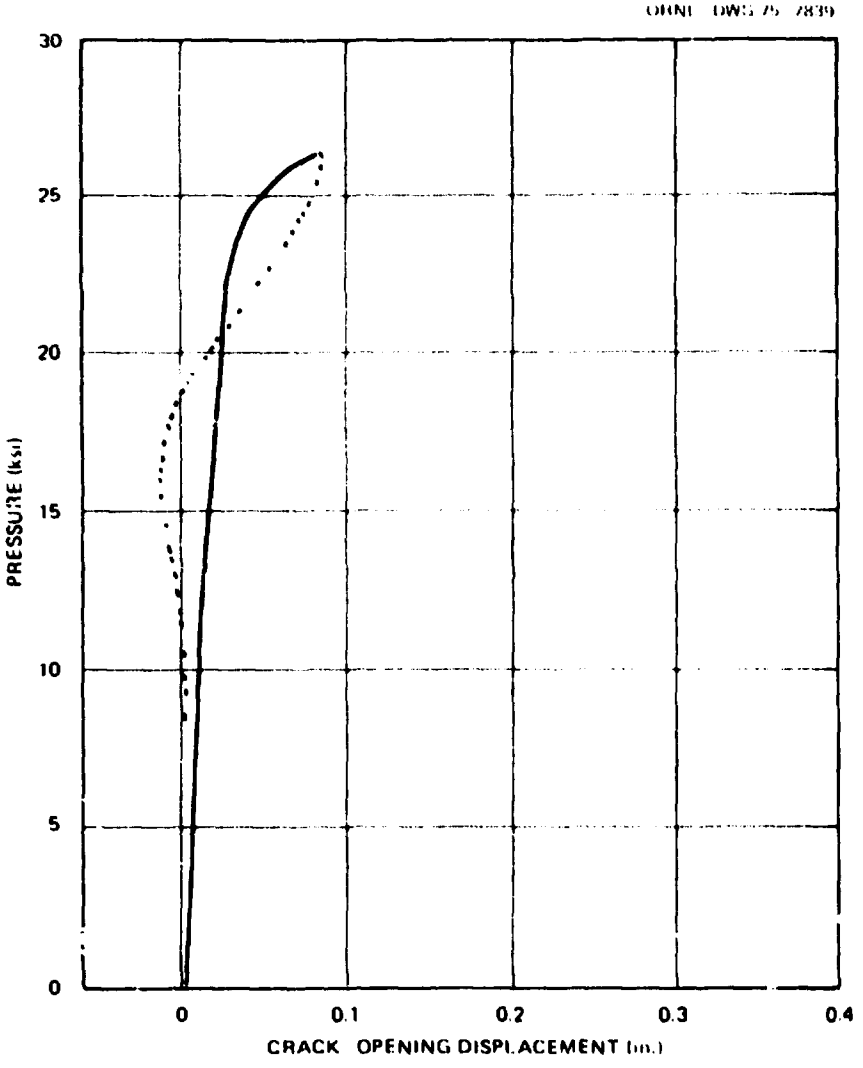

Fig. 3.22. Pressure vs COD (base metal flaw) – intermediate test vessel V-4.

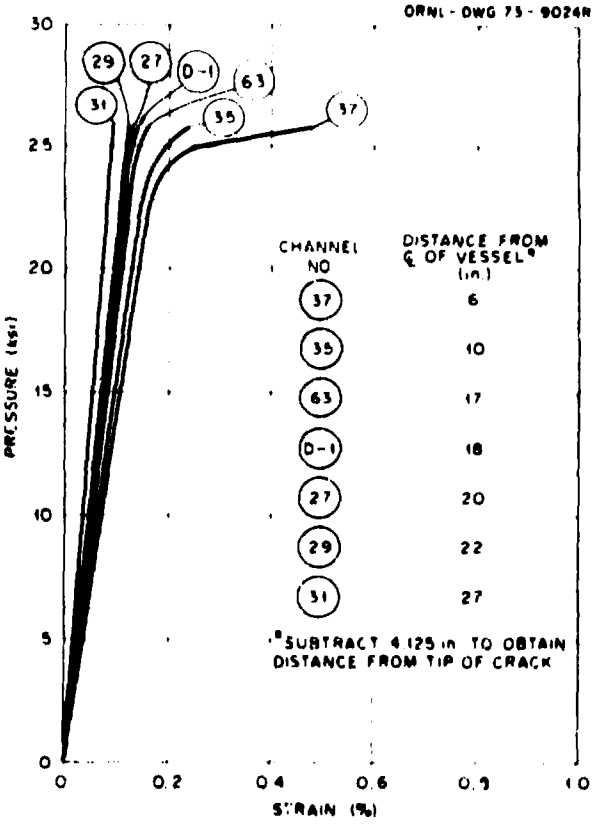

Fig. 3.23. Pressure vs outside surface circumferential strain aligned with flaw in weld metal – intermediate test vessel V-4.

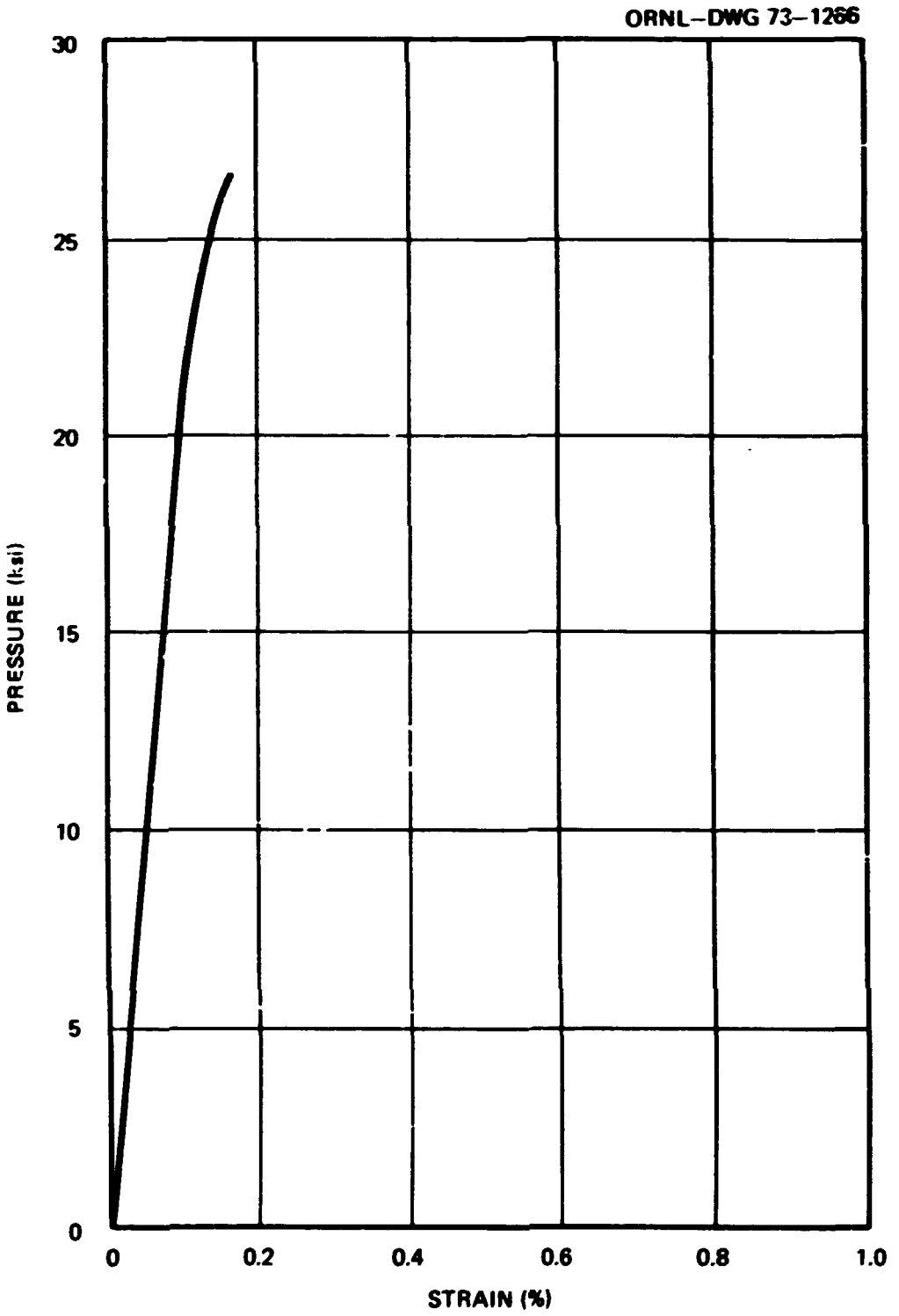

Fig. 3.24. Pressure vs outside surface circumferential strain 190° from flaw in base metal for intermediate test vessel V-4. Traced from x-y plot of channel 65.

Fig. 3.25. View of weld metal flaw after failure – intermediate test vessel V-4.

Fig. 3.26. View of intermediate test vessel V-4 with small steel model tested under the same conditions.

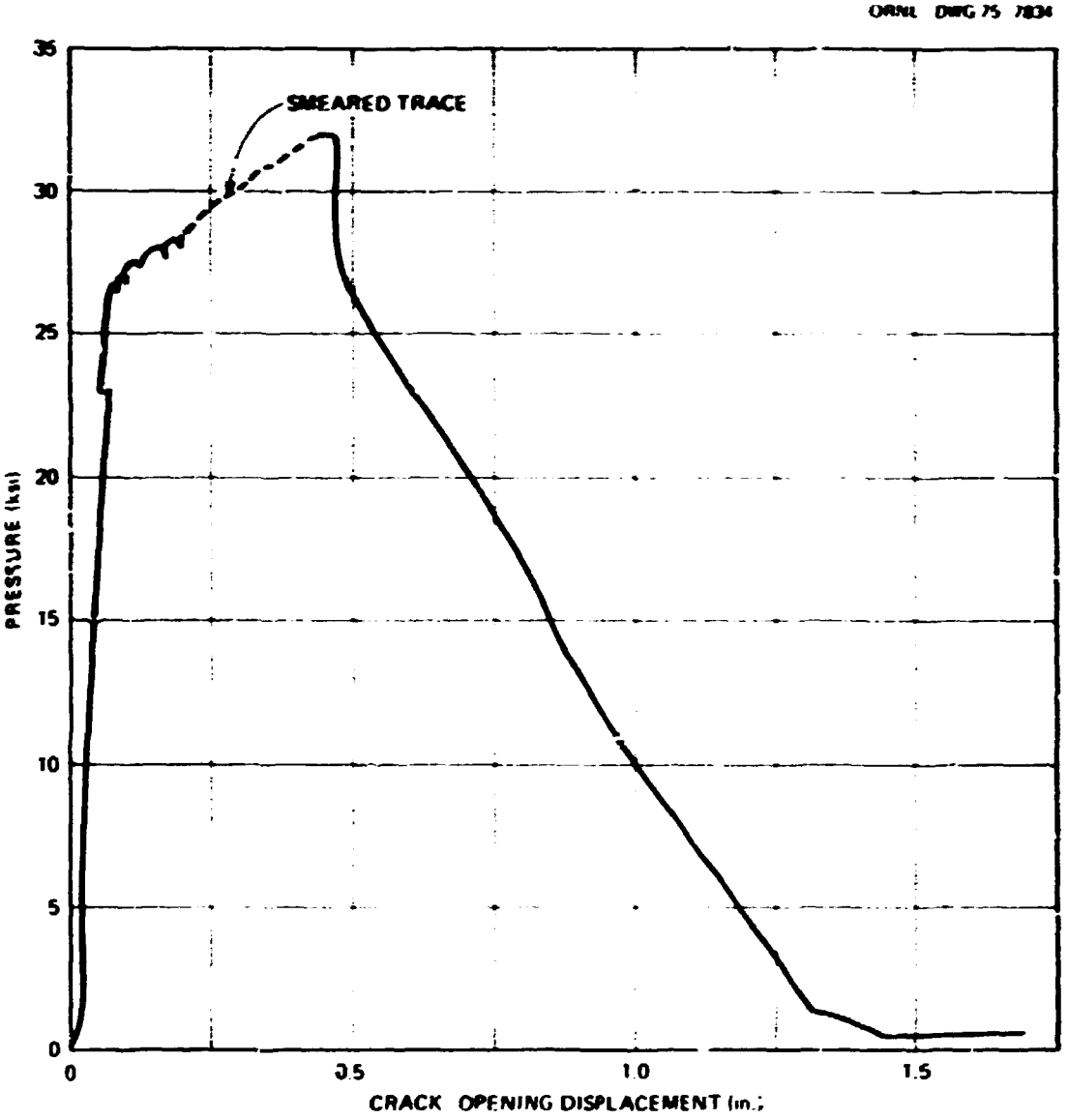

Fig. 3.27. Pressure vs COD (inside flaw in weld metal) – intermediate test vessel V-6.

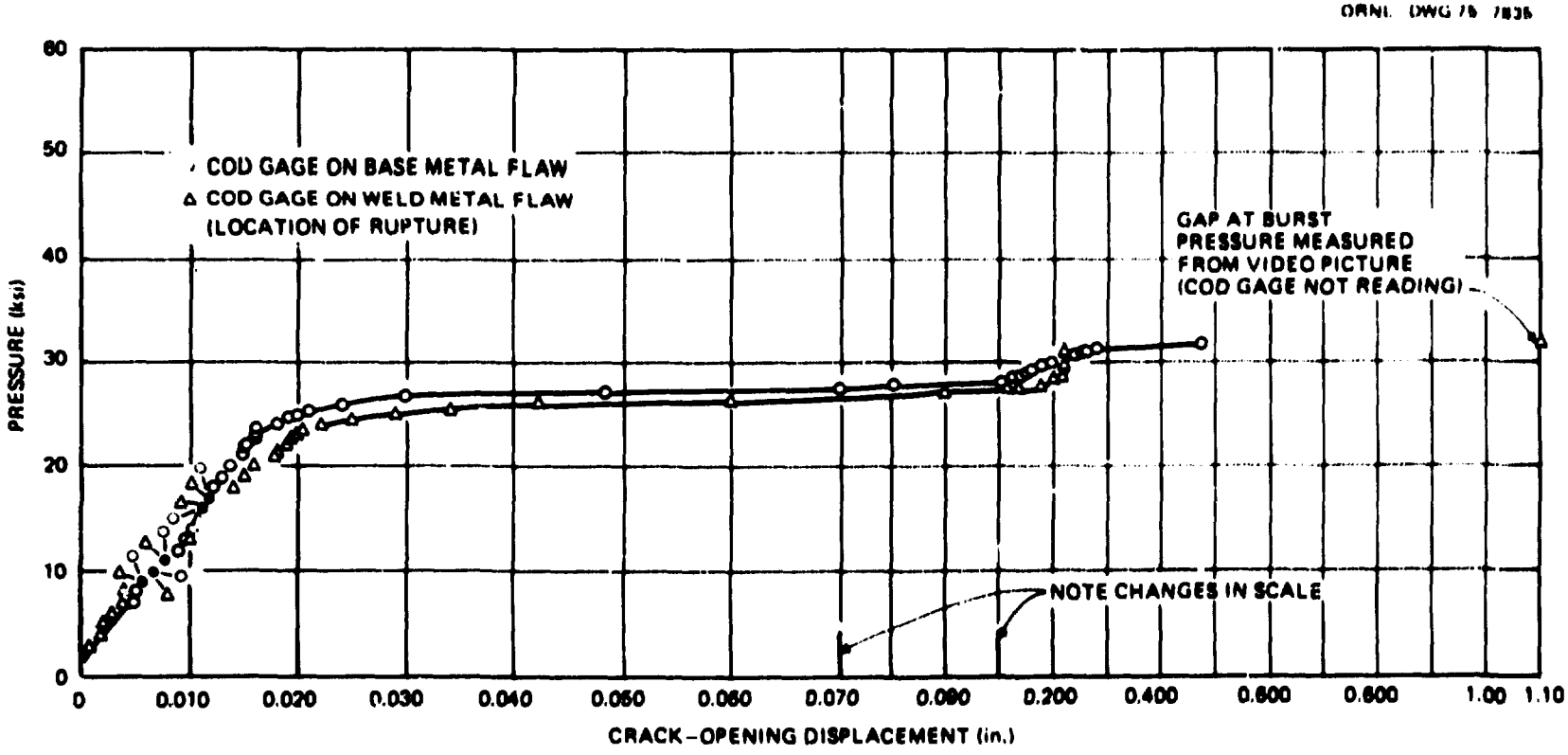

Fig. 3.28. Pressure vs COD (outside flaws) -- intermediate test vessel V-6.

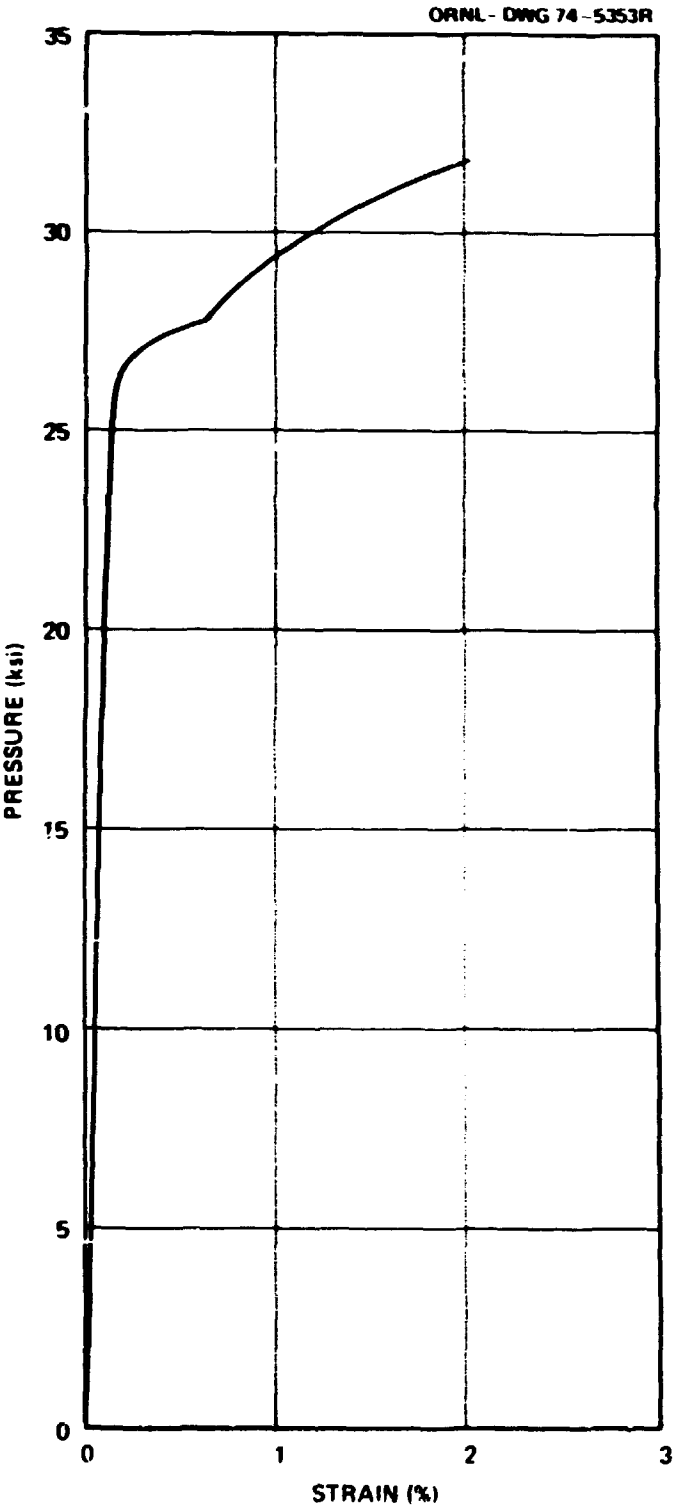

Fig. 3.29. Outside surface pressure vs circumferential strain curve at center of vessel 90° from any flaw – intermediate test vessel V-6.

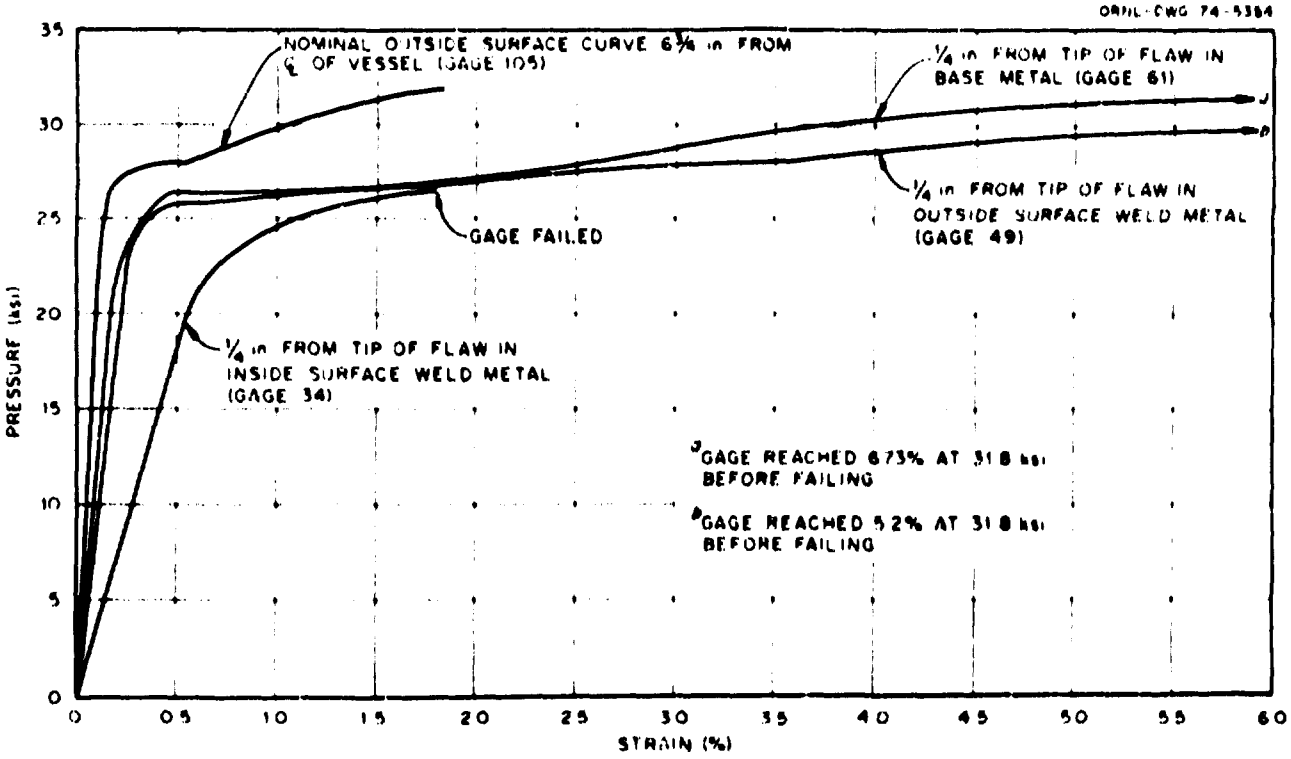

Fig. 3.30. Comparison of pressure-circumferential strain curves obtained ¼ in. from crack tip with nominal curve 90° from nearest flaw — intermediate test vessel V-8.

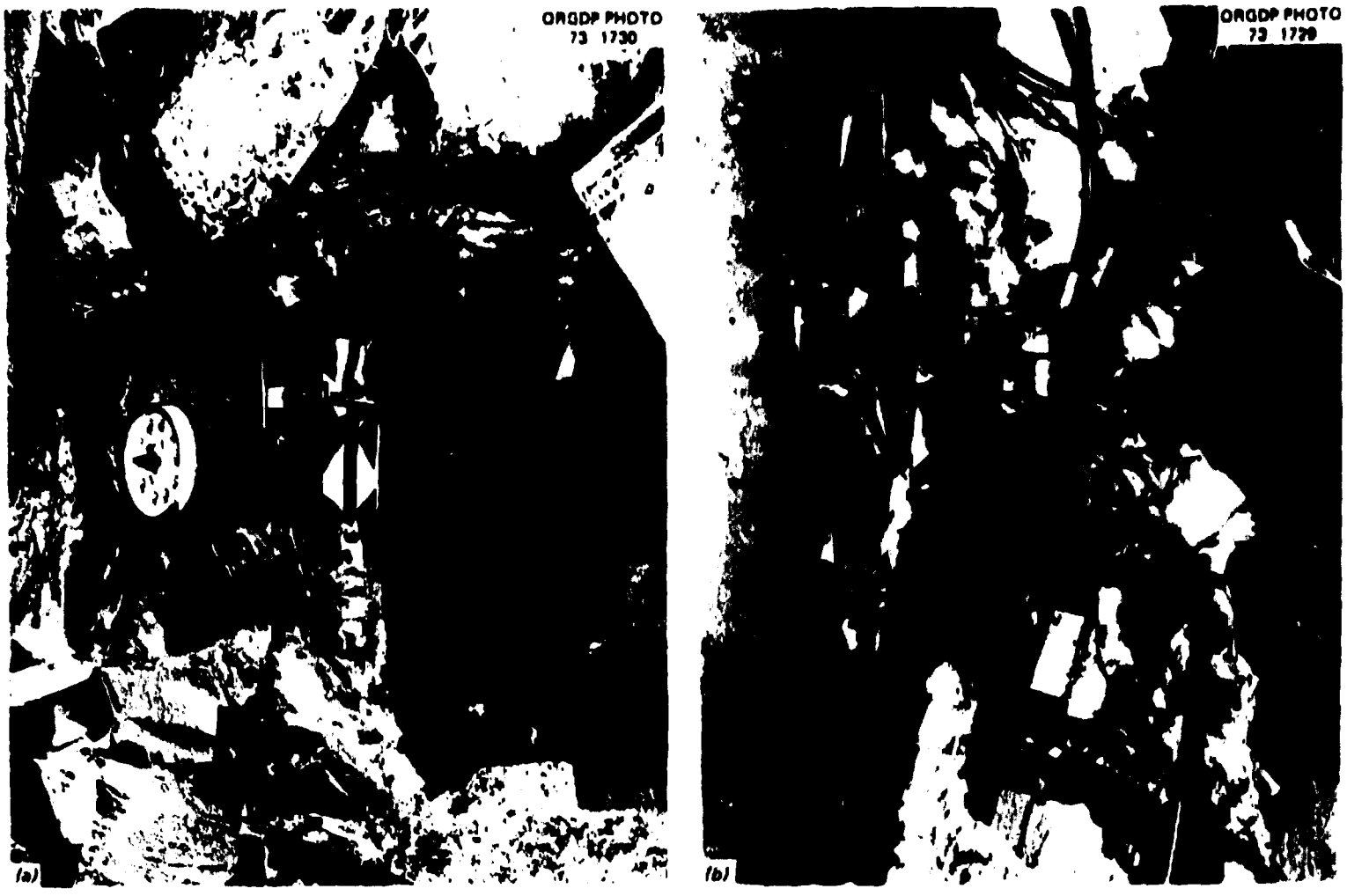

Fig. 3.31. View of outside flaws after failure (weld metal flaw A, on right) — intermediate test vessel V-6.

occurred. flaw A. is on the right. A section of the vessel was cut out in order to examine the inside surface flaw. which is shown in Fig. 3.32. A full view of V-6 in Fig. 3.33 shows quite clearly the degree of barreling and local yielding. Huge shear lips can be seen in the closeup in Fig. 3.34.

Acoustic Surveillance During Testing of Intermediate Test Vessels V-3, V-4, and V-6*

During the pressure tests, this series of vessels was acoustically monitored by Westinghouse Nuclear Energy Systems. A report[16] of these efforts by Schmidt and Lumetti is summarized below.

Introduction

An acoustic emission is a transient elastic wave that is generated when a material undergoes plastic deformation. The elastic wave is the result of the rapid release of energy when the material is strained beyond its limits of elasticity. The amplitude of the wave is a function of the fundamental metallurgical structure of the material (i.e., grain size).

The monitoring of acoustic emission activity and concurrent recording of its behavior over a given time period shows promise as a technique for predicting inception of flaw growth. A significant effort is being made to develop this technique as a nondestructive testing tool for in-service monitoring of the integrity of nuclear reactor pressure vessels and pressure boundaries.

To obtain additional data for developing this technique, Westinghouse Nuclear Energy Systems participated in this series of vessel rupture tests conducted by ORNL to (1) evaluate the capability of an acoustic monitoring system to locate acoustic activity, (2) obtain base-line acoustic emission data under conditions of impending vessel rupture, and (3) gain additional knowledge of acoustic emission phenomena.

System description

A simplified acoustic emission monitoring system is shown in Fig. 3.35. The acoustic wave propagating on the metal surface is converted to an electrical signal by the transducer. The analog amplifier stage adds the necessary gain, and the discriminator stage converts the signal into digital form. The on-line analysis and readout equipment was unique for each of the three vessel rupture tests in which Westinghouse participated. The basic operational functions of the on-line and readout equipment consisted of totalizing, triangulating, and displaying acoustic events. Both analog and digital signals were recorded on magnetic tape for subsequent laboratory analysis.

Transducers

The transducers are designed to provide optimum efficiency in the 300- to 700-kHz range and to operate at temperatures in excess of 550°F and at radiation exposures >100 R/hr with no degradation in sensitivity. They are held in place by magnetic mounts which incorporate a loading spring.

---

*Work performed by Westinghouse Electric Corporation for the Oak Ridge National Laboratory and supported in part under Purchase Order 11Y-7327V.

Fig. 3.32. View of inside flaw (weld metal) after failure – intermediate test vessel V-6.

PHOTO 417' 74

Fig. 3.3A Full view of intermediate test vessel V-6 after failure.

Fig. 3.34. View of post-test fracture in intermediate test vessel V-6.

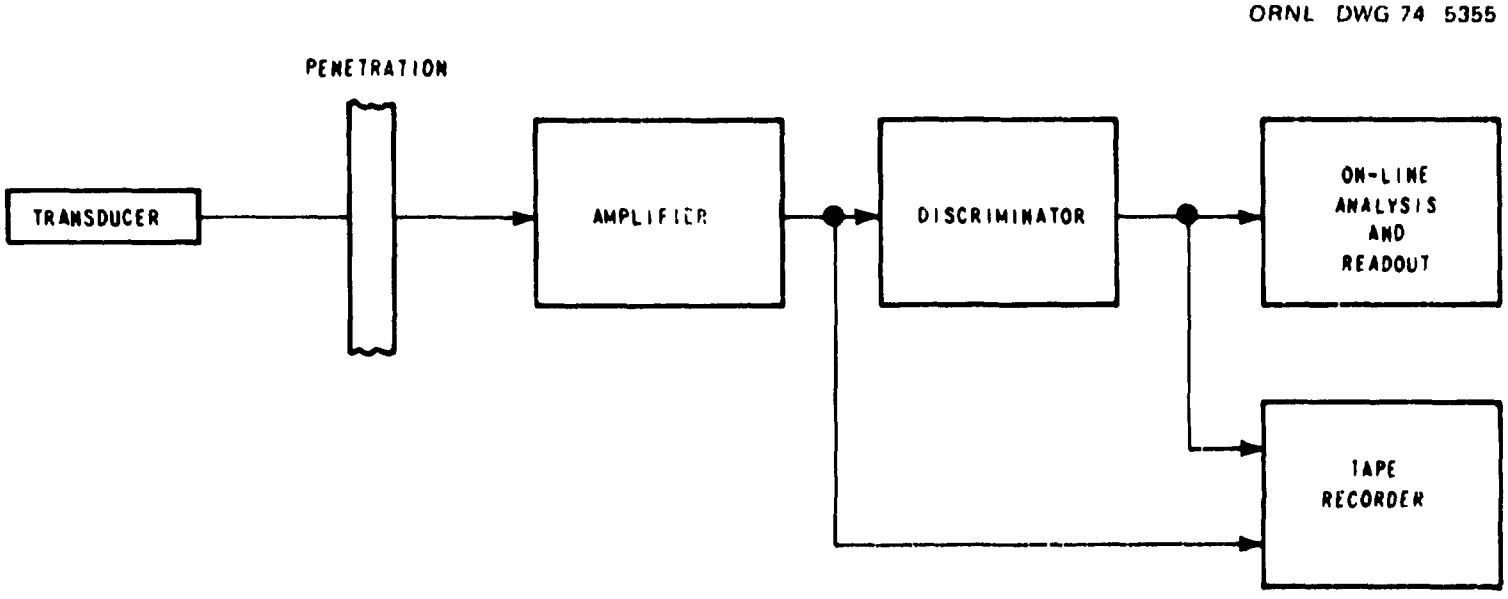

Fig. 3.35. Simplified block diagram of the acoustic emission monitoring system.

Amplifier/discriminator

The electrical signals are conditioned by a low-noise, high-gain (80- to 100-dB) amplifier. A bandpass filter with sharp cutoff characteristics (60 dB per octave) is used to pass only frequencies in the range of 300 to 700 kHz. The filtered and amplified signal then goes into the discriminator stage, which employs an adjusted threshold voltage to eliminate unwanted background noise. Analog signals above the threshold voltage produce digital pulses which go to various analysis units.

Analysis and readout

The digital pulses are used as input for various analysis equipment. The totalizer sums the digital pulses and provides an analog signal for strip-chart recording. The Westinghouse hyperbolic triangular display measures the signal and visually displays the acoustic emission location by energizing a light-emitting diode (LED). The LED unit is a free-standing system, operated from a NIM-BIN supply, requiring no computer or other support equipment. The LED matrix coordinates correspond to a location found from a hyperbolic map which includes transducer position information. The computer-controlled Westinghouse on-line triangulation system measures the time differences between signals for an unlimited number of acoustic channels. Using the time difference information and the transducer position information, the system locates the source of the acoustic event and displays it on a CRT. The CRT display shows a planar layout of the structure under surveillance, the transducer locations, and a history of triangulated acoustic events. A listing of triangulated acoustic event coordinates is provided by a hard-copy unit and a teletype listing.

Test of intermediate test vessel V-3

A flaw was placed in the side of vessel V-3 as shown in Fig. 3.36. The outside surface of the vessel was covered with plate coils for heating which were tightened in place with a bolt and clamp arrangement. After the installation of the heating coils, there was a ribbon of space about 1 in. wide along the girth and length of the surface of the vessel. The acoustic transducers were located within this inch of space. The transducer mounts in this test were glued to the vessel.

Four transducers were used to monitor the test vessel. Figure 3.36 also shows the layout of the four transducers. Because of the surface space limitations imposed by the heating jackets, the existing magnet mounts could not be used. Instead, alternate mounts were installed with Eastman 910 cement.

A fifth transducer was attached to the vessel and was pulsed with a pulse generator. The sensitivity and response of each transducer and also the signal propagation time for the vessel were determined in this manner.

Figure 3.37 shows the totalized acoustic counts for channel 1, which exemplifies the responses obtained. All four transducers showed an exponential increase in activity. The on-line analysis equipment accurately described the shape and location of the flaw.

Test of intermediate test vessel V-4

Figure 3.38 illustrates the array used to monitor the acoustic emission activities originating from the two flaws. The transducers were mounted using magnetic holders, and proper operation of the transducers was ensured by placing an electronic pulser on the vessel and monitoring the response. The transducers were coupled to the electronics using 150-ft runs of RG-22 B/U cable.

Figure 3.39 shows the acoustic counts detected as a function of pressure for channel 1. Failure was preceded by relatively few emissions, most probably due to brittle fracture.

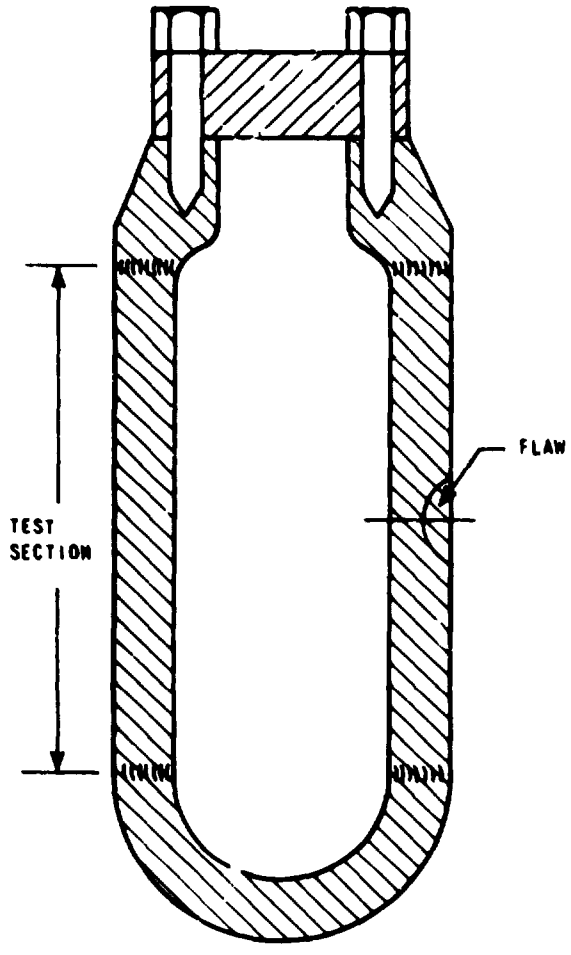

CROSS SECTION OF TEST VESSEL

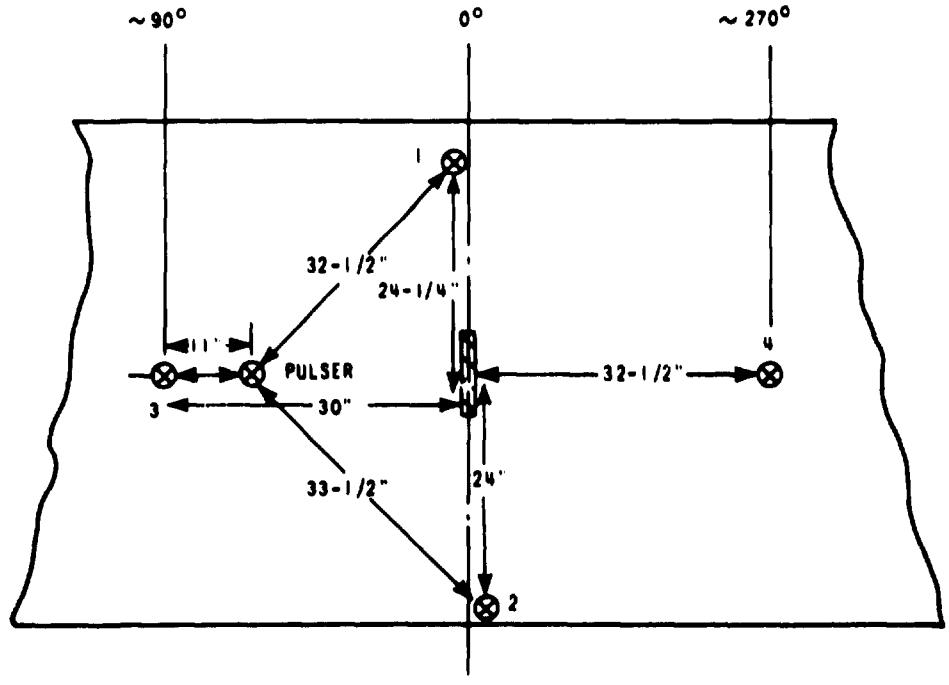

PARTIAL DEVELOPMENT OF EXTERIOR SURFACE SHOWING TRANSDUCER LOCATION

Fig. 3.36. Test specimen and transducer array -- intermediate test vessel V-3.

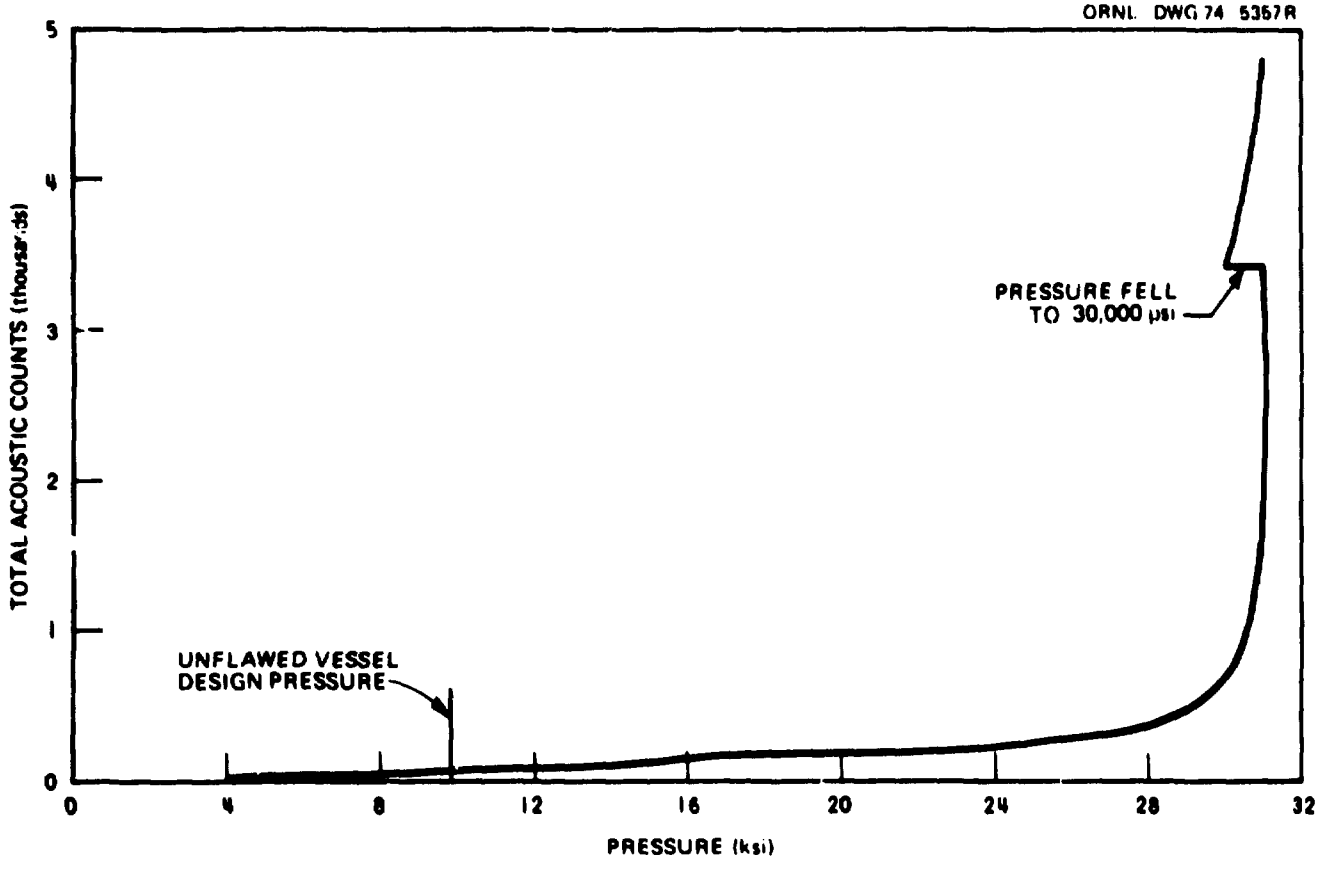

Fig. 3.37. Total acoustic counts vs applied pressure, channel 1 – intermediate test vessel V-3.

ORNL - DWG 74-5358R

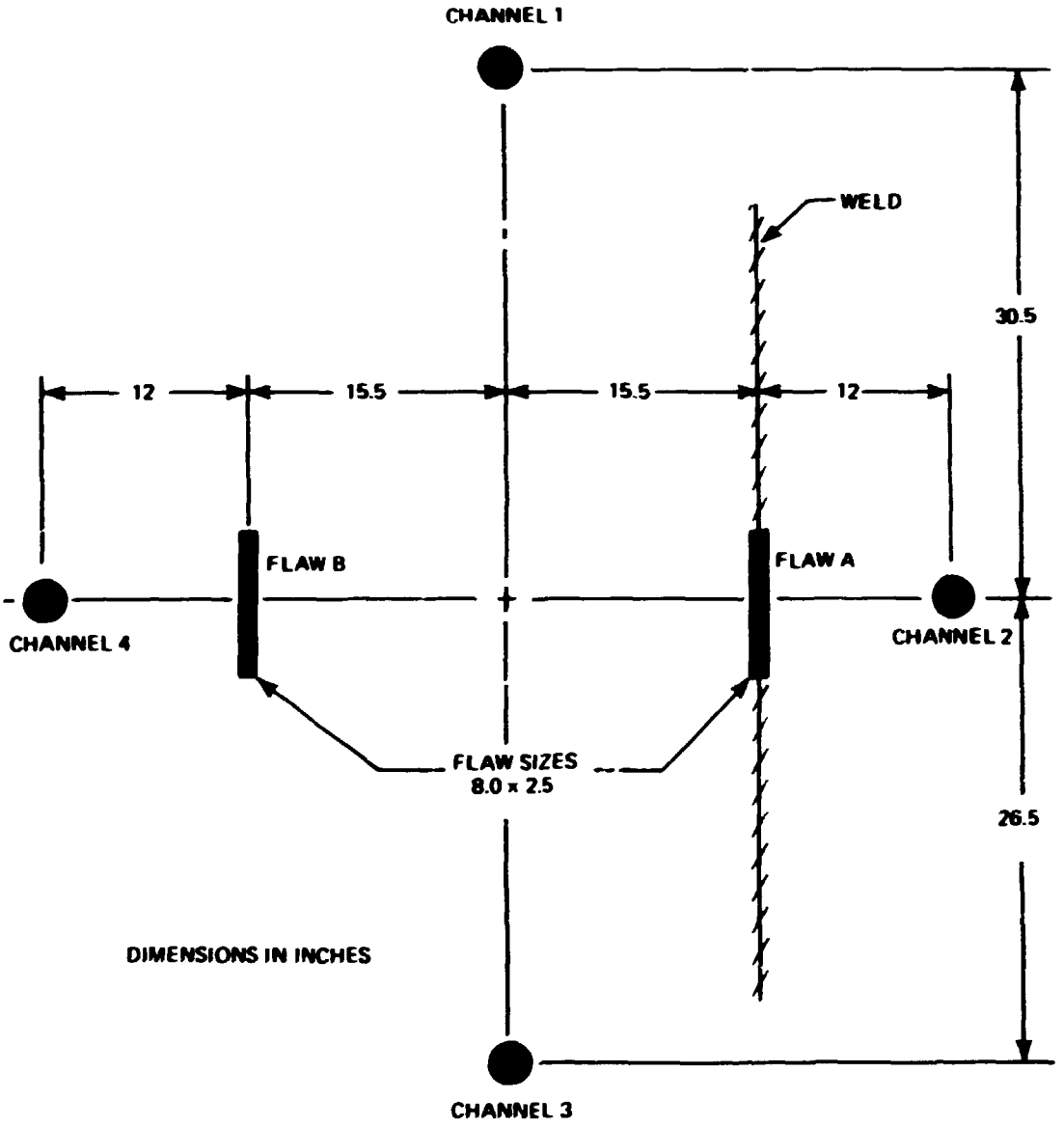

Fig. 3.38. Transducer array – intermediate test vessel V-4.

During the test the acoustic emission activity was monitored on an oscilloscope. Channels 2 and 4 were chosen for monitoring because of their proximity to the weld and base metal flaws, respectively. Throughout the test the weld flaw acoustic emission activity was greater; count-vs-pressure curves also indicate more activity in the weld flaw area.

Triangulation was accomplished on the acoustic emissions originating from both flaws. The greatest number of triangulated emissions occurred during pressurization from 26,000 psi to rupture. These triangulated emission locations concentrated near the top of the weld flaw.

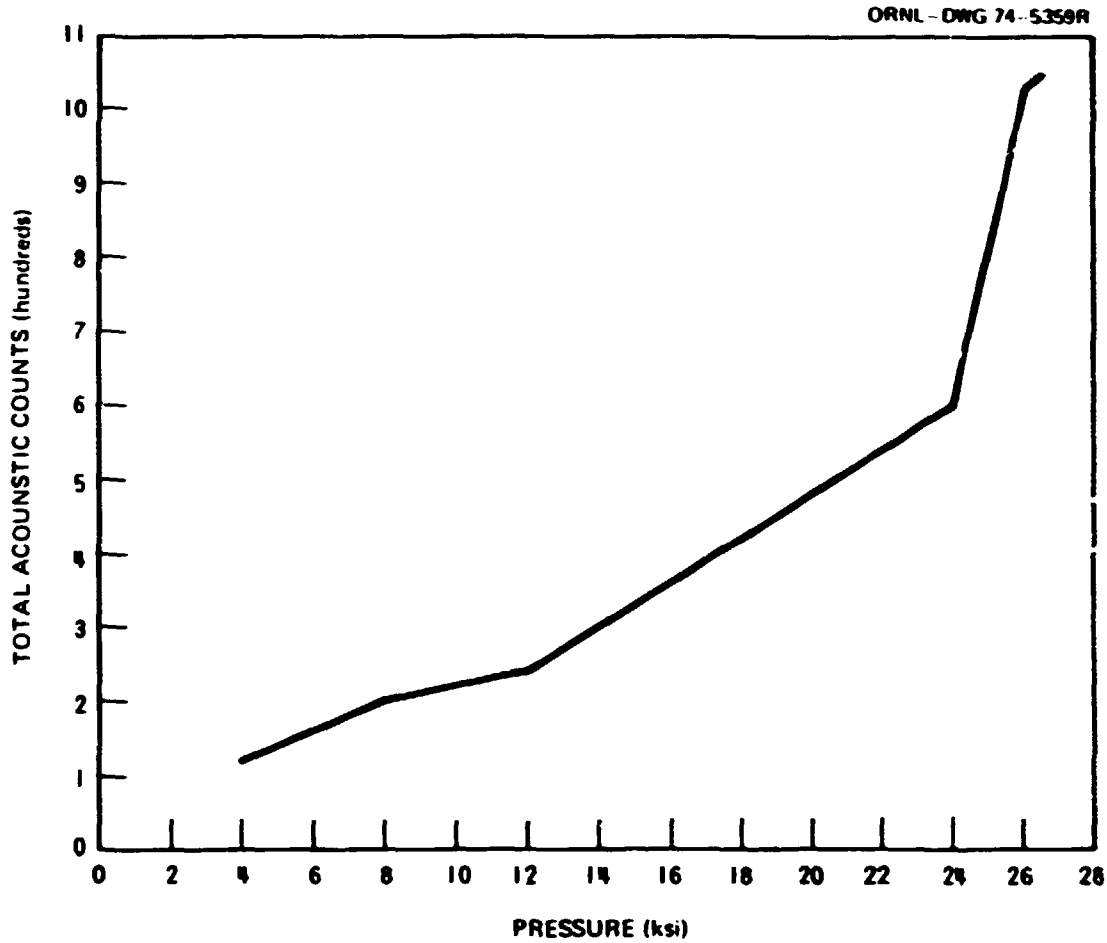

Fig. 3.39. Total acoustic counts vs applied pressure, channel 1 – intermediate test vessel V-4.

Test of intermediate test vessel V-6

Three flaws were cut in vessel V-6 as shown in Fig. 3.40. Flaw A was located on the vessel exterior 0° weld line, flaw B was on the exterior base metal, and flaw C was on the 180° weld line in the vessel interior. The vessel temperature was maintained at 190°F with heating sleeves and heated circulating fluid.

In addition to the eight transducers used in monitoring the test specimen, three transducers were installed to be used as simulators. The function of the simulators was to ensure adequate transducer sensitivity and coupling and proper amplifier gain, and to assess the on-line analysis and processing equipment performance prior to testing.

The transducers and simulators were held in place by magnetic mounts which adjusted to the contour of the test vessel. Figure 3.40 also shows the transducer and simulator positions. Optimum selection of transducer positions was not possible due to the ORNL strain gage and heating strip locations.

Figure 3.41 shows the acoustic counts as a function of applied pressure for channel 2. The characteristic exponential curve, indicative of gross flaw failure, is not predominant. The counts reflect the acoustic activity of the total vessel rather than the state of an individual flaw. Prior to failure, two of the flaws most

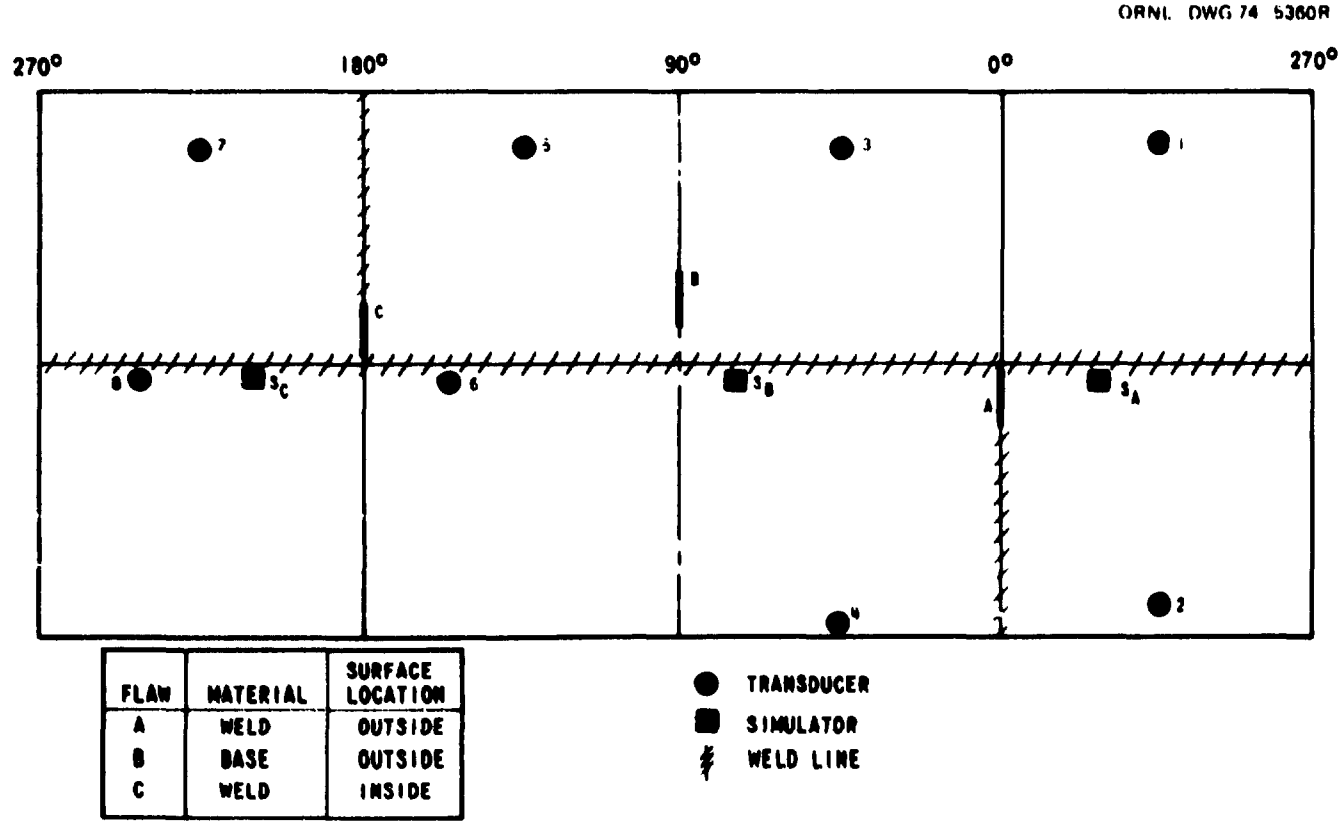

Fig. 3.40. Test specimen and transducer array – intermediate test vessel V-6.

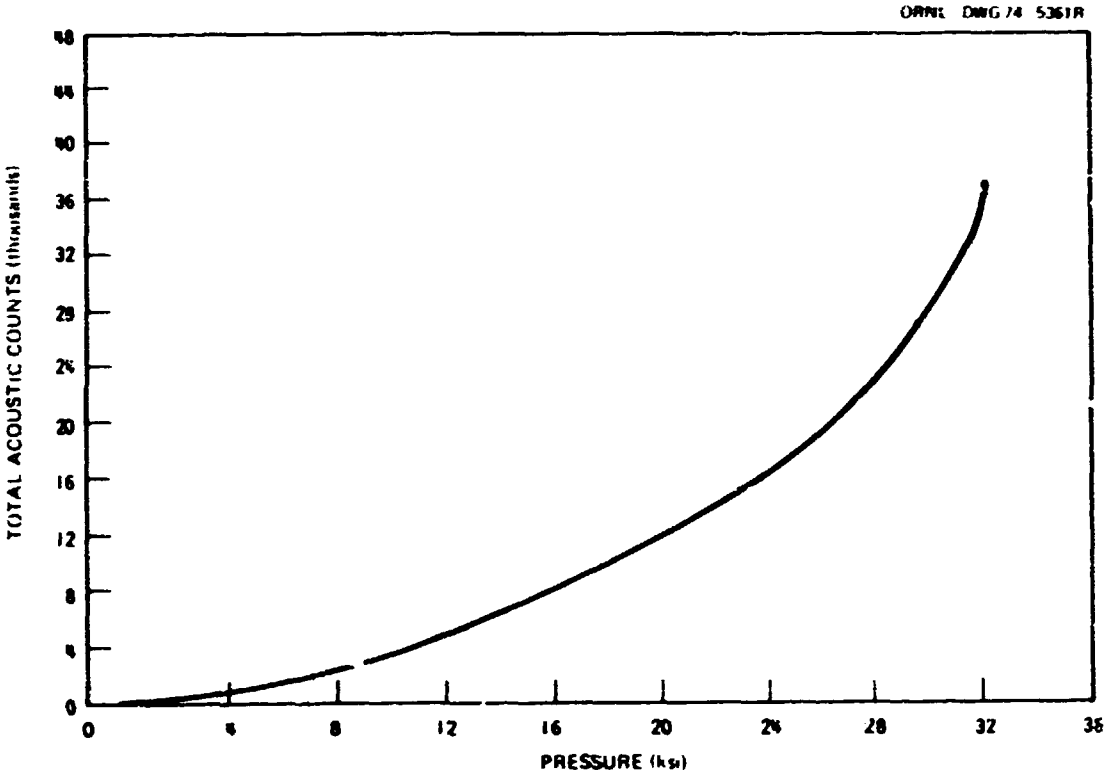

Fig. 3.41. Total acoustic counts vs applied pressure, channel 2 – intermediate test vessel V-6.

probably had not reached a critical state and thus did not emit acoustic activity at an exponential rate. The critical flaw activity would be at an exponential rate, and the resulting total vessel activity is the sum of the two noncritical and critical flaws.

The total counts for the transducers in the proximity of the critical flaw would not necessarily be definitive due to the relatively small vessel size, resulting in limited attenuation and "wraparound" of signals. Also, the total counts did not reflect the valuable information obtained during pressure holding periods. Totalization during holding was not possible due to the use of an ultrasonic pulser to monitor crack growth. The operation of an ultrasonic pulser was incompatible with the on-line acoustic data acquisition equipment being used.

The acoustic monitoring during holding is indicative of the integrity of the reactor vessel. During a static condition, only a few emissions are expected from uniformly stressed material; however, if a flaw is propagating, the stress intensity can increase even at a constant pressure. It is during the increase in stress intensity that plastic deformation will proceed, resulting in acoustic emissions. While holding at 32,000 psi, the vessel ruptured at flaw A.

Analysis of the rate of emissions appears to better exemplify the instability of the structure under surveillance (Fig. 3.42). The onset of failure coincided with a major increase in the rate of emissions.

During the final pressure increase to 32,000 psi, the count rate, with the exception of one channel, exceeded 1000 counts/min (typical 1350 counts/min). Secondary peaking in the rate occurred, with the major secondary peak at 27,000 psi. This is probably due to structural yielding, which results in continuous low-amplitude emissions.

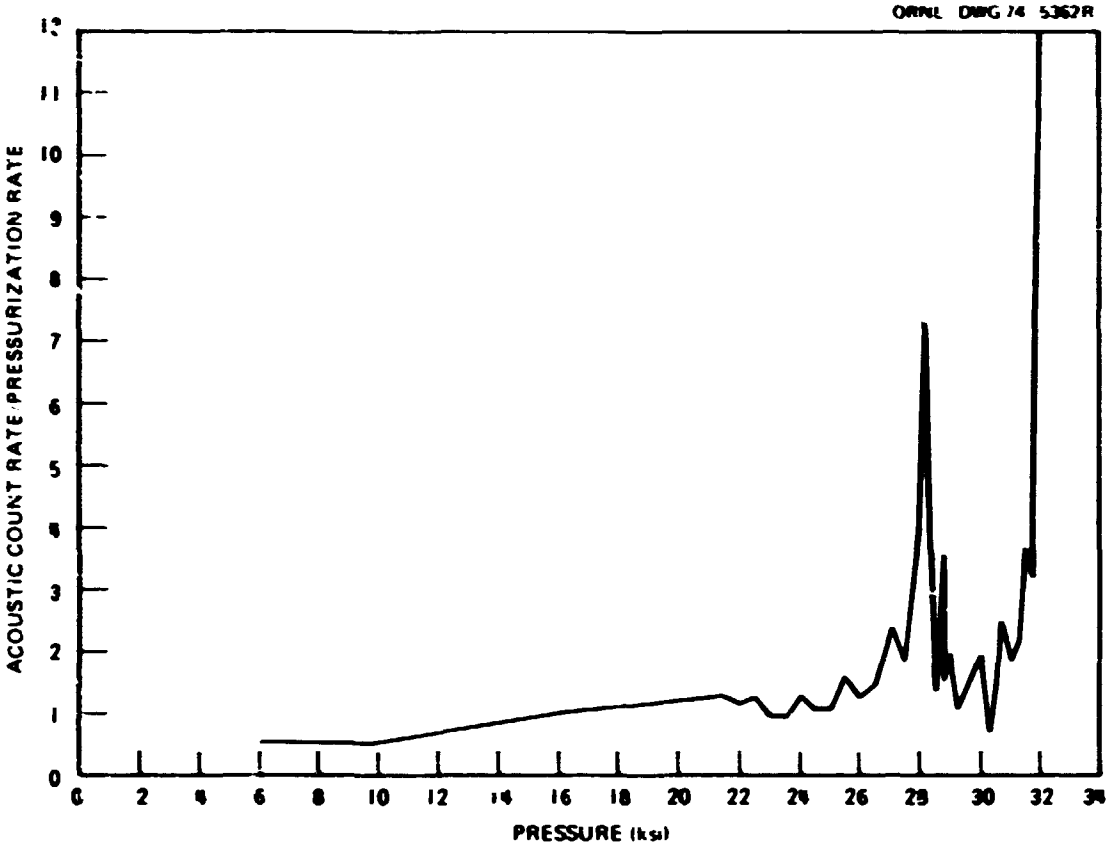

Fig. 3.42. Acoustic counts/ΔP vs applied pressure, channel 2 – intermediate test vessel V-6.

In the initial stages of testing, the majority of triangulated emissions concentrated in the vicinity of flaw C. This trend continued until approximately 29,000 psi, when most of the emissions triangulated near flaws A and B. The final pressure increase from 31,750 to 32,000 psi resulted in the most triangulations. A holding period followed, during which totalizing was not possible due to an ultrasonic pulser, but data were recorded on tape. During subsequent tape playback of triangulation in the zone encompassing flaw C, the ultrasonic pulser was inhibited to permit triangulation in zones A and B. Figure 3.43 shows the triangulations near flaw A during these 2 min of holding at 32,000 psi.

Ultrasonic Monitoring of Crack Growth

An attempt was made to ultrasonically monitor the crack growth at the three flaws in V-6. K. K. Klindt and S. P. Baker of ORNL were in charge of these efforts. The equipment used was an Automation Industries model 725 "immerscope," two Sperry model 721 "Reflectoscope" ultrasonic detectors, three 5-MHz $\frac{3}{4}$-in.-diam ultrasonic transducers, and one Sony model EV 310 video tape recorder modified to operate with an external sync generator. A network was built to modify the video signal and detector sync pulse in order to make them compatible with the tape recorder.

Each of the three transducers were oil-coupled to the outer surface of the vessel at a notch location and were held in place with magnets. The transducer for the inside flaw was positioned directly through the wall

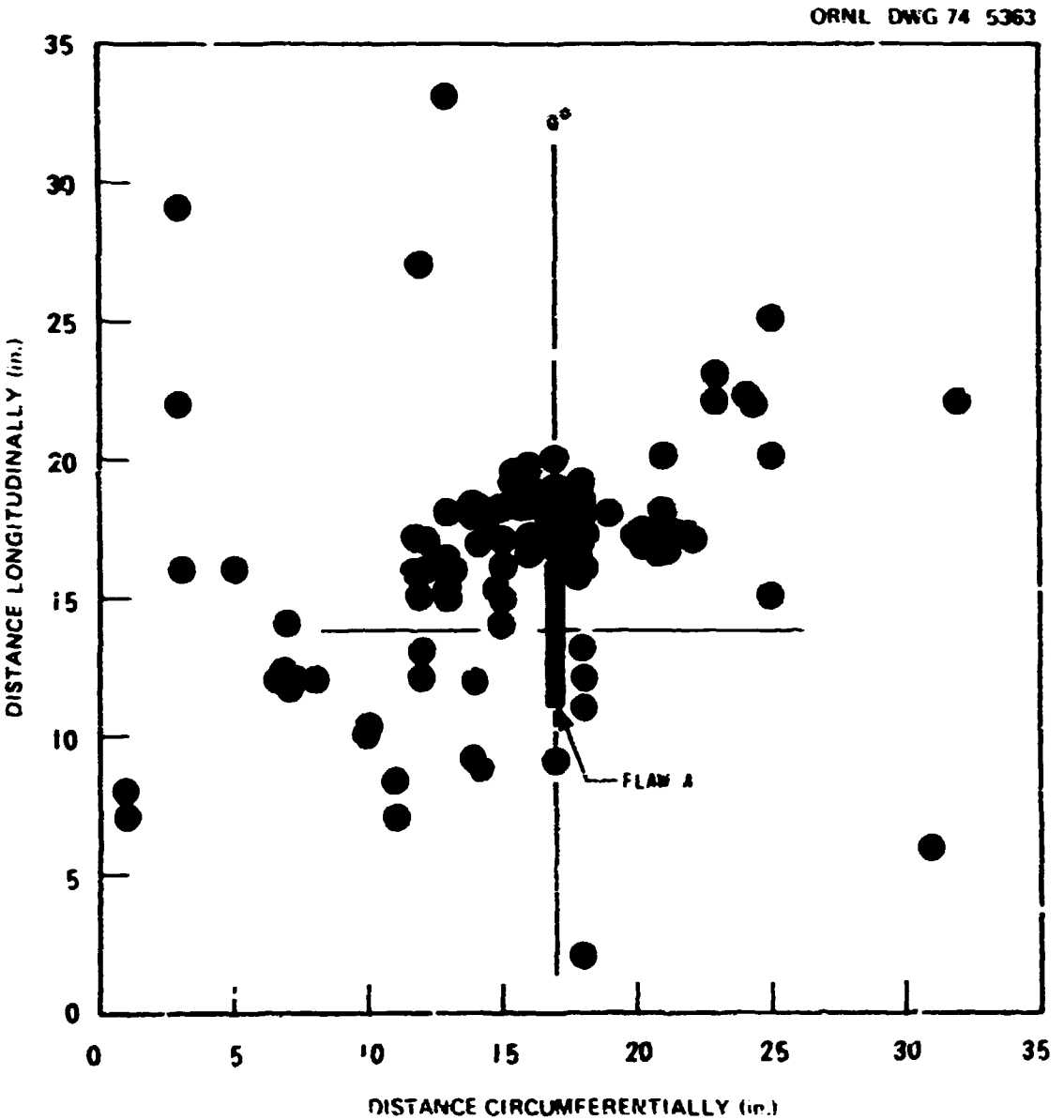

Fig. 3.43. Triangulated acoustic emissions during 2-min hold at 22,000 psi – intermediate test vessel.

from the flaw. Transducers for the outside flaws were positioned so that the ultrasonic waves were reflected from the inside surface and back to the crack front.

The three transducers were each monitored by a separate ultrasonic detector in order to simultaneously view the action at each flaw. With only one video recorder, the selection of the flaw to be recorded during the pressure hold periods was arbitrary and depended upon the activity observed at each flaw. Unfortunately, the vessel failed during the switching operation, thereby precluding the recording of the notch activity at failure and indicating the need for a separate tape recorder for each flaw on future tests.

Nevertheless, crack growth from ultrasonic indications was observed on the inside flaw, and valuable base-line information and experience were obtained that will be useful in future tests.

Small Steel Models and Strain-Gage Development

Eight 5½-in.-diam 0.85-in.-wall steel models (a scale factor of 7.06) were tested to provide information on which to (1) base understanding and predictions of full-scale vessel behavior and (2) properly determine flaw sizes and temperatures of the intermediate vessel tests. The results are summarized in Table 3.2. See Appendix F for a complete tabulation of strain data.

Since there were to be three flaws in vessel V-6 when tested, three of the models were tested to establish the behavior of the flaws projected for vessel V-6. The target size for the flaws to produce significant nominal strain at failure in vessel V-6 was 1¾ in. deep by 5 in. long. Two flaws were to be located on the outer surface (one in base metal and one in weld metal), and one was to be on the inner surface in weld metal.

Three model vessels were tested to failure at 200°F, the highest test temperature chosen to that date. The cylindrical bodies of these vessels were from vessel V-4 prolongation and were fabricated as described in Ref. 1. The flaws were placed in base metal alone.

Since some analyses showed that inside surface flaws would be much more severe than similar-sized outside surface flaws, the behavior of model vessel V4.7 suggested that a larger flaw could be tolerated. Two additional vessels were tested with flaws about the same size, one containing an inside surface flaw and the other an outside surface flaw, both modeled after the target flaw size for vessel V-6. Within the usual scatter, it was concluded from the last two tests that an inside surface flaw is no more severe than an outside surface flaw of the same size for the cylindrical geometry being investigated. Also, from prior intermediate vessel tests, it was concluded that significant nominal strain would be obtained for an intermediate vessel containing the target flaw size on the outside surface; this conclusion was supported by the data from the tests discussed here.

The model tests were performed in a water bath. In the initial tests, all the strain gages ceased to function properly on the first two model vessels (V4.7 and V4.6) prior to failure. The gaging techniques employed at that time on the inner surfaces depended on the integrity of the layer of a microcrystalline wax, which melts at about 170 to 180°F. Additional layers of a flexible two-part coating (Micro-measurements M-Kote 5) were added to retain the wax until the pressure built up to the point at which the wax refroze. The vessels were regaged using improved techniques and retested, and the last model vessel tested (V4.4) had a high gage survival rate. The improved techniques were used in gaging the inside surface of vessel V-6.

In addition to the above strain gage installation, eight experimental weldable strain gages (Ailtech SG-125) were used on the inside of V-6. The successful results of these gages (shown in Table 3.3) provide an alternate gage installation for future tests. This type of gage installation had never been used on tests above 10,000 psi hydrostatic pressure.

Although the weldable gage installation costs more, it has some advantages over the foil-gage installation. The time required for installation is about one-half that of the foil gage. The gage is also useful to higher temperatures, and its sensitivity exhibits less change at higher pressures. The latter was determined by the same qualification methods described in Ref. 1. It was concluded, however, that the foil gage would be slightly more preferable if the test temperature is 150°F or below and pressures greater than 30,000 psi are anticipated. J. H. Butler, ORNL, performed the qualification tests of the weldable gages.

Table 3.2. Summary of test data for small steel models tested for V-3 V-4, and V-6

(See Appendix F for a complete tabulation of strain vs pressure.)

Model No.	Date tested	Model diameter (in.)	Test temperature (°F)	Material tested	Model of intermediate vessel No.	Flaw depth (in.)	Size length (in.)	Orientation	Failure conditions		Mode of failure
									P_f (ksi)	λ_f (%)	
V3-A4	12/8/72	5½	130	V-3	V-3	0.38	1.42	Outside	31.8	2.75	Leak
V2-A1-C	1/24/73	5½	130	V-2	V-4	0.37	1.10	Outside	33.3	2.11	Burst
V2-A1-E	2/27/73	5½	130	V-2	V-4	0.37	1.20	Outside	33.5	2.31	Burst
V4.7	4/12/73	5½	200	V-4	V-6	0.15	0.52	Inside	37.5	>2[a]	
V4.6	4/25/73	5½	200	V-4	V-6	0.26	0.88	Inside	34.2	1.23	Burst
V4.4	5/1/73	5½	200	V-4	V-4	0.25	0.83	Outside	34.5	2.81	
V4.2	8/10/73	5½	130	V-4	V-4	0.44	1.150	Outside	33.0	1.702	Burst
V4.1	11/2/73	5½	130	V-4	V-3	0.221	1.204	Outside	33.1	2.20	Burst

[a]Strain data not reliable because gages failed.

Table 3.3. Summary of Ailtech weldable SG-125 strain gage performance

Gage No.	Strain encountered (%)	Ultimate integrity	Pressure at failure of gage[a] (psi)	Survival pressure (psi)
108	1.55	Failed	28,750	
102	1.6	Failed	30,000	
103	1.5	Failed	30,000	
107	2.97	Failed	31,250	
101	2.38	Failed	31,000	
104	7.03	Survived		31,900
112	6.57	Survived		31,900
106	4.36	Survived		31,900

[a]Failure mode in all cases was a short to ground with collapsed housing.

4. FRACTURE ANALYSIS METHODS AND RESULTS

Analytical Implications of the Test Results from Series 1, Intermediate Test Vessels V-1 and V-2

The experimental and analytical results obtained from series 1 of the intermediate test vessels,[1] consisting of vessels V-1 and V-2, were studied carefully to determine the types of improvements needed in the methods of analysis being applied to the vessels. The test results from vessel V-2, which was tested at 32°F, showed that the estimates of fracture strain based on linear elastic fracture mechanics were quite accurate. These results also indicated that an accurate elastic-plastic stress analysis of the cylindrical region of the unflawed vessel should be used to relate the estimated failure strain to the corresponding failure pressure, or the reverse. Furthermore, the test results obtained from vessel V-2 indicated that the occurrence of nominal plastic strain in the region of a surface flaw in a cylindrical pressure vessel does not necessarily elevate the fracture toughness above its plane strain value, even though this appears to occur in the case of surface-cracked tensile bars, through-cracked beams, and through-cracked plates loaded in uniaxial tension.

The test results from vessel V-1, which was tested at 130°F, indicated that substantial stable crack growth (slow crack extension under rising load) had probably occurred before final failure and that the onset of failure was probably induced by the onset of plastic instability in the region surrounding the slowly growing flaw. For future tests, it was deemed desirable to attempt to develop a means for nondestructive measurement of the amount of stable crack extension that occurs during a test as a function of the applied load. This development was eventually successful (see Chapter 2), and an attempt was made to measure stable crack growth during the test of vessel V-6 (see Chapter 3). While it was possible to estimate the pressure at the onset of plastic instability near the flaw for vessel V-1, an estimate of the corresponding nominal strain at failure was deferred, pending the development of the elastic-plastic stress analysis mentioned above, including the effects of strain hardening. Model data could have been used for this purpose, but the effects of yield stress variations through the thickness of the prolongation materic due to quenching made such estimates somewhat uncertain.

The fracture analysis methods applied to vessels V-1 and V-2 were examined to determine which methods could best be expected to produce reasonable estimates of failure conditions within definable ranges of temperature and flaw size, which methods were potentially suitable for application to the design and safety analysis of actual reactor pressure vessels, and the types of improvements needed for each of the methods. For predicting failure prior to the onset of through-thickness yielding, an estimate of the failure strain by linear elastic fracture mechanics, with the corresponding failure pressure being determined from a computed nonlinear pressure-strain curve, appeared to be the best approach. A more accurate method for estimating the nonlinear pressure-strain curve was the improvement most needed to improve the accuracy of this method with respect to pressure. For failure in the fully plastic range of strain, the equivalent-energy method had shown reasonable potential accuracy. The improvement most needed in this method was a consistent procedure for estimating the shape factor in the basic equation of the method. The test data being obtained from the 1/7-scale steel models of the intermediate test vessels were considered to be the best basis for this improvement.

The British stress concentration method,[1] although reasonably accurate in the fully plastic range, was known to be potentially unconservative at low temperatures, because of its strong dependence on total tensile elongation, which does not vary strongly with temperature just below the upper shelf.[17] Further applications of this method were left to its proponents. The tangent modulus method, while still in an early

stage of development, had shown good accuracy with respect to the first six intermediate tension specimens.[1] Its trial application to vessel V-2 had helped to reveal the difference in toughness behavior, in the presence of plastic strain, between surface cracks in the cylindrical region of a pressure vessel and surface cracks in tension specimens. This method was considered worthy of further development, provided that it could successfully analyze at least some of the existing steel model test data. The plastic instability method[1] of analysis had proven accurate for vessel V-1, and this accuracy was expected to be maintained in the upper-shelf temperature range. The improvements most needed in this method were a quantitative procedure for modeling stable crack growth and the same elastic-plastic stress and strain analysis needed to improve the accuracy of the pressure estimate obtained from the linear elastic fracture mechanics analysis based on strain. In this case, the elastic-plasic analysis is used in the reverse manner, namely, for relating pressure to strain instead of strain to pressure.

Analyses and Evaluations Performed in Support of the Series 2 Intermediate Pressure Vessel Tests

Pressure-strain curve calculations

The analytical and experimental results of the tests of vessels V-1 and V-2 made clear the desirability of predicting both the pressure and the strain at failure for the intermediate test vessels. Therefore, an effort was undertaken to develop a closed-form elastic-plastic stress and strain analysis of a thick-walled hollow cylinder, considering both the ideally plastic and the strain-hardening branches of the type of stress-strain curve characteristic of low-alloy pressure vessel steels. For example, a typical stress-strain curve for A508 class 2 forging steel is shown in Fig. 4.1. The analytical development required was the extension of the existing solution of Bland,[18] which used the Tresca (maximum shear stress) yield criterion and a bilinear

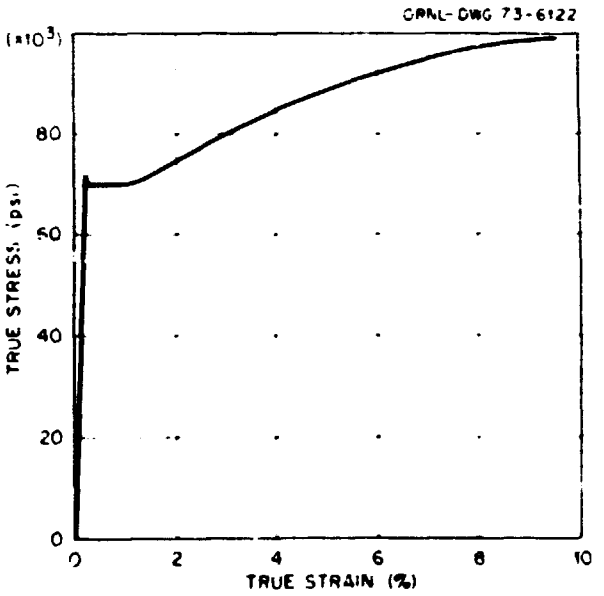

Fig. 4.1. Typical circumferential stress-strain curve at half thickness from intermediate test vessel V-1 prolongation.

(elastic-linear strain hardening) stress-strain curve, to consider a trilinear stress-strain curve describing an elastic ideally plastic linear strain-hardening material. This development proved to be quite straightforward, especially since, for the ratio of the outer to the inner radii of the intermediate test vessels, no more than one internal boundary ever exists between regions of different material behavior at any given load level. Since ideally plastic (zero strain hardening) behavior is a special case of linear strain hardening, it was not necessary to derive or solve any new differential equations.

The results of an analysis of an intermediate test vessel cylinder based on a trilinear stress-strain curve are shown in Fig. 4.2. The value of the yield stress used for this calculation was 75 ksi, and the linear

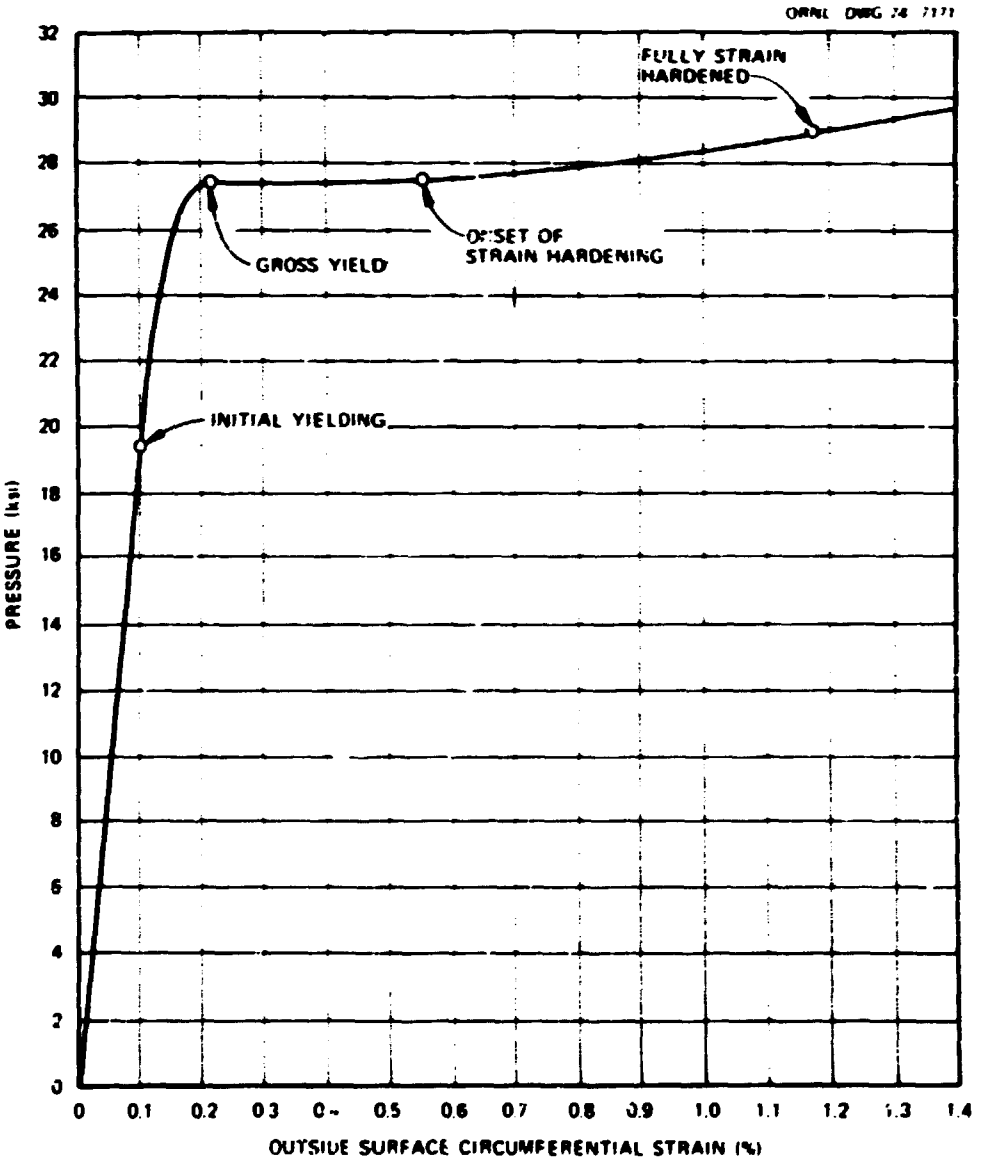

Fig. 4.2. Calculated pressure vs outside circumferential strain curve for intermediate test vessel geometry based on a yield stress of 75 ksi, the Tresca (maximum shear stress) yield criterion, and a trilinear stress-strain curve.

strain-hardening branch of the stress-strain curve was a straight line intersecting the curve shown in Fig. 4.1 at the strain values of 1.2 and 4.0%. The point labeled "initial yielding" in Fig. 4.2 is the point at which yielding first occurs at the inside surface of the vessel. Under increasing pressure, the ideally plastic region expands radially outward from the inside surface of the vessel until the point labeled "gross yield" is reached, at which point the vessel cylinder is completely yielded through the thickness. This is the ideally plastic collapse pressure for the vessel cylinder. At this pressure the vessel expands radially outward until strain hardening commences at the inside surface, which occurs at the point labeled "onset of strain hardening." Under increasing pressure, the strain-hardening region then expands radially outward from the inside surface of the vessel until the point labeled "fully strain hardened" is reached, beyond which the entire cylinder is in the strain-hardening range of strain. Following these initial calculations, the analysis was completely reviewed, and a computer program was written for performing the calculations.[19] Appendix C describes this analysis in more detail.

Transverse restraint effects

Perhaps the most elusive of all the phenomena involved in the process of fracture is the phenomenon called transverse restraint. Fundamentally, this term describes the inability of the plastic zone at the tip of a crack to freely contract in length along the crack front, because of the restraining effects of the surrounding elastic material. The more this contraction is prohibited, the higher is the tensile stress acting in the plastic zone in the direction parallel to the crack front and, consequently, the higher is the hydrostatic tensile component of stress in the plastic zone.[20] The hydrostatic tensile component of stress in the plastic zone is considered to be directly related to the value of the fracture toughness, because, at least implicitly, the ductility of the material in the plastic zone at the tip of a crack is considered to decrease as the hydrostatic tensile component of stress increases.

In conventional fracture toughness testing, the effects of transverse restraint are usually expressed in terms of the ratio of the computed plastic zone size to the specimen thickness. In fracture analysis, attempts have been made to implicitly correlate the amount of nominal plastic strain developed in the region of a flaw, normal to the plane of the flaw, with the degree to which transverse restraint has decreased and therefore fracture toughness has presumably increased.[1] Comparison of the test results from vessel V-2 with the pretest and posttest calculations indicated that the development of nominal plastic strain in the region of the flaw, normal to the plane of the flaw, does not necessarily elevate the fracture toughness. Nevertheless, this had appeared to be the case for the surface-cracked intermediate tension specimens tested previously.[1] Consequently, it was considered imperative to obtain, from existing data if possible, a more complete and fundamental understanding of the phenomenon of transverse restraint, so that this phenomenon could be properly considered in subsequent analyses of intermediate test vessels. For this purpose, the experimental data obtained from surface-flawed intermediate tension specimen 15, which was tested at −40°F, proved to be extremely useful, because the specimen failed in the linear elastic range of stress but the material appeared to possess more than its plane strain value of fracture toughness. An analysis of transverse restraint effects for this specimen is given in Appendix E, from which it is concluded that the nominal strain acting tangential to the crack tip, in the plane of the crack, is a fundamental parameter governing transverse restraint. On the basis of this conclusion, it is postulated that, since the axial strain in a cylindrical pressure vessel under internal pressure is nearly zero, even after yielding, the fracture toughness of the material at the tip of a surface crack lying in a plane perpendicular to the circumferential direction should retain its plane strain value even after plastic strain has developed in the circumferential direction.

Stable crack growth and plastic instability

Most of the flawed steel specimens tested under the HSST program have failed in the plastic range of strain rather than in the elastic range, because of the high toughness of the material. Several of the larger specimens, both surface-cracked tensile specimens and pressure vessels, which were tested at temperatures of 130°F or higher, have apparently undergone considerable stable crack growth prior to failure and finally reached their maximum loads by what appears to be the development of plastic instability and necking in the region surrounding the flaw. An analysis of the failure of a series of 1- and 6-in.-thick flawed tensile specimens that failed in the fully plastic range of strain is given in Appendix D. It is concluded that stable crack growth and plastic instability are important modes of physical behavior that should be explicitly considered in a fracture analysis, especially for large cracks, in order to obtain consistently accurate estimates of fracture conditions for the fully plastic range of strain.

Analysis methods development

Since some inconsistencies had been observed in the values of the experimentally determined shape factor used in the equivalent-energy method of elastic-plastic fracture analysis, additional ½-scale steel model test data were obtained and analyzed to provide a better basis for estimating this parameter. These studies are described in detail in Appendix G. The most important conclusion reached in Appendix G is that the experimentally determined shape factor used in the equivalent-energy method is apparently not a constant: it is a decreasing function of flaw size and failure strain, at least in the strain-hardening range of strain. Despite its potential significance, this fact has not been considered in any of the equivalent-energy calculations for intermediate test vessels V-3, V-4, and V-6 to be discussed later in this chapter.

Concurrent with the steel model studies described above, the tangent modulus method was undergoing further development and evaluation. The principal objectives of the developments in the tangent modulus method that were accomplished between the testing of vessels V-2 and V-4 were (1) to test the hypothesis that surface flaws in tensile specimens and cylindrical pressure vessels are subject to different conditions of transverse restraint and (2) to develop a rational analytical procedure that can take this difference into account if it exists. In Appendix E, it was concluded that the transverse restraint conditions for surface cracks in tensile specimens and cylindrical pressure vessels are in fact different. In Appendix H, this hypothesis was further tested by analyzing a series of small steel model pressure vessels by the tangent modulus method without allowing for incomplete transverse restraint. This analysis was quite successful, and it was therefore concluded that the hypothesis concerning the different degrees of transverse restraint that exist for surface cracks in tensile specimens and cylindrical pressure vessels is correct and that it can be taken into account analytically. The complete details of this and other developments in the method are presented in Appendix H.

The tangent modulus method[2] is based on the equation proposed by Neuber[21] for estimating the elastic-plastic stress and strain concentration factors at the tip of a notch.

$$K_\sigma K_\epsilon = K_t^2 . \tag{4.1}$$

where the subscripts σ and ϵ denote notch tip stress and strain, respectively. Equation (4.1) has been used successfully for estimating the elastic-plastic strain range at the tip of a machined notch being cycled in fatigue,[22,23] for relating the fracture toughness of a material to basic mechanical properties and a characteristic root radius,[24] and for demonstrating that the equivalent-energy method is an approximation for estimating the value of the J integral.[25] The basic innovation in the analysis, which was also used

successfully in Ref. 24, was to define K_σ and K_ε in terms of the ratios of stress and strain increments instead of in terms of the corresponding total stresses and strains.[1] This approach was originally proposed by Drucker[26] for the case of strain only. Appendix H includes the successful analyses of several sets of fracture test data for specimens of A533, grade B, class 1 steel by the tangent modulus method. It is concluded that the method is potentially a rational and practical method of elastic-plastic fracture analysis.

Test Objectives for Series 2, Intermediate Test Vessels V-3, V-4, and V-6

The test objectives for series 1 and 2 of the intermediate test vessels are summarized in Table 4.1. The series 1 vessels each contained one external surface flaw located in base metal,[1] and the series 2 vessels contained flaws in welds as well as in base metal. Vessel V-3 duplicated the testing conditions of vessel V-1, except that the external surface flaw was located in weld metal instead of in base metal (see Fig. 2.8). Vessel V-4 contained two external surface flaws, one located in weld metal and the other in base metal (see Fig. 2.9). Vessel V-6 contained an inside surface flaw in weld metal and two external surface flaws, one in weld metal and the other in base metal (see Fig. 2.10). Failure initiated at the external surface flaw in weld metal for all three vessels of series 2.

Table 4.1. Objectives of series 1 and 2 of the intermediate test vessel experiments[a]

Test objectives	Series 1		Series 2		
	V-1	V-2	V-3	V-4	V-6
Demonstrate [illegible]th	√	√	√	√	√
Test prediction methods	√	√	√	√	√
Compare weld metal and base metal			√	√	√
Determine flaw size effects					√
Compare performance of inside and outside surface flaws					√
Observe mode and extent of crack propagation in the dynamic upper-shelf range of temperature					√

[a]Test temperatures: V-1, 130°F; V-2, 32°F; V-3, 130°F; V-4, 75°F; V-6, 190°F.

Material Properties

Extensive material property measurements were made for intermediate test vessels V-3, V-4, and V-6 using specimens taken from the prolongations of the cylindrical regions of each of the vessels. These data are tabulated, plotted, and discussed in Chapter 2 and in Appendix A. The data include tensile properties, Charpy V-notch impact energy, and static fracture toughness K_{Ic} values obtained from specimens ranging from 0.394 to 4 in. in thickness. Table 4.2 identifies the locations of specific items of material property data in this report.

Table 4.2. Locations of material property data in this report for vessels V-3, V-4, and V-6

Type of data	Metal	Specimen size	Vessel V-3			Vessel V-4			Vessel V-6		
			Table	Figure: Cutting plan	Figure: Plot of data	Table	Figure: Cutting plan	Figure: Plot of data	Table	Figure: Cutting plan	Figure: Plot of data
Tensile	Base		2.1			2.1, A.5	A.4, 6		2.1, A.5	A.8, 9	2.21
	Weld	0.178 in. diam	2.2, A.5	A.1, 2, 3	2.19	2.2, A.5	A.4, 6	2.20	2.2, A.5	A.8, 9	2.21
Charpy impact energy	Base	Std. Charpy V-notch	2.1			2.1, A.6	A.4, 6	2.22	2.1		
	Weld	Std. Charpy V-notch	2.2			2.2, A.6	A.4, 5, 6	2.23	2.2		
Fracture toughness	Base	PCVV		No data of this type		A.3	A.4, 6	2.24	A.3	A.8, 9	2.25
	Weld	PCVV	A.3	A.1, 2, 3	2.26	A.3	A.4 to 7	2.27, 2.28	A.3	A.8, 9	2.29
Fracture toughness	Base	C_v-T		No data of this type			No data of this type			No data of this type	
	Weld	C_v-T	A.6	2.15	2.31		No data of this type			No data of this type	
Fracture toughness	Base	0.85T-T[a]		No data of this type		A.7	2.17	2.30	A.8	2.18	
	Weld	0.85T-T[a]	A.6	2.15	2.31	A.7	2.16	2.32	A.8	2.18	
Fracture toughness	Base	3T-T[a]		No data of this type			No data of this type			No data of this type	
	Weld	3T-T[a]	A.6	2.15	2.31		No data of this type			No data of this type	
Fracture toughness	Base	4T-T[a]		No data of this type		A.7	2.17	2.30	A.8	2.18	
	Weld	4T-T[a]		No data of this type		A.7	2.16	2.32	A.8	2.18	

[a] 200° F only.

Pretest Fracture Strength Calculations for Vessel V-3

Since the testing conditions for vessel V-3 were intended to be nominally the same as for vessel V-1 and since the material property and estimated flaw size data required for analysis were not made available until the day before the test, only one pretest calculation, performed by the equivalent-energy method, was made for vessel V-3.

The equivalent-energy method (analysis performed by F. J. Witt, ORNL)

The static fracture toughness of a 6-in.-thick section of weld metal at 130°F was estimated by using the data given in Table A.6. Three 0.85-in.-thick compact-tension (0.85T-CT) weld specimens were tested at 130°F, and one 3T-CT weld specimen was tested at 130°F, giving a value of $K_{Ic3} = 287.0$ ksi $\sqrt{in.}$ Defining the volumetric energy ratio[13] as

$$s_{d,p} = \frac{p}{d}\left(\frac{K_{Icd}}{K_{Icp}}\right)^2 \tag{4.2}$$

and assuming this quantity to be approximately a linear function of specimen thickness resulted in the following values of $s_{d,p}$ based on the average value of K_{Icd} for d = 0.85 in.:

p (in.)	$s_{d,p}$
0.85	1.00
3.0	1.64
6.0	2.53

Note that the data from the 0.394-in.-thick specimens were not used in this estimate. Reversing Eq. (4.2) gives[13]

$$K_{Icp} = K_{Icd}\sqrt{\frac{p/d}{s_{d,p}}} \tag{4.3}$$

Consequently,

$$K_{Ic6} = 195\sqrt{\frac{6}{(0.85)(2.53)}} = 325 \text{ ksi } \sqrt{in.}$$

The estimated flaw dimensions in vessel V-3, based on ultrasonic data obtained during fatigue sharpening of the flaw, were a = 2.55 in. and 2b = 8.25 in. These dimensions differ somewhat from those given in Table 2.4. The depth dimension given here apparently neglects the reduction in crack depth caused by the machining of a flat surface around the entrance to the notch. This flat surface was necessary for seating the seal block that was used during fatigue precracking of the notch by cyclic pressurization. Because no small models fabricated from vessel V-3 material and containing flaws in welds were tested prior to the test of vessel V-3, an equivalent-energy shape factor value of C = 1.145 was calculated from the data obtained from vessel V-1 (see Table G.1). Since the estimated fracture toughness[1] of vessel V-3 weld metal exceeded that of vessel V-1 base metal by only a small amount, 311 ksi $\sqrt{in.}$, and since the estimated flaw depth in vessel V-3 was almost exactly the same as the actual flaw depth[1] in vessel V-1, identical test results

were expected from both vessels. The following series of calculations completes this estimate. Rearranging Eq. (G-1) gives

$$p_f^* = \frac{K_{I,d}}{C\sqrt{\pi a_d}} \tag{4.4}$$

Thus,

$$p_f^* = \frac{325}{1.145\sqrt{2.55\pi}} = 100.29 \text{ ksi}$$

From Eq. (G-4),

$$E_d = \frac{(p_f^*)^2}{2M} \tag{4.5}$$

and from Ref. 1, $M = 191.5 \text{ ksi}(\%)^{-1}$. Consequently, at failure,

$$E_d = 26.26 \text{ ksi} \cdot \%$$

From Eq. (G-9),

$$m = \frac{(p_f - p_Y)^{-1}}{\epsilon_{ef} - \epsilon_{eY}} \tag{4.6}$$

Therefore, using the data for vessel V-1 listed in Table G.2,

$$m = \frac{\frac{28.8}{27.6} - 1}{0.9 - 0.144} = 0.0575(\%)^{-1}$$

From Eq. (G-8),

$$\epsilon_{e0} = \epsilon_{eY} + \frac{1}{m}\left\{\sqrt{1 + m\left|2\left(\frac{E_d}{p_Y}\right) - \epsilon_{eY}\right|} - 1\right\} \tag{4.7}$$

Therefore,

$$\epsilon_{e0} = 0.144 + 17.38\left\{\sqrt{1 + (0.0575)\left|2\left(\frac{26.3}{27.6}\right) - 0.144\right|} - 1\right\} = 1.0\%$$

Based on graphical methods rather than the bilinear approximation method used above and a value of E_d = 252 psi instead of 263 psi, the originally stated estimate of failure strain was 0.9%.

From Eq. (G.11),

$$p = p_y [1 + m(\epsilon_{\theta\theta} - \epsilon_{\theta y})] \tag{4.8}$$

Consequently, the estimated failure pressure is

$$p = 27.6[1 + (0.0575)(1.00 - 0.144)] = 29.0 \text{ ksi}$$

Posttest Fracture Strength Calculations for Vessel V-3

Linear elastic fracture mechanics based on strain (analysis performed by J. G. Merkle, ORNL)

An important hypothesis resulting from the analyses of the series 1 vessels[1] and substantiated by the analyses discussed in Appendix H is that a linear elastic fracture mechanics analysis expressed in terms of strain should be accurate below gross yield and conservative thereafter. Therefore, this type of calculation was made for each of the series 2 vessels. This type of calculation was expected to be conservative for vessel V-3, because gross yielding preceded failure.

The actual flaw depth a in vessel V-3 was 2.11 in. (see Table 2.4); the fracture toughness K_c used was 325 ksi $\sqrt{\text{in.}}$; and the shape factor C relating pressure to K_I used was 1.66 (p. 183 of Ref. 1). The modulus M relating pressure to strain is 191.5 ksi (Ref. 1). The estimated failure strain is calculated from the equation*

$$\lambda_f = \frac{K_c}{MC\sqrt{\pi a}} \tag{4.9}$$

Thus,

$$\lambda_f = \frac{325}{(191.5)(1.66)\sqrt{2.11\pi}} = 0.397\%$$

Referring to the calculated pressure-strain curve shown in Fig. 4.2, the corresponding failure pressure is 27.5 ksi.

Plastic instability (analysis performed by J. G. Merkle, ORNL)

Since plastic instability analyses have shown good accuracy in the static upper-shelf temperature range (see Ref. 1 and Appendices D and H), this method of analysis was applied to both vessels V-3 and V-6. For an external surface flaw in a cylindrical pressure vessel, this analysis is described in detail on pp. 161–63 of Ref. 1. Allowing for 15% stable crack growth (an arbitrary estimate), the crack area of a semielliptical crack

*Note that in this chapter the terms $\epsilon_{\theta\theta}$ and λ are used interchangeably to denote outside surface circumferential strain.

at maximum load is given by

$$A_c = \frac{(1.15)^2 \pi a (2b)}{4} = 1.039 a (2b) . \qquad (4.10)$$

where a and 2b are the initial dimensions of the crack. The effective trapezoidal load-bearing area at maximum load, including the area of the crack, is given by

$$A = [1.15(2b) + t]t . \qquad (4.11)$$

The failure pressure is calculated from

$$p_f = \sigma^* (Y \quad 1)\left(1 \quad \frac{A_c}{A}\right) . \qquad (4.12)$$

where

$$Y = \frac{\sigma_u}{\sigma_y} . \qquad (4.13)$$

and σ^* is a "flow stress" which is physically the hoop stress at plastic instability in a thin-walled hollow cylinder under internal pressure with closed ends. Following Ref. 1, the value of σ^* is taken here as 88.3 ksi.

The actual surface length of the flaw in vessel V-3 at zero load, 2b, was 8.50 in. (see Table 2.4). Thus, from Eq. (4.10),

$$A_c = (1.039)(2.11)(8.50) = 18.63 \text{ in.}^2$$

The load-bearing area, from Eq. (4.11), is

$$A = [(1.15)(8.50) + 6]6 = 94.65 \text{ in.}^2 .$$

For the intermediate test vessels, Y = 1.444; therefore, the failure pressure is estimated from Eq. (4.12) as

$$p_f = (88.3)(0.444)\left(1 \quad \frac{18.63}{94.65}\right) = 31.5 \text{ ksi}$$

The corresponding strain at failure falls beyond the range of the calculated curve in Fig. 4.2, but it can be calculated, for fully strain hardening conditions, from Eq. (H-71), which is

$$\lambda_f = \frac{2(p_f \quad S_y' \ln Y)}{(Y^2 \quad 1)(HS_y')} \qquad (4.14)$$

Using $S'_y = S_y \quad 5 = 70$ ksi and $HS'_y = 5.15$ ksi(%)$^{-1}$.

$$\lambda_1 = \frac{2\,[31.5 \quad (70)(0.367)]}{(1.085)(5.15)} = 2.08$$

The equivalent-energy method (analysis performed by F. J. Witt, ORNL)

Following the test of vessel V-3, a 0.85-m-thick model fabricated from vessel V-3 material and containing a flaw in a weld was tested. The experimentally determined shape factor for this model, which was designated model V3-A4, was 1.055 (see Table G-1). Note that the value of $K_{Ic(0.85)} = 174.5$ ksi$\sqrt{\text{in.}}$ used for the analysis of model V3-A4 was slightly erroneous for CT specimen V3A2A2-2 (see Table A-6). The value of K_{Ic6} was reestimated using the following toughness values:

Specimen No.	a (in.)	K_{Iq} (ksi$\sqrt{\text{in.}}$)
V3A1-3	0.85	178
V3A1-5	0.85	235
V2A2A1-1	3.0	286

None of the above values agree exactly with Table A-6, but the differences are minor. Following the previously described procedure,

$$K_{Ic(0.85)} = \frac{178 + 235}{2} = 206 \text{ ksi}\sqrt{\text{in.}} \;;$$

$$\gamma_{0.85,3} = \frac{3}{0.85}\left(\frac{206}{286}\right)^2 = 1.83 \;;$$

$$\gamma_{0.85,6} = 1.00 + \frac{(0.83)(5.15)}{(2.15)} = 3.0 \;;$$

$$K_{Ic6} = 206\sqrt{\frac{6}{(0.85)(3.0)}} = 315 \text{ ksi}\sqrt{\text{in.}} \;.$$

Using a = 2.1 in.,

$$\sigma_Y^* = \frac{3.5}{1.055\sqrt{2.1\pi}} = 116.2 \text{ ksi}$$

Then, using the bilinear approximation method,

$$E_d = \frac{(116.2)^2}{2(191.5)} = 35.25 \text{ ksi} \cdot \%$$

For model V3-A4 (see Table C-2), p_f = 31.5 ksi, p_y = 26.2 ksi, $\epsilon_{\theta f}$ = 2.75%, and $\epsilon_{\theta y}$ = 0.137%. Therefore,

$$m = \frac{\left(\frac{31.5}{26.2} - 1\right)}{2.75 - 0.137} = 0.0774(\%)^{-1}$$

$$\epsilon_{\theta m} = 0.137 + 12.92\left\{\sqrt{1 + (0.0774)\left[2\left(\frac{35.3}{26.2}\right) - 0.137\right]} - 1\right\} = 1.36\%$$

$$p_f = 26.2[1 + (0.0774)(1.36 - 0.137)] = 28.7 \text{ ksi}.$$

The strain estimate based on the bilinear approximation method is better than the pretest estimate, although the pressure estimate is lower by a slightly greater amount because of the lower gross yield pressure of model V3-A4.

The calculation based on the measured pressure-strain curve of vessel V-3 shown in Fig. 4.3 comes considerably closer with respect to pressure. At a pressure of 22.0 ksi, the pressure-strain curve is still ostensibly linear and the measured strain is 0.12%. From these values, $E = 183.3 \text{ ksi}(\%)^{-1}$. The difference between this value and the elastically calculated value of 191.5 ksi$(\%)^{-1}$ will be disregarded. Consequently,

$$E_d = \frac{(116.2)^2}{2(183.3)} = 36.83 \text{ ksi-\%} = 368.3 \text{ psi}.$$

The area under the test curve shown in Fig. 4.3 up to the point p = 31.1 ksi and $\epsilon_{\theta\theta}$ = 1.45% is 400.7 psi. The difference between the measured and the calculated energies is thus 32.4 psi. Dividing this energy difference by a stress of 31.0 ksi gives

$$\Delta\epsilon_{\theta\theta} = \frac{3.24 \text{ ksi-\%}}{31.0 \text{ ksi}} = 0.10\%.$$

Thus, the estimated failure strain is 1.45 − 0.10 = 1.35%, and the corresponding pressure, read from the pressure-strain curve in Fig. 4.3, is 30.8 ksi.

The normalized crack-opening-displacement approach (analysis performed by J. G. Merkle, ORNL)

This method of analysis, recently proposed[27] in the United Kingdom for determining allowable crack sizes for given strain levels, or the reverse, is based on the diagram shown in Fig. 4.4. The curve in Fig. 4.4 relates the normalized crack opening displacement (COD),

$$\phi = \frac{\delta_c}{2\pi\epsilon_y a}, \tag{4.15}$$

where δ_c is the critical crack opening displacement, to the strain ratio ϵ/ϵ_y. The effective crack size a is related to actual crack size a by

$$a = C^2 a. \tag{4.16}$$

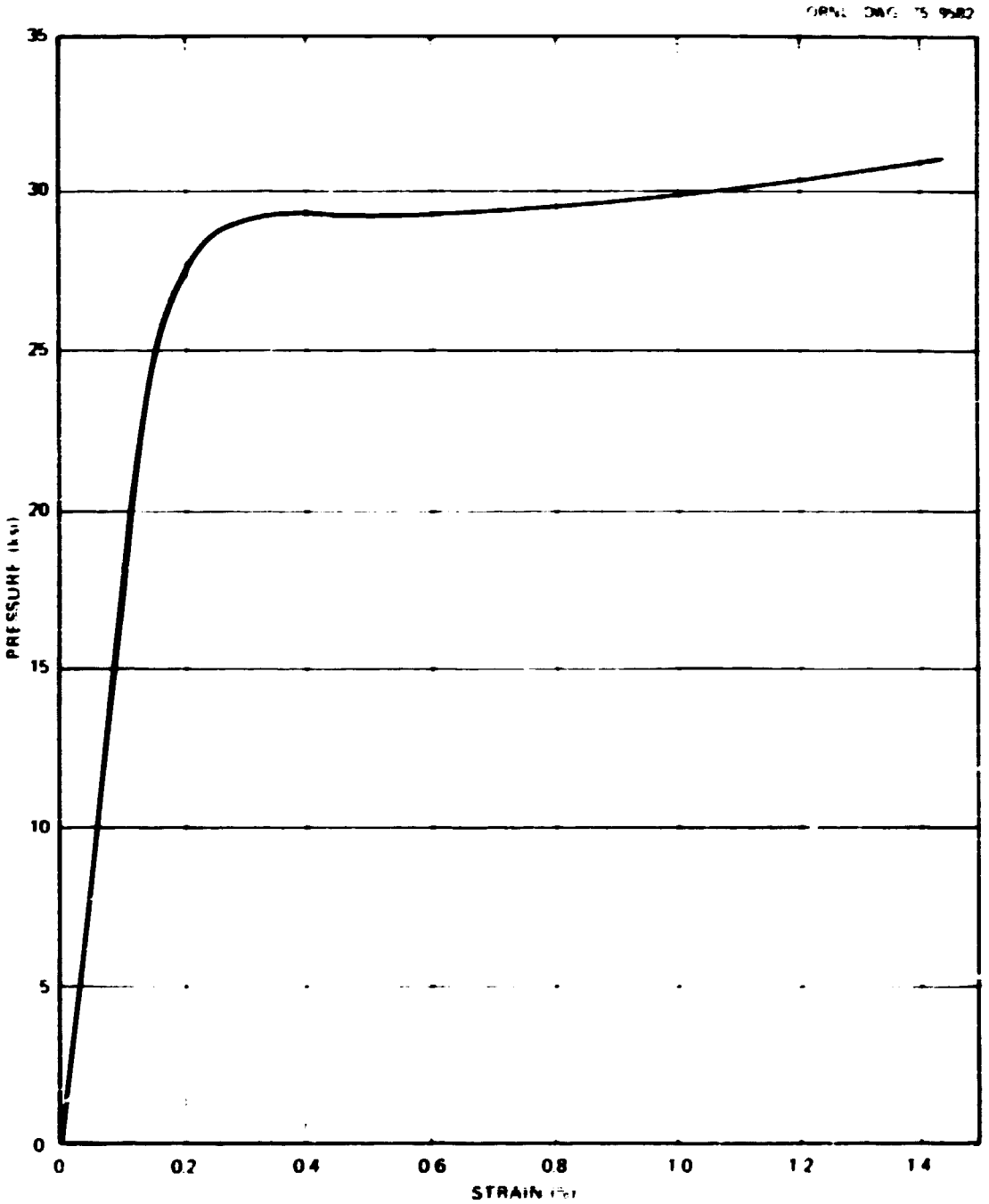

Fig. 4.3. Measured pressure vs outside circumferential strain curve for intermediate test vessel V-3.

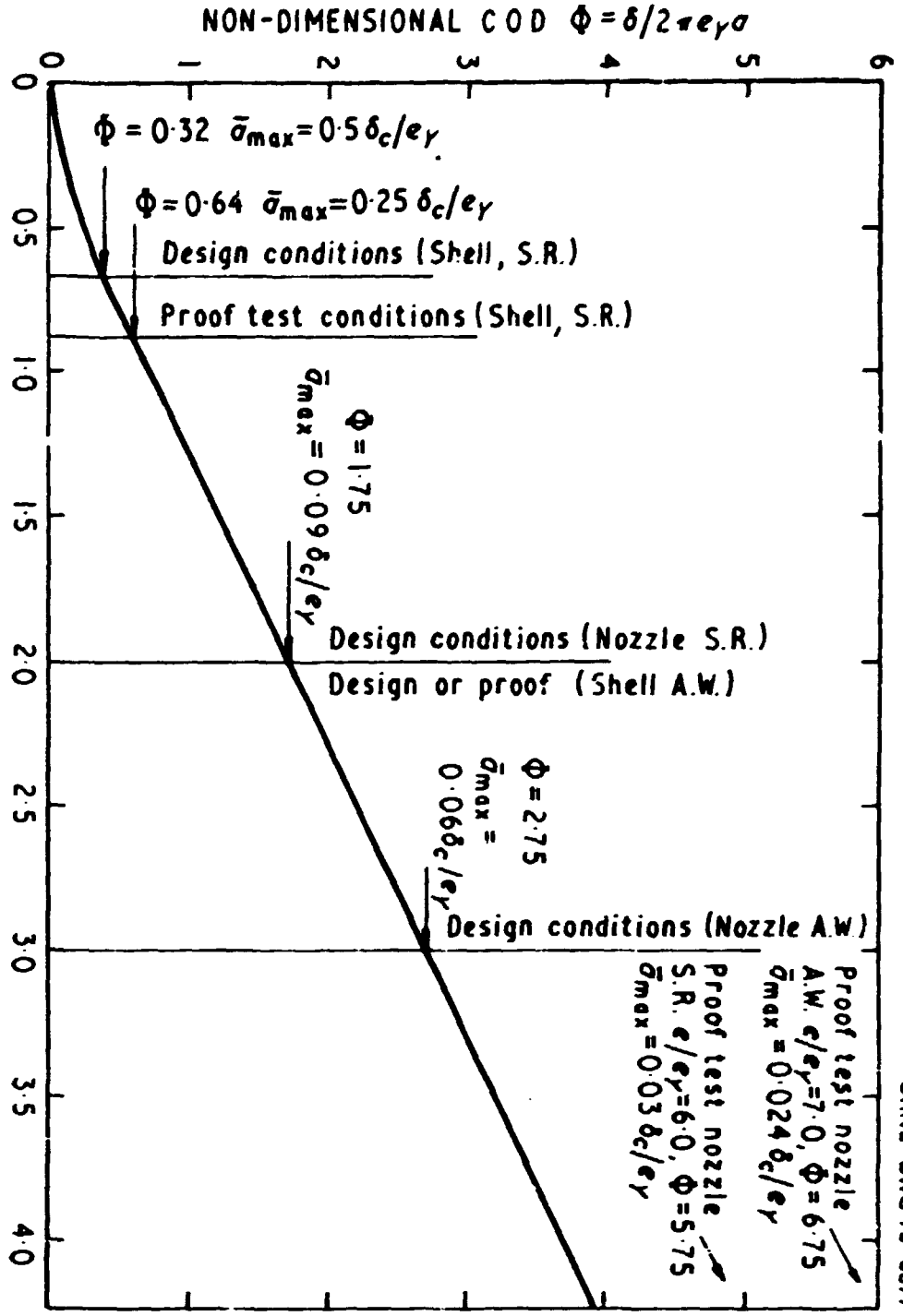

Fig. 4.4. Normalized crack-opening-displacement (COD) design curve.

where C is the fracture mechanics shape factor based on the elastically calculated nominal stress at the location of the flaw. Using the relation

$$K_{Ic}^2 = EG_{Ic} = E\sigma_Y\delta_c \ . \tag{4.17}$$

it follows that

$$\frac{\delta_c}{\epsilon_Y} = \left(\frac{K_{Ic}}{\sigma_Y}\right)^2 \ . \tag{4.18}$$

so that

$$\phi = \frac{(K_{Ic}/\sigma_Y)^2}{2\pi\, a} \ . \tag{4.19}$$

Dawes[28] recently proposed the following equations for representing the curve shown in Fig. 4.4:

$$\phi = \frac{1}{2}\left(\frac{\epsilon}{\epsilon_Y}\right)^2 \quad \epsilon \leq 0.5\epsilon_Y \ . \tag{4.20}$$

and

$$\phi = \frac{\epsilon}{\epsilon_Y} \quad 0.25 \quad \epsilon \geq 0.5\epsilon_Y \ . \tag{4.21}$$

Equation (4.20) incorporates a safety factor of 2 on flaw size in the elastic range for $\epsilon \leq 0.5\epsilon_Y$.

For vessel V-3, using σ_Y = 70 ksi and C = 0.9,

$$a = (0.9)^2\,(2.11) = 1.709 \text{ in.}$$

and

$$\phi = \frac{(325/70)^2}{2\pi\,(1.709)} = 2.007 \ .$$

Rearranging Eq. (4.21),

$$\frac{\epsilon}{\epsilon_Y} = \phi + 0.25 \quad \epsilon \geq 0.5\epsilon_Y \ . \tag{4.22}$$

Thus, the allowable strain is given by

$$\epsilon = 0.233\,(2.007 + 0.25) = 0.53\% \ .$$

By comparison with the test data for vessel V-3, this strain is conservative by about a factor of 3; the corresponding pressure from Fig. 4.2 is 27.5 ksi.

A recent examination of this method of analysis[29] shows that Eqs. (4.20) and (4.21) can be derived by using the equivalent-energy approximation for the J integral and assuming an elastic ideally plastic stress-strain curve.

The Berkeley Nuclear Laboratories two-criteria approach (analysis performed by J. G. Merkle, ORNL)

Another approach to inelastic fracture analysis recently developed in the United Kingdom is a generalization of the strip yield model in fracture mechanics,[17,30] in which the stress terms are arbitrarily replaced by load terms.[31] The result is the equation

$$\frac{L_f}{L_u} = \frac{2}{\pi} \cos^{-1} \exp - \left(\frac{\pi L_K}{\sqrt{8}\, L_u} \right)^2 . \tag{4.23}$$

where the loads L_K, L_u, and L_f are the failure load predicted by linear elastic fracture mechanics, the ultimate load based on a plastic collapse analysis, and the actual failure load, respectively.

For a surface crack in a cylindrical pressure vessel, L_K is estimated, in terms of pressure, from

$$L_K = \frac{K_{Ic}}{2.8\sqrt{\pi a}} . \tag{4.24}$$

The shape factor value of 2.8 is larger than would be expected based on elastic analysis, but it will be used here to be consistent with the method as proposed.[31]

For vessel V-3,

$$L_K = \frac{325}{2.8\sqrt{2.11\pi}} = 45.1 \text{ ksi} .$$

Since the exact method for estimating L_u is not completely described in Ref. 31, the previously described method for estimating failure pressures for plastic instability, but assuming no stable crack growth, will be used. Thus.

$$A_c = \frac{\pi (2.11)(8.50)}{4} = 14.09 \text{ in.}^2 .$$

$$A = (8.50 + 6)\,6 = 87.0 \text{ in.}^2 .$$

$$L_u = (88.3)(0.444)\left(1 - \frac{14.09}{87.0}\right) = 32.9 \text{ ksi} .$$

The calculations pertaining to Eq. (4.23) are

$$\frac{\pi L_K}{\sqrt{8}\, L_u} = \frac{\pi(45.1)}{\sqrt{8}\,(32.9)} = 1.523 .$$

$$e^{-(1.523)^2} = 0.09844 = \cos 84.35^\circ .$$

$$L_f = \left(\frac{84.35}{90}\right)(32.9) = 30.8 \text{ ksi} .$$

The corresponding strain is estimated from

$$\lambda_f = \frac{2[30.8 - (70)(0.367)]}{(1.085)(5.15)} = 1.83\% .$$

The above method of analysis is similar, in principle, to a method based on linear interpolation between the yield and ultimate stresses described in Ref. 32. However, the latter method, because it is based on uniaxial stresses, is not fully developed for application to cases involving multiaxial stress states.

Pretest Fracture Strength Calculations for Vessel V-4

Vessel V-4 contained two external surface flaws, 90° apart, as shown in Fig. 2.9. The pretest estimates of the flaw sizes based on ultrasonic data are shown in Table 2.4. Static fracture toughness K_{Icd} data were obtained from precracked Charpy V-notch specimens, 0.85T-CT specimens, and 4T-CT specimens. The latter two sets of toughness data are listed in Table A-7, and all the toughness data available before the test are plotted in Figs. 4.5 and 4.6. The tensile data available before the test are shown in Fig. 4.7. Of special importance is the fact, shown in Fig. 4.6, that at the test temperature of 75°F the toughness values for weld metal specimens do not vary systematically with specimen size as is normally expected.[13] This fact has a significant bearing on the comparisons between analytical results and experimental data to be discussed.

Linear elastic fracture mechanics based on strain (analysis performed by C. Buchalet, Westinghouse PWR Systems Division)

This method of analysis, which is identical in principle to the previously described posttest analysis of vessel V-3, is described in detail on pp. 191–95 of Ref. 1. Referring to Figs. 4.5, 4.6, and 4.8, the following results were obtained:

Flaw	Location	K_{Ic} (ksi $\sqrt{\text{in.}}$)	$\epsilon_{\theta 0}$ (%)	Pf (ksi)
A	Weld metal	200	0.20	27.0
B	Base metal	300	0.28	28.5

The flaw in weld metal, flaw A, was expected to be the failure origin.

The equivalent energy method (analysis performed by F. J. Witt, ORNL)

Several different equivalent-energy analyses were performed for vessel V-4, mostly based on various strain readings obtained from vessel V-3. In general, these analyses indicated that failure would initiate at flaw A at a pressure of approximately 29.0 ksi and at a strain of between 0.3 and 0.4% measured 17 in. from the vessel midplane.

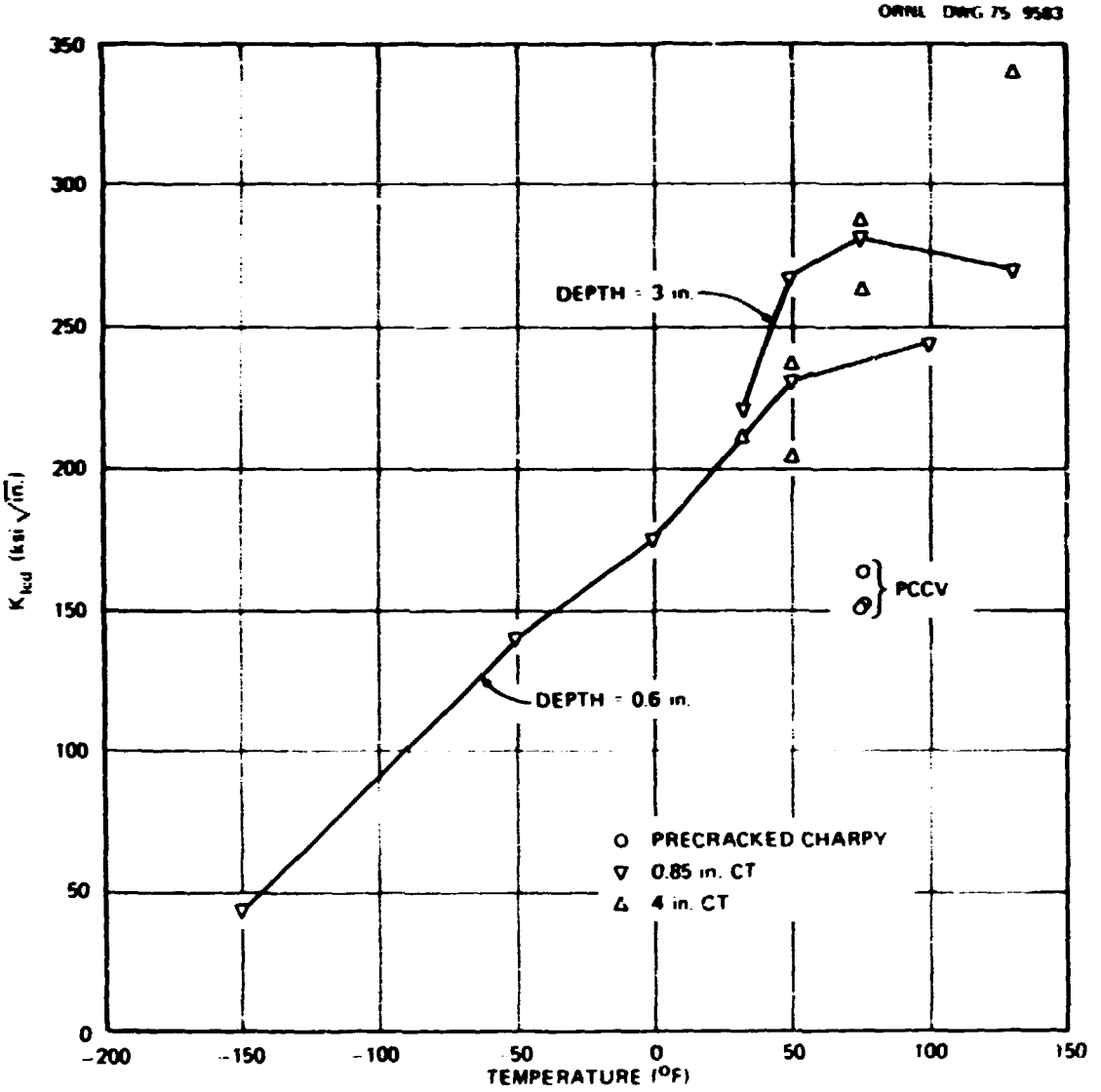

Fig. 4.5. Fracture toughness K_{Icd} values vs temperature for intermediate test vessel V-4 base metal.

The following calculation by the bilinear approximation method for the failure pressure and nominal strain at the flaw location is probably typical. The estimated fracture toughness K_{Ic6} for the weld region flaw is 200 ksi $\sqrt{in.}$, and the estimated flaw depth is 2.6 in. Using a value of C = 1.145, based on the test results from vessel V-1 (see Table G.1).

$$p_f^* = \frac{200}{1.145\sqrt{2.6\pi}} = 61.12 \text{ ksi} .$$

$$E_d = \frac{(61.12)^2}{(2)(191.5)} = 9.75 \text{ ksi}\cdot\% .$$

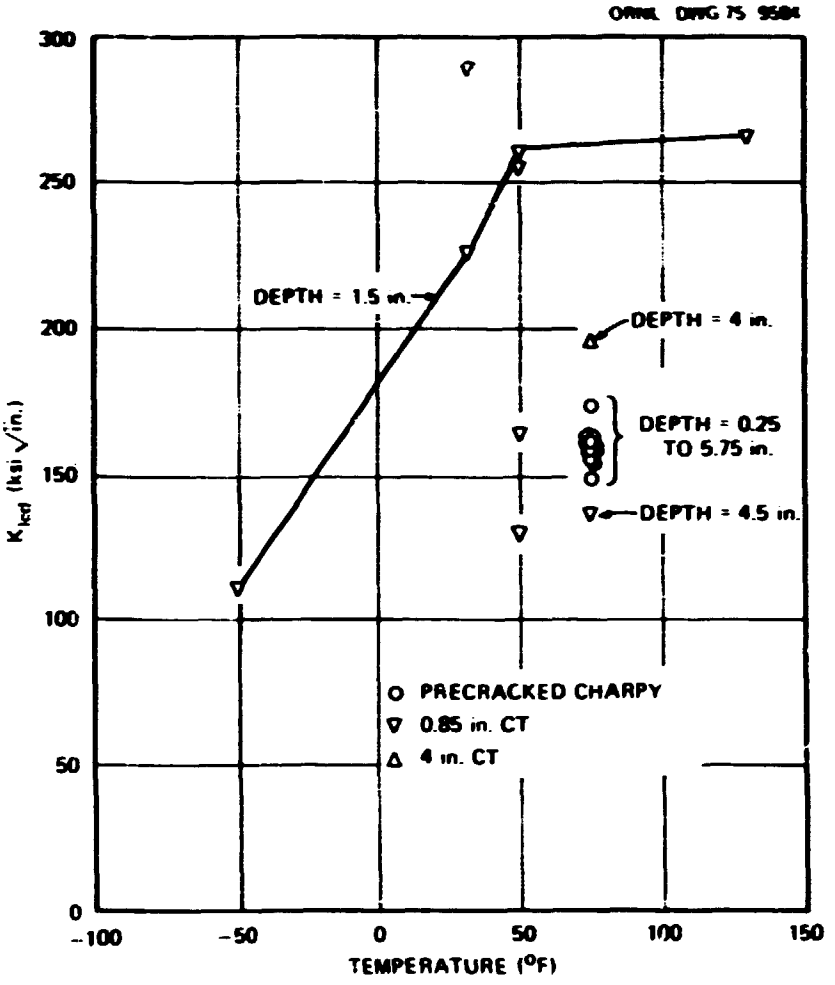

Fig. 4.6. Plot of fracture toughness K_{Icd} values vs temperature for intermediate test vessel V-4 weld metal.

The following parameters were estimated from the plot of pressure vs strain in the longitudinal weld of vessel V-3 shown in Fig. 4.9: $p_Y = 28.0$ ksi. $\epsilon_{\theta Y} = 0.146\%$. $p_f = 30.8$ ksi. $\epsilon_{\theta f} = 1.28\%$. Therefore.

$$m = \frac{(30.8/28.0) \quad 1}{1.28 \quad 0.146} = 0.0882\,(\%)^{-1} .$$

$$\frac{1}{m} = 11.34\% .$$

$$\epsilon_{\theta 0} = 0.146 + 11.34 \left\{ \sqrt{1 + (0.0882)\left| 2\left(\frac{9.75}{28.0}\right) \quad 0.146 \right|} \quad 1 \right\} = 0.146 + 0.272 = 0.418\% .$$

$$p_f = 28.0\,[1 + (0.0882)(4.18 \quad 0.146)] = 28.7 \text{ ksi} .$$

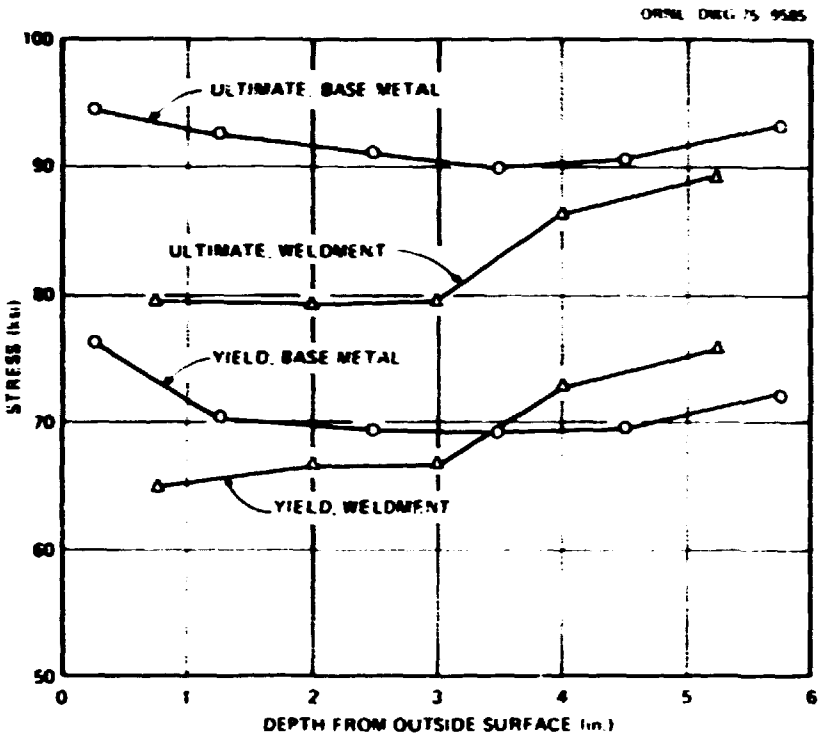

Fig. 4.7. Plot of yield and ultimate stresses vs thickness position for intermediate test vessel V-4 base metal and weld metal at 75°F.

The tangent modulus method (analysis performed by J. G. Merkle, ORNL)

These calculations were based on the method of analysis described in Appendix H. From Eq. (H-64), it follows that

$$f(\lambda) = \frac{K_{Ic}/S_Y}{\sqrt{a}} \tag{4.25}$$

Therefore, if a model and a prototype fail at the same strain,

$$\frac{(K_{Ic}/S_Y)_m}{\sqrt{a_m}} = \frac{(K_{Ic}/S_Y)_p}{\sqrt{a_p}} , \tag{4.26}$$

and, consequently,

$$\left(\frac{K_{Ic}}{S_Y}\right)_m = \sqrt{\frac{a_m}{a_p}}\left(\frac{K_{Ic}}{S_Y}\right)_p . \tag{4.27}$$

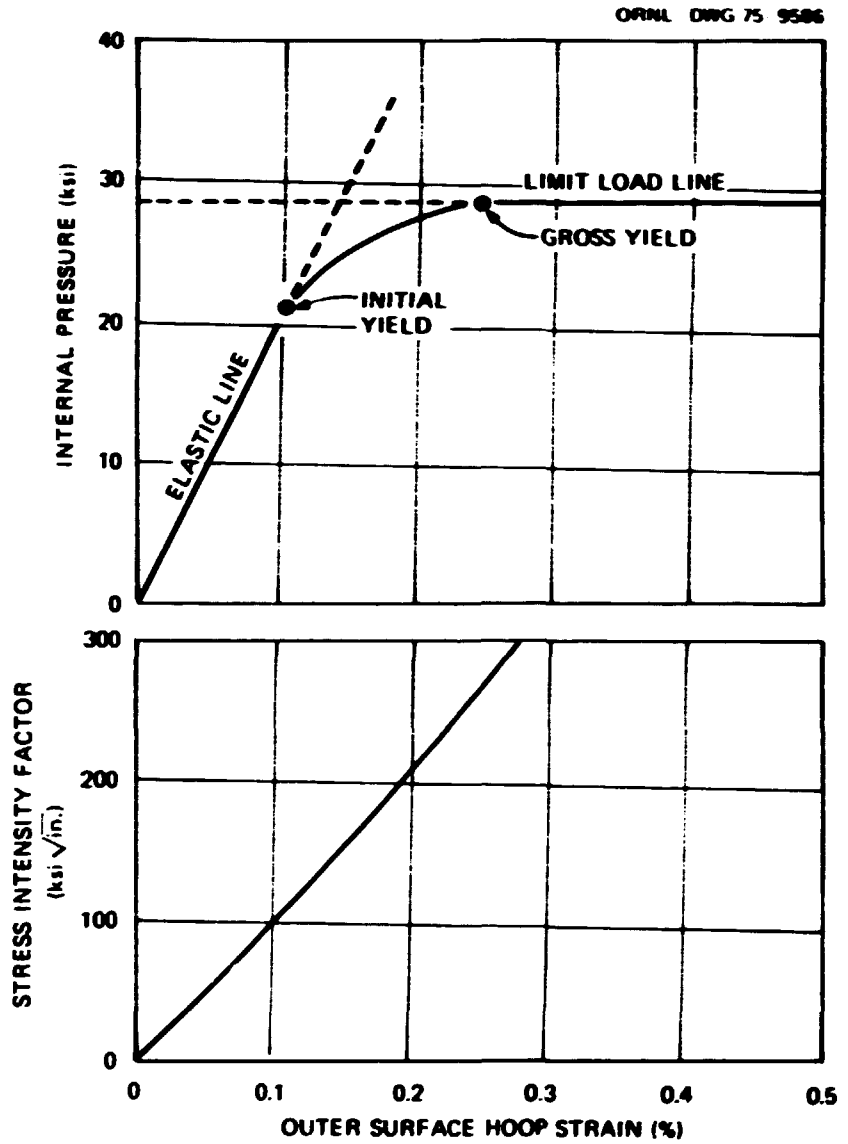

Fig. 4.8. Figure used by Westinghouse to predict failure conditions for intermediate test vessel V-4 by the method of linear elastic fracture mechanics based on strain.

Equation (4.27) allows the calculations previously made for the 6½-in.-diam model vessels in Appendix H to be used for the analysis of vessel V-4. For the models, $a_m = 0.4$ in., and for the prototype, $a_p = 2.60$ in. Therefore,

$$\sqrt{\frac{a_m}{a_p}} = \sqrt{\frac{0.4}{2.6}} = 0.392 \ .$$

A yield stress of 70 ksi was assumed for both weld metal and base metal.

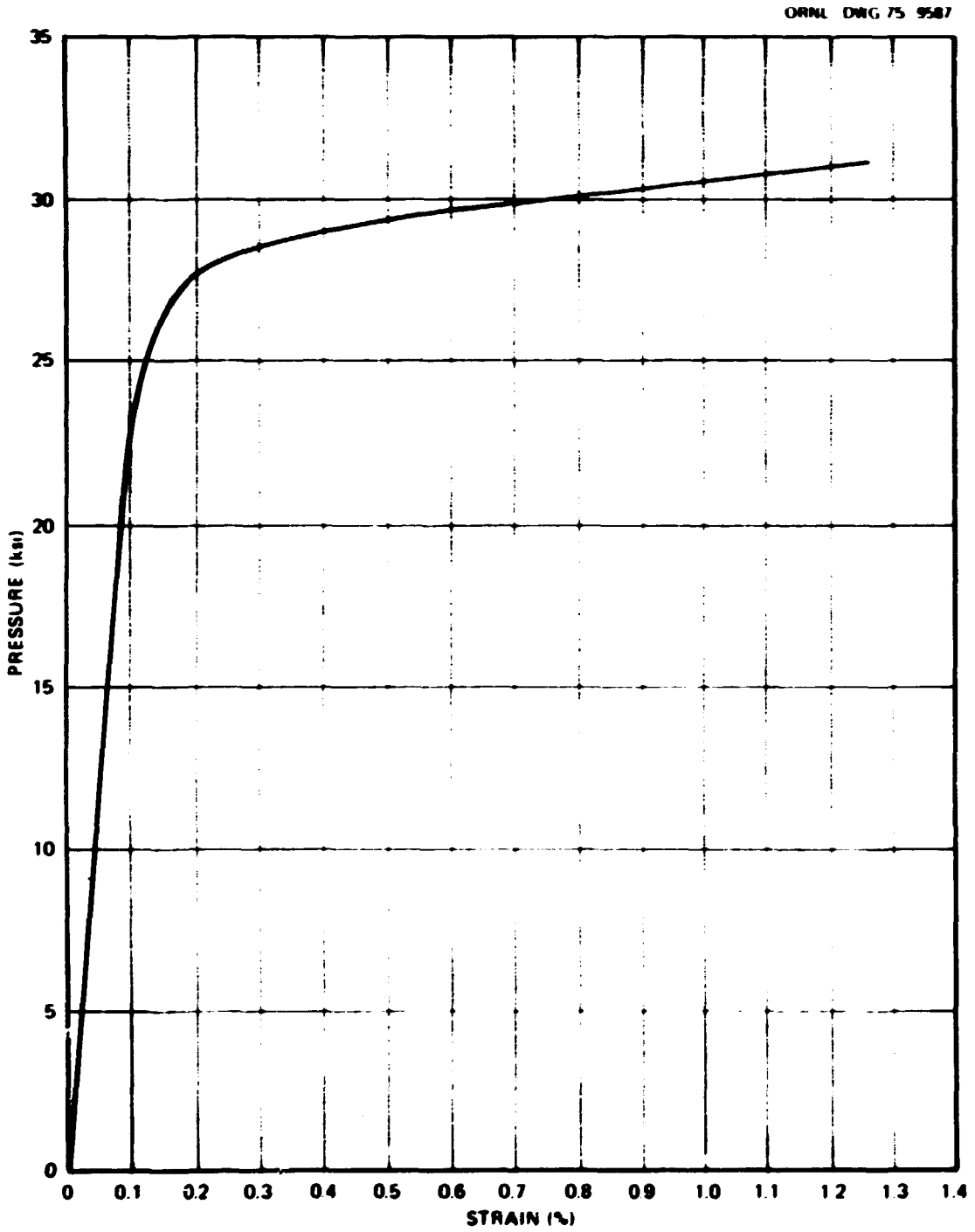

Fig. 4.9. Measured pressure vs outside circumferential strain curve in the longitudinal weld of intermediate test vessel V-3.

For flaw A, the weld flaw, the value of K_{Ic} was estimated from Fig. 4.6 as 200 ksi $\sqrt{in.}$ Thus,

$$\left(\frac{K_{Ic}}{S_Y}\right)_p = \frac{200}{70} = 2.86\sqrt{in.}$$

$$\left(\frac{K_{Ic}}{S_Y}\right)_m = (0.392)(2.86) = 1.12\sqrt{in.}$$

By linear interpolation in Table H-5, $\lambda_f = 0.41\%$. The pressure corresponding to this strain, from Fig. 4.2, is 27.5 ksi; but assuming a constrained yield stress of 77 ksi instead of 75 ksi, this pressure was multiplied by 77/75 to give 28.2 ksi.

For flaw B, the base metal flaw, the value of K_{Ic} was estimated from Fig. 4.5 as 275 ksi $\sqrt{in.}$ Thus,

$$\left(\frac{K_{Ic}}{S_Y}\right)_p = \frac{275}{70} = 3.93\sqrt{in.}$$

$$\left(\frac{K_{Ic}}{S_Y}\right)_m = (0.392)(3.93) = 1.54\sqrt{in.}$$

By linear interpolation in Table H-5, $\lambda_f = 0.89\%$. From Fig. 4.2, the corresponding pressure is about 28.2 ksi and, multiplying this value by 77/75, gives a pressure of 29.0 ksi. Failure was therefore expected to initiate at the weld metal flaw, flaw A.

Posttest Fracture Strength Calculations for Vessel V-4

Although it was generally estimated that vessel V-4 would fail at weld flaw A at a pressure between 28.0 and 29.0 ksi, it actually failed at 26.5 ksi. Failure occurred at a strain of 0.168%, prior to the onset of gross yielding instead of afterward as expected. Although some of this difference can be attributed to the difference between the actual flaw depth and the predicted flaw depth (3.0 vs 2.6 in.), it is also apparent that the toughness of the weld metal surrounding flaw A may have been less than estimated. This is assumed to be the case in some of the posttest analyses to be discussed. The fact that the weld metal toughness in vessel V-4 may have varied appreciably at 75°F is implicit in Fig. 4.6, which shows that the toughness values at this temperature do not vary consistently with specimen size as normally expected.[13] The phenomenon of weld property variability and its influence on fracture safety is widely recognized.[33] It is one of the prime reasons for the use of safety factors on load or toughness in Sections III and XI of the ASME Boiler and Pressure Vessel Code, which apply to nuclear pressure vessels.

Linear elastic fracture mechanics based on strain (analysis performed by J. G. Merkle, ORNL)

Recognizing the possible overestimate of fracture toughness made in the pretest analyses, Fig. 4.6 was reexamined, and a fracture toughness of 160 ksi $\sqrt{in.}$ was selected based on the data shown in the figure for the 13 precracked Charpy V-notch specimens. Consequently,

$$\lambda_f = \frac{160}{(191.5)(1.66)\sqrt{3.0\pi}} = 0.16\%.$$

From Fig. 4.2, this strain corresponds to a pressure of 26.2 ksi. Using the flaw depth of 2.95 in. listed in Table 2.4 gives a strain value of 0.165% and a pressure of 26.3 ksi.

The equivalent-energy method (analysis performed by F. J. Witt, ORNL)

The main revision in this analysis was in the value of the shape factor. Choosing a value of C = 1.60, which is the value originally used for the pretest analysis of vessel V-1 (see Ref. 1, p. 174), and using a fracture toughness value of 194.4 ksi $\sqrt{\text{in.}}$, which is the value obtained from the 4T-CT weld metal specimen (see Table A.7),

$$p_f^* = \frac{194}{1.6\sqrt{3.0\pi}} = 39.6 \text{ ksi} .$$

Calculating a modulus from the pressure-strain curve recorded by channel 63 on vessel V-4, as shown in Fig. 3.23, gives

$$M = \frac{20 \text{ ksi}}{0.11\%} = 181.82 \text{ ksi}(\%)^{-1} .$$

It follows that

$$E_d = \frac{(39.6)^2}{2(181.82)} = 4.31 \text{ ksi} \cdot \% = 43.1 \text{ psi} .$$

The area under the actual pressure-strain curve in Fig. 3.23 is 25.3 psi. The strain difference is estimated approximately by

$$\Delta\epsilon = \frac{4.31 - 2.53}{26.7} = 0.067\% .$$

Therefore, the estimated failure strain is 0.168 + 0.067 = 0.235%, and, by extending the pressure-strain curve shown in Fig. 3.23, the estimated failure pressure is about 27.0 ksi.

The normalized crack-opening-displacement approach (analysis performed by J. G. Merkle, ORNL)

Using the method previously described and a yield stress of 70 ksi,

$$a = (0.9)^2 (2.95) = 2.39 \text{ in.}$$

and

$$\phi = \frac{(160/70)^2}{2\pi(2.39)} = 0.348 .$$

The allowable strain is thus

$$\epsilon = (0.233)(0.348 + 0.25) = 0.139\% .$$

This strain is conservative, but by a factor of 1.2 rather than $\sqrt{2.0}$. From Fig. 4.2, the corresponding pressure is 24.2 ksi, which is approximately 10% less than the actual failure pressure.

The Berkeley Nuclear Laboratories two-criteria approach (analysis performed by J. G. Merkle, ORNL)

Using the method previously described and a value of K_{Ic} = 160 ksi $\sqrt{in.}$,

$$L_K = \frac{160}{2.8\sqrt{2.95\pi}} = 18.77 \text{ ksi} .$$

$$A_c = \frac{\pi(2.95)(8.25)}{4} = 19.11 \text{ in.}^2 .$$

$$A = (8.25 + 6)6 = 85.5 \text{ in.}^2 .$$

$$L_u = (88.3)(0.444)\left(1 - \frac{19.11}{85.5}\right) = 30.44 \text{ ksi} .$$

$$\frac{\pi L_K}{\sqrt{8}\, L_u} = \frac{\pi(18.77)}{\sqrt{8}(30.44)} = 0.6849 .$$

$$e^{-(0.6849)^2} = 0.62558 = \cos 51.28^\circ .$$

$$L_f = \left(\frac{51.28}{90}\right)(30.44) = 17.3 \text{ ksi} .$$

The corresponding strain by elastic analysis is 0.09%. This estimate is extremely conservative, due basically to the fact that the shape factor value of 2.8 based on pressure is larger than the elastically calculated value as noted previously.

Pretest Fracture Strength Calculations for Vessel V-6

Linear elastic fracture mechanics based on strain (analysis performed by C. Buchalet, Westinghouse PWR Systems Division)

The fracture toughness data used for this analysis are listed in Table A.8, and the estimated flaw size values are given in Table 2.4. Linear elastic fracture mechanics shape factors were calculated for each of the three flaws by the procedure described on pp. 191–95 of Ref. 1. The final results are shown graphically in Fig. 4.10. Failure was predicted to occur at flaw C, the inside weld metal flaw, at a pressure of 28.5 ksi and a strain of 0.3%. This prediction was known to be very conservative, because gross yielding was actually expected to precede failure.

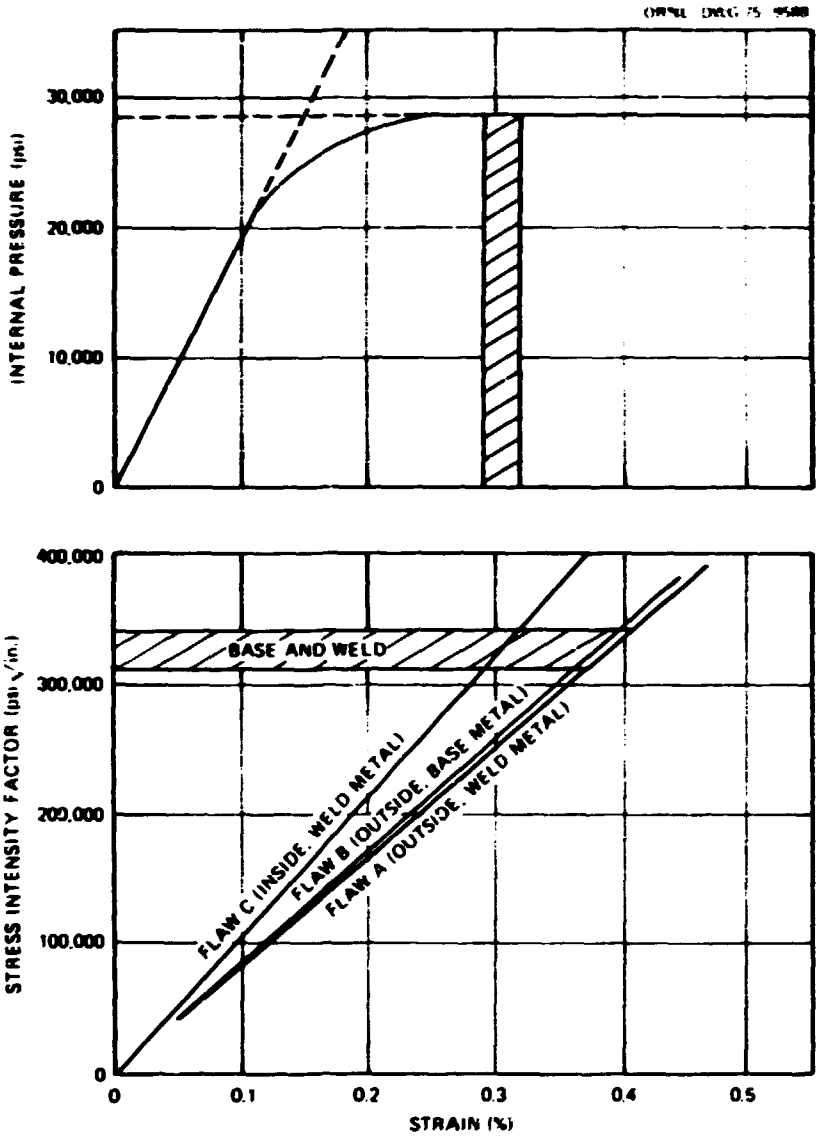

Figure 4.10. Figure used by Westinghouse to predict failure conditions for intermediate test vessel V-6 by the method of linear elastic fracture mechanics based on strain.

Plastic instability (analysis performed by J. G. Merkle, ORNL)

This analysis was a modification of the analysis used previously, taking into account the effect of pressure acting on the faces of an inside surface crack. The resulting equation is

$$p_f = \frac{\sigma^*(Y - 1)(1 - A_c/A)}{1 + (Y - 1)A_c/A} . \qquad (4.28)$$

Allowing for 20% stable crack growth.

$$A_c = \frac{(1.2)^2 \pi (1.77)(5.30)}{4} = 10.61 \text{ in.}^2 .$$

$$A = [(1.2)(5.30) + 6]\, 6 = 74.16 \text{ in.}^2 .$$

$$\frac{A_c}{A} = 0.1431 .$$

$$p_f = \frac{(88.3)(0.444)(1 - 0.1431)}{1 + (0.444)(0.1431)} = 31.6 \text{ ksi} .$$

Using the pressure-strain curve for model vessel V2-A1-E shown in Fig. G-9, this corresponds to an outside circumferential strain of 1.34%. These are the predicted failure conditions for the inside weld flaw, flaw C.

The equivalent-energy method (analysis performed by F. J. Witt, ORNL)

The equivalent-energy estimates made for each of the three flaws placed in vessel V-6 were based on independent toughness calculations for the individual CT specimens listed in Table A-8. The toughness calculations for the CT specimens, given in Table 4.3, were used to make the following estimates of K_{Ic6} for the material surrounding the three flaws in vessel V-6.

Table 4.3. Fracture toughness values for vessel V-6 material at 200°F

Specimen No.	Position	Thickness (in.)	K_{Icd} (ksi $\sqrt{\text{in.}}$)	Value of K_{Icd} used for analysis
		Weld metal		
V6-W5	OD	0.85	223.4	$K_{Ic0.85}$ = 220 ksi $\sqrt{\text{in.}}$ for flaw A
V6-W6	1/6T	0.85	224.6	
V6-W7	1/2T	0.85	190.0	$K_{Ic0.85}$ = 182 ksi $\sqrt{\text{in.}}$ for flaw C
V6-W8	3/6T	0.85	180.3	
V6-W9	ID	0.85	221.2	K_{Ic4} = 341.9 ksi $\sqrt{\text{in.}}$
V6-W1	OD + 1 3/8 in.	4.0	341.9	
		Base metal		
V6-13	OD + 3/16 in.	0.85	229.3	$K_{Ic0.85}$ = 220 ksi $\sqrt{\text{in.}}$ for flaw B
V6-10	OD + 3/16 in.	0.85	199.1	
V6-14	1/2T	0.85	243.3	
V6-11	1/2T	0.85	207.2	
V6-12	ID 3/16 in.	0.85	217.0	
V6-15	ID 3/16 in.	0.85	231.7	
V6-2	1/2T	4.0	315.6	K_{Ic4} = 325 ksi $\sqrt{\text{in.}}$
V6-3	1/2T	4.0	336.4	
V6-4	1/2T	4.0	322.8	

For flaw A (outside surface, weld).

$$s_{0.85,4} = \frac{4}{0.85}\left(\frac{220}{341.9}\right)^2 = 1.92 .$$

$$s_{0.85,6} = 1.00 + \frac{(0.92)(5.15)}{3.15} = 2.50 .$$

$$K_{Ic6} = 220\sqrt{\frac{6}{(0.85)(2.50)}} = 369 \text{ ksi}\sqrt{\text{in.}}$$

For flaw B (outside surface, base metal).

$$s_{0.85,4} = \frac{4}{0.85}\left(\frac{220}{325}\right)^2 = 2.14 .$$

$$s_{0.85,6} = 1.00 + \frac{(1.14)(5.15)}{3.15} = 2.85 .$$

$$K_{Ic6} = 220\sqrt{\frac{6}{(0.85)(2.85)}} = 346 \text{ ksi}\sqrt{\text{in.}}$$

For flaw C (inside surface, weld).

$$s_{0.85,4} = \frac{4}{0.85}\left(\frac{182}{341.9}\right)^2 = 1.34 .$$

$$s_{0.85,6} = 1.00 + \frac{(0.34)(5.15)}{3.15} = 1.55 .$$

$$K_{Ic6} = 182\sqrt{\frac{6}{(0.85)(1.55)}} = 390 \text{ ksi}\sqrt{\text{in.}}$$

Shape factors based on pressure were obtained from model data, but an adjustment was made for the differences in flaw shape between the model and prototype flaws using the equation

$$C' = C\frac{\Phi_m}{\Phi_p} , \qquad (4.29)$$

where C' is the shape factor for the prototype, C is the shape factor for the model, and the subscripts m and p denote model and prototype, respectively. The symbol Φ is an elliptical integral that can be closely

approximated by Eq. (H-63), which is

$$\Phi^2 = 1 + 4.593\left(\frac{a}{2b}\right)^{1.65} \quad (4.30)$$

The resulting shape factors for the vessel V-6 flaws are given in Table 4.4.

Table 4.4. Shape factors from models, adjusted for flaw shape for application to pretest equivalent-energy analyses of vessel V-6

Flaw	$\frac{a}{2b}$	Φ_p	Model No.	$\frac{a}{2b}$	Φ_m	C	C'
A	0.368	1.371	V4.4	0.298	1.273	1.215	1.125
B	0.332	1.319	V4.4	0.295	1.273	1.215	1.173
C	0.334	1.323	V4.6	0.296	1.271	1.232	1.185

The predictions of fracture strain and pressure for vessel V-6 were based on an extrapolation of the measured pressure-strain curve for vessel V-3 that was used for the posttest calculations for vessel V-3 (see Fig. 4.3). However, a value of M = 200 ksi $(\%)^{-1}$ was used for computing the volumetric energy values. For vessel V-6, the bilinear approximation method based on the curve shown in Fig. 4.9 gives almost exactly the same values of strain and pressure at failure as were obtained by the graphical solution based on the curve shown in Fig. 4.3. The latter values are shown below in parentheses along with the calculated values.

For flaw A (outside surface, weld).

$$p_f^* = \frac{369}{1.125\sqrt{1.87\pi}} = 135.5 \text{ ksi} .$$

$$E_d = \frac{(135.5)^2}{2(200)} = 45.8 \text{ ksi} \cdot \% .$$

$$\epsilon_{no} = 0.146 + 11.34\left\{\sqrt{1 + (0.0882)\left|2\left(\frac{45.8}{28.0}\right) \quad 0.146\right|} \quad 1\right\} = 1.61\% \ (1.6\%) .$$

$$p_f = 28.0\,[1 + (0.0882)(1.61 \quad 0.146)] = 31.6 \text{ ksi } (31.7 \text{ ksi}) .$$

For flaw B (outside surface, base metal).

$$p_f^* = \frac{346}{1.173\sqrt{1.72\pi}} = 127 \text{ ksi} .$$

$$E_d = \frac{(127)^2}{2(200)} = 40.3 \text{ ksi} \cdot \%\ .$$

$$\epsilon_{\theta\theta} = 0.146 + 11.34 \left\{ \sqrt{1 + (0.0882) \left| 2\left(\frac{40.3}{28.0}\right) - 0.146 \right|} - 1 \right\} = 1.439\% \ (1.435\%)\ .$$

$$p_f = 28.0[1 + (0.0882)(1.439 - 0.146)] = 31.2 \text{ ksi } (31.2 \text{ ksi})\ .$$

For flaw C (inside surface, weld),

$$p_f^{\bullet} = \frac{390}{1.185\sqrt{1.77\pi}} = 139 \text{ ksi}\ .$$

$$E_d = \frac{(139)^2}{2(200)} = 48.2 \text{ ksi} \cdot \%\ .$$

$$\epsilon_{\theta\theta} = 0.146 + 11.34 \left\{ \sqrt{1 + (0.0882) \left| 2\left(\frac{48.2}{28.0}\right) - 0.146 \right|} - 1 \right\} = 1.689\% \ (1.68\%)\ .$$

$$p_f = 28.0[1 + (0.0882)(1.689 - 0.146)] = 31.8 \text{ ksi } (32.0 \text{ ksi})\ .$$

Although, strictly speaking, the flaw expected to cause the failure was the outside surface flaw in base metal, flaw B, all the estimates were quite close to each other and, as can be seen, also quite close to the actual failure conditions.

Crack-arrest analysis (analysis performed by J. G. Merkle, ORNL)

This analysis was performed to determine if a through crack of length equal to double the vessel wall thickness would be stable or unstable with respect to a propagating flat (mode I) fracture at a nominal stress equal to the yield stress. Referring to Table 1 of Ref. 34, a value of $(K_{Ia}/\sigma_Y) = 2.1$ is required to satisfy this condition for a wall thickness of 6 in. Using the relation between toughness and temperature given in Ref. 34, it follows that

$$T = T_{-} \quad \frac{A_T}{K_{Ia}/\sigma_Y}\ . \tag{4.31}$$

For dynamic conditions,

$$T_{-} = NDT + 197\ . \tag{4.32}$$

For an NDT of +10°F,

$$T_{-} = 10 + 197 = 207°F\ .$$

Using $A_T = 125°F\sqrt{in.}$.

$$T = 207 \quad \frac{125}{3.1} = 167°F .$$

Therefore, for a test at 190°F, there is a 23°F margin against a propagating flat (mode I) fracture.

Posttest Fracture Strength Calculations for Vessel V-6

Linear elastic fracture mechanics based on strain (analysis performed by J. G. Merkle, ORNL)

In principle, this analysis is identical to the pretest analysis performed by Buchalet of Westinghouse. Because failure occurred well after the onset of gross yielding, this analysis will be quite conservative. For flaw A, the outside surface weld metal flaw at which failure occurred, the toughness used will be $K_c = 369$ ksi $\sqrt{in.}$, based on Witt's pretest estimate. The actual flaw depth was 1.87 in. Therefore, using a shape factor of C = 1.66 based on pressure,

$$\lambda_f = \frac{369}{(191.5)(1.66)\sqrt{1.87\pi}} = 0.479\% .$$

From Fig. 4.2, this strain corresponds to a pressure of 27.5 ksi.

Plastic instability (analysis performed by J. G. Merkle, ORNL)

This analysis follows the procedure described in Ref. 1 and summarized in the posttest analyses of vessel V-3. Since the actual surface length of flaw A was 5.25 in. and, allowing for 15% stable crack growth,

$$A_c = (1.039)(1.87)(5.25) = 10.20 \text{ in.}^2 .$$

$$A = [(1.15)(5.25) + 6]6 = 72.23 \text{ in.}^2 .$$

$$p_f = (88.3)(0.444)\left(1 - \frac{10.20}{72.23}\right) = 33.7 \text{ ksi} .$$

The fact that this calculated value of pressure exceeds the actual failure pressure of 31.9 ksi implies that more than 15% stable crack growth occurred prior to failure. The strain corresponding to a pressure of 33.7 ksi is estimated from

$$\lambda_f = \frac{2[33.7 - (70)(0.367)]}{(1.085)(5.15)} = 2.86\% .$$

which again exceeds the actual failure strain.

The normalized crack-opening-displacement approach (analysis performed by J. G. Merkle, ORNL)

Using the method as previously described and a yield stress of 70 ksi.

$$a = (0.9)^2 (1.87) = 1.51 \text{ in.}$$

and

$$\phi = \frac{(369/70)^2}{2\pi(1.51)} = 2.93 .$$

The allowable strain is thus $\epsilon = (0.233)(2.93 + 0.25) = 0.741\%$, which is conservative. From Fig. 4.2, the corresponding pressure is 27.7 ksi.

The Berkeley Nuclear Laboratories two-criteria approach (analysis performed by J. G. Merkle, ORNL)

Using the method previously described and $K_c = 369 \text{ ksi}\sqrt{\text{in.}}$.

$$L_K = \frac{369}{2.8\sqrt{1.87\pi}} = 54.37 \text{ ksi} .$$

$$A_c = \frac{\pi(1.87)(5.25)}{4} = 7.71 \text{ in.}^2 .$$

$$A = (5.25 + 6)6 = 67.50 \text{ in.}^2 .$$

$$L_a = (88.3)(0.444)\left(1 - \frac{7.71}{67.50}\right) = 34.73 \text{ ksi} .$$

$$\frac{\pi L_K}{\sqrt{8} L_a} = \frac{\pi(54.37)}{\sqrt{8}(34.73)} = 1.7388 .$$

$$e^{-(1.7388)^2} = 0.04863 = \cos 87.21^\circ .$$

$$L_f = \frac{(87.21)}{90}(34.73) = 33.7 \text{ ksi} .$$

This estimate agrees exactly with the plastic instability analysis based on an allowance of 15% stable crack growth, which is evidently an insufficient allowance for stable crack growth in the dynamic upper-shelf temperature range.

Summary

Table 4.5 summarizes the analytical results for the series 2 vessels, vessels V-3, V-4, and V-6. As in the case of the series 1 vessels,[1] vessels V-1 and V-2, no method of prediction overpredicted a failure pressure by more than 10%.

Table 4.5. Summary of analytical results for HSST program intermediate test vessels V-3, V-4, and V-6

Analytical method	Vessel V-3			Vessel V-4			Vessel V-6		
	Pressure (ksi)	Strain (in./in.)	Remarks	Pressure (ksi)	Strain (in./in.)	Remarks	Pressure (ksi)	Strain (in./in.)	Remarks
				Pretest estimates[a]					
Linear elastic fracture mechanics based on strain				27.0	0.20	K_{Ic} 200 ksi $\sqrt{in}$	28.4	0.30	Conservative
Plastic instability	30.3[b]	1.61[c]	15% stable crack growth				31.6	1.34	3% stable crack growth
Equivalent energy	29.0	1.0	J_{Id} 263 psi (n = 0.145)	29.0	0.1–0.4	J_{Id} = 98 psi (n = 0.145)	31.7	1.6	J_{Id} = 458 psi, (flaw 3) (n = 0.125)
Tangent modulus				28.2	0.41	K_{Ic} = 200 ksi $\sqrt{in}$.			
				Test results					
	31.0	1.47	J_{Id} 401 psi	26.5	0.168	Outside weld flaw	31.9	2.0	Outside weld flaw (flaw 4)
				Posttest calculations[a]					
Linear elastic fracture mechanics based on strain	27.5	0.397	Conservative	26.2	0.161	K_{Ic} 160 ksi $\sqrt{in}$	27.6	0.479	Conservative
Plastic instability	31.5	2.08					33.7	2.86	1% stable crack growth
Equivalent energy	30.8	1.35	J_{Id} = 368 psi (n = 0.055)	27.0	0.235	K_{Ic} 194 ksi $\sqrt{in}$. (n = 1.60)			
Normalized C(M)	27.5	0.53	Conservative	24.2	0.139	Conservative	27.7	0.741	Conservative
Berkeley two-criteria approach	30.8	1.83		17.4	0.09	(n = 3.80)	33.7	2.86	

[a]Underlined values were determined by the method indicated, other values were determined from the calculated values and an estimate of the pressure-strain curve.
[b]Corrected pretest estimate for vessel V-3.
[c]Based on Eq. 4.14.

5. CONCLUSIONS

The tests in series 2 were tests of flaws in weldments. The three test temperatures were so chosen that each test was in a different toughness range. The test conditions and pretest fracture toughness determinations are shown in Table 5.1. Vessel V-3 had a static toughness on the upper shelf, as did the first vessel, V-1, tested in series 1. Vessel V-4 was tested at a temperature substantially above the temperature of the V-2 test of series 1, but the static fracture toughness was still well down in the transition region. Vessel V-6 was tested at 190°F, a temperature higher than any of the previous tests and one at which both the static and dynamic toughnesses were on the upper shelf.

The flaws at which failure occurred in both series were located and oriented identically, although two vessels of series 2 contained multiple flaws, one being an inside surface flaw. The flaws had essentially the same shape, and sizes ranged from 1.87 to 3.00 in. deep and 5.25 to 8.50 in. long. Thus, test conditions were sufficiently similar in the two series for qualitative comparisons to be made of weld metal and base metal. Test results are summarized in Table 5.2.

Table 5.1. Intermediate vessel test conditions for series 1 and 2

Vessel No.	Flaw a (in.)	Size $2b$ (in.)	Test temperature (°F)	Fracture toughness K_{Ic} (ksi $\sqrt{in.}$)	Flaw description	
					Location	Material
2[a]	2.53	8.50	32	184	Outside	A508-2
4[b]	2.95	8.25	75	160	Outside	Weld
1[a]	2.56	8.25	130	311	Outside	A508-2
3[b]	2.11	8.50	130	325	Outside	Weld
6[b]	1.87	5.25	190	369	Outside	Weld

[a]Series 1 tests.
[b]Series 2 tests.

Table 5.2. Intermediate vessel test results for series 1 and 2

Vessel No.	Maximum pressure p_f (ksi) and strain λ_f (–) at failure		Mode of failure	Calculated results		Load factor $(p_f/p_d)^b$	Remarks
				LEFM[a] based on strain	Plastic instability		
2	p_f	27.9	Flat	27.4[c]		2.87	
	λ_f	0.194		0.206			
4	p_f	26.5	Mixed	26.2		2.73	Transition range
	λ_f	0.168		0.163			
1	p_f	28.8	Mixed	27.5[c]	29.9	2.96	Static upper shelf
	λ_f	0.92		0.345			
3	p_f	31.0	Mixed	27.5[c]	3.15	3.19	Static upper shelf
	λ_f	1.47		0.397			
6	p_f	31.9	Shear	27.5	33.7	3.28	Static and dynamic upper shelf
	λ_f	2.0		0.479			

[a]Linear elastic fracture mechanics.
[b]p_d, design pressure = 9.71 ksi.
[c]Earlier estimates of pressure, including those of reference 1, were based upon a less accurate estimate of the pressure-strain relationship for the intermediate vessels.

Vessel V-3, tested at 130°F, behaved as V-1. Both vessels attained strains in the unflawed sections far into the plastic range. The vessels ruptured when a condition of plastic instability in the net flawed section was attained, and the rupture propagated in a mixed mode the full length of the test sections.

Vessels V-1 and V-3 were tested at the same temperature, and fracture toughnesses were nearly identical. Crack geometry was also believed to be the same in both vessels before the test of V-3. Hence, analyses of V-1 were expected to apply to V-3. The test results generally confirmed these expectations. LEFM based on strain was very conservative, as was expected in these two tests. Both the plastic instability analysis and the equivalent-energy method gave reasonable estimates of both failure pressure and strain. The crack arrest estimate for vessel V-1 applies also to V-3 and proved to be correct in both tests.

The test of vessel V-6 at 140°F generally gave further confirmation of the conclusions drawn from the tests conducted at 130°F. In situations in which LEFM (based on strain) predicts gross yielding in the unflawed section, plastic instability in the net flawed section provides a better estimate of failure pressure and strain.

The V-6 test was the first intermediate vessel test to exhibit crack arrest. The final fracture was a full shear extending about 1½ ft from each end of the flaw. Arrest had been predicted in pretest analysis; however, the validity of that prediction was not assured by this test, since it is not known whether the drop in load during crack propagation was a significant factor.

The tests at 130°F and above, in which gross yielding in the unflawed section preceded fracture, demonstrate the importance of properly accounting for stable crack growth in estimating the strength of structures and in the conducting and interpretation of fracture-specimen testing.

The test vessel V-4 at 75°F demonstrated the fracture behavior of a structure in the fracture toughness transition regime. As was the case in the V-2 test, LEFM, based on strain, predicted the failure conditions reasonably well. However, the pretest estimates of failure pressure and strain were higher than the true values. Some estimates had indicated that gross yielding would precede fracture.

Variability of fracture toughness was known to be characteristic of weld metal. From posttest evaluation, it is evident that the values of fracture toughness used before the test were too high, and the actual crack depth had been substantially underestimated by pretest measurements. Nevertheless, the fracture pressure was only slightly overestimated by the method of LEFM based on strain.

The following general conclusions have been drawn from the tests of the first two series.

1. Experimental methods have been developed for observing flaw behavior in structures. Although the techniques are not always precise, they have proved to be useful. An ultrasonic method for precisely monitoring crack growth during specimen preparation was developed. Acoustic emission monitoring of test vessels was satisfactorily demonstrated, although the interpretation of such data requires further development and experience.

2. The techniques of strain gaging the intermediate vessels and acquiring reliable strain data have been demonstrated.

3. Fracture toughness values determined by testing small specimens have been useful in predicting the fracture behavior of the intermediate vessels as well as the model vessels.

4. Fracture behavior of weld metal is essentially like that of the base material of the intermediate vessels. Variability of toughness in weld material may be a significant factor in predicting flaw behavior.

5. Crack initiation prior to gross yield is satisfactorily predicted by the method of LEFM based on strain

6. Stable crack growth is a factor that should not be neglected in analyzing thick sections loaded beyond gross yield. In future tests it is important to try to measure stable crack extension with increasing load.

7. Pretest predictions of initiation and arrest were correct, but the test in which arrest was observed was somewhat inconclusive because the effect of decreasing load cannot be estimated.

8. All methods of analysis used in series 2 produced either accurate, conservative, or slightly unconservative estimates of failure pressure. For plastic behavior, both the plastic-instability and equivalent-energy methods produced reasonable results for both pressure and strain. However, the correct pressure-strain relationship was not always known *a priori* without test data

REFERENCES

1. R. W. Derby et al., *Test of 6-Inch-Thick Pressure Vessels. Series 1: Intermediate Test Vessels V-1 and V-2*, ORNL-4895 (February 1974).
2. C. J. Childress, *Fabrication and Mechanical Test Data for Acceptance of the First Six 6-Inch-Thick Intermediate Test Vessels of the Heavy Section Steel Technology Program*, ORNL-TM-4351 (October 1973).
3. A. A. Abbatiello and R. W. Derby, *Notch Sharpening in a Large Tensile Specimen by Local Fatigue*, ORNL-TM-3925 (November 1972).
4. *HSST Program Semiannu. Progr. Rep., Period Ending Feb. 28, 1971*, ORNL-4681, p. 60.
5. *HSST Program Semiannu. Progr. Rep., Period Ending Feb. 28, 1973*, ORNL-4918, pp. 53–60.
6. *HSST Program Semiannu. Progr. Rep., Period Ending Aug. 31, 1973*, ORNL-4971, pp. 66–74.
7. *HSST Program Semiannu. Progr. Rep., Period Ending Feb. 20, 1973*, ORNL-4918, pp. 60–68.
8. *HSST Program Semiannu. Progr. Rep., Period Ending Aug. 31, 1973*, ORNL-4971, pp. 74–79.
9. Personal communication with D. A. Canonico, ORNL.
10. Tentative Method of Test for Plane-Strain Fracture Toughness of Metallic Materials, ASTM E399-70T.
11. F. J. Witt, *A Procedure for Determining Bounding Values on Fracture Toughness K_{Ic} at Any Temperature*, HSST 5th Annual Information Meeting, Paper 13, March 197[illegible].
12. T. R. Mager, *Experimental Verification of Lower Bound K_{Ic} Values Utilizing the Equivalent Energy Concept*, HSST 6th Annual Information Meeting, Paper 23, April 1972.
13. F. J. Witt and T. R. Mager, *A Procedure for Determining Bounding Values on Fracture Toughness K_{Ic} at Any Temperature*, ORNL-TM-3894 (October 1972).
14. W. O. Shabbits, W. H. Pryle, and E. T. Wessel, *Heavy Section Fracture Toughness Properties of A533 Grade B, Class 1 Steel Plate and Submerged Arc Weldment*, HSST Program Technical Report No. 6 (December 1969).
15. D. A. Canonico, "Investigation of Weld-Metal Heat-Affected Zone," *HSST Program Semiannu. Progr. Rep., Period Ending Aug. 31, 1972*, ORNL-4853, p. 3, and *HSST Program Semiannu. Progr. Rep., Period Ending Feb. 28, 1973*, ORNL-4918, p. 9.
16. A. F. Schmidt and W. K. Lumetti, *Acoustic Surveillance During Vessel Rupture Testing at the Oak Ridge National Laboratory*, Westinghouse Electric Corp. (no date).
17. P. T. Heald and B. Edmundson, "A Review of Fracture Mechanics Methods for Assessing the Integrity of Pressurized Structures," pp. 95–99 in *Periodic Inspection of Pressurized Components*, The Institution of Mechanical Engineers, London, 1974.
18. D. R. Bland, "Elastoplastic Thick-Walled Tubes of Work-Hardening Material Subject to Internal and External Pressures and to Temperature Gradients," *J. Mech. Phys. Solids* 4, 209–29 (1956).
19. M. N. Raftenberg, "Determination of Stress and Strain Fields for an Internally Pressurized Elastic-Plastic Thick-Walled Hollow Cylinder, Using a Trilinear Stress-Strain Curve," *Quarterly Progress Report on Reactor Safety Programs Sponsored by the NRC Division of Reactor Safety Research for October–December 1974*, ORNL-TM-4805, Vol. II.
20. M. E. Shank (ed.), *Control of Steel Construction to Avoid Brittle Failure*, Welding Research Council, 1957.
21. H. Neuber, "Theory of Stress Concentration for Shear-Strained Prismatical Bodies with Arbitrary Nonlinear Stress-Strain Law," *J. Appl. Mech.*, ASME, pp. 544–50, December 1961.
22. T. H. Topper, R. M. Wetzel, and J. Morrow, "Neuber's Rule Applied to Fatigue of Notched Specimens," *J. Mater.* 4(1), 200–9 (March 1969).
23. J. G. Merkle, "An Analytical Basis for Notch Sharpening by Fatigue," ASME Paper 71-PVP-46, May 1971 (see also Paper 19, HSST Program 5th Annual Information Meeting, Oak Ridge National Laboratory, Oak Ridge, Tenn., March 1971).
24. J. G. Merkle, *An Elastic-Plastic Thick-Walled Hollow Cylinder Analogy for Analyzing the Strains in the Plastic Zone Just Ahead of a Notch Tip*, ORNL-TM-4071 (January 1973).
25. J. G. Merkle, "Analytical Applications of the J-Integral," *Progress in Flaw Growth and Fracture Toughness Testing*, ASTM STP 536, American Society for Testing and Materials, pp. 264–80, 1973.

26. D. C. Drucker "A Continuum Approach to the Fracture of Metals," pp. 5–50 in *Fracture of Solids*, proceedings of a conference on fracture held at Maple Valley, Wash., Aug. 21–24, 1962, Wiley, 1963.
27. F. M. Burdekin and M. G. Dawes, "Practical Use of Linear Elastic and Yielding Fracture Mechanics with Particular Reference to Pressure Vessels," pp. 28–37 in *Practical Application of Fracture Mechanics to Pressure Vessel Technology*, Institution of Mechanical Engineers, London, 1971.
28. M. G. Dawes, "Fracture Control in High Yield Strength Weldments," *Welding J.* 53(9), 369s–379s (September 1974).
29. J. G. Merkle, *Analytical Relations Between Elastic-Plastic Fracture Criteria* (to be published).
30. J. N. Goodier and F. A. Field, "Plastic Energy Dissipation in Crack Propagation," pp. 103–118 in *Fracture of Solids*, edited by D. C. Drucker and J. J. Gilman, Interscience, 1962.
31. A. R. Dowling, *The Effect of Defects on Structural Failure: A Two-Criteria Approach*, RD/B/N2921, Berkeley Nuclear Laboratories, Central Electricity Generating Board, England (March 1974).
32. E. K. Lynn, "Critical Flaw Size for Inelastic Stresses," Appendix 6 in *PVRC Recommendations on Toughness Requirements for Ferritic Materials*, WRC Bulletin No. 175, the Welding Research Council, August 1972.
33. F. J. Loss, *Engineering Significance of Statistical and Temperature-Induced Fracture Mechanics Toughness Variations on Fracture-Safe Assurance*, NRL-7353 (Dec. 2, 1971).
34. J. G. Merkle, "Fracture Safety Analysis Concepts for Nuclear Pressure Vessels Considering the Effects of Irradiation," *J. Basic Eng., ASME, Series D*, 93(2), 265–73 (June 1971).

APPENDICES

Appendix A

MATERIAL PROPERTIES OF PROLONGATIONS

Properties of base and weld metal of the prolongation of vessels V-3, V-4, and V-6 were determined by W. J. Stelzman of the Metals and Ceramics Division of Oak Ridge National Laboratory and by T. R. Mager, S. E. Yanichko, and L. R. Singer of Westinghouse Electric Corporation.*[1]

Stelzman tested precracked Charpy V-notch specimens taken from the prolongations of the three vessels. The locations of the specimens in the prolongations are shown in Fig. A.1 through A.9 and Tables A.1 and A.2; orientations are as defined in Fig. 2.14; and the data and fracture toughness values determined from these specimens are given in Table A.3. When these slow-bend tests were made, the specimen deflection was obtained from the crosshead motion; consequently, conservative (low-fracture toughness) values were deduced. These results were available at the time of the vessel tests. Subsequently, the system was changed so that specimen deflection is presently measured directly. By correlation of results obtained by both methods, data accumulated to date are sufficient to determine corrections for K_{Icd} data up to 125 ksi $\sqrt{in.}$ This correlation is shown in Fig. A.10. The adjusted values are included in Table A.3 under the heading "From specimen deflection." It should be noted that deflections for the adjusted values are taken from the correlation, of which the portion above the data points shown is an assumed linear fit to the data.

The value of K_{Icd} is calculated in accordance with the expression given in ASTM E-399-72 for bend specimens,[2] with the load P_Q being given the value P_{eq} prescribed by the equivalent-energy method, namely

$$P_{eq} = \sqrt{2\,k\,E_{max}}\,,$$

where k is the slope of the linear portion of the load-deflection curve and E_{max} is the area under the curve up to maximum load. The dimensional parameters shown in Table A.3 are as defined in ASTM E-399-72. The span length was 1.576 in. for all specimens; the width and thickness of the specimens were nominally 0.394 in., but actual measurements were used in calculating K_{Icd}.

Stelzman's measurements of Charpy-impact and tensile properties of the prolongations are given in Tables A.4 and A.5, respectively. Locations of these specimens are also shown in Fig. A.1 through A.9, and orientations are as defined in Fig. 2.14.

Fracture toughness was determined by Mager and his co-workers by testing compact-tension specimens machined from materials in prolongations of the test cylinders of vessels V-3, V-4, and V-6.

The pieces of the prolongation of vessel V-3 identified as V3A1, V3A2A1, and V3A2A2-I in Figs. A.1, A.2, and A.3 were sent to Westinghouse Electric Corporation for this purpose. Five 0.85T CT specimens (V3A1-1, V3A1-2, V3A1-3, V3A1-4, and V3A1-5) were cut from piece V3A1. One 3T CT specimen (V3A2A1-1) and six 0.394T CT specimens (V3A2A1-2 through V3A2A1-7) were cut from piece V3A2A1. Piece V3A2A2-I was cut into four 0.85T CT specimens (V3A2A2-1 through V3A2A2-4). Locations of the specimens are shown in Fig. 2.15.

The parts of the prolongation of vessel V-4 sent to Westinghouse for machining and testing of compact-tension specimens are pieces V4A1A1, V4A1A2-1, V4A2B, and V4C as identified in Figs. A.4 and A.5. One 4T CT specimen (V4A1A1-1) was cut from piece V4A1A1, four 0.85T CT specimens (V4A1A2-1

---

*Work sponsored by the HSST program under UCCND Subcontract 3196 between Union Carbide Corporation and Westinghouse Electric Corporation.

BLANK PAGE

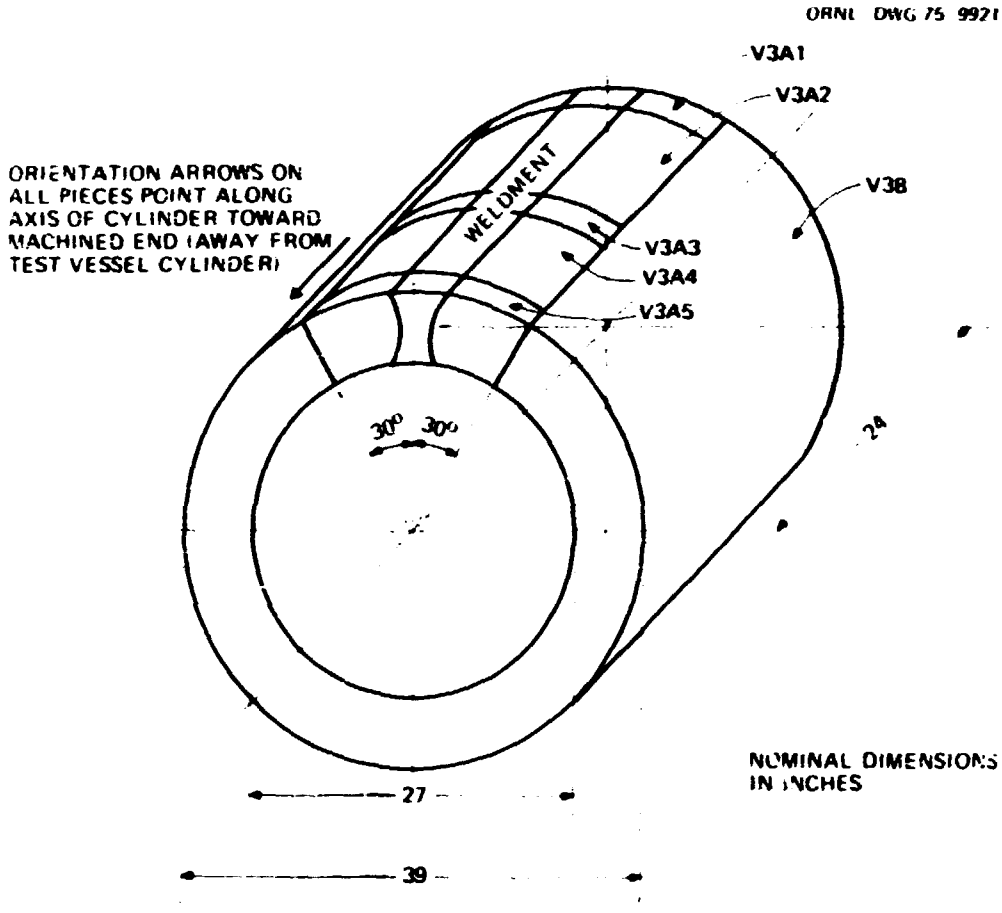

Fig. A.1. Cutting plan for the prolongation of vessel V-3.

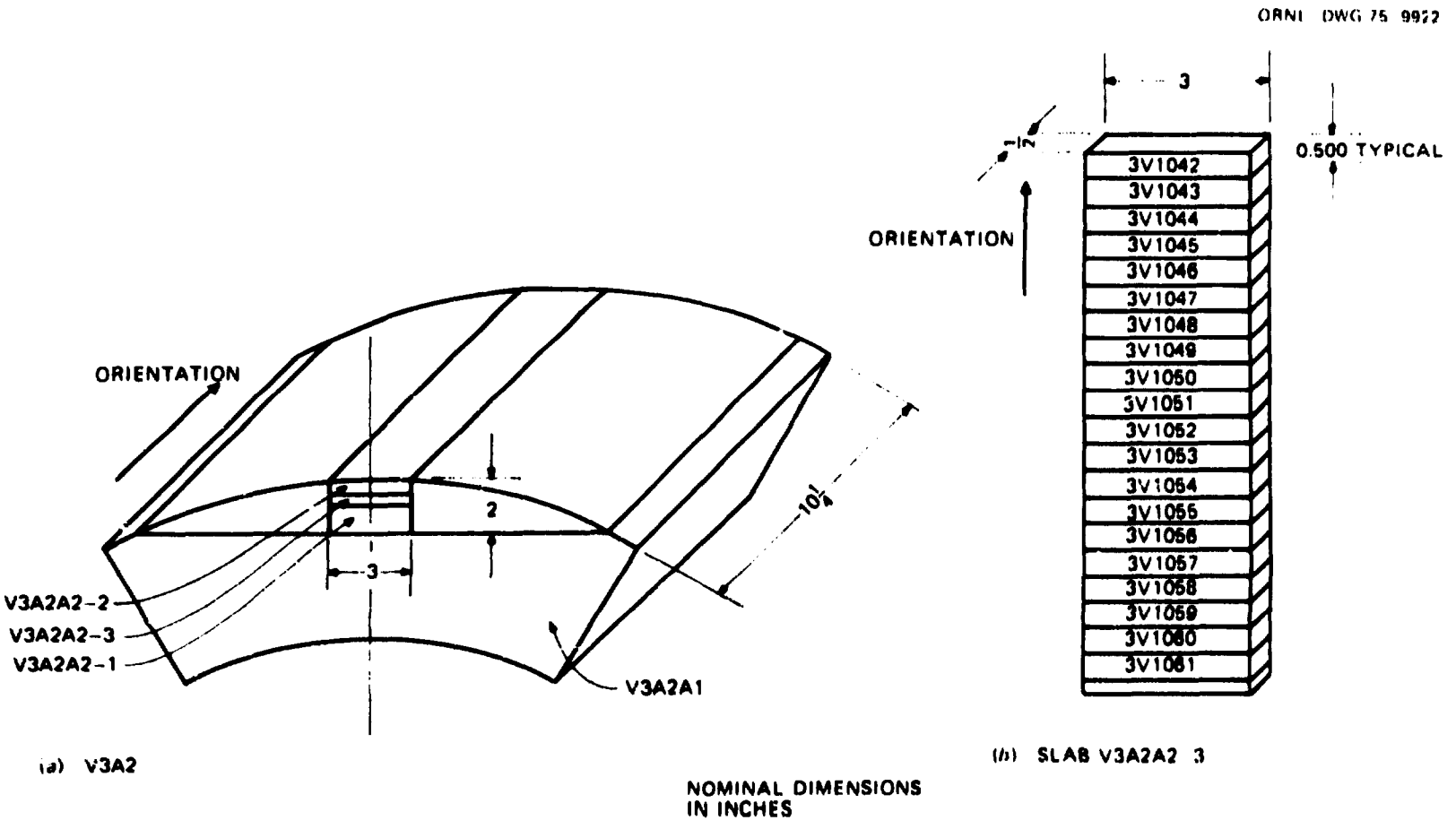

Fig. A.2. Cutting plan for piece V3A2 from the prolongation of vessel V-3.

SLAB NO	SPECIMEN NO FOR BLANK											
	a	b	c	d	e	f	g	h	i	j	k	l
V3A3 1	3V1000	3V1001	3V1002	3V1003	3V1004	3V1005	3V1006	3V1007	3V1008	3V1009	3V1010	3V1011
V3A3 2	3V1012	3V1013	3V1014	3V1015	3V1016	3V1017	3V1018	3V1019	3V1020	3V1021	3V1022	3V107
V3A3 3	3V1024	3V1025	3V1026	3V1027	3V1028	3V1029	3V1030	3V1031	3V1032	3V1033	3V1034	3V1035
V3A3 4	3V1036	3V2000	3V2001	3V1037	3V2002	3V2003	3V1038	3V1039	3V2004	3V1040	3V2005	3V1041

TYPE SPECIMEN CHARPY
MINIATURE TENSILE

1000 SERIES SPECIMEN NUMBERS
2000 SERIES SPECIMEN NUMBERS

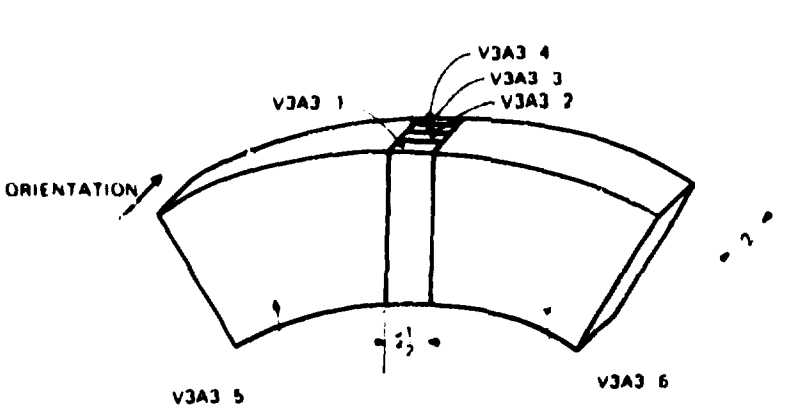

(a) V3A3

OUTSIDE SURFACE

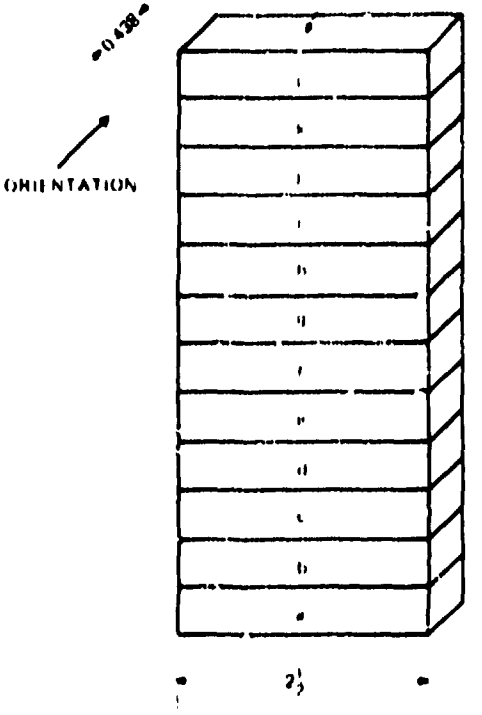

(b) TYPICAL SLAB

NOMINAL DIMENSIONS
IN INCHES

Fig. A.3. Cutting plan for piece V3A3 from the prolongation of vessel V-3.

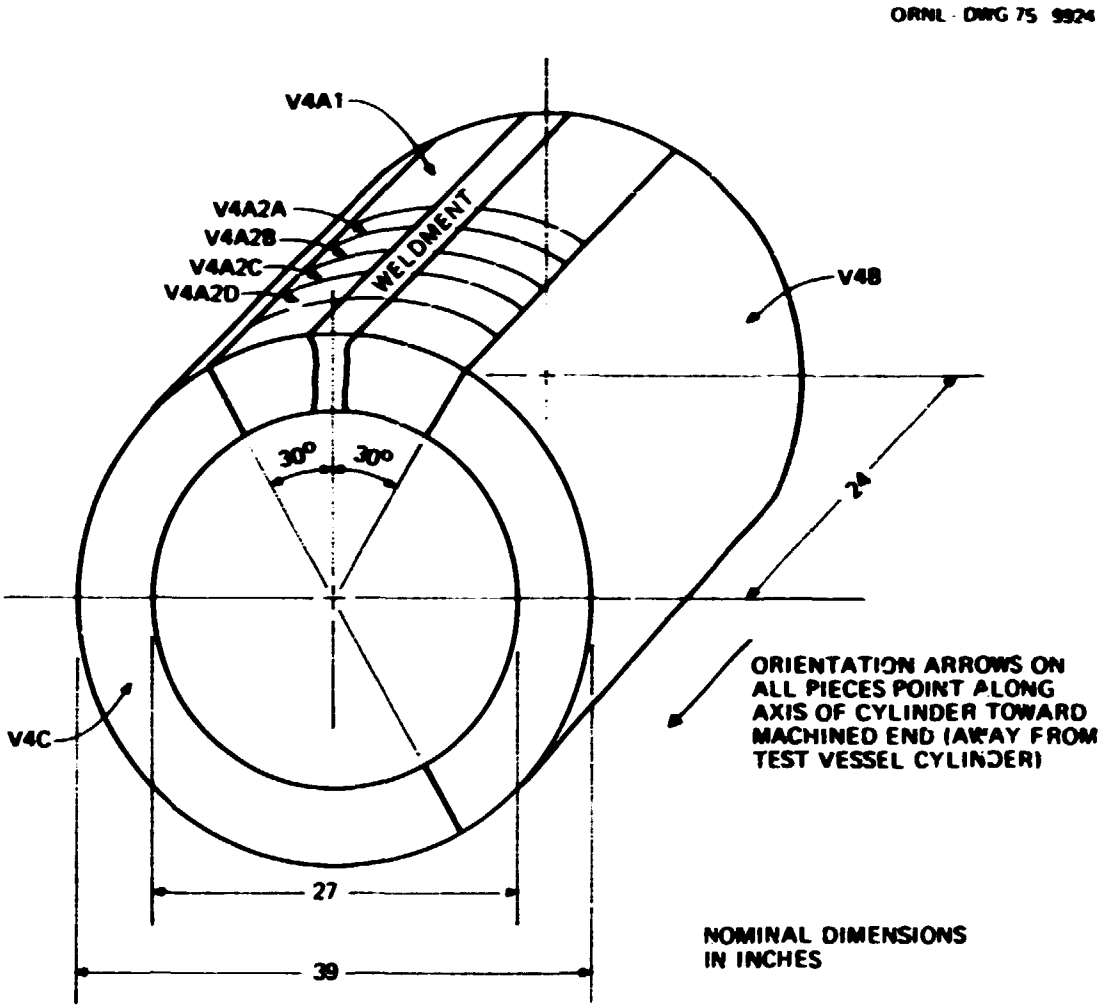

Fig. A.4. Cutting plan for the prolongation of vessel V-4.

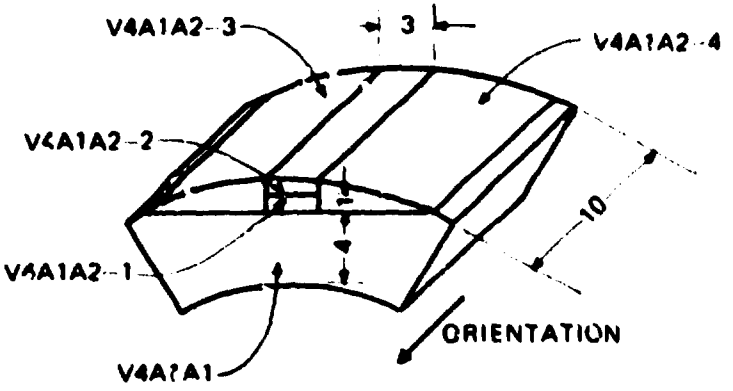

(a) V4A1

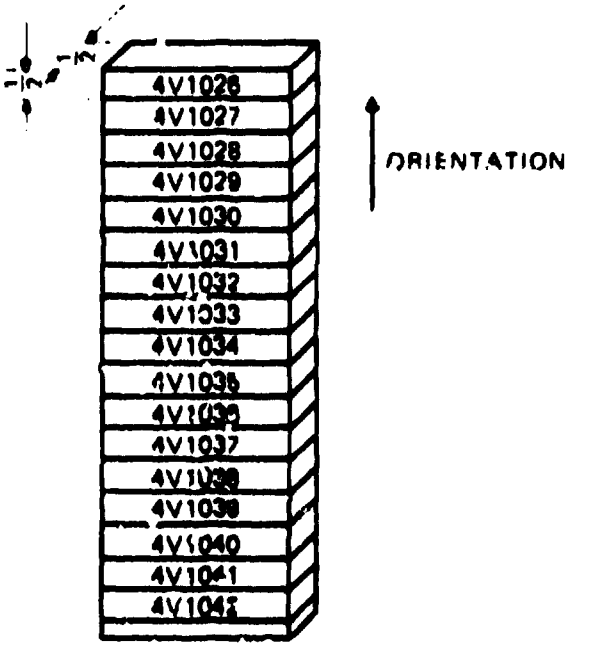

(b) SLAB V4A1A2 2

NOMINAL DIMENSIONS IN INCHES

Fig. A.8. Cutting plan for piece V4A1 from the prolongation of vessel V-4.

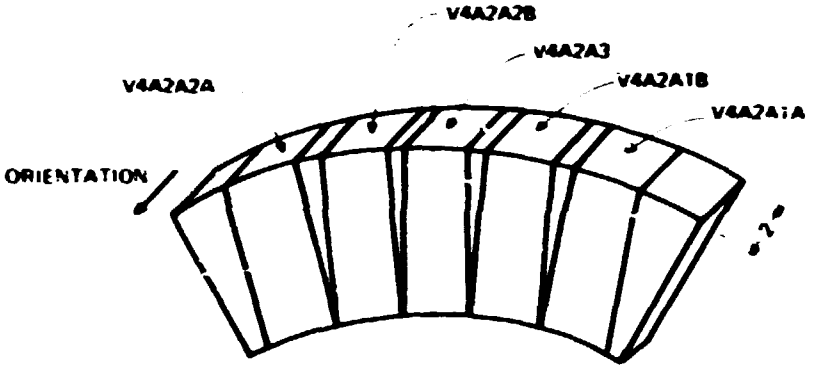

(a) V4A2A

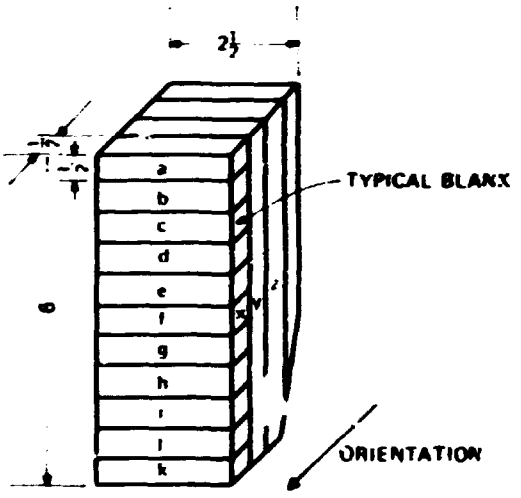

NOMINAL DIMENSIONS IN INCHES

PIECE NO.	SLAB NO. FOR SLAB		
	x	y	z
V4A2A3	V4A2A3A	V4A2A3B	V4A2A3C
V4A2A1A	V4A2A1A-1	V4A2A1A-2	V4A2A1A-3
V4A2A1B	V4A2A1B-1	V4A2A1B-2	V4A2A1B-3
V4A2A2B	V4A2A2B-1	V4A2A2B-2	V4A2A2B-3

(b) TYPICAL SLABS CUT FROM PIECES V4A2A3, V4A2A1A, V4A2A1B, AND V4A2A2B

Fig. A.6. Cutting plan for piece V4A2A from the prolongation of vessel V-4. See Table A.1 for specimen numbers.

ORNL DWG 75 9927

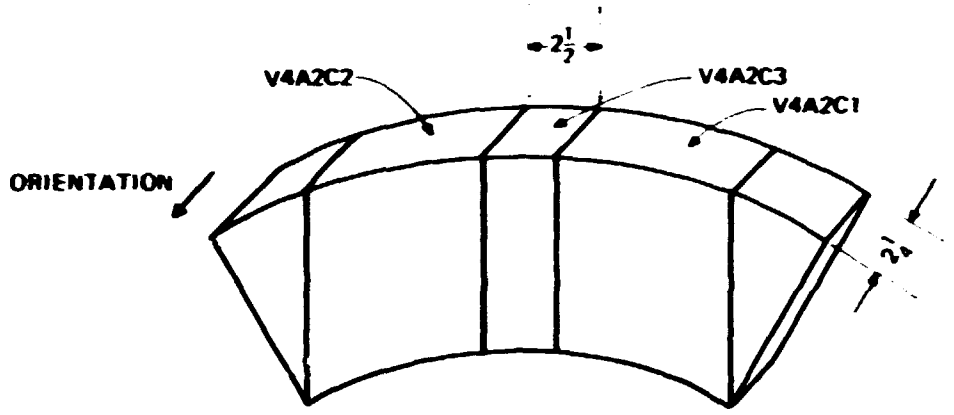

(a) V4A2C

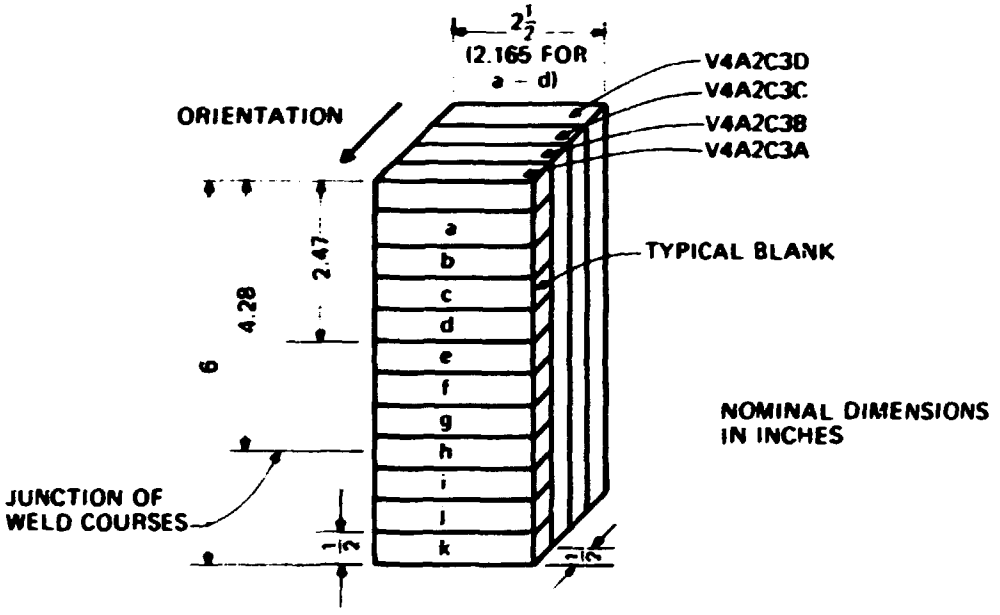

(b) V4A2C3

Fig. A.7. Cutting plan for piece V4A2C from the prolongation of vessel V-4. See Table A.1 for specimen numbers.

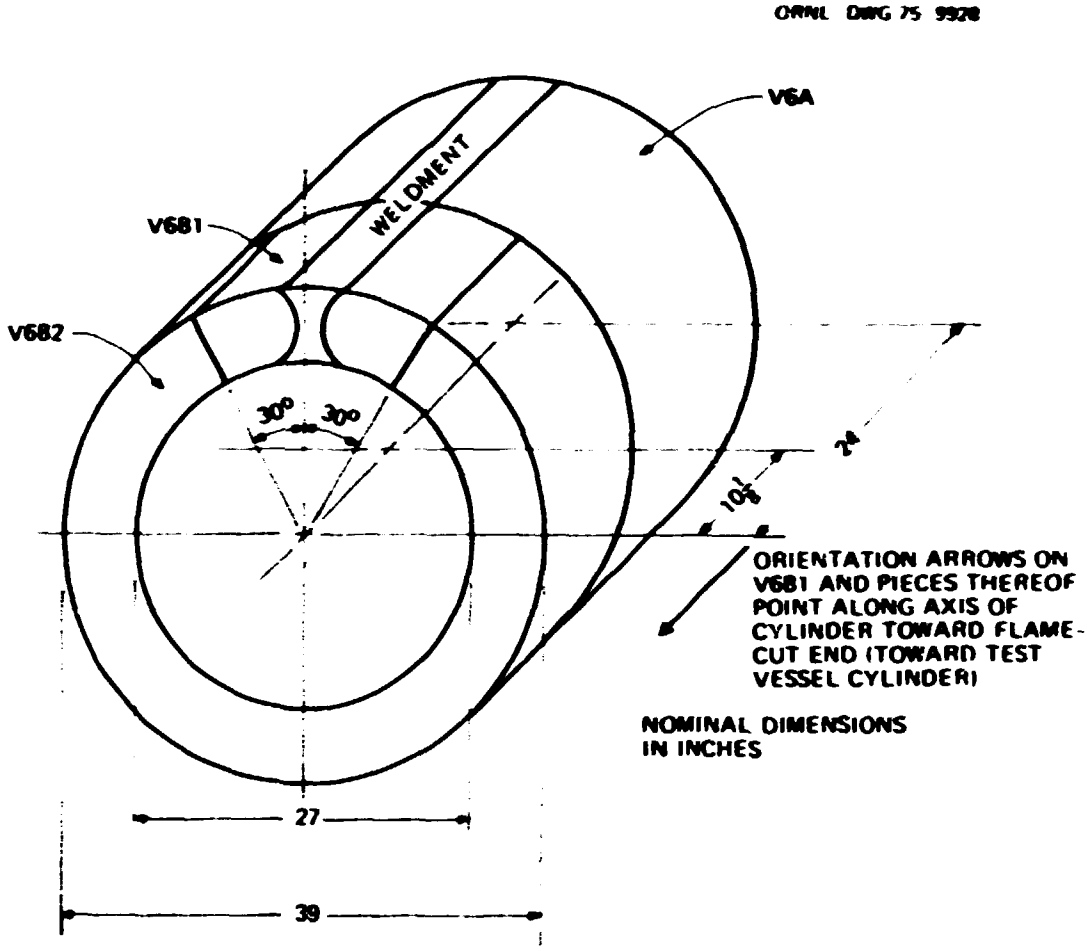

Fig. A.8. Cutting plan for the prolongation of vessel V-6.

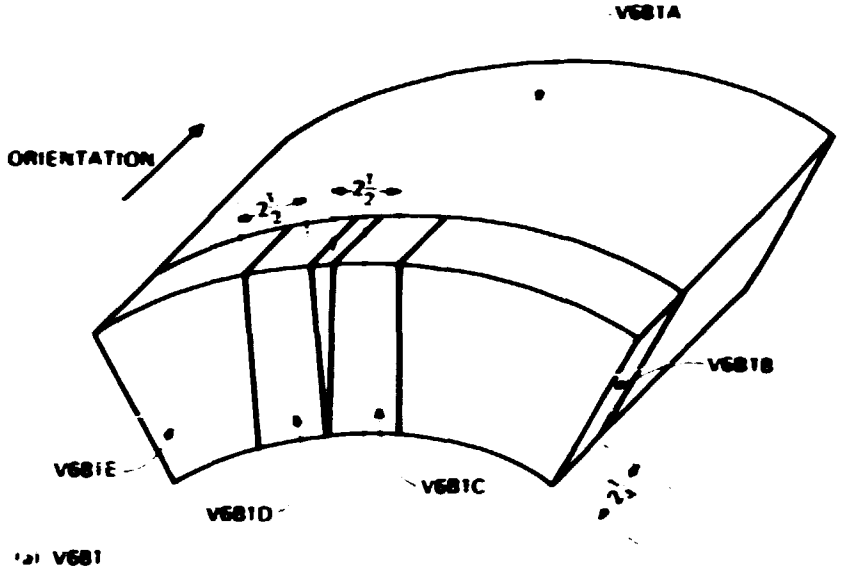

(a) V681

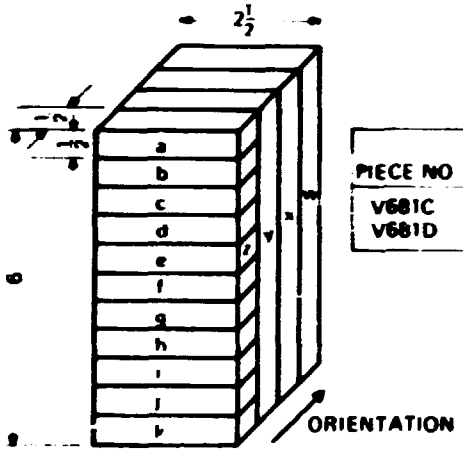

PIECE NO	SLAB NO FOR SLAB w	x	y	z
V681C	V681C1	V681C2	V681C3	V681C4
V681D	V681D1	V681D2	V681D3	V681D4

NOMINAL DIMENSIONS IN INCHES

(b) TYPICAL SLABS CUT FROM PIECES V681C AND V681D

Fig. A.9. Cutting plan for piece V681 from the prolongation of vessel V-6. See Table A.2 or specimen numbers.

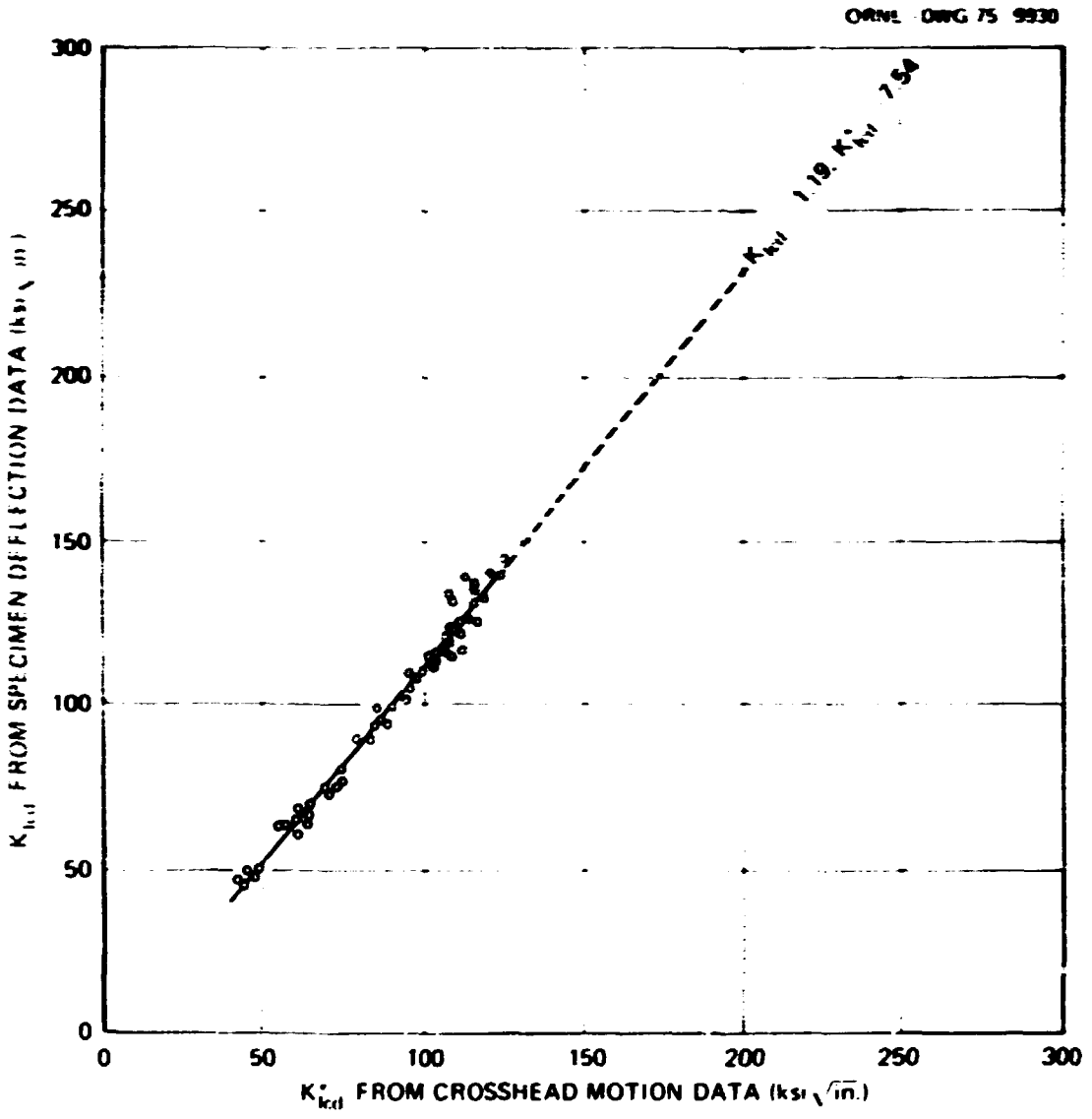

Fig. A.10. Comparison of static fracture toughness as computed from deflectometer measurements and crosshead motion.

Table A.1. Specimen numbers of tensile and Charpy V-notch specimens for vessel V-4 for slabs identified in Figs. A.6 and A.7

Slab	Specimen No. for blank										
	a	b	c	d	e	f	g	h	i	j	k
V4A2A3A	4V1000	4V2000	4V1001	4V2001	4V1002	4V2002	4V1003	4V2003	4V1004	4V2004	4V1005
V4A2A3B	4V1006	4V1007	4V1008	4V1009	4V1010	4V1011	4V1012	4V1013	4V1014	4V1015	4V1016
V4A2A3C	4V1017	4V1018	4V1019	4V1020	4V1021	4V1022	4V1023	4V1024	4V1025		
V4A2A1A-1	4V2005	4V2006	4V2007	4V2008	4V2009	4V2010	4V2011	4V2012	4V2013	4V2014	4V2015
V4A2A1A-2	4V1043	4V1044	4V1045	4V1046	4V1047	4V1048	4V1049	4V1050	4V1051	4V1052	4V1053
V4A2A1A-3	4V1054	4V1055	4V1056	4V1057	4V1058	4V1059	4V1060	4V1061			
V4A2A1B-1	4V1062	4V1063	4V1064	4V1065	4V1066	4V1067	4V1068	4V1069	4V1070	4V1071	4V1072
V4A2A1B-2	4V1073	4V1074	4V1075	4V1076	4V1077	4V1078	4V1079	4V1080	4V1081	4V1082	4V1083
V4A2A1B-3	4V1084	4V1085	4V1086	4V1087	4V1088	4V1089	4V1090	4V1091			
V4A2A2B-1	4V1092	4V1093	4V1094	4V1095	4V1096	4V1097	4V1098	4V1099	4V1100	4V1101	4V1102
V4A2A2B-2	4V1103	4V1104	4V1105	4V1106	4V1107	4V1108	4V1109	4V1110	4V1111	4V1112	4V1113
V4A2A2B-3	4V1114	4V1115	4V1116	4V1117	4V1118	4V1119	4V1120	4V1121			
V4A2C3A	4V1150	4V1151	4V1152	4V1153	4V1122	4V1123	4V1124	4V1125	4V1126	4V1142	4V1143
V4A2C3B	4V1154	4V1155	4V1156	4V1157	4V1127	4V1128	4V1129	4V1130	4V1131	4V1144	4V1145
V4A2C3C	4V1158	4V1159	4V1160	4V1161	4V1132	4V1133	4V1134	4V1135	4V1136	4V1146	4V1147
V4A2C3D	4V1162	4V1163	4V1164	4V1165	4V1137	4V1138	4V1139	4V1140	4V1141	4V1148	4V1149

Table A.2. Specimen numbers for tensile and Charpy V-notch specimens for vessel V-6 for slabs identified in Fig. A.9

Slab	Specimen No. for blank										
	a	b	c	d	e	f	g	h	i	j	k
V6P1C1	6V1000	6V1001	6V1002	6V1003	6V1004	6V1005	6V1006	6V1007	6V1008	6V1009	6V1010
V6B1C2	6V1011	6V1012	6V1013	6V1014	6V1015	6V1016	6V1017	6V1018	6V1019	6V1020	6V1021
V6B1C3	6V1022	6V1023	6V1024	6V1025	6V1026	6V1027	6V1028	6V1029	6V1030	6V1031	6V1032
V6V1C4	6V1033	6V2000	6V1034	6V2001	6V1035	6V2002	6V1036	6V2003	6V1037	6V2004	6V1038
V6B1D1	6V1039	6V1040	6B1041	6V1042	6V1043	6V1044	6V1045	6V1046	6V1047	6V1048	6V1049
V6B1D2	6V1050	6V1051	6V1052	6V1053	6V1054	6V1055	6V1056	6V1057	6V1058	6V1059	6V1060
V6B1D3	6V1061	6V1062	6V1063	6V1064	6V1065	6V1066	6V1067	6V1068	6V1069	6V1070	6V1071
V6B1D4	6V1072	6V2005	6V1073	6V2006	6V1074	6V2007	6V1075	6V2008	6V1076	6V2009	6V1077

Table A3 [illegible]

[illegible]	[illegible]	[illegible]	[illegible]		[illegible]	[illegible]	[illegible]			[illegible]		[illegible]	
			a	[illegible]			Maximum	[illegible]	[illegible]	Maximum [illegible]	[illegible]	Maximum [illegible]	[illegible]
							[illegible]						
[illegible]	[illegible]	[illegible]	.209	[illegible]	[illegible]	[illegible]	[illegible]	--	--	[illegible]	--	[illegible]	--
[illegible]	[illegible]	[illegible]	.207	[illegible]	[illegible]	[illegible]	[illegible]	--	--	[illegible]	--	[illegible]	--
[illegible]	[illegible]	[illegible]	[illegible]	[illegible]	[illegible]	[illegible]	[illegible]	--	--	[illegible]	--	[illegible]	--
[illegible]	[illegible]	[illegible]	.208	[illegible]	[illegible]	[illegible]	[illegible]	--	--	[illegible]	--	[illegible]	--
[illegible]	[illegible]	[illegible]	[illegible]	[illegible]	[illegible]	[illegible]	[illegible]	--	--	[illegible]	--	[illegible]	--
[illegible]	[illegible]	[illegible]	[illegible]	[illegible]	[illegible]	[illegible]	[illegible]	--	--	[illegible]	--	[illegible]	--
[illegible]	[illegible]	[illegible]	.201	.193	[illegible]	[illegible]	[illegible]	[illegible]	[illegible]	[illegible]	[illegible]	[illegible]	[illegible]
[illegible]	[illegible]	[illegible]	.201	[illegible]	[illegible]	[illegible]	--	[illegible]	[illegible]	[illegible]	[illegible]	--	[illegible]
[illegible]	[illegible]	[illegible]	.220	[illegible]	[illegible]	[illegible]	[illegible]	[illegible]	[illegible]	[illegible]	[illegible]	[illegible]	[illegible]
[illegible]	[illegible]	[illegible]	.220	[illegible]	[illegible]	[illegible]	--	[illegible]	[illegible]	--	[illegible]	--	[illegible]
[illegible]	[illegible]	[illegible]	[illegible]	[illegible]	[illegible]	[illegible]	--	[illegible]	[illegible]	--	[illegible]	--	[illegible]
[illegible]	[illegible]	[illegible]	.210	[illegible]	[illegible]	[illegible]	[illegible]	--	--	[illegible]	--	[illegible]	--
[illegible]	[illegible]	[illegible]	[illegible]	[illegible]	[illegible]	[illegible]	[illegible]	--	--	[illegible]	--	[illegible]	--
[illegible]	[illegible]	[illegible]	.199	[illegible]	[illegible]	[illegible]	--	[illegible]	[illegible]	--	[illegible]	--	[illegible]
[illegible]	[illegible]	[illegible]	.209	[illegible]	[illegible]	[illegible]	--	[illegible]	[illegible]	--	[illegible]	--	[illegible]
[illegible]	[illegible]	[illegible]	[illegible]	[illegible]	[illegible]	[illegible]	--	[illegible]	[illegible]	--	[illegible]	--	[illegible]
[illegible]	[illegible]	[illegible]	[illegible]	[illegible]	[illegible]	[illegible]	[illegible]	--	--	[illegible]	--	[illegible]	[illegible]
[illegible]	[illegible]	[illegible]	.200	[illegible]	[illegible]	[illegible]	--	[illegible]	[illegible]	--	[illegible]	--	[illegible]
[illegible]	[illegible]	[illegible]	[illegible]	[illegible]	[illegible]	[illegible]	[illegible]	--	--	[illegible]	--	[illegible]	--
[illegible]	[illegible]	[illegible]	[illegible]	[illegible]	[illegible]	[illegible]	--	[illegible]	[illegible]	--	[illegible]	--	[illegible]
[illegible]	[illegible]	[illegible]	.209	[illegible]	[illegible]	[illegible]	--	[illegible]	[illegible]	--	[illegible]	--	[illegible]
[illegible]	[illegible]	[illegible]	.233	[illegible]	[illegible]	[illegible]	--	[illegible]	[illegible]	--	[illegible]	--	[illegible]
[illegible]	[illegible]	32	[illegible]	[illegible]	[illegible]	[illegible]	[illegible]	--	--	[illegible]	--	[illegible]	--
[illegible]	[illegible]	[illegible]	.207	[illegible]	[illegible]	[illegible]	[illegible]	--	--	[illegible]	--	[illegible]	--
[illegible]	[illegible]	[illegible]	.208	[illegible]	[illegible]	[illegible]	[illegible]	--	--	[illegible]	--	[illegible]	--
[illegible]	[illegible]	[illegible]	[illegible]	[illegible]	[illegible]	[illegible]	[illegible]	--	--	[illegible]	--	[illegible]	--
							[illegible]						
[illegible]-1000	[illegible]	-100	.208	.186	.527	[illegible]	--	[illegible]	[illegible]	--	[illegible]	--	[illegible]
-1001	.22	-50	.212	.182	.538	[illegible]	--	[illegible]	[illegible]	--	[illegible]	--	[illegible]
-1002	[illegible]	32	.205	.199	.521	[illegible]	1210	--	--	[illegible]	--	[illegible]	--
-1003	.59	74	.186	.208	.472	[illegible]	[illegible]	--	--	[illegible]	--	[illegible]	--
-1004	[illegible]	130	.221	.172	.563	3.30	1290	--	--	[illegible]	--	[illegible]	--
-1005	[illegible]	74	.198	.202	.488	2.57	1390	--	--	[illegible]	--	[illegible]	--
-1006	[illegible]	-100	.195	.199	.496	2.43	--	[illegible]	[illegible]	--	[illegible]	--	[illegible]
-1007	.13	74	.195	.179	[illegible]	[illegible]	1380	--	--	[illegible]	--	[illegible]	--
-1008	.22	-50	.188	.206	.478	[illegible]	--	[illegible]	[illegible]	--	[illegible]	--	[illegible]
-1009	[illegible]	74	.207	.187	.525	2.90	1140	--	--	[illegible]	--	[illegible]	--
-1010	.41	50	.170	.224	.432	2.16	1655	--	--	[illegible]	--	[illegible]	--
-1011	.50	74	.185	.209	.470	2.42	1465	--	--	[illegible]	--	[illegible]	--
-1012	[illegible]	50	.171	.222	.435	2.18	1665	--	--	[illegible]	--	[illegible]	--
-1013	[illegible]	74	.204	.190	.517	2.81	[illegible]	--	--	[illegible]	--	[illegible]	--
-1014	[illegible]	130	.211	.183	.535	2.99	1205	--	--	[illegible]	--	[illegible]	--
-1015	[illegible]	74	.200	.186	.507	2.72	1350	--	--	[illegible]	--	5.2	--
-1016	[illegible]	50	.210	.185	.532	2.96	1165	--	--	[illegible]	--	4.7	--
-1017	[illegible]	74	.208	.193	.512	2.77	1270	--	--	[illegible]	--	4.2	--
-1018	.13	74	.179	.215	.455	2.32	1470	--	--	[illegible]	--	[illegible]	--
-1019	.22	32	.214	.190	[illegible]	[illegible]	1120	1035	[illegible]	[illegible]	.112	[illegible]	--
-1020	.32	[illegible]	.162	.232	.412	2.03	1675	--	--	.079	--	[illegible]	--
-1021	[illegible]	50	.200	[illegible]	.507	2.72	[illegible]	[illegible]	[illegible]	.067	.123	[illegible]	--
-1022	.50	74	.201	.192	.511	2.75	1225	[illegible]	[illegible]	[illegible]	.122	[illegible]	--
-1023	.59	50	.204	.190	[illegible]	[illegible]	1225	--	--	.059	--	5.0	--
-1024	[illegible]	74	.181	.213	.459	2.34	1545	--	--	.063	--	6.6	--
-1025	.77	74	.213	.181	.540	3.04	1185	--	--	[illegible]	--	3.8	--
-1026	.09	-100	.205	.188	.523	2.87	--	[illegible]	[illegible]	--	.014	--	0.7
-1027	.09	-50	.204	.190	.517	2.81	--	1090	[illegible]	--	.022	--	[illegible]
-1028	.09	0	.203	.190	.517	2.81	--	1200	900	--	.045	--	3.6
-1029	.09	32	.194	.200	.493	[illegible]	1340	1330	1140	.072	.086	[illegible]	--
-1030	.09	32	.211	.183	.536	3.00	--	1165	960	--	.070	--	5.7
-1031	.09	74	.196	.200	.492	2.60	1330	1060	910	.066	.137	6.0	13.3
-1032	.09	50	.194	.200	.492	2.60	1360	1050	900	.084	.152	[illegible]	--
-1033	.09	50	.172	.222	.436	2.19	1640	1410	1280	.074	.127	[illegible]	--
-1034	.09	130	.217	.177	.551	3.17	1050	--	--	.069	--	5.2	--
-1035	.09	74	.166	.228	.421	2.10	1650	--	--	.077	--	[illegible]	--
-1036	.09	74	.201	.193	.510	2.75	1210	--	--	.068	--	5.6	--
-1037	.09	130	.205	.189	.519	2.83	1180	--	--	.065	--	5.4	--
-1038	.09	200	.211	.183	.536	3.00	1100	--	--	.067	--	5.2	--

BLANK PAGE

[prolongations of V-3, V-4, and V-6 as determined from slow bend (0.100 in./min) tests
Notched Charpy V-notch specimens, CA orientation except as noted

Load (lb)		Crosshead deflection (in.)		Energy (ft-lb)		Slope of linear load-displacement curve (10^6 lb/in.)	Lateral expansion (10^{-3} in.)	K_{Ied} (ksi$\sqrt{in.}$)	
Start of fracture	Fracture arrest	Maximum load	Start of fracture	Maximum load	Start of fracture			From crosshead motion	From specimen deflection[c]
	V-3 weld metal								
--	--	.060	--	4.9	--	8.76	33	152	173
--	--	.063	--	5.3	--	8.97	39	157	179
--	--	.070	--	5.4	--	7.92	39	161	184
--	--	.071	--	6.1	--	9.21	43	164	186
--	--	.061	--	4.6	--	8.31	40	155	177
--	--	.068	--	6.1	--	8.76	31	163	186
1250	1090	.067	.097	6.1	9.3	8.37	30	155	177
1330	990	--	.069	--	4.3	9.12	17	137	155
1120	1085	.057	.066	5.3	7.5	8.04	28	165	189
1105	600	--	.038	--	2.7	8.13	19	125	141
990	220	--	.054	--	3.5	8.04	20	144	164
--	--	.066	--	5.6	--	7.92	39	157	179
--	--	.069	--	6.0	--	8.39	36	169	194
1175	490	--	.030	--	2.2	9.09	17	96	107
1160	415	--	.028	--	2.2	9.15	17	143	163
965	285	--	.012	--	0.5	8.46	7	49	51
--	--	.061	--	4.8	--	8.52	33	148	169
1210	190	--	.020	--	1.3	9.12	10	74	81
--	--	.071	--	5.4	--	7.83	37	153	175
960	230	--	.014	--	0.6	7.98	5	56	59
1140	185	--	.020	--	1.2	8.40	3	74	81
1010	360	--	.053	--	3.7	7.62	13	154	176
--	--	.069	--	5.7	--	7.68	32	164	188
--	--	.064	--	5.6	--	8.64	32	160	183
--	--	.056	--	4.7	--	8.40	33	146	166
--	--	.072	--	7.3	--	10.08	35	175	201
	V-4 weld metal								
1150	130	--	.026	--	2.0	8.04	7	92	102
1005	410	--	.021	--	1.3	8.43	12	79	86
--	--	.074	--	6.4	--	8.64	38	168	192
--	--	.068	--	6.3	--	8.58	43	142	161
--	--	.050	--	3.5	--	7.62	29	135	153
--	--	.070	--	6.9	--	9.06	37	161	184
1175	120	--	.015	--	0.8	9.00	5	56	59
--	--	.078	--	7.4	--	9.00	44	169	101
1360	430	--	.034	--	3.0	9.60	12	108	119
--	--	.079	--	5.3	--	8.46	44	154	176
--	--	.083	--	9.7	--	9.60	46	165	189
--	--	.075	--	7.6	--	8.82	43	157	179
--	--	.073	--	8.4	--	10.11	46	159	182
--	--	.076	--	6.7	--	7.59	46	159	182
--	--	.046	--	3.8	--	8.64	28	135	153
--	--	.067	--	6.2	--	8.67	40	159	182
--	--	.059	--	4.7	--	6.00	29	124	140
--	--	.071	--	6.2	--	8.46	43	158	180
--	--	.064	--	8.7	--	8.88	51	161	184
1035	770	.062	.112	4.8	--	7.80	24	149	170
--	--	.079	--	8.9	--	9.60	51	148	169
1115	1070	.067	.123	6.1	--	8.76	42	157	179
1070	945	.073	.122	6.3	--	8.13	39	157	179
--	--	.059	--	5.0	--	8.46	39	145	165
--	--	.063	--	6.6	--	8.79	49	140	159
--	--	.048	--	3.8	--	7.35	26	128	145
1045	260	--	.014	--	0.7	8.10	6	54	57
1090	855	--	.022	--	1.4	8.52	14	77	84
1200	900	--	.045	--	3.6	8.76	23	125	141
1330	1140	.072	.086	6.8	--	9.36	30	164	188
1165	960	--	.070	--	5.7	8.01	29	161	184
1080	910	.066	.137	6.0	13.3	8.94	36	151	172
1050	900	.084	.152	8.2	--	9.24	36	180	207
1410	1280	.074	.127	8.4	--	10.14	51	160	183
--	--	.069	--	5.2	--	7.86	30	161	184
--	--	.077	--	8.8	--	9.84	40	155	177
--	--	.068	--	5.6	--	8.16	35	148	169
--	--	.065	--	5.4	--	9.00	31	157	179
--	--	.067	--	5.2	--	8.28	35	156	178

Table A.3. continued

Specimen No.	Depth[a]	Test temperature °F	Average crack[b] dimensions (in.) a	c	a/W	f(a/W)	Load (lb) Maximum	Start of fracture	Fracture arrest	Crosshead deflection (in.) Maximum load	Start of fracture	Energ Maximum load
							V-- weld metal - continued					
-V-1122	.--	0	.211	.183	.535	2.99	--	1105	535	--	.063	--
-1123	.55	71	.202	.1--	.513	2.77	1195	725	670	.070	.185	5.9
-1124	.53	71	.204	.1-0	.517	2.81	1190	--	--	.065	--	5.3
-1125	.71	71	.199	.1-6	.504	2.69	1275	--	--	.057	--	5.4
-1126	.-0	71	.210	.1-4	.533	2.97	11-0	--	--	.070	--	5.7
-1127	.--	0	.200	.19-	.506	2.71	1290	--	--	.066	--	5.9
-1128	.55	50	.204	.1--	.515	2.79	1260	910	870	.066	.153	5.8
-1129	.53	50	.217	.179	.5--	3.13	1060	680	660	.061	.116	--.7
-1130	.71	200	.220	.175	.557	3.23	1160	--	--	.05-	--	4.-
-1131	.-0	50	.217	.179	.5--	3.13	1165	750	720	.065	.160	5.2
-1132	.--	75	.205	.190	.519	2.84	1150	--	--	.066	--	5.3
-1133[d]	.55	71	.200	.195	.506	2.71	1220	--	--	.06-	--	5.4
-1134	.53	0	.210	.184	.533	2.97	1210	1210	-50	.065	--	5.1
-1135	.71	0	.212	.182	.539	3.03	1260	975	330	.0--	.099	3.7
-1136	.-0	130	.211	.183	.535	2.99	1185	--	--	.065	--	5.-
-1137	.--	32	.205	.189	.520	2.84	1270	1170	810	.069	--	6.1
-1138[d]	.5-	50	.190	.205	.-60	2.50	1365	1355	765	.076	.066	7.5
-1139	.53	130	.194	.200	.493	2.60	1335	--	--	.067	--	6.2
-1140	.71	130	.189	.206	.-77	2.48	1525	--	--	.059	--	6.2
-1141	.-0	0	.194	.201	.-90	2.56	1460	1340	550	.068	.097	7.0
-1142	.5-	50	.195	.199	.-95	2.62	1385	1360	1230	.075	.080	7.4
-1143	.-7	50	.195	.199	.495	2.62	1310	1120	860	.073	.123	6.9
-1144	.--	75	.197	.19-	.499	2.65	1295	1190	1180	.068	.119	6.2
-1145	.97	75	.191	.204	.-6-	2.53	1365	1060	1070	.066	.133	6.2
-1146[d]	.--	0	.190	.195	.504	2.69	1325	990	560	.068	.133	6.4
-1147	.97	0	.190	.205	.-61	2.51	1290	1265	-40	.060	.075	5.5
-1148	.5-	32	.202	.192	.512	2.77	1355	1160	900	.063	.115	5.9
-1149	.97	32	.19-	.201	.-91	2.59	1-65	1080	730	.057	.1-1	5.6
							V-4 base metal					
-V-1063	.0-	130	.199	.19-	.507	2.72	1360	--	--	.055	--	5.0
-1064	.13	130	.207	.185	.529	2.93	1180	--	--	.052	--	5.1
-1067	.-1	130	.219	.175	.555	3.21	1075	--	--	.067	--	5.1
-1068	.50	130	.215	.17-	.5-7	3.11	1125	--	--	.067	--	5.2
-1052	.56	130	.210	.182	.535	2.99	1205	--	--	.073	--	6.1
-1053	.95	130	.211	.181	.539	3.03	1255	--	--	.068	--	5.9
-1054	.0-	7-	.221	.172	.562	3.29	1130	--	--	.059	--	4.-
-1055	.13	50	.202	.192	.512	2.77	1365	--	--	.073	--	7.0
-1056	.-1	7-	.19-	.201	.-88	2.56	1455	--	--	.068	--	6.6
-1057	.50	7-	.180	.214	.-57	2.33	1590	--	--	.06-	--	7.3
-1060	.5-	7-	.199	.19-	.506	2.71	1325	--	--	.072	--	6.-
-1062	.0-	50	.21-	.180	.5--	3.0-	1225	--	--	.057	--	5.0
-1063	.13	32	.201	.192	.511	2.76	1-35	--	--	.065	--	6.3
-1066	.-1	50	.191	.202	.-85	2.5-	1-90	--	--	.076	--	7.9
-1067	.50	50	.185	.20-	.-69	2.41	1620	--	--	.08-	--	8.-
-1071	.--	7-	.18-	.210	.-67	2.-0	1550	--	--	.06-	--	7.0
-1072	.95	7-	.191	.202	.467	2.56	1515	--	--	.07-	--	8.0
-1073	.0-	32	.197	.196	.502	2.6-	1455	--	--	.066	--	6.6
-1074	.13	-50	.20-	.189	.518	2.-9	1390	1385	390	.06-	--	5.6
-1077	.-1	32	.21-	.180	.5--	3.0-	1200	1190	820	.06-	--	5.2
-1078	.50	32	.193	.200	.-92	2.60	1505	1500	890	.076	--	7.-
-1082	.--	32	.20-	.186	.52-	2.92	1330	1230	995	.068	--	6.2
-1083	.95	50	.193	.200	.-92	2.60	1530	--	--	.07-	--	7.7
-1084	.0-	0	.201	.191	.513	2.77	1-00	--	--	.066	--	6.3
-1085	.13	7-	.19-	.195	.503	2.69	1385	--	--	.072	--	6.-
-1088	.-1	0	.191	.201	.-87	2.56	--	1-70	610	--	.060	--
-1089	.50	0	.195	.19-	.-96	2.63	--	1-60	75-	--	.05-	--
-1092	.0-	-50	.195	.199	.495	2.62	--	1500	7-0	--	.056	--
-1096	.-1	-50	.197	.196	.500	2.66	--	1170	390	--	.080	--
-1097	.50	-50	.20-	.18-	.520	2.--	--	1260	390	--	.037	--
-1101	.--	-50	.207	.186	.527	2.91	--	1320	-00	--	.050	--
-1102	.95	32	.199	.195	.505	2.70	1-0-	--	--	.066	--	6.5
-1103	.0-	-100	.210	.182	.535	2.99	--	1380	300	--	.055	--
-1113	.95	0	.20-	.186	.52-	2.89	1350	10-0	-70	.077	.1--	7.2

Table A.3. continued

Load (lb)			Crosshead deflection (in.)		Energy (ft-lb)		Slope of linear load-displacement curve (10^6 lb/in.)	Lateral expansion (10^{-3} in.)	K_{Ied} (ksi $\sqrt{in.}$)	
Maximum	Start of fracture	Fracture arrest	Maximum load	Start of fracture	Maximum load	Start of fracture			From crosshead motion	From specimen deflection[c]
		V-notch weld metal - continued								
--	1105	525	--	.063	--	5.0	8.40	26	153	175
1195	725	670	.070	.185	5.9	--	8.34	43	153	175
1190	--	--	.065	--	5.3	--	8.22	41	148	166
1375	--	--	.077	--	5.4	--	8.70	39	145	165
1140	--	--	.070	--	5.7	--	7.62	40	154	176
1230	--	--	.095	--	5.9	--	8.12	38	156	178
1270	910	870	.086	.153	5.8	--	8.46	31	154	176
1060	980	960	.081	.116	4.7	--	8.43	31	155	177
1100	--	--	.094	--	4.4	--	8.34	29	154	176
1165	790	720	.069	.160	5.2	--	8.13	34	160	183
1150	--	--	.086	--	5.3	--	8.04	42	146	166
1220	--	--	.094	--	5.4	--	8.40	44	144[c]	164
1210	1210	450	.065	--	5.1	--	8.40	23	154	176
1260	975	330	.084	.099	3.7	--	7.56	24	126	142
1165	--	--	.065	--	5.4	--	8.52	37	160	183
1270	1170	810	.089	--	6.1	--	8.70	27	163	186
1315	1355	765	.076	.086	7.5	--	9.06	29	162[c]	185
1335	--	--	.067	--	6.2	--	9.46	36	157	179
1525	--	--	.095	--	6.2	--	9.42	41	149	170
1460	1340	580	.068	.097	7.0	--	9.24	30	164	188
1385	1380	1230	.079	.080	7.4	--	9.00	36	164	184
1310	1120	870	.073	.123	6.9	--	9.06	37	171	196
1295	1190	1150	.088	.119	6.2	--	8.82	38	155	177
1365	1080	1070	.086	.133	6.2	--	9.00	36	149	170
1325	990	550	.069	.133	6.4	--	8.70	35	159[c]	182
1290	1265	440	.080	.075	5.5	--	9.60	26	145	165
1355	1160	900	.063	.115	5.9	--	8.76	39	158	180
1465	1080	730	.057	.141	5.6	--	9.30	34	148	169
		V-notch base metal								
1360	--	--	.051	--	5.0	--	9.18	33	146	166
1150	--	--	.052	--	4.1	--	9.12	31	143	163
1075	--	--	.067	--	5.1	--	7.98	35	162	185
1125	--	--	.067	--	5.2	--	8.04	34	160	183
1205	--	--	.073	--	6.1	--	8.16	37	169	194
1255	--	--	.068	--	5.9	--	8.52	36	172	197
1130	--	--	.059	--	4.4	--	7.08	32	145	165
1365	--	--	.073	--	7.0	--	9.48	33	179	205
1455	--	--	.068	--	6.6	--	8.58	25	153	175
1530	--	--	.069	--	7.3	--	9.30	39	153	175
1325	--	--	.072	--	6.4	--	7.98	38	154	176
1225	--	--	.059	--	5.0	--	7.86	33	158	180
1435	--	--	.065	--	6.3	--	8.73	35	163	186
1490	--	--	.076	--	7.9	--	9.75	41	177	203
1620	--	--	.080	--	8.6	--	9.72	39	177	203
1550	--	--	.068	--	7.0	--	8.49	39	147	167
1515	--	--	.078	--	8.0	--	9.12	43	174	200
1455	--	--	.066	--	6.6	--	9.12	36	165	189
1390	1385	350	.080	--	5.6	--	8.28	18	153	175
1200	1190	820	.064	--	5.2	--	8.34	29	161	184
1505	1500	690	.078	--	7.6	--	9.30	33	175	201
1330	1230	995	.068	--	6.2	--	8.52	33	169	194
1530	--	--	.078	--	7.7	--	9.60	36	177	203
1400	--	--	.066	--	6.3	--	8.61	31	163	186
1365	--	--	.072	--	6.8	--	7.98	35	157	179
--	1470	610	--	.060	--	5.8	9.12	24	149	170
--	1460	750	--	.054	--	5.2	9.48	25	147	167
--	1500	790	--	.056	--	5.7	9.30	24	152	173
--	1170	590	--	.020	--	1.2	8.61	17	68	73
--	1260	330	--	.037	--	2.9	8.28	11	111	125
--	1320	400	--	.050	--	4.2	8.28	12	136	154
1460	--	--	.066	--	6.5	--	8.79	35	161	184
--	1360	300	--	.058	--	5.2	7.38	14	147	167
1360	1040	470	.077	.144	7.2	--	8.40	33	179	205

2

BLANK PAGE

Table A.3 continued

Specimen No.	Depth[a]	Test temperature (°F)	Average crack dimensions[b] (in.) a	c	a/W	c/a/W	Load (lb) Maximum	Start of fracture	Fracture arrest	Crosshead deflection (in.) Maximum load	Start of fracture	Energy (ft-lb) Maximum load	Start of fracture
							V-6 weld metal						
6S-1000	.06	250	.205	.198	.523	2.77	1145	--	--	.055	--	4.4	--
-1001	.13	200	.198	.201	.489	2.57	1250	--	--	.062	--	5.4	--
-1002	.22	200	.195	.196	.496	2.62	1175	--	--	.06-	--	5.3	--
-1003	.31	200	.186	.207	.473	2.44	1385	--	--	.071	--	6.6	--
-1004	.41	200	.186	.205	.479	2.49	1390	--	--	.062	--	5.7	--
-1005	.50	200	.197	.197	.500	2.66	1435	--	--	.052	--	4.4	--
-1006	.59	200	.187	.206	.476	2.47	1360	--	--	.059	--	5.6	--
-1007	.69	200	.189	.205	.479	2.49	1445	--	--	.055	--	5.4	--
-1008	.77	200	.194	.200	.492	2.60	1480	--	--	.056	--	4.9	--
-1009	.86	200	.183	.211	.465	2.39	1529	--	--	.059	--	6.1	--
-1010	.95	200	.186	.207	.473	2.44	1370	--	--	.056	--	5.5	--
-1012	.13	150	.196	.195	.503	2.60	1160	--	--	.067	--	5.7	--
-1015	.41	150	.175	.219	.448	2.27	1535	--	--	.066	--	7.0	--
-1016	.68	150	.158	.205	.478	2.48	1395	--	--	.061	--	5.9	--
-1019	.77	150	.191	.202	.486	2.54	1430	--	--	.062	--	6.1	--
-1020	.86	150	.200	.190	.517	2.81	1310	--	--	.050	--	4.5	--
-1023	.23	75	.203	.190	.516	2.80	1190	--	--	.062	--	5.1	--
-1026	.41	75	.196	.200	.493	2.60	1310	--	--	.062	--	5.6	--
-1029	.68	75	.205	.191	.515	2.70	1270	950	810	.060	--	5.4	--
-1030	.86	75	.198	.196	.504	2.69	1230	965	790	.060	.114	5.1	--
-1031	.59	75	.202	.198	.512	2.77	1220	--	--	.048	--	3.9	--
-1032	.77	75	.196	.198	.497	2.64	1490	--	--	.054	--	5.5	--
-1033	.95	75	.195	.199	.494	2.61	1290	--	--	.063	--	5.7	--
-1034	.04	0	.205	.189	.480	2.50	1220	1030	600	.059	.109	5.0	--
-1035	.41	0	.197	.197	.499	2.65	1330	--	--	.062	--	5.8	--
-1036	.59	0	.197	.197	.500	2.66	--	1255	620	--	.032	--	2.6
-1037	.77	0	.187	.207	.476	2.47	--	1500	635	--	.033	--	3.2
-1042	.04	-50	.191	.203	.486	2.53	1460	1430	230	.063	.083	6.2	--
-1043	.31	-50	.199	.195	.506	2.71	1335	1245	255	.070	.107	6.6	--
-1021	.95	-50	.187	.207	.475	2.46	--	1400	350	--	.086	--	2.1
-1027	.50	-50	.200	.194	.508	2.73	1395	1380	120	.060	.077	5.7	--
-1024	.86	-50	.195	.198	.496	2.63	--	1330	350	--	.031	2.5	--
-1028	.95	0	.193	.200	.491	2.59	1425	1280	495	.068	.112	6.8	--
							V-6 base metal						
6T-1039	.04	200	.198	.203	.486	2.55	1470	--	--	.079	--	8.1	--
-1040	.13	200	.196	.196	.498	2.64	1375	--	--	.073	--	6.7	--
-1041	.22	200	.188	.206	.476	2.47	1495	--	--	.079	--	7.9	--
-1042	.31	200	.179	.195	.505	2.70	1285	--	--	.073	--	6.5	--
-1043	.41	200	.195	.199	.495	2.62	1480	--	--	.089	--	8.9	--
-1044	.50	200	.275	.119	.697	5.58	510	--	--	.069	--	2.5	--
-1045	.59	200	.193	.208	.489	2.57	1400	--	--	.072	--	7.1	--
-1046	.68	200	.197	.197	.500	2.66	1315	--	--	.068	--	6.1	--
-1047	.77	200	.195	.200	.494	2.61	1375	--	--	.079	--	7.5	--
-1048	.86	200	.204	.190	.517	2.81	1280	--	--	.071	--	6.2	--
-1049	.95	200	.204	.190	.517	2.81	1300	--	--	.076	--	6.9	--
-1053	.31	150	.206	.188	.522	2.86	1210	--	--	.075	--	6.3	--
-1059	.50	75	.203	.191	.515	2.79	1290	--	--	.084	--	7.6	--
-1057	.68	150	.189	.205	.481	2.51	1415	--	--	.072	--	7.0	--
-1054	.31	75	.194	.200	.492	2.60	1440	--	--	.075	--	7.5	--
-1056	.50	75	.201	.193	.511	2.75	1290	--	--	.066	--	5.7	--
-1060	.68	75	.190	.204	.483	2.52	1515	835	675	.078	.208	7.9	--
-1058	.22	-100	.199	.196	.504	2.69	--	1350	200	--	.031	--	2.6
-1054	.41	-50	.196	.198	.496	2.63	--	1415	335	--	.045	--	4.2
-1056	.59	0	.196	.198	.498	2.64	--	1375	595	--	.051	--	4.6
-1063	.22	-100	.198	.196	.503	2.68	--	1205	180	--	.019	--	1.2
-1065	.41	-50	.187	.207	.476	2.47	--	1490	440	--	.041	--	3.9
-1367	.59	0	.203	.191	.515	2.79	--	1340	715	--	.059	--	5.3
-1050	.04	0	.193	.201	.498	2.59	1510	1500	960	.027	.095	9.4	--
-1060	.95	0	.199	.195	.505	2.70	1490	--	--	.057	--	5.6	--
-1061	.04	-50	.189	.205	.479	2.49	--	1690	920	--	.049	--	5.3
-1062	.13	0	.193	.201	.489	2.57	--	1570	690	--	.049	--	7.3
-1071	.95	-50	.187	.207	.473	2.44	--	1480	880	--	.031	--	2.8
-1072	.04	-100	.188	.207	.476	2.47	--	1515	250	--	.026	--	3.3
-1073	.22	-50	.199	.195	.505	2.70	--	1165	400	--	.025	--	1.8
-1074	.41	-100	.198	.200	.497	2.52	--	1295	140	--	.038	--	1.5
-1077	.59	0	.185	.209	.470	2.48	--	1610	820	--	.052	--	6.6
-1076	.77	-50	.193	.201	.489	2.57	--	1380	400	--	.035	--	3.0
-1077	.95	-100	.188	.206	.478	2.48	--	1480	380	--	.026	--	2.2

[a] Fraction of wall thickness from outside.

[b] Dimension a is the average of 6 measurements; c = W − a.

[c] Adjusted values determined from a correlation defined in the text.

[d] Specimen orientation CR.

Table A.3 continued

Load (lb)		Crosshead deflection (in.)		Energy (ft-lb)		Slope of linear load-displacement curve (10^6 lb/in.)	Lateral expansion (10^{-3} in.)	K_{Ied} (ksi $\sqrt{in.}$)	
Start of fracture	Fracture arrest	Maximum load	Start of fracture	Maximum load	Start of fracture			From crosshead motion	From specimen deflection[c]
	V-6 weld metal								
--	--	.055	--	4.3	--	8.64	33	135	153
--	--	.062	--	5.4	--	8.70	35	140	159
--	--	.064	--	5.3	--	9.06	39	145	165
--	--	.071	--	6.6	--	9.36	39	152	173
--	--	.062	--	5.7	--	9.72	35	147	167
--	--	.052	--	4.4	--	8.82	34	131	148
--	--	.059	--	5.6	--	9.36	35	142	161
--	--	.055	--	5.4	--	8.91	31	137	155
--	--	.056	--	4.9	--	9.84	29	143	163
--	--	.059	--	6.1	--	9.90	34	147	167
--	--	.058	--	5.5	--	9.48	35	140	159
--	--	.067	--	5.7	--	8.52	31	148	169
--	--	.066	--	7.0	--	10.08	36	151	172
--	--	.061	--	5.9	--	9.54	33	146	169
--	--	.062	--	6.1	--	9.24	42	152	173
--	--	.050	--	4.5	--	8.64	35	139	158
--	--	.062	--	5.1	--	8.28	45	144	164
--	--	.062	--	5.6	--	9.30	34	149	170
950	810	.060	--	5.4	--	8.64	33	152	173
865	750	.060	.114	5.1	--	8.43	36	140	159
--	--	.048	--	3.9	--	8.61	39	127	144
--	--	.054	--	5.5	--	9.12	30	148	169
--	--	.063	--	5.7	--	8.82	39	147	167
1030	680	.059	.109	5.0	--	8.58	29	130	147
--	--	.062	--	5.2	--	8.82	36	150	171
1245	680	--	.038	--	2.6	9.12	24	103	115
1500	695	--	.033	--	3.2	9.48	21	108	121
1430	830	.063	.083	6.2	--	9.12	18	151	172
1245	755	.070	.107	6.6	--	8.64	21	142	165
1400	350	--	.086	--	2.1	9.72	17	88	97
1200	120	.060	.077	5.7	--	9.08	15	155	177
1330	350	--	.031	2.5	--	9.18	13	100	111
1250	695	.068	.112	6.8	--	9.93	28	149	196
	V-6 base metal								
--	--	.079	--	8.1	--	9.36	31	176	202
--	--	.073	--	6.7	--	8.34	32	156	178
--	--	.079	--	7.9	--	9.36	36	168	192
--	--	.073	--	6.5	--	8.94	31	163	186
--	--	.089	--	8.9	--	9.06	35	186	214
--	--	.069	--	8.5	--	9.42	32	153	175
--	--	.078	--	7.1	--	9.60	36	168	192
--	--	.068	--	6.1	--	9.06	30	157	179
--	--	.079	--	7.5	--	9.24	36	172	197
--	--	.071	--	6.2	--	8.40	31	161	184
--	--	.076	--	6.9	--	8.70	30	173	198
--	--	.075	--	6.3	--	9.00	31	171	195
--	--	.084	--	7.6	--	8.28	35	175	200
--	--	.078	--	7.0	--	9.48	40	168	195
--	--	.075	--	7.5	--	9.24	40	171	195
--	--	.066	--	5.7	--	9.00	36	156	178
935	675	.076	.208	7.9	--	9.54	37	173	198
1350	700	--	.031	--	2.6	8.94	11	105	115
1415	350	--	.045	--	4.2	9.60	13	138	150
1375	595	--	.031	--	4.6	8.76	22	133	151
1205	180	--	.018	--	1.2	9.12	6	70	76
1490	440	--	.041	--	3.9	10.20	14	128	145
1340	715	--	.059	--	5.3	8.70	22	152	172
1500	960	.087	.095	9.4	--	9.36	36	180	201
--	--	.057	--	5.6	--	9.36	32	155	177
1490	980	--	.049	--	5.3	9.06	36	162	184
1570	690	--	.039	--	7.1	9.60	24	170	191
1480	880	--	.031	--	2.8	9.48	21	160	111
1515	370	--	.036	--	3.3	9.81	6	111	167
1165	540	--	.018	--	1.8	8.58	5	84	98
1295	140	--	.016	--	1.5	9.10	2	74	88
1610	880	--	.088	--	6.6	9.54	36	158	173
1380	480	--	.035	--	3.0	9.18	11	107	120
1480	380	--	.026	--	2.2	9.60	11	90	100

[c] Adjusted values determined from a correlation defined in the text.

[d] Specimen orientation CR.

2

Table A.4. Charpy impact data from prolongation of vessel V-4 — CA orientation

Specimen No.	Depth[a]	Test temperature (°F)	Energy (ft-lb)	Lateral expansion (mils)
		V-4 weld metal		
4V-1039	.09	0	48	40
-1040	.09	-10	30	24
-1041	.09	50	74	63
-1042	.09	65	94	64
-1150	.04	-100	6	5
-1151	.13	25	56	48
-1154	.04	0	91	72
-1155	.13	-25	13	13
-1158	.04	100	125	91
-1159	.13	-50	10	11
-1162	.04	200	122	92
-1163	.13	50	43	39
		V-4 base metal		
4V-1049	.59	130	80.5	65
-1120	.59	75	49	43
-1068	.59	50	39	36
-1079	.59	32	38	31
-1090	.59	0	29	24
-1098	.59	-50	11	9
-1109	.59	-100	6	3
-1050	.68	200	88	70
-1061	.68	130	88.5	76
-1069	.68	100	67	55
-1080	.68	72	56	44
-1091	.68	50	49	42
-1099	.68	25	37	33
-1110	.68	0	30	27
-1121	.68	-50	13	9

[a]Fraction of wall thickness from outside.

Table A.5. Tensile properties for material from the prolongations of vessels V-3, V-4, and V-6 — circumferential (C) orientation

Specimen No.	Depth[a]	Temperature (°F)	Lower yield (ksi)	Ultimate strength (ksi)	Total elongation (%)	Reduction in area (%)
			V-3 weld metal			
3V-2000	.86	76	69.7	83.3	17.3	73.3
-2002	.59	76	72.2	84.8	14.5	71.8
-2004	.32	76	66.5	78.4	16.2	73.7
-2005	.13	76	68.0	81.2	19.4	73.1
-2001	.77	200	67.3	78.1	14.3	73.2
			V-4 base metal			
4V-2005	.04	74	76.2	94.5	18.1	65.4
-2007	.22	74	70.4	92.4	19.1	64.9
-2009	.41	74	69.3	91.1	19.0	63.5
-2011	.59	74	69.2	89.9	19.1	63.3
-2013	.77	74	69.5	90.6	18.1	64.0
-2015	.95	74	72.2	93.3	18.3	67.4
			V-4 weld metal			
4V-2000	.13	74	65.9	79.6	18.2	74.0
-2001	.31	74	66.6	79.2	15.7	73.7
-2002	.50	74	66.7	79.6	14.8	71.4
-2003	.68	74	72.9	86.4	14.3	71.1
-2004	.86	74	75.0	89.4	13.7	70.8
			V-6 weld metal			
6V-2000	.13	200	65.3	76.1	14.3	73.1
-2001	.31	200	66.1	78.0	14.6	72.5
-2002	.50	200	67.3	80.0	15.9	72.9
-2003	.68	200	78.9	90.6	12.7	69.5
-2004	.86	200	75.5	88.0	13.3	71.4
			V-6 base metal			
6V-2005	.13	200	64.7	85.5	17.2	67.7
-2006	.31	200	64.2	83.8	17.1	67.4
-2007	.50	200	64.5	83.9	16.7	65.4
-2008	.68	200	63.6	83.6	16.8	67.1
-2009	.86	200	66.5	87.5	16.5	68.7

[a]Fraction of wall thickness (6 in.) from outside.

Table A.8. Fracture toughness results determined from testing 3T, 0.85ST, and 0.394T CT specimens from the weldment of vessel V-3 prolongation – CA orientation

Specimen No.	Test temp. (°F)	Crack length (in.)	Maximum load (lb)	Energy to maximum load (in.-lb)	P_Q (lb)	Energy to P_Q (in.-lb)	K_{Ica} (ksi $\sqrt{in.}$)
0.394T CT specimens							
V3A2A1-2	−100	0.414	1,850	16.3	1,000	5.0	55.0
V3A2A1-3	−50	0.418	2,510	61.1	1,000	4.8	110.0
V3A2A1-4	+32	0.421	2,320	197.3	1,000	5.0	197.0
V3A2A1-5	+75	0.405	2,490	152.2	1,000	4.7	166.3
V3A2A1-6	+130	0.410	2,275	197.5	1,000	4.4	198.5
V3A2A1-7	+200	0.410	2,250	159.0	1,000	4.8	171.5
0.85ST CT specimens							
V3A1-1	−50	0.881	5,800	64.8	4,000	30.7	53.0
V3A1-4	+32	0.918	8,270	133.3	4,000	32.8	86.7
V3A1-2	+100	0.886	11,300	963.4	4,000	28.2	215.1
V3A1-3	+130	0.883	11,000	780.6	4,000	30.6	184.6
V3A1-5	+130	0.890	11,590	1,034.1	4,000	29.3	221.4
0.85ST CT specimens							
V3A2A2-4	0	0.926	9,800	263.0	4,000	32.2	113.3
V3A2A2-3	+32	0.911	9,540	232.1	4,000	31.5	104.4
V3A2A2-2	+130	0.878	11,600	838.3	4,000	33.8	189.5
V3A2A2-1	+200	0.880	11,200	553.0	4,000	31.4	152.4
3T CT specimen							
V3A2A-1	+130	3.356	113,500	11,600.0	40,000	554.0	287.0

Table A.7. Fracture toughness results determined from testing 0.85ØT and 4T CT specimens from the prolongation of vessel V-4 – CA orientation

Specimen No.	Test temp. (°F)	Crack length (in.)	Maximum load (lb)	Energy to maximum load (in.-lb)	P_Q (lb)	Energy to P_Q (in.-lb)	K_{Icd} (ksi $\sqrt{in.}$)
Base metal 0.85ØT CT specimens (outside surface)							
V4C-7	−150	0.871	4,750	40.7	4,000	15.2	44.0
V4C-8	−50	0.853	12,250	369.4	4,000	23.2	139.0
V4C-9	0	0.872	11,975	723.4	4,000	30.8	174.0
V4C-10	+32	0.867	11,900	1,176.8	4,000	28.3	230.4
V4C-11	+100	0.864	11,750	1,182.0	4,000	25.3	243.0
Base metal 0.85ØT CT specimens (center thickness region)							
V4C-12	+32	0.855	12,200	1,054.1	4,000	26.4	226.3
V4C-13	+50	0.883	11,600	1,394.5	4,000	26.0	269.0
V4C-16	+50	0.855	12,000	1,483.3	4,000	27.1	258.0
V4C-14	+75	0.881	11,650	1,624.8	4,000	27.8	280.0
V4C-15	+130	0.878	11,300	1,059.6	4,000	29.8	220.1
Base metal 4T CT specimens (center thickness region)							
V4C-1	+32	4.120	208,000	12,972.0	80,000	1,504.0	289.9
V4C-2	+50	4.138	214,000	15,436.0	80,000	1,428.0	235.0
V4C-5	+50	4.166	199,500	12,000.0	80,000	1,572.0	203.0
V4C-3	+75	4.139	221,000	20,260.0	80,000	1,520.0	261.0
V4C-6	+75	4.205	218,000	23,808.0	80,000	1,564.0	286.0
V4C-4	+130	4.156	222,000	31,752.0	80,000	1,432.0	338.6
Weldment 0.85ØT CT specimens							
V4A2B-2	+32	0.878	11,200	1,734.5	4,000	27.4	289.5
V4A2B-5	+50	0.883	10,350	342.7	4,000	27.6	129.3
V4A2B-4	+50	0.871	11,350	541.7	4,000	26.0	164.1
V4A2B-1	+50	0.881	11,100	1,348.8	4,000	27.8	255.0
V4A2B-3	+75	0.887	11,600	361.4	4,000	27.6	133.7
Weldment 0.85ØT CT specimens							
V4A1A2-1	50	0.887	9,900	228.8	4,000	26.0	112.7
V4A1A2-2	+32	0.876	11,150	930.1	4,000	26.0	226.3
V4A1A2-3	+50	0.888	10,600	1,231.7	4,000	26.0	262.0
V4A1A2-4	+130	0.863	10,850	1,475.3	4,000	26.2	266.0
Weldment 4T CT specimen							
V4A1A1-1	+75	3.963	197,500	9,600.0	80,000	1,136.0	194.4

Table A.8. Fracture toughness results determined from testing 0.85T and 4T CT specimens from the prolongation of vessel V-6 - CA orientation

Specimen No.	Test temp. (°F)	Crack length (in.)	Maximum load (lb)	Energy to maximum load (in.-lb)	P_Q (lb)	Energy to P_Q (in.-lb)	K_{Icd} (ksi $\sqrt{in.}$)
Base metal 0.85T CT specimens (outside surface)							
V6-10	+200	0.882	12,250	910.5	4,000	28.0	208.4
V6-13	+200	0.897	12,000	1,414.0	4,000	28.0	267.0
Base metal 0.85T CT specimens (center thickness region)							
V6-11	+200	0.880	11,890	1,369.0	4,000	28.0	255.0
V6-14	+200	0.867	12,400	1,467.0	4,000	27.0	262.2
Base metal 0.85T CT specimens (inside surface)							
V6-12	+200	0.892	12,100	915.0	4,000	27.0	217.0
V6-15	+200	0.877	12,690	1,160.0	4,000	28.0	233.1
Base metal 4T CT specimen (inside surface)							
V6-4	+200	4.122	223,500	30,316.2	80,000	1520.0	317.6
Base metal 4T CT specimens (center thickness region)							
V6-2	+200	4.172	216,000	28,334.5	80,000	1560.0	309.0
V6-3	+200	4.162	215,500	37,237.4	80,000	1680.0	342.7
Weldment 0.85T CT specimens (through the thickness)							
V6-W5	+200	0.883	11,350	1,294.4	4,000	28.0	249.3
V6-W6	+200	0.875	11,800	898.0	4,000	28.0	204.5
V6-W7	+200	0.885	11,600	999.3	4,000	26.0	228.0
V6-W8	+200	0.890	12,600	687.2	4,000	28.0	184.0
V6-W9	+200	0.883	12,060	1,313.6	4,000	28.0	251.1
Weldment 4T CT specimen							
V6-W1	+200	3.980	272,000	34,767.0	80,000	1440.0	321.6

through V4A1A2-4) were cut from piece V4A1A2-1, and five 0.85T CT specimens (V4A2B-1 through V4A2B-5) were cut from piece V4A2B. Westinghouse cut 16 CT specimens from piece V4C: six 4T specimens (V4C-1 through V4C-6) and ten 0.85T specimens (V4C-7 through V4C-16). Locations of all the Westinghouse specimens from the V-4 prolongation are shown in Figs. 2.16 and 2.17.

Piece V6A, shown in Fig. A.8, was set to Westinghouse. Westinghouse cut four 4T (V6-W1 and V6-2 through V6-4) and eleven 0.85T (V6-W5 through V6-W9 and V6-10 through V6-15) compact-tension specimens from this piece, as shown in Fig. 2.18.

The results of the compact-tension specimen tests are given in Tables A.6 through A.8 for vessels V-3, V-4, and V-6, respectively.

References

1. T. R. Mager, S. E. Yanichko, and L. R. Singer, *Fracture Toughness Characterization of HSST Intermediate Pressure Vessel Material*, WCAP-8456 (December 1974).

2. ASTM E-399-72, "Method of Test for Plane-Strain Fracture Toughness of Metallic Materials", *ASTM Standards*, Part 31, 1973.

Appendix B

INTERMEDIATE VESSEL TEST DATA

Strains recorded by the computer-controlled data-acquisition system and by BLH strain indicators are tabulated completely in this appendix. The strain gage layouts, showing locations of gages by data channel number, are presented in Figs. 3.5 through 3.10.

Table B.1. Pressure strain data from V-3 te

Channel No.	Strain (μin./in.) a						
	4030	8080	12060	16110	18720	20110	
85	-.2228391E+03	-.4496185E+03	-.6428809E+03	-.8814961E+03	-.1087705E+04	-.1084614E+04	-
86	-.2172754E+03	-.4424180E+03	-.6538014E+03	-.8718768E+03	-.1087367E+04	-.1082426E+04	-
35	-.3985118E+03	-.8053443E+03	-.1184278E+04	-.1575248E+04	-.1827212E+04	-.1973864E+04	-
37	-.4282549E+03	-.8986453E+03	-.1297346E+04	-.1782213E+04	-.1968873E+04	-.2114716E+04	-
48	-.2267831E+03	-.4594363E+03	-.6988095E+03	-.9367129E+03	-.1096447E+04	-.1191184E+04	-
49	-.2129789E+03	-.4396765E+03	-.6547130E+03	-.8795241E+03	-.1017566E+04	-.1094475E+04	-
87	-.1755184E+03	-.3608432E+03	-.5324473E+03	-.7099298E+03	-.8183913E+03	-.8755801E+03	-
84	-.3175804E+03	-.6388993E+03	-.9345815E+03	-.1228178E+04	-.1414669E+04	-.1648772E+04	-
85	-.1499778E+04	-.2835563E+04	-.2434329E+04	-.2793567E+04	-.3158692E+04	-.3178294E+04	-
86	-.3274824E+03	-.6667842E+03	-.9842894E+03	-.1311572E+04	-.1687193E+04	-.1855145E+04	-
87	-.4164873E+02	-.8538317E+02	-.1229974E+03	-.1646714E+03	-.1944319E+03	-.2083854E+03	-
88	-.2128435E+03	-.4363349E+03	-.6426613E+03	-.8570187E+03	-.9939169E+03	-.1067217E+04	-
89	-.6568948E+05	-.6609222E+05	-.6646718E+05	-.6685218E+05	-.6718415E+05	-.6724488E+05	-
30	-.1848565E+03	-.2874956E+03	-.2958763E+02	+.7573529E+03	-.3259286E+03	-.2394485E+04	-
31	-.1284666E+03	-.2675448E+03	-.4084665E+03	-.5414522E+03	-.6387337E+03	-.6762297E+03	-
32	-.2599838E+03	-.5853275E+03	-.9662377E+03	-.1325383E+04	-.1531723E+04	-.1674492E+04	-
33	-.6561239E+05	-.1825835E+02	-.8266443E+01	-.4185458E+01	-.4188458E+01	-.6282535E+01	-
36	-.8210869E+02	-.1591758E+03	-.2345635E+03	-.3137854E+03	-.3633862E+03	-.3893883E+03	-
50	-.2425593E+03	-.5265866E+03	-.8637479E+03	-.1284989E+04	-.1413943E+04	-.1546869E+04	-
51	-.6113284E+02	-.1321789E+03	-.2129789E+03	-.2918600E+03	-.3352446E+03	-.3510288E+03	-
53	-.1321258E+04	-.6464887E+05	-.6465894E+05	-.6465894E+05	-.6465894E+05	-.6464896E+05	-
56	-.2918600E+03	-.6388992E+03	-.9585171E+03	-.1269986E+04	-.1482964E+04	-.1593398E+04	-
58	-.4042655E+03	-.8262887E+03	-.1218712E+04	-.1619634E+04	-.1863566E+04	-.1975971E+04	-
59	-.7848668E+03	-.1551918E+04	-.2171282E+04	-.2711537E+04	-.3044818E+04	-.3288698E+04	-
60	-.4042655E+03	-.8242747E+03	-.1214768E+04	-.1613118E+04	-.1857649E+04	-.2001688E+04	-
61	-.6783773E+03	-.1392166E+04	-.1954279E+04	-.2590531E+04	-.2888166E+04	-.2944236E+04	-
62	-.1368419E+03	-.2888335E+03	-.4121537E+03	-.5462515E+03	-.6338287E+03	-.6783773E+03	-
63	-.2149589E+03	-.4397663E+03	-.6468249E+03	-.8637479E+03	-.9998178E+03	-.1074755E+04	-
66	-.2129789E+03	-.4338505E+03	-.6389368E+03	-.8499437E+03	-.9848416E+03	-.1058979E+04	-
67	-.7296588E+02	-.1538158E+03	-.2248111E+03	-.3017282E+03	-.3498488E+03	-.3746851E+03	-
68	-.2078629E+03	-.4288479E+03	-.6211886E+03	-.8262794E+03	-.9683772E+03	-.1031378E+04	-
70	-.7698986E+02	-.1479271E+03	-.2287551E+03	-.2997481E+03	-.3498488E+03	-.3786292E+03	-
71	-.2078629E+03	-.4228297E+03	-.6231686E+03	-.8282514E+03	-.9782374E+03	-.1044894E+04	-
72	-.2192586E+03	-.4463328E+03	-.6597278E+03	-.8789777E+03	-.1021194E+04	-.1098228E+04	-
73	+.9876154E+01	-.6520149E+02	-.9876154E+02	+.1106129E+03	+.1659194E+03	+.4358012E+03	+
74	-.2172754E+03	-.4444779E+03	-.6577518E+03	-.8758272E+03	-.1017243E+04	-.1092382E+04	-
75	-.4936877E+02	-.9681799E+02	-.1482413E+03	-.1777787E+03	-.2814735E+03	-.2034487E+03	-
77	-.3278883E+03	-.6577275E+03	-.9639126E+03	-.1264147E+04	-.1477472E+04	-.1736227E+04	-
78	-.4464821E+03	-.8552176E+03	-.1222668E+04	-.1598061E+04	-.1864618E+04	-.2117447E+04	-
79	+.1364854E+04	+.1313364E+04	+.1714588E+04	+.1145634E+04	+.9540364E+03	+.9816896E+03	+
97	-.4287841E+03	-.8552871E+03	-.1256247E+04	-.1653268E+04	-.1864618E+04	-.2206333E+04	-
98	-.3397397E+03	-.6833966E+03	-.1003417E+04	-.1321429E+04	-.1619689E+04	-.1852766E+04	-
99	-.3476486E+03	-.7012922E+03	-.1027128E+04	-.1349883E+04	-.1627598E+04	-.1982147E+04	-
101	-.5135600E+02	-.1066841E+03	-.1619689E+03	-.2172754E+03	-.2528295E+03	-.2686313E+03	-
102	-.2073992E+03	-.4225929E+03	-.6241729E+03	-.8315721E+03	-.9737887E+03	-.1064649E+04	-
103	-.1876469E+03	-.3852196E+03	-.5688664E+03	-.7565134E+03	-.8758272E+03	-.9382346E+03	-
104	-.6784493E+02	-.1366698E+03	-.1952387E+03	-.2603876E+03	-.3036922E+03	-.3273565E+03	-
105	-.3963775E+03	-.8026151E+03	-.1177388E+04	-.1563817E+04	-.1818289E+04	-.1954279E+04	-
106	-.1366698E+03	-.2780558E+03	-.4101817E+03	-.5442795E+03	-.6318487E+03	-.6744333E+03	-
107	-.3983495E+03	-.8066430E+03	-.1175328E+04	-.1561846E+04	-.1818289E+04	-.1962167E+04	-
108	-.1735647E+03	-.3550136E+03	-.5226663E+03	-.6922864E+03	-.8007643E+03	-.8559895E+03	-
109	-.1814548E+03	-.3707972E+03	-.5463866E+03	-.7297686E+03	-.8441555E+03	-.9033253E+03	-
110	-.1873710E+03	-.3846035E+03	-.5660299E+03	-.7554988E+03	-.8757127E+03	-.9388272E+03	-

BLANK PAGE

-3 test (computer output)

ı.) at pressure (psi)					
22220	23300	24100	25120	26120	27120
-.1198998E+04	-.1260125E+04	-.1342951E+04	-.1427683E+04	-.1575576E+04	-.1751168E+04
-.1191064E+04	-.1260197E+04	-.1333288E+04	-.1435897E+04	-.1568333E+04	-.1742152E+04
-.2299951E+04	-.2299227E+04	-.2388567E+04	-.2553167E+04	-.2805182E+04	-.3188737E+04
-.2358736E+04	-.2561895E+04	-.2789245E+04	-.3083587E+04	-.3825785E+04	-.3541411E+04
-.1386335E+04	-.1588321E+04	-.1698827E+04	-.1938364E+04	-.2393874E+04	-.3571341E+04
-.1246321E+04	-.1348866E+04	-.1461272E+04	-.1628847E+04	-.1932488E+04	-.3036988E+04
-.9781255E+03	-.1041238E+04	-.1182363E+04	-.1181155E+04	-.1889618E+04	-.1486988E+04
-.2013747E+04	-.2384738E+04	-.2682324E+04	-.2973958E+04	-.3156478E+04	-.3299489E+04
-.3267578E+04	-.3491758E+04	-.3184246E+04	-.3535397E+04	-.3590947E+04	-.3597188E+04
-.2470156E+04	-.2823292E+04	-.3168491E+04	-.3525595E+04	-.3751768E+04	-.3986486E+04
-.2281445E+03	-.2459996E+03	-.2618789E+03	-.2717985E+03	-.2856778E+03	-.2876814E+03
-.1174348E+04	-.1243785E+04	-.1317189E+04	-.1416285E+04	-.1545339E+04	-.1788873E+04
-.6747383E+05	-.6757428E+05	-.6768927E+05	-.6783211E+05	-.6808273E+05	-.6889866E+05
-.2939988E+04	-.3724967E+05	-.2192847E+04	-.3668074E+04	-.5358914E+05	+.1114478E+04
-.7476504E+03	-.7873286E+03	-.8218549E+03	-.8647089E+03	-.9183147E+03	-.9628678E+03
-.1948271E+04	-.2147646E+04	-.2484571E+04	-.2821621E+04	-.2993791E+04	-.4761726E+04
-.8266443E+01	-.8266443E+01	-.8266443E+01	-.6882535E+01	-.8266443E+01	-.4188458E+01
-.4218589E+03	-.4349382E+03	-.4428738E+03	-.4468417E+03	-.4588095E+03	-.4447315E+03
-.1832813E+04	-.2841848E+04	-.2309244E+04	-.2689765E+04	-.3594869E+04	-.5388697E+04
-.3944054E+03	-.4356188E+03	-.5867830E+03	-.7533288E+03	-.7967826E+03	-.1089678E+04
-.6465094E+05	-.6465094E+05	-.6465094E+05	-.6464493E+05	-.6464698E+05	-.6465094E+05
-.1766936E+04	-.1851733E+04	-.1918782E+04	-.2087488E+04	-.2868277E+04	-.2153459E+04
-.2884432E+04	-.2232335E+04	-.2423622E+04	-.2608818E+04	-.2868849E+04	-.3322865E+04
-.3433299E+04	-.3561481E+04	-.3715299E+04	-.3947782E+04	-.4261314E+04	-.4748753E+04
-.2281635E+04	-.2425593E+04	-.2688992E+04	-.2823786E+04	-.3086848E+04	-.3447184E+04
-.3397883E+04	-.3697551E+04	-.4081243E+04	-.4294809E+04	-.4566932E+04	-.5038641E+04
-.7493783E+03	-.7848668E+03	-.8144472E+03	-.8479419E+03	-.8913238E+03	-.9367129E+03
-.1163216E+04	-.1252237E+04	-.1327174E+04	-.1427698E+04	-.1599808E+04	-.1737356E+04
-.1169412E+04	-.1238545E+04	-.1289766E+04	-.1396561E+04	-.1475816E+04	-.1611146E+04
-.4141257E+03	-.4299819E+03	-.4456781E+03	-.4594681E+03	-.4870668E+03	-.5166711E+03
-.1141883E+04	-.1196992E+04	-.1254209E+04	-.1321208E+04	-.1415868E+04	-.1534837E+04
-.4239858E+03	-.4377988E+03	-.4476581E+03	-.4456846E+03	-.4476565E+03	-.4377988E+03
-.1232517E+04	-.1321258E+04	-.1408028E+04	-.1514465E+04	-.1642639E+04	-.1882433E+04
-.1224643E+04	-.1297726E+04	-.1376736E+04	-.1477339E+04	-.1611788E+04	-.1793589E+04
+.2378277E+02	+.2311828E+03	+.2398829E+03	+.3594465E+03	+.1362989E+03	+.9481188E+02
-.1218816E+04	-.1275999E+04	-.1353833E+04	-.1451783E+04	-.1582139E+04	-.1763881E+04
-.1422166E+03	-.8691815E+02	-.9876154E+01	+.1164936E+03	+.8864084E+03	+.5412138E+03
-.2190538E+04	-.2486816E+04	-.2818654E+04	-.3138462E+04	-.3391471E+04	-.3587819E+04
-.2636933E+04	-.3067533E+04	-.3401347E+04	-.3671721E+04	-.3887234E+04	-.4192678E+04
+.1135758E+04	+.6696832E+03	+.9856491E+03	+.9459940E+03	+.1114838E+04	+.1216742E+04
-.2397938E+04	-.2561874E+04	-.2731744E+04	-.3049631E+04	-.3675984E+04	-.5734894E+04
-.2486816E+04	-.2862189E+04	-.3225551E+04	-.3571883E+04	-.3816146E+04	-.4011693E+04
-.2573726E+04	-.3049756E+04	-.3434926E+04	-.3756783E+04	-.4017619E+04	-.4207241E+04
-.2863637E+03	-.3101112E+03	-.3278883E+03	-.3496471E+03	-.3812195E+03	-.4246746E+03
-.1226618E+04	-.1313589E+04	-.1398463E+04	-.1499326E+04	-.1619689E+04	-.1763881E+04
-.1054773E+04	-.1129832E+04	-.1198965E+04	-.1289818E+04	-.1414265E+04	-.1643992E+04
-.3688889E+03	-.3727131E+03	-.3766572E+03	-.3727830E+03	-.3668673E+03	-.3353166E+03
-.2230362E+04	-.2386153E+04	-.2543915E+04	-.2884171E+04	-.3074382E+04	-.3482506E+04
-.7395102E+03	-.7758867E+03	-.8045671E+03	-.8360875E+03	-.8614412E+03	-.9327105E+03
-.2169229E+04	-.2356572E+04	-.2534055E+04	-.2899994E+04	-.3151134E+04	-.3583883E+04
-.9486888E+03	-.1007859E+04	-.1061111E+04	-.1138161E+04	-.1216939E+04	-.1341167E+04
-.1007859E+04	-.1074917E+04	-.1136059E+04	-.1216858E+04	-.1317493E+04	-.1472837E+04
-.1055194E+04	-.1128178E+04	-.1197282E+04	-.1285866E+04	-.1402826E+04	-.1601419E+04

2

Table

Channel No.	27500	28100	28000	28300	28350	28
65	-.1865537E+04	-.2186125E+04	-.2186125E+04	-.2163314E+04	-.2273747E+04	-.2
96	-.1848816E+04	-.2024611E+04	-.2073992E+04	-.2131274E+04	-.2218389E+04	-.2
35	-.3329125E+04	-.3664026E+04	-.3765888E+04	-.3867888E+04	-.4043678E+04	-.4
37	-.3753788E+04	-.4108844E+04	-.4214385E+04	-.4317488E+04	-.4488119E+04	-.4
48	-.4945844E+04	-.7186867E+04	-.7983885E+04	-.8172881E+04	-.8876894E+04	-.9
49	-.4648158E+04	-.7154514E+04	-.7771759E+04	-.8018262E+04	-.8678975E+04	-.9
57	-.1697915E+04	-.2224447E+04	-.2374321E+04	-.2465834E+04	-.2682796E+04	-.2
24	-.3374893E+04	-.3466158E+04	-.3488237E+04	-.3525873E+04	-.3557688E+04	-.3
25	-.3507818E+04	-.3622892E+04	-.2611175E+04	-.3699286E+04	-.3788413E+04	-.2
26	-.3976188E+04	-.4055489E+04	-.4069569E+04	-.4121157E+04	-.4168848E+04	-.4
27	-.2876614E+03	-.2797452E+03	-.2757961E+03	-.2797644E+03	-.2777883E+03	-.2
28	-.1825826E+04	-.2001895E+04	-.2059513E+04	-.2115869E+04	-.2288325E+04	-.2
29	-.6833485E+05	-.6854853E+05	-.6[illegible]59835E+05	-.6866979E+05	-.6875788E+05	-.6
30	+.1818874E+04	-.5359123E+05	+.[illegible]787787E+03	+.2978787E+03	-.9814391E+03	-.5
31	-.9977796E+03	-.1045396E+04	-.1055477E+04	-.1079287E+04	-.1103897E+04	-.1
32	-.6784894E+04	-.1118484E+05	-.1245861E+05	-.1289784E+05	-.1397444E+05	-.1
33	-.4188458E+01	-.2284426E+01	-.2894118E+01	-.1899618E+00	-.1899618E+00	-.6
38	-.5022684E+03	-.4038668E+03	-.3938171E+03	-.3969855E+03	-.3858885E+03	-.3
50	-.6811388E+04	-.1015594E+05	-.1117948E+05	-.1152255E+05	-.1248293E+05	-.1
51	-.1248485E+04	-.1761820E+04	-.1946399E+04	-.2039876E+04	-.2267831E+04	-.2
53	-.6465894E+05	-.6464896E+05	-.6465891E+05	-.6465894E+05	-.6465894E+05	-.6
56	-.2216559E+04	-.2257971E+04	-.2248111E+04	-.2275719E+04	-.2281635E+04	-.2
58	-.3632474E+04	-.4194582E+04	-.4368049E+04	-.449 222E+04	-.4721833E+04	-.5
59	-.5864166E+04	-.5657746E+04	-.5874668E+04	-.6834483E+04	-.6367675E+04	-.6
60	-.3683747E+04	-.4086848E+04	-.4226854E+04	-.4346348E+04	-.4575183E+04	-.4
61	-.5487298E+04	-.6257242E+04	-.6592487E+04	-.6831102E+04	-.7326881E+04	-.8
62	-.9623492E+03	-.9958738E+03	-.9978457E+03	-.1015594E+04	-.1085454E+04	-.1
63	-.1843845E+04	-.2082872E+04	-.2084432E+04	-.2143594E+04	-.2238258E+04	-.2
66	-.1698827E+04	-.1888461E+04	-.1851739E+04	-.1891174E+04	-.1944419E+04	-.2
67	-.5285038E+03	-.5581956E+03	-.5521676E+03	-.5628278E+03	-.5699158E+03	-.5
68	-.1599314E+04	-.1664391E+04	-.1731440E+04	-.1764964E+04	-.1812893E+04	-.1
70	-.4259579E+03	-.3352446E+03	-.3865173E+03	-.3845453E+03	-.3727131E+03	-.3
71	-.1895118E+04	-.1989775E+04	-.2110869E+04	-.2159378E+04	-.2248223E+04	-.2
72	-.1982147E+04	-.2181646E+04	-.2166828E+04	-.2226885E+04	-.2332934E+04	-.2
73	-.1469572E+04	-.1665128E+04	-.1726351E+04	-.1783633E+04	-.1880514E+04	-.2
74	-.1872519E+04	-.2077943E+04	-.2141150E+04	-.2196432E+04	-.2301286E+04	-.2
75	+.6913307E+03	+.9362593E+03	+.1019219E+04	+.1054773E+04	+.1145743E+04	+.1
77	-.3695657E+04	-.3818820E+04	-.3831948E+04	-.3861328E+04	-.3928962E+04	-.4
78	-.4095866E+04	-.4377111E+04	-.4418591E+04	-.4479823E+04	-.4574924E+04	-.4
79	+.1341181E+04	+.1761986E+04	+.1617714E+04	+.1933751E+04	+.1947 82E+04	+.2
97	-.8568551E+04	-.1177405E+05	-.1254469E+05	-.1291998E+05	-.1377218E+05	-.1
98	-.4184589E+04	-.4213167E+04	-.4238919E+04	-.4284275E+04	-.4329966E+04	-.4
99	-.4309953E+04	-.4432417E+04	-.4454145E+04	-.4507476E+04	-.4557812E+04	-.4
101	-.4523878E+03	-.5076343E+03	-.5254114E+03	-.5412132E+03	-.5668734E+03	-.6
102	-.1858791E+04	-.2002884E+04	-.2044364E+04	-.2093744E+04	-.2168793E+04	-.2
103	-.1834989E+04	-.2708115E+04	-.2984573E+04	-.3107838E+04	-.3316546E+04	-.3
104	-.3036922E+03	-.2286340E+03	-.1938587E+03	-.1833985E+03	-.1480139E+03	-.6
105	-.3756712E+04	-.4275811E+04	-.4444949E+04	-.4575183E+04	-.4805838E+04	-.5
106	-.9668933E+03	-.1033878E+04	-.1051898E+04	-.1078699E+04	-.1116167E+04	-.1
107	-.3772468E+04	-.4288186E+04	-.4328599E+04	-.4442977E+04	-.4638288E+04	-.4
108	-.1433681E+04	-.1658712E+04	-.1751425E+04	-.1818484E+04	-.1938879E+04	-.2
109	-.1603501E+04	-.1905149E+04	-.1998076E+04	-.2074887E+04	-.2187389E+04	-.2
110	-.1782982E+04	-.2329162E+04	-.2562851E+04	-.2672581E+04	-.2879596E+04	-.3

B-1. (continued)

ain (min./in.) at pressure (psi)

	2830	2860	2890	2910	2900	2910
E+04	-.2437425E+04	-.2526167E+04	-.2988748E+04	-.3184823E+04	-.3478748E+04	-.3549649E+04
E+04	-.2476939E+04	-.2688388E+04	-.3296666E+04	-.3888344E+04	-.4163786E+04	-.4426774E+04
E+04	-.4374780E+04	-.4525495E+04	-.4889212E+04	-.5065150E+04	-.5354821E+04	-.5535368E+04
E+04	-.4811198E+04	-.4963968E+04	-.5259588E+04	-.5537347E+04	-.5846856E+04	-.6037324E+04
E+04	-.9887744E+04	-.1083761E+05	-.1031173E+05	-.1055488E+05	-.1075149E+05	-.1083826E+05
E+04	-.9741814E+04	-.9937844E+04	-.1035708E+05	-.1066275E+05	-.1091517E+05	-.1103152E+05
E+04	-.2961984E+04	-.3068474E+04	-.3261733E+04	-.3399775E+04	-.3516124E+04	-.3575885E+04
E+04	-.3688848E+04	-.3696306E+04	-.3751859E+04	-.3787571E+04	-.3827258E+04	-.3848965E+04
E+04	-.2557467E+04	-.2618924E+04	-.3434489E+04	-.3648684E+04	-.3340976E+04	-.2615804E+04
E+04	-.4259844E+04	-.4331269E+04	-.4412615E+04	-.4491976E+04	-.4579274E+04	-.4648778E+04
E+03	-.2678411E+03	-.2678411E+03	-.2658738E+03	-.2599849E+03	-.2579889E+03	-.2539589E+03
E+04	-.2396627E+04	-.2409877E+04	-.3837469E+04	-.3978564E+04	-.3823146E+04	-.3971949E+04
E+05	-.6892747E+05	-.6903668E+05	-.6922786E+05	-.6939174E+05	-.6958419E+05	-.6971782E+05
E+05	-.5359588E+05	-.5359382E+05	-.5359382E+05	-.5285317E+05	-.2201933E+05	
E+04	-.1144598E+04	-.1176342E+04	-.1214809E+04	-.1243799E+04	-.1275544E+04	
E+05	-.1551915E+05	-.1572358E+05	-.1619372E+05	-.1668827E+05	-.1695955E+05	
E+01	-.6172498E+01	-.4188458E+01	-.4188458E+01	-.2284426E+01	-.4188458E+01	
E+03	-.3733863E+03	-.3792584E+03	-.3792584E+03	-.3792584E+03	-.3832265E+03	
E+05	-.1371545E+05	-.1387124E+05	-.1421634E+05	-.1451886E+05	-.1474682E+05	
E+04	-.2648432E+04	-.2741118E+04	-.2944236E+04	-.3078334E+04	-.3196656E+04	
E+05	-.6465291E+05	-.6465894E+05	-.6465894E+05	-.6464896E+05	-.6465894E+05	
E+04	-.2275719E+04	-.2313188E+04	-.2332988E+04	-.2350656E+04	-.2370377E+04	
E+04	-.5105578E+04	-.5259396E+04	-.5533508E+04	-.5768891E+04	-.5992998E+04	
E+04	-.7115874E+04	-.7422718E+04	-.8081367E+04	-.8564513E+04	-.9022824E+04	
E+04	-.5885858E+04	-.5898837E+04	-.5710991E+04	-.6822571E+04	-.6332179E+04	
E+04	-.8418695E+04	-.8832709E+04	-.9649129E+04	-.1027426E+05	-.1089545E+05	
E+04	-.1037886E+04	-.1058979E+04	-.1078811E+04	-.1088670E+04	-.1092583E+04	
E+04	-.2463834E+04	-.2666188E+04	-.3332726E+04	-.3668854E+04	-.3947998E+04	
E+04	-.2085272E+04	-.2076544E+04	-.2149589E+04	-.2190922E+04	-.2273747E+04	
E+03	-.5758319E+03	-.5837288E+03	-.5916882E+03	-.5896361E+03	-.5975842E+03	
E+04	-.1877378E+04	-.1922726E+04	-.1975971E+04	-.2021388E+04	-.2072688E+04	
E+03	-.3332726E+03	-.3273565E+03	-.2977761E+03	-.2681957E+03	-.2405873E+03	
E+04	-.2344748E+04	-.2397985E+04	-.2453282E+04	-.2482782E+04	-.2522222E+04	
E+04	-.2544097E+04	-.2579651E+04	-.2571758E+04	-.2569775E+04	-.2575788E+04	
E+04	-.2834487E+04	-.2121397E+04	-.2174729E+04	-.2388153E+04	-.2681379E+04	
E+04	-.2516444E+04	-.2615285E+04	-.2981614E+04	-.3130741E+04	-.3255180E+04	
E+04	+.1343157E+04	+.1386612E+04	+.1585126E+04	+.1586110E+04	+.1655243E+04	
E+04	-.4047247E+04	-.4126257E+04	-.4226993E+04	-.4298102E+04	-.4379886E+04	
E+04	-.4693148E+04	-.4780058E+04	-.4896597E+04	-.4989433E+04	-.5090169E+04	
E+04	+.2078841E+04	+.2202382E+04	+.2289292E+04	+.2295818E+04	+.2305894E+04	
E+05	-.1534557E+05	-.1573271E+05	-.1656823E+05	-.1716278E+05	-.1768226E+05	
E+04	-.4416615E+04	-.4487724E+04	-.4568709E+04	-.4637842E+04	-.4714875E+04	
E+04	-.4649693E+04	-.4730677E+04	-.4801785E+04	-.4853141E+04	-.4918284E+04	
E+03	-.6182815E+03	-.6360243E+03	-.6933868E+03	-.7347858E+03	-.7999684E+03	
E+04	-.2269540E+04	-.2332747E+04	-.2403855E+04	-.2419657E+04	-.2425582E+04	
E+04	-.3656150E+04	-.3754913E+04	-.3936635E+04	-.4078958E+04	-.4191439E+04	
E+02	-.4930868E+02	-.2967166E+02	+.2948547E+02	+.7493783E+02	+.1124855E+03	
E+04	-.5859396E+04	-.5454418E+04	-.5836931E+04	-.6178473E+04	-.6511633E+04	
E+04	-.1185188E+04	-.1222581E+04	-.1275822E+04	-.1311398E+04	-.1348866E+04	
E+04	-.4979369E+04	-.5142757E+04	-.5426711E+04	-.5671558E+04	-.5931857E+04	
E+04	-.2065825E+04	-.2122179E+04	-.2177481E+04	-.2289995E+04	-.2234645E+04	
E+04	-.2319455E+04	-.2376586E+04	-.2453481E+04	-.2498937E+04	-.2542388E+04	
E+04	-.3159666E+04	-.3248291E+04	-.3372457E+04	-.3473866E+04	-.2569989E+04	

2

BLANK PAGE

Table 8.1. (

Channel No.	Strain (					
	29110	29110	29320	29320	29260	29380
65	-.3593033E+04	-.3942082E+04	-.4847248E+04	-.5482235E+04	-.6085675E+04	-.6434724E+04
96	-.4558832E+04	-.5024986E+04	-.5728169E+04	-.6235803E+04	-.6747388E+04	-.7043672E+04
35	-.5650442E+04	-.6118673E+04	-.7169719E+04	-.8005488E+04	-.8975680E+04	-.9557001E+04
37	-.6152397E+04	-.6634517E+04	-.7691480E+04	-.8531252E+04	-.9497476E+04	-.1007284E+05
43	-.1098165E+05	-.1104532E+05	-.1142001E+05	-.1180861E+05	-.1203134E+05	-.1216346E+05
47	-.1109068E+05	-.1133718E+05	-.1185788E+05	-.1232122E+05	-.1262689E+05	-.1279057E+05
57	-.[illegible]10E+04	-.3733047E+04	-.3963775E+04	-.4164921E+04	-.4324655E+04	-.4415369E+04
24	-.3986772E+04	-.3936374E+04	-.4078995E+04	-.4243898E+04	-.4426429E+04	-.4557375E+04
25	-.3340840E+04	-.3359816E+04	-.3208053E+04	-.3079267E+04	-.2368984E+04	-.2[illegible]710E+04
26	-.4636411E+04	-.4855054E+04	-.5253579E+04	-.5640730E+04	-.6017138E+04	-.6376807E+04
27	-.2519688E+03	-.2408646E+03	-.2083054E+03	-.1845117E+03	-.1587193E+03	-.1446311E+03
28	-.4647342E+04	-.4462005E+04	-.5378249E+04	-.5971853E+04	-.6535319E+04	-.6834987E+04
29	-.4981434E+05	-.7018535E+05	-.7184486E+05	-.7167139E+05	-.7239755E+05	-.7282618E+05
30	-.5359123E+05	-.5359322E+05	-.5358715E+05	-.5359123E+05	-.5359123E+05	-.5359123E+05
31	-.1315[illegible]5E+04	-.1374745E+04	-.1499551E+04	-.1579[illegible]1E+04	-.1676318E+04	-.1739587E+04
32	-.1716[illegible]7E+05	-.1749953E+05	-.1822822E+05	-.1887415E+05	-.1924516E+05	-.1944753E+05
33	-.2204426E+01	-.4188458E+01	-.6282535E+01	-.2204426E+01	-.2204426E+01	-.2204426E+01
34	-.3[illegible]917[illegible]6E+03	-.3951[illegible]06E+03	-.4031957E+03	-.4090189E+03	-.4149710E+03	-.4229071E+03
56	-.1[illegible]8[illegible]63E+05	-.1588009E+05	-.1558493E+05	-.1603850E+05	-.1638472E+05	-.1645854E+05
51	-.3291313E+04	-.3439215E+04	-.3740935E+04	-.3955884E+04	-.4141257E+04	-.4239858E+04
53	-.6464896E+05	-.6465[illegible]4E+05	-.6464896E+05	-.6464896E+05	-.6464896E+05	-.6464896E+05
54	-.2409817E+04	-.2461696E+04	-.2567579E+04	-.2644488E+04	-.2747033E+04	-.2810139E+04
58	-.6229634E+04	-.6604291E+04	-.7539068E+04	-.8294344E+04	-.9233631E+04	-.9814779E+04
59	-.9414458E+04	-.9972541E+04	-.1094672E+05	-.1164679E+05	-.1233503E+05	-.1275981E+05
60	-.4645731E+04	-.7144654E+04	-.[illegible]359003E+04	-.9444838E+04	-.1074952E+05	-.1[illegible]45551E+05
61	-.1147128E+05	-.1229953E+05	-.1386532E+05	-.1492438E+05	-.1598328E+05	-.1660841E+05
62	-.1110251E+04	-.1131944E+04	-.1159132E+04	-.1226601E+04	-.1264869E+04	-.1293650E+04
63	-.4233942E+04	-.4719061E+04	-.5703102E+04	-.6388515E+04	-.6885291E+04	-.7207759E+04
64	-.23[illegible]8F+04	-.2425593E+04	-.2585328E+04	-.2839719E+04	-.3208488E+04	-.3427383E+04
67	-.6133[illegible]5E+03	-.6487969E+03	-.7[illegible]79578E+03	-.7296[illegible]E+03	-.7631745E+03	-.7[illegible]922[illegible]E+03
68	-.2151482E+04	-.2277691E+04	-.2399957E+04	-.2492642E+04	-.2549831E+04	-.2632656E+04
70	-.2129799E+03	-.1656503E+03	-.6507689E+02	+.3944854E+01	+.7493703E+02	+.1104335E+03
71	-.2575467E+04	-.2881131E+04	-.3715299E+04	-.4299819E+04	-.4986484E+04	-.5277144E+04
72	-.2593477E+04	-.2601379E+04	-.2680388E+04	-.2718816E+04	-.2913465E+04	-.3077489E+04
73	-.2[illegible]95982E+04	-.3[illegible]58689E+04	-.628[illegible]3E+03	-.1260197E+04	-.1036996E+04	-.1183163E+04
74	-.3369743E+04	-.3575167E+04	-.4035396E+04	-.4373161E+04	-.4598337E+04	-.4833390E+04
75	+.1716476E+04	+.1817212E+04	+.2036463E+04	+.2194481E+04	+.2348549E+04	+.2427558E+04
77	-.4462046E+04	-.4568[illegible]7E+04	-.4789934E+04	-.5083259E+04	-.5259864E+04	-.5423983E+04
78	-.[illegible]66782E+04	-.5342999E+04	-.5684714E+04	-.5977048E+04	-.6302961E+04	-.6492583E+04
79	+.2374202E+04	+.1716476E+04	+.1511851E+04	+.1592036E+04	+.1684871E+04	+.1724376E+04
97	-.1809509E+05	-.1870148E+05	-.1993285E+05	-.2092362E+05	-.2179074E+05	-.2228868E+05
98	-.4831414E+04	-.4965730E+04	-.5273866E+04	-.5562250E+04	-.5903964E+04	-.6125190E+04
99	-.5011160E+04	-.5117922E+04	-.5364726E+04	-.5619531E+04	-.5921741E+04	-.6111364E+04
101	-.8631758E+03	-.9263832E+03	-.1082426E+04	-.1193039E+04	-.1301677E+04	-.1366860E+04
102	-.2449838E+04	-.2729769E+04	-.3387508E+04	-.3824846E+04	-.4327730E+04	-.4600312E+04
103	-.4288226E+04	-.4424517E+04	-.4697098E+04	-.4944882E+04	-.5163253E+04	-.5285717E+04
104	+.1459[illegible]0E+03	+.1952307E+03	+.2996363E+03	+.3667970E+03	+.4299819E+03	+.4594823E+04
105	-.6858822E+04	-.7371438E+04	-.8437981E+04	-.9144290E+04	-.9860136E+04	-.1027229E+05
106	-.1384363E+04	-.1433663E+04	-.1534141E+04	-.1605230E+04	-.1674251E+04	-.1713691E+04
107	-.6200853E+04	-.6633899E+04	-.7684541E+04	-.8454080E+04	-.9274443E+04	-.9753646E+04
108	-.2270147E+04	-.2307621E+04	-.2384483E+04	-.2423989E+04	-.2463435E+04	-.2496964E+04
109	-.2587692E+04	-.2635827E+04	-.2743335E+04	-.2828315E+04	-.2909181E+04	-.2968461E+04
110	-.3654720E+04	-.3773059E+04	-.4085534E+04	-.4203826E+04	-.4372646E+04	-.4475287E+04

BLANK PAGE

B.1. (continued)

Strain (in./in.) at pressure (psi

SG	29040	29370	29550	29180	29560	29700
724E+04	-.6827158E+04	-.6892235E+04	-.7359606E+04	-.7637661E+04	-.7686961E+04	-.7884165E
672E+04	-.7399214E+04	-.7462421E+04	-.7916725E+04	-.8211834E+04	-.8262398E+04	-.8455963E
881E+04	-.1010392E+05	-.1013634E+05	-.1118663E+05	-.1107478E+05	-.1114826E+05	-.1161918E
284E+05	-.1085184E+05	-.1098550E+05	-.1236323E+05	-.1315603E+05	-.1327110E+05	-.1400611E
346E+05	-.1225812E+05	-.1229559E+05	-.1236855E+05	-.1252040E+05	-.1256181E+05	-.1265844E
857E+05	-.1293255E+05	-.1297397E+05	-.1310412E+05	-.1331512E+05	-.1336246E+05	-.1351835E
369E+04	-.4492278E+04	-.4521858E+04	-.4614543E+04	-.4709281E+04	-.4738781E+04	-.4829494E
375E+04	-.4715829E+04	-.4767683E+04	-.5067563E+04	-.5297428E+04	-.5354956E+04	-.5611222E
710E+04	-.1688388E+04	-.2545562E+04	-.2472284E+04	-.1432521E+04	-.2527706E+04	-.2196486E
807E+04	-.6731598E+04	-.6817262E+04	-.7448588E+04	-.7848958E+04	-.7934272E+04	-.8387894E
311E+03	-.1249813E+03	-.1249908F+03	-.8134888E+02	-.5753369E+02	-.5554966E+02	-.2388826E
987E+04	-.7411379E+04	-.7275362E+04	-.7724288E+04	-.7985646E+04	-.8035247E+04	-.8174684E
610E+05	-.7339499E+05	-.7350662E+05	-.7455677E+05	-.7513353E+05	-.7522678E+05	-.7570957E
123E+05	-.5359112F+05	-.5359123E+05	+.2717028E+04	-.6918867E+04	-.6962516E+04	-.1719545E
887E+04	-.1846735E+04	-.1874722E+04	-.2150731E+04	-.2340969E+04	-.2372714E+04	-.2545579E
753E+05	-.1966306E+05	-.1965784E+05	-.1976421E+05	-.2008981E+05	-.2007052E+05	-.2027817E
426E+01	-.1825035E+02	-.2284426E+01	+.1874195E+01		-.2284426E+01	+.1874195E
871E+03	-.4250187E+03	-.4328273E+03	-.4485735E+03		-.4546517E+03	-.4723834E
854E+05	-.1657894E+05	-.1661432F+05	-.1669715E+05		-.1694366E+05	-.1708762E
858E+04	-.4350292E+04	-.4370812E+04	-.4559326E+04		-.4723005E+04	-.4864991E
896E+05	-.6465291E+05	-.6464896E+05	-.6464896E+05		-.6464896E+05	-.6464896E
139E+04	-.2896907E+04	-.2939322E+04	-.3180579E+04			-.3494432E
779E+04	-.1057598E+05	-.1076311E+05	-.1207078E+05			-.1360187E
598E+05	-.1335062E+05	-.1347091E+05	-.1478626E+05			-.1673868E
551E+05	-.1223248E+05	-.1235475E+05	-.1344528E+05			-.1469949E
841E+05	-.1743469E+05	-.1758862E+05	-.1902612E+05			-.2072809E
650E+04	-.1319286E+04	-.1335062E+04	-.1411972E+04			-.1528321E
759E+04	-.7580472E+04	-.7647521E+04	-.8107804E+04			-.8664898E
383E+04	-.3756712E+04	-.3823760E+04	-.4456781E+04			-.5087830E
228E+03	-.7828948E+03	-.7986710E+03	-.8382235E+03			-.8854402E
656E+04	-.2752950E+04	-.2802250E+04	-.3206516E+04			-.3839536E
335E+03	+.1676223E+03	+.1617862E+03	+.2583355E+03			+.3707411E
144E+04	-.5783956E+04	-.5874641E+04	-.6939563E+04			-.8248998E
489E+04	-.3243323E+04	-.3302586E+04	-.4065025E+04			-.5092145E
163E+04	-.1754084E+04	-.1819639E+04	-.2086834E+04			-.2360401E
390E+04	-.5260039E+04	-.5350988E+04	-.6281234E+04			-.7316254E
558E+04	+.2538172E+04	+.2546147E+04	+.2735694E+04			+.2996425E
983E+04	-.5603738E+04	-.5680763E+04	-.6854082E+04			-.6660478E
583E+04	-.6707883E+04	-.6786893E+04	-.7181938E+04			-.7829814E
376E+04	+.1799435E+04	+.1803336E+04	+.1957454E+04			+.2196456E
866E+05	-.2287712E+05	-.2299751E+05	-.2412152E+05			-.2686317E
519E+04	-.6397772E+04	-.6468836E+04	-.6960713E+04			-.7717226E
364E+04	-.6344441E+04	-.6411598E+04	-.6844174E+04			-.7551387E
660E+04	-.1445869E+04	-.1459695E+04	-.1643392E+04			-.1846840E
312E+04	-.5183996E+04	-.5181030E+04	-.5947428E+04			-.6888620E
517E+04	-.5464231E+04	-.5437810E+04	-.5597804E+04			-.5917791E
823E+03	+.5867836E+03	+.5867836E+03	+.5837208E+03			+.6823214E
229E+05	-.1060079E+05	.1090728E+05	-.1198086E+05			
691E+04	-.1755104E+04	-.1772852E+04	-.1843845E+04			
646E+04	-.1039850E+05	-.1052471E+05	-.1188146E+05			
964E+04	-.2512743E+04	-.2534438E+04	-.2583747E+04			
461E+04	-.3001880E+04	-.3025548E+04	-.3106413E+04			
507E+04	-.4585657E+04	-.4619187E+04	-.4778946E+04			

2

BLANK PAGE

29370	29550	29180	29560	29700
192235E+04	-.7359686E+04	-.7637661E+04	-.7686961E+04	-.7884165E+04
162421E+04	-.7916725E+04	-.8211834E+04	-.8262390E+04	-.8455963E+04
113634E+05	-.1118663E+05	-.1187478E+05	-.1114026E+05	-.1161918E+05
198550E+05	-.1236323E+05	-.1315683E+05	-.1327110E+05	-.1408611E+05
229559E+05	-.1236855E+05	-.1252848E+05	-.1256181E+05	-.1265844E+05
297397E+05	-.1310412E+05	-.1331512E+05	-.1336246E+05	-.1351835E+05
821858E+04	-.4614540E+04	-.4709201E+04	-.4738781E+04	-.4829494E+04
767683E+04	-.5067563E+04	-.5297428E+04	-.5354956E+04	-.5611222E+04
645562E+04	-.2472284E+04	-.1432521E+04	-.2527706E+04	-.2196486E+04
817262E+04	-.7448508E+04	-.7848958E+04	-.7934272E+04	-.8387894E+04
249908F+03	-.8134888E+02	-.5753369E+02	-.5554966E+02	-.2388826E+02
275362E+04	-.7724288E+04	-.7985646E+04	-.8035247E+04	-.8174684E+04
358662E+05	-.7455677E+05	-.7513353E+05	-.7522678E+05	-.7578957E+05
359123E+05	+.2717828E+04	-.6918867E+04	-.6962516E+04	-.1719545E+04
874722E+04	-.2150731E+04	-.2348969E+04	-.2372714E+04	-.2545579E+04
9A57P4E+05	-.1976421E+05	-.2008981E+04	-.2007852E+05	-.2027817E+05
804426E+01	+.1874195E+01		-.2284426E+01	+.1874195E+01
328273E+03	-.4485735E+03		-.4546517E+03	-.4723834E+03
661432E+05	-.1669715E+05		-.1694366E+05	-.1708762E+05
870812E+04	-.4559326E+04		-.4723885E+04	-.4864991E+04
464896E+05	-.6464896E+05		-.6464896E+05	-.6464896E+05
933322E+04	-.3180879E+04			-.3494432E+04
876311E+05	-.1207078E+05			-.1368107E+05
347091E+05	-.1478626E+05			-.1673868E+05
235475E+05	-.1344528E+05			-.1469949E+05
750862E+05	-.1902612E+05			-.2072089E+05
335842E+04	-.1411972E+04			-.1528321E+04
647521E+04	-.8107884E+04			-.8684888E+04
823764E+04	-.4456781E+04			-.5087838E+04
986719E+03	-.8382235E+03			-.8854482E+03
389225E+04	-.3206516E+04			-.3839536E+04
1617842E+03	+.2583355E+03			+.3787411E+03
887641E+04	-.6939563E+04			-.8248998E+04
1382586E+04	-.4865825E+04			-.5892145E+04
1619659E+04	-.2006934E+04			-.2360481E+04
635E9E4E+04	-.6281234E+04			-.7316254E+04
254147E+04	+.2735694E+04			+.2996425E+04
568763E+04	-.6054082E+04			-.6668478E+04
678693E+04	-.7181938E+04			-.7829814E+04
1803336E+04	+.1957454E+04			+.2196456E+04
2299751E+05	-.2412152E+05			-.2686317E+05
646886E+04	-.6968713E+04			-.7717226E+04
641159E+04	-.6844174E+04			-.7551307E+04
1459695E+04	-.1643392E+04			-.1846840E+04
5181030E+04	-.5947428E+04			-.6808628E+04
5437816E+04	-.5597884E+04			-.5917791E+04
508783E+03	+.5837208E+03			+.6823214E+03
1898728E+05	-.1198886E+05			
1772852E+04	-.1843845E+04			
1052471E+05	-.1188146E+05			
2534438E+04	-.2583747E+04			
3025548E+04	-.3106413E+04			
4619187E+04	-.4778946E+04			

3

Table B-1.

Channel No.	Strain (μin./in.)					
	29730	29490	29660	30030	29800	30
65	-.8594366E+04	-.8771577E+04	-.8915535E+04	-.9976485E+04	-.1019930E+05	-.1032
96	-.9119864E+04	-.9277689E+04	-.9413949E+04	-.1089688E+05	-.1052688E+05	-.1063
35	-.1264812E+05	-.1297833E+05	-.1338887E+05	-.1658814E+05	-.1755395E+05	-.1787
37	-.1638271E+05	-.1678195E+05	-.1713997E+05	-.1967287E+05	-.2023041E+05	-.2046
48	-.1335062E+05	-.1358613E+05	-.1363854E+05	-.1409777E+05	-.1468455E+05	-.1479
49	-.1499185E+05	-.1489695E+05	-.1472730E+05	-.1563817E+05	-.1598648E+05	-.1599
57	-.5261360E+04	-.5363914E+04	-.5044767E+04	-.5868836E+04	-.5975848E+04	-.6032
24	-.6688988E+04	-.6867198E+04	-.7188889E+04	-.8976358E+04	-.9486755E+04	-.9611
25	-.1998818E+04	-.1129818E+04	-.1964241E+04	-.1698468E+04	-.7588366E+03	
26	-.9708844E+04	-.1082688E+05	-.1331789E+05	-.1242287E+05	-.1291698E+05	
27	+.5952488E+02	+.7738373E+02	+.8988468E+02	+.2282438E+03	+.2468378E+03	
28	-.8664085E+04	-.8791756E+04	-.8916157E+04	-.9738268E+04	-.9934638E+04	
29	-.7693588E+05	-.7718388E+05	-.7741128E+05	-.7887488E+05	-.7982351E+05	
30	+.2910888E+04	+.2814858E+04	+.2388291E+04	+.4842445E+04	+.4896818E+04	
31	-.3057285E+04	-.3166488E+04	-.3253624E+04	-.3813455E+04	-.3944889E+04	
32	-.2159624E+05	-.2198999E+05	-.2211884E+05	-.2361948E+05	-.2486568	
33	-.2284426E+01	-.1899618E+00	-.4108458E+01	+.1874195E+01		
38	-.4943323E+03	-.4942991E+03	-.5102846E+03	-.5577822E+03		
50	-.1888866E+05	-.1821167E+05	-.1834774E+05	-.1933178E+05		
51	-.5383634E+04	-.5494068E+04	-.5572949E+04	-.6267188E+04		
53	-.6464896E+05	-.6465894E+05	-.6465894E+05	-.6464896E+05		
56	-.3892781E+04	-.3969698E+04	-.4042376E+04	-.4561299E+04		
58	-.1575255E+05	-.1628888E+05	-.1656395E+05	-.1942644E+05		
59	-.1989514E+05	-.1953884E+05	-.1987686E+05	-.2224447E+05		
60	-.1650567E+05	-.1691999E+05	-.1726115E+05	-.1978535E+05		
61	-.2278197E+05	-.2309835E+05	-.2341191E+05	-.2539576E+05		
62	-.1699867E+04	-.1729468E+04	-.1772852E+04	-.1983859E+04		
63	-.9448894E+04	-.9611668E+04	-.9757598E+04	-.1067261E+05		
64	-.5774895E+04	-.5916881E+04	-.6044263E+04	-.6883494E+04		
67	-.9584052E+03	-.9722894E+03	-.9998178E+03	-.1139832E+04		
68	-.4579847E+04	-.4728921E+04	-.4859874E+04	-.5728858E+04		
70	+.5363914E+03	+.5758319E+03	+.5896361E+03	+.7631745E+03		
71	-.9511886E+04	-.9728122E+04	-.9873940E+04	-.1064186E+05		
72	-.6825929E+04	-.7128608E+04	-.7367618E+04	-.8858984E+04		
73	-.3098966E+04	-.3128765E+04	-.3086301E+04	-.3393444E+04		
74	-.8467364E+04	-.8685889E+04	-.8856934E+04	-.1005590E+05		
75	+.3487822E+04	+.3492288E+04	+.3543564E+04	+.4157868E+04		
77	-.7685159E+04	-.7952279E+04	-.8207883E+04	-.1023968E+05		
78	-.8923531E+04	-.9198658E+04	-.9459388E+04	-.1155985E+05		
79	+.2630768E+04	+.2731744E+04	+.2887778E+04	+.3511960E+04		
97	-.2889983E+05	-.2948427E+05	-.2992879E+05	-.3284018E+05		
98	-.8923544E+04	-.9212476E+04	-.9498984E+04	-.1170126E+05		
99	-.8753885E+04	-.9054458E+04	-.9338891E+04	-.1159855E+05		
101	-.2887742E+04	-.2135224E+04	-.2174788E+04	-.2439410E+04		
102	-.8175189E+04	-.8444111E+04	-.8667312E+04	-.9951212E+04		
103	-.6549589E+04	-.6780933E+04	-.6826397E+04	-.7569884E+04		
104	+.8261348E+03	+.8617739E+03		+.1027269E+04		
105	-.1539675E+05	-.1580974E+05		-.1896984E+05		
106	-.2074443E+04	-.2106125E+04		-.2326847E+04		
107	-.1587286E+05	-.1632641E+05		-.1927736E+05		
108	-.2788868E+04	-.2888592E+04		-.3068921E+04		
109	-.3587438E+04	-.3654788E+04		-.4210654E+04		
110	-.5656868E+04	-.5788776E+04		-.6598981E+04		

ontinued)

ressure (psi)						
	30280	30340	30280	30050	30040	29970
05	-.1048724E+05	-.1102363E+05	-.1124844E+05	-.1141409E+05	-.1143053E+05	-.1147325E+05
05	-.1078881E+05	-.1127659E+05	-.1147016E+05	-.1163806E+05	-.1165854E+05	-.1169732E+05
05	-.1938713E+05	-.1992883E+05	-.2049834E+05	-.2089786E+05	-.2080183E+05	-.2068873E+05
05	-.2083955E+05	-.2205187E+05	-.2251815E+05	-.2291308E+05	-.2295665E+05	-.2304990E+05
05	-.1481584E+05	-.1536684E+05	-.1559479E+05	-.1578668E+05	-.1580688E+05	-.1584189E+05
05	-.1613709E+05	-.1678984E+05	-.1705814E+05	-.1726984E+05	-.1729187E+05	-.1733412E+05
04	-.6097508E+04	-.6377536E+04	-.6493866E+04	-.6594458E+04	-.6606718E+04	-.6628955E+04
04	-.9934699E+04	-.1096351176JE+05	-.1134741E+05	-.1165496E+05	-.1169868E+05	-.1176821E+05
	-.1525841E+04		-.1363148E+04	-.3412997E+03	-.4186818E+03	-.2489918E+03
	-.1351812E+05		-.1513581E+05	-.1549633E+05	-.1553799E+05	-.1562569E+05
	+.2817518E+03		+.3738238E+03	+.3928646E+03	+.3948488E+03	+.3988171E+03
	-.1018668E+05		-.1087313E+05		-.1105369E+05	-.1109139E+05
	-.7967788E+05		-.8084457E+05		-.8115013E+05	-.8181560E+05
	+.3572288E+04		+.5476998E+04		+.5574814E+04	+.5564892E+04
	-.4883308E+04		-.4458385E+04		-.4643466E+04	-.4587275E+04
	-.2445672E+05		-.2607581E+05		-.2655399E+05	-.2663336E+05
	+.1874195E+01		+.1874195E+01		-.1099618E+08	-.1099618E+08
	-.5894487E+03		-.6311168E+03		-.6370685E+01	-.6398526E+03
	-.1982479E+05		-.2872286E+05		-.2896584E+05	-.2100603E+05
	-.6628095E+04		-.7195927E+04		-.7332481E+04	-.7353689E+04
	-.6464896E+05		-.6464896E+05		-.6465497E+05	-.6465894E+05
	-.4823578E+04		-.5162767E+04		-.5245917E+04	-.5265312E+04
	-.2877925E+05		-.2269814E+05		-.2314388E+05	-.2323845E+05
	-.2333383E+05		-.2493836E+05		-.2531054E+05	-.2531294E+05
	-.2108406E+05		-.227157 8E+05		-.2315185E+05	-.2324231E+05
	-.2640150E+05		-.2785082E+05		-.2827077E+05	-.2835978E+05
	-.208A		-.2222474E+04		-.2252172E+04	-.2259999E+04
			-.1184794E+05		-.1203483E+05	-.1207875E+05
			-.7773731E+04		-.7986318E+04	-.7937489E+04
			-.1335062E+04		-.1343827E+04	-.1348866E+04
			-.6732500E+04		-.6661878E+04	-.6898235E+04
			+.8992444E+03		+.9427821E+03	+.9465738E+03
			-.1169018E+05		-.1185258E+05	-.1188738E+05
			-.1048658E+05		-.1069856E+05	-.1074328E+05
			-.3885279E+04		-.1170000E+05	-.1179805E+05
			-.1150177E+05		-.1169402E+05	-.1173602E+05
			+.5078318E+04		+.5179416E+04	+.5139558E+04
			-.1277776E+05		-.1313816E+05	-.1320441E+05
			-.1438462E+05		-.1465911E+05	-.1473324E+05
			+.4399038E+04		+.4539446E+04	+.4568783E+04
			-.3556798E+05		-.3688851E+05	-.3611314E+05
			-.1457918E+05		-.1497128E+05	-.1505126E+05
			-.1445276E+05		-.1484663E+05	-.1498879E+05
			-.2733719E+04		-.2779278E+04	-.2787058E+04
			-.1088945E+05		-.1107954E+05	-.1110855E+05
			-.8615956E+04		-.8792288E+04	-.8827306E+04
			+.1139832E+04		+.1151664E+04	+.1155688E+04
			-.2219122E+05		-.2268981E+05	-.2271972E+05
			-.2567899E+04		-.2630464E+04	-.2638578E+04
			-.2217347E+05		-.2268038E+05	-.2269409E+05
			-.3408179E+04		-.3477818E+04	-.3492969E+04
			-.4966316E+04		-.5086601E+04	-.5114841E+04
			-.7638818E+04		-.7816327E+04	-.7853681E+04

2

BLANK PAGE

Table B.1. (continu

Channel No.	Strain (μin./						
	29950	30510	30280	30670	30230	30800	
65	-.1150886E+05	-.1171976E+05	-.1192090E+05	-.1450831E+05	-.1446570E+05	-.1257562E+05	-.1
96	-.1172176E+05	-.1193839E+05	-.1209236E+05	-.1437573E+05	-.1434018E+05	-.1265728E+05	-.1
35	-.1861928E+05	-.1917683E+05	-.1543947E+05	-.2169845E+05	-.2119861E+05	-.2166100E+05	-.2
37	-.2310348E+05	-.2356975E+05	-.2397897E+05	-.2916541E+05	-.2916937E+05	-.2528406E+05	-.2
48	-.1586101E+05	-.1599511E+05	-.1613513E+05	-.2191514E+05	-.2378415E+05	-.1683717E+05	-.1
49	-.1735778E+05	-.1752935E+05	-.1775416E+05	-.2566593E+05	-.2883812E+05	-.1872045E+05	-.1
57	-.6641787E+04	-.6746305E+04	-.6844906E+04	-.1088495E+05	-.1060821E+05	-.7324109E+04	-.7
24	-.1188576E+05	-.1219869E+05	-.1252525E+05	-.1636632E+05	-.1772719E+05		
25	-.3333631E+03	-.1410760E+04	-.3849518E+03	-.8868501E+03	-.4583530E+03		
26		-.1615110E+05	-.1658068E+05		-.2284947E+05		
27		+.4345319E+03	+.4682987E+03		+.7955034E+03		
28		-.1134536E+05	-.1152516E+05		-.1398749E+05		
29		-.8165212E+05	-.8194273E+05		-.8587245E+05		
30		+.5544452E+04	+.5546806E+04		+.8896241EA		
31		-.4708389E+04	-.4795217E+04				
32		-.2691511E+05	-.2722295E+05				
33		+.1874195E+01	-.4188458E+01				
38		-.6797357 E+03	-.6887674E+03				
5h		-.2115591E+05	-.2124070E+05				
.		-.7507507E+04	-.7643577E+04				
--		-.6464896E+05	-.6465894E+05				
56		-.5432935E+04	-.5509844E+04				
58		-.2377673E+05	-.2420663E+05				
59		-.2554169E+05	-.2580792E+05				
60		-.2376095E+05	-.2415339E+05				
61		-.2881920E+05	-.2913670E+05				
62		-.2325020E+04	-.2346684E+04				
63		-.1230939E+05	-.1247307E+05				
66		-.8136584E+04	-.8264746E+04				
67		-.1486055E+04	-.1433663E+04				
68		-.7893381E+04	-.7223535E+04				
70		+.9564332E+03	+.9741814E+03				
71		-.1208063E+05	-.1220685E+05				
72		-.1182376E+05	-.1123313E+05				
73		-.1203903E+05	-.1221877E+05				
74		-.1201533E+05	-.1221877 +05				
75		+.5250163E+04	+.5333123+ 04				
77		-.1367254E+05	-.1402414E+05				
78		-.1525273E+05	-.1563987E+05				
7?		+.4722777E+04	+.4864993E+04				
97		-.3657337E+05	-.3689928E+05				
98		-.1559642E+05	-.1600332E+05				
99		-.1545618E+05	-.1585122E+05				
101		-.2818654E+04	-.2854206E+04				
102		-.1137733E+05	-.1157090E+05				
103		-.9018903E+04	-.9174947E+04				
104		+.1163496E+04	+.1194681E+04				
105		-.2328372E+05	-.2372607E+05				
106		-.2703649E+04	-.2740947E+04				
107		-.2323639E+05	-.2364119E+05				
108		-.3627107E+04	-.3711775E+04				
109		-.5297667E+04	-.5431448E+04				
110		-.8056924E+04	-.8218159E+04				

BLANK PAGE

(continued)

(μin./in.) at pressure (psi)					
30810	30850	30910	30920	30970	31031
-.1279845E+05	-.1302524E+05	-.1324216E+05	-.1346508E+05	-.1368784E+05	-.1391462E+05
-.1285875E+05	-.1305035E+05	-.1324985E+05	-.1344737E+05	-.1364884E+05	-.1385229E+05
-.2205783E+05	-.2237781E+05	-.2315754E+05	-.2337721E+05	-.2382904E+05	-.2389458E+05
-.2574240E+05	-.2617128E+05	-.2660975E+05	-.2704895E+05	-.2749189E+05	-.2793744E+05
-.1717213E+05	-.1754512E+05	-.1790483E+05	-.1825111E+05	-.1859830E+05	-.1893146E+05
-.1911888E+05	-.1954082E+05	-.1998058E+05	-.2040653E+05	-.2082066E+05	-.2124078E+05
-.7523283E+04	-.7724430E+04	-.7945297E+04	-.8158388E+04	-.8349563E+04	-.8542822E+04

2

Table B-1. (continued)

Channel No.	Strain (μin./in.) at press					
	31000	31080	31000	31010	30100	2990
65	-.1413746E+05	-.1434847E+05	-.1441749E+05	-.1448256E+05	-.1446887E+05	-.14451
96	-.1405376E+05			-.1434610E+05	-.1433425E+05	-.14322
35	-.2376754E+05			-.2246671E+05	-.2997841E+05	-.28254
37	-.283778+E+05			-.2904055E+05	-.2917334E+05	-.29173
48	-.1920851E+05			-.2077925E+05	-.2496783E+05	-.25857
49	-.2168441E+05			-.2381222E+05	-.2881329E+05	-.29915
57	-.8736866E+04			-.9530807E+04	-.1075346E+05	-.10893
24					-.1813188E+05	-.18702
25					-.3373422E+03	+.13476
26					-.2309149E+05	-.23443
27					+.7955834E+03	+.79942
28					-.1398153E+05	-.13978
29					-.8587642E+05	-.85875
30					-.4791862E+03	-.98676
31					-.5883523E+04	-.58751
32					-.6542923E+05	-.65425
33					-.1234343E+02	-.16420
38					-.9429135E+03	-.93110
50					-.6686894E+05	-.66860
51					-.3778404E+04	-.21889
53					-.6465094E+05	-.64650
56					-.6730529E+04	-.67246
58					-.2844057E+05	-.27908
59					-.2783911E+05	-.27430
60					-.3212826E+05	-.32495
61					-.3596189E+05	-.36263
62					-.2896907E+04	-.28870
63					-.1473893E+05	-.14729
66					-.1084551E+05	-.10833
67					-.1703831E+04	-.16900
68					-.8933283E+04	-.89214
70					+.1222656E+04	+.12266
71					-.1326977E+05	-.13165
72					-.1408734E+05	-.14085
73					-.1451795E+05	-.14482
74					-.1485176E+05	-.14833
75					+.4096628E+04	+.38991
77					-.1902344E+05	-.19513
78					-.2094535E+05	-.21330
79					-.6607146E+05	-.66071
97					-.4411677E+05	-.44382
98					-.2212653E+05	-.22675
99					-.2202579E+05	-.22628
101					-.3146518E+04	-.31346
102					-.1295158E+05	-.12860
103					-.1432635E+05	-.14508
104					+.1820181E+04	+.18594
105					-.3071235E+05	-.30895
106					-.3648250E+04	-.36559
107					-.2930629E+05	-.29339
108					-.7412000E+04	-.75082
109					-.1005097E+05	-.10176
110					-.1350648E+05	-.13673

tinued)

) at pressure (psi)

29900	29770	30120	580	0
-.1445102E+05	-.1445298E+05	-.1451806E+05	-.9828789E+04	-.9829172E+04
-.1432240E+05	-.1431737E+05		+.6735724E+05	+.6479951E+05
-.2025493E+05	-.1998645E+05		-.4611345E+05	-.2796437E+05
-.2917345E+05	-.2917334E+05		-.2658237E+05	-.2704618E+05
-.2585722E+05	-.2630298E+05		-.6435684E+05	-.6436705E+05
-.2991565E+05	-.3054078E+05		-.6370410E+05	-.6371431E+05
-.1089348E+05	-.1094278E+05		-.6439036E+05	-.6440058E+05
-.1870207E+05	-.1901863E+05		+.6448524E+05	+.6452377E+05
+.1347649E+03	+.1625711E+03		+.3323438E+04	+.3291593E+04
-.2344319E+05	-.2365489E+05		+.6389968E+05	+.6393840E+05
+.7994225E+03			-.6494950E+05	-.6497616E+05
-.1397070E+05			-.9279172E+04	-.9280195E+04
-.8587511E+05			-.8590169E+05	-.8592012E+05
-.9067680E+04			-.7025312E+04	-.4728310E+04
-.5875126E+04			-.5916681E+04	-.5946184E+04
-.6542515E+05			-.6537215E+05	-.6539881E+05
-.1642039E+02			-.7428098E+05	-.7566980E+05
-.9311066E+03			-.6743183E+05	-.6745849E+05
-.6606094E+05			-.6604884E+05	-.6605905E+05
-.2188950E+04			-.6549076E+05	-.6550097E+05
-.6465094E+05			-.6463884E+05	-.6464905E+05
-.6724612E+04			-.6467039E+05	-.6468061E+05
-.2790813E+05			-.6432726E+05	-.6433747E+05
-.2743089E+05			-.2613442E+05	-.2581739E+05
-.3249506E+05			-.4976273E+05	-.4865490E+05
-.3626360E+05			-.4762541E+05	-.4758601E+05
-.2887048E+04			-.6500564E+05	-.6501585E+05
-.1472907E+05			-.6514368E+05	-.6515389E+05
-.1003367E+05			-.6514171E+05	-.6515192E+05
-.1690027E+04			-.6473941E+05	-.6474963E+05
-.8921451E+04			-.6515354E+05	-.6516375E+05
+.1226601E+04			-.6518509E+05	-.6519531E+05
-.1316525E+05			-.6531327E+05	-.6532348E+05
-.1408537E+05			-.6665839E+05	-.6408645E+05
-.1448239E+05			-.6768946E+05	-.6511752E+05
-.1483398E+05			-.1042760E+05	-.1058979E+05
+.3899105E+04			+.6665604E+05	+.6409830E+05
-.1951330E+05			+.6699183E+05	+.6443409E+05
-.2133051E+05			+.6732169E+05	+.6476395E+05
-.6607146E+05			-.6864152E+05	-.6606958E+05
-.4430245E+05			+.6620963E+05	+.6365190E+05
-.2267565E+05			-.6747416E+05	-.6490222E+05
-.2262824E+05			-.6939014E+05	+.6263465E+05
-.3134691E+04			-.1902782E+04	-.1854804E+04
-.1286073E+05			-.7084391E+05	-.6827197E+05
-.1458807E+05			-.6850128E+05	-.6592934E+05
+.1659412E+04			-.6612772E+05	-.6613390E+05
-.3089591E+05			-.3499138E+05	-.3496601E+05
-.3655910E+04			-.6463687E+05	-.6464305E+05
-.2933999E+05			-.2748106E+05	-.2744273E+05
-.7506265E+04			-.6606054E+05	-.6606672E+05
-.1017656E+05			-.6466639E+05	-.6467257E+05
-.1367327E+05			-.6448690E+05	-.6449308E+05

2

BLANK PAGE

Table B. . [illegible]

Pressure (psi)	[illegible]								
[illegible]									

Table B.3. Pressure-strain data from V-4 – computer output

Channel No.	Strain (uin./in.) at pressure (psi)								
	5950	7970	11990	16130	18056	19890	21960	22960	25970
16	-.3625586E+03	-.7152345E+03	-.1040150E+04	-.1365056E+04	-.1805556E+04	-.1648359E+04	-.1838527E+04	-.1987579E+04	-.2055434E+04
17	-.1960649E+03	-.3883267E+03	-.5726400E+03	-.7628290E+03	-.8919414E+03	-.9811511E+03	-.1034294E+04	-.1077329E+04	-.1131320E+04
18	-.1941668E+03	-.3883267E+03	-.5705756E+03	-.7587897E+03	-.8479788E+03	-.9751045E+03	-.1039161E+04	-.1083659E+04	-.1139615E+04
19	-.2139703E+03	-.4239894E+03	-.6201143E+03	-.8400284E+03	-.9391167E+03	-.1040115E+04	-.1151058E+04	-.1206530E+04	-.1271902E+04
20	-.2059670E+03	-.4081995E+03	-.6023615E+03	-.8004754E+03	-.8935476E+03	-.9867020E+03	-.1069721E+04	-.1114235E+04	-.1200665E+04
21	-.1466690E+03	-.2932263E+03	-.4359050E+03	-.5785448E+03	-.6458904E+03	-.7136520E+03	-.7905262E+03	-.8301469E+03	-.8973399E+03
22	-.1505641E+03	-.2991701E+03	-.4418140E+03	-.5864369E+03	-.6557967E+03	-.7211541E+03	-.7964375E+03	-.8320977E+03	-.8697992E+03
23	-.6971265E+02	-.1386801E+03	-.2040965E+03	-.2676890E+03	-.2992076E+03	-.3189965E+03	-.3407913E+03	-.3477155E+03	-.3506966E+03
24	-.8150215E+02	-.1624032E+03	-.2396519E+03	-.3188975E+03	-.3586078E+03	-.3961616E+03	-.4357934E+03	-.4516934E+03	-.4675202E+03
25	-.2138915E+03	-.4259706E+03	-.6281177E+03	-.8341558E+03	-.9331730E+03	-.1030288E+04	-.1131326E+04	-.1180095E+04	-.1240213E+04
26	-.2021334E+03	-.4041768E+03	-.5943061E+03	-.7906405E+03	-.8836415E+03	-.9727050E+03	-.1057894E+04	-.1095554E+04	-.1135158E+04
27	-.1617762E+03	-.3225329E+03	-.4757593E+03	-.6328652E+03	-.7078632E+03	-.7800163E+03	-.8493098E+03	-.8801469E+03	-.9133995E+03
28	-.1902756E+03	-.3823829E+03	-.5646007E+03	-.7547897E+03	-.8430163E+03	-.9330918E+03	-.1018293E+04	-.1051959E+04	-.1089564E+04
29	-.3623675E+03	-.7944898E+03	-.1157231E+04	-.1466099E+04	-.1604619E+04	-.1755345E+04	-.1955440E+04	-.2045955E+04	-.2181299E+04
30	-.1485999E+03	-.2952076E+03	-.4353872E+03	-.5788955E+03	-.6477217E+03	-.7132145E+03	-.7795900E+03	-.8063259E+03	-.8306118E+03
31	-.1406255E+03	-.2793575E+03	-.4114098E+03	-.5508081E+03	-.6102277E+03	-.6676951E+03	-.7291103E+03	-.7567330E+03	-.7806176E+03
32	-.2654662E+03	-.5270149E+03	-.7763757E+03	-.1000512E+04	-.1091673E+04	-.1194513E+04	-.1353154E+04	-.1466079E+04	-.1568947E+04
33	-.2634298E+03	-.5250336E+03	-.7727367E+03	-.1030284E+04	-.1155074E+04	-.1271995E+04	-.1694813E+04	-.1467009E+04	-.1616700E+04
34	-.2971014E+03	-.5904152E+03	-.8599185E+03	-.1143221E+04	-.1273549E+04	-.1408669E+04	-.1557279E+04	-.1638523E+04	-.1719731E+04
35	-.3030361E+03	-.5884714E+03	-.8680413E+03	-.1123419E+04	-.1252145E+04	-.1382984E+04	-.1549365E+04	-.1658325E+04	-.1738815E+04
36	-.3664498E+03	-.7251408E+03	-.1060015E+04	-.1408695E+04	-.1571139E+04	-.1735954E+04	-.1936778E+04	-.2027998E+04	-.2136948E+04
37	-.2957619E+03	-.5875771E+03	-.8815633E+03	-.1175446E+04	-.1309106E+04	-.1446835E+04	-.1615675E+04	-.1289777E+04	-.1400715E+04
38	-.1939091E+03	-.3877640E+03	-.5697897E+03	-.7597296E+03	-.8467954E+03	-.9357314E+03	-.1034747E+04	-.1066210E+04	-.1119750E+04
39	-.7716790E+02	-.1524743E+03	-.2217235E+03	-.2909722E+03	-.3246074E+03	-.3524117E+03	-.3900015E+03	-.4015777E+03	-.4166957E+03
40	-.2273465E+03	-.4511815E+03	-.6648640E+03	-.8844520E+03	-.9853446E+03	-.1092259E+04	-.1212519E+04	-.1270215E+04	-.1337135E+04
41	-.2255677E+03	-.4491847E+03	-.6628671E+03	-.8805066E+03	-.9805693E+03	-.1086241E+04	-.1206906E+04	-.1265215E+04	-.1331135E+04
42	-.2117170E+03	-.4253922E+03	-.6232178E+03	-.8269861E+03	-.9259546E+03	-.1026732E+04	-.1139467E+04	-.1214901E+04	-.1285920E+04
43	-.2136957E+03	-.4254336E+03	-.6252662E+03	-.8290559E+03	-.9260044E+03	-.1029872E+04	-.1154537E+04	-.1213914E+04	-.1282159E+04
44	-.1998450E+03	-.3957598E+03	-.5797651E+03	-.7697030E+03	-.8587751E+03	-.9517201E+03	-.1070441E+04	-.1127519E+04	-.1191100E+04
45	-.2552677E+03	-.4867979E+03	-.6886091E+03	-.8825061E+03	-.9699619E+03	-.1060595E+04	-.1165457E+04	-.1220036E+04	-.1282165E+04
46	-.2987782E+03	-.5876682E+03	-.8627927E+03	-.1127910E+04	-.1254496E+04	-.1377062E+04	-.1509711E+04	-.1586067E+04	-.1668544E+04
47	-.4076048E+03	-.8033536E+03	-.1173521E+04	-.1559136E+04	-.1741161E+04	-.1913157E+04	-.2111149E+04	-.2200135E+04	-.2320777E+04
48	-.5719888E+03	-.7361350E+03	-.1068508E+04	-.1412774E+04	-.1576993E+04	-.1733296E+04	-.1899495E+04	-.1997295E+04	-.2095972E+04
49	-.5540268E+02	-.1108345E+03	-.1642951E+03	-.2178757E+03	-.2453968E+03	-.2730941E+03	-.3126467E+03	-.3303452E+03	-.3477502E+03
50	-.4432207E+03	-.8948352E+03	-.1295642E+04	-.1698507E+04	-.1822259E+04	-.2006250E+04	-.2206127E+04	-.2301096E+04	-.2425614E+04
51	-.1978664E+03	-.3957687E+03	-.5797730E+03	-.7677442E+03	-.8577472E+03	-.9517399E+03	-.1070451E+04	-.1127529E+04	-.1191450E+04
52	-.4214554E+03	-.8350416E+03	-.1216878E+04	-.1618522E+04	-.1806548E+04	-.1998595E+04	-.2212004E+04	-.2311011E+04	-.2396664E+04
53	-.7518925E+02	-.1488190E+03	-.2190466E+03	-.2908741E+03	-.3264573E+03	-.3601292E+03	-.3998952E+03	-.4173007E+03	-.4358636E+03
54	-.2196317E+03	-.4352778E+03	-.6390675E+03	-.8507715E+03	-.9516759E+03	-.1052516E+04	-.1167355E+04	-.1230541E+04	-.1309710E+04
55	-.9101895E+02	-.1820645E+03	-.2651690E+03	-.3522198E+03	-.3917652E+03	-.4356366E+03	-.4793613E+03	-.4974126E+03	-.5207426E+03
56	-.5788126E+02	-.1148278E+03	-.1682484E+03	-.2256261E+03	-.2513471E+03	-.2771292E+03	-.2993521E+03	-.3126171E+03	-.3255447E+03
57	-.2255677E+03	-.4472154E+03	-.6588195E+03	-.8765587E+03	-.9794428E+03	-.1082324E+04	-.1194161E+04	-.1254545E+04	-.1325670E+04
58	-.4194768E+03	-.8291544E+03	-.1209054E+04	-.1604742E+04	-.1790725E+04	-.1980877E+04	-.2186790E+04	-.2290204E+04	-.2385471E+04
59	-.2255900E+03	-.4473517E+03	-.6608340E+03	-.8826506E+03	-.9862715E+03	-.1090111E+04	-.1191190E+04	-.1252259E+04	-.1327906E+04
60	-.2255900E+03	-.4452100E+03	-.6509965E+03	-.8686962E+03	-.9734589E+03	-.1077271E+04	-.1189120E+04	-.1251744E+04	-.1317444E+04
61	-.4333274E+03	-.8568218E+03	-.1250951E+04	-.1666045E+04	-.1861920E+04	-.2059750E+04	-.2275022E+04	-.2308125E+04	-.2408225E+04
62	-.2176590E+02	-.4362399E+02	-.5747377E+02	-.7152356E+02	-.7950210E+02	-.8556789E+02	-.9239531E+02	-.9517772E+03	-.9802950E+03
63	-.4333274E+03	-.8607046E+03	-.1258991E+04	-.1677586E+04	-.1877417E+04	-.2071451E+04	-.2290655E+04	-.2411741E+04	-.2522406E+04
64	-.2542585E+04	-.2671589E+04	-.2952556E+04	-.3273901E+04	-.3871513E+04	-.2802557E+04	-.3777224E+02	-.3871470E+04	-.4036417E+04
65	-.6727458E+02	-.1366476E+03	-.1979824E+03	-.2652827E+03	-.2929524E+03	-.3227336E+03	-.3505446E+03	-.3650300E+03	-.3798734E+03
66	-.4174981E+03	-.8310716E+03	-.1212930E+04	-.1614576E+04	-.1802555E+04	-.1994413E+04	-.2208136E+04	-.2326462E+04	-.2411134E+04
67	-.4359299E+03	-.8620650E+03	-.1256432E+04	-.1670614E+04	-.1866450E+04	-.2049889E+04	-.2227509E+04	-.2296792E+04	-.2436060E+04
68	-.3249078E+03	-.6460518E+03	-.9452967E+03	-.1254650E+04	-.1401160E+04	-.1551666E+04	-.1734055E+04	-.1342966E+04	-.1400302E+04
69	-.9964127E+01	-.9908770E+01	-.1585405E+02	-.1981754E+02	-.2179929E+02	-.2377919E+02	-.2576290E+02	-.2677457E+02	-.2776456E+02
70	-.2799656E+03	-.5095107E+03	-.6896504E+03	-.1014658E+04	-.1086354E+04	-.1081449E+04	-.1125036E+04	-.1267722E+04	-.1254359E+04
71	-.4994212E+03	-.1016640E+04	-.1551713E+04	-.2261181E+04	-.2600061E+04	-.2395266E+04	-.3250075E+04	-.3469883E+04	-.3640207E+04
72	-.2972415E+03	-.5945262E+03	-.8759365E+03	-.1173598E+04	-.1317866E+04	-.1466468E+04	-.1674582E+04	-.1782105E+04	-.2006963E+04
73	-.2611004E+03	-.5231831E+03	-.7649570E+03	-.1026548E+04	-.1149617E+04	-.1276217E+04	-.1454730E+04	-.1549682E+04	-.1712235E+04
74	-.5460399E+03	-.1125636E+04	-.1676964E+04	-.2348178E+04	-.2587682E+04	-.2651270E+04	-.2704325E+04	-.2737136E+04	-.2727136E+04
75	-.2259004E+03	-.4478764E+03	-.6559606E+03	-.8759353E+03	-.9789865E+03	-.1083200E+04	-.1194998E+04	-.1256987E+04	-.1341647E+04
76	-.2258805E+03	-.4439129E+03	-.6539788E+03	-.8719717E+03	-.9730412E+03	-.1078096E+04	-.1189052E+04	-.1248699E+04	-.1319045E+04
77	-.2179593E+03	-.4300405E+03	-.6341615E+03	-.8442272E+03	-.9413353E+03	-.1040421E+04	-.1149417E+04	-.1208496E+04	-.1279504E+04
78	-.2159982E+03	-.4300405E+03	-.6321795E+03	-.8422655E+03	-.9413353E+03	-.1038619E+04	-.1149417E+04	-.1218729E+04	-.1305975E+04
79	-.6155081E+02	-.1228587E+03	-.1805396E+03	-.2397922E+03	-.2715005E+03	-.3012952E+03	-.3358697E+03	-.3402580E+03	-.3471855E+03
80	-.2398005E+03	-.4776027E+03	-.6975774E+03	-.9175521E+03	-.9750240E+03	-.1028676E+04	-.1220760E+04	-.1329675E+04	-.1434790E+04
81	-.1678786E+02	-.1129799E+03	-.1248905E+03	-.1169235E+03	-.5969079E+04	-.6965127E+04	-.6809326E+04	-.6895159E+04	-.6994120E+04
82	-.2060589E+03	-.4082615E+03	-.6004714E+03	-.8006286E+03	-.8937711E+03	-.9869081E+03	-.1084019E+04	-.1139936E+04	-.1191044E+04
83	-.1544966E+03	-.3091556E+03	-.4553821E+03	-.6044550E+03	-.6757781E+03	-.7471664E+03	-.8204461E+03	-.8521928E+03	-.8960075E+03
84	-.2119845E+03	-.4240955E+03	-.6222708E+03	-.8269914E+03	-.9254791E+03	-.1020616E+04	-.1129599E+04	-.1198962E+04	-.1260215E+04
85	-.3586992E+03	-.7154152E+03	-.1042402E+04	-.1369192E+04	-.1512078E+04	-.1650768E+04	-.1834699E+04	-.1940078E+04	-.2075478E+04
86	-.4057564E+01	-.0000000E+00	-.5945262E+01	-.5945262E+01	-.5945262E+01	-.1689947E+03	-.5574476E+03	-.6364807E+03	-.6966790E+03
87	-.2257999E+03	-.4498981E+03	-.6658876E+03	-.8858625E+03	-.9860135E+03	-.1088549E+04	-.1194998E+04	-.1266996E+04	-.1342744E+04
88	-.7834532E+03	-.1281997E+04	-.1788442E+04	-.2405669E+04	-.2473931E+04	-.2731981E+04	-.2922004E+04	-.3084224E+04	-.3204970E+04
89	-.1978617E+02	-.6162099E+02	-.5945262E+02	-.7129361E+02	-.5177354E+02	-.3576077E+02	-.7905493E+02	-.1500275E+03	-.2000902E+03
90	-.0000000E+00	-.4043082E+01	-.9977925E+01	-.9977925E+01	-.9977925E+01	-.1402057E+02	-.9977925E+01	-.9977925E+01	-.9977925E+01
91	-.2294960E+03	-.4971567E+03	-.6708124E+03	-.8923814E+03	-.9972310E+03	-.1100246E+04	-.1209908E+04	-.1282105E+04	-.1357404E+04
92	-.3996403E+03	-.7875078E+03	-.1147597E+04	-.1521655E+04	-.1699566E+04	-.1869708E+04	-.2059761E+04	-.2172685E+04	-.2272465E+04
93	-.2097122E+03	-.4217235E+03	-.6215110E+03	-.8510101E+03	-.9299240E+03	-.1029902E+04	-.1141602E+04	-.1202929E+04	-.1277126E+04
94	-.2037770E+03	-.4097944E+03	-.5955106E+03	-.7935008E+03	-.8863198E+03	-.9782827E+03	-.1082171E+04	-.1137565E+04	-.1200869E+04

2

ble B.3. Pressure-strain data from V-4 – computer output

	Strain (μin./in.) at pressure (psi)								
	19[illegible]0	21960	22960	23970	24[illegible]	25240	2[illegible]	[illegible]	[illegible]
04	-.15[illegible]E-04	-.1535271E-04	-.1927679E-04	-.2055434E-04	-.2207014E-04	-.2343717E-04	-.24[illegible]E-04	[illegible]	[illegible]
03	-.9411111E-03	-.1034244E-04	-.11[illegible]29E-04	-.1131320E-04	-.1175306E-04	-.1206504E-04	-.124[illegible]E-04	[illegible]	[illegible]
03	-.9551745E-03	-.1034151E-04	-.1085699E-04	-.1139161E-04	-.1130755E-04	-.1200577E-04	-.122[illegible]E-04	[illegible]	[illegible]
03	-.1040115E-04	-.1151358E-04	-.1265530E-04	-.1271908E-04	-.1323417E-04	-.1361059E-04	-.14001[illegible]E-04	[illegible]	[illegible]
03	-.9867020E-03	-.1069721E-04	-.1141231E-04	-.1200665E-04	-.1246231E-04	-.1277929E-04	-.151[illegible]E-04	[illegible]	[illegible]
03	-.7132620E-03	-.7905262E-03	-.8014398E-03	-.8737599E-03	-.9099943E-03	-.9311369E-03	-.962[illegible]E-03	[illegible]	[illegible]
03	-.7211541E-03	-.7984375E-03	-.8209778E-03	-.8697992E-03	-.8954940E-03	-.9034136E-03	-.91[illegible]E-03	[illegible]	[illegible]
03	-.3139965E-03	-.3407910E-03	-.3437155E-03	-.3506966E-03	-.3526775E-03	-.3447532E-03	-.3[illegible]E-03	[illegible]	[illegible]
03	-.3961615E-03	-.4357349E-03	-.4516334E-03	-.4635202E-03	-.4694636E-03	-.4655013E-03	-.4[illegible]E-03	[illegible]	[illegible]
03	-.1050236E-04	-.1131326E-04	-.1130855E-04	-.1246215E-04	-.1305060E-04	-.1351232E-04	-.14[illegible]E-04	[illegible]	[illegible]
03	-.9727050E-03	-.1057394E-04	-.1093554E-04	-.1135153E-04	-.1174731E-04	-.1212422E-04	-.12[illegible]E-04	[illegible]	[illegible]
04	-.2125396E-04	-.2258632E-04	-.2343820E-04	-.2442877E-04	-.2547773E-04	-.2656340E-04	-.27[illegible]E-04	[illegible]	[illegible]
03	-.9350915E-03	-.1015250E-04	-.1051959E-04	-.1093564E-04	-.1127243E-04	-.1152998E-04	-.1142[illegible]E-04	[illegible]	[illegible]
04	-.1755345E-04	-.1955440E-04	-.2048553E-04	-.2181289E-04	-.2323951E-04	-.2454636E-04	-.25[illegible]E-04	[illegible]	[illegible]
03	-.7132145E-03	-.7759900E-03	-.8063259E-03	-.8340615E-03	-.8538731E-03	-.8637738E-03	-.8[illegible]E-03	[illegible]	[illegible]
03	-.5675971E-03	-.7291103E-03	-.7537330E-03	-.3063746E-03	-.3479734E-03	-.3779955E-03	-.[illegible]E-03	[illegible]	[illegible]
04	-.1145155E-04	-.1353154E-04	-.1460079E-04	-.1534967E-04	-.1582023E-04	-.1753343E-04	-.1[illegible]E-04	[illegible]	[illegible]
04	-.1271943E-04	-.1694215E-04	-.1470096E-04	-.1616700E-04	-.1922738E-04	-.2040665E-04	-.2[illegible]E-04	[illegible]	[illegible]
04	-.1406894E-04	-.1557270E-04	-.1636523E-04	-.1719731E-04	-.1751146E-04	-.1820769E-04	-.1[illegible]E-04	[illegible]	[illegible]
04	-.1302942E-04	-.1549363E-04	-.1558325E-04	-.1588157E-04	-.2361624E-04	-.3536441E-04	-.4[illegible]E-04	[illegible]	[illegible]
04	-.1789643E-04	-.1927750E-04	-.2023758E-04	-.2143694E-04	-.2240769E-04	-.2314072E-04	-.2431[illegible]E-04	[illegible]	[illegible]
03	-.1004433E-04	-.1136752E-04	-.1259771E-04	-.1400715E-04	-.1483926E-04	-.1547319E-04	-.1614[illegible]E-04	[illegible]	[illegible]
03	-.9557314E-03	-.1034747E-04	-.1084210E-04	-.1137530E-04	-.1181055E-04	-.1208755E-04	-.1235[illegible]E-04	[illegible]	[illegible]
03	-.3524117E-03	-.3500065E-03	-.3918777E-03	-.3998937E-03	-.4013721E-03	-.3979153E-03	-.39[illegible]E-03	[illegible]	[illegible]
03	-.1092275E-04	-.1212919E-04	-.1275233E-04	-.1373170E-04	-.1460220E-04	-.1537379E-04	-.1600[illegible]E-04	[illegible]	[illegible]
03	-.1062241E-04	-.1200960E-04	-.1275215E-04	-.1373133E-04	-.1460134E-04	-.1539320E-04	-.1612511E-04	[illegible]	[illegible]
03	-.1028732E-04	-.1153467E-04	-.1214301E-04	-.1235926E-04	-.1347257E-04	-.1366826E-04	-.1432[illegible]E-04	[illegible]	[illegible]
03	-.1023672E-04	-.1153517E-04	-.1210914E-04	-.1282109E-04	-.1341462E-04	-.1379051E-04	-.1422[illegible]E-04	[illegible]	[illegible]
03	-.9517201E-03	-.1070441E-04	-.1127319E-04	-.1191106E-04	-.1235591E-04	-.1255375E-04	-.12521[illegible]E-04	[illegible]	[illegible]
03	-.64[illegible]E-03	-.69[illegible]92E-03	-.[illegible]7303E-03	-.7536930E-03	-.3161750E-03	-.9882973E-03	-.[illegible]22[illegible]E-03	[illegible]	[illegible]
03	-.10[illegible]E-04	-.1165417E-04	-.1220836E-04	-.1252163E-04	-.1337564E-04	-.1377132E-04	-.1416[illegible]E-04	[illegible]	[illegible]
04	-.1577[illegible]2E-04	-.1505711E-04	-.1565067E-04	-.1625342E-04	-.1579750E-04	-.1709436E-04	-.17[illegible]E-04	[illegible]	[illegible]
04	-.19191[illegible]E-04	-.2111149E-04	-.2200157E-04	-.2302970E-04	-.2405369E-04	-.2645236E-04	-.2[illegible]E-04	[illegible]	[illegible]
04	-.1772[illegible]E-04	-.1799495E-04	-.19[illegible]E-04	-.2059725E-04	-.2136363E-04	-.2138322E-04	-.22[illegible]E-04	[illegible]	[illegible]
03	-.27[illegible]1E-03	-.3126457E-03	-.3413452E-03	-.3779502E-03	-.4056431E-03	-.4333469E-03	-.4[illegible]E-03	[illegible]	[illegible]
04	-.200[illegible]E-04	-.2200127E-04	-.2301096E-04	-.2425647E-04	-.2717452E-04	-.2989495E-04	-.32[illegible]E-04	[illegible]	[illegible]
03	-.961[illegible]E-03	-.1070451E-04	-.1127429E-04	-.1179150E-04	-.1236632E-04	-.1256416E-04	-.1277[illegible]E-04	[illegible]	[illegible]
04	-.1[illegible]E-04	-.2212074E-04	-.2511011E-04	-.2959964E-04	-.3369696E-04	-.3723536E-04	-.4[illegible]E-04	[illegible]	[illegible]
03	-.3612292E-03	-.3999939E-03	-.4173207E-03	-.4353606E-03	-.4392659E-03	-.4353090E-03	-.4[illegible]01E-03	[illegible]	[illegible]
03	-.10[illegible]E-04	-.1167337E-04	-.12[illegible]51E-04	-.1309710E-04	-.13[illegible]E-04	-.1425415E-04	-.14[illegible]E-04	[illegible]	[illegible]
03	-.4[illegible]E-03	-.4[illegible]E-03	-.4[illegible]10E-03	-.4405526E-03	-.4729179E-03	-.4491774E-03	-.4[illegible]E-03	[illegible]	[illegible]
03	-.2771232E-03	-.2990321E-03	-.3126412E-03	-.3354542E-03	-.3572383E-03	-.3519[illegible]E-03	-.4015[illegible]E-03	[illegible]	[illegible]
03	-.10[illegible]E-04	-.1179164E-04	-.1246545E-04	-.1325670E-04	-.1394910E-04	-.1450510E-04	-.15[illegible]E-04	[illegible]	[illegible]
04	-.1900[illegible]E-04	-.2447500E-04	-.2[illegible]2034E-04	-.2525471E-04	-.3011205E-04	-.3250851E-04	-.3[illegible]E-04	[illegible]	[illegible]
03	-.1090111E-04	-.1171130E-04	-.1222739E-04	-.1279060E-04	-.13[illegible]92E-04	-.1416550E-04	-.152[illegible]E-04	[illegible]	[illegible]
03	-.1077271E-04	-.1179120E-04	-.12[illegible]E-04	-.1337444E-04	-.1412624E-04	-.1475935E-04	-.1539400E-04	[illegible]	[illegible]
04	-.2059750E-04	-.2239222E-04	-.2355113E-04	-.2530623E-04	-.2643397E-04	-.2729465E-04	-.27[illegible]10E-04	[illegible]	[illegible]
02	-.[illegible]9E-02	+.7279651E-02	-.1[illegible]72E-03	+.3025956E-03	+.4271[illegible]E-03	+.6150955E-03	+.3035576E-03	[illegible]	[illegible]
04	-.2071412E-04	-.2343653E-04	-.24[illegible]13E-04	-.2528496E-04	-.25[illegible]E-04	-.2670942E-04	-.2756279E-04	[illegible]	[illegible]
04	-.25[illegible]E-04	+.[illegible]224E-02	+.[illegible]70E-03	+.1153417E-04	-.44[illegible]50E-04	-.4357193E-04	+.4713179E-04	[illegible]	[illegible]
03	-.322[illegible]E-03	-.3305446E-03	-.[illegible]3500E-03	-.3296759E-03	-.3122466E-03	-.2772550E-03	-.2495116E-03	[illegible]	[illegible]
04	-.1944413E-04	-.2201136E-04	-.2342462E-04	-.2431104E-04	-.2505744E-04	-.2740277E-04	-.2906658E-04	[illegible]	[illegible]
04	-.2043669E-04	-.2225509E-04	-.2296792E-04	-.2340660E-04	-.2437497E-04	-.2516753E-04	-.2610069E-04	[illegible]	[illegible]
04	-.1551566E-04	-.1734155E-04	-.1742966E-04	-.1946042E-04	-.2053202E-04	-.2104541E-04	-.2159612E-04	[illegible]	[illegible]
02	-.2377913E-02	+.2575270E-02	-.3170571E-02	-.2774456E-02	-.2774245E-02	-.2972403E-02	-.2774666E-02	[illegible]	[illegible]
04	-.1051449E-04	-.1125636E-04	-.1257722E-04	-.1264359E-04	-.1499629E-04	-.1677776E-04	-.1[illegible]E-04	[illegible]	[illegible]
04	-.2555266E-04	-.3250075E-04	-.3465383E-04	-.3902074E-04	-.4292023E-04	-.4831226E-04	-.56[illegible]E-04	[illegible]	[illegible]
04	-.1466446E-04	-.1674542E-04	-.1827103E-04	-.2066969E-04	-.2326474E-04	-.2619755E-04	-.3129[illegible]	[illegible]	[illegible]
04	-.1275217E-04	-.1454790E-04	-.1547652E-04	-.1712255E-04	-.1544545E-04	-.2015565E-04	-.255[illegible]57E-04	[illegible]	[illegible]
04	-.5517270E-04	-.7043255E-04	-.7256208E-04	-.7574106E-04	-.7274253E-04	-.6792808E-04	-.6[illegible]E-04	[illegible]	[illegible]
03	-.1082004E-04	-.1194998E-04	-.1256597E-04	-.1341647E-04	-.1413881E-04	-.1482293E-04	-.15[illegible]1E-04	[illegible]	[illegible]
03	-.1075095E-04	-.1179052E-04	-.1243499E-04	-.1319843E-04	-.1351258E-04	-.1426245E-04	-.14[illegible]E-04	[illegible]	[illegible]
03	-.1040421E-04	-.1149417E-04	-.1204396E-04	-.1277504E-04	-.1325775E-04	-.1365408E-04	-.14[illegible]E-04	[illegible]	[illegible]
03	-.1056412E-04	-.1169417E-04	-.1217729E-04	-.1305975E-04	-.1379261E-04	-.1454727E-04	-.14[illegible]E-04	[illegible]	[illegible]
03	-.5012952E-03	-.5506974E-03	-.6023580E-03	-.6716574E-03	-.5410724E-03	-.6203376E-03	-.6[illegible]E-03	[illegible]	[illegible]
03	-.1028[illegible]E-04	-.12[illegible]0750E-04	-.1329671E-04	-.1434790E-04	-.14[illegible]202E-04	-.1551614E-04	-.1625165E-04	[illegible]	[illegible]
04	-.6465127E-04	-.6309325E-04	-.6895159E-04	-.6938120E-04	-.6621676E-04	-.6752465E-04	-.6[illegible]E-04	[illegible]	[illegible]
03	-.9989071E-03	-.1064019E-04	-.1129536E-04	-.1191034E-04	-.1262559E-04	-.1290159E-04	-.131[illegible]E-04	[illegible]	[illegible]
03	-.7471564E-03	-.8204461E-03	-.8521928E-03	-.8698075E-03	-.9215469E-03	-.9415661E-03	-.9651[illegible]E-03	[illegible]	[illegible]
03	-.1029616E-04	-.1127997E-04	-.1199962E-04	-.1290215E-04	-.1355550E-04	-.1405052E-04	-.1450622E-04	[illegible]	[illegible]
04	-.1650758E-04	-.1846904E-04	-.1940776E-04	-.2076278E-04	-.2229394E-04	-.2376035E-04	-.259[illegible]E-04	[illegible]	[illegible]
01	+.1689547E-05	-.5574475E-05	+.6364177E-05	+.6566790E-05	+.2550565E-05	-.3549920E-05	+.4014779E-0[illegible]	[illegible]	[illegible]
03	-.1988549E-04	-.1194998E-04	-.1266996E-04	-.1365447E-04	-.1452669E-04	-.1524067E-04	-.15[illegible]E-04	[illegible]	[illegible]
04	-.2731951E-04	-.2922004E-04	-.3084224E-04	-.3204900E-04	-.3321475E-04	-.3216635E-04	-.3[illegible]E-04	[illegible]	[illegible]
02	-.3575077E-02	+.7905495E-02	+.1502755E-03	+.2669929E-03	+.3954404E-03	+.5576904E-03	+.64[illegible]E-03	[illegible]	[illegible]
01	+.1402057E-02	+.9977923E-01	+.9977923E-01	+.9977923E-01	+.1402057E-02	+.1402057E-02	+.3956[illegible]E-01	[illegible]	[illegible]
03	-.1100204E-04	-.1209908E-04	-.1282105E-04	-.1379042E-04	-.1466166E-04	-.1539558E-04	-.16[illegible]E-04	[illegible]	[illegible]
04	-.1865706E-04	-.2039758E-04	-.2124834E-04	-.2229683E-04	-.2322666E-04	-.2410298E-04	-.2552250E-04	[illegible]	[illegible]
03	-.1023902E-04	-.1141602E-04	-.1202929E-04	-.1276125E-04	-.1339474E-04	-.1394972E-04	-.1450509E-04	[illegible]	[illegible]
03	-.9792877E-03	-.1082171E-04	-.1157655E-04	-.1200959E-04	-.1250292E-04	-.1279965E-04	-.1315647E-04	[illegible]	[illegible]

BLANK PAGE

Table B.4. Pressure-strain data from V-4 test (manual readout from BLH indicator)

Pressure (psi)	Strain (μin./in.) at gage No. —		
	D-1	D-2	D-3
0	0000	0000	0000
4,000	00220	00220	00220
[illegible],000	00450	00450	00440
12,000	00640	00660	00650
16,000	00860	00880	00870
18,000	00950	00970	00960
20,000	01050	01080	01070
22,000	01140	01190	01180
23,000	01170	01260	01240
24,000	01220	01360	01320
25,000	01280	01440	01400
25,500	01340	01520	01470
26,000	01420	01590	01520
26,500			01630

Table B.5. Pressure-strain data from V-6 test - computer output

Channel No.	Strain (μin./in.) at pressure (psi) –								
	4100	8070	12080	16060	20000	21030	21520	22040	22230
91	−.2232282E+03	−.4406834E+03	−.6504965E+03	−.8583407E+03	−.1069956E+04	−.1127771E+04	−.1154629E+04	−.1185419E+04	−.1197053E+04
92	−.2213039E+03	−.4387590E+03	−.6465368E+03	−.8524585E+03	−.1062259E+04	−.1118040E+04	−.1145007E+04	−.1175797E+04	−.1187322E+04
90	−.2213039E+03	−.4368346E+03	−.6446972E+03	−.8506189E+03	−.1060334E+04	−.1116200E+04	−.1143082E+04	−.1173872E+04	−.1183558E+04
94	−.2155307E+03	−.4291371E+03	−.6312121E+03	−.8332848E+03	−.1037241E+04	−.1093092E+04	−.1118066E+04	−.1148856E+04	−.1160450E+04
88	−.2232282E+03	−.4445322E+03	−.6542973E+03	−.8640680E+03	−.1075729E+04	−.1133498E+04	−.1160402E+04	−.1191192E+04	−.1202780E+04
41	−.5484688E+03	−.1031420E+04	−.1472939E+04	−.1912479E+04	−.2506451E+04	−.2720281E+04	−.2828176E+04	−.2934111E+04	−.2985589E+04
40	−.4732275E+03	−.9089111E+03	−.1314792E+04	−.1726633E+04	−.2261188E+04	−.2447299E+04	−.2536395E+04	−.2625491E+04	−.2665089E+04
97	−.2116820E+03	−.4214395E+03	−.6215572E+03	−.8255544E+03	−.1027619E+04	−.1083437E+04	−.1110368E+04	−.1143082E+04	−.1154644E+04
85	−.2155307E+03	−.4272127E+03	−.6311982E+03	−.8351954E+03	−.1041090E+04	−.1095003E+04	−.1119990E+04	−.1150780E+04	−.1160436E+04
42	−.1980031E+01	−.6048482E+01	−.4068574E+01	−.6048482E+01	−.6048482E+01	−.6048482E+01	−.4068574E+01	−.4068574E+01	−.6048482E+01
39	−.3792089E+03	−.7521006E+03	−.1103875E+04	−.1457273E+04	−.1822585E+04	−.1915898E+04	−.1959577E+04	−.2007226E+04	−.2038992E+04
86	−.2251526E+03	−.4464565E+03	−.6581144E+03	−.8755832E+03	−.1049200E+04	−.1146938E+04	−.1175797E+04	−.1208512E+04	−.1220069E+04
96	−.2213039E+03	−.4387590E+03	−.6465331E+03	−.8601529E+03	−.1073805E+04	−.1133632E+04	−.1160402E+04	−.1195041E+04	−.1208487E+04
87	−.2251526E+03	−.4483809E+03	−.6581228E+03	−.8755916E+03	−.1093049E+04	−.1152720E+04	−.1181570E+04	−.1214284E+04	−.1227775E+04
105	−.2169669E+03	−.4300937E+03	−.6355403E+03	−.8371467E+03	−.1046431E+04	−.1104035E+04	−.1130916E+04	−.1163557E+04	−.1176998E+04
84	−.2116820E+03	−.4195151E+03	−.6157471E+03	−.8120463E+03	−.1012225E+04	−.1066080E+04	−.1093049E+04	−.1125763E+04	−.1139212E+04
99	−.2290014E+03	−.4599272E+03	−.6793453E+03	−.8968140E+03	−.1121914E+04	−.1185489E+04	−.1216209E+04	−.1254697E+04	−.1270167E+04
82	−.2251526E+03	−.4445322E+03	−.6561956E+03	−.8640418E+03	−.1073805E+04	−.1129623E+04	−.1156429E+04	−.1185419E+04	−.1195056E+04
83	−.2309257E+03	−.4618515E+03	−.6811650E+03	−.8967093E+03	−.1116141E+04	−.1175762E+04	−.1202738E+04	−.1237377E+04	−.1248893E+04
48	−.5349596E+03	−.1160660E+04	−.1962103E+04	−.2740353E+04	−.3520534E+04	−.3746477E+04	−.3831447E+04	−.3974352E+04	−.4034218E+04
61	−.3437647E+03	−.6836673E+03	−.1023548E+04	−.1371153E+04	−.1761244E+04	−.1880974E+04	−.1942771E+04	−.2027741E+04	−.2074089E+04
33	−.1296259E+03	−.1296177E+06	−.1296299E+06	−.1296299E+06	−.1296299E+06	−.1296299E+06	−.1296299E+06	−.1296299E+06	−.1296299E+06
62	−.3263833E+03	−.6430853E+03	−.9501367E+03	−.1270706E+04	−.1620243E+04	−.1718730E+04	−.1772803E+04	−.1836530E+04	−.1869360E+04
63	−.2742392E+03	−.5444577E+03	−.8148175E+03	−.1077652E+04	−.1351674E+04	−.1421195E+04	−.1459818E+04	−.1502304E+04	−.1517753E+04
65	−.2549266E+03	−.5099427E+03	−.7513353E+03	−.9927279E+03	−.1237983E+04	−.1303641E+04	−.1332609E+04	−.1371231E+04	−.1386681E+04
100	+.2515546E+02	+.2268924E+02	+.4646378E+02	+.6540824E+02	+.8977047E+02	+.9451147E+02	+.9815562E+02	+.1023948E+03	+.1038837E+03
101	−.4804779E+03	−.9421545E+03	−.1380385E+04	−.1812842E+04	−.2254068E+04	−.2370649E+04	−.2425369E+04	−.2475506E+04	−.2479286E+04
102	−.4825670E+03	−.9421545E+03	−.1363753E+04	−.1783675E+04	−.2214376E+04	−.2328947E+04	−.2381588E+04	−.2439992E+04	−.2452208E+04
103	−.4888340E+03	−.9379765E+03	−.1349222E+04	−.1756609E+04	−.3089682E+04	−.2285168E+04	−.2337629E+04	−.2391944E+04	−.2408428E+04
8	−.3772234E+03	−.7345506E+03	−.1084021E+04	−.1429478E+04	−.1731257E+04	−.1806702E+04	−.1846410E+04	−.1890088E+04	−.1898030E+04
9	−.3593550E+03	−.6968430E+03	−.1014533E+04	−.1330209E+04	−.1620075E+04	−.1689564E+04	−.1725301E+04	−.1763023E+04	−.1772950E+04
10	−.3295742E+03	−.6274428E+03	−.9291610E+03	−.1215056E+04	−.1469186E+04	−.1512864E+04	−.1528748E+04	−.1544631E+04	−.1536689E+04
11	−.3355304E+03	−.6571900E+03	−.9589418E+03	−.1254764E+04	−.1528748E+04	−.1570441E+04	−.1592280E+04	−.1608163E+04	−.1600221E+04
12	−.3494281E+03	−.6829795E+03	−.9926934E+03	−.1300428E+04	−.1588310E+04	−.1639930E+04	−.1665740E+04	−.1685593E+04	−.1679737E+04
13	−.3454573E+03	−.6789403E+03	−.1004605E+04	−.1318297E+04	−.1616105E+04	−.1671695E+04	−.1707432E+04	−.1727286E+04	−.1719345E+04
14	−.3434719E+03	−.6751111E+03	−.9827665E+03	−.1290501E+04	−.1574411E+04	−.1631988E+04	−.1669710E+04	−.1691550E+04	−.1689564E+04
15	−.4268581E+03	−.8377920E+03	−.1236896E+04	−.1641915E+04	−.2052890E+04	−.2164071E+04	−.2217677E+04	−.2283195E+04	−.2310990E+04
16	−.4209020E+03	−.8240607E+03	−.1203144E+04	−.1582353E+04	−.1969503E+04	−.2072744E+04	−.2120393E+04	−.2166057E+04	−.2170028E+04
17	−.6035576E+03	−.1137591E+04	−.1522791E+04	−.1903986E+04	−.2295107E+04	−.2402318E+04	−.2449967E+04	−.2491660E+04	−.2497617E+04
18	−.5956160E+02	−.1173657E+03	−.1707432E+03	−.2243687E+03	−.2779541E+03	−.2898665E+03	−.2958226E+03	−.3037642E+03	−.3077349E+03
19	−.4129604E+03	−.8299488E+03	−.1234911E+04	−.1612134E+04	−.1997299E+04	−.2100539E+04	−.2152159E+04	−.2195838E+04	−.2195838E+04
20	−.4189166E+03	−.8239543E+03	−.1203130E+04	−.1586324E+04	−.1973474E+04	−.2076714E+04	−.2124364E+04	−.2168042E+04	−.2172013E+04
21	−.4050189E+03	−.7982178E+03	−.1171378E+04	−.1536689E+04	−.1917883E+04	−.2017153E+04	−.2068773E+04	−.2116422E+04	−.2116422E+04
22	−.5479667E+03	−.1026331E+04	−.1467201E+04	−.1911928E+04	−.2352683E+04	−.2487689E+04	−.2565119E+04	−.2642569E+04	−.2676301E+04
23	−.4089897E+03	−.8101326E+03	−.1191232E+04	−.1564484E+04	−.1949650E+04	−.2052890E+04	−.2104510E+04	−.2152159E+04	−.2156130E+04	
24	−.4268581E+03	−.8591738E+03	−.1254764E+04	−.1639930E+04	−.2029065E+04	−.2132305E+04	−.2179955E+04	−.2229588E+04	−.2238516E+04
25	−.4248728E+03	−.8378222E+03	−.1230940E+04	−.1616105E+04	−.2009211E+04	−.2112451E+04	−.2164071E+04	−.2215691E+04	−.2227604E+04
26	−.1489040E+03	−.3892955E+03	−.4943613E+03	−.5459814E+03	−.6015722E+03	−.6156699E+03	−.6194407E+03	−.6253969E+03	−.6273822E+03
27	−.4169312E+03	−.8214120E+03	−.1203144E+04	−.1584339E+04	−.1965533E+04	−.2062817E+04	−.2108480E+04	−.2156130E+04	−.2160100E+04
28	−.4328143E+03	−.8318631E+03	−.1215056E+04	−.1610149E+04	−.2003255E+04	−.2114437E+04	−.2173998E+04	−.2235545E+04	−.2259370E+04
29	−.4367851E+03	−.8477301E+03	+.6467993E+05	+.6467794E+05	+.6467794E+05	+.6467794E+05	+.6467993E+05	+.6467993E+05	+.6467794E+05
30	−.5439960E+03	−.1103877E+04	−.1630002E+04	−.2173998E+04	−.2948799E+04	−.3238165E+04	−.3389055E+04	−.3581637E+04	−.3706717E+04
31	−.7226808E+03	−.1399731E+04	−.2025094E+04	−.2684243E+04	−.3581637E+04	−.3893343E+04	−.4081955E+04	−.4286450E+04	−.4425427E+04
32	−.2422172E+03	−.3931676E+03	−.4486974E+03	−.4328143E+03	−.3017787E+03	−.2283195E+03	−.1985387E+03	−.1469186E+03	−.1052255E+03
34	−.9789757E+03	−.2162030E+04	−.3317581E+04	−.4431383E+04	−.5668279E+04	−.6138819E+04	−.6434638E+04	−.6778110E+04	−.6954810E+04
35	−.3097203E+03	−.7266855E+03	−.1054240E+04	−.1278589E+04	−.1270647E+04	−.1234911E+04	−.1217042E+04	−.1201159E+04	−.1167607E+04
36	−.6035576E+03	−.1266539E+04	−.1937738E+04	−.2565119E+04	−.3172648E+04	−.3362345E+04	−.3478397E+04	−.3625316E+04	−.3694790E+04
37	−.5936306E+03	−.1185219E+04	−.1741184E+04	−.2297092E+04	−.2924475E+04	−.3156765E+04	−.3291771E+04	−.3454573E+04	−.3547886E+04
38	−.4983320E+03	−.9409864E+03	−.1350065E+04	−.1753096E+04	−.2136276E+04	−.2253414E+04	−.2312976E+04	−.2376522E+04	−.2406303E+04
43	−.5108481E+03	−.9741829E+03	−.1401843E+04	−.1793864E+04	−.2219545E+04	−.2379917E+04	−.2470993E+04	−.2575927E+04	−.2647204E+04
44	−.2645829E+03	−.5291424E+03	−.7801909E+03	−.1035102E+04	−.1297736E+04	−.1369189E+04	−.1405881E+04	−.1450297E+04	−.1471519E+04
45	−.2781018E+03	−.5619888E+03	−.8362108E+03	−.1118157E+04	−.1417484E+04	−.1500523E+04	−.1543008E+04	−.1593218E+04	−.1620254E+04
46	−.2974144E+03	−.6141734E+03	−.9495033E+03	−.1340282E+04	−.1722648E+04	−.1823067E+04	−.1873277E+04	−.1935074E+04	−.1954385E+04
49	−.4364652E+03	−.9849480E+03	−.1452284E+04	−.1884860E+04	−.2255639E+04	−.2348334E+04	−.2394681E+04	−.2460340E+04	−.2475789E+04
50	−.8690680E+02	−.1602946E+03	−.2845762E+03	−.4325855E+03	−.7106698E+03	−.7801909E+03	−.8091580E+03	−.8361940E+03	−.8497120E+03
51	−.3032081E+03	−.6236970E+03	−.9384730E+03	−.1274492E+04	−.1624028E+04	−.1712861E+04	−.1755346E+04	−.1805555E+04	−.1830660E+04
52	−.2781018E+03	−.5561953E+03	−.8304173E+03	−.1112363E+04	−.1402035E+04	−.1475418E+04	−.1514041E+04	−.1556526E+04	−.1571975E+04
53	−.2723079E+03	−.5407696E+03	−.7937491E+03	−.1058315E+04	−.1320950E+04	−.1388560E+04	−.1417908E+04	−.1454199E+04	−.1469648E+04

101	-.4804779E+03	-.9421543E+03	-.1380385E+04	-.1812842E+04	-.2254068E+04	-.2370649E+04	-.2429369E+04	-.2479506E+04	-.2479386E+04
102	-.4825670E+03	-.9421545E+03	-.1363753E+04	-.1783675E+04	-.2214376E+04	-.2328947E+04	-.2383588E+04	-.2439992E+04	-.2452208E+04
103	-.4888340E+03	-.9379765E+03	-.1349222E+04	-.1756609E+04	-.3089682E+04	-.2285168E+04	-.2337629E+04	-.2391944E+04	-.2408428E+04
8	-.3772234E+03	-.7345506E+03	-.1084021E+04	-.1429478E+04	-.1731257E+04	-.1806702E+04	-.1846410E+04	-.1890088E+04	-.1898030E+04
9	-.3593550E+03	-.6968650E+03	-.1014533E+04	-.1330209E+04	-.1620075E+04	-.1689564E+04	-.1725301E+04	-.1763023E+04	-.1772950E+04
10	-.3295742E+03	-.6274428E+03	-.9[illegible]E+03	-.1215056E+04	-.1469186E+04	-.1512864E+04	-.1528748E+04	-.1544631E+04	-.1536689E+04
11	-.3355304E+03	-.6571900E+03	-.95[illegible]E+03	-.1254764E+04	-.1528748E+04	-.1570461E+04	-.1592280E+04	-.1608163E+04	-.1600221E+04
12	-.3494281E+03	-.6829795E+03	-.9926934E+03	-.1300428E+04	-.1588310E+04	-.1639930E+04	-.1665740E+04	-.1685593E+04	-.1679737E+04
13	-.3454573E+03	-.6789403E+03	-.1004605E+04	-.1318297E+04	-.1616105E+04	-.1671695E+04	-.1707432E+04	-.1727286E+04	-.1719345E+04
14	-.3434719E+03	-.6751111E+03	-.9827665E+03	-.1290501E+04	-.1574611E+04	-.1631988E+04	-.1669710E+04	-.1691550E+04	-.1689564E+04
15	-.4268581E+03	-.8377920E+03	-.1236896E+04	-.1641915E+04	-.2052890E+04	-.2164071E+04	-.2217677E+04	-.2283195E+04	-.2310990E+04
16	-.4209020E+03	-.8240607E+03	-.1203144E+04	-.1582353E+04	-.1969503E+04	-.2072744E+04	-.2120393E+04	-.2166057E+04	-.2170078E+04
17	-.6035576E+03	-.1137591E+04	-.1522791E+04	-.1903986E+04	-.2295107E+04	-.2402318E+04	-.2449967E+04	-.2491660E+04	-.2497617E+04
18	-.5956160E+02	-.1173657E+03	-.1707432E+03	-.2243487E+03	-.2779541E+03	-.2898665E+03	-.2958226E+03	-.3037642E+03	-.3077349E+03
19	-.4129604E+03	-.8299488E+03	-.1234911E+04	-.1612134E+04	-.1997299E+04	-.2120539E+04	-.2152159E+04	-.2195838E+04	-.2195838E+04
20	-.4189166E+03	-.8239543E+03	-.1205130E+04	-.1586324E+04	-.1973474E+04	-.2076714E+04	-.2124364E+04	-.2168042E+04	-.2172013E+04
21	-.4050189E+03	-.7982178E+03	-.1171378E+04	-.1536689E+04	-.1917883E+04	-.2017153E+04	-.2068773E+04	-.2116422E+04	-.2116422E+04
22	-.5479667E+03	-.1026331E+04	-.1467201E+04	-.1911928E+04	-.2352683E+04	-.2487689E+04	-.2565119E+04	-.2642549E+04	-.2676301E+04
23	-.4088997E+03	-.8101326E+03	-.1191232E+04	-.1564484E+04	-.1949650E+04	-.2052890E+04	-.2104510E+04	-.2152159E+04	-.2156130E+04
24	-.4268581E+03	-.8591738E+03	-.1254764E+04	-.1639930E+04	-.2029065E+04	-.2132305E+04	-.2179955E+04	-.2229589E+04	-.2239516E+04
25	-.4248728E+03	-.8378222E+03	-.1230940E+04	-.1616105E+04	-.2009211E+04	-.2112451E+04	-.2160071E+04	-.2215691E+04	-.2227604E+04
26	-.1489040E+03	-.3892955E+03	-.4943613E+03	-.5459814E+03	-.6015722E+03	-.6154699E+03	-.6194407E+03	-.6253969E+03	-.6273822E+03
27	-.4169312E+03	-.8214120E+03	-.1203144E+04	-.1584339E+04	-.1965533E+04	-.2062817E+04	-.2108460E+04	-.2156130E+04	-.2160100E+04
28	-.4328143E+03	-.8518631E+03	-.1215056E+04	-.1610149E+04	-.2003255E+04	-.2114437E+04	-.2173998E+04	-.2235545E+04	-.2259370E+04
29	-.4367851E+03	-.8477301E+03	+.6467993E+05	+.6467994E+05	+.6467994E+05	+.6467994E+05	+.6467993E+05	+.6467993E+05	+.6467994E+05
30	-.5419960E+03	-.1103877E+04	-.1630002E+04	-.2173998E+04	-.2948299E+04	-.3238165E+04	-.3389055E+04	-.3581637E+04	-.3706717E+04
31	-.7226808E+03	-.1399731E+04	-.2025094E+04	-.2684243E+04	-.3581637E+04	-.3893543E+04	-.4081955E+04	-.4286450E+04	-.4425437E+04
32	-.2422172E+03	-.3931676E+03	-.4486974E+03	-.4328143E+03	-.3017787E+03	-.2283195E+03	-.1985387E+03	-.1469186E+03	-.1052255E+03
34	-.9789757E+03	-.2162030E+04	-.3317581E+04	-.4431383E+04	-.5668279E+04	-.6138815E+04	-.6434638E+04	-.6778110E+04	-.6954810E+04
35	-.3097203E+03	-.7246855E+03	-.1054240E+04	-.1278589E+04	-.1270647E+04	-.1234911E+04	-.1217042E+04	-.1201159E+04	-.1167407E+04
36	-.6035576E+03	-.1266539E+04	-.1937738E+04	-.2565119E+04	-.3172648E+04	-.3363245E+04	-.3478397E+04	-.3625316E+04	-.3696790E+04
37	-.5936306E+03	-.1185219E+04	-.1741184E+04	-.2297092E+04	-.2924475E+04	-.3156765E+04	-.3291771E+04	-.3454573E+04	-.3547886E+04
38	-.4983320E+03	-.9409848E+03	-.1350063E+04	-.1753096E+04	-.2136276E+04	-.2253414E+04	-.2312976E+04	-.2374522E+04	-.2404503E+04
43	-.5108481E+03	-.9741829E+03	-.1401843E+04	-.1793864E+04	-.2219545E+04	-.2379917E+04	-.2470593E+04	-.2575927E+04	-.2647204E+04
44	-.2645829E+03	-.5291429E+03	-.7801909E+03	-.1035102E+04	-.1297730E+04	-.1369189E+04	-.1405881E+04	-.1450297E+04	-.1471539E+04
45	-.2781018E+03	-.5619888E+03	-.8362108E+03	-.1118157E+04	-.1417484E+04	-.1500523E+04	-.1543008E+04	-.1593218E+04	-.1620254E+04
46	-.2974144E+03	-.6141734E+03	-.9695033E+03	-.1340282E+04	-.1722648E+04	-.1823067E+04	-.1873277E+04	-.1935074E+04	-.1954385E+04
49	-.4366652E+03	-.9849480E+03	-.1452284E+04	-.1884860E+04	-.2256639E+04	-.2348334E+04	-.2394681E+04	-.2460340E+04	-.2475789E+04
50	-.8690680E+02	-.1602946E+03	-.2645762E+03	-.4325855E+03	-.7106698E+03	-.7801909E+03	-.8091580E+03	-.8361940E+03	-.8497120E+03
51	-.3032081E+03	-.6236970E+03	-.9384730E+03	-.1274492E+04	-.1624028E+04	-.1712861E+04	-.1755346E+04	-.1805555E+04	-.1830660E+04
52	-.2781018E+03	-.5561953E+03	-.8304173E+03	-.1112363E+04	-.1402035E+04	-.1475419E+04	-.1514041E+04	-.1556576E+04	-.1571975E+04
53	-.2723079E+03	-.5407696E+03	-.7937491E+03	-.1058315E+04	-.1320950E+04	-.1388540E+04	-.1417508E+04	-.1454199E+04	-.1469648E+04
54	-.1892637E+03	-.3766176E+03	-.5542825E+03	-.7358098E+03	-.9057502E+03	-.9501664E+03	-.9714090E+03	-.9945827E+03	-.1004238E+04
55	-.2491328E+03	-.4905237E+03	-.7203295E+03	-.9597910E+03	-.1191528E+04	-.1251393E+04	-.1280360E+04	-.1313189E+04	-.1326708E+04
56	-.2472015E+03	-.4943804E+03	-.7299796E+03	-.9731034E+03	-.1214696E+04	-.1278424E+04	-.1307390E+04	-.1344082E+04	-.1357600E+04
57	-.2549266E+03	-.5060217E+03	-.7474144E+03	-.9907382E+03	-.1237924E+04	-.1301652E+04	-.1332550E+04	-.1371173E+04	-.1386622E+04
58	-.2510641E+03	-.5098106E+03	-.7569966E+03	-.1004182E+04	-.1255231E+04	-.1324752E+04	-.1359512E+04	-.1394273E+04	-.1411584E+04
59	-.7531923E+03	-.1507034E+03	-.2202244E+03	-.2974701E+03	-.3805091E+03	-.4036828E+03	-.4152697E+03	-.4307188E+03	-.4403745E+03
60	-.2896893E+03	-.5735362E+03	-.8477582E+03	-.1127774E+04	-.1413582E+04	-.1490828E+04	-.1529451E+04	-.1573867E+04	-.1595110E+04
64	-.6373165E+03	-.1294341E+03	-.1892995E+03	-.2588206E+03	-.3361351E+03	-.3570088E+03	-.3669645E+03	-.3804824E+03	-.3882070E+03
66	-.2472015E+03	-.4944060E+03	-.7372981E+03	-.9656044E+03	-.1205066E+04	-.1270725E+04	-.1301622E+04	-.1340246E+04	-.1351832E+04
68	-.2491328E+03	-.4963580E+03	-.7319572E+03	-.9714187E+03	-.1210880E+04	-.1272677E+04	-.1303575E+04	-.1340267E+04	-.1353784E+04
70	-.1776761E+03	-.3515154E+03	-.5214538E+03	-.6913962E+03	-.8458875E+03	-.8767858E+03	-.8922349E+03	-.8999595E+03	-.9038217E+03
71	-.1738136E+03	-.3418079E+03	-.5001614E+03	-.6681706E+03	-.8110751E+03	-.8342488E+03	-.8400422E+03	-.8496979E+03	-.8496979E+03
72	-.5580707E+02	-.1096897E+03	-.1597590E+03	-.2213431E+03	-.3232961E+03	-.3522092E+03	-.3675569E+03	-.3791031E+03	-.3868502E+03
73	-.1693456E+03	-.3348424E+03	-.4966637E+03	-.6504239E+03	-.7274163E+03	-.7389510E+03	-.7428113E+03	-.7505089E+03	-.7466499E+03
74	-.1635724E+03	-.3175230E+03	-.4618114E+03	-.5695835E+03	-.6138777E+03	-.6023000E+03	-.5946339E+03	-.5907852E+03	-.5830550E+03
75	-.1539505E+03	-.3040523E+03	-.4425837E+03	-.5311108E+03	-.5388268E+03	-.5389088E+03	-.5349781E+03	-.5349781E+03	-.5272618E+03
76	-.1654968E+03	-.3194473E+03	-.4368531E+03	-.5253802E+03	-.5965583E+03	-.6042848E+03	-.6042559E+03	-.6061802E+03	-.6062093E+03
77	-.1654968E+03	-.3232961E+03	-.4542503E+03	-.5735694E+03	-.6273484E+03	-.6428515E+03	-.6504410E+03	-.6542897E+03	-.6505495E+03
78	-.1828162E+03	-.3560106E+03	-.5234819E+03	-.7601957E+03	-.9371739E+03	-.9622684E+03	-.9602664E+03	-.9679639E+03	-.9680419E+03
79	-.3656325E+02	-.7120212E+02	-.1058244E+03	-.1808800E+03	-.2597915E+03	-.2713116E+03	-.2828841E+03	-.2848085E+03	-.2848010E+03
80	-.1847406E+03	-.3656325E+03	-.5426862E+03	-.7197404E+03	-.9968297E+03	-.1023812E+04	-.1035317E+04	-.1050712E+04	-.1054604E+04
81	-.1982113E+03	-.3848763E+03	-.5580707E+03	-.7716904E+03	-.9987541E+03	-.1041120E+04	-.1064183E+04	-.1081501E+04	-.1085384E+04
89	-.4810533E+02	-.9814347E+02	-.1423194E+03	-.1923565E+03	-.2405477E+03	-.2539405E+03	-.2578671E+03	-.2655646E+03	-.2693365E+03
93	-.6158021E+02	-.1250848E+03	-.1828289E+03	-.2463374E+03	-.3155986E+03	-.3348645E+03	-.3425399E+03	-.3540862E+03	-.3618075E+03
98	-.1751187E+03	-.3483130E+03	-.5118243E+03	-.6754069E+03	-.8351816E+03	-.8755552E+03	-.8948376E+03	-.9198544E+03	-.9275167E+03

BLANK PAGE

Table B.5 (continued)

Channel No.	Strain (uin./in.) at pressure (psi) –								
	22550	22510	23060	22990	23520	23500	24060	24040	24510
91	−.1221982E+04	−.1221982E+04	−.1254697E+04	−.1256712E+04	−.1289336E+04	−.1291260E+04	−.1329748E+04	−.1335521E+04	−.1368235E+04
92	−.1212360E+04	−.1212360E+04	−.1245075E+04	−.1248906E+04	−.1281638E+04	−.1283562E+04	−.1322050E+04	−.1327823E+04	−.1360538E+04
90	−.1208512E+04	−.1208512E+04	−.1241226E+04	−.1243217E+04	−.1275865E+04	−.1277789E+04	−.1314352E+04	−.1318202E+04	−.1350916E+04
94	−.1185419E+04	−.1185419E+04	−.1218134E+04	−.1220110E+04	−.1252772E+04	−.1256621E+04	−.1293184E+04	−.1298958E+04	−.1331672E+04
88	−.1227755E+04	−.1227755E+04	−.1260470E+04	−.1262460E+04	−.1295109E+04	−.1298958E+04	−.1337465E+04	−.1343218E+04	−.1375933E+04
41	−.3064785E+04	−.3094684E+04	−.3181599E+04	−.3259132E+04	−.3338012E+04	−.3379591E+04	−.3484526E+04	−.3530063E+04	−.3631039E+04
40	−.2726466E+04	−.2744285E+04	−.2819522E+04	−.2876986E+04	−.2950196E+04	−.2979894E+04	−.3078889E+04	−.3128387E+04	−.3231322E+04
97	−.1177721E+04	−.1177721E+04	−.1210436E+04	−.1212379E+04	−.1243150E+04	−.1246999E+04	−.1283562E+04	−.1289336E+04	−.1322050E+04
85	−.1185419E+04	−.1185419E+04	−.1216209E+04	−.1220096E+04	−.1250852E+04	−.1254697E+04	−.1291260E+04	−.1297033E+04	−.1329748E+04
42	−.6048682E+01	−.6048682E+01	−.6048682E+01	−.1980031E+01	−.6048682E+01	−.6048682E+01	−.6048682E+01	−.6048682E+01	−.6068574E+01
39	−.2098354E+04	+.3273803E+04	+.3819884E+04	+.3849144E+04	+.3917168E+04	+.4044232E+04	+.7266515E+04	+.4733162E+04	+.7763008E+04
86	−.1246999E+04	−.1246999E+04	−.1281638E+04	−.1285502E+04	−.1318202E+04	−.1323976E+04	−.1364386E+04	−.1372084E+04	−.1406723E+04
96	−.1233528E+04	−.1233453E+04	−.1268168E+04	−.1273921E+04	−.1306655E+04	−.1312428E+04	−.1350916E+04	−.1360538E+04	−.1395177E+04
87	−.1252772E+04	−.1254697E+04	−.1289336E+04	−.1295113E+04	−.1327823E+04	−.1333596E+04	−.1374008E+04	−.1383630E+04	−.1418269E+04
105	−.1201958E+04	−.1201958E+04	−.1236519E+04	−.1240383E+04	−.1273000E+04	−.1278761E+04	−.1317162E+04	−.1324842E+04	−.1359460E+04
84	−.1166175E+04	−.1168100E+04	−.1200814E+04	−.1204694E+04	−.1241226E+04	−.1246999E+04	−.1289336E+04	−.1298958E+04	−.1335521E+04
99	−.1300882E+04	−.1300882E+04	−.1337445E+04	−.1343298E+04	−.1379781E+04	−.1385555E+04	−.1429815E+04	−.1435589E+04	−.1472152E+04
82	−.1220058E+04	−.1220058E+04	−.1254697E+04	−.1258565E+04	−.1293184E+04	−.1297033E+04	−.1339370E+04	−.1347067E+04	−.1385555E+04
83	−.1277789E+04	−.1277789E+04	−.1314352E+04	−.1320099E+04	−.1356689E+04	−.1362462E+04	−.1404723E+04	−.1414420E+04	−.1450983E+04
48	−.4155879E+04	−.4182915E+04	−.4318095E+04	−.4389759E+04	−.4524727E+04	−.4625146E+04	−.4886539E+04	−.5009444E+04	−.5326151E+04
61	−.2151334E+04	−.2174508E+04	−.2255616E+04	−.2329102E+04	−.2402383E+04	−.2468041E+04	−.2618671E+04	−.2719089E+04	−.2877444E+04
33	−.1296299E+06	−.1296299E+06	−.1296299E+06	−.1296420E+06	−.1296299E+06	−.1296299E+06	−.1296299E+06	−.1296299E+06	−.1296299E+06
62	−.1921501E+04	−.1936950E+04	−.1996815E+04	−.2037481E+04	−.2095303E+04	−.2130064E+04	−.2278552E+04	−.2284555E+04	−.2390768E+04
63	−.1556376E+04	−.1556376E+04	−.1606585E+04	−.1622260E+04	−.1664519E+04	−.1676106E+04	−.1741765E+04	−.1768801E+04	−.1834460E+04
65	−.1417579E+04	−.1421441E+04	−.1461995E+04	−.1471621E+04	−.1514136E+04	−.1525723E+04	−.1577864E+04	−.1595244E+04	−.1649315E+04
100	+.1045407E+03	+.1170340E+03	+.1109800E+03	+.1112828E+03	+.1159124E+03	+.1159124E+03	+.1208449E+03	+.1223246E+03	+.1277503E+03
101	−.2500576E+04	−.2483862E+04	−.2527732E+04	−.2493910E+04	−.2544444E+04	−.2529820E+04	−.2577868E+04	−.2577868E+04	−.2659341E+04
102	−.2483862E+04	−.2473416E+04	−.2523553E+04	−.2496080E+04	−.2546513E+04	−.2531309E+04	−.2579957E+04	−.2571601E+04	−.2619649E+04
103	−.2444170E+04	−.3651632E+04	−.3676701E+04	−.3668195E+04	−.3674612E+04	−.3699868E+04	−.3705947E+04	−.3741461E+04	−.3779063E+04
8	−.1921854E+04	−.1921854E+04	−.1969503E+04	−.1973595E+04	−.2025094E+04	−.2029065E+04	−.2092598E+04	−.2112451E+04	−.2191867E+04
9	−.1800746E+04	−.1798760E+04	−.1846410E+04	−.1850479E+04	−.1902000E+04	−.1913912E+04	−.1983601E+04	−.2005240E+04	−.2074729E+04
10	−.1540660E+04	−.1520806E+04	−.1548601E+04	−.1520802E+04	−.1552572E+04	−.1544631E+04	−.1588310E+04	−.1588310E+04	−.1631988E+04
11	−.1602207E+04	−.1564339E+04	−.1612134E+04	−.1576428E+04	−.1610149E+04	−.1598246E+04	−.1635959E+04	−.1633973E+04	−.1671695E+04
12	−.1683608E+04	−.1665740E+04	−.1695520E+04	−.1659838E+04	−.1693535E+04	−.1675666E+04	−.1709418E+04	−.1701462E+04	−.1741184E+04
11	−.1727288E+04	−.1711403E+04	−.1739199E+04	−.1711530E+04	−.1743170E+04	−.1715374E+04	−.1735228E+04	−.1723316E+04	−.1747160E+04
14	−.1695520E+04	−.1681622E+04	−.1711403E+04	−.1681606E+04	−.1715374E+04	−.1693535E+04	−.1711403E+04	−.1687579E+04	−.1705447E+04
15	−.2362610E+04	−.2368566E+04	−.2440040E+04	−.2460037E+04	−.2529383E+04	−.2547251E+04	−.2636048E+04	−.2660418E+04	−.2741819E+04
16	−.2189881E+04	−.2179955E+04	−.2235545E+04	−.2215654E+04	−.2275253E+04	−.2277238E+04	−.2336654E+04	−.2338635E+04	−.2515485E+04
17	−.2513499E+04	−.2501587E+04	−.2549237E+04	−.2521563E+04	−.2581003E+04	−.2579017E+04	−.2630637E+04	−.2636594E+04	−.2731892E+04
18	−.3117057E+03	−.3117057E+03	−.3156765E+03	−.3134756E+03	−.3196473E+03	−.3176618E+03	−.3196473E+03	−.3156756E+03	−.3196473E+03
19	−.2211720E+04	−.2195838E+04	−.2235545E+04	−.2207779E+04	−.2251428E+04	−.2239516E+04	−.2281195E+04	−.2281195E+04	−.2354668E+04
20	−.2189881E+04	−.2172013E+04	−.2211720E+04	−.2176065E+04	−.2221648E+04	−.2201779E+04	−.2231560E+04	−.2219662E+04	−.2265326E+04
21	−.2136276E+04	−.2120393E+04	−.2156130E+04	−.2120383E+04	−.2160100E+04	−.2136276E+04	−.2160071E+04	−.2152159E+04	−.2195838E+04
22	−.2702111E+04	−.2712038E+04	−.2757702E+04	−.2771823E+04	−.2821235E+04	−.2817264E+04	−.2858957E+04	−.2866924E+04	−.2914547E+04
23	−.2179955E+04	−.2166071E+04	−.2207750E+04	−.2179946E+04	−.2219662E+04	−.2195838E+04	−.2223611E+04	−.2207750E+04	−.2247458E+04
24	−.2265326E+04	−.2255399E+04	−.2303048E+04	−.2275841E+04	−.2322902E+04	−.2307019E+04	−.2350698E+04	−.2338786E+04	−.2382537E+04
25	−.2255399E+04	−.2243487E+04	−.2295107E+04	−.2271384E+04	−.2318931E+04	−.2307019E+04	−.2350698E+04	−.2342756E+04	−.2390406E+04
26	−.6313530E+03	−.6293676E+03	−.6315323E+03	−.6311940E+03	−.6392965E+03	−.6371091E+03	−.6531922E+03	−.6571630E+03	−.6730461E+03
27	−.2193852E+04	−.2183929E+04	−.2231575E+04	−.2206390E+04	−.2249443E+04	−.2231575E+04	−.2279224E+04	−.2289151E+04	−.2350698E+04
28	−.2287166E+04	−.2285180E+04	−.2326981E+04	−.2326981E+04	−.2380678E+04	−.2378693E+04	−.2426157E+04	−.2422172E+04	−.2469821E+04
29	+.6467794E+05	+.6467794E+05	+.6467794E+05	+.6468203E+05	+.6467794E+05	+.6467794E+05	+.6467794E+05	+.6467794E+05	+.6467794E+05
30	−.3863562E+04	−.3927095E+04	−.4042247E+04	−.4177445E+04	−.4268581E+04	−.4373807E+04	−.4586241E+04	−.4735147E+04	−.4927729E+04
31	−.4590216E+04	−.4677571E+04	−.4806621E+04	−.4977557E+04	−.5084558E+04	−.5191786E+04	−.5414149E+04	−.5602781E+04	−.5835052E+04
32	−.4566389E+02	−.1985387E+02	+.1985387E+01	+.6957870E+02	+.7941547E+02	+.1350061E+03	+.2201779E+03	+.2819249E+03	+.3531988E+03
34	−.7256588E+04	−.7357843E+04	−.7675505E+04	−.7928067E+04	−.8241340E+04	−.8431937E+04	−.8886620E+04	−.9152631E+04	−.9648980E+04
35	−.1157481E+04	−.1133655E+04	−.1149539E+04	−.1099908E+04	−.1127700E+04	−.1089977E+04	−.1076080E+04	−.1030415E+04	−.1012547E+04
36	−.3807972E+04	−.3847680E+04	−.3982686E+04	−.4098153E+04	−.4220932E+04	−.4308289E+04	−.4488003E+04	−.4586241E+04	−.4809807E+04
37	−.3678922E+04	−.3726371E+04	−.3849664E+04	−.3922991E+04	−.4081955E+04	−.4169312E+04	−.4317807E+04	−.4488974E+04	−.4689483E+04
38	−.2436069E+04	−.2446011E+04	−.2499602E+04	−.2521629E+04	−.2577032E+04	−.2581003E+04	−.2634208E+04	−.2634231E+04	−.2687287E+04
63	−.2726401E+04	−.2765999E+04	−.2853115E+04	−.2954207E+04	−.3035266E+04	−.3086764E+04	−.3201554E+04	−.3266916E+04	−.3367891E+04
44	−.1508231E+04	−.1515955E+04	−.1562303E+04	−.1581704E+04	−.1629893E+04	−.1649204E+04	−.1718725E+04	−.1749624E+04	−.1823007E+04
45	−.1664670E+04	−.1676257E+04	−.1730329E+04	−.1761242E+04	−.1817230E+04	−.1848129E+04	−.1933099E+04	−.1979464E+04	−.2077141E+04
46	−.2000733E+04	−.2012319E+04	−.2077978E+04	−.2112801E+04	−.2176535E+04	−.2217020E+04	−.2305853E+04	−.2375174E+04	−.2502829E+04
49	−.2522136E+04	−.2529861E+04	−.2607106E+04	−.2630379E+04	−.2715295E+04	−.2738424E+04	−.2838864E+04	−.2892915E+04	−.3031957E+04
50	−.8709545E+03	−.8767480E+03	−.8999217E+03	−.9096245E+03	−.9269576E+03	−.9346822E+03	−.9638493E+03	−.9694427E+03	−.9906855E+03
51	−.1880869E+04	−.1890525E+04	−.1948460E+04	−.1979544E+04	−.2025705E+04	−.2045016E+04	−.2120331E+04	−.2166678E+04	−.2245167E+04
52	−.1614660E+04	−.1618323E+04	−.1668533E+04	−.1691786E+04	−.1741915E+04	−.1761227E+04	−.1842135E+04	−.1880955E+04	−.1956341E+04
53	−.1500566E+04	−.1504409E+04	−.1548625E+04	−.1562391E+04	−.1608691E+04	−.1624140E+04	−.1689798E+04	−.1716826E+04	−.1790218E+04
54	−.1021618E+04	−.1019687E+04	−.1046723E+04	−.1044813E+04	−.1071828E+04	−.1071828E+04	−.1102727E+04	−.1104658E+04	−.1132831E+04

BLANK PAGE

19	−.2211720E+04	−.2195838E+04	−.2235565E+04	−.2207779E+04	−.2251428E+04	−.2239516E+04	−.2283195 4	−.2 8 1	−.
20	−.2189881E+04	−.2172013E+04	−.2211720E+04	−.2174065E+04	−.2221648E+04	−.2203779E+04	−.2243560E+04	−.2219662E+04	−.2265326E+04
21	−.2136276E+04	−.2120393E+04	−.2156130E+04	−.2120383E+04	−.2160100E+04	−.2136276E+04	−.2164071E+04	−.2152159E+04	−.2195838E+04
22	−.2702111E+04	−.2712033E+04	−.2757702E+04	−.2771823E+04	−.2821235E+04	−.2817264E+04	−.2858957E+04	−.2862927E+04	−.2914547E+04
23	−.2179955E+04	−.2164071E+04	−.2207750E+04	−.2179946E+04	−.2219662E+04	−.2195838E+04	−.2223633E+04	−.2207750E+04	−.2247458E+04
24	−.2265326E+04	−.2255399E+04	−.2303048E+04	−.2275841E+04	−.2322902E+04	−.2307019E+04	−.2350698E+04	−.2318786E+04	−.2372517E+04
25	−.2255399E+04	−.2243487E+04	−.2295107E+04	−.2271384E+04	−.2318931E+04	−.2307019E+04	−.2350698E+04	−.2314756E+04	−.2390404E+04
26	−.6313533E+03	−.6293676E+03	−.6353238E+03	−.6331940E+03	−.6392945E+03	−.6373091E+03	−.6531922E+03	−.6571 0E+03	−.6730461E+03
27	−.2193852E+04	−.2183925E+04	−.2231575E+04	−.2206390E+04	−.2249443E+04	−.2231575E+04	−.2279224E+04	−.2289151E+04	−.2350698E+04
28	−.2287166E+04	−.2285180E+04	−.2326873E+04	−.2326981E+04	−.2380478E+04	−.2378493E+04	−.2426157E+04	−.2422172E+04	−.2466821E+04
29	+.6467794E+05	+.6467794E+05	+.6467794E+05	+.6468203E+05	+.6467794E+05	+.6467794E+05	+.6467794E+05	+.6467794E+05	+.6467793E+05
30	−.3863562E+04	−.3927095E+04	−.4042247E+04	−.4177445E+04	−.4268581E+04	−.4373807E+04	−.4586241E+04	−.4735147E+04	−.4927729E+04
31	−.4590214E+04	−.4677571E+04	−.4806621E+04	−.4977557E+04	−.5084576E+04	−.5191786E+04	−.5414149E+04	−.5602761E+04	−.5835052E+04
32	−.4566389E+02	−.1985387E+02	+.1985387E+01	+.6957870E+02	+.7941547E+02	+.1350063E+03	+.2203779E+03	+.2819249E+03	+.3531988E+03
34	−.7256585E+04	−.7357843E+04	−.7675505E+04	−.7928067E+04	−.8241340E+04	−.8431917E+04	−.8882620E+04	−.9152603E+04	−.9648980E+04
35	−.1157481E+04	−.1133655E+04	−.1149539E+04	−.1099908E+04	−.1127700E+04	−.1089977E+04	−.1176080E+04	−.1030415E+04	−.1012547E+04
36	−.3807972E+04	−.3847680E+04	−.3982686E+04	−.4098153E+04	−.4220932E+04	−.4309289E+04	−.4481001E+04	−.4586243E+04	−.4808607E+04
37	−.3678922E+04	−.3726571E+04	−.3849664E+04	−.3972991E+04	−.4081955E+04	−.4169312E+04	−.4373807E+04	−.4486974E+04	−.4689483E+04
38	−.2436049E+04	−.2446011E+04	−.2499602E+04	−.2521629E+04	−.2577032E+04	−.2581003E+04	−.2632623E+04	−.2674608E+04	−.2678287E+04
43	−.2726401E+04	−.2765999E+04	−.2853115E+04	−.2954207E+04	−.3035266E+04	−.3084764E+04	−.3203558E+04	−.3266916E+04	−.3 789.E+04
44	−.1508231E+04	−.1515955E+04	−.1562303E+04	−.1581704E+04	−.1629893E+04	−.1649204E+04	−.1718725E+04	−.1749624E+04	−.1823007E+04
45	−.1666670E+04	−.1676257E+04	−.1730329E+04	−.1763242E+04	−.1817230E+04	−.1848129E+04	−.1913099E+04	−.1979446E+04	−.2072141E+04
46	−.2005733E+04	−.2012319E+04	−.2077978E+04	−.2112801E+04	−.2174535E+04	−.2217020E+04	−.2305853E+04	−.2375374E+04	−.2502829E+04
49	−.2522136E+04	−.2529861E+04	−.2607106E+04	−.2630379E+04	−.2715250E+04	−.2738424E+04	−.2838843E+04	−.2892915E+04	−.3031957E+04
50	−.8709545E+03	−.8767480E+03	−.8999217E+03	−.9096245E+03	−.9269576E+03	−.9346822E+03	−.9613649E+03	−.9694427E+03	−.9906853E+03
51	−.1880869E+04	−.1890525E+04	−.1948460E+04	−.1979544E+04	−.2025705E+04	−.2045016E+04	−.2120331E+04	−.2166678E+04	−.2265167E+04
52	−.1614460E+04	−.1618123E+04	−.1668533E+04	−.1691786E+04	−.1741915E+04	−.1761227E+04	−.1842305E+04	−.1880958E+04	−.1954341E+04
53	−.1500546E+04	−.1504409E+04	−.1548825E+04	−.1562391E+04	−.1608691E+04	−.1624140E+04	−.1689798E+04	−.1716834E+04	−.1790218E+04
54	−.1021618E+04	−.1019687E+04	−.1046723E+04	−.1044813E+04	−.1071828E+04	−.1071828E+04	−.1102727E+04	−.1104658E+04	−.1127631E+04
55	−.1353744E+04	−.1353744E+04	−.1392366E+04	−.1394371E+04	−.1432920E+04	−.1438714E+04	−.1485061E+04	−.1492786E+04	−.1535271E+04
56	−.1388499E+04	−.1390430E+04	−.1429052E+04	−.1436859E+04	−.1475400E+04	−.1483125E+04	−.1533333E+04	−.1546852E+04	−.1595131E+04
57	−.1617520E+04	−.1621386E+04	−.1661936E+04	−.1671621E+04	−.1712146E+04	−.1721802E+04	−.1775874E+04	−.1793254E+04	−.1847326E+04
58	−.1444483E+04	−.1444483E+04	−.1486968E+04	−.1498659E+04	−.1541039E+04	−.1552627E+04	−.1606699E+04	−.1626010E+04	−.1687806E+04
59	−.4519613E+03	−.4558237E+03	−.4674105E+03	−.4770217E+03	−.4905841E+03	−.4983087E+03	−.5214925E+03	−.5330693E+03	−.5601053E+03
60	−.1633732E+04	−.1639526E+04	−.1689736E+04	−.1707216E+04	−.1757326E+04	−.1774706E+04	−.1848089E+04	−.1880918E+04	−.1962026E+04
64	−.3978627E+03	−.3997939E+03	−.4113807E+03	−.4171526E+03	−.4287610E+03	−.4345544E+03	−.4519347E+03	−.4615904E+03	−.4809018E+03
66	−.1382731E+04	−.1382731E+04	−.1425216E+04	−.1432996E+04	−.1475425E+04	−.1483150E+04	−.1533360E+04	−.1552671E+04	−.1606743E+04
68	−.1382752E+04	−.1384683E+04	−.1423305E+04	−.1431065E+04	−.1469653E+04	−.1475446E+04	−.1525656E+04	−.1537243E+04	−.1581 9E+04
70	−.9192708E+03	−.9.54086E+03	−.9385823E+03	−.9347309E+03	−.9578937E+03	−.9578937E+03	−.9810674E+03	−.9926542E+03	−.1023553E+04
71	−.8574225E+03	−.8516291E+03	−.8728716E+03	−.8652055E+03	−.8902519E+03	−.8902519E+03	−.9192190E+03	−.9269436E+03	−.9578418E+03
72	−.3887251E+03	−.3906494E+03	−.3964226E+03	−.4022462E+03	−.4118176E+03	−.4118176E+03	−.4175908E+03	−.4252883E+03	−.4310615E+03
73	−.7505089E+03	−.7428113E+03	−.7620551E+03	−.7581960E+03	−.7774502E+03	−.7812989E+03	−.8159178E+03	−.8390304E+03	−.8698205E+03
74	−.5850120E+03	−.5734657E+03	−.5888608E+03	−.5734325E+03	−.5946339E+03	−.5811612E+03	−.6254260E+03	−.6292728E+03	−.6542897E+03
75	−.5272806E+03	−.5118855E+03	−.5311293E+03	−.5157148E+03	−.5349781E+03	−.5349781E+03	−.5465244E+03	−.5426796E+03	−.5657682E+03
76	−.6100290E+03	−.5984827E+03	−.6158021E+03	−.6062093E+03	−.6273484E+03	−.6254260E+03	−.6523654E+03	−.6542897E+03	−.6791067E+03
77	−.6619873E+03	−.6465922E+03	−.6658360E+03	−.6582475E+03	−.6773824E+03	−.6773824E+03	−.7120212E+03	−.7197187E+03	−.7428113E+03
78	−.9698883E+03	−.9602664E+03	−.9795103E+03	−.9718005E+03	−.9968297E+03	−.1010300E+04	−.1035317E+04	−.1041090E+04	−.1062259E+04
79	−.2828841E+03	−.2809597E+03	−.2828841E+03	−.2771050E+03	−.2790353E+03	−.2694134E+03	−.2617159E+03	−.2540196E+03	−.2501696E+03
80	−.1062259E+04	−.1058410E+04	−.1081503E+04	−.1077697E+04	−.1093049E+04	−.1096897E+04	−.1127687E+04	−.1135185E+04	−.1162326E+04
81	−.1094973E+04	−.1094973E+04	−.1118066E+04	−.1116176E+04	−.1143082E+04	−.1145007E+04	−.1179646E+04	−.1183494E+04	−.1204663E+04
89	−.2732622E+03	−.2713378E+03	−.2771109E+03	−.2751100E+03	−.2809597E+03	−.2790353E+03	−.2828841E+03	−.2790353E+03	−.2809597E+03
93	−.3675569E+03	−.3675569E+03	−.3771788E+03	−.3791280E+03	−.3849007E+03	−.3887251E+03	−.3983470E+03	−.4002714E+03	−.4079689E+03
98	−.9429470E+03	−.9429470E+03	−.9660 5E+03	−.9640823E+03	−.9891322E+03	−.9891322E+03	−.1016 3E+04	−.1017998E+04	−.1039166E+04

Table B-5 (continued)

Channel No.	Strain [illegible] at pressure (psi)								
	24500	24990	29940	25560	25510	26020	25940	26510	26410
91	-.1374008E+04	-.1412496E+04	-.1426042E+04	-.1479849E+04	-.1497169E+04	-.1545279E+04	-.1570406E+04	-.1633918E+04	-.1658933E+04
92	-.1368235E+04	-.1408647E+04	-.1422118E+04	-.1479849E+04	-.1501017E+04	-.1558825E+04	-.1595116E+04	[illegible]	[illegible]
90	-.1354784E+04	-.1393252E+04	-.1402874E+04	-.1456757E+04	-.1470227E+04	-.1504866E+04	-.1510728E+04	[illegible]	[illegible]
94	-.1339370E+04	-.1377857E+04	-.1391327E+04	-.1445059E+04	-.1470227E+04	-.1524110E+04	-.1562671E+04	[illegible]	[illegible]
88	-.1381706E+04	-.1422118E+04	-.1435589E+04	-.1491395E+04	-.1508715E+04	-.1558825E+04	-.1589605E+04	[illegible]	[illegible]
41	-.3678556E+04	-.3787451E+04	-.3854768E+04	-.4042859E+04	-.4157694E+04	-.4335886E+04	-.4504572E+04	[illegible]	[illegible]
40	-.3280840E+04	-.3383795E+04	-.3445172E+04	-.3601585E+04	-.[illegible]0E+04	-.3862933E+04	-.4025404E+04	[illegible]	[illegible]
97	-.1327823E+04	-.1362462E+04	-.1372084E+04	-.1420193E+04	-.142[illegible]5E+04	-.1470227E+04	-.1487583E+04	[illegible]	[illegible]
85	-.1337445E+04	-.1372084E+04	-.1383630E+04	-.1433664E+04	-.1447115E+04	-.1491395E+04	-.1508771E+04	[illegible]	[illegible]
42	-.6048482E+01	-.6048482E+01	-.6048482E+04	-.6068574E+01	-.6068574E+01	-.6068574E+01	-.1980031E+01	[illegible]	[illegible]
39	+.3718629E+04	+.3792089E+04	+.1015776E+05	+.8130158E+04	+.1069726E+05	+.1157281E+05	+.1126151E+05	[illegible]	[illegible]
86	-.1414420E+04	-.1454832E+04	-.1468303E+04	-.1526035E+04	-.1543354E+04	-.1595312E+04	-.1620365E+04	[illegible]	[illegible]
96	-.1402874E+04	-.1441361E+04	-.1454832E+04	-.1508715E+04	-.1524110E+04	-.1570295E+04	-.1591563E+04	[illegible]	[illegible]
87	-.1427891E+04	-.1468303E+04	-.1481774E+04	-.1543354E+04	-.1562598E+04	-.1616480E+04	-.1647317E+04	[illegible]	[illegible]
105	-.1367083E+04	-.1487405E+04	-.1420881E+04	-.1478447E+04	-.1495727E+04	-.1545849E+04	-.1576415E+04	[illegible]	[illegible]
84	-.1345143E+04	-.1385555E+04	-.1402874E+04	-.1466179E+04	-.1487547E+04	-.1537581E+04	-.1562602E+04	[illegible]	[illegible]
99	-.1477925E+04	-.1518337E+04	-.1526035E+04	-.1579917E+04	-.1581766E+04	-.1624178E+04	-.1624276E+04	[illegible]	[illegible]
82	-.1393252E+04	-.1435589E+04	-.1449059E+04	-.1512564E+04	-.1529881E+04	-.1581842E+04	-.1608424E+04	[illegible]	[illegible]
83	-.1464454E+04	-.1508715E+04	-.1520281E+04	-.1591463E+04	-.1597208E+04	-.1635724E+04	-.1641491E+04	[illegible]	[illegible]
48	-.5513471E+04	-.5940254E+04	-.6124551E+04	-.7224452E+04	-.8054853E+04	-.9308164E+04	-.1100727E+05	[illegible]	[illegible]
61	-.2997174E+04	-.3225049E+04	-.3394989E+04	-.3634451E+04	-.3715559E+04	-.3916397E+04	-.4175188E+04	[illegible]	[illegible]
33	-.1296299E+06	-.1296299E+06	-.1296299E+06	-.1296259E+06	-.1296299E+06	-.1296299E+06	-.1296380E+06	[illegible]	[illegible]
62	-.2468013E+04	-.2624436E+04	-.2769771E+04	-.3035769E+04	-.3163224E+04	-.3327171E+04	-.3621116E+04	[illegible]	[illegible]
63	-.1869220E+04	-.1965777E+04	-.2054610E+04	-.2274760E+04	-.2379041E+04	-.2525808E+04	-.2850543E+04	[illegible]	[illegible]
65	-.1672489E+04	-.1742010E+04	-.1788358E+04	-.1944780E+04	-.2041269E+04	-.2307815E+04	-.2678660E+04	[illegible]	[illegible]
100	+.1287367E+03	+.1341624E+03	+.1361354E+03	+.1464936E+03	+.1494530E+03	+.1588260E+03	+.1630767E+03	[illegible]	[illegible]
101	-.2690676E+04	-.2816018E+04	-.2903758E+04	-.3169065E+04	-.3311119E+04	-.3547180E+04	-.3759944E+04	[illegible]	[illegible]
102	-.2630094E+04	-.2715744E+04	-.2776327E+04	-.3052079E+04	-.3217113E+04	-.3463619E+04	-.3670191E+04	[illegible]	[illegible]
103	-.1776974E+04	-.1894138E+04	-.1944097E+04	-.4098685E+04	-.4104952E+04	-.4073617E+04	-.4251072E+04	[illegible]	[illegible]
8	-.2227604E+04	-.2322903E+04	-.2386518E+04	-.2485704E+04	-.2553135E+04	-.2640564E+04	-.2712205E+04	[illegible]	[illegible]
9	-.2098554E+04	-.2160100E+04	-.2183925E+04	-.2289151E+04	-.2314961E+04	-.2408274E+04	-.2458045E+04	[illegible]	[illegible]
10	-.1635959E+04	-.1679637E+04	-.1698608E+04	-.1747140[illegible]4	-.1766994E+04	-.1818614E+04	-.1834512E+04	[illegible]	[illegible]
11	-.1675666E+04	-.1721330E+04	-.1729272E+04	-.1784862E+04	-.1794790E+04	-.1858122E+04	-.1882197E+04	[illegible]	[illegible]
12	-.1745155E+04	-.1792804E+04	-.1800746E+04	-.1868249E+04	-.1878176E+04	-.1941869E+04	-.1969578E+04	[illegible]	[illegible]
13	-.1743170E+04	-.1782877E+04	-.1782877E+04	-.1834497E+04	-.1842419E+04	-.1905971E+04	-.1929937E+04	[illegible]	[illegible]
14	-.1701476E+04	-.1741184E+04	-.1739199E+04	-.1790819E+04	-.1792804E+04	-.1946410E+04	-.1866273E+04	[illegible]	[illegible]
15	-.2765644E+04	-.2831015E+04	-.2884676E+04	-.2997934E+04	-.3033671E+04	-.3119043E+04	-.3158937E+04	[illegible]	[illegible]
16	-.2577032E+04	-.2797410E+04	-.2962197E+04	-.3265961E+04	-.3387070E+04	-.3537959E+04	-.3696860E+04	[illegible]	[illegible]
17	-.2781527E+04	-.2964182E+04	-.3095217E+04	-.3608909E+04	-.3549872E+04	-.3752381E+04	-.3925320E+04	[illegible]	[illegible]
18	-.1117057E+03	-.3037642E+03	-.2858957E+03	-.2422172E+01	-.2104510E+03	-.1826556E+03	-.1387505E+03	[illegible]	[illegible]
19	-.2378493E+04	-.2525412E+04	-.2588944E+04	-.2811307E+04	-.2950285E+04	-.3188511E+04	-.3414970E+04	[illegible]	[illegible]
20	-.2279224E+04	-.2376508E+04	-.2461865E+04	-.2811329E+04	-.2988007E+04	-.3272803E+04	-.3496415E+04	[illegible]	[illegible]
21	-.2199808E+04	-.2279224E+04	-.2330844E+04	-.2588944E+04	-.2755717E+04	-.3121024E+04	-.3395082E+04	[illegible]	[illegible]
22	-.2946314E+04	-.3041611E+04	-.3111705E+04	-.3391040E+04	-.3513258E+04	-.4201078E+04	-.4604450E+04	[illegible]	[illegible]
23	-.2247458E+04	-.2307019E+04	-.2330844E+04	-.2613262E+04	-.2843074E+04	-.3115595E+04	-.3641282E+04	[illegible]	[illegible]
24	-.2374522E+04	-.2440040E+04	-.2491660E+04	-.2819010E+04	-.2991965E+04	-.3216180E+04	-.3441316E+04	[illegible]	[illegible]
25	-.2394376E+04	-.2465850E+04	-.2521441E+04	-.2862927E+04	-.3057495E+04	-.3347362E+04	-.3585792E+04	[illegible]	[illegible]
26	-.6790023E+03	-.6809877E+03	-.6770169E+03	-.6611338E+03	-.6313590E+03	-.5976014E+03	-.5438460E+03	[illegible]	[illegible]
27	-.2366581E+04	-.2469821E+04	-.2541295E+04	-.2847045E+04	-.2958226E+04	-.3126984E+04	-.3278566E+04	[illegible]	[illegible]
28	-.2491660E+04	-.2586959E+04	-.2646520E+04	-.2916201E+04	-.3065417E+04	-.3291756E+04	-.3496447E+04	[illegible]	[illegible]
29	+.6467794E+05	+.6467794E+05	+.6467794E+05	+.6467794E+05	+.6467794E+05	+.6467794E+05	+.6468207E+05	[illegible]	[illegible]
30	-.5052809E+04	-.5249362E+04	-.5455846E+04	-.5980450E+04	-.6236100E+04	-.6642074E+04	-.7185495E+04	[illegible]	[illegible]
31	-.6017707E+04	-.6248012E+04	-.6508098E+04	-.6899502E+04	-.7421176E+04	-.7939561E+04	-.8618985E+04	[illegible]	[illegible]
32	+.4129604E+03	+.5102444E+03	+.6072428E+03	+.8274209E+03	+.9708541E+03	+.1167407E+04	+.1387958E+04	[illegible]	[illegible]
34	-.9912889E+04	-.1051461E+05	-.1096926E+05	-.1203541E+05	-.1271640E+05	-.1370909E+05	-.1473043E+05	[illegible]	[illegible]
35	-.9248249E+03	-.9589418E+03	-.9051364E+03	-.8136771E+03	-.7663591E+03	-.7147192E+03	-.6231857E+03	[illegible]	[illegible]
36	-.4915817E+04	-.5158015E+04	-.5312748E+04	-.5765561E+04	-.6021661E+04	-.6444565E+04	-.6850073E+04	[illegible]	[illegible]
37	-.4804636E+04	-.5040897E+04	-.5221567E+04	-.5664046E+04	-.5892627E+04	-.6281761E+04	-.6671301E+04	[illegible]	[illegible]
38	-.2680272E+04	-.2727921E+04	-.2727921E+04	-.2781521E+04	-.2779541E+04	-.2811147E+04	-.2841294E+04	[illegible]	[illegible]
43	-.3419368E+04	-.3526284E+04	-.3595580E+04	-.3743094E+04	-.3821290E+04	-.3934144E+04	-.4021424E+04	[illegible]	[illegible]
44	-.1861600E+04	-.1958187E+04	-.2013413E+04	-.2231477E+04	-.2427454E+04	-.3211497E+04	-.3050250E+04	[illegible]	[illegible]
45	-.2155180E+04	-.2248294E+04	-.2498921E+04	-.2881220E+04	-.3111865E+04	-.4126875E+04	-.5210545E+04	[illegible]	[illegible]
46	-.2607111E+04	-.2804087E+04	-.2970165E+04	-.3298459E+04	-.3653789E+04	-.4186784E+04	-.5106257E+04	[illegible]	[illegible]
49	-.3116927E+04	-.3340940E+04	-.3541778E+04	-.3962767E+04	-.4414654E+04	-.5167799E+04	-.6322952E+04	[illegible]	[illegible]
50	-.9868230E+03	-.1002272E+04	-.9844891E+03	-.9655804E+03	-.9365445E+03	-.9346822E+03	-.9482497E+03	[illegible]	[illegible]
51	-.2323101E+04	-.2471799E+04	-.2589958E+04	-.2784644E+04	-.3091695E+04	-.3680693E+04	-.4635029E+04	[illegible]	[illegible]
52	-.2000688E+04	-.2097246E+04	-.2193801E+04	-.2545270E+04	-.3024193E+04	-.3730991E+04	-.4862918E+04	[illegible]	[illegible]

24	-.2374522E+04	-.2440040E+04	-.2491660E+04	-.2539910E+04	-.2591396E+04	-.2736180E+04	-.3461336E+04	[illegible]
25	-.2394378E+04	-.2465850E+04	-.2521441E+04	-.2586292E+04	-.3057495E+04	-.3157302E+04	-.3535702E+04	[illegible]
26	-.6790021E+03	-.6809877E+03	-.6770169E+03	-.6611318E+03	-.6611590E+03	-.5970014E+03	-.5438660E+03	[illegible]
27	-.2386581E+04	-.2466982E+04	-.2541295E+04	-.2584705E+04	-.2958226E+04	-.3126984E+04	-.3278566E+04	[illegible]
28	-.2491660E+04	-.2586955E+04	-.2666520E+04	-.2934460E+04	-.3065417E+04	-.3293756E+04	-.3498447E+04	[illegible]
29	+.6467794E+03	+.6467794E+03	+.6467794E+03	+.6467794E+03	+.6467794E+03	+.6467794E+03	+.6468203E+03	[illegible]
30	-.5052809E+04	-.5249302E+04	-.5465384E+04	-.5904540E+04	-.6216100E+04	-.6640704E+04	-.7185495E+04	[illegible]
31	-.6017707E+04	-.6248012E+04	-.6508098E+04	-.6996502E+04	-.7421376E+04	-.7939561E+04	-.8618985E+04	[illegible]
32	+.4129604E+03	+.5102444E+03	+.6075283E+03	+.8259209E+03	+.9708541E+03	+.1167607E+04	+.1387958E+04	[illegible]
34	-.9932889E+04	-.1051461E+05	-.1096926E+05	-.1201541E+05	-.1271640E+05	-.1370909E+05	-.1473043E+05	[illegible]
35	-.9748249E+03	-.9589418E+03	-.9053304E+03	-.8118771E+03	-.7663591E+03	-.7147392E+03	-.6231857E+03	[illegible]
36	-.4915817E+04	-.5158035E+04	-.5312748E+04	-.5765363E+04	-.6023663E+04	-.6446585E+04	-.6850073E+04	[illegible]
37	-.4804636E+04	-.5040897E+04	-.5221567E+04	-.5640484E+04	-.5892627E+04	-.6281763E+04	-.6671951E+04	[illegible]
38	-.2680272E+04	-.2727921E+04	-.2727921E+04	-.2781527E+04	-.2779541E+04	-.2833147E+04	-.2841296E+04	[illegible]
43	-.3419368E+04	-.3526284E+04	-.3595580E+04	-.3742094E+04	-.3821290E+04	-.3934144E+04	-.4023424E+04	[illegible]
44	-.1861610E+04	-.1958187E+04	-.2015433E+04	-.2230477E+04	-.2427454E+04	-.3211497E+04	-.5050350E+04	[illegible]
45	-.2155180E+04	-.2348294E+04	-.2498921E+04	-.2883220E+04	-.3311865E+04	-.4126875E+04	-.5210545E+04	[illegible]
46	-.2607111E+04	-.2804087E+04	-.2970165E+04	-.3298459E+04	-.3653782E+04	-.4186784E+04	-.5106257E+04	[illegible]
49	-.3116927E+04	-.3340940E+04	-.3541778E+04	-.3962767E+04	-.4414654E+04	-.5167799E+04	-.6122952E+04	[illegible]
50	-.9568230E+03	-.1002272E+04	-.9848918E+03	-.9655804E+03	-.9385445E+03	-.9146822E+03	-.9482497E+03	[illegible]
51	-.2323101E+04	-.2471799E+04	-.2589598E+04	-.2786644E+04	-.3091695E+04	-.3680693E+04	-.4615029E+04	[illegible]
52	-.2000688E+04	-.2097246E+04	-.2193801E+04	-.2545270E+04	-.3024191E+04	-.3730991E+04	-.4862913E+04	[illegible]
53	-.1836565E+04	-.1965951E+04	-.2110787E+04	-.2390801E+04	-.2762270E+04	-.3425894E+04	-.4316371E+04	[illegible]
54	-.2131694E+04	-.2180660E+04	-.2196452E+04	-.2201215E+04	-.2205077E+04	-.2237906E+04	-.2245864E+04	[illegible]
55	-.1546857E+04	-.1597067E+04	-.1616179E+04	-.1697487E+04	-.1730116E+04	-.1821080E+04	-.1900162E+04	[illegible]
56	-.1610580E+04	-.1670445E+04	-.1701134E+04	-.1807556E+04	-.1865490E+04	-.1992946E+04	-.2089626E+04	[illegible]
57	-.1668568E+04	-.1741952E+04	-.1784417E+04	-.1935066E+04	-.2008450E+04	-.2079902E+04	-.2161082E+04	[illegible]
58	-.1710980E+04	-.1788226E+04	-.1842298E+04	-.2004514E+04	-.2046999E+04	-.2108795E+04	-.2275027E+04	[illegible]
59	-.5794167E+03	-.6257661E+03	-.6817677E+03	-.8208091E+03	-.7512882E+03	-.7454948E+03	-.7628486E+03	[illegible]
60	-.2021892E+04	-.2151278E+04	-.2236248E+04	-.2388809E+04	-.2486878E+04	-.2491159E+04	-.2612110E+04	[illegible]
64	-.4982821E+03	-.5369049E+03	-.5851834E+03	-.7531927E+03	-.7184121E+03	-.7010519E+03	-.6991169E+03	[illegible]
66	-.1622192E+04	-.1691713E+04	-.1730136E+04	-.1873241E+04	-.1985247E+04	-.2298092E+04	-.2707629E+04	[illegible]
68	-.1595177E+04	-.1649249E+04	-.1674354E+04	-.1780980E+04	-.1826916E+04	-.1971750E+04	-.2236402E+04	[illegible]
70	-.1035198E+04	-.1073782E+04	-.1100798E+04	-.1174181E+04	-.1208942E+04	-.1278466E+04	-.1317121E+04	[illegible]
71	-.9712909E+03	-.1015776E+04	-.1040881E+04	-.1114264E+04	-.1149024E+04	-.1216614E+04	-.1268839E+04	[illegible]
72	-.4426074E+03	-.4522297E+03	-.4714735E+03	-.4807173E+03	-.5292050E+03	-.5599511E+03	-.6081680E+03	[illegible]
73	-.8852155E+03	-.9275519E+03	-.9667958E+03	-.1012225E+04	-.1039166E+04	-.1108444E+04	-.1160965E+04	[illegible]
74	-.6619873E+03	-.6831555E+03	-.6696884E+03	-.7218411E+03	-.7197187E+03	-.7928452E+03	-.8197687E+03	[illegible]
75	-.5734657E+03	-.6004071E+03	-.5965538E+03	-.7235075E+03	-.7466601E+03	-.7928452E+03	-.7812960E+03	[illegible]
76	-.6812311E+03	-.7062481E+03	-.7177944E+03	-.7312650E+03	-.7466601E+03	-.8082403E+03	-.8275270E+03	[illegible]
77	-.7466601E+03	-.7812989E+03	-.7928452E+03	-.8351810E+03	-.8582742E+03	-.1135185E+04	-.1224051E+04	[illegible]
78	-.1060134E+04	-.1057296E+04	-.1089200E+04	-.1112298E+04	-.1146931E+04	-.1264118E+04	-.1408678E+04	[illegible]
79	-.2482452E+03	-.2560184E+03	-.2482452E+03	-.2560184E+03	-.2560184E+03	-.2461965E+03	-.2328415E+03	[illegible]
80	-.1162326E+04	-.1256624E+04	-.1297033E+04	-.1377857E+04	-.1462530E+04	-.1616480E+04	-.1662744E+04	[illegible]
81	-.1212360E+04	-.1256021E+04	-.1295109E+04	-.1350916E+04	-.1395177E+04	-.1512584E+04	-.1606924E+04	[illegible]
89	-.2771109E+03	-.2790353E+03	-.2751865E+03	-.2751865E+03	-.2694161E+03	-.2751865E+03	-.2770353E+03	[illegible]
93	-.4118176E+03	-.4231398E+03	-.4227127E+03	-.4645322E+03	-.4503053E+03	-.4676247E+03	-.4811267E+03	[illegible]
98	-.1043015E+04	-.1068032E+04	-.1069956E+04	-.1102671E+04	-.1104595E+04	-.1111516E+04	-.1111518E+04	[illegible]

2

BLANK PAGE

Table B.5 (continued)

Channel No.	Strain (μin./in.) at pressure (psi)								
	26990	26800	27430	27190	27540	27360	27640	27870	27610
91	-.1785866E+04	-.2003419E+04	-.2467334E+04	-.2761673E+04	-.2859823E+04	-.3073442E+04	-.3110015E+04	-.3561088E+04	-.3978989E+04
92	-.1941701E+04	-.2064899E+04	-.2472889E+04	-.2724999E+04	-.2790431E+04	-.3023897E+04	-.3065731E+04	-.3458141E+04	-.3987652E+04
90	-.1830087E+04	-.2039806E+04	-.2455655E+04	-.2777043E+04	-.2834780E+04	-.2938703E+04	-.2971294E+04	-.3418578E+04	-.3956105E+04
94	-.1914759E+04	-.2053419E+04	-.2409452E+04	-.2601902E+04	-.2642316E+04	-.2777032E+04	-.2809899E+04	-.3237206E+04	-.3580402E+04
88	-.1880121E+04	-.2038014E+04	-.2432537E+04	-.2717653E+04	-.2784721E+04	-.2965284E+04	-.3004859E+04	-.3488097E+04	-.3957858E+04
41	-.5636689E+04	-.6070777E+04	-.7102373E+04	-.7693209E+04	-.7838945E+04	-.8351773E+04	-.8442854E+04	-.9726168E+04	-.1106698E+05
40	-.5112854E+04	-.5512405E+04	-.6522284E+04	-.7100082E+04	-.7238996E+04	-.7726083E+04	-.7815185E+04	-.8934317E+04	-.1087037E+05
97	-.1637648E+04	-.1680033E+04	-.1855162E+04	-.1961010E+04	-.2001425E+04	-.2105368E+04	-.2134899E+04	-.2434088E+04	-.2673897E+04
85	-.1698289E+04	-.1764730E+04	-.2009142E+04	-.2174649E+04	-.2228535E+04	-.2361525E+04	-.2386454E+04	-.2684054E+04	-.3118644E+04
42	-.4068574E+01	-.1980031E+01	-.1980031E+01	-.6048482E+01	-.1980031E+01	-.1980031E+01	-.6048482E+01	-.1980031E+01	-.1980031E+01
39	+.1241462E+05	+.1175193E+05	+.8497676E+04	+.1105661E+05	+.8646508E+04	+.9549710E+04	+.1157185E+05	+.1088786E+05	+.8817915E+04
86	-.1891667E+04	-.1997568E+04	-.2288168E+04	-.2359374E+04	-.2392091E+04	-.2415184E+04	-.2449914E+04	-.2735987E+04	-.3604587E+04
96	-.1810843E+04	-.1899534E+04	-.2139946E+04	-.2272737E+04	-.2305454E+04	-.2378811E+04	-.2397880E+04	-.2654984E+04	-.3077778E+04
87	-.1964793E+04	-.2093786E+04	-.2388250E+04	-.2546059E+04	-.2623059E+04	-.2771226E+04	-.2807910E+04	-.3249081E+04	-.4164364E+04
105	-.1900860E+04	-.2023817E+04	-.2286882E+04	-.2294563E+04	-.2321445E+04	-.2430797E+04	-.2461619E+04	-.2817568E+04	-.3493027E+04
84	-.1882398E+04	-.1849335E+04	-.2030256E+04	-.2109161E+04	-.2145726E+04	-.2224631E+04	-.2234696E+04	-.2530390E+04	-.3114047E+04
99	-.1693456E+04	-.1693058E+04	-.1807103E+04	-.1891781E+04	-.1943743E+04	-.2090005E+04	-.2124775E+04	-.2813618E+04	-.3908145E+04
82	-.1941701E+04	-.2051459E+04	-.2409417E+04	-.2676922E+04	-.2778921E+04	-.3146901E+04	-.3204377E+04	-.3746932E+04	-.4813673E+04
83	-.1722328E+04	-.1737716E+04	-.2084127E+04	-.2290049E+04	-.2357406E+04	-.2728835E+04	-.2805889E+04	-.3609866E+04	-.4861769E+04
48	-.2546023E+05	-.2962749E+05	-.3836645E+05	-.4183823E+05	-.4229850E+05	-.4584153E+05	-.4408878E+05	-.5[illegible]007E+05	-.5611098E+05
61	-.1263763E+05	-.1564322E+05	-.2054476E+05	-.2169972E+05	-.2180008E+05	-.2280179E+05	-.2287151E+05	-.2461090E+05	-.2930897E+05
35	-.1296358E+06	-.1296358E+06	-.1296420E+06	-.1296358E+06	-.1296420E+06	-.1296378E+06	-.1296420E+06	-.1296358E+06	-.1296358E+06
62	-.1187846E+05	-.1446129E+05	-.1872938E+05	-.1989270E+05	-.2002332E+05	-.2049841E+05	-.2057953E+05	-.2359877E+05	-.2842954E+05
63	-.1111938E+05	-.1307078E+05	-.1601402E+05	-.1694371E+05	-.1703760E+05	-.1734660E+05	-.1740440E+05	-.1977659E+05	-.2351501E+05
65	-.1041476E+05	-.1204721E+05	-.1418705E+05	-.1497419E+05	-.1505612E+05	-.1526470E+05	-.1531684E+05	-.1735811E+05	-.1781596E+05
100	+.2140680E+03	+.2252294E+03	+.2661712E+03	+.2789031E+03	+.2814627E+03	+.2895951E+03	+.2911491E+03	+.3544675E+03	+.3604400E+03
101	-.6744197E+04	-.6980016E+04	-.5464702E+04	-.5636014E+04	-.5702868E+04	-.5769721E+04	-.5809829E+04	-.6337974E+04	-.6919731E+04
102	-.6685615E+04	-.6940403E+04	-.5494032E+04	-.5688324E+04	-.5759356E+04	-.5838744E+04	-.5880425E+04	-.6[illegible]344E+04	-.[illegible]E+04
103	-.6748375E+04	-.6942589E+04	-.5289387E+04	-.5381310E+04	-.5414737E+04	-.5479501E+04	-.5496769E+04	-.5[illegible]845E+04	-.[illegible]E+04
8	-.3248093E+04	-.3403163E+04	-.3796294E+04	-.4030335E+04	-.4106034E+04	-.4264611E+04	-.4309756E+04	-.4[illegible]E+04	-.[illegible]E+04
9	-.2948899E+04	-.3132974E+04	-.3633468E+04	-.3927095E+04	-.4010715E+04	-.4207034E+04	-.4252875E+04	-.4[illegible]E+04	-.[illegible]E+04
10	-.2056568E+04	-.2219702E+04	-.2477818E+04	-.2616739E+04	-.2672398E+04	-.2775570E+04	-.2811584E+04	-.[illegible]E+04	-.[illegible]E+04
11	-.2144218E+04	-.2275342E+04	-.2541587E+04	-.2668359E+04	-.2730010E+04	-.2835152E+04	-.2[illegible]E+04	-.[illegible]E+04	-.[illegible]E+04
12	-.2859377E+04	-.2364699E+04	-.2634724E+04	-.2765644E+04	-.2827319E+04	-.2934401E+04	-.2[illegible]E+04	-.[illegible]E+04	-.[illegible]E+04
13	-.2299078E+04	-.2438228E+04	-.2827588E+04	-.[illegible]E+04	-.[illegible]E+04	-.[illegible]E+04	-.[illegible]E+04	-.[illegible]E+04	-.[illegible]E+04
14	-.2156150E+04	-.2[illegible]E+04	-.[illegible]E+04	-.[illegible]E+04	-.[illegible]E+04	-.[illegible]E+04	-.[illegible]E+04	-.[illegible]E+04	-.[illegible]E+04
15	-.3492299E+04	-.3651344E+04	-.[illegible]E+04	-.[illegible]E+04	-.[illegible]E+04	-.[illegible]E+04	-.[illegible]E+04	-.[illegible]E+04	-.[illegible]E+04
16	-.4677571E+04	-.4911935E+04	-.[illegible]E+04	-.[illegible]E+04	-.[illegible]E+04	-.[illegible]E+04	-.[illegible]E+04	-.[illegible]E+04	-.[illegible]E+04
17	-.4888066E+04	-.5130525E+04	-.[illegible]E+04	-.[illegible]E+04	-.[illegible]E+04	-.[illegible]E+04	-.[illegible]E+04	-.[illegible]E+04	-.[illegible]E+04
18	+.1131670E+03	+.1[illegible]E+03	-.[illegible]E+03	-.[illegible]E+04	-.[illegible]E+04	-.[illegible]E+04	-.[illegible]E+04	-.[illegible]E+04	-.[illegible]E+04
19	-.4391675E+04	-.4650105E+04	-.[illegible]E+04	-.[illegible]E+04	-.[illegible]E+04	-.[illegible]E+04	-.[illegible]E+04	-.[illegible]E+04	-.[illegible]E+04
20	-.4320201E+04	-.4596822E+04	-.[illegible]E+04	-.[illegible]E+04	-.[illegible]E+04	-.[illegible]E+04	-.[illegible]E+04	-.[illegible]E+04	-.[illegible]E+04
21	-.4244757E+04	-.4467259E+04	-.[illegible]E+04	-.[illegible]E+04	-.[illegible]E+04	-.[illegible]E+04	-.[illegible]E+04	-.[illegible]E+04	-.[illegible]E+04
22	-.5586878E+04	-.5897455E+04	-.[illegible]E+04	-.[illegible]E+04	-.[illegible]E+04	-.[illegible]E+04	-.[illegible]E+04	-.[illegible]E+04	-.[illegible]E+04
23	-.4550506E+04	-.4[illegible]E+04	-.[illegible]E+04	-.[illegible]E+04	-.[illegible]E+04	-.[illegible]E+04	-.[illegible]E+04	-.[illegible]E+04	-.[illegible]E+04
24	-.4429398E+04	-.4694194E+04	-.[illegible]E+04	-.[illegible]E+04	-.[illegible]E+04	-.[illegible]E+04	-.[illegible]E+04	-.[illegible]E+04	-.[illegible]E+04
29	-.4598155E+04	-.4[illegible]E+04	-.[illegible]E+04	-.[illegible]E+04	-.[illegible]E+04	-.[illegible]E+04	-.[illegible]E+04	-.[illegible]E+04	-.[illegible]E+04
26	-.2203779E+03	-.1149755E+04	-.[illegible]E+04	-.[illegible]E+04	-.[illegible]E+04	-.[illegible]E+04	-.[illegible]E+04	-.[illegible]E+04	-.[illegible]E+04
27	-.4191151E+04	-.4490165E+04	-.[illegible]E+04	-.[illegible]E+04	-.[illegible]E+04	-.[illegible]E+04	-.[illegible]E+04	-.[illegible]E+04	-.[illegible]E+04
28	-.4687498E+04	-.4997494E+04	-.[illegible]E+04	-.[illegible]E+04	-.[illegible]E+04	-.[illegible]E+04	-.[illegible]E+04	-.[illegible]E+04	-.[illegible]E+04
29	+.6467993E+03	+.[illegible]E+03	-.[illegible]E+04	-.[illegible]E+04	-.[illegible]E+04	-.[illegible]E+04	-.[illegible]E+04	-.[illegible]E+04	-.[illegible]E+04
90	-.1145766E+05	-.1271[illegible]E+05	-.[illegible]E+05	-.[illegible]E+05	-.[illegible]E+05	-.[illegible]E+05	-.[illegible]E+05	-.[illegible]E+05	-.[illegible]E+05
91	-.1428351E+05	-.[illegible]E+04	-.[illegible]E+05	-.[illegible]E+05	-.[illegible]E+05	-.[illegible]E+05	-.[illegible]E+05	-.[illegible]E+05	-.[illegible]E+05
92	-.9420821E+04	-.[illegible]E+04	-.[illegible]E+04	-.[illegible]E+04	-.[illegible]E+04	-.[illegible]E+04	-.[illegible]E+04	-.[illegible]E+04	-.[illegible]E+04
34	-.1601810E+05	-.1333[illegible]E+05	-.[illegible]E+05	-.[illegible]E+05	-.[illegible]E+05	-.[illegible]E+05	-.[illegible]E+05	-.[illegible]E+05	-.[illegible]E+05
33	-.5168006E+02	-.[illegible]E+02	-.[illegible]E+04	-.[illegible]E+04	-.[illegible]E+04	-.[illegible]E+04	-.[illegible]E+04	-.[illegible]E+04	-.[illegible]E+04
96	-.1109037E+05	-.1275101E+05	-.[illegible]E+05	-.[illegible]E+05	-.[illegible]E+05	-.[illegible]E+05	-.[illegible]E+05	-.[illegible]E+05	-.[illegible]E+05
37	-.1064763E+05	-.1212351E+05	-.[illegible]E+05	-.[illegible]E+05	-.[illegible]E+05	-.[illegible]E+05	-.[illegible]E+05	-.[illegible]E+05	-.[illegible]E+05
38	-.3142657E+04	-.3288036E+04	-.[illegible]E+04	-.[illegible]E+04	-.[illegible]E+04	-.[illegible]E+04	-.[illegible]E+04	-.[illegible]E+04	-.[illegible]E+04
43	-.4613198E+04	-.4948099E+04	-.[illegible]E+04	-.[illegible]E+04	-.[illegible]E+04	-.[illegible]E+04	-.[illegible]E+04	-.[illegible]E+04	-.[illegible]E+04
44	-.1243465E+05	-.1320790E+05	-.1410207E+05	-.1[illegible]E+05	-.[illegible]E+05	-.[illegible]E+05	-.[illegible]E+05	-.[illegible]E+05	-.[illegible]E+05
45	-.1306615E+05	-.1412718E+05	-.[illegible]E+05	-.[illegible]E+05	-.[illegible]E+05	-.[illegible]E+05	-.[illegible]E+05	-.[illegible]E+05	-.[illegible]E+05
46	-.1358578E+05	-.1507545E+05	-.[illegible]E+05	-.[illegible]E+05	-.[illegible]E+05	-.[illegible]E+05	-.[illegible]E+05	-.[illegible]E+05	-.[illegible]E+05
49	-.1850426E+05	-.2126520E+05	-.[illegible]E+05	-.[illegible]E+05	-.[illegible]E+05	-.[illegible]E+05	-.[illegible]E+05	-.[illegible]E+05	-.[illegible]E+05
50	-.1919145E+04	-.2170739E+04	-.[illegible]E+04	-.[illegible]E+04	-.[illegible]E+04	-.[illegible]E+04	-.[illegible]E+04	-.[illegible]E+04	-.[illegible]E+04
51	-.1446680E+05	-.1572820E+05	-.[illegible]E+05	-.[illegible]E+05	-.[illegible]E+05	-.[illegible]E+05	-.[illegible]E+05	-.[illegible]E+05	-.[illegible]E+05
52	-.1407818E+05	-.1513337E+05	-.[illegible]E+05	-.[illegible]E+05	-.[illegible]E+05	-.[illegible]E+05	-.[illegible]E+05	-.[illegible]E+05	-.[illegible]E+05
53	-.1256403E+05	-.1363857E+05	-.[illegible]E+05	-.[illegible]E+05	-.[illegible]E+05	-.[illegible]E+05	-.[illegible]E+05	-.[illegible]E+05	-.[illegible]E+05
54	-.1924675E+04	-.1423340E+04	-.[illegible]E+04	-.[illegible]E+04	-.[illegible]E+04	-.[illegible]E+04	-.[illegible]E+04	-.[illegible]E+04	-.[illegible]E+04
55	-.2893671E+04	-.6468003E+04	-.[illegible]E+04	-.[illegible]E+04	-.[illegible]E+04	-.[illegible]E+04	-.[illegible]E+04	-.[illegible]E+04	-.[illegible]E+04
[illegible]	[illegible]	[illegible]	[illegible]	[illegible]	[illegible]	[illegible]	[illegible]	[illegible]	[illegible]

BLANK PAGE

Table B-5 (continued)

Channel No.	Strain (in./in.) at pressure (psi)			
	2950	3150	3350	0
91	.1001511E-03	.1856794E-03	-.2130112E-03	.1442716E-03
92	.1041118E-03	.1870679E-03	-.2208611E-03	.1528981E-03
93	.1006548E-03	.1822884E-03	-.2111891E-03	.1401548E-03
94	.9141612E-04	.1751774E-03	-.2065410E-03	.1392290E-03
95	.9791812E-04	.1804181E-03	-.2105018E-03	.1412406E-03
96	.2271913E-03	*.6889120E-03	*.6889725E-03	.6211110E-03
97	.2049615E-03	.1701600E-03	-.4446449E-03	.1486256E-03
98	.5588096E-04	.1015051E-03	-.1186551E-03	.5885912E-04
99	.8851111E-04	.1248272E-03	-.1458179E-03	.9181160E-04
100	.6048482E-01	*.4157668E-02	*.4760902E-02	.1198820E-02
101	.2185910E-04	*.7112011E-01	*.8615908E-04	.1021865E-03
102	.7551680E-04	.1466645E-03	-.1725609E-03	.1113255E-03
103	.7155199E-04	.1388405E-03	-.1501287E-03	.9927484E-04
104	.8581829E-04	.1611325E-03	-.1899165E-03	.1251425E-03
105	.8184420E-04	.1588565E-03	-.1856091E-03	.1215967E-03
106	.9889625E-04	.1743005E-03	-.1982498E-03	.1311274E-03
107	.9209581E-04	.1601174E-03	-.1856259E-03	.1459258E-03
108	.1590109E-03	.2078815E-03	-.2661697E-03	.2271857E-03
109	.1191036E-03	.2029864E-03	-.2112914E-03	.1772156E-03
110	.8630598E-03	.8642588E-03	-.8625492E-03	.8641285E-03
111	.1262088E-03	.5855267E-03	-.1270921E-03	.7811551E-03
112	.1298178E-03	.1291159E-03	-.1291122E-03	.1290779E-03
113	.1180011E-03	.5168411E-03	-.1888887E-03	.1359801E-03
114	.2652217E-03	.1915047E-03	-.5085401E-03	.1765151E-03
115	.2340184E-03	.4005113E-03	-.4867858E-03	.2320651E-03
100	*.4920912E-01	*.8112149E-01	*.4881118E-01	*.8175507E-01
101	.1499865E-03	.2113244E-03	*.5965446E-03	.5211514E-03
102	.1240402E-03	*.6006129E-03	*.6894967E-03	.4130647E-03
103	.1159011E-03	*.6241487E-03	*.6246124E-03	.1076972E-03
8	.1278589E-03	.2520444E-03	.1109115E-03	.1803718E-03
9	.1123459E-03	.2530218E-03	.1128572E-03	-.8519505E-04
10	.1118421E-03	.2160516-03	.2467419E-03	-.1190011E-03
11	.1141593E-03	.2129200E-03	.1455128E-03	*.6105526E-03
12	.1208121E-03	.2215410E-03	.6578551E-03	.6589528E-03
13	.1804398E-03	.2428787E-03	.2872855E-03	*.1302098E-03
14	.1248861E-03	.2119696E-03	.2781924E-03	-.4408749E-03
15	.1998490E-03	.6519005E-03	.6519218E-03	.6525172E-03
16	.1453104E-03	.2719679E-03	.1201621E-03	.1588556E-03
17	.1495195E-03	.2787708E-03	.1216180E-03	.4174402E-03
18	*.1731257E-04	*.1801551E-04	*.5116196E-04	.6880951E-03
19	.1685089E-03	.2707265E-03	.2118188E-03	.8351190E-03
20	.1502918E-03	.2823248E-03	.1271108E-03	.8819279E-03
21	.1511659E-03	.1122225E-03	-.1122188E-03	-.1465048E-03
22	.1706455E-03	.1132161E-03	-.1581042E-03	.6429079E-03
23	-.1575881E-03	.2948525E-03	.1422509E-03	*.1275849E-03
24	.1804191E-03	.5201746E-03	.5791956E-03	-.5709910E-03
25	.1827620E-03	.1018186E-03	-.1622914E-03	.4290817E-03
26	*.2136278E-04	*.4605823E-04	.6791795E-03	*.8211282E-03
27	.1614715E-03	.1092195E-03	.1618817E-03	.4152516E-03
28	.1701066E-03	.1188136E-03	.1745214E-03	.4875117E-03
29	*.6467794E-03	*.6472547E-03	*.6471155E-03	*.6467199E-03
30	.1181369E-03	.5568801E-03	.6605181E-03	.5568414E-03
31	.9115615E-04	.8586170E-04	-.8136619E-04	.1151126E-03
32	*.1580017E-04	*.1664708E-04	*.1589506E-04	.9086290E-04
34	.1170718E-03	.1162801E-03	.1161846E-03	.1045688E-03
35	*.6866416E-04	*.1586159E-04	*.1302411E-04	*.8151752E-04
36	.1286498E-03	.1188769E-03	-.1192421E-03	.1538131E-03
37	.2911607E-03	.2286428E-03	.2270200E-03	.2373111E-03
38	.1809680E-03	*.6556111E-03	*.6559279E-03	.2058449E-03
41	.2261219E-03	.1790020E-03	.4297105E-03	.8598048E-03
44	.2257891E-03	.4131225E-03	.8130408E-03	.8144958E-03
45	.2777715E-03	.5015198E-03	.8106098E-03	.4821682E-03
46	.1598782E-03	.6906499E-03	.6800914E-03	.1278802E-03
49	.6031150E-03	.5212994E-03	.1274554E-03	-.1278107E-03
50	.8291599E-04	*.1797198E-03	*.4771655E-03	*.6310582E-03
51	.2818854E-03	.5412912E-03	-.1218260E-03	-.1266390E-03
52	-.2818629E-03	-.4038154E-03	-.4635127E-03	-.1271811E-03
53	-.2226610E-03	-.4141661E-03	-.1719182E-03	-.6400075E-03
54	-.1070559E-04	-.5301488E-04	-.6438615E-04	-.8880951E-03

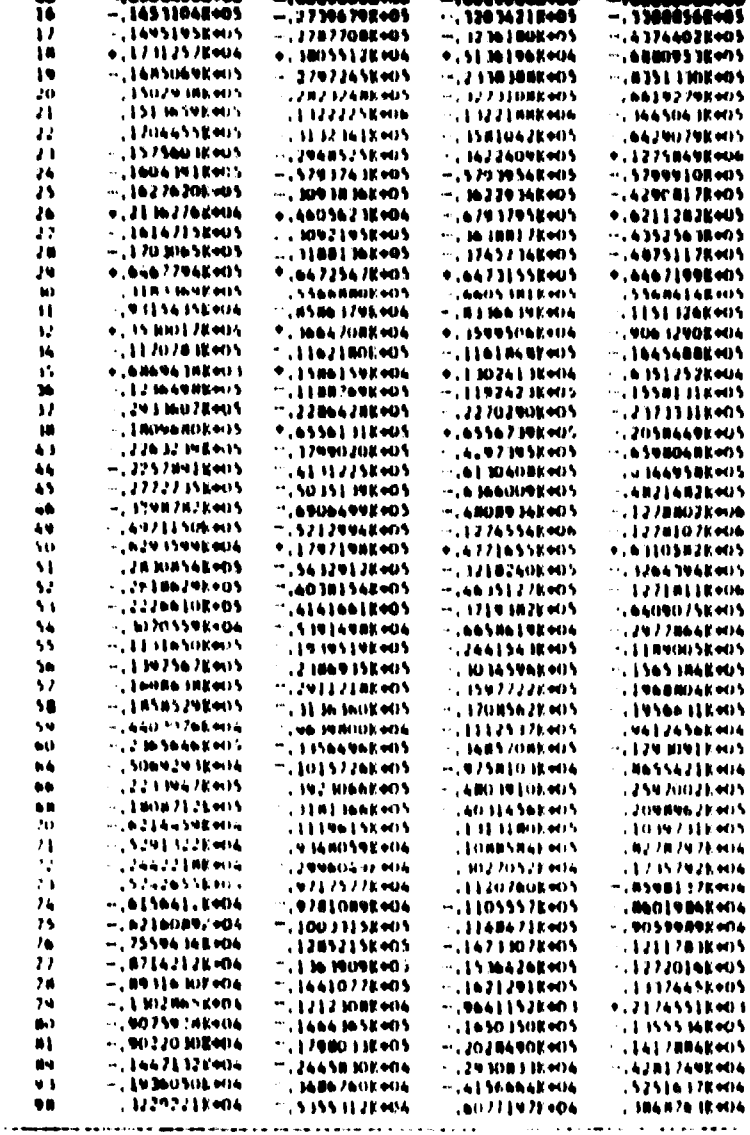

BLANK PAGE

Table B.6. Pressure-strain data from V-6 test
(manual readout from BLH boxes)

Pressure (psi)	Strain (μin./in.) at gage No. -							
	104	106	107	108	109	110	111	112
0	0	0	0	0	0	0	0	0
4,000	630	470	450	490	160	250	250	540
8,000	1,250	910	890	940	250	490	450	1,070
12,000	1,850	1,330	1,280	1,370	450	720	660	1,590
16,000	2,460	1,740	1,660	1,800	640	950	880	2,140
20,000	3,160	2,160	2,110	2,260	840	1,190	1,090	2,790
21,000	3,420	2,310	2,240	2,400	870	1,250	1,150	3,040
21,500	3,570	2,390	2,310	2,490	880	1,280	1,180	3,180
22,000	3,760	2,460	2,390	2,580	890	1,310	1,210	3,360
22,500	3,960	2,540	2,470	2,680	890	1,350	1,250	3,570
23,000	4,210 (4,360)	2,630	2,550	2,780	870	1,400	1,280	3,790 (3,870)
23,500	4,460 (4,620)	2,740	2,620	2,890	860	1,440	1,320	3,970 (4,110)
24,000	4,810 (4,970)	2,870	2,720	3,030	820	1,500	1,360	4,300 (4,420)
24,500	5,150 (5,350)	2,980	2,810	3,160	780	1,560	1,410	4,600 (4,750)
25,000	5,550 (5,830)	3,240	2,930	3,340	740	1,640	1,460	4,980 (5,180)
25,500	6,240 (6,630)	3,400	3,140	3,660	640	1,820 (2,070)	1,550	5,610 (5,890)
26,000	6,960 (7,510)	3,720	3 390	4,030	450	2,580 (2,980)	1,610	6,270 (6,670)
26,500	8,310 (9,210)	4,430	3,920	4,810	160	4,570 (5,790)	1,780	7,520 (8,190)
27,000	12,100 (13,100)	5,310	4,620	5,750	260 (350)	10,050 (10,760)	4,000 (4,890)	11,100 (11,820)
27,500	16,490	6,750	5,790	7,250	770	13,470	7,150	14,850
27,500	17,730	7,120	6,060	7,550	910	14,180	7,530	15,730
27,500	17,850 (18,140)	7,380	6,280	7,830	1,020 (1,110)	14,280 (14,470)	7,620	15,850 (16,040)
27,500	18,260					14,550		16,140
27,900	21,130	10,390	8,890	10,770	1,690	16,270	8,300	18,910
27,600	21,610	10,690	9,150	11,030	1,750	16,750	8,410	18,830
27,900	21,740	10,890	9,350	11,200	1,850	16,850	8,460	18,960
27,800	21,860					16,940		19,050
27,900	21,950					17,000		19,130
28,250	23,890	13,760	12,160	13,750	2,250	17,900	8,550	21,060
27,900	24,690					18,380		21,560
28,250	24,890	14,320	12,670	14,230	2,320	18,490	8,620	21,760
28,100	25,280					18,590		22,090
28,250	25,380	14,620	12,950	14,490	2,360	18,620	8,650	22,180
28,200	25,500					18,650		22,290
28,500	25,630	14,830	13,150	14,690	2,380	18,700	8,680	22,430
28,300	26,020					18,750		22,760
28,500	26,200	15,210	13,490	15,020	2,400	18,790	8,710	22,930
28,400	26,440					18,850		23,120
28,750	26,750	15,800	14,060	15,580	2,380	18,970	8,750	23,450
28,500	27,400					19,190		24,000
28,750	27,660	16,440	14,620	9,740	2,370	19,340	8,930	24,310
28,600	28,320					19,750		24,826
28,750	28,470	17,120	15,180	9,470	2,380	19,870	9,080	24,970

BLANK PAGE

27,800	21,860							
27,900	21,950					17,000		19,130
28,250	23,890	13,760	12,160	13,750	2,250	17,900	8,550	21,660
27,900	24,690					18,380		21,560
28,250	24,890	14,320	12,670	14,230	2,320	18,490	8,620	21,760
28,100	25,280					18,590		22,090
28,250	25,580	14,620	12,950	14,490	2,360	18,620	8,650	22,180
28,200	25,500					18,650		22,290
28,500	25,630	14,830	13,150	14,690	2,380	18,700	8,680	22,430
28,300	26,020					18,750		22,760
28,500	26,200	15,210	13,490	15,020	2,400	18,790	8,710	22,930
28,400	26,440					18,850		23,120
28,750	26,750	15,800	14,060	15,580	2,380	18,970	8,750	23,450
28,500	27,400					19,190		24,000
28,750	27,660	16,440	14,620	9,740	2,370	19,340	8,930	24,310
28,600	28,320					19,750		24,826
28,750	28,470	17,120	15,180	9,470	2,380	19,870	9,080	24,970
28,600	28,890					20,160		25,310
28,750	28,980	17,470	15,490		2,400	20,210	9,150	25,410
28,700	29,160					20,340		25,560
29,000	29,450	17,970	15,930		2,390	20,540	9,330	25,920
28,700	30,110					20,980		26,400
29,000	30,290	18,590	16,450		2,350	21,110	9,530	26,580
28,800	30,690					21,370		26,930
29,000	30,810	19,000	16,810		2,320	21,460	9,670	27,040
28,900	31,190					21,680		27,350
29,250	31,550	19,600	17,330		2,250	21,900	9,930	27,780
	(32,270)					(22,340)		(28,350)
29,250	32,520	20,300	17,910		2,160	22,490	10,170	28,630
29,100	33,050					22,850		29,050
29,250	33,230	20,760	18,320		2,080	22,940	10,340	29,220
29,100	33,500					23,110		29,440
29,500	33,870	21,340	18,850		1,950	23,330	10,610	29,890
29,150	34,800					23,880		30,590
29,500	34,970	22,060	19,450		1,780	23,980	10,850	30,800
29,300	35,510					24,310		31,230
29,500	35,640	22,520	19,836		1,640	24,390	11,040	31,370
29,500	35,820					24,480		31,520
29,750	35,970	22,790	20,090		1,520	24,590	11,160	31,700
29,600	36,510					24,930		32,150
29,750	36,750	23,290	20,500		1,270	25,100	11,370	32,410
29,600	37,270					25,500		32,910
29,750	37,360	23,710	20,890		1,050	25,570	11,550	32,940
30,000	38,060	24,320	21,410			26,060	11,790	33,650

Table B.6. (continued)

Pressure (psi)	Strain (μin./in.) at gage No. –							
	104	106	107	108	109	110	111	112
29,700	38,960					26,610		34,340
30,000	39,130	25,050	22,040		270	26,750	12,150	34,640
29,800	39,730					27,120		35,120
30,000	39,930	25,520	22,450		30	27,200	12,370	35,280
29,900	40,360					27,450		35,630
30,000	40,500	25,900	22,760		280	27,550	12,530	35,790
29,800	41,050	26,250	23,080		540	27,890	12,680	36,270
30,000	41,140	26,300	23,140		560	27,930	12,720	36,350
30,250	41,310	26,430	23,260		670	28,010	12,790	36,520
30,200	41,690					28,190		36,880
30,500	41,950	26,840	23,610		1,220	28,370	12,990	37,270
30,100	43,290				2,070	29,360		38,470
30,500	43,470	27,660	24,370		2,230	29,460	13,410	38,700
30,400	44,050					29,820		39,230
30,750	44,600	28,500	25,080		3,330	30,210	13,830	40,030
30,200	45,980	29,170	25,660		4,090	31,220	14,090	41,110
30,750	46,250	29,490	25,940		4,480	31,380	14,240	41,520
30,500	47,190				5,000	31,790		42,250
30,750	47,270	30,080	26,480		5,320	31,880	14,480	42,450
30,600	47,770					32,160		42,900
31,000	48,400	30,960	27,280		7,550	32,640	14,950	44,030
30,500	49,700					33,470		44,880
31,000	50,000	31,740	27,970		8,840	33,690	15,280	45,360
30,750	50,750					34,150		46,000
31,000	51,020	32,340	28,510		10,130	34,350	15,550	46,440
30,800	51,840	32,700	28,820		10,800	34,860	15,680	47,140
31,250	52,520	33,260	29,350		12,900	35,170	16,050	48,160
30,850	53,790	33,760	29,710		14,110	36,340	16,260	49,160
31,250	54,170	34,100	144,530		15,450	36,570	16,500	49,640
31,000	55,020					37,020		50,390
31,500	56,800	35,630			18,940	38,430	17,270	52,600
31,000	58,050	36,120			19,040	39,400	17,500	53,480
31,500	58,450	36,450			19,210	39,630	17,670	53,950
31,250	59,230	36,850			19,440	40,020	17,820	54,550
31,750	60,470	37,650			20,270	41,500	18,100	56,220
31,250	61,740	38,060			20,220	42,050	18,440	57,100
31,750	62,310	38,570			20,190	42,840	18,690	57,940
31,400	63,300	38,950			20,100	43,340	18,980	58,620
31,600	70,160	43,580			17,000	50,520	21,380	65,720
31,900	70,390						21,240	

Appendix C

DETERMINATION OF STRESS AND STRAIN FIELDS FOR AN INTERNALLY PRESSURIZED ELASTIC-PLASTIC THICK-WALLED HOLLOW CYLINDER USING A TRILINEAR STRESS-STRAIN CURVE

The closed-form solution for the elastic-plastic stress and strain fields in a long, closed-end cylinder loaded by internal pressure has been extended to include material with a trilinear stress-strain curve. The solution for a bilinear material was presented by Bland,[1] and the geometry of the problem is described in Fig. C.1. The following features are built into the problem.

1. The cylinder is assumed to be "long" in the sense that all quantities F are assumed independent of z; that is,

$$\frac{\partial F}{\partial z} = 0 . \tag{C.1}$$

The results obtained are therefore restricted to the central section of the cylinder sufficiently distant from the ends.

2. The problem is completely axisymmetric, both in terms of geometry and applied load. No circumferential displacement and no θ dependence in any quantities are admitted, so

$$v \equiv 0 , \quad \frac{\partial(F)}{\partial \theta} = 0 . \tag{C.2}$$

3. The condition of "closed ends" is used, so that both the axial stress and the axial strain are nonzero at every point.

ORNL-DWG 75-321

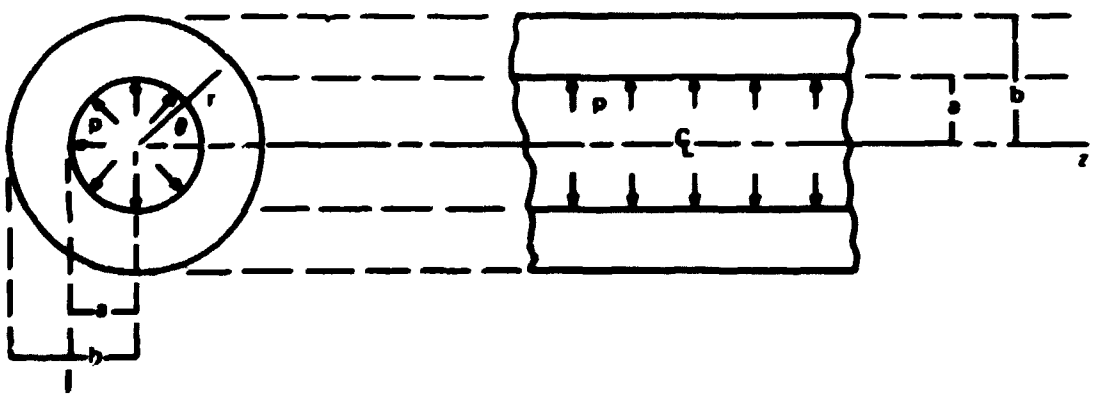

Fig. C.1. Circular cylinder with internal pressure.

BLANK PAGE

4. The Tresca yield condition is used. Since for the thick-walled cylinder, $\sigma_\theta > \sigma_z > \sigma_r$ for all r and p, the Tresca condition reduces to the statement that yield (further plastic strain) occurs at some r if at that position the yield function given by

$$f = \sigma_\theta - \sigma_r \tag{C.3}$$

is equal to the hardening parameter K.

5. No creep (time dependence) is included.

6. Body forces are neglected.

7. The material, when tested in uniaxial tension, produces a trilinear stress-strain curve as shown in Fig. C.2. The curve of Fig. C.2 exhibits three distinct regions: (1) region A ($0 < \sigma < Y_{\sigma 1}$) – linear elastic behavior, with Young's modulus E and Poisson's ratio ν; (2) region B ($Y_{\sigma 1} < \sigma < \sigma_s$) – plastic behavior

ORNL-DWG 75-322

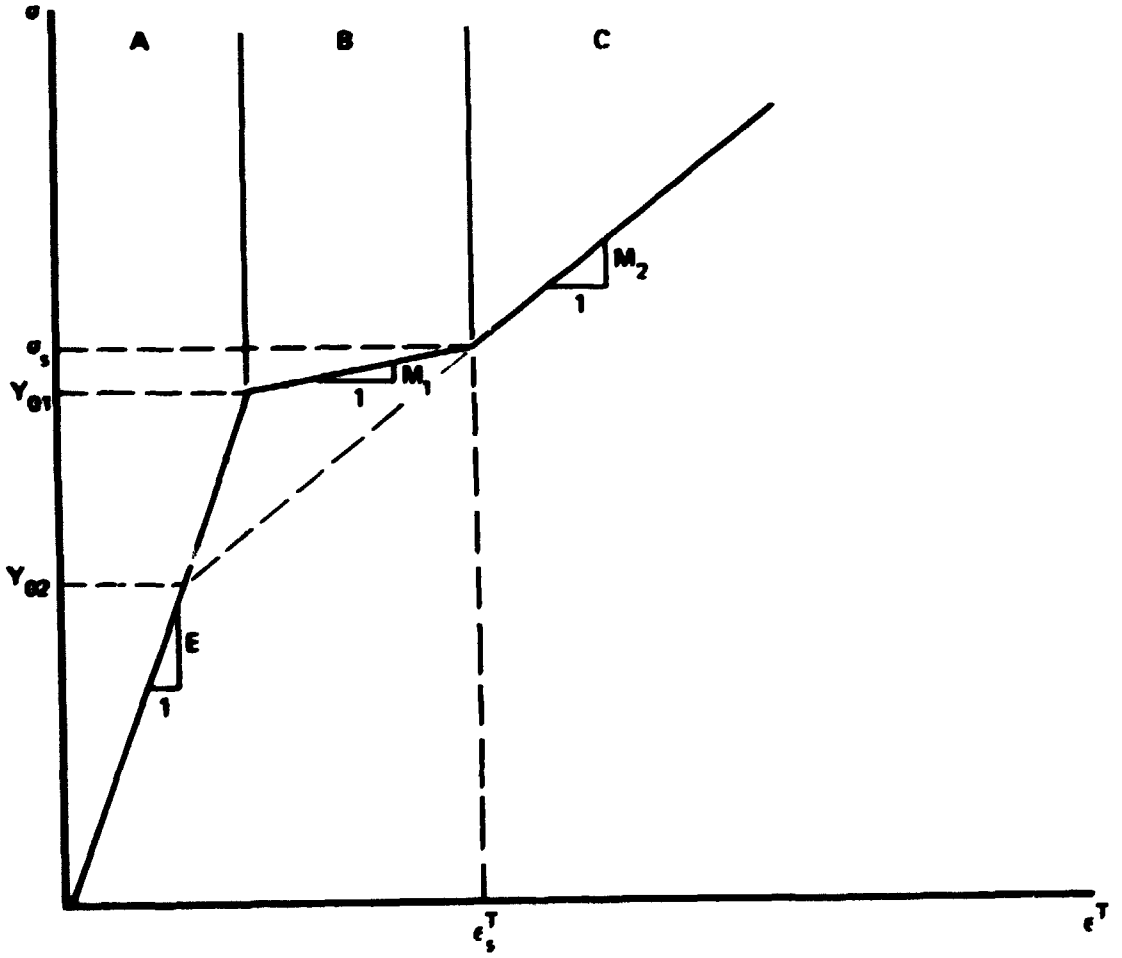

Fig. C.2. Stress-strain curve from a uniaxial tension test for a trilinear material; true stress vs true total strain.

with linear strain hardening, with the hardening parameter described by

$$K = Y_{\sigma 1} + M_1 (\epsilon^T - Y_{\sigma 1}/E) = Y_{\sigma 1} (1 + \eta_1 \epsilon^P) . \tag{C.4}$$

where $M_1 \geq 0$; and (3) region C ($\sigma > \sigma_s$) – plastic behavior with linear strain hardening, with the hardening parameter described by

$$K = Y_{\sigma 2} + M_2 (\epsilon^T - Y_{\sigma 2}/E) = Y_{\sigma 2} (1 + \eta_2 \epsilon^P) . \tag{C.5}$$

where $M_2 \geq M_1$.

Conventional pressure vessel steel is well represented by this trilinear model. In the HSST program intermediate vessel tests, cylindrical steel vessels with surface flaws were pressurized to rupture. This analysis affords a means of predicting nominal surface strains in the central region of the vessel, at points remote from the test flaws. These strains are used for predicting fracture in the elastic-plastic range.

The solution also finds use as a standard with which to assess the operation of a finite-element code in solving an elastic-plastic problem with strain hardening. As a test problem, the pressurized cylinder is convenient to model with finite elements and has sufficient complexity to bring into focus much of the workings of the code in question.

Qualitative Summary of the Response

As the internal pressure is increased from zero, the cylinder responds in five stages, as represented in Fig. C.3. Note that it has been assumed that the elastic zone will disappear before the inside wall enters region C. A necessary and sufficient condition for this to occur is that

$$\frac{b}{a} < \left\{ 1 + \left| \frac{E + Y_{\sigma 1}(1 - \nu^2)\eta_1}{Y_{\sigma 1}(1 - \nu^2)} \right| \epsilon_s^P \right\}^{1/2} . \tag{C.6}$$

Formulation

The equations governing the problem are the following.

Equilibrium

Radial (using axisymmetry): $$\frac{d\sigma_r}{dr} = \frac{\sigma_\theta - \sigma_r}{r} . \tag{C.7}$$

Axial (neglecting weight): $$\int_a^b \sigma_z 2\pi r dr = p\pi a^2 . \tag{C.8}$$

Strain displacement

$$\epsilon_r = \frac{du}{dr} . \tag{C.9}$$

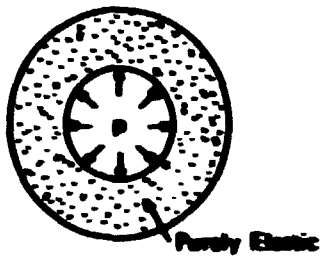

Stage I: Purely Elastic ($0 < p < p_a$)
The entire cylinder is in region A of the stress–strain curve. (See Fig. 1.3)

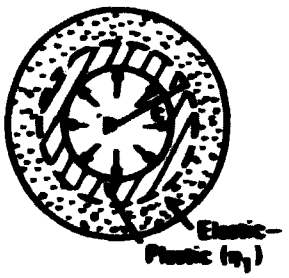

Stage II: Elastic–Plastic (η_1) ($p_a < p < p_b$)
At $p = p_a$ the inside wall just yields. A plastic region develops and progresses across the cylinder as the pressure is increased. For some p in this range, the elastic–plastic interface is at $r = c$, the plastic portion being in region B of the stress–strain curve.

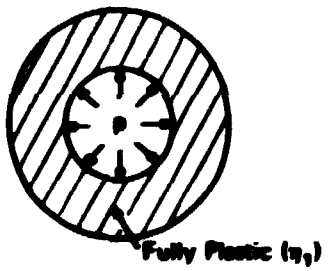

Stage III: Fully Plastic (η_1) ($p_b < p < p_c$)
At $p = p_b$ the outside wall just yields. In this stage the entire cylinder is in region B.

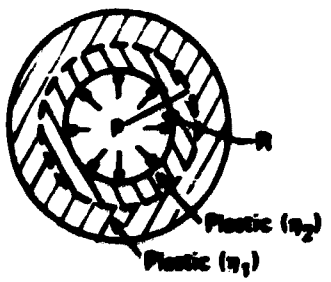

Stage IV: Plastic (η_1)–Plastic (η_2) ($p_c < p < p_d$)
At $p = p_c$ the inside wall enters region C. As p increases, the interface at $r = R$ separating the η_1 and the η_2 material moves radially outward. At $p = p_d$, $R = b$.

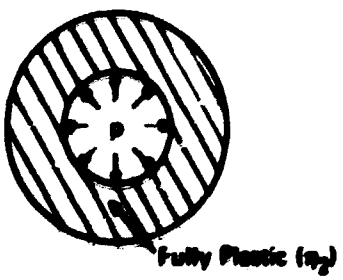

Stage V: Fully Plastic (η_2) ($p > p_d$)
Next follows a stage for which the entire cylinder is in region C. The material continues to harden as the pressure increases.

Fig. C.1. Behavior of the cylinder as pressure is increased, exhibiting five distinct stages.

$$\epsilon_\theta = \frac{u}{r}. \tag{C.10}$$

No warpage of r–θ plane

$$\epsilon_z = \text{constant (independent of r)}. \tag{C.11}$$

This is a condition termed "generalized plane strain."

In addition, in the zones indicated, the following relationships hold.

Elastic zone constitutive relations

At all points in region A, Hooke's law:

$$\epsilon_r = \frac{1}{E}(\sigma_r - \nu\sigma_\theta - \nu\sigma_z),$$

$$\epsilon_\theta = \frac{1}{E}(-\nu\sigma_r + \sigma_\theta - \nu\sigma_z), \tag{C.12}$$

$$\epsilon_z = \frac{1}{E}(-\nu\sigma_r - \nu\sigma_\theta + \sigma_z).$$

Plastic zone constitutive relations

At all points in regions B or C, the yield condition is satisfied; that is, the yield function equals the hardening parameter.

$$f = K. \tag{C.13}$$

Strain hardening. Equations (C.4) and (C.5) are generalized to this triaxial problem as

$$K = \begin{cases} Y_{\theta 1}(1 + \eta_1 \epsilon_\theta^p); & \text{all points in region B} \\ Y_{\theta 2}(1 + \eta_2 \epsilon_\theta^p); & \text{all points in region C} \end{cases} \tag{C.14}$$

It can be proved from incremental theory that this is the only generalization consistent with the Tresca yield condition. So from Eq. (C.13),

$$\sigma_\theta \quad \sigma_r = \begin{cases} Y_{\theta 1}(1 + \eta_1 \epsilon_\theta^p); & \text{all points in region B} \\ Y_{\theta 2}(1 + \eta_2 \epsilon_\theta^p); & \text{all points in region C} \end{cases} \tag{C.15}$$

Normality. The flow rule relates plastic strain increments to f by

$$d\epsilon_{ij}^p = \lambda \frac{\partial f}{\partial \sigma_{ij}}. \tag{C.16}$$

In particular,

$$d\epsilon_z^P = \lambda \frac{\partial f}{\partial \sigma_z} = 0 .$$

because f is not a function of σ_z; so

$$\epsilon_z^P = 0 . \tag{C.17}$$

Plastic incompressibility. From Eq. (C.16),

$$d\epsilon_r^P = \lambda \frac{\partial f}{\partial \sigma_r} = -\lambda . \tag{C.18}$$

$$d\epsilon_\theta^P = \lambda \frac{\partial f}{\partial \sigma_\theta} = \lambda . \tag{C.19}$$

Integrating Eqs. (C.17), (C.18), and (C.19), the dilatation for small strain is

$$\epsilon_r^P + \epsilon_z^P + \epsilon_\theta^P = 0 , \tag{C.20}$$

with the physical interpretation that no volume change accompanies plastic strain.

Hooke's law. ϵ_z and the elastic components of ϵ_r and ϵ_θ are still related to stress by Hooke's law in all regions of the cylinder. Therefore,

$$\epsilon_r^E = \frac{1}{E}(\sigma_r - \nu\sigma_\theta - \nu\sigma_z) .$$

$$\epsilon_\theta^E = \frac{1}{E}(-\nu\sigma_r + \sigma_\theta - \nu\sigma_z) . \tag{C.21}$$

$$\epsilon_z = \frac{1}{E}(-\nu\sigma_r - \nu\sigma_\theta + \sigma_z) .$$

Boundary condition

$$\sigma_r(r = a) = -p , \tag{C.22}$$

$$\sigma_r(r = b) = 0 . \tag{C.23}$$

Continuity at interface

In stage II at $r = c$ and in stage IV at $r = R$, all components of stress, strain, and displacement are continuous across the internal boundaries.

Results

Details to the solution procedure and closed-form expressions for σ_r, σ_θ, σ_z, ϵ_r, ϵ_θ, and ϵ_z as functions of r for the five stages of the problem will be presented in a future report.

A FORTRAN IV program has been written to evaluate and plot these functions. (A listing of the program is attached to this appendix.) Material behavior is described by inputting the six constants ν, E, M_1, M_2, Y_{01}, and ϵ_z^I (see Fig. C.2) that are required for the analysis. The program has been run on the IBM 360/91 for a large range of pressures. Values for the material constants were easily obtained from stress-strain curves from uniaxial tension tests[2] performed on specimens taken from the prolongation of intermediate vessel V-1.

Graphs of stresses and strains corresponding to a pressure in stage II are presented in Fig. C.4 and Fig. C.5, respectively. Note from the σ_r curve that the boundary conditions of Eqs. (C.22) and (C.23) are met. An interesting feature is that σ_θ reaches a maximum at r = c.

The quantities that are measured by strain gages in these intermediate vessel tests are ϵ_z and ϵ_θ at the inside and outside walls (i.e., at r = a and r = b respectively). For all values of p and r, ϵ_z is found to be

$$\epsilon_z = \frac{(1 - 2\nu)}{E(b^2/a^2 - 1)}\, p. \tag{C.24}$$

The computed curve of circumferential strain at the outside wall, $\epsilon_{\theta b}$, vs pressure, p, is sketched in Fig. C.6. The curve is linear for all values of pressure corresponding to stages I, III, and V and nonlinear in stages II and IV. This nonlinearity is a consequence of the internal boundary present in stages II and IV (see Fig. C.3).

Expressions for p_a, p_b, p_c and p_d, and $\epsilon_{\theta b}$, the circumferential strain at the outside wall at these pressures, follow. Much of the curve in Fig. C.6 can be constructed from them.

$$p_a = \frac{Y_{01}}{2}(1 - a^2/b^2). \tag{C.25a}$$

$$p_b = \frac{Y_{01}}{K_1}\left|\ln(b/a) + \frac{Y_{01}\eta_1(1 - \nu^2)(b^2/a^2 - 1)}{2E}\right|. \tag{C.25b}$$

$$p_c = \frac{Y_{01}}{K_1}\left|\ln(b/a) + \frac{Y_{01}\eta_1(b^2/a^2 - 1)}{2b^2/a^2}\right| + \left|\epsilon_z^P + \frac{Y_{01}(1 - \nu^2)}{K_1}\right|. \tag{C.25c}$$

$$p_d = \frac{Y_{02}}{K_2}\left[\ln(b/a) + \eta_2(b^2/a^2 - 1)/2\right]. \tag{C.25d}$$

At pressure p_a,

$$\epsilon_{\theta b} = \frac{(1 - \nu/2)Y_{01}a^2/b^2}{E}. \tag{C.26a}$$

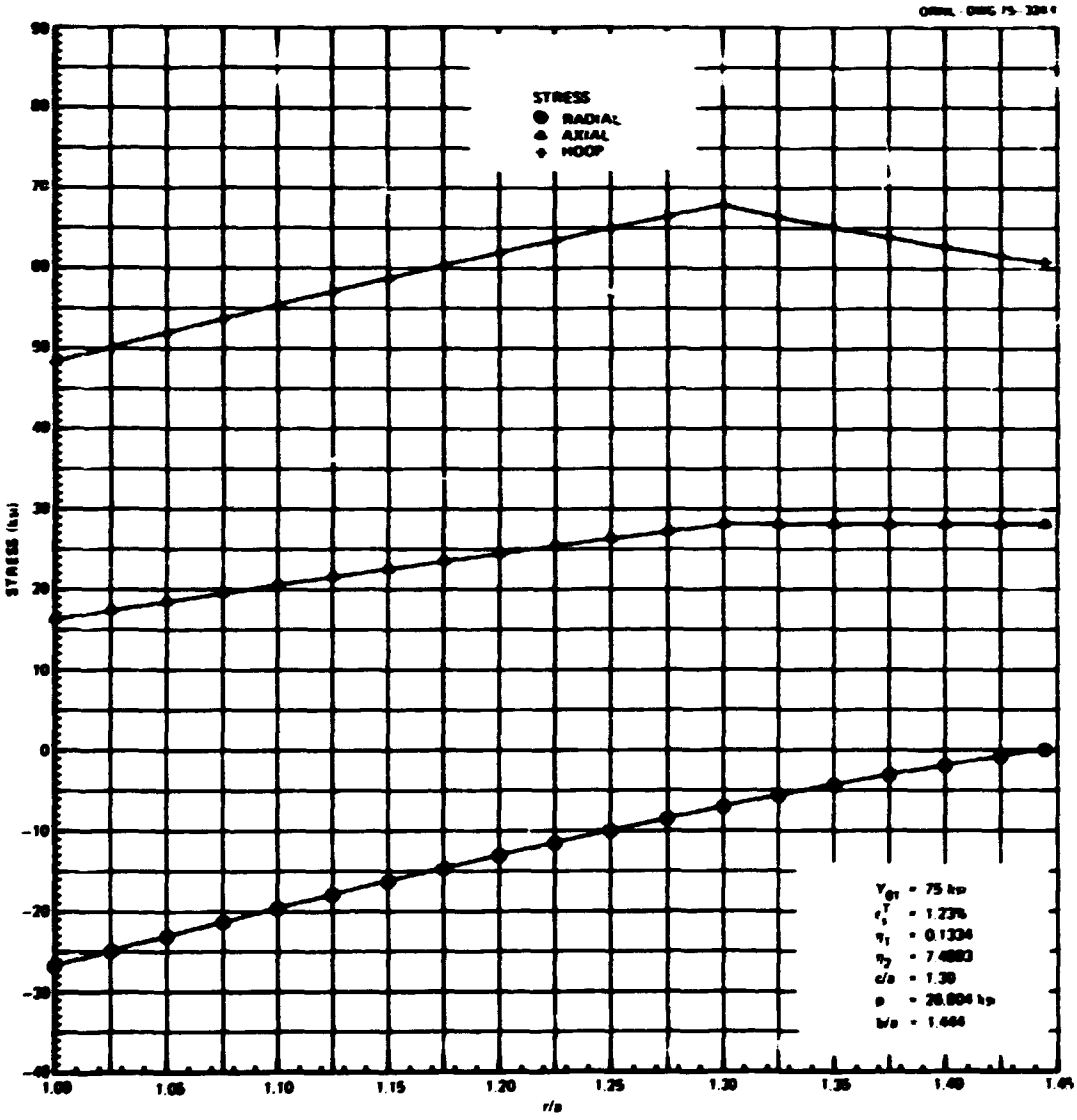

Fig. C.4. Stress vs r/a for a pressure in stage II.

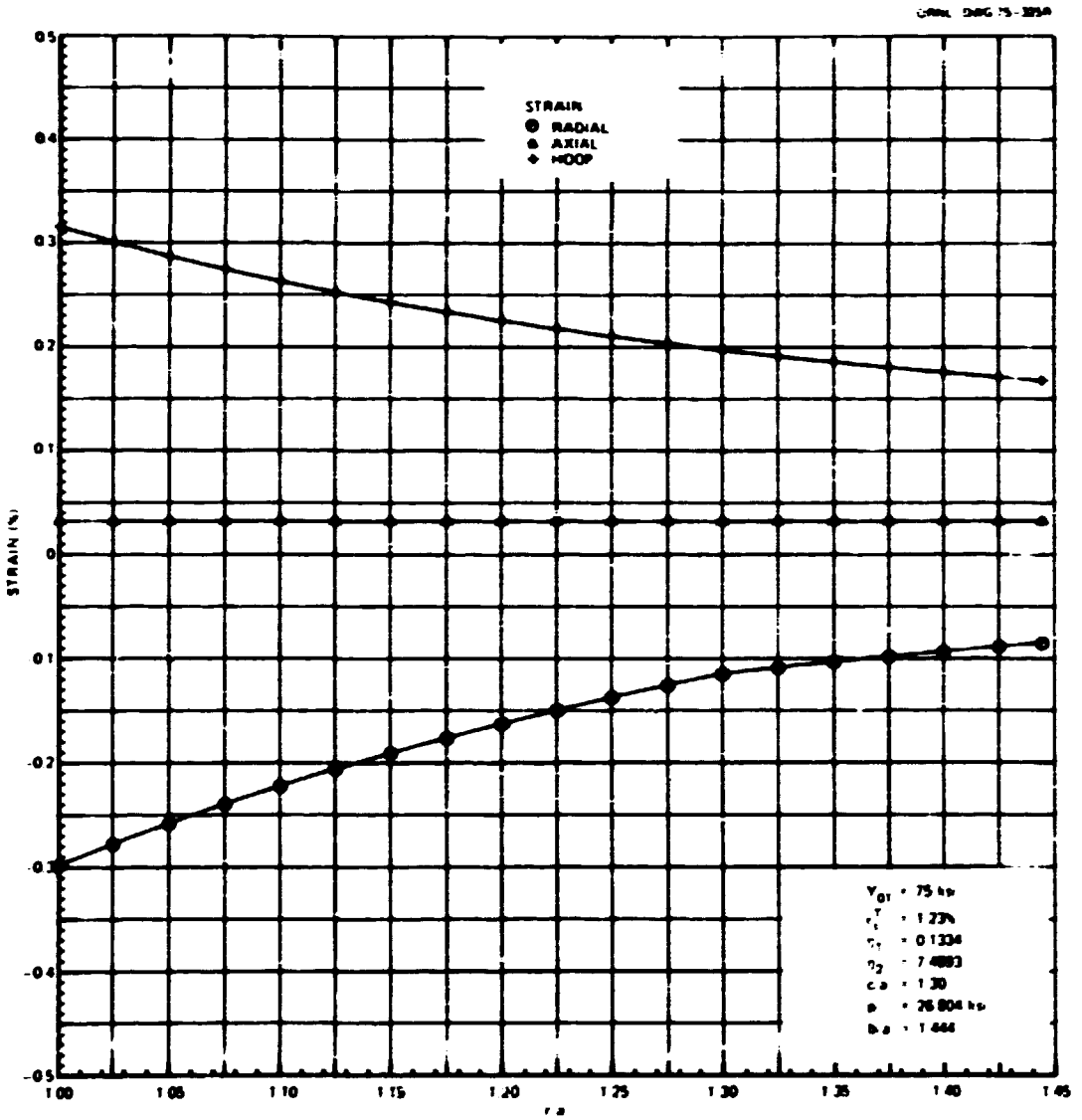

Fig. C.5. Strain vs r/a for a pressure in stage II.

ORNL DWG 75 326

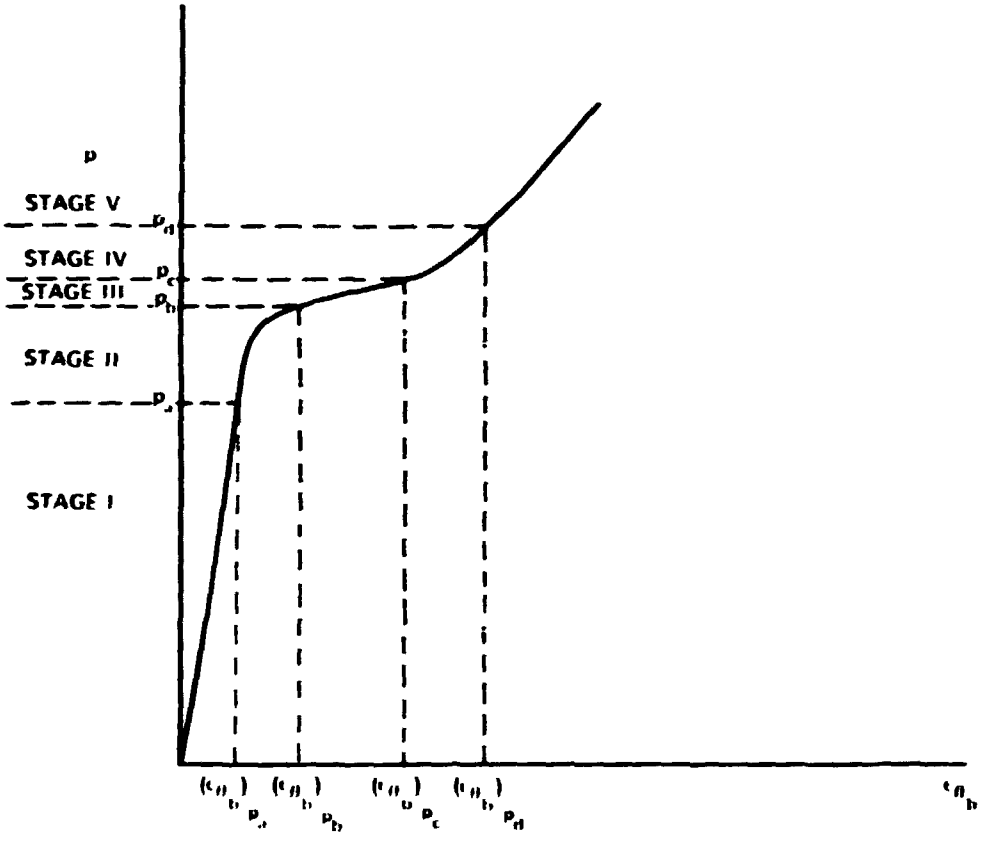

Fig. C.6. Computed pressure vs circumferential strain at the outside wall.

At pressure p_b.

$$\epsilon_{\theta b} = -\frac{\nu(1-2\nu)Y_{01}}{(b^2/a^2-1)K_1}\left[\ln b/a + \frac{Y_{01}\eta_1(1-\nu^2)(b^2/a^2-1)}{2E}\right] + \frac{Y_{01}(1-\nu^2)}{E}. \qquad \text{(C.26b)}$$

At pressure p_c.

$$\epsilon_{\theta b} = \frac{\nu(1-2\nu)Y_{01}}{(b^2/a^2-1)K_1}\ln b/a + \left\{\frac{(1-2\nu)Y_{01}\eta_1[(b^2/a^2-1)(1+\nu)-\nu]+2K_1}{2Eb^2/a^2}\right\} \times \left[\epsilon_s^p + \frac{Y_{01}(1-\nu^2)}{K_1}\right]. \qquad \text{(C.26c)}$$

At pressure p_d.

$$\epsilon_{\theta b} = \frac{\nu(1-2\nu)Y_{02}}{(b^2/a^2-1)K_2}\left[\ln b/a + \frac{\eta_2(b^2/a^2-1)Q}{2}\right] + Q, \qquad \text{(C.26d)}$$

where

$$K_1 = E + Y_{\theta 1}\eta_1(1 - \nu^2), \tag{C.27}$$

$$K_2 = E + Y_{\theta 2}\eta_2(1 - \nu^2), \tag{C.28}$$

$$Q = \frac{K_1 Y_{\theta 2} - K_2 Y_{\theta 1}}{K_2 Y_{\theta 1}\eta_1 - K_1 Y_{\theta 2}\eta_2}. \tag{C.29}$$

Comparison with Experimental Data

Comparison will be made with vessel V-1 test data, since material constants can be furnished for the prolongation of this vessel. The comparison is complicated by the fact that the properties of the vessel are not uniform. As a result of the quenching process, the steel near the walls of the vessel has a significantly higher yield stress than the center material. Figure C.7 shows a successful match.

References

1. D. R. Bland, "Elastoplastic Thick-Walled Tubes of Work-Hardening Material Subject to Internal and External Pressures and to Temperature Gradients," *J. Mech. Phys. Solids* 4, 209–29 (1955–56).

2. R. W. Derby et al., *Test of 6-Inch-Thick Pressure Vessels. Series 1: Intermediate Test Vessels V-1 and V-2*, ORNL-4895, Tables D-1 and D-4 (February 1974).

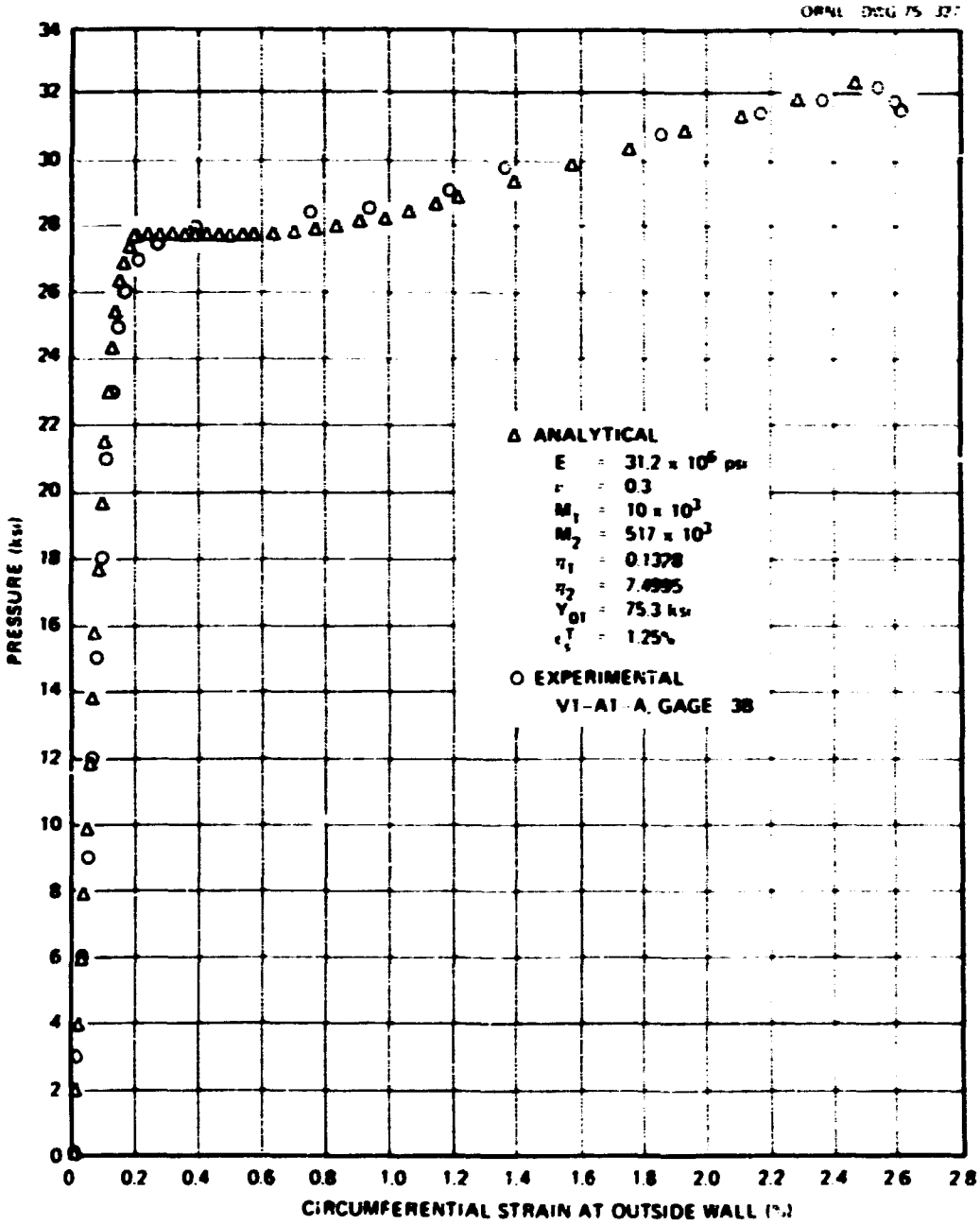

Fig. C.7. Pressure vs circumferential strain at the outside wall (analytical vs experimental), h/a = 1.444.

FORTRAN IV LISTING

```
C                                                                       10
C       THIS PROGRAM COMPUTES STRESSES AND STRAINS FOR A 'TRILINEAR'    20
C     ELASTIC-PLASTIC HOLLOW CYLINDER UNDER INTERNAL PRESSURE.  FOR     30
C     EACH SELECTED PRESSURE, THE OUTPUT GIVES RADIAL, AXIAL, AND HOOP  40
C     STRESSES AND STRAINS AT THE DESIRED RADIAL LOCATIONS.  THE FOUR   50
C     TRANSITION PRESSURES PA, PB, PC, AND PD ARE ALSO OUTPUT.          60
C                                                                       70
C                                                                       80
C                                                                       90
C          IDENTIFICATION OF VARIABLES                                 100
C                                                                      110
C     BA        RATIO OF OUTER TO INNER RADIUS OF CYLINDER (B/A)       120
C     CA        IN STAGE II, RATIO OF ELASTIC-PLASTIC(N1) INTERFACE TO 130
C               INNER RADIUS OF CYLINDER (C/A)                         140
C     E         YOUNG'S MODULUS, OR SLOPE OF REGION A OF STRESS-STRAIN 150
C               CURVE                                                  160
C     EP1       SLOPE OF REGION B OF STRESS-STRAIN CURVE               170
C     EP2       SLOPE OF REGION C OF STRESS-STRAIN CURVE               180
C     EPSA      AXIAL STRAIN                                           190
C     EPSR      RADIAL STRAIN                                          200
C     EPST      HOOP STRAIN                                            210
C     EPSSP     THE PLASTIC STRAIN AT WHICH REGION B ENDS AND REGION C 220
C               BEGINS ON THE STRESS-STRAIN CURVE                      230
C     EPSST     THE TOTAL STRAIN AT WHICH REGION B ENDS AND REGION C   240
C               BEGINS ON THE STRESS-STRAIN CURVE                      250
C     ETA1      MATERIAL COEFFICIENT APPEARING IN REGION B STRAIN-     260
C               HARDENING EXPRESSION                                   270
C     ETA2      MATERIAL COEFFICIENT APPEARING IN REGION C STRAIN-     280
C               HARDENING EXPRESSION                                   290
C     NPINT1    NUMBER OF EQUALLY-SPACED INTERVALS OF PRESSURE IN      300
C               STAGE I, RANGING FROM ZERO TO PA                       310
C     NPINT2    NUMBER OF EQUALLY-SPACED INTERVALS OF PRESSURE IN      320
C               STAGE II, RANGING FROM PA TO PB                        330
C     NPINT3    NUMBER OF EQUALLY-SPACED INTERVALS OF PRESSURE IN      340
C               STAGE III, RANGING FROM PB TO PC                       350
C     NPINT4    NUMBER OF EQUALLY-SPACED INTERVALS OF PRESSURE IN      360
C               STAGE IV, RANGING FROM PC TO PD                        370
C     NPINT5    NUMBER OF 500 PSI PRESSURE INCREMENTS ABOVE PD IN      380
C               STAGE V                                                390
C     NOTE THAT OUTPUT IS OBTAINED FOR THE PRESSURES THAT BOUND EACH   400
C               INTERVAL                                               410
C     NRINT     NUMBER OF EQUALLY-SPACED INTERVALS OF RADIUS RANGING   420
C               FROM THE INNER TO THE OUTER RADIUS OF THE CYLINDER     430
C               OUTPUT IS OBTAINED AT THE END POINTS OF EACH INTERVAL  440
C     P         INTERNAL PRESSURE                                      450
C     PA        FIRST TRANSITION PRESSURE, SEPARATING STAGES I AND II  460
C     PB        SECOND TRANSITION PRESSURE, SEPARATING STAGES II AND III 470
C     PC        THIRD TRANSITION PRESSURE, SEPARATING STAGES III AND IV 480
C     PD        FOURTH TRANSITION PRESSURE, SEPARATING STAGES IV AND V  490
C     POIS      POISSON RATIO                                          500
C     RA        RATIO OF THE RADIUS OF A SELECTED POINT IN THE CYLINDER 510
C               TO THE INSIDE RADIUS (R/A)                             520
C     RSA       IN STAGE IV, RATIO OF PLASTIC(N1)-PLASTIC(N2) INTERFACE 530
C               RADIUS TO INNER RADIUS OF CYLINDER (RS/A)              540
C     SIGA      AXIAL STRESS                                           550
C     SIGR      RADIAL STRESS                                          560
C     SIGT      HOOP STRESS                                            570
C     X         ARRAY THAT STORES THE RADIAL POSITIONS FOR WHICH OUTPUT 580
C               IS DESIRED                                             590
C     YO1       FIRST YIELD STRESS, APPEARING IN REGION B STRAIN-      600
C               HARDENING EXPRESSION                                   610
C     YO2       SECOND YIELD STRESS, APPEARING IN REGION C STRAIN-     620
C               HARDENING EXPRESSION                                   630
C                                                                      640
C                                                                      650
C                                                                      660
```

```
C          INPUT                                                          670
C                                                                         680
C          THE USER SUPPLIES THE FOLLOWING FOUR INPUT CARDS               690
C                                                                         700
C     CARD 1  -  TITLE                                                    710
C                READ(5,1000) TITLE                                       720
C           1000 FORMAT(20A4)                                             730
C                                                                         740
C     CARD 2  -  MATERIAL PROPERTIES                                      750
C                READ(5,1020) E,POIS,YC1,EM1,EM2,EPSST                    760
C           1020 FORMAT(6F10.0)                                           770
C                                                                         780
C     CARD 3  -  GEOMETRY                                                 790
C                READ(5,1030) BA,NPINT                                    800
C           1030 FORMAT(F10.0,I5)                                         810
C                                                                         820
C     CARD 4  -  PRESSURE INCREMENTS                                      830
C                READ(5,1040) NPINT1,NPINT2,NPINT3,NPINT4,NPINT5          840
C           1040 FORMAT(5I5)                                              850
C                                                                         860
C                                                                         870
C                                                                         880
C                                                                         890
      DIMENSION X(1000),TITLE(20)                                         900
C                                                                         910
C     READ INPUT                                                          920
C                                                                         930
      READ(5,1000) TITLE                                                  940
 1000 FORMAT(20A4)                                                        950
      WRITE(6,1010) TITLE                                                 960
 1010 FORMAT(1H1,20A4///)                                                 970
      READ(5,1020) E,POIS,YC1,EM1,EM2,EPSST                               980
 1020 FORMAT(6F10.0)                                                      990
      READ(5,1030) BA,NPINT                                              1000
 1030 FORMAT(F10.0,I5)                                                   1010
      READ(5,1040) NPINT1,NPINT2,NPINT3,NPINT4,NPINT5                    1020
 1040 FORMAT(5I5)                                                        1030
C                                                                        1040
C     DEFINE CONVENIENT INTERMEDIATE VARIABLES                           1050
C                                                                        1060
      NPIN=NPINT+1                                                       1070
      NPIN1=NPINT1+1                                                     1080
      NPIN2=NPINT2+1                                                     1090
      NPIN3=NPINT3+1                                                     1100
      NPIN4=NPINT4+1                                                     1110
      NPIN5=NPINT5+1                                                     1120
      P1=1.-2.*POIS                                                      1130
      P2=1.+POIS                                                         1140
      P3=1.-POIS**2                                                      1150
      B=BA**2-1.                                                         1160
      YC2=((EM1-EM2)*EPSST+(1.-EM1/E)*YC1)/(1.-EM2/E)                    1170
      ETA1=EM1/(YC1*(1.-EM1/E))                                          1180
      ETA2=EM2/(YC2*(1.-EM2/E))                                          1190
      K1=E*YC1*ETA1*P3                                                   1200
      K2=E*YC2*ETA2*P3                                                   1210
      EPSSP=(1.-EM1/E)*(EPSST-YC1/E)                                     1220
      EC=YC1*P3*B/K1                                                     1230
C                                                                        1240
C     TEST TO MAKE SURE THAT IN PRESSURE LOADING FROM ZERO, THE OUTSIDE  1250
C          OF THE CYLINDER WILL LEAVE REGION A (ELASTIC) BEFORE THE      1260
C          INSIDE ENTERS REGION C.  THIS IS AN ASSUMPTION IMPLICIT IN    1270
C          THE ANALYSIS.                                                 1280
C                                                                        1290
      IF(EPSSP.GT.EC)GO TO 10                                            1300
      PRINT 1050,EPSSP                                                   1310
 1050 FORMAT(1H0,'EPSSP =',F11.8,', TOO SMALL FOR THE ELASTIC REGION TO  1320
     1DISAPPEAR PRIOR TO THE ONSET OF THE ETA2 REGION')                  1321
      GO TO 210                                                          1330
```

```
C                                                                       1340
C     COMPUTE THE FOUR TRANSITION PRESSURES                             1350
C                                                                       1360
 10   VR=B**2*PRES                                                     1370
      B=(R1*VR2-R2*VR1)/(R2*VR1*ETA1-R1*VR2*ETA2)                       1380
      PA=.5*TB1*(1.-1./BA**2)                                           1390
      PB=F*VR1*(ALOG(BA)+ETA1*B*VC1*PI/12.*PI*PI/R1                     1400
      PC=(EPSSP*VR1*PI/R1)/12.*BA**2/(ETA1*VC1*B))+VR1*E*ALOG(BA)/R1    1410
      PD=F*VR2*(ALOG(BA)+.5*ETA2*B*PI/R2                                1420
      PRINT 1000, E,PRIS,EPS,ER2,ETA1,ETA2,VC1,VR2,EPSST,EPSSP,BA,NPINT 1430
 1000 FORMAT(1H0,'MATERIAL PROPERTIES'//'0      E =',F14.0/'0      PRIS =',
     1F6.4/'0      ER1 =',F12.0/'0      ER2 =',F12.0/'0      ETA1 =',F8.4/
     2'0      ETA2 =',F8.4/'0      VC1 =',F10.2/'0      VR2 =',F10.2/
     3'0      EPSST =',F10.8/'0      EPSSP =',F10.8//////'GEOMETRY'/
     4'0      B/A =',F9.3/'0      NPINT =',I5)                         1440
      PRINT 1010, NPINT1,NPINT2,NPINT3,NPINT4,NPINT5,PA,PB,PC,PD        1450
 1010 FORMAT(1H1,'PRESSURE INCREMENTS'//'0      NPINT1 =',I5/
     1'0      NPINT2 =',I5/'0      NPINT3 =',I5/'0      NPINT4 =',I5/
     2'0      NPINT5 =',I5//////'TRANSITION PRESSURES'//'0      PA =',
     3F11.3/'0      PB =',F11.3/'0      PC =',F11.3/'0      PD =',F11.3)
C                                                                       1470
C     CREATE THE R ARRAY TO SPECIFY RADIAL POSITIONS                    1480
C                                                                       1490
      DO 20 I=1,NPIN                                                    1500
      X(I)=1.0+FLOAT(I-1)*(BA-1.)/NPINT                                 1510
 20   CONTINUE                                                          1520
C                                                                       1530
C     STAGE I CALCULATIONS                                              1540
C                                                                       1550
      DO 40 J=1,NPINT                                                   1560
      PRINT 1020                                                        1570
 1020 FORMAT(1H1,' STAGE I -   PURELY ELASTIC')                         1580
      P=FLOAT(J-1)*PA/NPINT1                                            1590
      PRINT 1030,P                                                      1600
 1030 FORMAT(1H ,'PRESSURE =',F11.3//)                                  1610
      PRINT 1100                                                        1620
 1100 FORMAT(1H ,'STRESSES'//'0R/A',16X,'SIGR',15X,'SIGA',15X,'SIGT'/)  1630
      DO 30 I=1,NPIN                                                    1640
      RA=X(I)                                                           1650
      SIGR=P*(1.-(BA/RA)**2)/B                                          1660
      SIGA=P/B                                                          1670
      SIGT=P*(1.+(BA/RA)**2)/B                                          1680
      PRINT 1110,RA,SIGR,SIGA,SIGT                                      1690
 1110 FORMAT(1H ,F9.3,14X,3(F11.3,6X))                                  1700
 30   CONTINUE                                                          1710
      PRINT 1120                                                        1720
 1120 FORMAT(1H0,' STRAINS'//'0R/A',16X,'EPSR',15X,'EPSA',15X,'EPST'/)  1730
      DO 40 I=1,NPIN                                                    1740
      RA=X(I)                                                           1750
      EPSR=P*(P1-P2*(BA/RA)**2)/(E*B)                                   1760
      EPSA=P*P1/(E*B)                                                   1770
      EPST=P*(P1+P2*(BA/RA)**2)/(E*B)                                   1780
      PRINT 1130,RA,EPSR,EPSA,EPST                                      1790
 1130 FORMAT(1H ,F9.3,14X,3(F12.9,7X))                                  1800
 40   CONTINUE                                                          1810
C                                                                       1820
C     STAGE II CALCULATIONS                                             1830
C                                                                       1840
      DO 100 J=1,NPINT2                                                 1850
      PRINT 1140                                                        1860
 1140 FORMAT(1H1,' STAGE II -   ELASTIC-PLASTIC(CETA II)')              1870
      CA=1.+FLOAT(J-1)*(BA-1.)/NPINT2                                   1880
      VR=(BA/CA)**2-1.                                                  1890
      PS=ALOG(CA)-.5*ETA1*(1.-CA**2)*VC1*P3/E                           1900
      Z=.5*CA/BA)**2                                                    1910
      P=VC1*(VR+Z*E*PS/R1)                                              1920
      PRINT 1150,P,CA                                                   1930
 1150 FORMAT(1H ,'PRESSURE =',F11.3,5X,'C/A =',F5.3//)                  1940
      PRINT 1160                                                        1950
      DO 70 I=1,NPIN                                                    1960
```

```
      RA=X(I)                                                          1970
      FL=ALOG(RA)-.5*ETA1*((CA/RA)**2-CA**2)*VD1**3/E                  1980
      B=1.+VDR*ETA1**3*(CA/RA)**2/E                                    1990
      S=FL-FS-VL*Z*XI/E                                                2000
      IF(RA.GE.CAOGO TO 50                                             2010
      SIGR=E*VDR*S/XI                                                  2020
      SIGA=P*P1/B+POIS*E*VC1*2.*S*B1/XI                                2030
      SIGT=E*VDR*(S+B1)/XI                                             2040
      GO TO 60                                                         2050
   50 SIGR=VDR*Z*(1.-(BA/RA)**2)                                       2060
      SIGA=P*P1/B+2.*POIS*Z*VDR                                        2070
      SIGT=VDR*Z*(1.+(BA/RA)**2)                                       2080
   60 PRINT 1110,RA,SIGR,SIGA,SIGT                                     2090
   70 CONTINUE                                                         2100
      PRINT 1120                                                       2110
      DO 100 I=1,NRIN                                                  2120
      RA=X(I)                                                          2130
      FL=ALOG(RA)-.5*ETA1*((CA/RA)**2-CA**2)*VD1**3/E                  2140
      B=1.+VDR*ETA1**3*(CA/RA)**2/E                                    2150
      S=FL-FS-VL*Z*XI/E                                                2160
      IF(RA.GE.CAOGO TO 80                                             2170
      EPSA=P*P1/(E*B)                                                  2180
      EPSR=-VDR*EPSA+P1*P2*VD1*(B*FL)/XI-VD1**3*(CA/RA)**2/E           2190
      EPST=-VDR*EPSA+P1*P2*VC1*FL/XI*VD1*P3*(CA/RA)**2/E               2200
      GO TO 90                                                         2210
   80 EPSA=P*P1/(E*B)                                                  2220
      EPSR=P2*Z*VDR*(P1-(BA/RA)**2)/E-POIS*EPSA                        2230
      EPST=P2*Z*VDR*(P1+(BA/RA)**2)/E-POIS*EPSA                        2240
   90 PRINT 1130,RA,EPSR,EPSA,EPST                                     2250
  100 CONTINUE                                                         2260
C                                                                      2270
C     STAGE III CALCULATIONS                                           2280
C                                                                      2290
      DO 120 J=1,NPINB                                                 2300
      PRINT 1140                                                       2310
 1140 FORMAT(1H1,' STAGE III -   FULLY PLASTIC(ETA1)')                 2320
      P=PB+FLOAT(J-1)*(PC-PB)/NPINT3                                   2330
      V1=XI**P/(VDR*E)-ALOG(BA)                                        2340
      PRINT 1090,P                                                     2350
      PRINT 1100                                                       2360
      DO 110 I=1,NRIN                                                  2370
      RA=X(I)                                                          2380
      SIGR=-P*VDR*E*(ALOG(BA)+V1*(BA**2-(BA/RA)**2)/B1/XI              2390
      SIGA=(P1/B-2.*POIS)*P+POIS*VD1*E*(2.*ALOG(RA)+1.+2.*BA**2*V1/B1/XI2400
      SIGT=-P*VDR*E*(ALOG(RA)+1.+V1*(BA**2+(BA/RA)**2)/B)*XI           2410
      PRINT 1110,RA,SIGR,SIGA,SIGT                                     2420
  110 CONTINUE                                                         2430
      PRINT 1120                                                       2440
      DO 120 I=1,NRIN                                                  2450
      RA=X(I)                                                          2460
      EPSR=-P*P1*(P2+POIS/B1/E+P1*P2*VDR*(ALOG(RA)+1.+V1*(BA**2+(BA/RA)*2470
     1*2)/B1/XI-2.*V1*(BA/RA)**2/(ETA1*B)                              2471
      EPSA=P*P1/(E*B)                                                  2480
      EPST=-P*P1*(P2+POIS/B1/E+P1*P2*VD1*(ALOG(RA)+V1*(BA**2-(BA/RA)**2)2490
     1/B1/XI+2.*V1*(BA/RA)**2/(ETA1*B)                                 2491
      PRINT 1130,RA,EPSR,EPSA,EPST                                     2500
  120 CONTINUE                                                         2510
C                                                                      2520
C     STAGE IV CALCULATIONS                                            2530
C                                                                      2540
      DO 180 J=1,NPINA                                                 2550
      PRINT 1170                                                       2560
 1170 FORMAT(1H1,' STAGE IV -   PLASTIC(ETA1)-PLASTIC(ETA2)')          2570
      RSA=1.+FLOAT(J-1)*(BA-1.)/NPINT4                                 2580
      FS1=ALOG(BA/RSA)+.5*ETA1*P**(1.-(RSA/BA)**2)                     2590
      FS2=ALOG(RSA)+.5*ETA2*P**(RSA**2-1.)                             2600
      P=E*(VDR*FS1/XI+VD2*FS2/XI2)                                     2610
      PRINT 1180,P,RSA                                                 2620
 1180 FORMAT(1H ,'PRESSURE =',F11.3 ,3X,'RS/A =',F5.3//)               2630
      PRINT 1100                                                       2640
```

```
      DO 150 I=1,NRIN                                                   2650
      RA=X(I)                                                           2660
      FL1=ALOG(RA/RSA)+.5*ETA1**2*(1.-(RSA/RA)**2)                      2670
      FL2=ALOG(RA)+.5*ETA2**2*(RSA**2-(RSA/RA)**2)                      2680
      B1=1.+ETA1**2*(RSA/RA)**2                                         2690
      B2=1.+ETA2**2*(RSA/RA)**2                                         2700
      IF(RA.GE.RSA)GO TO 130                                            2710
      SIGR=-P*E*VB2*FL2/R2                                              2720
      SIGA=(PI/B-2.*POIS)*P+POIS*E*VB2*(2.*FL2*B2)/R2                   2730
      SIGT=-P*E*VB2*(FL2+B2)/R2                                         2740
      GO TO 140                                                         2750
  130 SIGR=-P*E*VB2*FS2/R2+E*VB1*FL1/R1                                 2760
      SIGA=(PI/B-2.*POIS)*P+2.*POIS*E*VB2*FS2/R2+POIS*E*VB1*(2.*FL1*B1)/
     1R1                                                                2771
      SIGT=-P*E*VB2*FS2/R2+E*VB1*(FL1+B1)/R1                            2780
  140 PRINT 1110,RA,SIGR,SIGA,SIGT                                      2790
  150 CONTINUE                                                          2800
      PRINT 1120                                                        2810
      DO 180 I=1,NRIN                                                   2820
      RA=X(I)                                                           2830
      FL1=ALOG(RA/RSA)+.5*ETA1**2*(1.-(RSA/RA)**2)                      2840
      FL2=ALOG(RA)+.5*ETA2**2*(RSA**2-(RSA/RA)**2)                      2850
      B1=1.+ETA1**2*(RSA/RA)**2                                         2860
      B2=1.+ETA2**2*(RSA/RA)**2                                         2870
      IF(RA.GE.RSA)GO TO 160                                            2880
      EPSA=P*P1/(E*B)                                                   2890
      EPSR=P1*P2*(-P+E*VB2*(FL2+B2)/R2)/E-POIS*EPSA-P*(RSA/RA)**2       2900
      EPST=P1*P2*(-P+E*VB2*FL2/R2)/E-POIS*EPSA+P*(RSA/RA)**2            2910
      GO TO 170                                                         2920
  160 EPSA=P*P1/(E*B)                                                   2930
      EPSR=P1*P2*(-P+E*VB2*FS2/R2+E*VB1*(FL1+B1)/R1)/E-POIS*EPSA-P*(RSA/
     1RA)**2                                                            2941
      EPST=P1*P2*(-P+E*VB2*FS2/R2+E*VB1*FL1/R1)/E-POIS*EPSA+P*(RSA/RA)**
     12                                                                 2951
  170 PRINT 1130,RA,EPSR,EPSA,EPST                                      2960
  180 CONTINUE                                                          2970
C                                                                       2980
C     STAGE V CALCULATIONS                                              2990
C                                                                       3000
      DO 200 J=1,NPINS                                                  3010
      PRINT 1190                                                        3020
 1190 FORMAT(1H1,' STAGE V -   FULLY PLASTIC(ETA2)')                    3030
      P=PO*FLOAT(J-1)*500.                                              3040
      V2=R2*P/(VB2*E)-ALOG(RA)                                          3050
      PRINT 1090,P                                                      3060
      PRINT 1100                                                        3070
      DO 190 I=1,NRIN                                                   3080
      RA=X(I)                                                           3090
      SIGR=-P*VB2*E*(ALOG(RA)+V2*(BA**2-(BA/RA)**2)/B)/R2               3100
      SIGA=(PI/B-2.*POIS)*P+POIS*VB2*E*(2.*ALOG(RA)+1.+2.*V2*BA**2/B)/R2 3110
      SIGT=-P*VB2*E*(ALOG(RA)+1.+V2*(BA**2+(BA/RA)**2)/B)/R2            3120
      PRINT 1110,RA,SIGR,SIGA,SIGT                                      3130
  190 CONTINUE                                                          3140
      PRINT 1120                                                        3150
      DO 200 I=1,NRIN                                                   3160
      RA=X(I)                                                           3170
      EPSR=-P*P1*(P2+POIS/B)/E+P1*P2*VB2*(ALOG(RA)+1.+V2*(BA**2+(BA/RA)*
     1*2)/B)/R2-2.*V2*(BA/RA)**2/(ETA2*B)                               3181
      EPSA=P*P1/(E*B)                                                   3190
      EPST=-P*P1*(P2+POIS/B)/E+P1*P2*VB2*(ALOG(RA)+V2*(BA**2-(BA/RA)**2)
     1/B)/R2+2.*V2*(BA/RA)**2/(ETA2*B)                                  3201
      PRINT 1130,RA,EPSR,EPSA,EPST                                      3210
  200 CONTINUE                                                          3220
  210 STOP                                                              3230
      END                                                               3240
```

Appendix D

STABLE CRACK GROWTH AND PLASTIC INSTABILITY

Introduction

It has been adequately demonstrated experimentally, and explained analytically,[1,2] that geometrically similar specimens containing sharp cracks should fracture at nominal stress levels that decrease with increasing crack size, if fracture precedes gross yielding. However, no equally satisfactory basis has been developed for determining if, and to what extent, geometric size effects should still exist in the fully plastic range. The purpose of this appendix is to present evidence indicating that size effects in the fully plastic range may be closely related to the occurrence of stable crack growth. More specifically, it will be shown that such size effects may be a consequence of the fact that the fractional increase in flaw size due to stable crack growth prior to maximum load tends to increase with increasing specimen size for geometrically similar specimens.

It has been found that both large[3] and small[4] surface-flawed tensile specimens can fail by tensile instability on the plane of the crack, if the material is sufficiently tough. This is most easily verified by observing that necking has occurred throughout the region containing the crack plane. However, tensile instability alone involves no size effect. Therefore, if necking has occurred at failure, but a size effect (i.e., a variation of gross section fracture stress with size) is still observed, the size effect must be due to some physical cause other than the final mode of failure.

A good example of size effects in the fully plastic range was provided by the data obtained by the Southwest Research Institute on two 6-in.-thick by 18-in.-wide intermediate tensile specimens[3,5,6] and two 1-in.-thick by 3-in.-wide scale models[3,7] of these specimens, all tested at temperatures of 200°F or slightly higher. One specimen of each size (intermediate tensile specimen 2 and ¼-scale model 2) contained a machined but unsharpened notch.[5] The other 6-in.-thick specimen (intermediate tensile specimen 1-B) contained a fatigue-sharpened notch,[6] and the other 1-in.-thick specimen (specimen 01H-2008) contained a notch that was sharpened by electron-beam welding and hydrogen charging.[7] All specimens were fabricated from A533, grade B, class 1 steel plate. The individual specimens and their notch preparation procedures are identified in Figs. D.1 through D.4.

The specimens were instrumented with both strain gages and displacement clip gages.[3,7] The analysis discussed below is based on the overall elongation of the test section as measured by two clip gages, one mounted on each side of the specimen and each measuring a displacement between gage points located in the grip regions of the specimen.[3,7] These two clip gages are gages 2 and 4 as shown in Fig. D.5. For purposes of analysis, it will be assumed that the entire displacement measured by clip gages 2 and 4 occurred within the test section of uniform width, the length of which is identified by the symbol L in Fig. D.5.

The data pertinent to the specimens to be analyzed are listed in Table D.1. The fact that in each specimen necking occurred throughout the region containing the crack plane implies that a condition of tensile instability was reached on the plane of the crack at maximum load. A simple model based on this premise is shown in Fig. D.6, where the dashed lines represent slip lines emanating from the tip of the flaw at maximum load. The intersection points of these slip lines with the back face of the specimen define a distance ℓ over which the strain at maximum load is assumed to be equal to the uniaxial necking strain, which, according to the stress-strain curve shown in Fig. D.7, is 10%. The average strain over the remainder of the gage length L is assumed to be the strain corresponding to the gross section stress, as determined

BLANK PAGE

Table D.1. Data from specimens and models used for study of size effects in the fully plastic range[a]

Specimen No	Thickness (in.)	Test temp. (°F)	Notch characteristics: Machined shape and sharpening procedure	Notch characteristics: Initial dimensions (in.) a	Notch characteristics: Initial dimensions (in.) b_0	Notch characteristics: Estimated dimensions at max. load (in.) a	Notch characteristics: Estimated dimensions at max. load (in.) b_0	Reference for chip gage data	Conditions at max. load: Gross stress σ_g (ksi)	Conditions at max. load: Axial strain $\Delta l/l$	Comments
					½-scale models						
Model 2	1	210[d,3]	Semielliptical, electric-discharge machining only	0.40	1.00	0.40	1.00	Ref. 1	76.9[d,1]	4.61[d,1]	Ref. 1 contains an error in the calculation of σ_g P_{max} = 2100 lb = 76.9 ksi
01N-2000	1	200[d,1]	Part circular, machined plus electron-beam and hydrogen charging	0.41	1.50	0.43	1.58	Ref. 1, p. A-11	71.6[d,1]	4.13[d,1]	
					Intermediate-section specimens (6 in. thick)						
2	6	32[d,3]	Semielliptical, electric-discharge machining only	2.16[d,1]	6.000[d,1]	1.50	7.00	Ref. 6, Fig. 3, p. 7	60.0[d,1]	1.81[d,1]	
14	6	200[d,6]	Part circular, machined plus local fatigue	2.55[d,6]	7.85[d,6]	3.00	8.45	Ref. 6, Fig. 2, p. B-4	61.0[d,6]	1.81[d,6]	Chip gage plots in Ref. 6 indicate gross stress at max. load of 62.3 ksi instead of 61.0, as listed in Table 1, p. 6 of Ref. 6

[a]Numbers in parentheses are reference numbers.

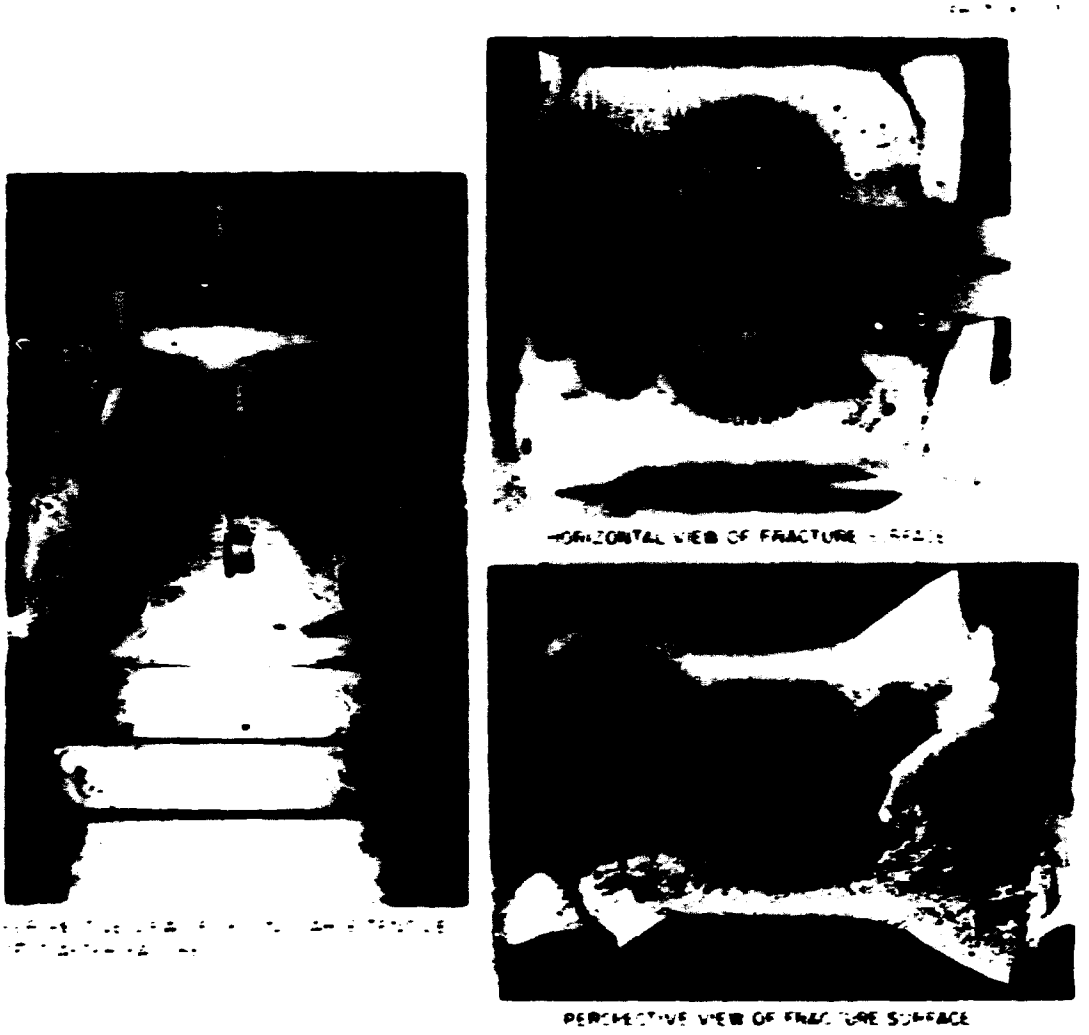

Fig. D.1. Intermediate tensile specimen 2 after fracture at 220 F: the flaw was produced by electric discharge machining without subsequent sharpening.[5]

from the uniaxial stress-strain curve shown in Fig. D.7. The gross section stress at maximum load is determined by assuming that the average stress on the remaining net section at maximum load equals the uniaxial ultimate stress, which, according to the figure, is 87 ksi. The remaining net section area is determined by estimating the dimensions, and therefore the area, of the flaw at maximum load. This was done by visually examining the actual fracture surfaces except for ¼-scale model 2, for which the estimate was based on Fig. D.2. The position of the flaw border at maximum load was estimated by locating the boundary of the region beyond which there was a perceptible decrease in the roughness of the flaw surface which was assumed to be due to the large shear displacements occurring as a result of tensile instability. The flaw dimensions at maximum load thus estimated generally equal or exceed those given in Refs. 5, 6, and 7, which were based on spraying paint into the notch at maximum load prior to complete separation of the

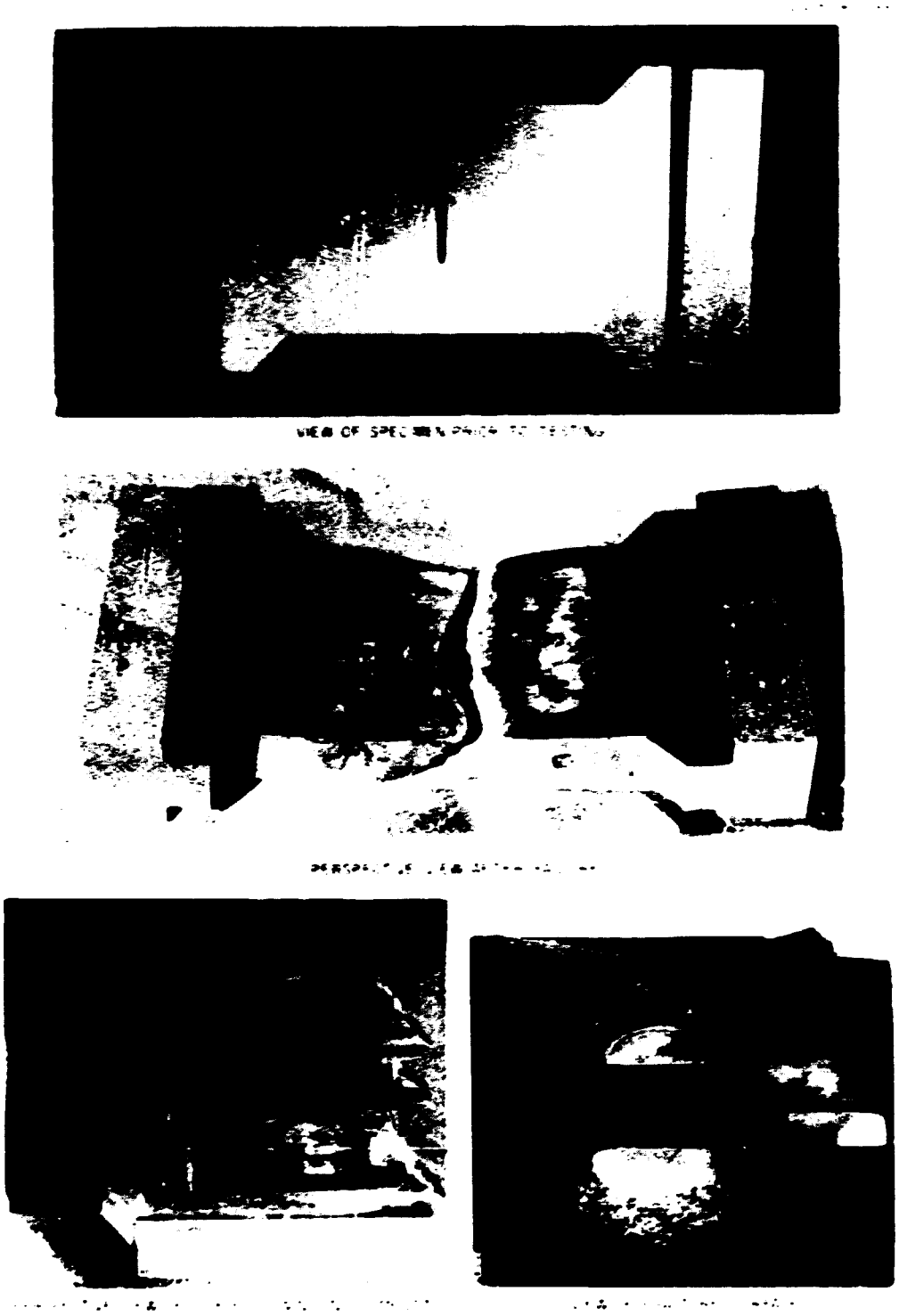

Fig. D.2. Several views of ¼-scale model 1, to which eight load cycles were applied to produce failure at 200 F; initial flaw size was the same as for ¼-scale model 2. The flaw was produced by electric discharge machining without subsequent sharpening.

Fig. D.1. Fracture surfaces of longitudinally oriented intermediate tensile specimens 14, 15, and 16; machined notches were sharpened by local fatiguing.[6]

Fig. D.4. Fracture surfaces of 1-in.-thick flawed tensile specimens from HSST plate 01 tested at various temperatures: machined notches were sharpened by electron-beam welding and hydrogen charging.

specimen. The differences between the two estimates are assumed to be due to incomplete penetration of the point into the flaws, which could have been caused by the tip region of the flaws being either not sufficiently open or not completely separated at maximum load.

The differences between the initial flaw dimensions and those estimated at maximum load, as listed in Table D.1, are assumed to be due to stable crack growth. The values given in the table imply that the flaws in the larger specimens underwent a proportionally greater amount of stable crack growth prior to maximum load than the flaws in the smaller specimens. While this conclusion is only tentative, it does lead to estimates of maximum loads and gage section elongations that are in good agreement with the experimental data.

ORNL-DWG 73-6140R

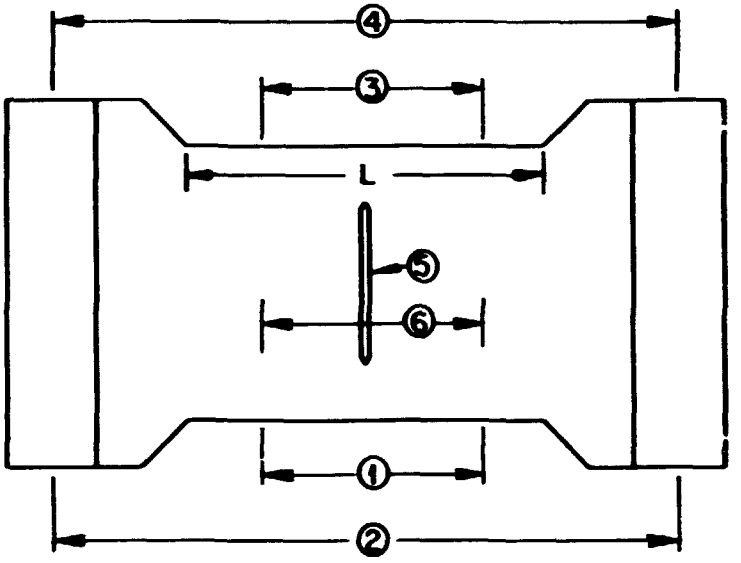

Fig. D.5. Clip gage locations and numbers (circled) for intermediate tensile specimens and ½-scale models; the distance L is the effective gage length for clip gages 2 and 4. For intermediate tensile specimens, L = 24 in.; for ½-scale models, L = 4 in.

ORNL-DWG 75-7628

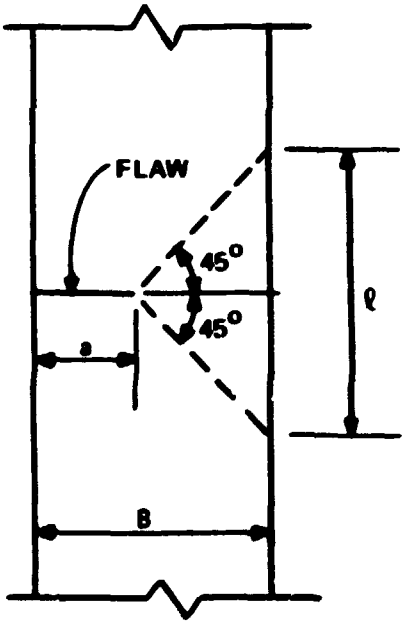

Fig. D.6. Vertical cross section bisecting a surface-flawed tensile specimen that has reached a condition of tensile instability on the net section.

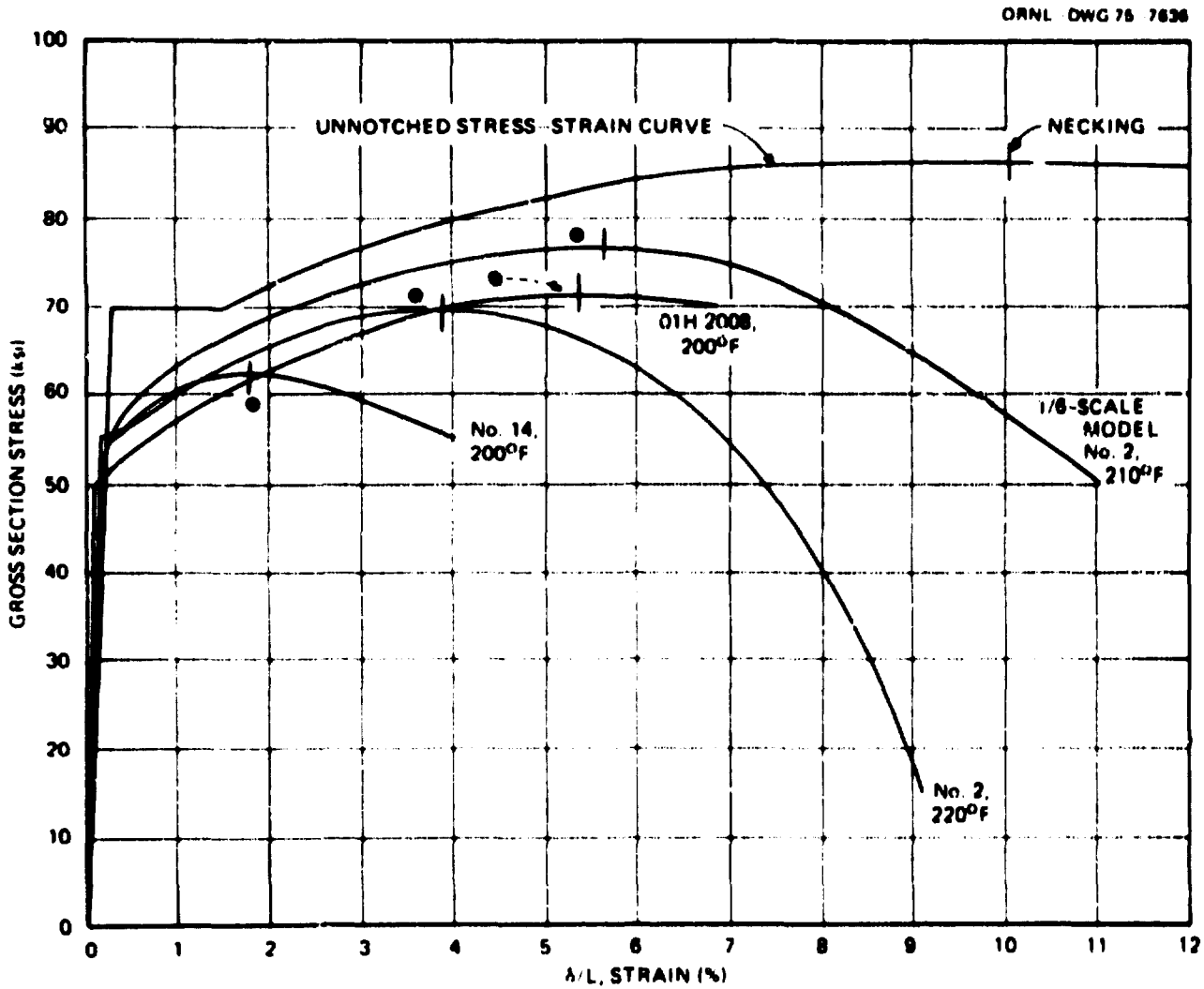

Fig. D.7. Clip gage curves and unnotched stress-strain curve for surface-flawed tensile specimens failing by tensile instability in the fully plastic range of strain.

Based on the assumptions stated above, the gross section stresses at maximum load for each specimen were estimated from the equation

$$\sigma_g = \sigma'_{ult}\left(1 - \frac{A_c}{A}\right) \quad . \tag{D.1}$$

where σ_g is the gross section stress, σ'_{ult} is the engineering ultimate tensile stress (87 ksi), A_c is the crack area, and A is the gross section area. Referring to Fig. D.6, the value of the distance ℓ over which the strain equals the uniaxial necking strain ϵ_1, which is 10%, is determined from the expression

$$\ell = 2(B - a) \quad . \tag{D.2}$$

where B is specimen thickness and a is estimated crack depth at maximum load. The average strain over the length of the test section at maximum load is estimated from

$$\epsilon_{av} = \frac{\delta}{L} = \epsilon_1\left(\frac{\ell}{L}\right) + \epsilon_g\left(1 - \frac{\ell}{L}\right) \quad . \tag{D.3}$$

where δ is elongation of the test section and ϵ_g is strain corresponding to the stress σ_g, according to the uniaxial stress-strain curve. Calculated values based on the above equations are summarized in Table D.2, and the resulting estimates of gross section stress and average test section strain at maximum load are plotted as points in Fig. D.7 along with a clip gage curve for each of the four specimens analyzed. It can be seen that the estimated and the actual maximum load conditions are in good agreement. This tends to substantiate the premise that the size effects observed with these specimens were due primarily to the occurrence of stable crack growth prior to maximum load in the larger specimens.

The results for the two specimens with unsharpened notches, cited above, were actually known prior to the test of intermediate test vessel V-1. Therefore, the same hypothesis concerning the proportionally greater amount of stable crack growth to be expected in larger specimens was applied to the posttest analysis of a 1/4-scale model of vessel V-1 and to the pretest analysis[8] of vessel V-1. Assuming no stable crack growth in the 1/4-scale model and 15% stable crack growth in vessel V-1 and using a plastic instability

Table D.2. Maximum load and average test section strain estimates based on the tensile instability model for four surface-cracked tensile specimens of A533, grade B, class 1 steel tested at temperatures near 200°F.

Specimen No.	σ_{ult} (ksi)	A (in.)	A_c (in.)	σ_g (ksi)	ℓ (in.)	ϵ_g (%)	$\epsilon_{av} = \delta/L$ (%)
Model[a]	87	3	0.314	78.0	1.20	3.35	5.34
01H 2008	87	3	0.482	73.1	1.14	2.18	4.41
2	87	108	19.2	71.5	5.00	1.80	3.51
14	87	108	26.8[b]	59.0	4.00	0.197	1.83

[a]One-sixth-scale model.

[b]Flaw assumed to be semielliptical in shape after stable crack growth.

failure analysis, the calculated failure pressure for the ¼-scale model (which failed at a pressure of 32.2 ksi) was 32.0 ksi, and the predicted failure pressure for vessel V-1 (which failed at a pressure of 28.8 ksi) was 29.5 ksi. Thus, analyses of both surface-flawed tensile specimens and experimental pressure vessels that have failed in the fully plastic range of strain indicate that stable crack growth and plastic instability are the physical phenomena that probably control the ultimate strength of flawed structures at high strains. It follows that any method of fracture analysis that ignores these phenomena cannot be expected to be consistently accurate in the fully plastic range of strain.

In addition to their implications regarding failure analysis, the above results also have a bearing on the techniques used for preparing cracks in structural test specimens and on the determination of fracture toughness values from material property specimens. Cracks in structural test specimens should be sharpened for tests at all temperatures, so that early stable crack growth will not be inhibited by lack of initial notch sharpness. Stable crack growth should be measured in fracture toughness specimens tested at elevated temperatures, and particular attention should be given to determining the relation between specimen size and the percentage of stable crack growth occurring prior to maximum load.

References

1. G. R. Irwin et al., "Basic Aspects of Crack Growth and Fracture," Chap. 7 in *Technology of Steel Pressure Vessels for Water-Cooled Nuclear Reactors*, G. D. Whitman, G. C. Robinson and A. W. Savolainen, Eds., ORNL-NSIC-21 (December 1967); see also NRL R-6598 (Nov. 21, 1967).
2. J. G. Merkle, "Fracture Safety Analysis Concepts for Nuclear Pressure Vessels Considering the Effects of Irradiation," *J. Basic Eng. ASME* 93, Series D(2), 265–73 (June 1971).
3. S. C. Grigory, *Tests of 6-in.-thick Flawed Tensile Specimens. First Technical Summary Report Longitudinal Specimens Numbers 1 Through 7*, HSSTP-TR-18, Southwest Research Institute, San Antonio, Tex. (June 1972).
4. P. N. Randall and J. G. Merkle, "Gross Strain Crack Tolerance of Steels," *Nucl. Eng. Des.* 17(1), 46–63 (August 1971).
5. S. C. Grigory, G. W. Deel, and R. Sherman, "Tests of Large Tensile Specimens," *HSST Program Semiannu. Progr. Rep. Feb. 28, 1970*, ORNL-4590, pp. 138–46, 168–212.
6. S. C. Grigory, *Tests of 6-inch-thick Flawed Tensile Specimens. Third Technical Summary Report Longitudinal Specimens Numbers 14 Through 16 (and) Unflawed Specimen Number 17*, HSSTP-TR-22, Southwest Research Institute, San Antonio, Tex. (October 1972).
7. S. C. Grigory, *Tests of 6-inch-thick Tensile Specimens. Fourth Technical Summary Report — Tests of 1-inch-thick Flawed Tensile Specimens for Size Effect Evaluation*, HSSTP-TR-23, Southwest Research Institute, San Antonio, Tex. (July 1973).
8. R. W. Derby et al., *Tests of 6-inch-thick Pressure Vessels. Series 1: Intermediate Test Vessels V-1 and V-2*, ORNL-4895, pp. 161–63 (February 1974).

Appendix E

TRANSVERSE RESTRAINT EFFECT STUDIES

Prior to the test of intermediate test vessel V-2, two attempts had been made to determine the effects of transverse restraint on the behavior of the surface flaws either in the intermediate test vessels or in the smaller scale steel model pressure vessels that had been tested previously. Evidence was available from drop weight tests,[1] gross strain tests,[2] and intermediate tensile specimen tests[3] to indicate that for these specimens, when fracture occurred in the plastic range, the total strain at fracture exceeded the predictions of linear-elastic fracture mechanics. In connection with the pretest analysis of vessel V-2, intermediate tensile specimen 5, which had failed at a strain of 0.48%, was successfully analyzed by the tangent modulus method.[3] The material of specimen 5 at 75 F had the same K_{Ic}/σ_y ratio as the material of vessel V-2 at 32°F. For this analysis, the Irwin β_{Ic} correction was used to elevate the fracture toughness above its plane strain value, based on the assumed existence of less than full transverse restraint. However, the same type of analysis overpredicted the fracture strain of vessel V-2, which was correctly predicted by a linear-elastic fracture mechanics analysis based on strain and assuming full transverse restraint.[3] Without the β_{Ic} correction, the tangent modulus analysis of vessel V-2 reduced essentially to the linear-elastic fracture mechanics analysis based on strain, which was accurate. This result implied that a real difference existed between the behavior of the surface flaws in intermediate tensile specimen 5 and in intermediate test vessel V-2.

Related evidence in the literature concerning the effects of transverse restraint is still scarce, inconclusive, and apparently contradictory. Vallun[4] developed an approximate expression for the plastic work performed per unit of increasing crack area at the tip of a slowly moving crack from which it was concluded that under biaxial in-plane tension the fracture stress for a through crack in a wide plate could be less than that under uniaxial loading. However, Erdogan, Kibler, and Roberts,[5] Kibler and Roberts,[6] and Erdogan and Ratwani[7] used various portions of the same set of experimental data obtained at Lehigh University to show that the effect of biaxial in-plane tension is to increase the fracture strength of through-cracked aluminum and/or plexiglass plates and thin-walled cylinders. Meanwhile, Harris and Dunegan[8] showed that local through-thickness compressive stresses could be used to arrest a wedge-induced precrack in a single-edge notched specimen of beryllium. Later, Maymon, Waldrop, and Busch[9] compared test results from surface-cracked tensile specimens and high-strength steel pressure vessels and concluded that in-plane transverse tensile stresses should reduce the fracture strength of surface-cracked specimens. Finally, Little and Bunting,[10] considering the Lehigh results,[5-7] postulated that transverse in-plane compressive stresses should reduce the fracture strength of through-cracked plates and cylinders.

Although the information from the literature summarized above may appear to be contradictory, there is a hypothesis that agrees with all the conclusions reached. However, the analysis presented in Ref. 4 appears to be in error, because it provides for no possible variation of the fracture toughness with temperature and assumes that the ratio of the intermediate to the major principal stress is the same throughout the plate. The unifying hypothesis is that the agent of transverse restraint is the strain in the direction tangent to the crack front in the plane of the crack at the point of fracture initiation. If lateral stresses cause this strain to become more negative, which occurs when either lateral in-plane tensile stresses or through-thickness compressive stresses are applied to a through-cracked plate or cylinder, the effective fracture toughness should increase. On the other hand, if lateral stresses cause this strain to become more positive, which occurs when lateral in-plane tensile stresses are applied to a surface-cracked bar or cylinder, the effective fracture toughness should decrease. This hypothesis is based on the assumption that the

effective fracture toughness depends on the magnitude of the hydrostatic stress in the plastic zone just ahead of the crack tip; that is, as the hydrostatic stress increases, the fracture toughness should decrease. The hydrostatic stress near the crack tip should increase or decrease as the tensile strain tangent to the crack tip in the plane of the crack increases or decreases. This hypothesis does not contradict the well-known analytical result that only the stresses normal to the crack plane influence the opening-mode stress-intensity factor. The phenomenon under consideration here is the probable variation of the fracture toughness of a material with the strain along the crack front, not a variation of the computed value of K_I produced by lateral stresses.

Although no experiments were performed specifically to test the foregoing hypothesis, data were already available from intermediate tensile specimen 15, tested at the Southwest Research Institute on June 16, 1972, that were ideally suited to this purpose. Specimen 15 was an 18-in.-wide, 6-in.-thick intermediate tensile specimen fabricated of A533, grade B, class 1 steel from HSST plate 04.[11] It contained a part-circular fatigue-sharpened part-through surface crack 2.22 in. deep and 8.02 in. long on the surface.[12] The nominal specimen temperature at fracture was −40°F and the failure load was 3.4×10^6 lb. The gross section stress at fracture was 31.5 ksi, which is well below the yield stress, and the fracture surface was completely flat.

By applying linear-elastic fracture mechanics to intermediate tensile specimen 15, the gross stress at fracture can be estimated from the equation

$$\sigma_f = \frac{K_c}{C\sqrt{\pi a}} , \tag{E.1}$$

where K_c is the fracture toughness of the material, C is the nondimensional shape factor for the geometry and the type of loading being considered, and a is the flaw depth. The value of C can be determined from the Smith and Alavi[13] solution for a part-circular surface crack.[14] Following Ref. 14, for uniform tension, the value of C is given by

$$C = \frac{\Phi_0}{\pi/2\sqrt{1 - D}} , \tag{E.2}$$

where

$$D = \frac{1 - (a/b)^2}{1 + (a/b)^2} \tag{E.3}$$

and 2b is the surface length of the crack. From Eq. (E.3), D = 0.53; therefore, by interpolation in Table 2 of Ref. 14, $\Phi_0 = 0.867$. Inserting these values into Eq. (E.2) thus gives C = 0.804. The value of K_{Ic} at −40°F was determined directly from the plot of the valid fracture toughness values obtained by Westinghouse[15] using compact specimens from HSST plate 02 material (Fig. E.1). At −40°F, K_{Ic} = 57 ksi $\sqrt{\text{in.}}$. Assuming full transverse restraint, the gross section fracture stress in intermediate tensile specimen 15 is estimated from Eq. (E.1) as

$$\sigma_f = \frac{K_{Ic}}{C\sqrt{\pi a}} = \frac{57}{0.804\sqrt{2.22\pi}} = 26.9 \text{ ksi}$$

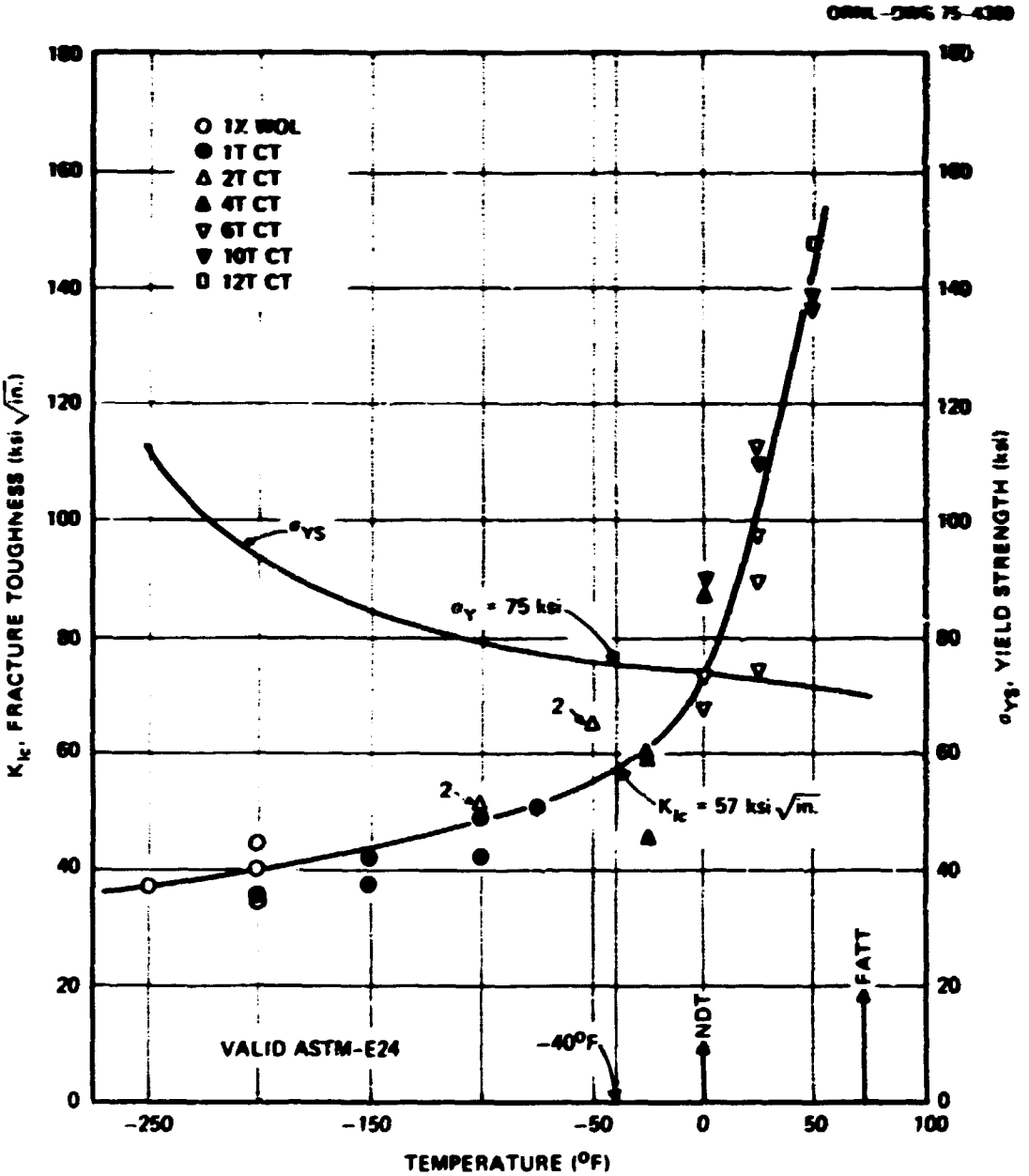

Fig. E.1. Temperature dependence of the K_{Ic} fracture toughness of a 12-in.-thick A533, grade B, class 1 plate (HSST plate 02).

This estimate is less than the actual gross section stress at fracture, indicating either that fracture occurred under conditions of less than full transverse restraint or that the values of K_{Ic} or C used in the calculation are inaccurate. The scatter in fracture toughness data illustrated in Fig. E.1 or plate-to-plate variations in fracture toughness could be responsible for the inaccuracy of the above calculations, but this is not believed to be the case. Furthermore, although values of C as low as 0.656 have been estimated by the finite-element method,[16] later estimates by the same method[17] produced values as high as 0.99. Neither of these calculations is considered as accurate as the value of 0.804 computed from the result of Ref. 13.

Additional information concerning shape factors for part-through surface cracks was obtained experimentally by Derby,[18] using fatigue-sharpened external surface cracks in bonde epoxy model pressure vessels. Two of these models had flaw depth ratios, a/t, close to that of intermediate tensile specimen 15, thus allowing an independent estimate to be made by interpolation for specimen 15. As shown in Table E.1, the estimated value of the shape factor for intermediate tensile specimen 15, based on Derby's epoxy model pressure vessel data,[18] is 0.795. This value is only 1% different from the value of 0.808 calculated from the results of Refs. 13 and 14.

Table E.1. Shape factors for part-through surface cracks from epoxy model pressure vessel data[18]

Model vessel No.	a (in.)	a/t	C	Remarks
110	0.24	0.407	0.845	Experimental
114	0.21	0.356	0.776	Experimental
		0.370	0.795	Calculated by interpolation between models 110 and 114

Witt attempted to explain the fracture strength of intermediate tensile specimen 15 by using the equivalent-energy method (Ref. 3, App. H). This explanation relied upon a previously estimated value of the shape factor for a part-through surface crack in a tensile bar.[19] Applying the equivalent-energy method to a 1-in.-thick flawed tensile specimen that failed at a strain of over 5%, Witt and Mager[17] estimated the value of the shape factor for the flaw in this specimen as 0.64. Applying this value to intermediate tensile specimen 15, assuming a fracture toughness of between 50 and 60 ksi $\sqrt{in.}$ and using pretest estimates of the crack depth ranging from 2.5 to 2.6 in., gave an estimated range of fracture stress of 27.4 to 33.5 ksi, which corresponds to a range of fracture loads of 3.0 to 3.6 X 10^6 lb. In view of the discrepancy between the estimated and the actual cracks depths and also the lack of proof that shape factors calculated by the equivalent-energy method are independent of strain level, the relative accuracy of these estimates may be fortuitous.

A more direct analysis of the effects of transverse restraint can be made by means of an elastic-plastic notch-tip stress and strain analysis developed specifically for the purpose of studying the effects of transverse restraint. This method of analysis, called the hollow cylinder analogy,[20] specifically considers the effects of strain along the crack front on the hydrostatic stress near a crack tip and provides equations relating the fracture toughness of a material to its triaxial ductility and the shape of its stress-strain curve. The analysis begins with an estimate of the strain tangent to the crack front in the plane of the crack at fracture.

In the case of intermediate tensile specimen 15, this estimate was made by averaging the readings of the transverse strain gages mounted on the front and back face portions of the net section and excluding those gages closest to the crack tip because they are located at points of high normal strain but low hydrostatic stress. The strain gage layout for intermediate tensile specimen 15 is shown in Fig. E.2, and the readings of

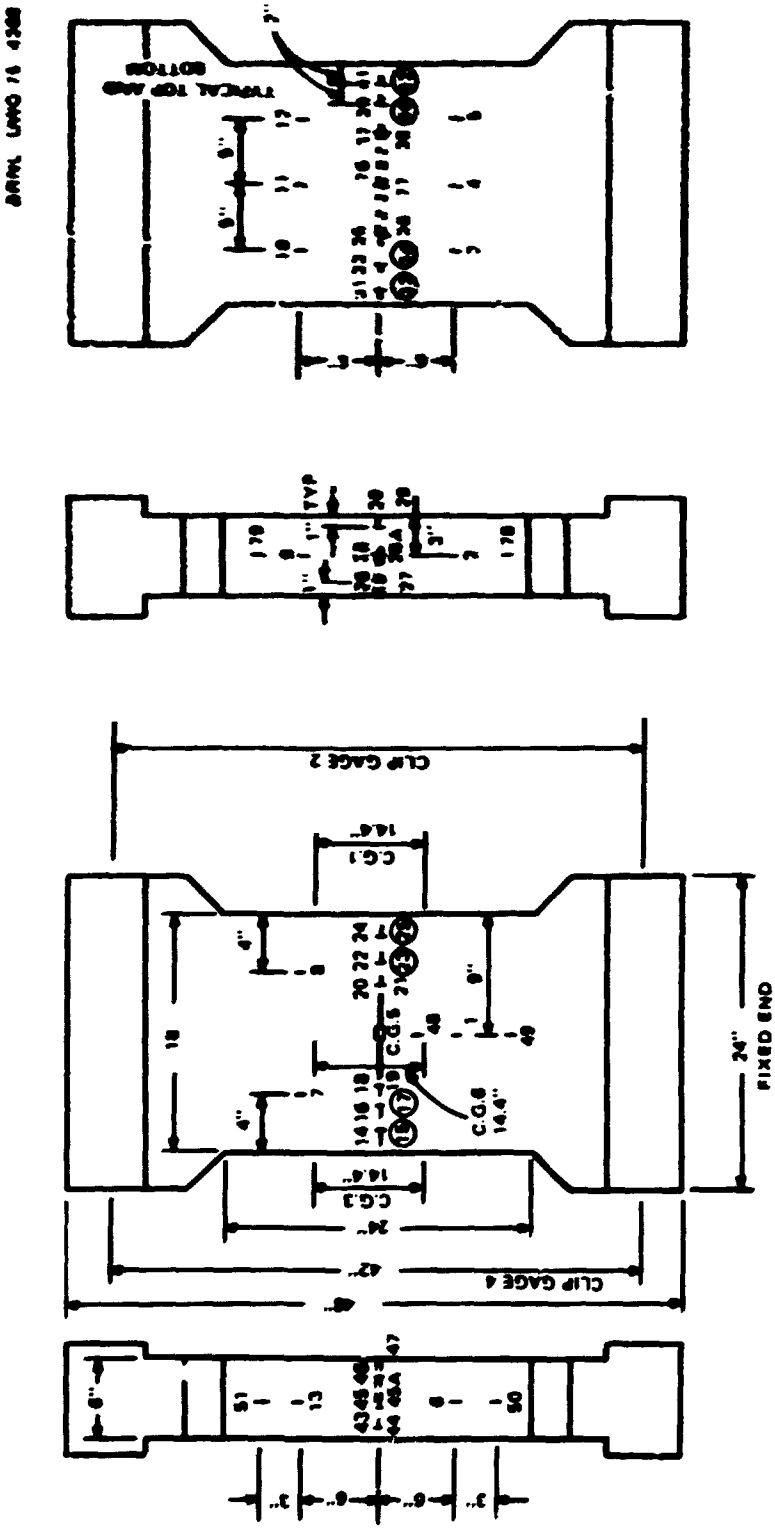

Fig. E.2. Strain gage and clip gage locations on intermediate tensile specimen 15 (Ref. 12).

all the transverse strain gages on the specimen at the fracture load of 3.4×10^5 lb are listed in Table E.2. The numbers of the inner and the back face strain gages remote from the crack, the readings from which were used to estimate the transverse strain near the deepest point of the crack, are shown circled in Fig. E.2; these readings are listed separately in Table E.2. From Table E.2, the estimated width direction contraction strain at the deepest point of the crack is -0.01497, which is less than half of the computed gross section contraction strain of -0.03157 based on a Poisson's ratio of 0.5 and the applied gross section stress of 31.5 ksi. Thus, the inner massive end sections used for gripping the specimen appear to have exerted a significant restraining influence on the transverse strains occurring throughout the test section. This conclusion agrees with the results of model tests conducted on smaller specimens of the same geometry,[21] as shown in Figs. E.3 and E.4, which demonstrated that a longer test section would have been required in order to achieve uniform transverse strains near the middle of the specimen.

The transverse restraint analysis of Ref. 20 begins with an expression for the transverse strain in the plane of the crack tangent to the crack tip of the form

$$\epsilon_t = n(1+\nu)\epsilon_y \tag{E.4}$$

From Eq. (E.4), it follows directly that

$$n = \frac{\epsilon_t}{\epsilon_y(1+\nu)} \tag{E.5}$$

Table E.2. Transverse strain-gage readings (μin./in.) from intermediate tensile specimen 15 at the failure load of 3.4×10^5 lb (Ref. 12)

Gage No.	Width direction		Thickness direction
	Remote from crack	Near crack	
44			145
45A			142
47			116
15	85		
17	76		
19		482	
21		442	
23	129		
25	231		
27			244
28A			200
29			Gage out
32	130		
34	149		
36		188	
77		297	
38		181	
40	164		
42	149		
Total	1113		
Average	139		

Fig. E.3. Grid pattern on ½, -scale model of unflawed Sn[illegible] tensile test specimen near maximum load.

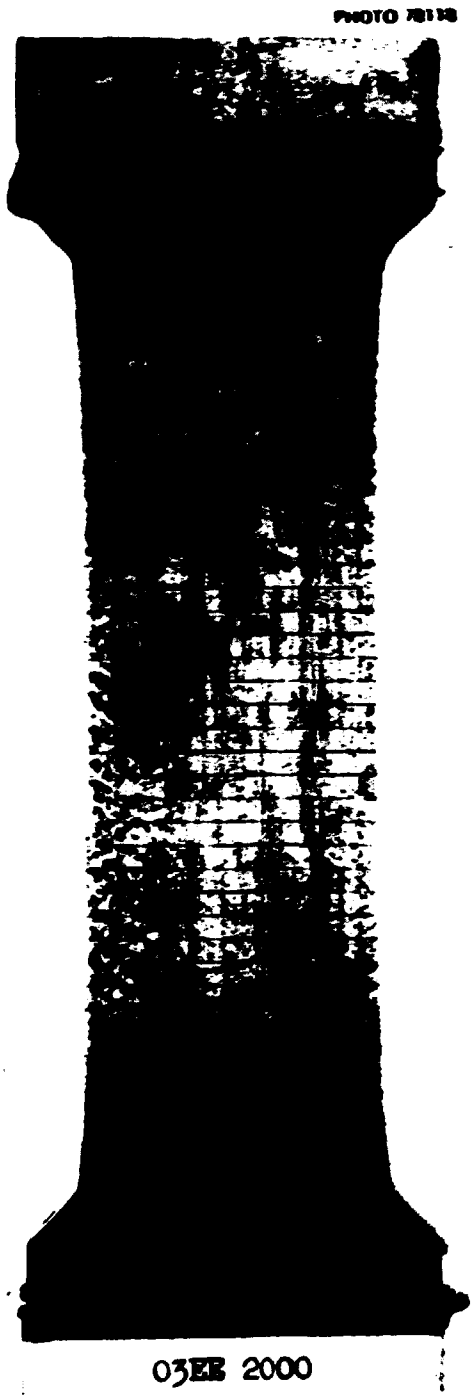

Fig. E.4. Grid pattern on unflawed elongated model of the SwRI tensile specimen near maximum load.

For a yield stress of 75 ksi, ϵ_y = 0.25%. Thus, for ϵ_y = 0.913% and r = 0.5, Eq. (E.5) gives n = 0.0428. Using an elastic–ideally plastic approximation for the stresses at the crack tip, the ratio of the maximum principal stress to the hydrostatic stress at the crack tip is given by[26]

$$\nu_o = \frac{2}{3}(1 + \pi/2 - n) \tag{E.6}$$

For n = 0.0428, Eq. (E.6) gives ν_o = 2.41. The triaxial ductility of the material is assumed to be expressed empirically by

$$\epsilon_f^P = \frac{1}{3}\left(e^{\nu_o} - 1\right) \tag{E.7}$$

If the value of the ductility under uniaxial tension is $\epsilon_{f,t}$ and the value of the ductility under plane strain tension is $\epsilon_{f,ps}$, it follows from Eq. (E.7) that

$$\nu = 2.32 \ln\left(\frac{\epsilon_{f,t}}{\epsilon_{f,ps}}\right) \tag{E.8}$$

and also that

$$I = \frac{\epsilon_{f,ps}}{(1.5)^{\nu}} \tag{E.9}$$

Reference 20 shows that $\epsilon_{f,ps}$ = 0.47 for A533, grade B, class 1 steel at −40°F. Thus, using a value of $\epsilon_{f,t}$ = 1.0, the value of ν from Eq. (E.8) is 1.75 and the value of I from Eq. (E.9) is 0.297. Consequently, setting ν = ν_o = 2.41 in Eq. (E.7) gives ϵ_f^P = 0.542.

Reference 20 also shows that the fracture toughness of a material can be related to the triaxial ductility of the material and the shape of its stress-strain curve by the equation

$$K_c = \frac{1}{3}\sqrt{\pi\rho_o}\sqrt{E_t E}\left[(1 + \epsilon^*_{\theta_o})^{3/2} - 1\right] , \tag{E.10}$$

where ρ_o is an effective root radius, E_t is the tangent modulus of the strain-hardening branch of the stress-strain curve, E is the elastic modulus, and $\epsilon^*_{\theta_o}$ is the notch root strain at fracture. Thus, using Eq. (E.10), an estimate of the ratio K_c/K_{Ic} can be obtained from

$$\frac{K_c}{K_{Ic}} = \frac{(1 + \epsilon_f^P)^{3/2} - 1}{(1 + \epsilon_{f,ps})^{3/2} - 1} , \tag{E.11}$$

where $\epsilon^*_{\theta_o}$ is set equal to ϵ_f^P for partial restraint and $\epsilon_{f,ps}$ for full restraint. By using L'Hopital's rule, it can be shown that using the elastic–ideally plastic approximation inherent in Eq. (E.6), for which E_t = 0, does not void Eq. (E.11) even though such an approximation would not give a physically meaningful result if used in Eq. (E.10). Thus, for ϵ_f^P = 0.542 and $\epsilon_{f,ps}$ = 0.470, the estimated value of K_c/K_{Ic} from Eq. (E.11) is 1.17. Multiplying the previously estimated value of the gross section stress at fracture, which was based

on the assumption of full transverse restraint by 1.17 gives (26.9) (1.17) = 31.5 ksi, which is exactly the same as the measured fracture stress.

From the above analysis, it can be concluded that the nominal strain acting tangent to a crack front in the plane of the crack has a fundamental influence on the fracture toughness of the material at the crack tip. Furthermore, as long as this strain remains nearly zero, as does the axial strain in a cylindrical pressure vessel under internal pressure even in the plastic range, the fracture toughness of a material containing surface cracks that are subject to this nearly zero transverse strain should be the plane strain value, notwithstanding the development of plastic strain normal to the plane of the crack.

On the other hand, if this transverse strain becomes a contraction, as is the case for a uniaxially loaded tensile specimen, the fracture toughness at the tip of a surface crack should be greater than the plane strain value. This hypothesis explains the observed difference in behavior between intermediate tensile specimens 5 and 15 and intermediate test vessel V-2.

References

1. L. W. Loechel, *The Effect of Testing Variables on the Transition Temperature in Steel*, HSSTP-TR-2, Martin Marietta Corp., Denver, Colo. (Nov. 20, 1969).
2. P. N. Randall and J. G. Merkle, "Gross Strain Crack Tolerance of Steels," *Nucl. Eng. Des.* 17(1), 46–63 (August 1971).
3. R. W. Derby et al., *Test of 6-inch-thick Pressure Vessels, Series I, Intermediate Test Vessels V-1 and V-2*, ORNL-4895 (February 1974).
4. S. R. Valluri, "Fracture under Biaxial Conditions in the Presence of a Crack," *Proceedings of the First International Conference on Fracture, Sendai, Japan, Sept. 12–17, 1965*, vol. 3, 1965.
5. F. Erdogan, J. J. Kibler, and R. Roberts, "Fatigue and Fracture of Thin-Walled Tubes Containing Cracks," pp. 771–80 in Part II, *Proceedings of the First International Conference on Pressure Vessel Technology, Delft, the Netherlands*, ASME, 1969.
6. J. J. Kibler and R. Roberts, "The Effect of Biaxial Stresses on Fatigue and Fracture," *J. Eng. Ind., Trans. ASME, Series B* 92, 727–34 (November 1970).
7. F. Erdogan and M. Ratwani, "Fracture of Cylindrical and Spherical Shells Containing a Crack," *Nucl. Eng. Des.* 20(1), 265–86 (June 1972).
8. D. O. Harris and H. L. Panegan, "Fracture Toughness of Beryllium," *J. Mater.* 3(1), 59–72 (March 1968).
9. H. W. Maynor, Jr., R. S. Waldrop, and C. C. Busch, "Crack Tolerating Ability of a High-Strength Biaxially Stressed Cylindrical Pressure Vessel Containing a Surface Crack," *Int. J. Mech. Sci.* 14, 205–13 (1972).
10. C. D. Little and P. M. Bunting, "The Surface Flaw in Aircraft Structures and Related Fracture Mechanics Analysis Problems," pp. 11–42 in *The Surface Crack, Physical Problems and Computational Solutions*, ASME, 1972.
11. C. E. Childress, *Fabrication History of the Third and Fourth ASTM A-533 Steel Plates of the Heavy-Section Steel Technology Program*, ORNL-4313-2, pp. 64-66 (February 1970).
12. S. C. Grigory, *Tests of 6-inch-thick Flawed Tensile Specimens: Third Technical Summary Report: Longitudinal Specimens Numbers 14 Through 16, Unflawed Specimen Number 17*, HSSTP-TR-22, Southwest Research Institute (October 1972).

13. F. W. Smith and M. J. Alavi. "Stress-Intensity Factors for a Part-Circular Surface Flaw." pp. 793–800 in Part II. *Proceedings of the First International Conference on Pressure Vessel Technology, Delft, the Netherlands*. ASME. 1969.

14. J. G. Merkle. *A Review of Some of the Existing Stress Intensity Factor Solutions for Part-Through Surface Cracks*. ORNL-TM-3983 (January 1973).

15. W. O. Shabbits, W. H. Pryle, and E. T. Wessel. *Heavy Section Fracture Toughness Properties of A533 Grade B Class 1 Steel Plate and Submerged Arc Weldment*. HSSTP-TR-6 (also WCAP-7414) (December 1969).

16. N. Levy and P. V. Marcal. *Three-Dimensional Elastic-Plastic Stress and Strain Analysis for Fracture Mechanics, Phase II: Improved Modelling*. HSSTP-TR-17. Brown University (November 1971).

17. P. V. Marcal, P. M. Stuart, and R. S. Bettes. *Elastic Plastic Behavior of a Longitudinal Semi-Elliptic Crack in a Thick Pressure Vessel*. HSSTP-TR-28. Brown University (June 1973).

18. R. W. Derby. "Experimentally Determined Shape Factors for Deep Part-Through Cracks in a Thick-Walled Pressure Vessel." pp. 482–91 in *Progress in Flaw Growth and Fracture Toughness Testing*. ASTM STP-536. ASTM. 1973.

19. F. J. Witt and T. R. Mager. "Fracture Toughness K_{Ic} Values at Temperatures Up to 550°F for ASTM A533, Grade B, Class 1 Steel." *Nucl. Eng. Des.* 17(1). 91–102 (August 1971).

20. J. G. Merkle. *An Elastic-Plastic Thick-Walled Hollow Cylinder Analogy for Analyzing the Strains in the Plastic Zone Just Ahead of a Notch Tip*. ORNL-TM-4071 (January 1973).

21. G. C. Robinson. *Discussion of SwRI Model Parametric Tests*. ORNL-TM-3313 (June 1971).

Appendix F

MODEL TEST DATA

Strains recorded as a function of pressure are tabulated completely in this appendix for models V3-A4, V2-A1-C, V2-A1-E, V4.6, V4.4, V4.2, and V4.1, which are described in Chapter 3. The strain gage layouts are shown in Fig. F.1.

BLANK PAGE

Table F.1. Pressure-strain dat

See Fi

Tes

Flaw size: 1

Pressure (psi)	1	2	3	4	5	6	7	8	9	10	11	12	13	1
0	-0002	-0002	-0002	-0001	-0001	0000	0000	0000	0000	-0002	0001	0000	0000	0
5,000	0026	0025	0026	0027	0027	0023	0022	0025	0026	0025	0022	0026	0024	0
10,200	0051	0050	0053	0055	0054	0047	0045	0051	0052	0052	0044	0052	0049	0
10,200	0052	0051	0052	0055	0055	0047	0046	0052	0053	0053	0043	0052	0049	0
15,000	0079	0076	0081	0063	0082	0071	0068	0076	0079	0079	0064	0078	0073	0
20,000	0106	0104	0108	0112	0114	0116	0084	0107	0107	0106	0089	0108	0096	0
24,000	0131	0132	0148	0145	0140	0135	0114	0134	0133	0133	0109	0135	0129	0
23,700	0131	0135	0154	0149	0141	0135	0115	0135	0133	0134	0108	0135	0128	0
25,600	0147	0182	0227	0205	0168	0138	0124	0150	0150	0157	0114	0149	0134	0
27,000	0159	0267	0343	0266	0222	0150	0136	0162	0165	0197	0144	0158	0135	0
27,000	0172	0310	0409	0336	0252	0157	0138	0171	0179	0233	0179	0165	0137	0
27,500	0185	0346	0459	0400	0283	0165	0146	0186	0210	0272	0201	0175	0141	0
28,000	0249	0474	0646	0564	0368	0204	0179	0281	0315	0394	0248	0222	0175	0
28,500	0405	0635	0901	0711	0450	0226	0250	0415	0479	0683	0328	0356	0246	0
26,500	0569	0826	1156	0852	0540	0254	0307	0510	0610	0893	0401	0488	0321	0
29,000	0722	1103	1507	1062	0675	0305	0372	0616	0740	1102	0493	0631	0413	0
29,600	0806	1283	1739	1224	0776	0356	0409	0680	0818	1231	0556	0705	0453	0
30,250	0898	1493	2032	1470	0945	0446	0454	0756	0910	1386	0646	0788	0504	0
31,000	1034	1866	2564	1981	1302	0609	0491	0844	1019	1573	0771	0894	0585	0
31,500	1108	2435	3741	2681	1858	0917	0509	0887	1077	1679	0972	0951	0616	0
31,800	1062	3204	14378	2437	1128	0481	0846	1032	1625	1618	1155	0908	0581	0

[a] To convert microinches/inch strain to percent strain, move decimal point four places to left.

[b] Multiply values in table by 10 except where noted.

BLANK PAGE

n data from model vessel V3-A4 (vessel V-3 prolongation)

ee Fig. F.1 for gage locations
Test temperature: 130°F
e: length, 1.42 in.; depth, 0.38 in.

Strain (μin./in.)[a,b] at gage No. –													
14	15	16	17	18	19	20	21	22	23	24	25	26	2
0000	-0001	-0002	-0001	-0001	-0002	-0002	-001x1	-003x1	-002x1	-002x1	-003x1	-003x1	-0
0021	0026	0026	0026	0027	0026	0025	122x1	119x1	117x1	124x1	124x1	123x1	12
0042	0050	0052	0054	0054	0053	0052	148x1	143x1	137x1	151x1	153x1	150x1	15
0042	0051	0052	0054	0054	0053	0052	053	047	042	055	058	155	15
0062	0076	0079	0081	0081	0081	0079	079	070	062	081	085	082	08
0084	0103	0105	0106	0106	0105	0106	106	088	066	111	114	106	11
0100	0127	0131	0134	0134	0131	0134	136	123	084	137	140	132	13
0099	0126	0130	0137	0136	0133	0135	136	123	084	137	139	131	13
0109	0149	0161	0219	0216	0207	0170	165	139	089	150	155	157	15
0126	0181	0213	0454	0453	0431	0226	202	161	093	163	177	208	17
0133	0210	0273	0594	0587	0567	0290	234	171	095	175	198	249	18
0155	0269	0352	0721	0694	0680	0391	305	196	099	198	235	301	20
0196	0430	0546	0886	0883	0866	0587	392	268	133	314	410	562	36
0227	0549	0691	1011	1027	1035	0757	470	312	189	468	619	904	56
0256	0645	0812	1169	1204	1237	0936	601	381	214	547	720	1063	69
0292	0777	0969	1547	1599	1646	1235	833	468	247	654	864	1265	86
0327	0874	1075	1811	1868	1919	1439	991	530	267	723	956	1384	95
0387	1008	1241	2110	2169	2223	1685	1195	611	293	810	1071	1540	106
0456	1212	1497	2472	2540	2594	1997	1448	733	331	912	1204	1740	120
0510	1348	1661	2678	2753	2799	2169	1600	790	336	957	1267	1840	127
0496	1336	1651	2671	2747	2791	2158	1580	775	299	904	1205	1760	121

2

BLANK PAGE

	21	22	23	24	25	26	27	28	29
?	-001x1	-003x1	-002x1	-002x1	-003x1	-003x1	-002x1	-001x1	-002x1
5	122x1	119x1	117x1	124x1	124x1	123x1	124x1	123x1	122x1
?	148x1	143x1	137x1	151x1	153x1	150x1	151x1	150x1	147x1
?	053	047	042	055	058	155	156	155	152
9	079	070	062	081	085	082	083	081	076
6	106	088	066	111	114	102	111	111	096
4	136	123	084	137	140	132	139	141	126
5	136	123	084	137	139	131	139	140	125
0	165	139	089	150	155	157	154	154	138
6	202	161	093	163	177	208	170	166	136
0	234	171	095	175	198	249	184	175	144
1	305	196	099	198	235	301	209	192	154
7	392	268	133	314	410	562	348	297	204
7	470	312	189	468	619	904	565	452	308
6	601	381	214	547	720	1063	695	549	372
5	833	468	247	654	864	1265	860	672	458
0	991	530	267	723	956	1384	951	750	522
5	1195	611	293	810	1071	1540	1067	853	604
7	1448	733	331	912	1204	1740	1207	973	691
0	1600	790	336	957	1267	1840	1278	1029	736
8	1580	775	299	904	1205	1760	1219	974	696

3

Table F.2. Pressure-strain data from model vessel V2-A1-C (vesse

See Fig. F.1 for gage locations
Test temperature: 130°F
Flaw size: length, 1.2 in.; depth, 0.37 in.

Pressure (psi)	Strain (μin./in.)[a] at gage No.														
	1	2	3	4	5	6	7	8	9	10	11	12	13	14	15
2,000	110	130	130	130	130	130	110	120	110	130	130	110	120	130	13
4,000	210	230	240	240	230	230	200	220	190	230	220	190	200	220	22
8,000	370	420	440	450	430	440	380	420	370	440	420	360	380	420	45
12,000	560	640	670	680	650	650	570	630	560	660	630	550	570	640	66
16,000	740	850	890	900	860	860	750	830	740	870	830	720	750	840	89
20,000	910	1040	1090	1110	1050	1060	920	1020	920	1060	1020	880	930	1030	109
22,000	1010	1140	1210	1230	1160	1170	1020	1120	1010	1170	1120	960	1030	1130	122
23,000	1050	1210	1290	1300	1220	1240	1070	1180	1060	1240	1170	1020	1090	1200	130
24,000	1130	1300	1410	1420	1310	1330	1130	1260	1130	1330	1230	1060	1150	1270	141
25,000	1190	1380	1520	1540	1400	1430	1190	1340	1190	1420	1300	1110	1210	1350	152
25,500	1210	1430	1570	1600	1440	1480	1230	1380	1220	1460	1320	1130	1240	1360	157
26,000	1240	1470	1660	1690	1490	1550	1260	1430	1250	1520	1370	1160	1290	1440	165
26,750	1280	1550	1800	1860	1570	1660	1320	1520	1290	1610	1440	1210	1340	1500	175
27,500	1320	1680	2110	2220	1710	1860	1420	1660	1340	1780	1540	1270	1410	1590	190
28,000	1380	1830	2620	2980	1870	2130	1560	1900	1360	2090	1720	1360	1470	1660	195
28,250	1420	1930	2990	3510	1970	2420	1690	2130	1390	2280	1920	1500	1510	1700	196
28,500	1490	2420	3800	4580	2390	3130	1930	2690	1480	2820	2290	1690	1570	1760	196
28,50C	1540	2540	4090	5110	2590	3530	2110	2960	1510	3120	2550	1820	1630	1830	193
29,000	1720	2960	4910	628C	3090	4580	2410	3610	1750	3670	3120	2080	1760	1960	197
29,000	1810	3090	5160	6630	3180	5090	2560	3860	1870	4290	3410	2170	1830	2040	226
29,000	1890	3220	5370	6880	3320	5500	2680	4070	1990	3630	3660	1950	1900	2130	263
29,200	2110	3520	5820	7370	3630	6130	2870	4446	2290	5230	4000	2350	2100	2320	344
29,500	2320	3810	6300	7880	4090	6670	3080	4790	2630	5770	4330	2480	2290	2560	454
29,300	1770	4380	6920	8660	4640	7390	3830	5290	3100	6620	4810	2710	2570	2970	595
30,000	2830	4690	7350	9230	5060	7820	3390	5610	3390	7160	5120	2860	2730	3260	672
30,300	3220	5270	8290	10180	5860	8830	3700	6390	3960	8290	5770	3170	3120	3910	829
31,000	3690	6200	9900	11790	6950	10320	4240	7530	4690	9900	6730	3650	3710	4870	1048
31,600	4260	7230	11720	13670	8180	11820	4880	8620	5510	11470	7750	4170	4380	5760	1233
32,000	4900	8460	13670	15770	9610	13210	5500	9630	6400	12890	9780	4630	4980	6620	1401
32,500	5640	10010	15860	18220	11320	14620	6150	10680	7450	14310	9770	5100	5580	7480	1563
32,800	6480	11810	18310	20890	13200	16150	6890	11830	8610	15820	10830	5610	6220	8420	1736
33,200	7510	14140	21550	24420	15580	17310	7490	12720	10040	16970	11650	6030	6660	9120	1857
33,250	9050	17630	27150	30620	19380	18230	7950	13420	12190	17880	12310	6340	6980	9620	1950
Burated	7960	21810	50140	59360	24770	14100	5470	10090	12300	13610	8860	3700	4850	7130	1667

[a] To convert microinches/inch strain to percent strain, move decimal point four places to left.

vessel W2-A1-C (vessel V-2 prolongation)

gge locations
e: 1307
in.; depth, 0.37 in.

in./in.)[a] at gage No. –												
13	14	15	16	17	18	19	20	21	22	23	24	25
120	130	130	130	130	120	93	121	121	148	109	152	153
200	220	220	220	220	210	161	212	214	259	192	269	261
380	420	450	440	440	420	321	418	424	512	379	532	502
570	640	660	660	650	620	482	635	643	774	576	808	753
750	840	890	880	870	820	635	838	848	1022	760	1067	993
930	1030	1090	1090	1070	1010	778	1038	1040	1254	933	1311	1217
1030	1130	1220	1220	1180	1120	859	1133	1151	1390	1032	1445	1338
1090	1200	1300	1300	1250	1180	905	1190	1212	1470	1090	1522	1405
1150	1270	1410	1410	1340	1250	963	1263	1289	1574	1162	1618	1486
1210	1350	1520	1530	1430	1330	1015	1324	1365	1679	1239	1709	1560
1240	1380	1570	1590	1470	1360	1039	1354	1397	1726	1272	1748	1590
1290	1440	1650	1660	1530	1420	1071	1393	1446	1802	1328	1805	1633
1340	1500	1750	1780	1620	1480	1116	1447	1517	1916	1411	1895	1692
1410	1590	1900	1910	1730	1570	1172	1524	1626	2130	1560	2030	1780
1470	1660	1950	1960	1820	1650	1222	1630	1743	2560	1910	2260	1660
1510	1700	1960	1960	1870	1690	1250	1770	2210	2970	2260	2530	1970
1570	1780	1960	1900	1920	1770	1330	1990	2660	3810	2980	3140	2240
1630	1830	1930	1860	1960	1830	1360	2160	3040	4460	3400	3480	2420
1760	1960	1970	1860	2040	2000	1470	2550	3800	5600	4220	4230	2850
1830	2040	2260	2150	2080	2120	1550	2750	4190	6040	4570	4650	3030
1900	2130	2630	2560	2150	2270	1610	2950	4460	6450	4850	4950	3190
2100	2320	3440	3430	2470	2610	1760	3340	4940	7230	5460	5460	3490
2290	2560	4540	4670	2950	2960	1900	3650	5360	7940	5880	5850	3750
2570	2970	5950	6310	3950	3960	2070	4050	6040	8990	6510	6420	4100
2730	3260	6720	7210	4560	3750	2200	4350	6540	9660	6920	6850	4330
3120	3910	8290	8920	5660	4280	2470	5060	7600	11110	7850	7780	4840
3710	4870	10420	11210	7040	4890	2880	6060	9000	12990	9260	9150	5670
4380	5760	12330	13270	8380	5570	3350	7000	10220	14760	10670	10690	6600
4980	6620	14010	15140	9650	6280	3800	7900	11350	16400	11960	12090	7470
5580	7480	15630	16900	10850	7000	4230	8800	12520	18070	13270	13510	8330
6220	8420	17360	18740	12110	7770	4690	9780	13790	19860	14670	15030	9360
6660	9120	18570	20080	13040	8380	5030	10530	14820	26500	21400	18800	10800
6980	9620	19500	21090	13730	8820	7000	14200	15600	27800	22500	19800	11400
4850	7130	16670	18320	11050	6390	4500	9500	11300	19600	15600	13200	7300

2

1

BLANK PAGE

Table F.5- Pressure-strain data from model vessel V2-A1-E (vessel V-2 prolongation)

See Fig. F.1 for gage locations
Test temperature: 130°F
Flaw size: length, 1.2 in.; depth, 0.37 in.

Pressure (psi)	Strain (μin./in.)[a] at gage No. –								
	1	2	3	4	5	6	7	8	9
				×1 scale					
0	000	000	000	000	000	000	000	--	000
5,000	249	264	270	262	248	267	266	--	254
10,000	508	544	544	535	498	536	537	--	516
15,000	787	823	826	815	754	810	812	--	776
20,200	1026	1109	1106	1092	1013	1088	1090	--	1045
22,500	1137	1260	1237	1226	1125	1219	1227	--	1158
25,000	1297	1474	1472	1461	1299	1453	1466	--	1335
25,500	1330	1517	1519	1509	1331	1504	1516	--	1375
26,000	1371	1508	1505	1579	1374	1574	1584	--	1420
26,500	1416	1661	1658	1651	1422	1653	1648	--	1473
27,250	1498	1789	1790	1778	1494	1790	1780	--	1542
27,500	1509	1822	1823	1804	1517	1825	1791	--	1570
28,000	1561	1896	1894	1906	1578	1925	1899	--	1666
28,400	1627	1973	1979	1962	1633	1996	1967	--	1766
				×10 scale[b]					
29,000	172	204	203	207	173	231	198	--	190
29,250	182	216	216	227	185	280	208	--	226
29,000	187	225	227	235	190	312	214	--	242
29,250	195	246	251	255	197	362	233	--	269
29,250	203	277	282	286	201	402	250	--	287
29,100	215	359	360	355	217	465	292	--	310
29,000	223	391	392	385	225	495	319	--	319
29,000	228	402	403	395	227	506	330	--	322
29,300	236	413	414	408	232	524	351	--	331
29,250	257	457	460	451	242	564	561	--	201
29,250	263	469	472	463	245	576	410	--	363
29,250	268	430	484	474	248	587	423	--	367
29,500	275	494	497	490	254	603	447	199	355
29,600	292	536	540	532	266	639	495	198	367
29,650	301	564	570	558	273	659	522	198	375
29,600	301	569	575	563	272	663	527	198	376
29,500	311	594	600	589	283	685	555	197	385
29,000	314	599	605	595	285	691	563	196	389
29,000	321	617	624	613	291	707	584	195	398
29,750	332	651	660	648	300	735	618	196	411
30,000	337	659	666	657	305	746	636	194	421
30,000	369	745	754	741	330	822	716	189	459
30,000	414	848	857	840	363	917	814	185	510
30,500	424	865	875	858	371	935	835	184	518
30,500	449	922	931	912	391	987	890	181	546
31,000	463	957	967	969	405	1026	944	178	573
31,000	533	1116	1121	1098	461	1169	1078	171	632
31,250	565	1144	1146	1121	472	1196	1104	170	643
31,500	554	1164	1165	1141	481	1215	1127	169	654
31,500	590	1273	1262	1215	510	1285	1198	165	684
31,500	605	1353	1273	1244	523	1316	1227	163	698
31,750	620	1408	1299	1289	534	1335	1263	162	704
31,750	645	1515	1369	1320	559	1389	1302	159	737
32,000	657	1565	1372	1362	570	1411	1325	158	750
32,000	710	--	1474	1441	617	1513	1424	152	808
32,000	731	--	1516	1480	636	1557	1459	150	829
32,000	816	--	1675	--	708	--	1610	--	958
				×100 scale[c]					
32,500	085	--	174	--	074	--	167	--	099
33,000	087	--	181	--	076	--	172	--	104
33,000	094	--	222	--	082	--	185	--	115
33,500	096	--	231	--	083	--	189	--	123
33,500	101	--	506	--	088	--	203	--	134
33,500+	103	--	--	--	090	--	213	--	179
0	077	--	627	--	065	--	181	--	--

[a]To convert microinches/inch strain to percent strain, move decimal point four places to left.
[b]Multiply tabulated values by 10.
[c]Multiply tabulated values by 100.

Table F.--. Pressure-strain data from model vessel V-6
(vessel V-- prolongation)

See Fig. F.1 for gage locations
Test temperature: 200°F
Flaw size: length, 0.-- in.; depth, 0.-- in.

Pressure (psi)	Strain (μin./in.)[a] at gage No. —							
	1	2	3	4	5	6	7	8
10,000	440	470	370	440	1--0	490	640	610
20,000	960	1,000	820	870	1,210	920	1,310	1,260
25,000	1,200	1,230	1,070	1,170	1,420	1,140	1,650	1,590
30,000	1,500	1,500	1,370	1,480	1,770	1,470	2,050	1,950
31,000	1,550	1,650	1,450	1,590	1,850	1,520	2,130	2,020
32,000	1,620	1,740	1,500	1,720	2,050	1,570	2,210	2,120
33,000	1,700	1,800	1,570	1,850	2,120	1,650	2,310	2,220
33,500	1,750	1,850	1,620	1,790	2,180	1,710	2,370	2,270
34,100	1,830	1,950	1,750	1,990	2,280	1,820	2,510	2,370
34,250	1,860	1,930	1,790	2,050	2,340	1,870	2,480	2,450
34,400	1,920	2,040	1,850	2,110	2,390	1,960	2,570	2,530
35,000	1,990	2,100	1,920	2,180	2,480	2,040	2,810	2,640
35,500	4,690	5,240	2,100	2,360	3,610	4,210	6,750	5,440
34,600	7,490	8,750	2,210	2,470	2,690	7,750	11,170	9,010
0	11,990		620	590	320		48,630	

[a]To convert microinches/inch strain to percent strain, move decimal point four places to left.

Table F.5. Pressure-strain data from model vessel V-4.
(vessel V-4 prolongation)

See Fig. F.1 for gage locations
Test temperature: [illegible]°F
Flaw size: length, 0.35 in.; depth, 0.25 in.

Pressure (psi)	Strain (μin./in.)[a] at gage No. —						
	1	2	3	4	5	6	7
5,000	260	260	260	290	230	300	290
10,000	520	520	520	540	540	560	560
15,000	830	810	780	770	840	900	880
20,000	1,030	1,030	1,020	970	1,070	1,160	1,130
25,000	1,350	1,370	1,360	1,270	1,470	1,720	1,730
27,000	1,650	1,750	1,610	1,450	1,740	4,390	4,740
27,500	1,970	2,050	1,630	1,550	1,770	7,[illegible]80	6,330
28,000	2,410	2,570	1,700	1,610	1,820	9,310	8,390
28,500	3,750	3,620	1,750	1,720	2,020	10,340	9,680
29,000	4,230	4,090	2,310	2,240	2,700	10,960	10,470
29,250	4,560	4,430	2,320	2,650	5,320	11,440	11,020
29,500	4,540	4,710	3,750	2,940	4,720	11,960	11,600
29,500	5,090	4,950	3,750	3,140	5,230	12,340	12,000
29,750	5,350	5,200	4,130	3,360	5,300	12,790	12,490
29,750	5,430	5,310	4,270	3,460	5,010	12,930	12,700
30,000	5,690	5,[illegible]00	4,550	3,620	5,420	13,330	13,100
30,250	5,950	5,730	4,940	3,790	6,070	13,830	13,700
30,250	6,420	6,150	5,420	4,080	7,570	14,580	14,450
30,500	6,980	6,710	6,120	4,430	8,430	15,550	15,490
31,000	7,590	7,290	6,360	4,540	9,340	16,600	16,600
31,200	8,150	7,840	7,560	5,240	10,170	17,590	17,660
31,400	9,260	8,900	8,770	5,950	11,700	19,590	19,770
31,800	9,670	9,290	9,210	6,260	12,250	20,050	20,460
32,000	10,630	10,220	10,150	6,550	13,440	22,170	22,430
32,300	11,340	10,[illegible]90	10,[illegible]60	7,310	14,350	23,490	23,890
32,500	12,300	11,790	11,690	7,560	15,470	25,390	25,830
32,700	13,190	12,700	12,550	8,420	16,570	27,370	27,360
33,000	13,490	13,670	13,440	9,020	17,770	29,470	30,050
33,300	15,410	14,930	14,540	9,750	19,250	32,340	32,960
33,700	17,020	16,560	15,[illegible]80	10,660	21,020	36,570	37,080
33,100	17,120	16,560	16,050	10,740	21,210	36,910	37,300
34,000	18,470	18,060	17,020	11,440	22,[illegible]80	43,090	41,210
34,200	19,170	18,790	17,650	11,890	23,290		43,420
34,300	19,060	21,070	19,040	12,870	25,160		50,510
34,500	24,750	24,500	20,600	13,990	27,220		63,440
0	51,370	50,300	1[illegible],010	11,460	24,610		

[a]To convert microinches/inch strain to percent strain, move decimal point four places to left.

Table F.6. Pressure-strain data from model vessel V4.2
(vessel V-4 prolongation)

See Fig. F.1 for gage locations
Test temperature: 130°F
Flaw size: length, 3.15 in.; depth, .64 in.

Pressure (psi)	Strain (μin./in.)[a] to gage No. –										
	1	2	3	4	5	6	7	8	9	10	11
0	0	0	20	0	10	0	0	0	10	0	
4,000	320	260	230	570	240	220	520	250	220	220	2
8,000	630	480	450	760	450	410	410	420	410	410	4
12,000	1,000	740	640	1,230	680	630	620	640	610	620	6
16,000	1,350	1,010	880	1,740	930	870	860	850	850	840	8
18,000	1,650	1,150	990	1,990	1,040	980	940	960	950	950	9
20,000	2,010	1,330	1,120	2,370	1,190	1,110	1,060	1,070	1,060	1,060	1,0
21,000	2,310	1,490	1,190	2,650	1,270	1,190	1,130	1,150	1,110	1,110	1,1
22,000	2,690	1,690	1,290	2,970	1,390	1,290	1,220	1,210	1,170	1,150	1,1
23,000	3,490	2,120	1,530	3,220	1,670	1,540	1,540	1,500	1,420	1,460	1,2
24,000	4,600	2,960	1,910	4,230	1,920	1,820	1,790	1,810	1,720	1,850	1,5
25,000	5,450	4,450	1,550	5,760	2,720	1,950	1,810	1,870	1,800	1,860	1,4
25,500	5,790	5,320	1,820	6,550	3,590	1,650	1,840	1,870	1,860	1,530	1,5
26,000	6,060	5,490	1,750	6,970	4,190	1,710	1,880	1,750	1,810	1,870	1,5
26,500	11,390	7,740	1,950	12,410	5,220	2,050	2,050	2,010	1,870	1,960	1,6
27,000	14,520	9,140	2,220	15,240	6,440	2,530	2,200	2,320	1,920	1,750	1,7
27,500	16,750	10,420	2,900	17,740	7,960	3,050	3,760	2,750	1,880	1,790	1,7
27,500	17,530	11,210	2,470	20,230	9,380	3,610	4,820	3,400	1,890	1,810	1,8
27,750	18,750	11,780	3,230	21,270	10,590	3,940	5,340	4,300	1,720	1,870	1,9
27,750	20,430	12,530	4,540	21,270	11,490	4,150	5,820	4,710	1,730	1,900	1,9
28,000	22,000	13,960	5,770	24,760	12,230	4,490	6,240	5,020	1,740	2,020	2,0
28,000	22,630	14,420	5,410	26,420	12,740	4,610	6,740	5,400	1,790	2,150	2,1
28,250	23,510	14,720	6,300	28,530	13,040	4,840	7,240	5,600	1,810	2,230	2,2
28,250	24,240	14,970	6,170	28,740	13,220	4,970	7,540	5,770	1,850	2,350	2,3
28,500	25,040	14,970	6,510	27,730	13,370	5,010	7,890	5,920	1,910	2,440	2,4
28,750	25,190	15,460	6,850	29,460	13,470	5,110	8,190	6,080	1,940	2,570	2,7
28,750	25,110	15,700	7,000	30,190	13,540	5,190	8,430	6,180	1,960	2,650	2,9
28,750	25,990	15,840	7,400	31,170	13,610	5,210	8,660	6,200	2,170	3,140	3,1
28,750	26,100	16,140	7,790	31,740	13,660	5,300	8,810	6,210	2,210	3,210	3,1
28,000	25,820	16,370	8,120	31,460	13,700	5,410	8,940	6,210	2,300	3,290	3,4
29,300	40,100	16,700	8,290	32,740	13,740	5,510	9,040	6,210	2,370	3,350	3,5
29,250	41,190	17,010	8,420	33,340	13,770	5,610	10,820	6,210	2,410	4,030	4,0
29,250	42,070	17,260	8,540	34,030	13,800	5,710	11,010	6,210	2,700	4,350	4,5
29,500	43,040	17,510	8,650	34,730	13,820	5,800	11,240	6,210	2,960	5,030	5,0
29,750	43,150	17,720	8,760	35,420	13,840	5,900	11,440	6,210	3,150	5,360	5,3
29,750	43,210	17,940	8,870	35,940	13,860	6,000	11,540	6,210	3,280	5,570	5,6
30,000	43,280	18,140	8,970	36,440	13,880	6,100	11,640	6,210	3,380	5,730	5,8
30,000	43,350	18,340	9,070	36,940	13,900	6,190	11,740	6,210	3,460	5,870	5,9
30,500	43,420	18,540	9,160	37,440	13,920	6,290	11,840	6,210	3,540	6,000	6,1
30,500	43,490	18,740	9,250	37,940	13,940	6,390	11,940	6,210	3,610	6,120	6,2
30,750	43,560	18,940	9,340	38,440	13,960	6,490	12,040	6,210	3,680	6,240	6,3
31,000	43,630	19,140	9,430	38,940	13,980	6,590	12,140	6,210	3,750	6,350	6,4
31,000	43,700	19,340	9,520	39,440	14,000	6,690	12,240	6,210	3,820	6,460	6,5
31,250	43,770	19,540	9,610	39,940	14,020	6,790	12,340	6,210	3,890	6,570	6,6
31,500	43,840	19,740	9,700	40,440	14,040	6,890	12,440	6,210	3,960	6,680	6,7
31,500	43,910	19,940	9,790	40,940	14,060	6,990	12,540	6,210	4,030	6,790	6,8
31,500	43,980	20,140	9,880	41,440	14,080	7,090	12,640	6,210	4,100	6,900	6,9
31,750	44,050	20,340	9,970	41,940	14,100	7,190	12,740	6,210	4,170	7,010	7,0
31,750	44,120	20,540	10,060	42,440	14,120	7,290	12,840	6,210	4,240	7,120	7,1
32,000	44,190	20,740	10,150	42,940	14,140	7,390	12,940	6,210	4,310	7,230	7,2
32,250	44,260	20,940	10,240	43,440	14,160	7,490	13,040	6,210	4,380	7,340	7,3
32,250	44,330	21,140	10,330	43,940	14,180	7,590	13,140	6,210	4,450	7,450	7,4
32,500	44,400	21,340	10,420	44,440	14,200	7,690	13,240	6,210	4,520	7,560	7,5
32,750	44,470	21,540	10,510	44,940	14,220	7,790	13,340	6,210	4,590	7,670	7,6
32,750	44,540	21,740	10,600	45,440	14,240	7,890	13,440	6,210	4,660	7,780	7,7
33,000	44,610	21,940	10,690	45,940	14,260	7,990	13,540	6,210	4,730	7,890	7,8
33,000	44,680	22,140	10,780	46,440	14,280	8,090	13,640	6,210	4,800	8,000	7,9
33,250	44,750	22,340	10,870	46,940	14,300	8,190	13,740	6,210	4,870	8,110	8,0
33,500	44,820	22,540	10,960	47,440	14,320	8,290	13,840	6,210	4,940	8,220	8,1
33,500	44,890	22,740	11,050	47,940	14,340	8,390	13,940	6,210	5,010	8,330	8,2
33,750	44,960	22,940	11,140	48,440	14,360	8,490	14,040	6,210	5,080	8,440	8,3
34,000	45,030	23,140	11,230	48,940	14,380	8,590	14,140	6,210	5,150	8,550	8,4
34,000	45,100	23,340	11,320	49,440	14,400	8,690	14,240	6,210	5,220	8,660	8,5
34,250	45,170	23,540	11,410	49,940	14,420	8,790	14,340	6,210	5,290	8,770	8,6
34,500	45,240	23,740	11,500	50,440	14,440	8,890	14,440	6,210	5,360	8,880	8,7
34,500	45,310	23,940	11,590	50,940	14,460	8,990	14,540	6,210	5,430	8,990	8,8
34,750	45,380	24,140	11,680	51,440	14,480	9,090	14,640	6,210	5,500	9,100	8,9
35,000	45,450	24,340	11,770	51,940	14,500	9,190	14,740	6,210	5,570	9,210	9,0

[a] To convert microinches/inch strain to percent strain, move decimal point four places to left.

6. Pressure-strain data from model vessel V6.2
(vessel V-4 prolongation)

See Fig. F.1 for gage locations
Test temperature: 130°F
Gage size: length, 1.15 in.; depth, .44 in.

	Strain (μin/in.)[a] to gage No. -							
)	6	7	8	9	10	11	12	13
10	0	0	0	10	0	10	10	10
840	220	320	230	220	220	220	220	210
150	410	410	420	410	410	420	420	390
680	630	620	640	610	620	650	620	590
950	870	840	850	850	840	840	840	790
840	960	960	950	950	950	950	950	870
130	1,110	1,060	1,070	1,050	1,050	1,050	1,050	990
870	1,150	1,150	1,150	1,110	1,110	1,110	1,110	1,040
390	1,210	1,220	1,210	1,170	1,150	1,170	1,170	1,100
570	1,340	1,340	1,300	1,240	1,260	1,250	1,270	1,150
820	1,420	1,430	1,410	1,320	1,350	1,340	1,370	1,220
720	1,540	1,710	1,570	1,400	1,460	1,450	1,500	1,290
390	1,650	1,940	1,670	1,460	1,530	1,520	1,590	1,360
190	1,810	2,130	1,850	1,510	1,570	1,590	1,670	1,380
220	2,050	2,750	2,010	1,570	1,660	1,670	1,750	1,420
440	2,650	3,200	2,320	1,620	1,730	1,750	1,850	1,440
640	3,000	3,760	2,750	1,660	1,790	1,790	1,930	1,470
360	3,410	4,620	3,400	1,690	1,810	1,840	1,990	1,510
790	3,940	5,540	4,400	1,720	1,870	1,900	2,060	1,550
960	4,750	5,620	4,710	1,750	1,900	1,930	2,090	1,540
520	5,440	6,440	5,320	1,740	2,020	2,050	2,130	1,560
780	6,110	6,940	6,030	1,750	2,130	2,150	2,290	1,570
900	6,470	7,240	6,390	1,810	2,230	2,250	2,370	1,570
200	6,740	7,570	6,620	1,850	2,330	2,340	2,460	1,600
570	6,910	8,390	7,020	1,910	2,490	2,490	2,590	1,620
070	7,160	8,750	7,240	2,020	2,750	2,740	2,720	1,650
320	7,390	9,130	7,470	2,090	2,930	2,910	2,970	1,670
560	7,610	9,430	9,200	2,170	3,140	3,100	3,150	1,710
760	7,810	9,690	9,410	2,200	3,210	3,190	3,220	1,710
790	7,940	9,850	9,540	2,300	3,440	3,400	3,430	1,730
950	8,210	9,970	9,740	2,370	3,620	3,570	3,590	1,770
200	8,370	10,320	10,200	2,600	4,070	4,040	4,010	1,790
600	8,530	10,970	10,970	2,830	4,440	4,370	4,310	1,810
120	8,700	11,280	11,140	3,15	5,050	5,010	4,970	2,050
690	9,100	11,790	11,750	3,550	5,790	5,730	5,630	2,260
860	9,140	11,970	11,920	3,950	6,390	6,300	6,140	2,440
340	9,420	12,400	12,370	4,390	6,960	6,860	6,670	2,640
730	9,820	12,730	12,750	4,820	7,470	7,360	7,150	2,840
140	9,490	13,250	13,290	5,290	7,970	7,860	7,630	3,050
910	9,970	13,940	14,060	5,850	8,520	8,410	8,170	3,190
670	9,720	13,280	13,240	5,720	10,020	9,910	9,610	3,410
290	9,890	13,990	13,970	6,370	10,470	10,340	10,040	3,640
090	9,970	14,390	14,290	6,870	11,050	10,910	10,610	3,720
550	10,290	17,010	17,120	9,390	11,740	11,640	11,340	3,940
170	10,370	17,190	17,720	9,990	12,450	12,360	11,990	4,110
940	10,490	17,390	17,770	10,240	12,780	12,660	12,310	4,270
650	11,760	19,150	19,090	10,790	14,110	14,020	13,610	4,440
920	11,910	20,720	20,410	11,410	14,410	14,310	13,920	4,610
460	12,190	20,900	21,100	11,950	15,220	15,090	14,700	4,740
020	12,370	21,190	21,370	12,370	15,590	15,510	14,920	4,910
360	12,280	21,710	21,470	9,040	16,150	15,970	14,990	5,050
570	12,970	22,290	22,550	9,190	16,490	16,250	15,210	5,200
750	13,520	23,240	23,470	9,350	17,070	16,920	15,750	5,1
	13,[illegible]	22,900	23,760	9,470	17,010	16,740	15,720	5,[illegible]

[a] Decimal point four places to left.

2

BLANK PAGE

Table P.7. Pressure-strain data from model vessel V4.1
(vessel V4 prolongation)

See Fig. P.1 for gage locations
Test temperature: 150°F
Flaw size: length, 1.204 in.; depth, 0.221 in.

Pressure (psi)	Strain (μin./in.)[a] at gage No. -										
	1	2	3	4	5	6	7	8	9	10	11
0	0	0	0	0	0	0	0	0	0	0	0
5,000	260	310	360	410	310	460	280	340	290	280	260
10,000	500	580	710	770	570	490	530	560	550	520	1,700
15,000	760	890	1,110	1,190	880	760	800	840	850	800	1,580
20,000	1,020	1,250	1,600	1,730	1,280	1,030	1,070	1,110	1,090	1,060	1,520
25,000	1,420	3,490	4,280	5,730	3,410	1,460	1,410	1,620	1,570	1,580	950
26,000	1,630	5,440	7,170	8,580	5,130	1,670	1,510	1,810	1,750	1,670	850
27,000	1,990	8,070	11,190	13,070	7,940	2,190	1,600	2,150	2,010	1,880	750
27,250	2,170	8,860	12,080	14,660	8,950	2,490	1,660	2,430	2,340	2,150	670
27,500	2,560	10,060	14,090	17,250	10,380	3,040	1,780	2,760	2,640	2,460	620
28,000	3,370	11,760	16,780	20,850	12,180	3,890	1,840	3,240	3,070	2,880	510
28,500	4,210	13,760	20,390	24,590	13,930	4,560	2,100	4,330	4,100	3,880	290
28,750	4,500	14,540	21,740	26,050	14,580	4,800	2,280	4,880	4,630	4,400	110
29,000	4,750	15,300	23,400	27,480	15,250	5,010	2,510	5,680	5,450	5,150	170
29,600	5,710	17,830	27,860	32,160	17,470	5,800	3,530	8,090	7,980	7,660	1,360
30,000	6,220	19,150	30,180	34,650	18,660	6,240	4,360	9,640	9,590	9,260	2,110
31,000	8,250	24,690	41,020	44,890	23,370	7,860	6,200	13,580	13,420	12,960	3,980
32,000	10,880	32,740		59,780	29,940	9,920	8,120	17,220	17,270	16,690	5,810
32,700	13,100	40,890		78,900	36,390	11,770	9,480	19,740	19,770	19,090	7,060
33,100	16,440	56,060			40,630	14,450	10,580	21,940	22,010	21,180	8,190
32,500	22,670					19,610	10,740	22,350	22,520	21,550	8,270
0	23,210					19,770	8,430	19,690	19,790	18,990	6,170

[a]To convert microinches/inch strain to percent strain, move decimal point four places to left.

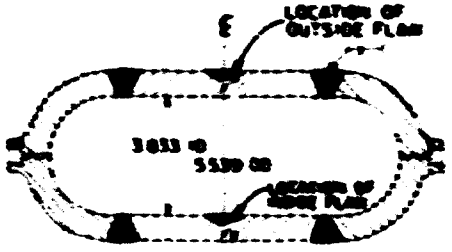

SKETCH OF MODELS

NOTE: WHERE NO DIMENSIONS ARE SHOWN, GAGES ARE PLACED SYMMETRICALLY ABOUT CENTER LINE OF FLAW. ALL ARE LOCATED ON OUTSIDE SURFACE

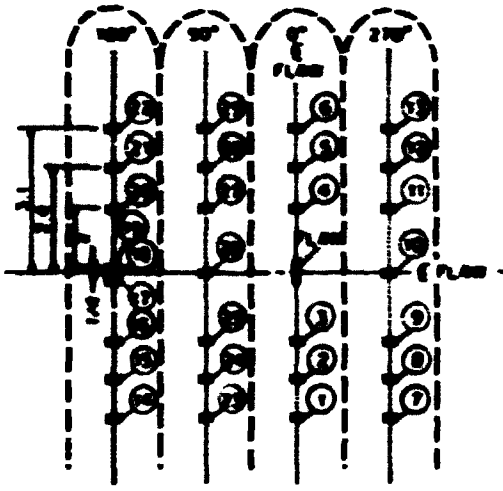

STRAIN GAGE LOCATIONS
MODEL V3-A4

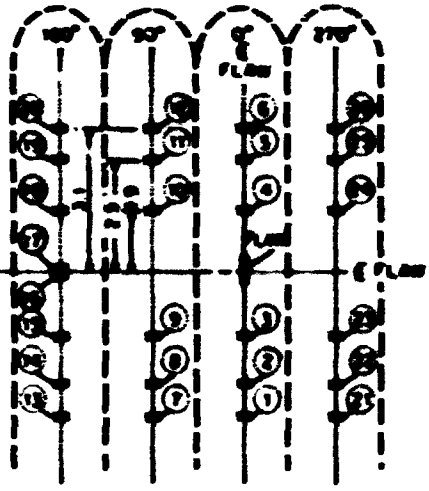

STRAIN GAGE LOCATIONS
MODEL V2-B?-C

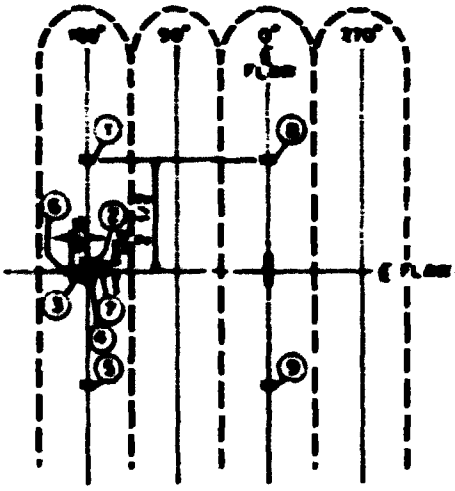

STRAIN GAGE LOCATIONS
MODEL V2-A1-E

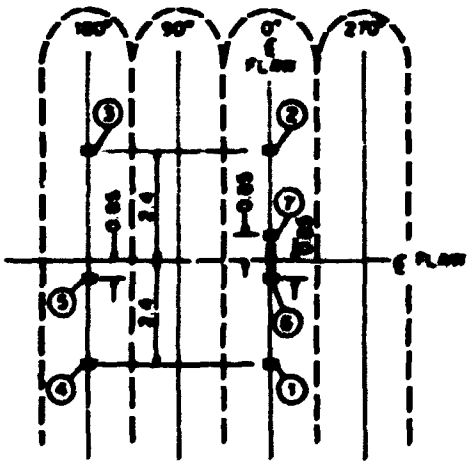

STRAIN GAGE LOCATIONS
MODEL V4-4

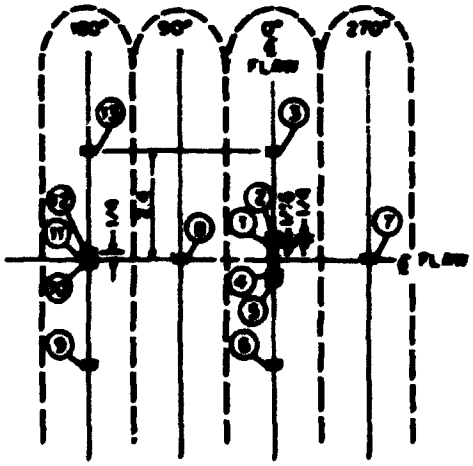

STRAIN GAGE LOCATIONS
MODEL V4-2

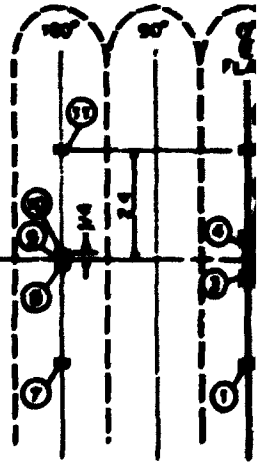

STRAIN GAGE LOCATIONS
MODEL V4-

Fig. F.1. Strain gage locations of models tested for V-3, V-4, and V-6.

NOTE WHERE NO DIMENSIONS ARE SHOWN, GAGES ARE PLACED SYMMETRICALLY ABOUT CENTER LINE OF FLAW. ALL GAGES ARE LOCATED ON OUTSIDE SURFACE

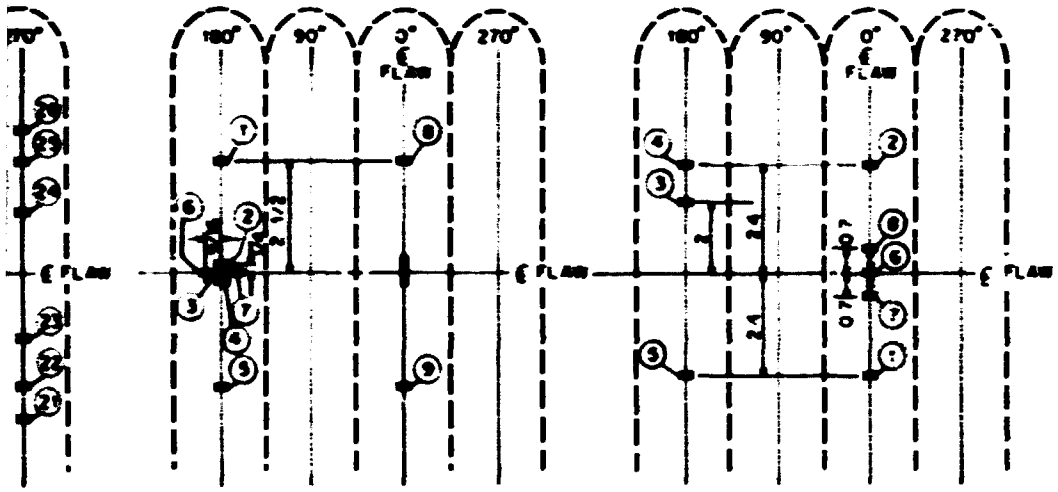

STRAIN GAGE LOCATIONS
MODEL V2-A1-E

STRAIN GAGE LOCATIONS
MODEL V4-6

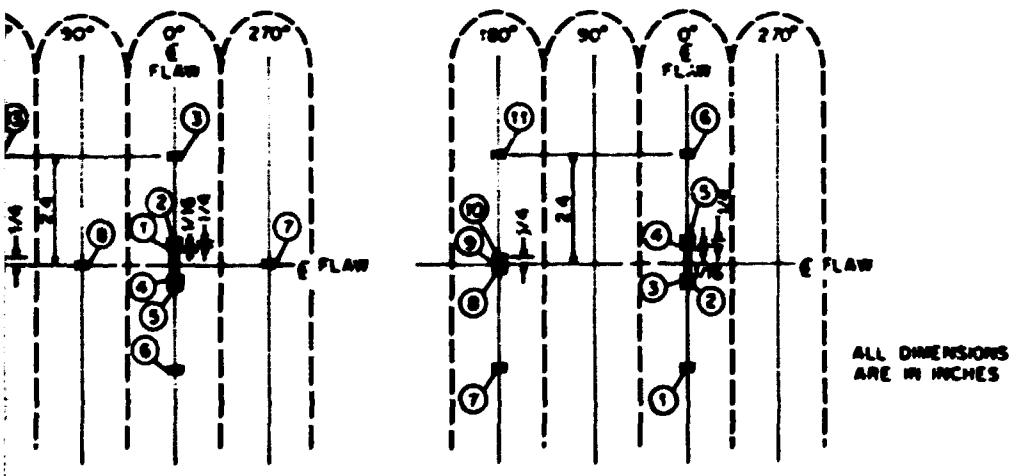

ALL DIMENSIONS ARE IN INCHES

STRAIN GAGE LOCATIONS
MODEL V4-2

STRAIN GAGE LOCATIONS
MODEL V4-1

...sections of models tested for V-2, V-4, and V-6.

2

Appendix G

ANALYSES OF MODEL VESSEL TEST DATA BY THE EQUIVALENT-ENERGY METHOD

In applying the equivalent-energy method of fracture analysis to intermediate test vessels V-1 and V-2, it was found that the accuracy of equivalent-energy calculations depends strongly on the value of the shape factor C used in the basic equation of the method,[1] which for a pressure vessel loaded by internal pressure, can be written as

$$K_{Icd} = C\, p_d^* \sqrt{\pi a_d} \,. \tag{G.1}$$

where the subscript d identifies the thickness of the component in the region of the flaw and p_d^* defines the end point of the extended initial tangent to the pressure-strain curve, the area under which is the same as the area under the actual pressure-strain curve at maximum load. When the equivalent-energy method was first developed, it was postulated that the shape factor C should be equal to the value calculated elastically for a linear-elastic fracture mechanics analysis.[2] This was, in fact, a necessity if the term C was to be a constant in Eq. (G.1), since the equivalent-energy method was formulated in such a way that it would automatically reduce to linear-elastic fracture mechanics for completely linear behavior. However, the pretest analysis of intermediate test vessel V-1 by the equivalent-energy method,[3] using a value of C = 1.60, which agreed with the linear elastic value, underestimated the failure strain of vessel V-1 by approximately a factor of 2. Subsequently,[1] a value of C = 1.132 was calculated from the test results obtained from model vessel V2-A1-B, and this value led to a more accurate posttest analysis of intermediate test vessel V-1.

The next pretest estimate made by the equivalent-energy method[3] was for intermediate test vessel V-2, using a value of C = 1.10, which was based on the test results obtained from model vessel V2-A1-F. In this case, the pretest estimate overpredicted the failure strain of vessel V-2 by approximately a factor of 2, implying that in this case the shape factor was too low instead of too high.

The apparently contradictory results described above led to the testing of additional ½-scale steel models of the vessels to examine the possible effects of flaw shape and size on the experimentally determined equivalent-energy shape factor. The results of these tests are summarized here, along with other model and intermediate pressure vessel data used in the pre- and posttest equivalent-energy analyses of intermediate test vessels V-3, V-4, and V-6.

In order to calculate an equivalent-energy shape factor from experimental pressure vessel data, Eq. (G.1) is rearranged to read

$$C = \frac{K_{Icd}}{p_f^* \sqrt{\pi a_d}} \,. \tag{G.2}$$

The value of K_{Icd} is determined by testing compact specimens having the same thickness as the thickness of the test vessel in the region of the flaw and the same test temperature as the vessel. The value of a_d is the flaw depth in the test vessel. The pseudoelastic failure pressure p_f^* in Eq.(G.2) is determined by measuring two areas under the vessel's nonlinear pressure-strain curve, a calculated example of which is shown in Fig. G.1. The pressure-strain curve is assumed to be linear up to or beyond point A and becomes nonlinear at or beyond point A. By definition,

$$\frac{(p_A)^2}{2M} = E_A \tag{G.3}$$

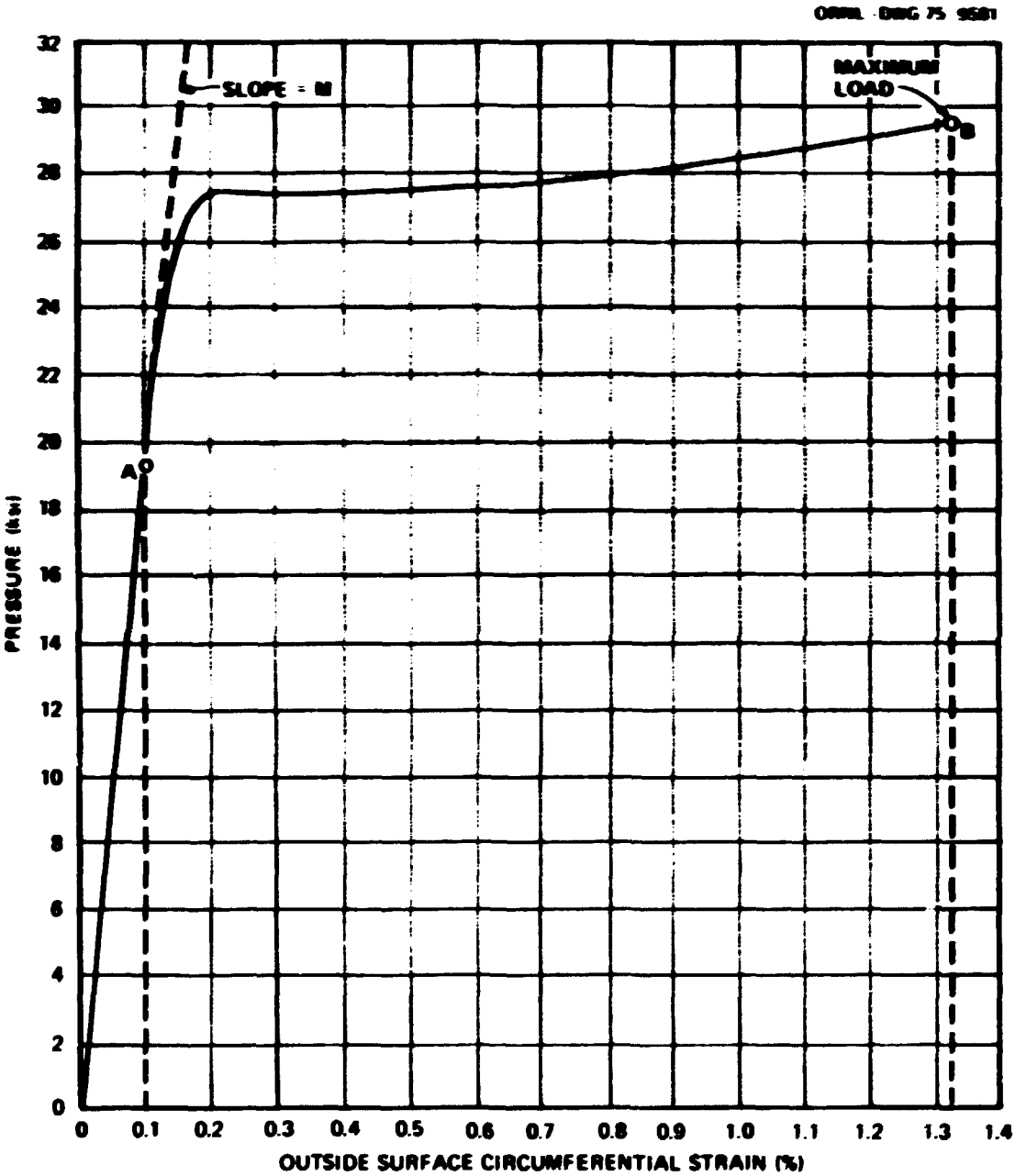

Fig. G.1. Typical pressure–outside circumferential strain curve for intermediate test vessel geometry showing points related to area measurements required for an equivalent-energy analysis.

and

$$\frac{(p_f^*)^2}{2M} = E_B \,. \tag{G.4}$$

where p_A is the pressure at point A; E_A and E_B are the areas under the curves OA and OAB, respectively; and M is the slope of the linear portion of the pressure-strain curve which includes the segment OA. Dividing Eq. (G.4) by Eq. (G.3) and rearranging gives

$$p_f^* = p_A \sqrt{\frac{E_B}{E_A}} \,. \tag{G.5}$$

Since, from Eq. (G.3),

$$\frac{p_A}{\sqrt{E_A}} = \sqrt{2M} \,. \tag{G.6}$$

it can be seen that the point A can be any point on the linear portion of the pressure-strain curve.

Because only the ratio E_B/E_A affects the value of p_f^*, the areas E_A and E_B can be measured by any convenient arbitrary scale. The usual practice is to plot the pressure-strain curve on graph paper having 20 lines to the inch in both directions and then to count the number of $\frac{1}{20} \times \frac{1}{20}$ in. grid line squares lying beneath the curve.

Table G.1 summarizes the experimental data and shape factor values that were used either for making the pre- and posttest equivalent-energy calculations for intermediate test vessels V-3, V-4, and V-6, as discussed in Chapter 4, or for the evaluation of flaw shape and size effects on the value of the experimentally determined shape factor. The pressure-strain curves for the specimens listed in Table G.1 are shown in Figs. G.2 through G.12.

The equivalent-energy method as described above requires the measurement of areas under nonlinear curves, but this step can usually be replaced, at least for checking purposes, by a straightforward calculation based on a bilinear approximation to the pressure-strain curve with no significant loss in accuracy. The initial elastic portion of the bilinear curve is best determined from the theoretical elastic equation relating pressure and strain. For the intermediate test vessels and their geometrically similar models, the straight line representing this equation passes through the point $p = 30$ ksi, $\epsilon_{\theta_\theta} = 0.157\%$, and fits the experimental curves shown in Figs. G.2 through G.12 with negligible error. The position of the strain-hardening branch of the approximate bilinear curve can be chosen by visually balancing the positive and negative areas lying between the actual curve and the bilinear curve.

For a bilinear curve, such as the one shown schematically in Fig. G.13, the value of p_f^* can be determined from

$$p_f^* = p_Y \sqrt{1 + \left(\frac{p_f}{p_Y} + 1\right)\left(\frac{\epsilon_{\theta f}}{\epsilon_{\theta Y}} - 1\right)} \,. \tag{G.7}$$

where the quantities are defined in Fig. G.13. The relationship between p_f^* and the energy at failure is given by Eq. (G.4). Note that when pressure is expressed in ksi and strain in percent, as indicated in Fig. G.13,

Table G.1 Summary of steel model and intermediate test vessel data pertaining to the evaluation of shape factors by the equivalent-energy method

Model or vessel No.	Date Tested	Test temp. (°F)	Flaw size (in.)		Failure conditions		Gage No.	Figure No.	$K_{Ic_{eq}}$ (ksi$\sqrt{in.}$)	p_f^* (ksi)	Shape factor Q	Comments
			Depth	Length	Pressure (ksi)	Strain (%)						
V1-A1-C	5/9/72	130	0.32	1.48	32.2	1.66	138	G-2	210.5	148	1.50	See Ref. 1, p. 167
V1-A1-F	5/24/72	130	0.32	1.48	32.5	1.90	138	G-3	210.5	149	1.41	See Ref. 1, p. 167
V-1	6/30/72	130	2.56	8.25	28.8	0.9	124,125	G-4	311	95.5	1.145	Data from X-Y plotter
V2-A1-B	9/7/72	130	0.36	1.14	34.7	2.30	5	G-5	198	164.4	1.132	See Ref. 1, p. 177
V2-A1-F	9/8/72	32	0.345	1.14	36.5	2.49	5	G-6	194	170	1.10	See Ref. 1, p. 180
V3-A4	12/8/72	130	0.30	1.39	31.5	2.75	18	G-7	174.5	169	1.055	Flaw in weld
V2-A1-C	1/30/73	130	0.37	1.10	33.3	2.11	17	G-8	200	142	1.31	
V2-A1-E	2/27/73	130	0.37	1.20	33.5	2.13	7	G-9	200	155	1.20	
V4.6	4/25/73	200	0.26	0.88	34.2	1.23	9(V4.4)	G-10	220	197	1.232	Inside flaw, raised; used V4.4 curve extended to 34.6 ksi = 3.0% strain
V4.4	5/1/73	200	0.25	0.83	34.5	2.81	9	G-10	220	204	1.215	Curve for page 9 extended to 3.23% to estimate strain at vessel midplane
V4.2	8/10/73	130	0.44	1.15	33.8	1.70]	11	G-11	220	138	1.36	
V4.1	11/2/73	130	0.31	1.32	33.1	2.20	9	G-12	220	153	1.45	

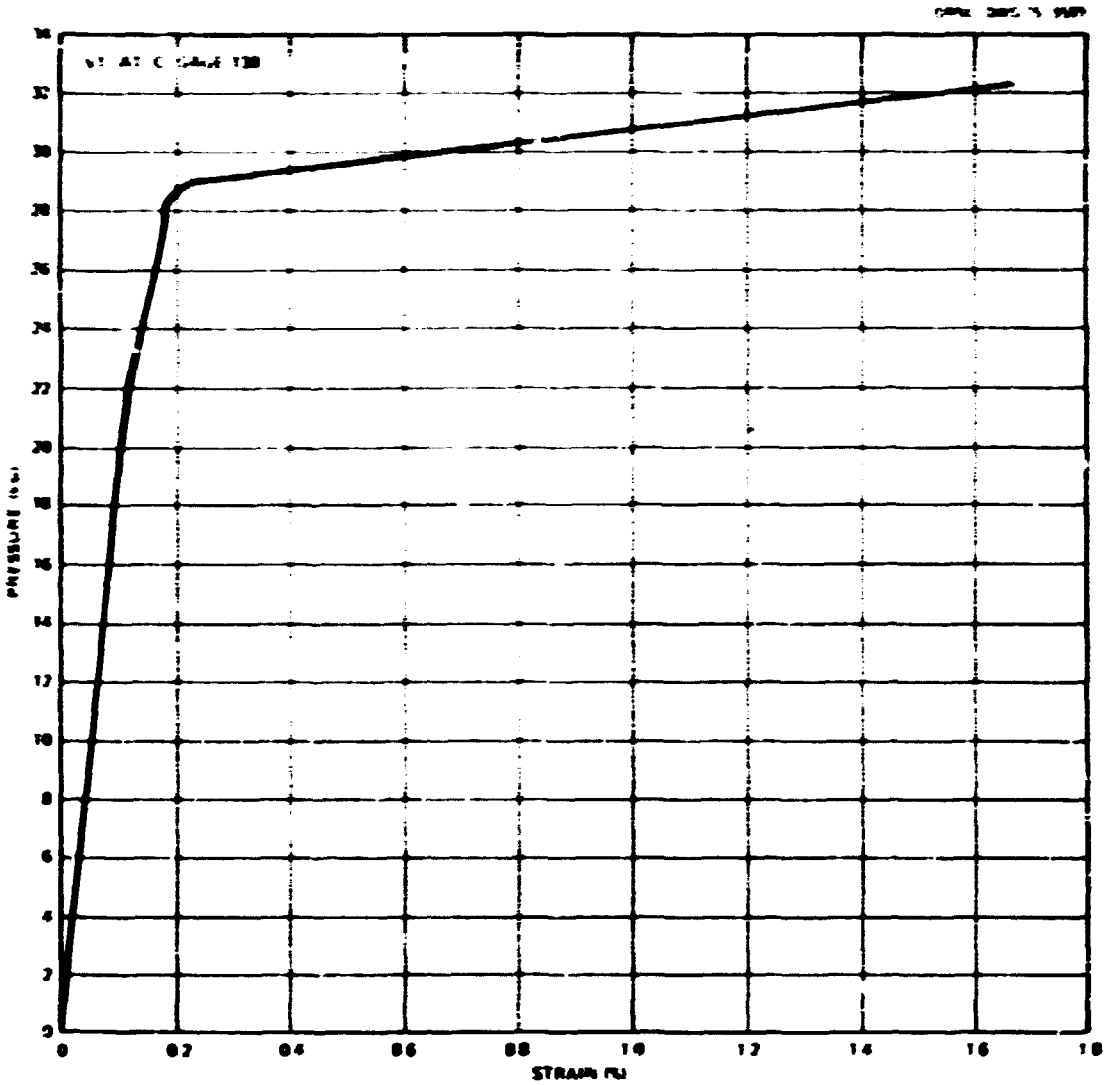

Fig. 6.2. Pressure - outside circumferential strain curve for model vessel VI-A1-C, tested at 130°F (gage 138).

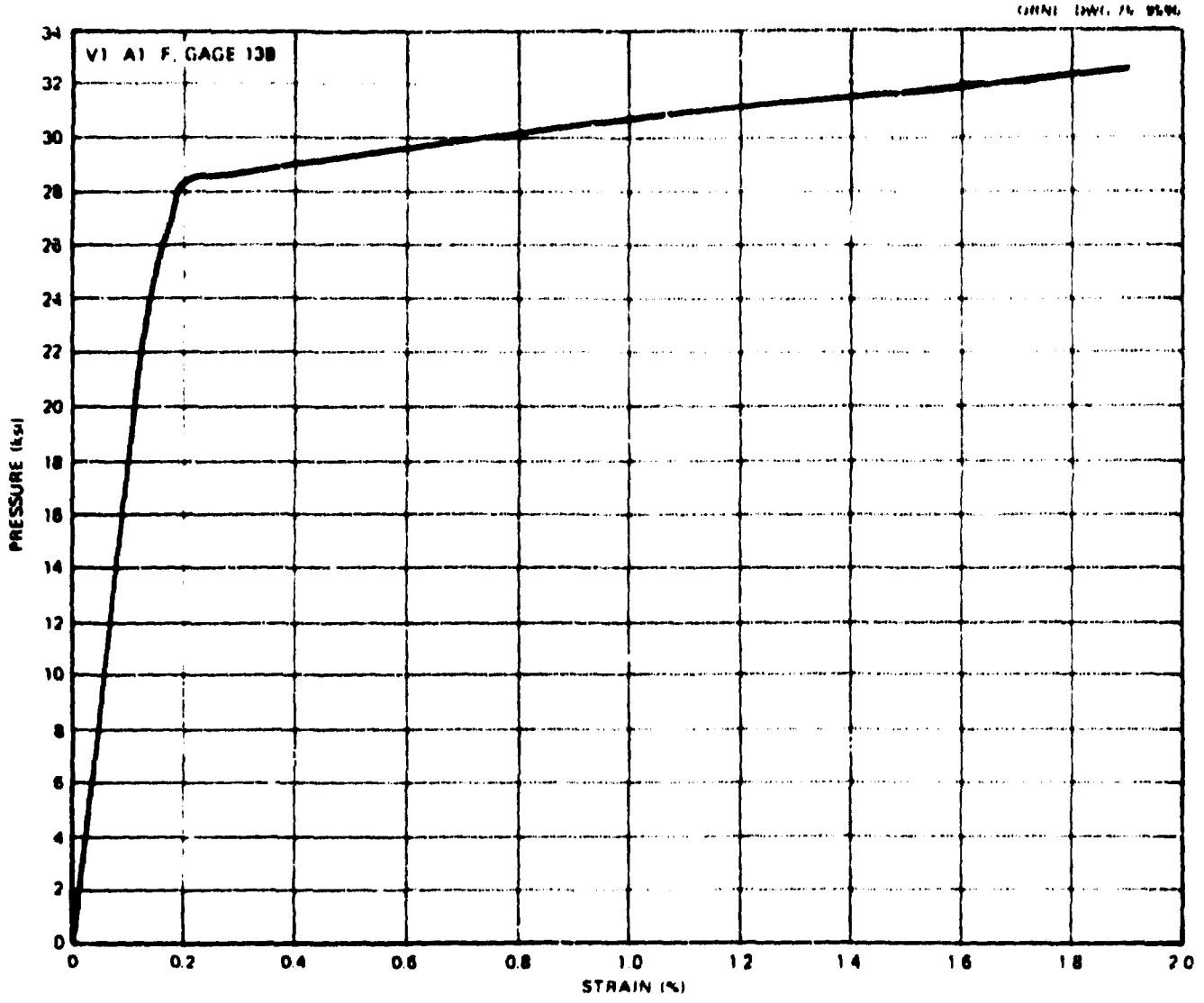

Fig. G.3. Pressure--outside circumferential strain curve for model vessel V1-A1-F, tested at 130°F (gage 138).

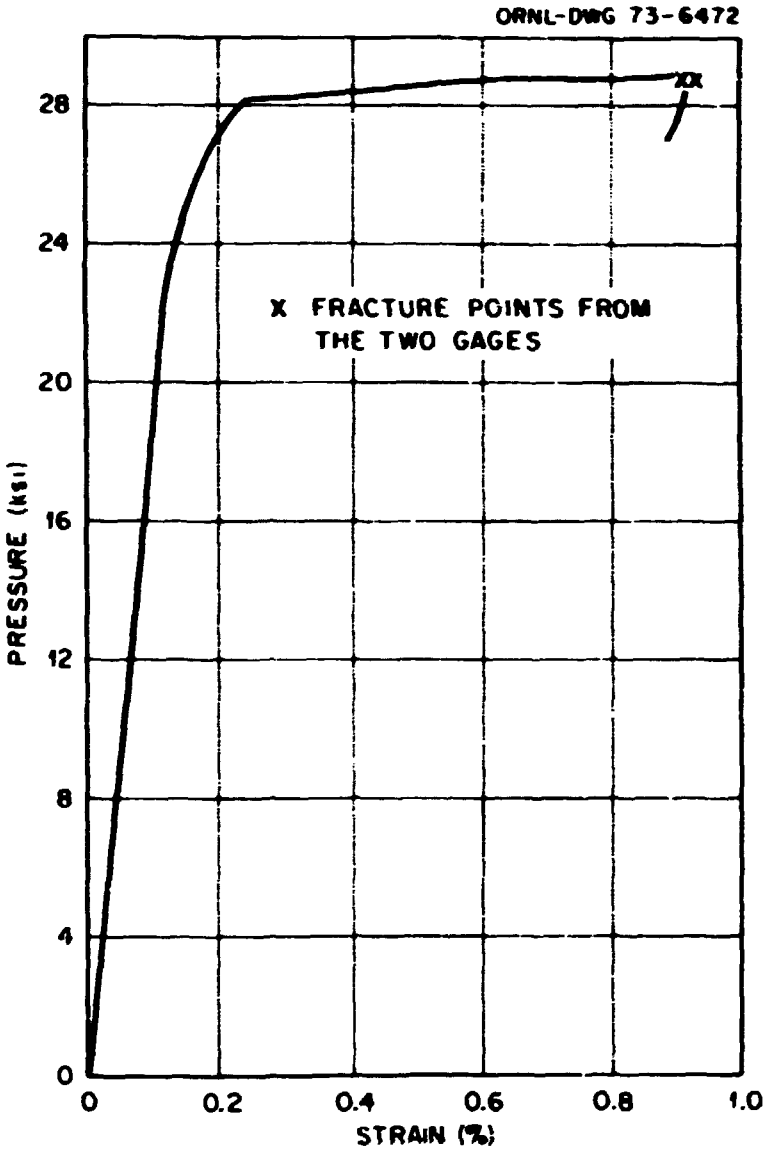

Fig. G.4. Pressure–outside circumferential strain curve for intermediate test vessel V-1, tested at 130°F (gages 124 and 125, X-Y plotter record).

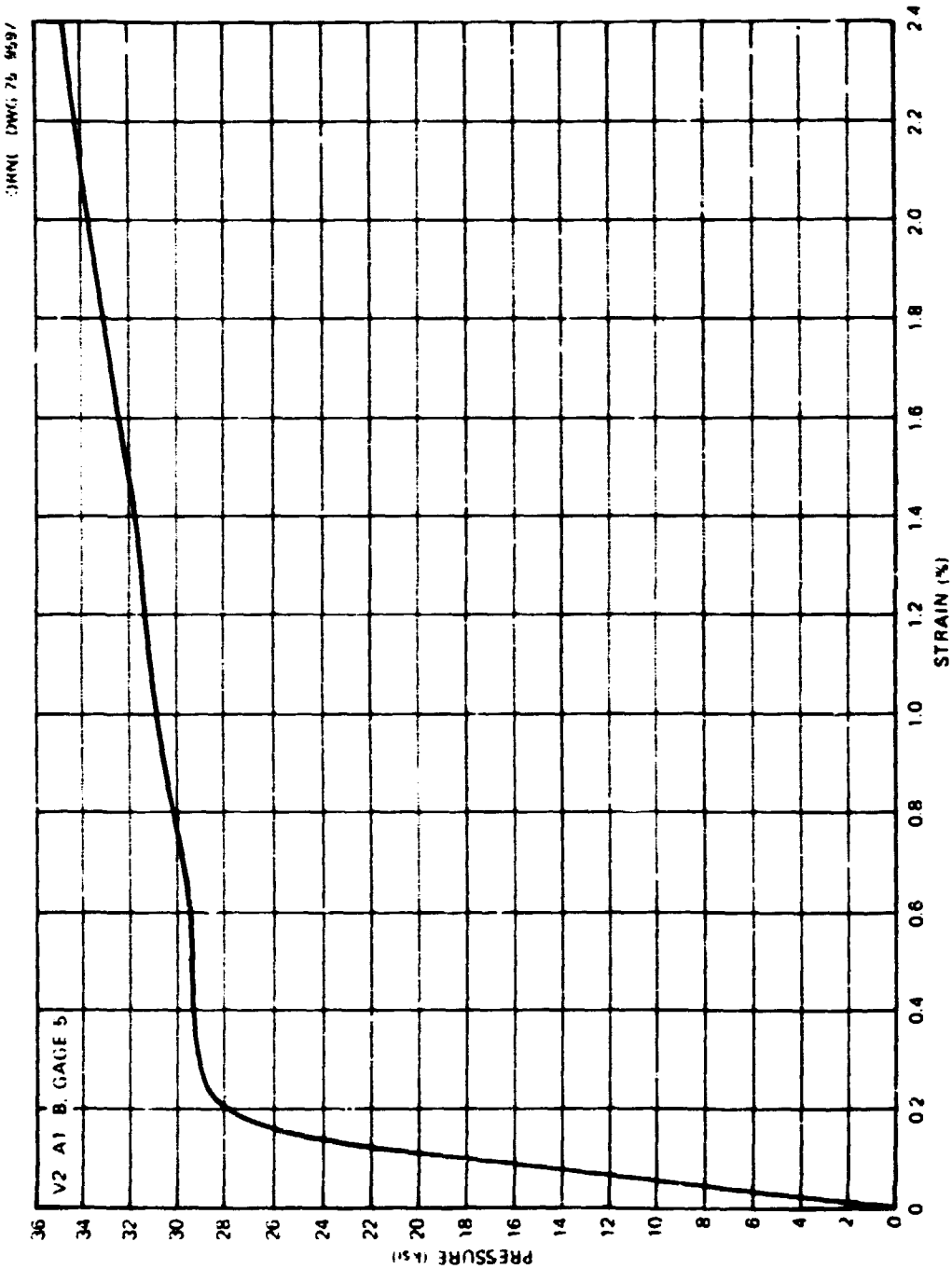

Fig. G.8. Pressure - outside circumferential strain curve for model vessel V2-A1-B, tested at 130°F (gage 5).

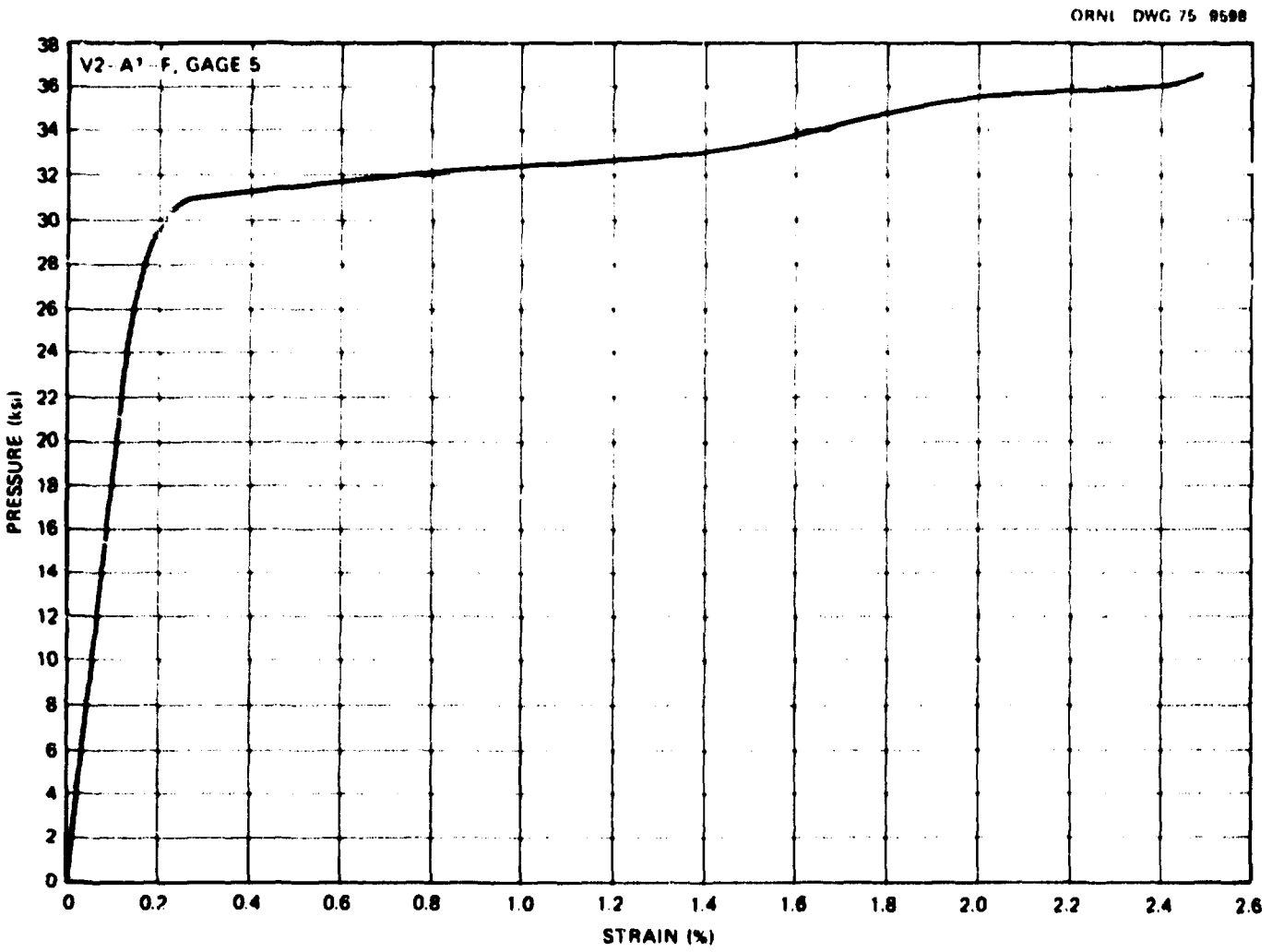

Fig. G.6. Pressure - outside circumferential strain curve for model vessel V2-A1-F, tested at 32°F (gage 5).

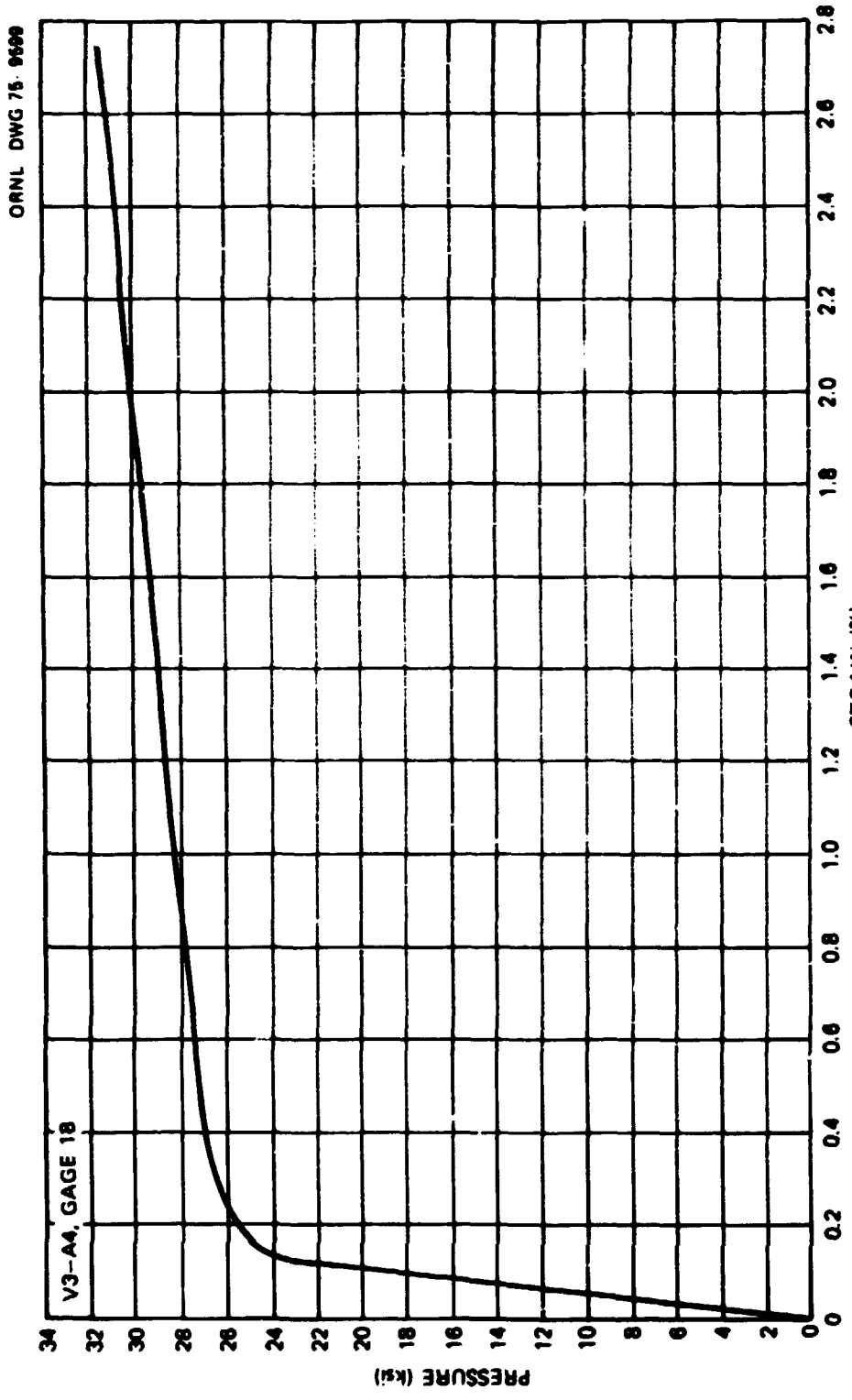

Fig. G.7. Pressure--outside circumferential strain curve for model vessel V3-A4, tested at 130°F (gage 18).

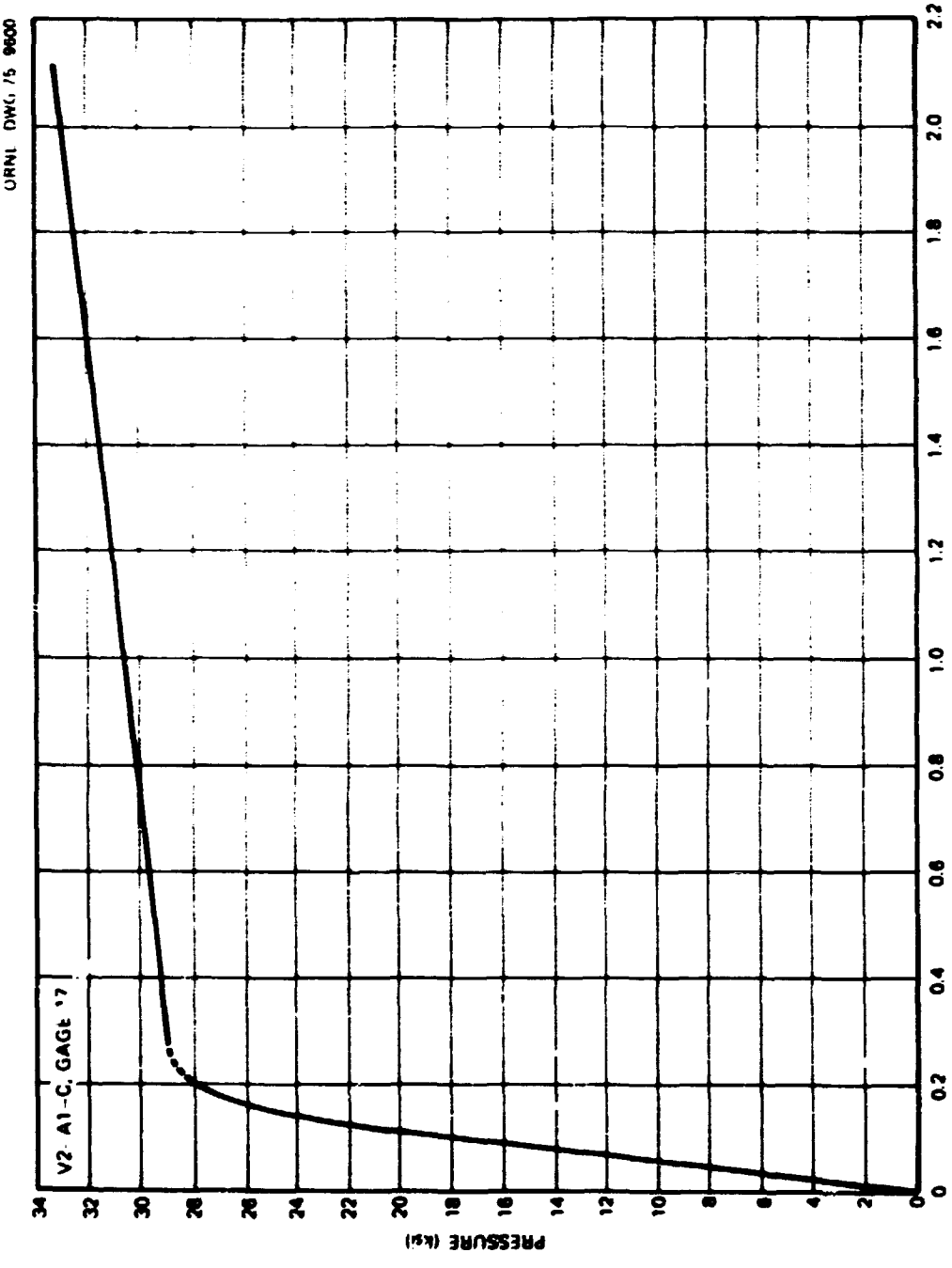

Fig. G.8. Pressure--outside circumferential strain curve for model vessel V2-A1-C, tested at 130°F (page 17).

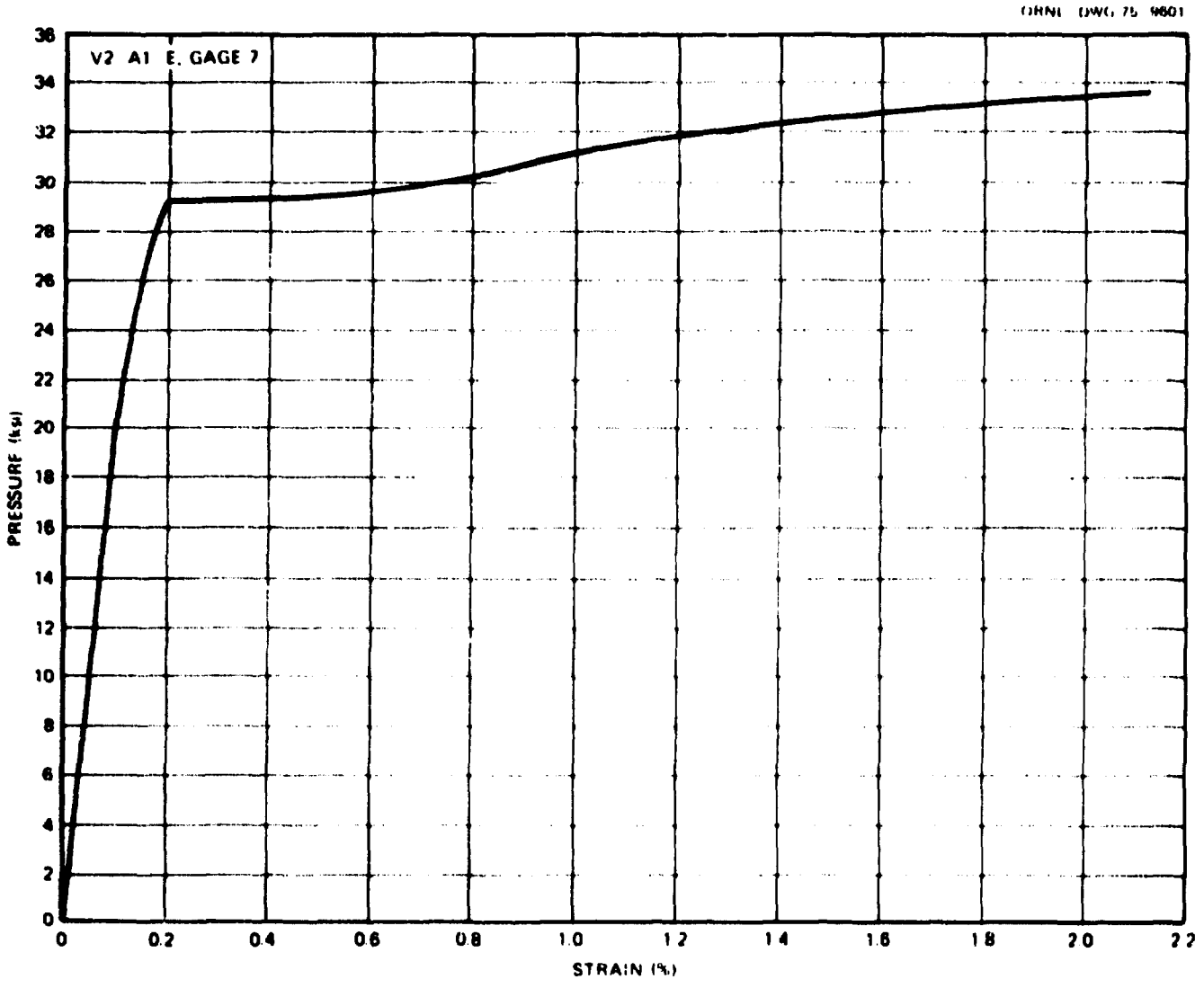

Fig. G.9. Pressure - outside circumferential strain curve for model vessel V2-A1-E, tested at 130°F (gage 7).

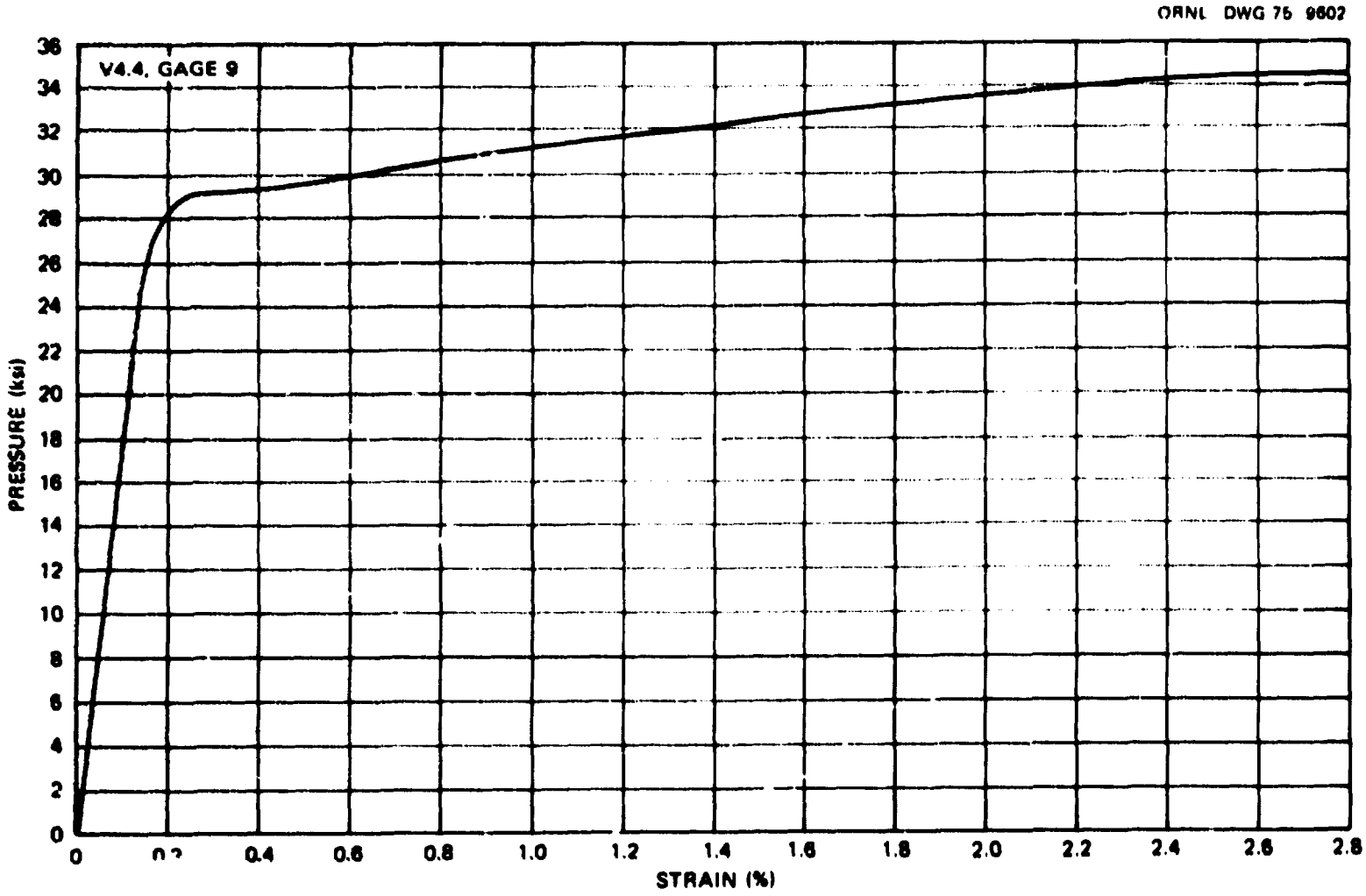

Fig. G.10. Pressure - outside circumferential strain curve for model vessel V4.4, tested at 200°F (gage 9).

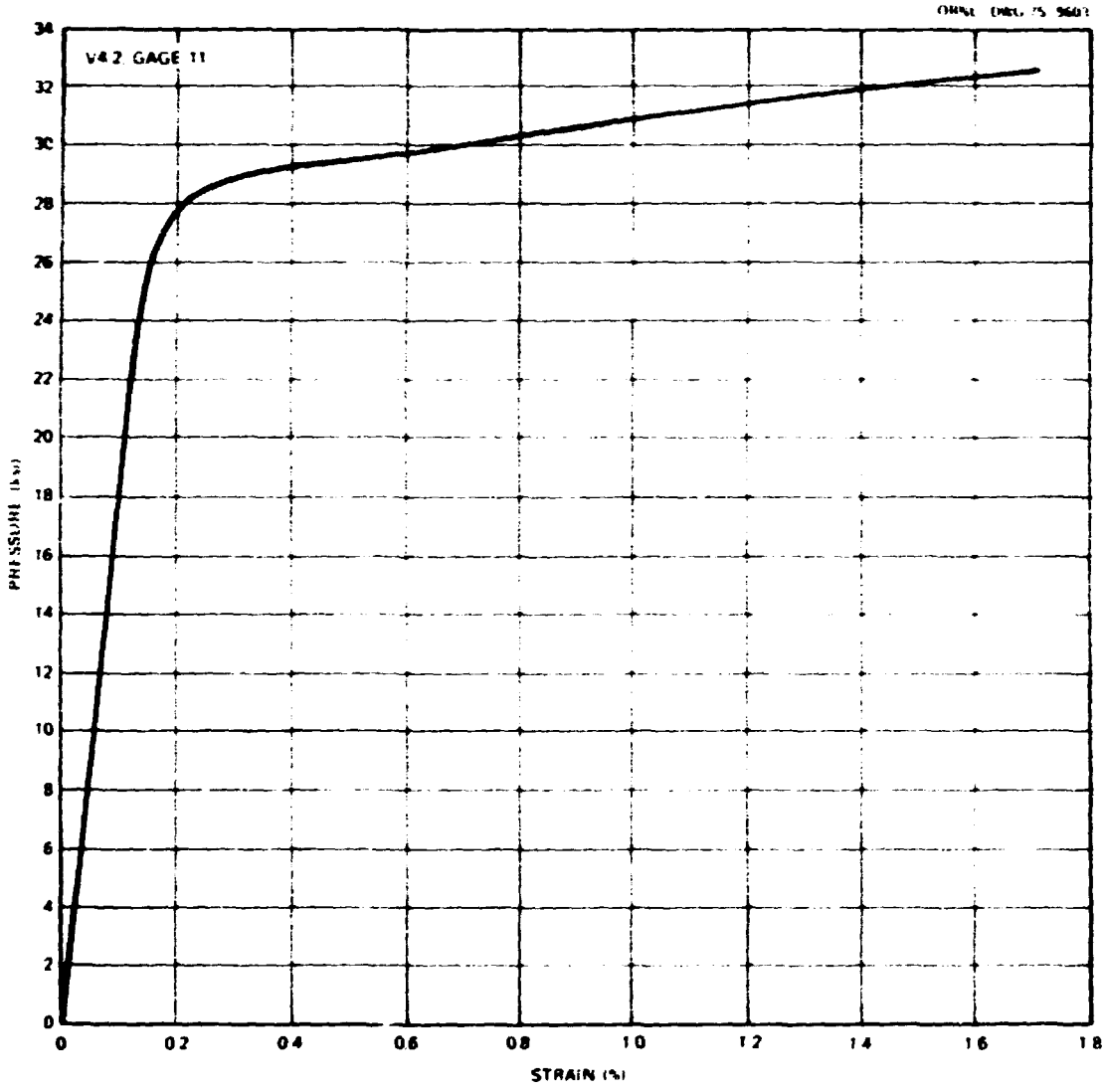

Fig. G.11. Pressure–outside circumferential strain curve for model vessel V4.2, tested at 130°F (gage 11).

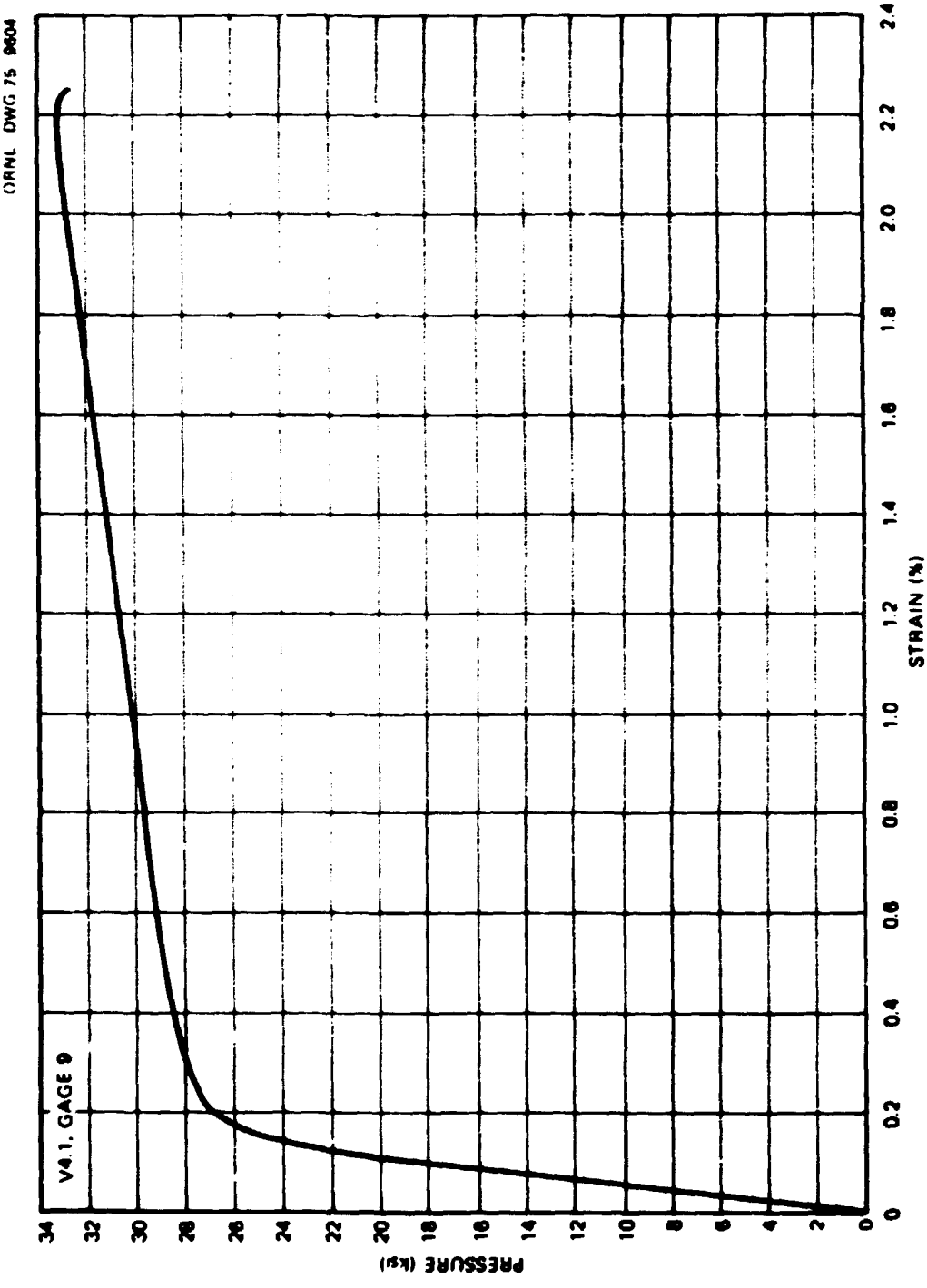

Fig. G.12. Pressure - outside circumferential strain curve for model vessel V4.1, tested at 200°F (gage 9).

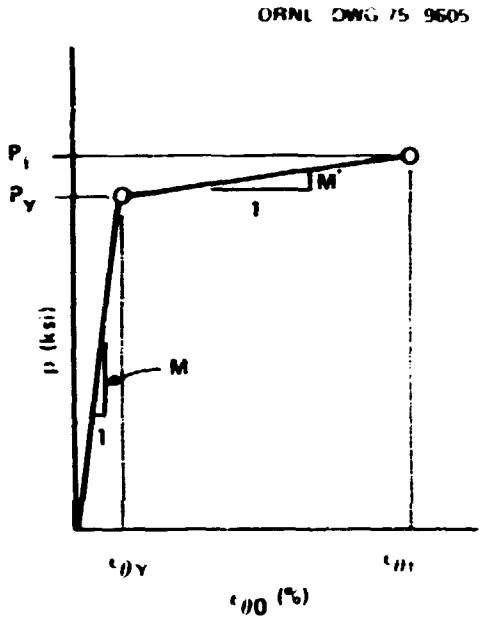

Fig. G.13. Schematic of bilinear pressure–outside circumferential strain curve.

energy will be expressed in ksi·%, which is one-tenth of the value in psi. For the bilinear curve shown in Fig. G.13, the strain corresponding to a given energy E_d, for $p_d^* \geq p_Y$, is given by

$$\epsilon_{\theta_0} = \epsilon_{\theta Y} + \frac{1}{m}\left\{\sqrt{1 + m\left[2\left(\frac{E_d}{p_Y}\right) - \epsilon_{\theta Y}\right]} - 1\right\}. \tag{G.8}$$

where

$$m = \frac{M'}{p_Y} = \frac{[(p_t/p_Y) - 1]}{(\epsilon_{\theta t} - \epsilon_{\theta Y})}. \tag{G.9}$$

Here, M' is the slope of the strain-hardening branch of the bilinear pressure-strain curve and the subscript d identifies the thickness of the component, which must be geometrically similar to the model tested. The pressure corresponding to a given strain for a bilinear pressure-strain curve is given by

$$p = M\epsilon_{\theta_0}, \tag{G.10}$$

for $p_d^* \leq p_Y$ and by

$$p = p_Y[1 + m(\epsilon_{\theta_0} - \epsilon_{\theta Y})] \tag{G.11}$$

for $p_d^* \geq p_Y$.

The bilinear approximation method described above was used to check the values of p_f^* given in Table G.1. Table G.2 gives the values of p_f^* computed from Eq. (G.7) based on bilinear approximations to the pressure-strain curves of each of the specimens listed in Table G.1. The maximum difference between an approximate value and an actual value is less than 6%, and the average of the approximate values is only 0.23% different from the average of the actual values. This is considered to be an adequate check on the values of p_f^* given in Table G.1 as well as a demonstration of the utility of the bilinear approximation method.

Table G.2. Estimates of p_f^* by the bilinear approximation method

Model or vessel No.	p_f (ksi)	p_Y (ksi)	$\varepsilon_{\theta f}$ (%)	$\varepsilon_{\theta Y}$ (%)	p_f^* (ksi)	p_f^* (Table G.1) (ksi)
V1-A1-C	32.2	28.8	1.66	0.150	136	140
V1-A1-F	32.5	28.4	1.90	0.148	146	149
V-1	28.8	27.6	0.9	0.144	94.4	95.5
V2-A1-B	35.0	28.7	2.30	0.150	164	164.4
V2-A1-F	36.5	29.9	2.49	0.156	175	170
V3-A4	31.5	26.2	2.75	0.137	172	169
V2-A1-C	33.0	29.0	2.00	0.152	150	142
V2-A1-F	33.5	28.8	2.13	0.150	154	155
V4.6	34.6	29.8	3.00	0.156	190	197
V4.4	34.7	30.0	3.23	0.157	197	204
V4.2	32.8	28.5	1.70	0.149	137	138
V4.1	33.1	27.7	2.20	0.145	157	153

In order to investigate the effects of flaw shape and size on the equivalent-energy shape factor for surface flaws in pressure vessels, the flaw dimensions for the 1/7-scale steel models listed in Table G.1 were converted to the flaw shape ratios a/2b and the flaw depth ratios a/t listed in Table G.3, with the results plotted in Fig. G.14. The initial implication drawn from Fig. G.14 was that the equivalent-energy shape factor is quite sensitive to flaw size and shape.[3] However, because the effects of flaw size and shape shown in the figure are something less than systematic, another possibility was considered, namely that C might vary systematically with failure strain. Figure G.15 shows a plot of the same shape factor values used to plot Fig. G.14, but with the independent variable being failure strain and the parameter being flaw size. In Fig. G.15, there appears to be a consistent relation between the flaw size and the value of the shape factor for a given failure strain. The shape factor tends to decrease as the flaw size increases. Because of this apparently consistent trend, the curve for a flaw depth of 0.32 in. was drawn by linearly interpolating between the points corresponding to the other flaw sizes. The shape of this curve leaves little doubt that for the 1/7-scale steel models of the intermediate test vessels, the equivalent-energy shape factor for a given flaw size is not constant but decreases with increasing failure strain. It is also apparent from Fig. G.15 that the equivalent-energy shape factor could easily become equal to the elastically calculated value of approximately 1.6 as the failure strain decreases and approaches the elastic range. The fact that an equivalent-energy shape factor still less than the elastic value agreed with the test results from intermediate tensile specimen 15 (see Appendix F), which failed at a gross stress well below the yield stress, does not alter this conclusion, because this result was due to a condition of partial transverse restraint that developed

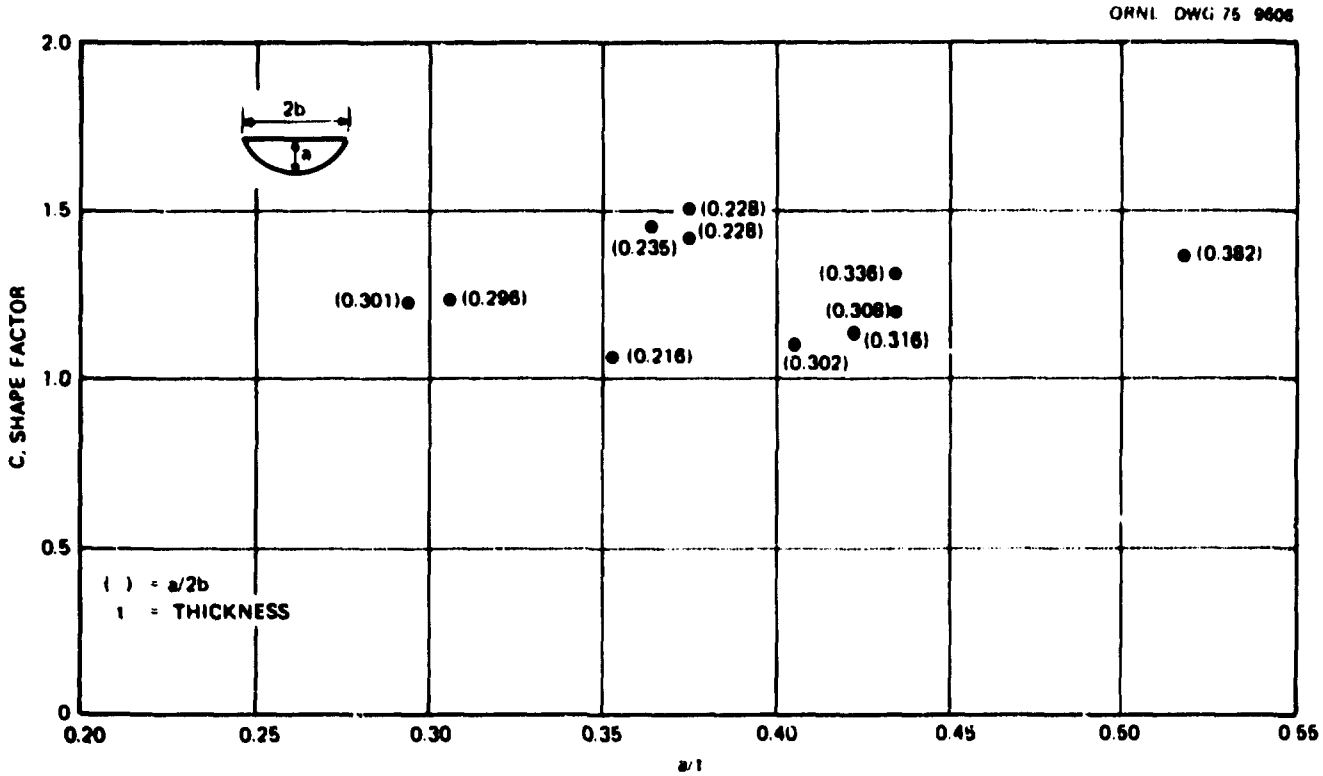

Fig. G.14. Variation of experimentally determined equivalent-energy shape factors for surface cracks in 0.85-in.-thick model pressure vessels of A508 class 2 forging steel with relative flaw depth and flaw shape.

Table G.3. Variation of the equivalent-energy shape factor with flaw shape and size for 0.85-in.-thick model vessels tested between 32 and 200°F

Model No.	$\frac{a}{t}$	$\frac{a}{2b}$	C
V1-A1-C	0.376	0.228	1.50
V1-A1-I	0.376	0.228	1.41
V2-A1-B	0.423	0.316	1.13
V2-A1-F	0.406	0.302	1.10
V3-A4	0.353	0.216	1.06
V2-A1-C	0.435	0.336	1.31
V2-A1-E	0.435	0.308	1.20
V4.6	0.306	0.296	1.23
V4.4	0.294	0.301	1.22
V4.2	0.518	0.382	1.36
V4.1	0.365	0.235	1.45

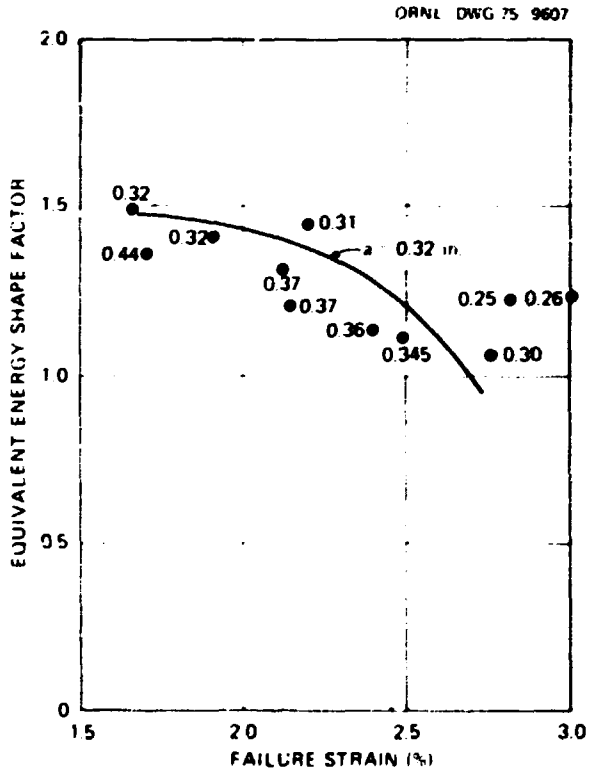

Fig. G.15. Variation of experimentally determined equivalent-energy shape factors for surface cracks in 0.85-in.-thick model pressure vessels of A508 class 2 forging steel with failure strain and flaw size.

in the tensile specimen but that does not develop in the wall of a pressure vessel, as explained in Appendix E. Considering the foregoing results, it is apparent that the overestimate of the failure strain for intermediate test vessel V-2 by the pretest equivalent-energy analysis was probably not due to yield point phenomena, as implied in Appendix H of Ref. 1, but rather mainly to the variation of the equivalent-energy shape factor with failure strain. However, this variation is not explicitly considered in any of the equivalent-energy analyses discussed elsewhere in this report.

References

1. R. W. Derby et al., *Test of 6-inch-thick Pressure Vessels, Series 1: Intermediate Test Vessels V-1 and V-2*, ORNL-4895 (February 1974).
2. F. J. Witt, "The Application of the Equivalent Energy Procedure for Predicting Fracture in Thick Pressure Vessels," pp. 163–67 in *Practical Applications of Fracture Mechanics to Pressure Vessel Technology*, Institution of Mechanical Engineers, London, 1971.
3. F. J. Witt, "Status of the Fracture Investigations of the Heavy-Section Steel Technology Program," paper prepared for presentation at the Second International Conference on Structural Mechanics in Reactor Technology, Berlin, Sept. 10–14, 1973 (unpublished).

Appendix H

DEVELOPMENT OF THE TANGENT MODULUS METHOD OF ELASTIC-PLASTIC FRACTURE ANALYSIS

ABSTRACT

The method of elastic-plastic fracture analysis discussed here is based on Neuber's equation for estimating the actual stress and strain concentration factors of a sharp notch in the elastic-plastic range. The innovation in the analysis is that the basic equation is written in terms of the increments of stress and strain instead of the total stresses and strains, because the former approach is known to provide a more accurate description of elastic-plastic behavior. The use of Neuber's equation as a starting point allows the effects of overall geometry on notch tip behavior to be accounted for by the elastically calculated fracture mechanics shape factor. The result is a simple differential equation that can be directly integrated, provided that the effective tangent modulus in the net section can be estimated as a function of the nominal strain. For this purpose, the average tangent modulus across the net section is used as the effective tangent modulus, and the method of analysis is called the tangent modulus method.

The fracture criterion used in the method is directly related to the value of K_{Ic} and therefore to the results of both standard and small specimen testing. Because the relation between the average tangent modulus across the net section and the nominal strain enters the analysis, predicted fracture strains are functions of both the shape of the stress-strain curve and the nominal strain gradient. These effects have been observed experimentally, but they are not predicted by other methods of fracture analysis presently proposed for structural components.

The method has been successfully applied to the analysis of both large and small surface-cracked tensile bars and a series of model pressure vessels containing surface cracks. Differences in transverse restraint between these two types of specimens have been observed, and these differences can be accounted for in the analysis. The method is presently believed to be a potentially rational and practical method of elastic-plastic fracture analysis for structural components.

Introduction

The need for a method of fracture analysis applicable in the elastic-plastic range of strain became evident at the outset of the HSST program. Randall[1-3] proposed and carried out a series of experiments that were intended to provide the basis for a direct experimental approach to the problem, but it was generally anticipated that eventually analytical methods would also be required. Randall's gross strain data for surface-cracked tensile and bend specimens provided an unusually clear and complete picture of fracture behavior in the elastic-plastic range. In particular, it was revealed that, for surface-cracked tensile specimens, the variation of fracture strain with temperature above the yield strain displays some important trends not predictable by simple extrapolations of linear-elastic fracture mechanics.[1,2,4] As shown in Fig. H.1, the most interesting and obvious feature of Randall's gross strain data was a very abrupt increase in the gross section strain at fracture, under tension loading, over the range of strain corresponding to the yield plateau of the uniaxial tensile stress-strain curve. (Materials without a yield plateau did not exhibit this phenomenon.[1]) Since fracture toughness is a continuous function of temperature, such a discontinuity was not expected to be predictable by a method of fracture analysis based on a relation between a continuous function of total stress or strain and the fracture toughness. In addition, since no such discontinuity had

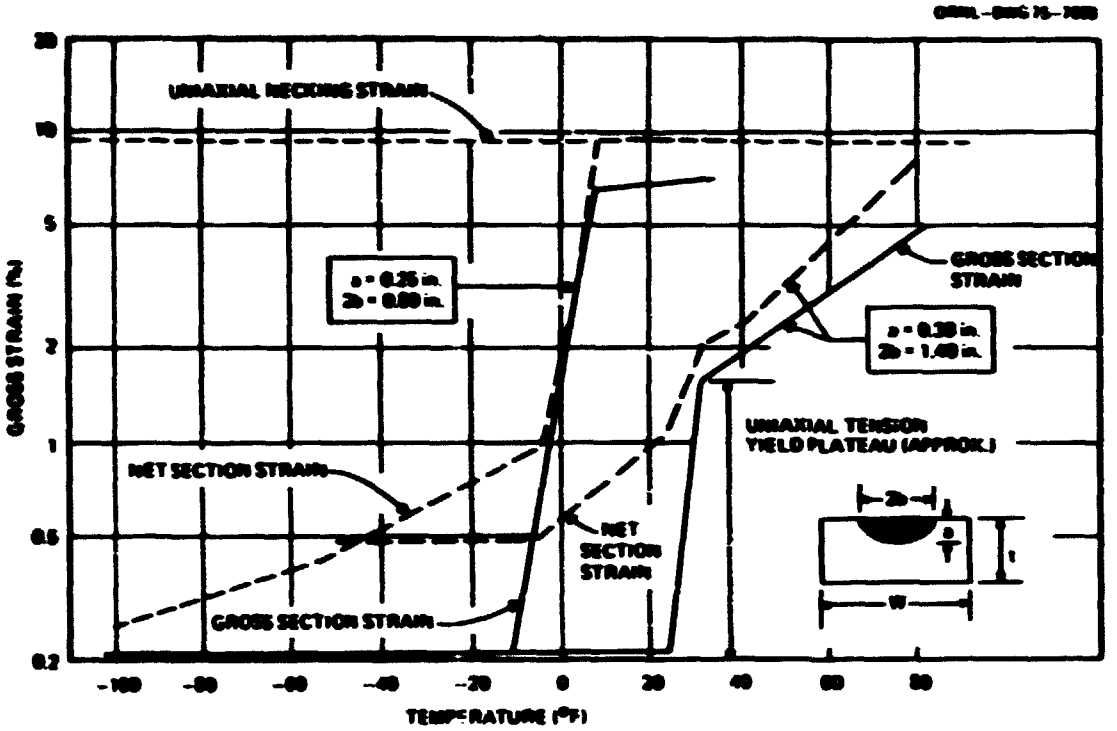

Fig. H.1. Uniaxial tensile gross strain crack tolerance curves for 0.25- and 0.38-in.-deep surface flaws in A533, grade B, class 1 steel.[1]

appeared in either Charpy V-notch impact energy data or dynamic-tear test data, it was evident that an effect of strain gradient on fracture strain should be postulated and that an abrupt increase in fracture strain with temperature should not be predicted for the case of bending.

In order to predict an abrupt rise in the fracture strain-vs-temperature curve through the strain range corresponding to the yield plateau, an incremental analysis rather than a total strain analysis appeared to be more appropriate. In addition, a function compatible with an incremental analysis and relatable to fracture strain was required as a factor that can become discontinuous at the extremities of the strain range corresponding to the yield plateau. The most obvious function that meets both of these requirements is the tangent modulus of the uniaxial stress-strain curve. As shown in Appendix C of Ref. 5, this function can be incorporated as a factor in a differential equation that relates the notch-tip strain increment to the flaw size and to the nominal strain increment at the location of the flaw. This equation is[5]

$$d\varepsilon\sqrt{\rho} = 2C\sqrt{a}\sqrt{\frac{E_t}{E_n}}\,d\lambda\,, \tag{H.1}$$

where ε = notch root strain, ρ = notch root radius, C = linear elastic fracture mechanics shape factor in the expression for K_I, a = crack depth, E_t = tangent modulus corresponding to the nominal (gross) strain λ, E_n = tangent modulus at the base of the notch, λ = nominal strain at the location of the flaw.

It was not immediately obvious whether Eq. (H.1) should be written in terms of the net or the gross section strain. Initial applications of the equation did not explicitly consider net section effects, although it

was tacitly assumed that the net section fracture strain curve should approach the gross section fracture strain curve as the ratio of the crack area to the gross section area becomes small.[6] However, it was later reasoned[2,5] that the crack-tip strain should be more directly related to the net section strain and, therefore, that it is the net section fracture strain that should be directly related to the flaw size and the fracture toughness. This hypothesis was further substantiated by the observation, shown in Fig. H.2, that the gross section fracture stress remains constant, at a value just below the yield stress, over a considerable range of temperature just below the transition temperature.[2,6] Furthermore, as shown in Fig. H.3b, within this same temperature range, the net section fracture strain continues to increase with temperature while passing through the strain range of the yield plateau.[2,6] Since there appears to be nothing significant about a stress just below the yield stress, this implies that the gross section fracture stress and strain are controlled by the net section fracture strain, rather than the reverse. Nevertheless, some interaction between the net and the gross section fracture strain was expected, because the gross section strain should control the transverse restraint applied to the net section. Thus, the analytical approach tentatively chosen was to relate the net section fracture strain to the flaw size and the fracture toughness by means of Eq. (H.1), but also to consider net section effects on transverse restraint, and then to determine the corresponding gross section fracture stress and strain by using equilibrium and the stress-strain curve.

Randall's gross strain data[6] also indicated that the net section stress-strain relation at fracture is still reasonably close to the uniaxial stress-strain curve. Nevertheless, the monotonic increase in the net section fracture strain with temperature through the strain range of the yield plateau implied that during initial yielding of the net section, the notch root strain continuously increases with increasing nominal strain. As a result, the effective value of the tangent modulus E_g in Eq. (H.1) is not necessarily zero during initial yielding of the net section, even though the tangent modulus of the uniaxial stress-strain curve is zero

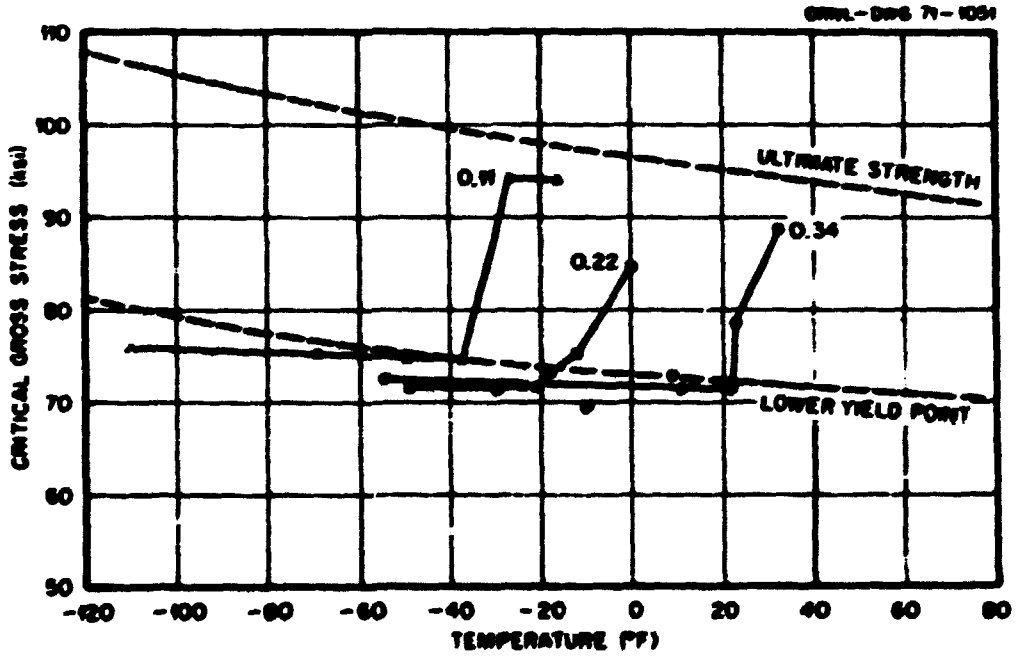

Fig. H.2. Effects of crack size and temperature on gross section stress at maximum load for surface-cracked tensile specimens of A533, grade B, class 1 steel.[2,5]

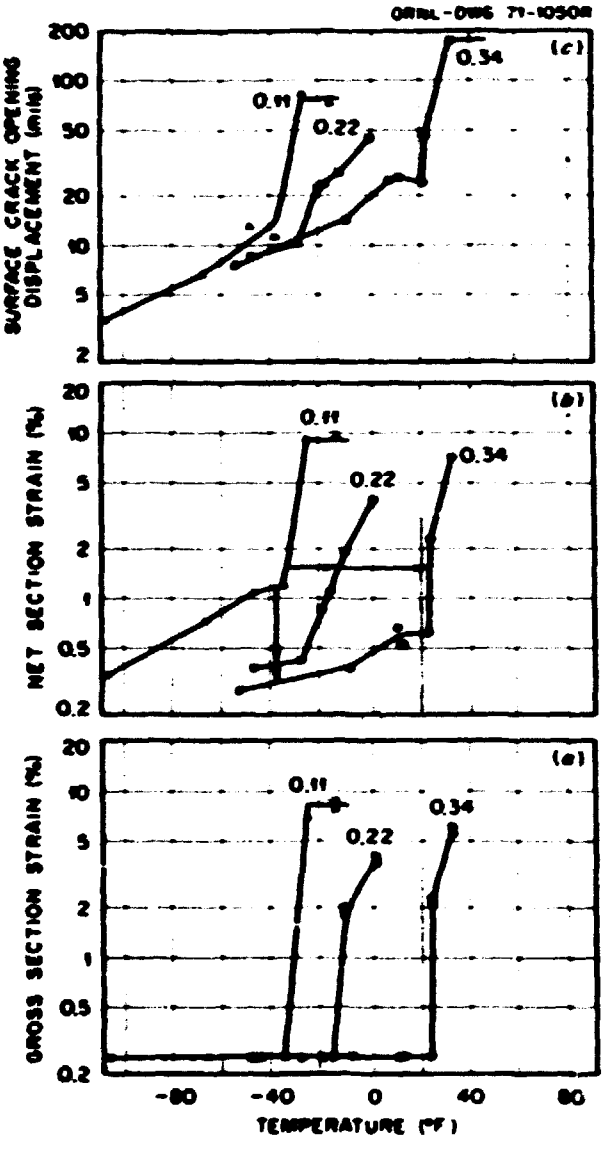

Fig. H.3. Effects of crack size on gross section strain, net section strain, and surface crack-opening displacement at maximum load for surface-cracked tensile specimens of A533, grade B, class 1 steel.[7,8]

within the strain range of the yield plateau. This fact, that the effective value of E_T *may be greater than the* tangent modulus of the uniaxial stress-strain curve, is probably due to the development of strain gradients across the net section and the restraining effects of the regions above and below the crack plane that are under lower stress than the net section. It thus appears that the value of the effective tangent modulus may be a characteristic of the volume of material containing the crack plane and not just of the crack plane itself. Presuming this to be the case, the tangent modulus E_T in Eq. (H.1) was redefined as an effective tangent modulus, a quantity that need not necessarily be equal to the tangent modulus of the uniaxial stress-strain curve at a given value of strain. On the other hand, for tension loading, the relation between the average net section stress and strain was still assumed to be the uniaxial stress-strain curve.

There was no completely analytical procedure available for determining the value of the effective tangent modulus that exists during initial yielding of the net section. Therefore, it was decided to evaluate E_s empirically by comparing trial calculations with several sets of experimental data obtained under different testing conditions. Thus, the overall approach taken was semiempirical. Rather than attempting to completely prove all the assumptions made mathematically, it was considered just as constructive to adequately justify them by comparing calculations with experimental data. The remainder of this appendix describes the developments that have been made thus far in the tangent modulus method, a significant portion of which was accomplished in preparation for the pretest analysis of intermediate test vessel V-4.

Piecewise Linear Representation of the Stress-Strain Curve

The integration of the right side of Eq. (H.1) can be made particularly straightforward by approximating the uniaxial stress-strain curve with a series of straight lines. Figure H.4 shows such an approximation for the true stress-strain curve of A533, grade B, class 1 steel. The true tensile stress S shown in Fig. H.4 is related to the engineering stress S' and to the strain λ by the equation[5]

$$S = S'e^{\lambda} . \tag{H.2}$$

For A533, grade B, class 1 steel, the value of the ultimate tensile stress S'_{ult} is approximately 87 ksi. The use of a value of 12% for the necking strain in Fig. H.4, in contrast to the value of approximately 10% indicated in Fig. H.1, is not considered to be a serious discrepancy in view of the usual variability of this quantity.

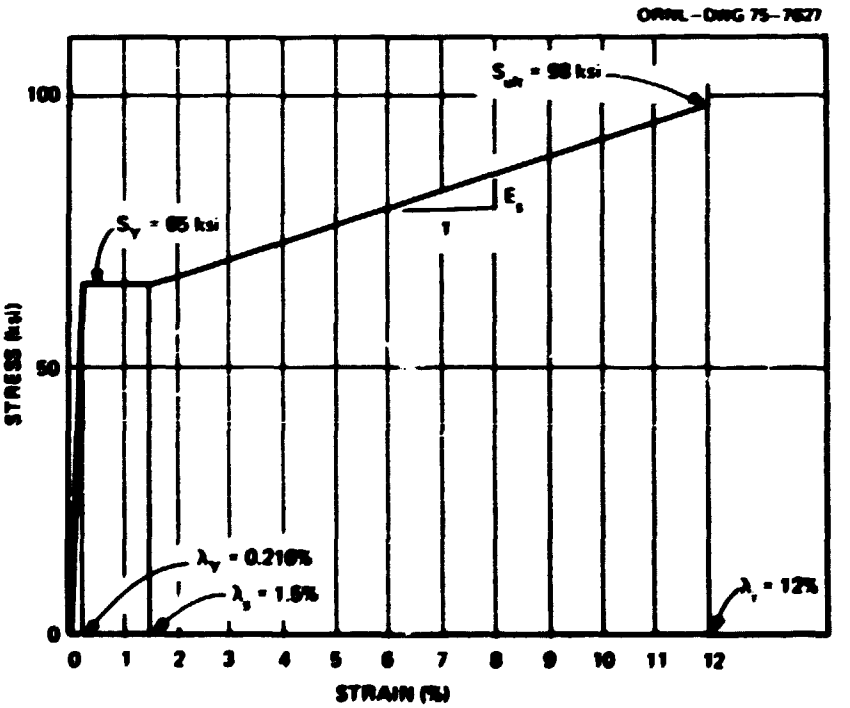

Fig. H.4. Piecewise linear approximation for the true stress-strain curve of A533, grade B, class 1 steel.

From Fig. H.4, the value of the tangent modulus in the strain-hardening range of strain E_s is evaluated as

$$E_s = \frac{(98 - 65)\,10^3}{(12.0 - 1.5)\,10^{-2}} = 3.15 \times 10^5 \text{ psi}. \tag{H.3}$$

Since the elastic modulus of steel is given approximately by

$$E = 3 \times 10^7 \text{ psi}, \tag{H.4}$$

a convenient and sufficiently accurate approximation for the ratio E/E_s should be

$$\frac{E}{E_s} \sim 100. \tag{H.5}$$

This ratio will be used for the analyses to be discussed later in this appendix.

Relations Between Notch-Tip Strain, Fracture Toughness, and Temperature

Although it is not possible to determine the values of the notch root strain ϵ and the notch root radius ρ separately, it is possible to determine an important combination of these factors, $\epsilon\sqrt{\rho}$, by integrating the right side of Eq. (H.1). The quantity $\epsilon\sqrt{\rho}$, known as the notch ductility factor,[5] is directly relatable to the value of the fracture toughness as conventionally measured. This relationship is established by combining the integral of the right side of Eq. (H.1) with the basic equation of linear elastic fracture mechanics:

$$K_c = CS_f\sqrt{\pi a}, \tag{H.6}$$

which describes the result of a fracture mechanics test conducted in the linear elastic range. Dividing both sides of Eq. (H.6) by the elastic modulus E and rearranging gives

$$\lambda_f = \frac{(K_c/S_f)\,\lambda_Y}{C\sqrt{\pi a}}. \tag{H.7}$$

where, for uniaxial loading, the strain λ is related to the stress S by

$$\lambda = \frac{S}{E}. \tag{H.8}$$

For failure under nominally elastic conditions, the integral of Eq. (H.1) gives

$$\epsilon_f\sqrt{\rho} = 2C\sqrt{a}\sqrt{\frac{E}{E_s}}\,\lambda_f. \tag{H.9}$$

Note that in integrating Eq. (H.1), the tip of the crack is assumed to enter the strain-hardening range immediately. Therefore, for all the analyses to be discussed, the tangent modulus E_m at the tip of the crack

is immediately set equal to E_s. Solving Eq. (H.9) for λ_f gives

$$\lambda_f = \frac{\epsilon_f \sqrt{\rho}}{2C \sqrt{2} \sqrt{E/E_s}} . \tag{H.10}$$

Then, equating the right sides of Eqs. (H.7) and (H.10) gives, after rearranging,

$$\epsilon_f \sqrt{\rho} = \frac{2}{\sqrt{\pi}} \sqrt{\frac{E}{E_s}} \left(\frac{K_c}{S_Y} \right) \lambda_Y . \tag{H.11}$$

Using Eq. (H.5), Eq. (H.11) becomes

$$\epsilon_f \sqrt{\rho} = \frac{20\lambda_Y}{\sqrt{\pi}} \left(\frac{K_c}{S_Y} \right) . \tag{H.12}$$

and, for $\lambda_Y = 0.216\%$, Eq. (H.12) becomes

$$\epsilon_f \sqrt{\rho} = 2.43 \times 10^{-2} \left(\frac{K_c}{S_Y} \right) . \tag{H.13}$$

Thus, the notch ductility factor at fracture, $\epsilon_f \sqrt{\rho}$, is directly proportional to the ratio K_c/S_Y. This relationship is assumed to hold regardless of whether the nominal strain at fracture is in the elastic or the plastic range. Therefore, the value of the ratio K_c/S_Y corresponding to a given value of the notch ductility factor at fracture is determined by rearranging Eq. (H.13) to read

$$\frac{K_c}{S_Y} = \frac{\epsilon_f \sqrt{\rho}}{2.43 \times 10^{-2}} . \tag{H.14}$$

To determine the temperature corresponding to a given value of the notch ductility factor at fracture, a relationship between the fracture toughness and the temperature is needed. For A533, grade B, class 1 steel, the variation of the static initiation fracture toughness with temperature can be expressed to a close approximation by the equation[7]

$$\frac{K_{Ic}}{S_Y} = \frac{A_T}{T_\infty - T} , \tag{H.15}$$

where K_{Ic} is the plane strain fracture toughness, A_T is an empirical coefficient having a value of about $125°F \sqrt{in.}$, and T_∞ is the temperature at the onset of upper-shelf conditions, which for A533, grade B, class 1 steel is about 125°F. Solving Eq. (H.15) for the temperature T gives

$$T = T_\infty - \frac{A_T}{K_{Ic}/S_Y} \tag{H.16}$$

If the value of the fracture toughness for a given set of conditions is believed not to be the plane strain value, Eq. (II.16) can be modified to read

$$T = T_o - \frac{A_1 (K_c - K_{Ic})}{K_c S_y} \qquad (II.17)$$

Therefore, the temperature corresponding to a given value of the notch ductility factor at fracture can be determined by applying Eqs. (II.14) and (II.16) or (II.17) as judged appropriate. The determination of whether or not the value of the fracture toughness applicable should be the plane strain value and the procedure to be used for estimating the ratio K_c/K_{Ic}, if needed, will be discussed later, along with the results of the trial calculations to be presented.

General Definition of the Effective Tangent Modulus

In order to integrate the right side of Eq. (II.1), the tangent modulus E_t must be shown as a function of the strain λ. If there is no strain gradient across the net section, the tangent modulus might be estimated as simply the slope of the tensile stress-strain curve at the current value of nominal strain. However, if there is a strain gradient across the net section, the tangent modulus will also vary across the net section once yielding has occurred. For this case, an estimate of the tangent modulus based on judgment appears to be required. Therefore, it was decided to estimate an effective value of the tangent modulus as the average tangent modulus across the net section, assuming a linearly varying strain distribution. By this definition, the equations that determine the effective tangent modulus are

$$E_\varepsilon = \frac{\int_0^t (ds/d\lambda)\, dx}{t} \qquad (II.18)$$

and

$$\lambda = \lambda_0 + \frac{\lambda_t - \lambda_0}{t} x, \qquad (II.19)$$

where t is thickness of the component in the region of the flaw, x is a distance measured in the thickness direction, and λ_0 and λ_t are the nominal strains at the front and the back surfaces of the cracked section. From Eq. (II.19),

$$dx = \frac{t}{\lambda_t - \lambda_0} d\lambda, \qquad (II.20)$$

Therefore, substituting Eq. (II.20) into Eq. (II.18) and integrating gives

$$E_\varepsilon = \frac{S_t - S_0}{\lambda_t - \lambda_0}. \qquad (II.21)$$

Consequently, the effective tangent modulus is the stress difference between the front and the back

surfaces divided by the strain difference between the same two locations. For the case of pure bending,

$$S_{\cdot} = S_{\cdot} \tag{III.22}$$

and

$$\varepsilon_{\cdot} = -\varepsilon_{\cdot} \tag{III.23}$$

so that substituting Eqs. (III.22) and (III.23) into Eq. (III.21) gives

$$E = \frac{S_{\cdot}}{\varepsilon_{\cdot}} = E_{s} \tag{III.24}$$

Consequently, the effective tangent modulus for the case of pure bending is the secant modulus of the stress-strain curve at the front and the back surfaces of the specimen. For uniform tensile loading, the effective tangent modulus thus far remains the tangent modulus of the uniaxial tensile stress-strain curve at the current value of nominal strain. These two idealized cases will now be considered in more detail.

Strain Tolerance Analyses for the Idealized Cases of Pure Tension and Pure Bending Without Net Section Effects

Before attempting to analyze actual test specimens, it is instructive to analyze the two idealized cases of pure tension and pure bending, omitting the net section effects that invariably occur when the area of the net section is less than that of the gross section due to the area removed by the crack. For these analyses, a 2.25-in-deep part-through surface crack in a specimen of A533, grade B, class 1 steel will be considered. Based on previous analyses,[7] the value of $C_{\cdot}$, the linear elastic fracture mechanics shape factor, will be taken as 0.9. For this analysis, the stress-strain curve will be represented by the piecewise linear curve shown in Fig. III.4.

For the case of pure tension, the integration of Eq. (III.1) is direct; the results are as shown below.

For $\varepsilon_{\cdot} \le \varepsilon_{Y}$ (the elastic range),

$$J = J \tag{III.25}$$

and therefore, letting $\Delta\varepsilon = \varepsilon_{\cdot}$,

$$\Delta\varepsilon\sqrt{a} = 2\sigma_{Y}\sqrt{\frac{J}{\pi E}} \tag{III.26}$$

For $\varepsilon_{\cdot} \le \varepsilon_{\cdot} \le \varepsilon_{\cdot}$ (the transition range),

$$J = 0, \tag{III.27}$$

and therefore

$$\Delta\varepsilon\sqrt{a} = 0 \tag{III.28}$$

For $\lambda \geq \lambda_s$ (the strain-hardening range),

$$E_z = E_s \,. \tag{H.29}$$

and therefore, letting $\Delta\lambda = \lambda - \lambda_s$,

$$\Delta\kappa\sqrt{\rho} = 2C\sqrt{a}\,(\lambda - \lambda_s) \,. \tag{H.30}$$

The total value of the notch ductility factor at a given value of nominal strain is the sum of the incremental values that occur up to that value of strain. The fact that $\Delta\kappa\sqrt{\rho}$ is zero in the transition range of strain, as indicated by Eq. (H.28), implies that for pure tensile loading the fracture strain will undergo an abrupt increase from the yield strain to the strain at the onset of strain hardening, at the temperature at which initial yielding and fracture coincide. Furthermore, in the strain-hardening range, the increase in nominal strain required to produce a given increase in the notch ductility factor is ten times the value that would be required in the elastic range.

For the case of pure bending, the solution in the elastic range is the same as for pure tension, as given by Eq. (H.26). In the elastic-plastic range, the solutions are as given below, with λ representing the surface bending strain.

For $\lambda_y \leq \lambda \leq \lambda_s$ (the transition range),

$$E_z = E_{sec} = \frac{S_y}{\lambda} \,. \tag{H.31}$$

and therefore, by direct integration between the limits λ_y and λ,

$$\Delta\kappa\sqrt{\rho} = 4C\sqrt{a}\sqrt{\frac{E}{E_s}}\,(\sqrt{\lambda\lambda_y} - \lambda_y) \,. \tag{H.32}$$

For $\lambda \geq \lambda_s$ (the strain-hardening range),

$$\frac{E_z}{E_s} = \frac{E_{sec}}{E_s} = 1 + \frac{\lambda_d}{\lambda} \,. \tag{H.33}$$

where

$$\lambda_d = \frac{S_y}{E_s} - \lambda_s \,. \tag{H.34}$$

Consequently, substituting Eq. (H.33) into Eq. (H.1) results in an integral, the value of which, for the limits λ_s and λ, is

$$\Delta\kappa\sqrt{\rho} = 2C\sqrt{a}\left[\sqrt{\lambda(\lambda + \lambda_d)} - \sqrt{\lambda_s(\lambda_s + \lambda_d)} + \lambda_d \ln\left(\frac{\sqrt{\lambda} + \sqrt{\lambda + \lambda_d}}{\sqrt{\lambda_s} + \sqrt{\lambda_s + \lambda_d}}\right)\right] \,. \tag{H.35}$$

The curves of fracture strain vs temperature for the idealized cases of pure tension and pure bending, based on the assumption that $K_c = K_{Ic}$ and on Eqs. (H.14), (H.16), and (H.25) through (H.35), are shown in Fig. H.5. Also shown by the dashed curve in Fig. H.5 is the prediction of linear elastic fracture mechanics extrapolated into the plastic range. Several important results are made evident by Fig. H.5. First, the curves for pure tension and pure bending are not the same, nor do they have the same shape. The bending curve does not exhibit a sudden rise in fracture strain through the strain range of the yield plateau, because the effective tangent modulus in the presence of a strain gradient is never zero. Also, the bending curve sweeps

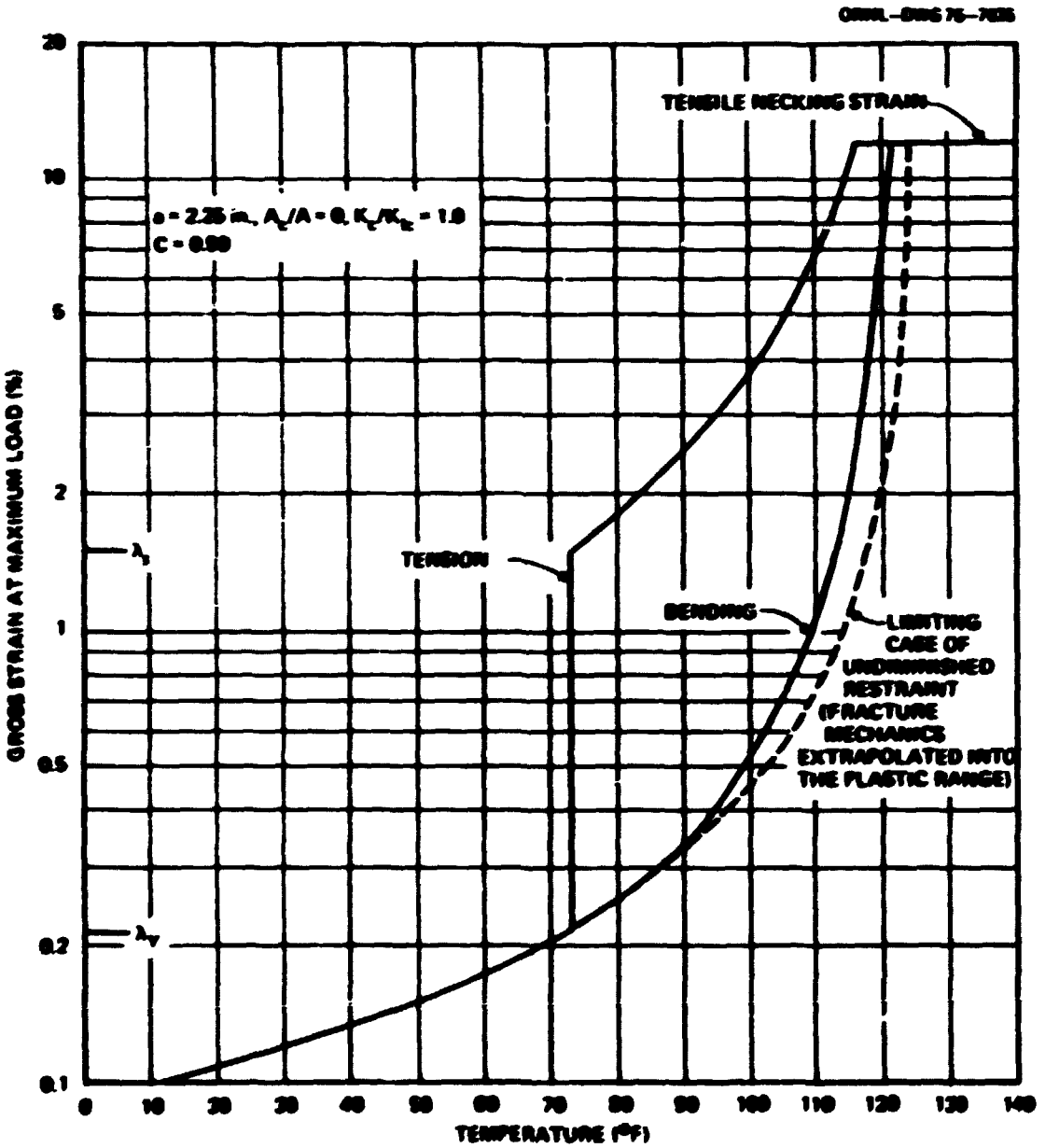

Fig. H.5. Calculated fracture strain-vs-temperature curves for the idealized cases of pure tension and pure bending, not considering net section effects, for a specimen of A533, grade B, class 1 steel containing a 2.25-in.-deep surface crack.

upward at higher temperatures than the tension curve, because the effective tangent modulus in bending equals or exceeds the effective tangent modulus in tension at all strain levels. Second, the curve representing the extrapolation of linear elastic fracture mechanics into the plastic range comes close to the bending curve but not to the tension curve. Third, conspicuous by its absence in Fig. H.5 is any indication of why experimental gross section fracture strains should remain constant, just below the yield strain, over a considerable range of temperature just below the transition temperature for tensile loading. In this regard, direct reasoning indicates that, in a surface-cracked tensile specimen of finite dimensions, the gross section and the net section cannot have the same areas and therefore cannot yield simultaneously. While the net section is yielding, the gross section stress and strain must remain constant, just below the yield point. This and other net section effects will now be considered.

Consideration of Net Section Effects in Surface-Cracked Tensile Specimens

The preceding analytical results indicate that the tangent modulus method has the apparent potential of being developed into a realistic method of elastic-plastic fracture analysis for structural components containing surface cracks. However, before this development can be considered adequate, certain additional important aspects of experimentally observed elastic-plastic fracture behavior must be considered. In particular, in the hypothetical example just considered, in which net section effects were ignored, the fracture strain-vs-temperature curve for pure tensile loading rose abruptly through the strain range of the yield plateau. Such a variation of fracture strain with temperature has actually been observed in the gross sections of real surface-cracked tensile specimens, and it can be explained on the basis of equilibrium considerations alone. However, as shown in Figs. H.1 and H.3b, the net section fracture strain in surface-cracked tensile specimens does not exhibit this phenomenon. Furthermore, because the gross section stress and strain remain constant at values just below the yield point while the net section fracture strain traverses the strain range of the yield plateau, it can be deduced that it is the net section strain that directly governs crack tip conditions and that should be represented by the term λ in Eq. (H.1). In addition, since the net section fracture strain-vs-temperature curve does not rise vertically through the strain range of the yield plateau, it follows that the effective tangent modulus for a real surface-cracked tensile specimen is *not zero* in the strain range of the yield plateau. This implies the existence of a strain gradient across the net section, a fact confirmed by Randall's experimental data.[1-6] In fact, Randall found it necessary to use special adjustable grips for loading surface-cracked tensile specimens in order to minimize the bending that would otherwise occur across the net section because of its eccentricity with respect to the line of action of the applied load.[1-4] No such provisions were made in the design of the gripping devices for the larger intermediate tensile specimens,[7] and significant strain gradients were measured across the net sections of these specimens.

Having established that net section eccentricity is the most likely cause of the observed continuous variation of the net section fracture strain with temperature over the strain range of the yield plateau, a consistent explanation of the elastic-plastic fracture behavior of surface-cracked tensile specimens can now be formulated. This explanation is summarized graphically and schematically in Fig. H.6. The net section strain and the gross section strain curves shown in Fig. H.6 are separate because of the area difference between the net and the gross sections. At the temperature T_1, the net section yields; between the temperatures T_1 and T_2, the average stress on the net section is the yield stress, and the net section strain is between the yield strain and the strain at the onset of strain hardening. In this temperature range, because the load remains constant, the gross section strain remains constant, at a value just below the yield strain.

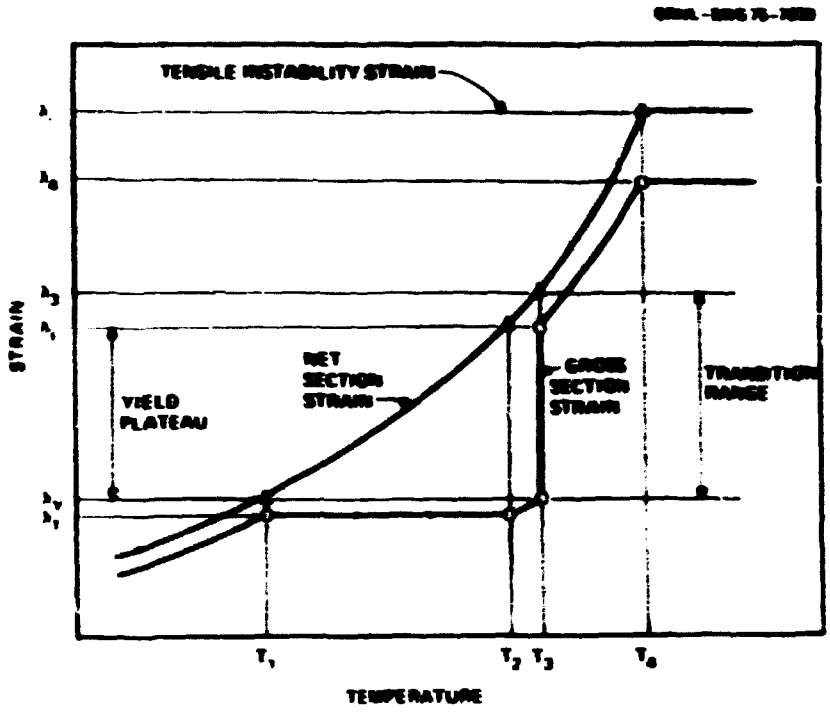

Fig. H.6. Schematic diagram of net and gross section fracture strain-vs-temperature curves for a material possessing an ideally plastic yield point elongation prior to strain hardening.

At the temperature T_2, the net section begins to strain harden and the load begins to increase, thereby causing the gross section strain to increase. At the temperature T_3, the gross section yields and the gross section strain immediately increases to the value of the strain at the onset of strain hardening. (T_3 is therefore the "transition temperature" of the specimen.) Above the temperature T_3, both the net section strain and the gross section strain are in the strain-hardening range. At and above the temperature T_4, the specimen fails by tensile instability on the net section at a load that does not depend on the fracture toughness (except for the effects of prior stable crack growth) and that is therefore relatively independent of temperature. The strains λ_1, λ_3, and λ_4 shown in Fig. H.6 are determined by equilibrium and the stress-strain curve. The above described points of temperature and strain transition are summarized in Table H.1.

Finally, utilizing the assumption that the apparently finite tangent modulus in the transition range of strain is caused by the bending that is induced by the eccentricity of the net section, a semiempirical method for estimating the effective tangent modulus in this range of strain was developed. In the process, the upper limit of the transition range of strain was extended from λ_3 to λ_2, assuming that transverse restraint does not diminish until the gross section yields, as concluded by Randall.[1,2] Assuming no adjustment of the line of action of the applied load, the effective tangent modulus was estimated as the ratio of the stress difference due to bending, when initial yielding just occurs at the cracked surface, divided by the difference between the strain at the onset of strain hardening and the bending strain at the opposite unyielded surface. Referring to Figs. H.7 and H.8, the effective tangent modulus in the transition range of

Table H.1. Net and gross section strains occurring at the temperatures T_1 through T_4 in surface-cracked tensile specimens that fall in the elastic-plastic range of strain

Temperature	Strains	
	Net section	Gross section
T_1	λ_Y	λ_1
T_2	λ_2	λ_2
T_3	λ_3	λ_Y, λ_3
T_4	λ_4	λ_4

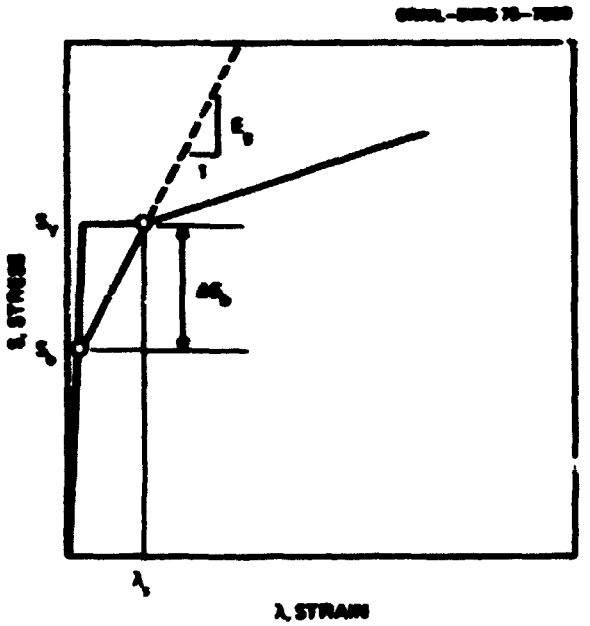

Fig. H.7. Definition of the effective tangent modulus in the transition range of strain for a surface-cracked tensile specimen.

strain is thus estimated by

$$E_g = \frac{\left(\frac{\Delta S_b}{S}\right) S_Y}{\lambda_s - \left(1 - \frac{\Delta S_b}{S}\right)\lambda_Y} , \qquad \text{(H.36)}$$

which describes conditions just prior to the onset of strain hardening at the cracked face, assuming that the stress and strain at the back face remain constant in the elastic range as yielding progresses inward from the

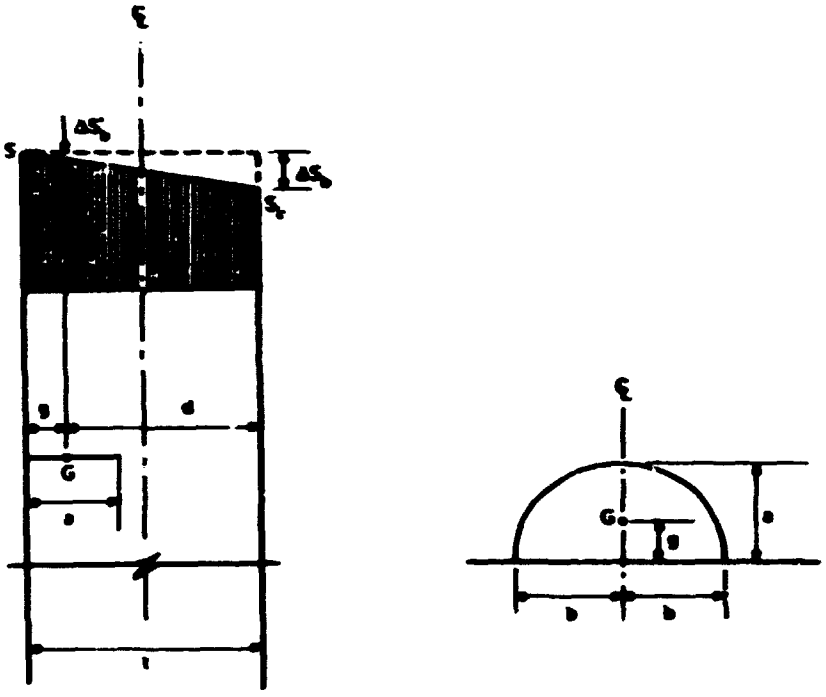

Fig. H.8. Effects of net section eccentricity on the nominal elastic stress distribution in the net section of a surface-cracked tensile specimen.

cracked face. Equation (H.36) has been used successfully to estimate the effective tangent modulus throughout the transition range of strain despite its obvious theoretical shortcomings.

The net section stress gradient shown in Fig. H.8 is determined by finding the linearly varying nominal stress distribution which, considering the area removed by the crack, still maintains the line of action of the applied load at the midpoint of the gross section. Referring to Fig. H.8, point G is the centroid of the crack, which is assumed to be semielliptical in shape. The distance g is the distance from the front face of the specimen to point G, which is given by

$$g = \frac{4}{3\pi} a . \tag{H.37}$$

Defining

$$k_1 = \frac{d}{t} = 1 - \frac{g}{t} , \tag{H.38}$$

it follows that

$$k_1 = 1 - \frac{4}{3\pi}\left(\frac{a}{t}\right) . \tag{H.39}$$

Taking the moment of the stress distribution shown in Fig. H.8 about the back face of the specimen; treating the nominal stress that would have acted over the area of the crack as being a uniform tensile stress equal to $(S - \Delta S_b')$, which is the nominal stress acting at the centroidal depth of the crack; and equating the resulting moment arm to t/2 gives

$$\frac{\Delta S_b}{S} = 6\left(1 - \frac{\Delta S_b'}{S}\right)\frac{A_c}{A}(2k_1 - 1). \tag{H.40}$$

Since

$$\frac{\Delta S_b'}{S} = \frac{\Delta S_b}{S}(1 - k_1), \tag{H.41}$$

it follows, by combining Eqs. (H.40) and (H.41), that

$$\frac{\Delta S_b}{S} = \frac{6(A_c/A)(2k_1 - 1)}{1 + 6(A_c/A)(2k_1 - 1)(1 - k_1)}. \tag{H.42}$$

For a semielliptical surface crack, the crack area is given by

$$A_c = \frac{\pi ab}{2}, \tag{H.43}$$

where a and b are the crack dimensions defined in Fig. H.8. Equation (H.42) gives the value of $\Delta S_b/S$ to be used for calculating the effective tangent modulus in the transition range of strain, from Eq. (H.36).

The values of λ_1, λ_2, and λ_3 are determined from equilibrium and the stress-strain curve, ignoring the effects of net section eccentricity. Since the load is the same on the net and the gross sections,

$$S_g A = S_n(A - A_c), \tag{H.44}$$

where S_g and S_n are the gross and the net section stresses, respectively. For determining λ_1, the net section stress is the yield stress; so that

$$S_{g1} = S_Y\left(1 - \frac{A_c}{A}\right), \tag{H.45}$$

and

$$\lambda_1 = \lambda_Y\left(1 - \frac{A_c}{A}\right). \tag{H.46}$$

For determining λ_3, the gross section stress is the yield stress so that, using Eq. (H.44),

$$S_{n3} = S_Y \left(\frac{A}{A - A_c} \right) \tag{H.47}$$

and

$$S_{n3} - S_Y = S_Y \left[\frac{A_c/A}{1 - (A_c/A)} \right] . \tag{H.48}$$

Thus,

$$\lambda_3 = \lambda_s + \frac{S_Y}{E_s} \left[\frac{A_c/A}{1 - (A_c/A)} \right] . \tag{H.49}$$

For determining λ_4, the net section stress is the engineering ultimate tensile stress. Therefore, using Eq. (H.44),

$$S_{g4} = S'_{uit} \left(1 - \frac{A_c}{A} \right) . \tag{H.50}$$

$$S'_{cit} - S_{g4} = S'_{uit} \left(\frac{A_c}{A} \right) . \tag{H.51}$$

and

$$\lambda_4 = \lambda_s - \frac{S'_{uit}}{E_s} \left(\frac{A_c}{A} \right) . \tag{H.52}$$

Note that because Eqs. (H.50) through (H.52) are written in terms of the nominal rather than the true ultimate tensile stress, the point (S_{g4}, λ_4) will fall slightly below the approximate true stress-strain curve, thus approximating a point on the nominal stress-strain curve.

Analysis of Intermediate Tensile Specimens

Formulation of the analysis

Although the experimental data from Randall's gross strain tension specimens[1] originally motivated the development of the tangent modulus method, these specimens were not the first to be successfully analyzed, the reason being that the experimental steps taken to minimize bending due to net section eccentricity caused the effective tangent modulus in the transition range of strain to be initially difficult to estimate. The first surface-cracked tensile specimens to be successfully analyzed were the first seven longitudinally oriented intermediate tensile specimens tested by the Southwest Research Institute[9] for the HSST program. These specimens were fabricated from A533, grade B, class 1, steel plate and had gross

sections measuring 18 in. wide and 6 in. thick. The pertinent data for these specimens are listed in Table H.2. No steps were taken to control bending due to net section eccentricity in these specimens.

In order to develop a clear graphical comparison between calculations and experimental data for the intermediate tensile specimens listed in Table H.2, values of net section fracture stress vs temperature were calculated for three crack sizes spanning the range of crack sizes listed in Table H.2. The resulting comparison is shown in Fig. H.9, which is an updated version of Fig. C-13 in Ref. 5. The difference between the two figures is due to the fact that some of the experimental net section fracture stress values used in Ref. 5 were calculated on the basis of preliminary estimates of net section area. The comparison between analysis and experiment illustrated by Fig. H.9 is certainly favorable. Therefore, an explanation of the calculations is in order.

The first calculations made were for a crack depth a of 2.25 in. and a ratio of crack area to gross section area, A_c/A, of 0.10. This corresponds to a crack surface length 2b of 6.10 in. and a flaw shape ratio a/2b of 0.369. The value of the linear elastic fracture mechanics shape factor C was taken as 0.90.

Assuming that full transverse restraint does not exist in a surface-cracked tensile specimen, the Irwin β_{1c} correction[7] was used to estimate the ratio K_c/K_{1c}. Irwin's equation for making this estimate is

$$\frac{K_c}{K_{1c}} = \sqrt{1 + 1.4\beta_{1c}^2} \quad . \tag{H.53}$$

where

$$\beta_{1c} = \frac{(K_{1c}/S_Y)^2}{B} \quad . \tag{H.54}$$

Here B represents the thickness of a through-cracked specimen, because Eqs. (H.53) and (H.54) were based mainly on data from specimens containing through-thickness cracks. However, for specimens containing part-through surface cracks, a modified definition of β_{1c} seemed appropriate. In a through-cracked specimen, the distance from the point of greatest restraint on the crack tip to the nearest free surface, not including the crack surface, is B/2. In a surface-cracked specimen, the corresponding distance is a, unless the crack depth exceeds half the thickness. Thus, it seemed appropriate to replace B in Eq. (H.54) with 2a, so that the definition of β_{1c} used for a part-through surface crack is

$$\beta_{1c} = \frac{(K_{1c}/S_Y)^2}{2a} \quad . \tag{H.55}$$

The corresponding definition of β_c is

$$\beta_c = \frac{(K_c/S_Y)^2}{2a} \quad . \tag{H.56}$$

The relation between K_c/K_{1c} and $1/\beta_c$ is shown graphically in Fig. H.10. This relation is discussed in more detail in Ref. 7.

Table H.2. Test data for surface-cracked longitudinal intermediate tensile specimens 1 through 7, fabricated from A533, grade B, class 1 steel plate

Specimen No.	Test temp. (°F)	Initial flaw dimensions (in.)		Maximum load conditions							Comments
		a	2b	Maximum load (kips)	Gross stress (ksi)	Flaw dimensions (in.) a	Flaw dimensions (in.) 2b	Flaw area ($in.^2$)	Net area ($in.^2$)	Net stress (ksi)	
1	215	2.375	6.598	7300	67.5	3.80	7.50	22.4	85.6	85.2	Max. load flaw size based on examination of fracture surface
2	220	2.160	6.000	7550	69.9	3.50	7.00	19.3	88.7	85.0	Max. load flaw size based on examination of fracture surface
3	50	2.05	8.37	5300	49.1	2.05	8.37	13.5	94.5	56.1	Max. load flaw dimensions from Ref. 9
4	100	2.05	8.20	7500	69.4	2.75	8.20	17.7	90.3	83.0	Max. load crack depth taken as the average between zero and max. load values, as given in Ref. 9
5	75	2.53	8.26	5900	54.6	2.53	8.26	16.4	91.6	64.4	Max. load flaw dimensions from Ref. 9
6	100	3.37	9.53	4700	43.5	4.38	10.75	37.0	71.0	66.2	Max. load flaw dimensions based on photograph (close to Ref. 9)
7	100	2.43	8.13	7050	65.2	2.80	8.20	18.0	90.0	78.3	Max. load flaw dimensions based on photograph (close to Ref. 9)

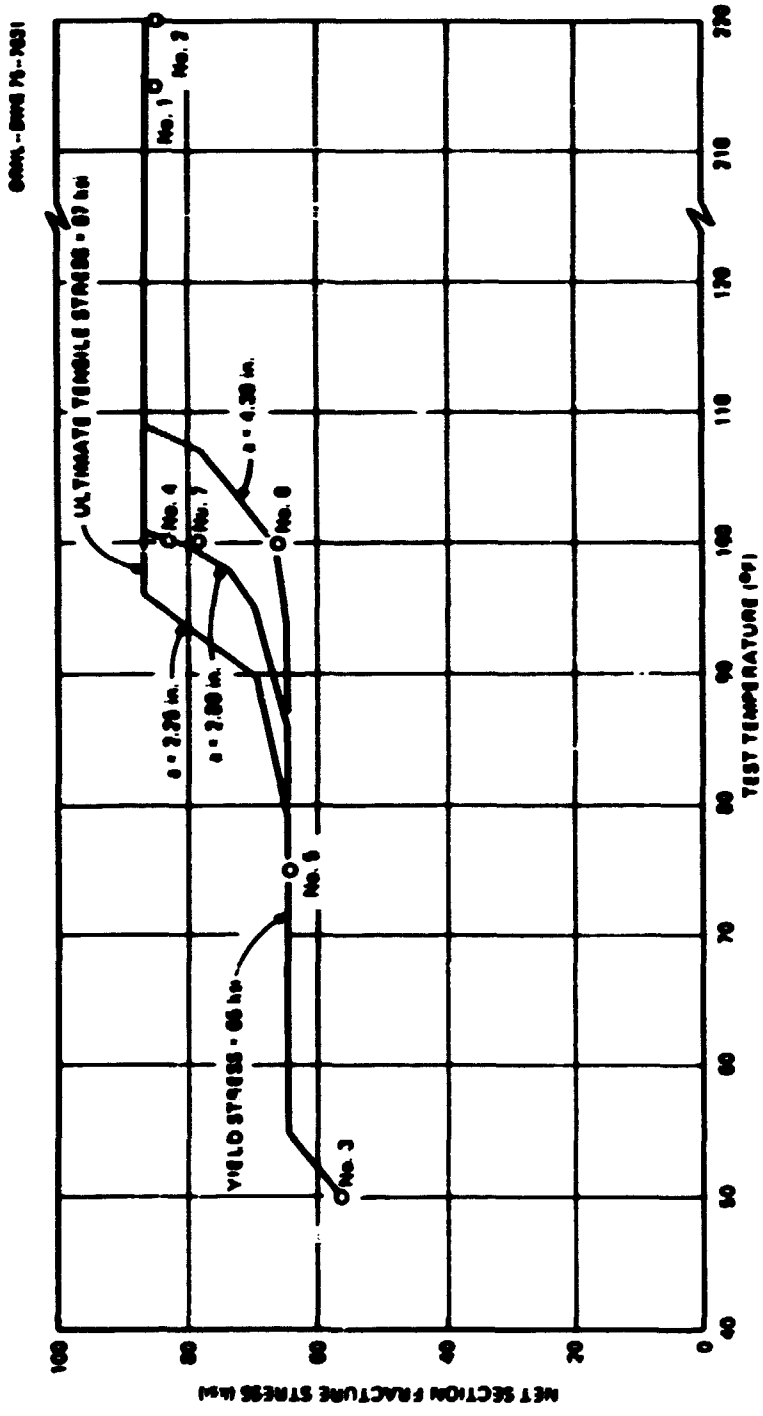

Fig. H.8. Comparison of longitudinal intermediate tensile specimen net section fracture stress data with fracture stress estimates made by the tangent modulus method; material is A533, grade B, class 1 steel (revision to Fig. C-13 of Ref. 5).

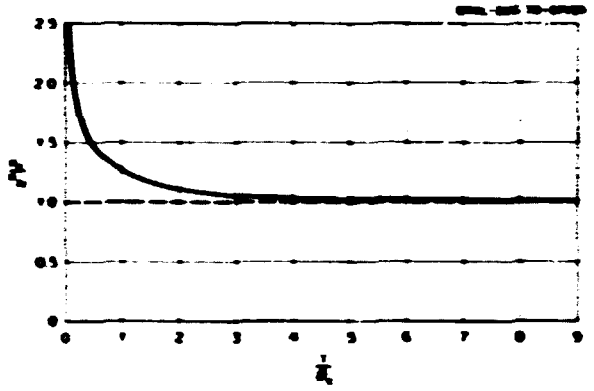

(10a)

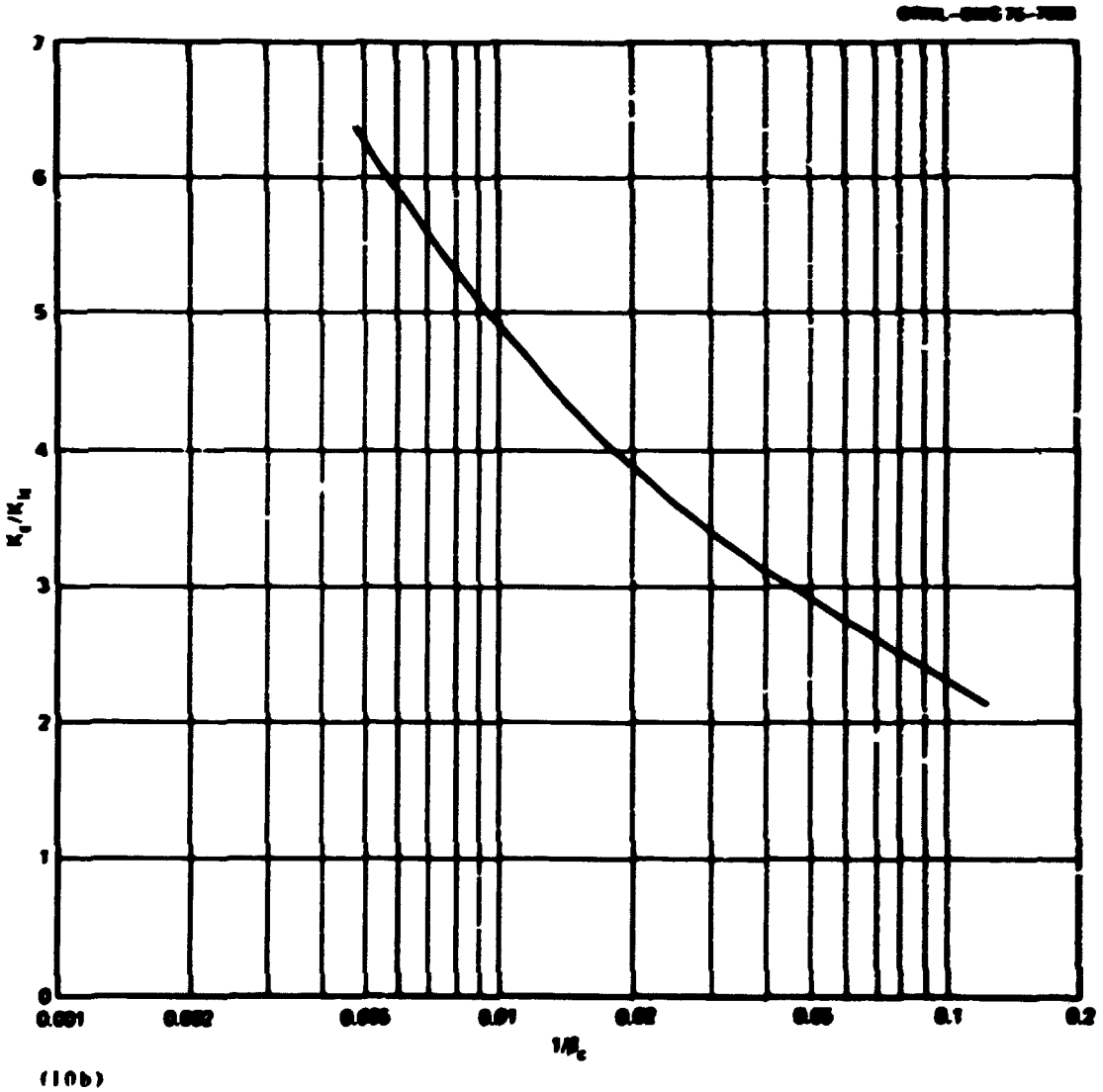

(10b)

Fig. H.10. Plots of the ratio K_c/K_{ic} vs the parameter $1/\beta_c$

Calculations for the temperature T_1 (a = 2.25 in.)

From Eq. (H.26),

$$\epsilon_f \sqrt{\rho} = (2)(0.90)\sqrt{2.25}\,(10)(2.16 \times 10^{-3}) = 5.83 \times 10^{-2}\ \sqrt{\text{in.}}$$

From Eq. (H.14),

$$\frac{K_c}{S_y} = \frac{5.83 \times 10^{-2}}{2.43 \times 10^{-2}} = 2.40\sqrt{\text{in.}}$$

From Eq. (H.56),

$$\frac{1}{\beta_c} = \frac{2a}{(K_c/S_y)^2} = \frac{(2)(2.25)}{(2.40)^2} = 0.78\ .$$

From Fig. H.10a,

$$\frac{K_c}{K_{Ic}} = 1.34\ .$$

Consequently, from Eq. (H.17),

$$T_1 = 125 - \frac{(125)(1.34)}{(2.40)} = 125 - 70 = 55^\circ\text{F}\ .$$

Calculations for the temperature T_2 (a = 2.25 in.)

From Eq. (H.39),

$$k_1 = 1 - \frac{4}{3\pi}\left(\frac{2.25}{6.00}\right) = 0.841\ .$$

From Eq. (H.42),

$$\frac{\Delta S_0}{S} = \frac{(6)(0.1)(0.682)}{1 + (6)(0.1)(0.682)(0.159)} = 0.384\ .$$

From Eq. (H.36),

$$E_2 = \frac{(0.384)(6.5 \times 10^6)}{[1.500 - (0.616)(0.216)] \times 10^{-7}} = 1.83 \times 10^6\ \text{psi}\ .$$

Therefore,

$$\frac{E_g}{E_s} = \frac{1.83 \times 10^6}{3.15 \times 10^5} = 5.80$$

and

$$\sqrt{\frac{E_g}{E_s}} = 2.41 .$$

Considering bending due to net section eccentricity, Eq. (H.28) is replaced by

$$\Delta\epsilon_f \sqrt{\rho} = 2C \sqrt{3} \sqrt{\frac{E_g}{E_s}} (0 \quad \lambda_g) . \tag{H.57}$$

From Eq. (H.57), using $\lambda = \lambda_s$,

$$\Delta\epsilon_f \sqrt{\rho} = (2)(0.90)(1.50)(2.41)(1.500 - 0.216) \times 10^{-2} = 8.36 \times 10^{-2} \sqrt{\text{in.}}$$

Thus,

$$\epsilon_f \sqrt{\rho} = (5.83 + 8.36) \times 10^{-2} = 14.19 \times 10^{-2} \sqrt{\text{in.}}$$

From Eq. (H.14),

$$\frac{K_s}{S_y} = \frac{14.19 \times 10^{-2}}{2.43 \times 10^{-2}} = 5.83 \sqrt{\text{in.}}$$

From Eq. (H.56),

$$\frac{1}{\rho'_c} = \frac{4.50}{(5.83)^2} = 0.132 .$$

From Fig. H.10a,

$$\frac{K_s}{K_{g_s}} = 2.13 .$$

Consequently, from Eq. (H.17),

$$T_2 = 125 \quad \frac{(125)(2.13)}{(5.83)} = 125 \quad 46 = 79^\circ\text{F} .$$

Calculations for the temperature T_3 (a = 2.25 in.)

From Eq. (H.49),

$$\lambda_3 = 1.50 + \frac{(6.5 \times 10^6)(0.1) \times 10^{-2}}{(3.15 \times 10^7)(0.9)} = 3.79\% .$$

The tangent modulus for $\lambda_2 \leq \lambda \leq \lambda_3$ has the same value as in Eq. (H.57); thus,

$$\Delta\sigma_f \sqrt{\rho} = 2C\sqrt{a}\sqrt{\frac{E_T}{E_s}}(\lambda - \lambda_2) . \qquad \text{(H.58)}$$

From Eq. (H.58) and the previous results for T_2, and, using $\lambda = \lambda_3$,

$$\Delta\sigma_f \sqrt{\rho} = \frac{2.29}{1.284}(8.36 \times 10^{-2}) = 14.92 \times 10^{-2} \sqrt{\text{in.}}$$

Thus,

$$\sigma_f \sqrt{\rho} = (14.19 + 14.92) \times 10^{-2} = 29.11 \times 10^{-2} \sqrt{\text{in.}}$$

From Eq. (H.14),

$$\frac{K_c}{S_y} = \frac{29.11 \times 10^{-2}}{2.43 \times 10^{-2}} = 11.98 \sqrt{\text{in.}}$$

From Eq. (H.56),

$$\frac{1}{A_c} = \frac{4.50}{(11.98)^2} = 0.0314 .$$

From Fig. H.10b,

$$\frac{K_c}{K_{Ic}} = 3.38 .$$

Consequently, from Eq. (H.17),

$$T_3 = 125 - \frac{(125)(3.38)}{(11.98)} = 125 - 35 = 90^\circ\text{F} .$$

Calculations for the temperature T_4 (a = 2.25 in.)

Since the transition range extends to λ_3, Eq. (H.30) is replaced by

$$\Delta\sigma_f \sqrt{\rho} = 2C\sqrt{a}(\lambda - \lambda_3) . \qquad \text{(H.59)}$$

From Eq. (H.59), using $\lambda = \lambda_1 = 1.25$,

$$\Delta\alpha_1 \sqrt{\rho} = (2)(0.9)(1.5)(12.00 - 3.79) \times 10^{-2} = 22.20 \times 10^{-2} \sqrt{\text{in.}}$$

Thus,

$$\alpha_1 \sqrt{\rho} = (29.11 + 22.20) \times 10^{-2} = 51.31 \times 10^{-2} \sqrt{\text{in.}}$$

From Eq. (H.14),

$$\frac{K_c}{S_y} = \frac{51.31 \times 10^{-2}}{2.43 \times 10^{-2}} = 21.1 \sqrt{\text{in.}}$$

From Eq. (H.56),

$$\frac{1}{\beta_c} = \frac{4.50}{(21.1)^2} = 0.0101 .$$

From Fig. H.10b,

$$\frac{K_c}{K_{Ic}} = 4.90 .$$

Consequently, from Eq. (H.17),

$$T_s = 125 \quad \frac{(125)(4.90)}{(21.1)} = 125 - 29 = 96^\circ\text{F} .$$

Calculations for 50°F, a temperature less than T_1 ($a = 2.25$ in.)

From Eq. (H.15),

$$\frac{K_{Ic}}{S_y} = \frac{125}{125 \quad 50} = 1.67 \sqrt{\text{in.}}$$

From Eq. (H.54),

$$\beta_{Ic} = \frac{(1.67)^2}{4.50} = 0.62 .$$

From Eq. (H.53),

$$\frac{K_c}{K_{Ic}} = \sqrt{1 + (1.4)(0.62)^2} = 1.24 .$$

Therefore,

$$\frac{K_c}{S_y} = (1.24)(1.67) = 2.07\sqrt{in.}$$

Since at T_1, $K_c/S_y = 2.40$, it follows that, at 50°F,

$$\lambda_y = \frac{2.07}{2.40}(0.216) = 0.186 .$$

Net section fracture stress calculations (a = 2.25 in.)

At T = 50°F,

$$S_f = (3 \times 10^2)(0.186) = 56 \text{ ksi} ;$$

at $T = T_1 = 55°F$,

$$S_f = S_y = 65 \text{ ksi} ;$$

at $T = T_2 = 79°F$,

$$S_f = S_y = 65 \text{ ksi} ;$$

and at $T = T_3 = 98°F$,

$$S_f = 65.0 + (3.15)(3.79 - 1.50) = 72.2 \text{ ksi},$$

which is a true stress. The engineering stress, from Eq. (H.2), is

$$S_f' = \frac{72.2}{e^{0.0379}} = 69.6 \sim 70 \text{ ksi} .$$

At $T = T_4 = 96°F$,

$$S_f = S_{ult} = 87 \text{ ksi} .$$

The foregoing calculations are summarized in Table H.3, along with the calculations for two other crack depths, 2.80 and 4.38 in., representing intermediate tensile specimens 7 and 6, respectively. The value of the shape factor C used for the two deeper cracks was 0.95.

In calculating the ratio K_c/K_{Ic} for very large values of δ_c, an approximation based on Eq. (H.53) was found useful. When the second term under the radical in Eq. (H.53) is large compared to unity,

$$\left(\frac{K_c}{K_{Ic}}\right)^2 \sim 1.4\delta_{Ic}^2 = \frac{1.4\delta_c^2}{(K_c/K_{Ic})^2} . \qquad \text{(H.68)}$$

Table H.3. Summary of calculations by the tangent modulus method for longitudinal intermediate tensile specimens fabricated from A533, grade B, class 1 steel

$\frac{a}{2b}$	$\frac{A_n}{A}$	Comp.	h_1	$\frac{\Delta h_0}{B}$	$\frac{P_0}{\sqrt{b_0}}$ (psi × 10^{-6})	$\frac{P_0}{\sqrt{b_0}}$	$\frac{K_{Iv}}{\sigma_Y}$ ($\sqrt{in.}$)	μ_{Iv}	λ_f (-)	$\frac{\Delta\sigma_f\sqrt{\rho}}{}$ ($\sqrt{in.}$ × 10^3)	$\frac{\sigma_f\sqrt{\rho}}{}$ ($\sqrt{in.}$ × 10^3)	$\frac{K_c}{\sigma_Y}$ ($\sqrt{in.}$)	$\frac{I}{\mu_c}$	$\frac{K_c}{K_{Ic}}$	$\frac{T}{\sigma_f}$ (-)	N_f (kcycles)	N_f (kcycles)
Case 1: a = 2.25 in., 2b = 6.10 in., C = 0.98																	
0.369	0.110	50°†					1.07	0.62	0.186			2.07		1.24	50		56
		T_1							0.216	5.83	5.83	2.68	0.78	1.36	55		65
		T_2	0.041	0.384	1.83	2.41			1.50	8.36	14.19	5.83	0.132	2.13	79		65
		T_3							3.79	14.02	28.11	11.98	0.0314	3.38	90	72.2	74
		T_4							12.00	22.20	51.31	21.1	0.0101	4.98	96	98	87
Case 2: a = 2.88 in., 2b = 8.20 in., C = 0.95																	
0.361	0.167	T_1							0.216	6.86	6.86	2.82	0.705	1.36	65		65
		T_2	0.082	0.56	2.58	2.81			1.50	11.40	18.26	7.52	0.0990	2.14	86		65
		95°†					4.17	3.11	3.79	30.4	38.7	15.9		3.81	95	72.2	74
		T_3							5.63	36.8	55.1	22.7	0.0100	4.87	98	78	74
		100°†					5.00	4.47	8.85	10.2	65.3	26.9		5.38	100	88.2	81
		T_4							12.00	20.2	75.3	31.0	0.172	5.89	100	98	87
Case 3: a = 4.38 in., 2b = 10.75 in., C = 0.95																	
0.408	0.361	T_1							0.216	8.48	8.48	3.46	0.73	1.35	76		65
		T_2	0.090	0.635	2.85	3.00			1.50	15.1	23.58	9.72	0.0993	2.39	94		65
		100°†					5.00	2.86	2.85	19.0	42.6	17.6		3.52	100	89.2	87
		107°†					6.95	5.52	7.70	88	112	46.0		6.60	107	84.5	78
		T_3 = T_4							12.2	137	181	62.1	1.441	8.00	100	98	87

so that

$$\frac{K_c}{K_{Ic}} \sim (1.4)^{1/6}\,\beta_c^{1/3} = 1.058\beta_c^{1/3} \quad . \tag{H.61}$$

By comparing Table H.3 with Fig. H.5, it can be seen that one of the results of considering net section effects has been an increase in the transition temperature for a 2.25-in.-deep crack from 73 to 90°F. In order to obtain the agreement between analysis and experiment indicated in Fig. H.9, it was necessary to consider the actual crack sizes in the test specimens at maximum load. Some of these crack sizes were estimated by examining the actual test specimens or photographs of them, while the crack dimensions for the other specimens were taken directly from Ref. 9, as indicated in Table H.2. The crack size at maximum load in intermediate tensile specimen 4 was estimated as the average of the values given in Ref. 9 for zero and maximum load because of the experimenter's stated uncertainty concerning the correct dimensions. In any case, it is evident that stable crack growth prior to maximum load should be considered in an elastic-plastic fracture analysis, at least for large cracks. (See also Appendix D.)

Evaluation of Strain Gradient Effects

As indicated by Fig. H.5, the tangent modulus method predicts that the fracture strain for a given surface crack geometry should be a function of the strain gradient in the region of the crack. Furthermore, the analysis implies that as the strain gradient becomes steeper, with the maximum tensile strain occurring at the cracked face, the fracture strain should decrease, approaching the strain predicted by linear elastic fracture mechanics. This hypothesis was tested by Randall,[3,10] using surface-cracked gross strain specimens of A533, grade B, class 1 steel loaded with controlled combinations of tensile and bending strain. The results are shown in Fig. H.11, which demonstrates that a systematic effect of strain gradient on fracture strain does exist and that the predictions of linear elastic fracture mechanics for the case of pure bending, expressed in terms of strain and extrapolated into the plastic range, do provide a lower bound to the experimental data.

The linear elastic fracture mechanics calculations plotted in Fig. H.11 were based on Eq. (H.7) and an assumed constant yield stress of 65 ksi. The value of the shape factor C for the case of bending for which the maximum value of C occurs at the front face of the specimen was obtained from Fig. 12 of Ref. 11. Accordingly,

$$C = \frac{M_1 M_2}{\Phi} \quad , \tag{H.62}$$

where

$$\Phi^2 = 1 + 4.593\left(\frac{a}{2b}\right)^{1.65} \quad . \tag{H.63}$$

For $a/2b = 0.324$, $M_1 M_2$ is about 0.95, and, from Eq. (H.63), $\Phi = 1.31$. Consequently, using Eq. (H.62), $C = 0.725$. Because the test specimens were not subject to any in-plane transverse tensile stresses, full transverse restraint was not assumed. Instead, after determining the ratio K_{Ic}/S_Y from Eq. (H.15), the value of β_{Ic} was determined from Eq. (H.54) and the value of K_c/K_{Ic} from Eq. (H.53). The value of K_c/S_Y was

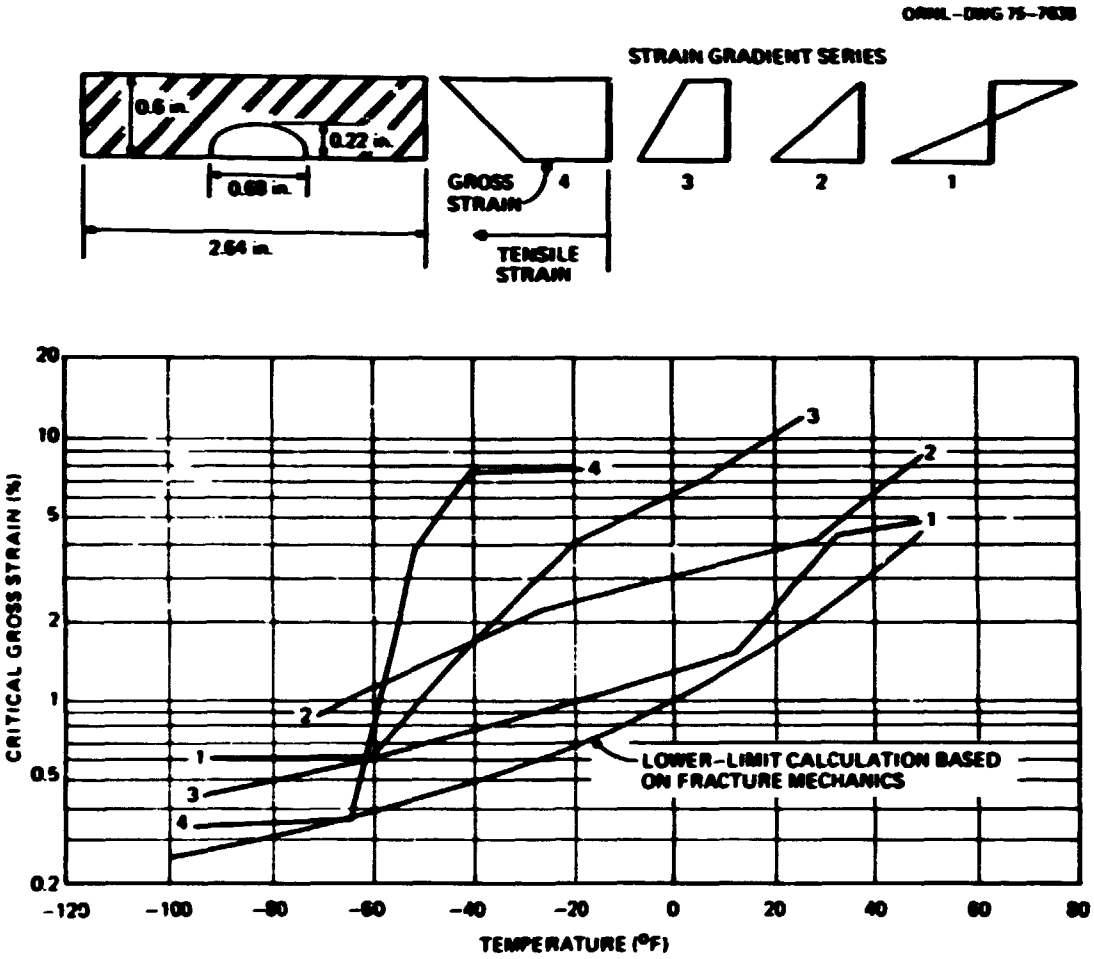

Fig. H.11. Gross section data for strain gradient specimens of A533, grade B, class 1 steel and comparison with the predictions of linear elastic fracture mechanics extrapolated into the plastic range.

then determined and used in Eq. (H.7). Thus, the linear elastic fracture mechanics curve in Fig. H.11 contains an allowance for incomplete transverse restraint. An allowance for incomplete transverse restraint is considered appropriate for uniaxial tensile loading but not necessarily for biaxial tensile loading, as discussed in Appendix E and in the following section of this appendix.

Analysis of 3- and 6.5-In.-Diam Steel Model Pressure Vessels

The analysis of the first seven intermediate tensile specimens and the evaluation of strain gradient effects just discussed were performed prior to the testing of intermediate test vessels V-1 and V-2. However, prior to these two tests, calculations by the tangent modulus method had not been made for any of the surface-cracked model pressure vessels that had already been tested. Nevertheless, as discussed in Ref. 5, a prediction of the failure strain for intermediate test vessel V-2 was made by the tangent modulus method, using the modified Irwin β_{Ic} correction, assuming that the occurrence of plastic strain in the direction

normal to the crack plane would cause a decrease in transverse restraint and a consequent increase in fracture toughness. This assumption proved to be incorrect for the reasons discussed in Appendix E, and a posttest analysis without the β_{1c} correction, thereby assuming full transverse restraint even in the presence of plastic strain normal to the crack plane, proved to be accurate. In order to further test the resulting hypothesis that the β_{1c} correction should not be used in the tangent modulus method for surface cracks in the cylindrical region of a pressure vessel, calculations were made for two series of small steel model pressure vessels that had been tested previously. These models were fabricated from A533, grade B, class 1 steel and had external surface flaws sharpened by electron-beam welding and subsequent hydrogen charge cracking. The experimental data from these model pressure vessels are summarized in Table H.4.

Table H.4. Data for 3- and 6.5-in.-diam steel model pressure vessels of A533, grade B, class 1 steel analyzed by the tangent modulus method

Model No.	Date tested	Model diam. (in.)	Test temp (°F)	Flaw size (in.)		Failure conditions		Temperature adjustment			
				Depth	Length	Pressure (ksi)	Strain (%)	$125 - T_{3.0}$ (°F)	$\sqrt{a_{3.0}/a_{0.5}}$	$125 - T_{0.5}$ (°F)	$T_{0.5}$ (°F)
5	2.1.71	3	50	0.150	0.750	30	0.64	175	0.612	107	18
3	2.5.71	3	-1	0.150	0.750	30	1.1	126	0.612	77	-48
7	2.5.71	3	26	0.150	0.750	31	2.9	99	0.612	61	-64
6	1.29.71	3	61	0.150	0.750	34	3.2	64	0.612	39	-86
4	2.22.71	3	180	0.130	0.750	31.7	3.2	No adjustment; $T_{3.0} > T_m$			180
1G1	2.29.72	6.5	65	0.39	1.50	27.0	0.164	No adjustment required			65
01-HB	7.29.71	6.5	50	0.40	1.45	31.5	3.57	No adjustment required			50
01-GB	2.23.72	6.5	197	0.43	1.52	29.5	~3.0	No adjustment required			197
1G3	2.10.72	6.5	200	0.40	1.51	31.0	2.15	No adjustment required			200

The value of the yield stress used for this analysis was 72 ksi instead of 65 ksi, and the strain at the onset of strain hardening was taken as 1.2% instead of 1.5%, because the later data for HSST plate 01 indicated that these values would be more appropriate estimates for most of the plate in the temperature range of interest (see Fig. H.2).

All nine of the specimens listed in Table H.4 had crack planes oriented perpendicular to the plate rolling direction. The failure strains cover the range from 0.164 to 3.57%. In order to simplify the comparison between calculation and experiment, the test temperatures for the 3-in.-diam models that were tested below 125°F were adjusted to the temperatures at which failure would have occurred at the same strains if the models and flaws had been of the larger sizes. This adjustment was based on Eqs. (H.1) and (H.11), which, when combined, imply that

$$\frac{K_c}{S_Y} = f(\lambda)\sqrt{a} . \tag{H.64}$$

By combining Eqs. (H.64) and (H.56), it follows that

$$\beta_c = \frac{1}{2} f^2(\lambda) \tag{H.65}$$

and therefore that

$$\frac{K_c}{K_{Ic}} = g(\lambda) \ . \tag{H.66}$$

Consequently, by substituting Eqs. (H.64) and (H.66) into Eq. (H.17), it follows that for failure at a given strain λ,

$$T = T_\infty - \frac{M(\lambda)}{\sqrt{a}} \ , \tag{H.67}$$

where

$$M(\lambda) = A_T \frac{g(\lambda)}{f(\lambda)} \ . \tag{H.68}$$

From Eq. (H.67), it follows that

$$T_\infty - T_{6.5} = (T_\infty - T_{3.0}) \sqrt{\frac{a_{3.0}}{a_{6.5}}} \ . \tag{H.69}$$

where the subscripts 6.5 and 3.0 indicate vessel diameter. The flaw depths in the 3- and the 6.5-in.-diam models were taken as 0.15 and 0.40 in., respectively. The resulting temperature adjustments are shown in Table H.4.

From Eq. (H.12), the relation between K_c/S_Y and $\epsilon_f \sqrt{\rho}$ for $\lambda_Y = 0.247$ is

$$\frac{K_c}{S_Y} = \frac{\epsilon_f \sqrt{\rho}}{2.71 \times 10^{-2}} \ . \tag{H.70}$$

Although the ratio of the crack area to the gross area was considerably smaller than that for the surface-cracked tensile specimens analyzed previously, some local bending due to the presence of the flaw was still expected. Accordingly, the tangent modulus in the transition range was arbitrarily estimated as 20 times the yield stress, or 1.44×10^6 psi, a value smaller than those used for the intermediate tensile specimens listed in Table H.3. This value corresponds to a value of $\Delta S_b/S$ of approximately 20%. Assuming a value of $E_s = 3.00 \times 10^5$ psi, the value of $\sqrt{E_g/E_s}$ in the transition range is 2.19. The difference between net and gross section strains was otherwise ignored for the flaw in the cylinder, because the flaw area was small compared to the gross section area. Thus, in contrast to the surface-cracked tensile specimens analyzed previously, failure at constant gross section strain over a range of temperature below the upper shelf was not expected, and the experimental data indicate that it did not occur.

The value of C used for this analysis, 0.863, is the elastically estimated[5] value for the flaws in intermediate test vessels V-1 and V-2. The transition range of strain was assumed to extend from the yield strain, 0.24%, to the strain at the onset of strain hardening in uniaxial tension, 1.2%. Thus, the analysis applied to the model vessels was basically a full restraint uniaxial tensile analysis, assuming, in effect, a small ratio of crack area to gross section area.

The pressure at failure by plastic instability in the upper-shelf temperature range was estimated for the 6.5-in.-diam model vessels by the method described in Ref. 5. Assuming a nominal ultimate tensile stress of 89 ksi, the flow stress for failure by plastic instability is 86.2 ksi, and the calculated failure pressure is 31.0 ksi, which agrees well with the experimental data listed in Table H.4. Based on the elastic-plastic pressure-strain analysis described in Appendix C, it can be shown that in the fully strain-hardened range of strain, the outside surface circumferential strain can be estimated from the equation

$$\lambda = \frac{2[p \quad S'_Y \ln(r_o/r_i)]}{[(r_o/r_i)^2 \quad 1](HS'_Y)}, \tag{H.71}$$

where HS'_Y is the slope of the straight line that best fits the initial portion of the strain-hardening branch of the stress-strain curve, taken here as 5.15×10^4 psi, and S'_Y is the intercept of this line with the elastic branch of the stress-strain curve, taken here as 67 ksi. For $r_o/r_i = 1.444$, Eq. (H.71) gives an estimated failure strain of 2.29%, which is nearly a lower bound to the experimental data in the upper-shelf range of temperature. Figure H.12 shows the assumed true stress-strain curve and related parameters that were used for this analysis.

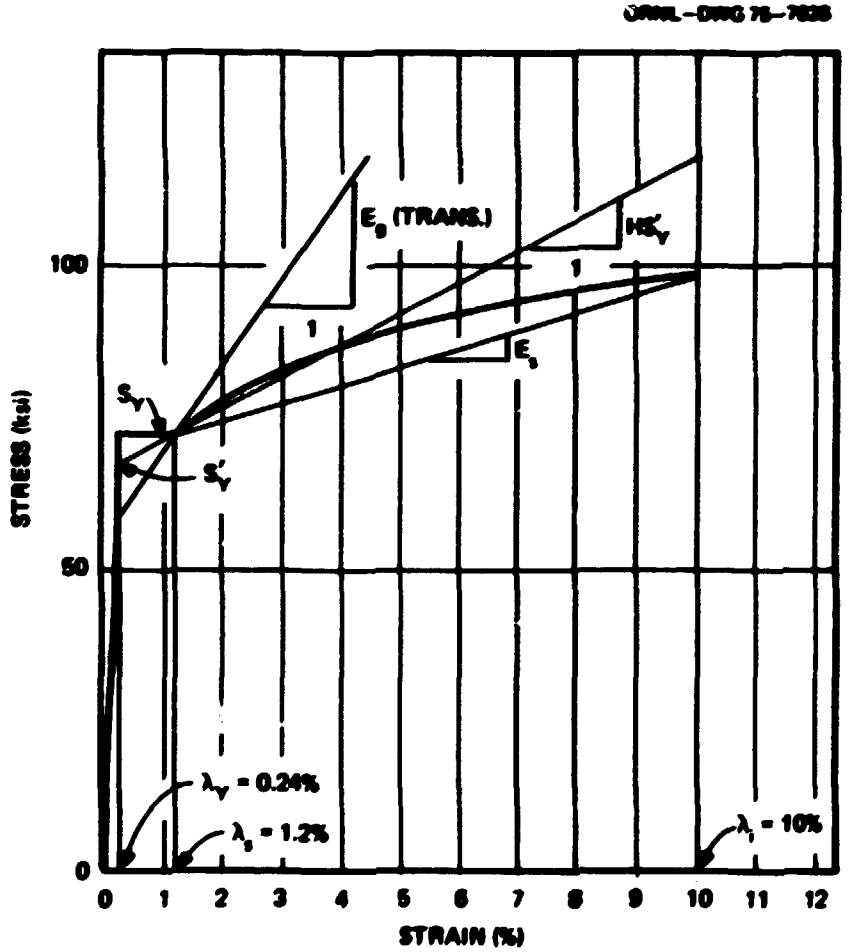

Fig. H.12. True stress-strain curve and associated parameters used for the analysis of surface-flawed 6.5- and 3-in.-OD steel model pressure vessels of A533, grade B, class 1 steel.

The analytical results are summarized in Table II.5 and plotted in Fig. II.13, along with the experimental data listed in Table II.4. The agreement between analysis and experiment shown in Fig. II.13 is considered good at all strain levels.

Table II.5. Summary of tangent modulus calculations for 6.5-in.-diam steel model pressure vessels of A533, grade B, class 1 steel; a = 0.40 in.

Gross strain, ε_g	$\frac{k_{\varepsilon_g}}{S_y}$	$\frac{12.5}{\varepsilon_g}$	$\frac{I}{\varepsilon_g}$	Remarks
0.14	0.565	221	96	
0.15	0.605	207	82	
0.16	0.645	194	69	
0.17	0.685	183	58	
0.18	0.725	172	47	
0.19	0.766	163	38	
0.20	0.806	155	30	
0.21	0.845	148	23	
0.22	0.886	141	16	
0.23	0.926	135	10	
0.24	0.969	129	04	Yield, $I = I_1$
0.27	0.995	125	01	
0.30	1.022	122	03	
0.35	1.066	117	08	
0.40	1.110	112	13	
0.50	1.198	104	21	
0.60	1.286	97	28	
0.70	1.374	91	34	
0.75	1.418	88	37	
0.90	1.550	81	44	
1.00	1.638	76	49	
1.10	1.726	72	53	
1.20	1.814	69	56	Onset of strain hardening, $I = I_2 = I_3$
1.50	1.935	65	60	
2.00	2.136	59	66	
2.29	2.253	56	69	Failure by plastic instability: $I = I_4$

Analysis of Gross Strain Tension Specimens Containing 0.25-in.-Deep Surface Cracks

Having developed an apparently workable procedure for considering the effects of net section bending and transverse restraint in surface-cracked specimens, an attempt was then made to estimate the transition temperature for a series of gross strain tension specimens containing 0.25-in.-deep surface cracks. Since net section bending in the test specimens had been reduced experimentally by adjusting the specimen grips,[1,2] the computed stress difference due to net section bending was arbitrarily reduced by a factor of 4. Otherwise, the analysis followed the same procedure and used the same material properties that were used for the intermediate tensile specimens discussed previously. The ratio of crack area to gross section area used was 0.10, and the linear elastic fracture mechanics shape factor C was taken as 0.90. The calculated

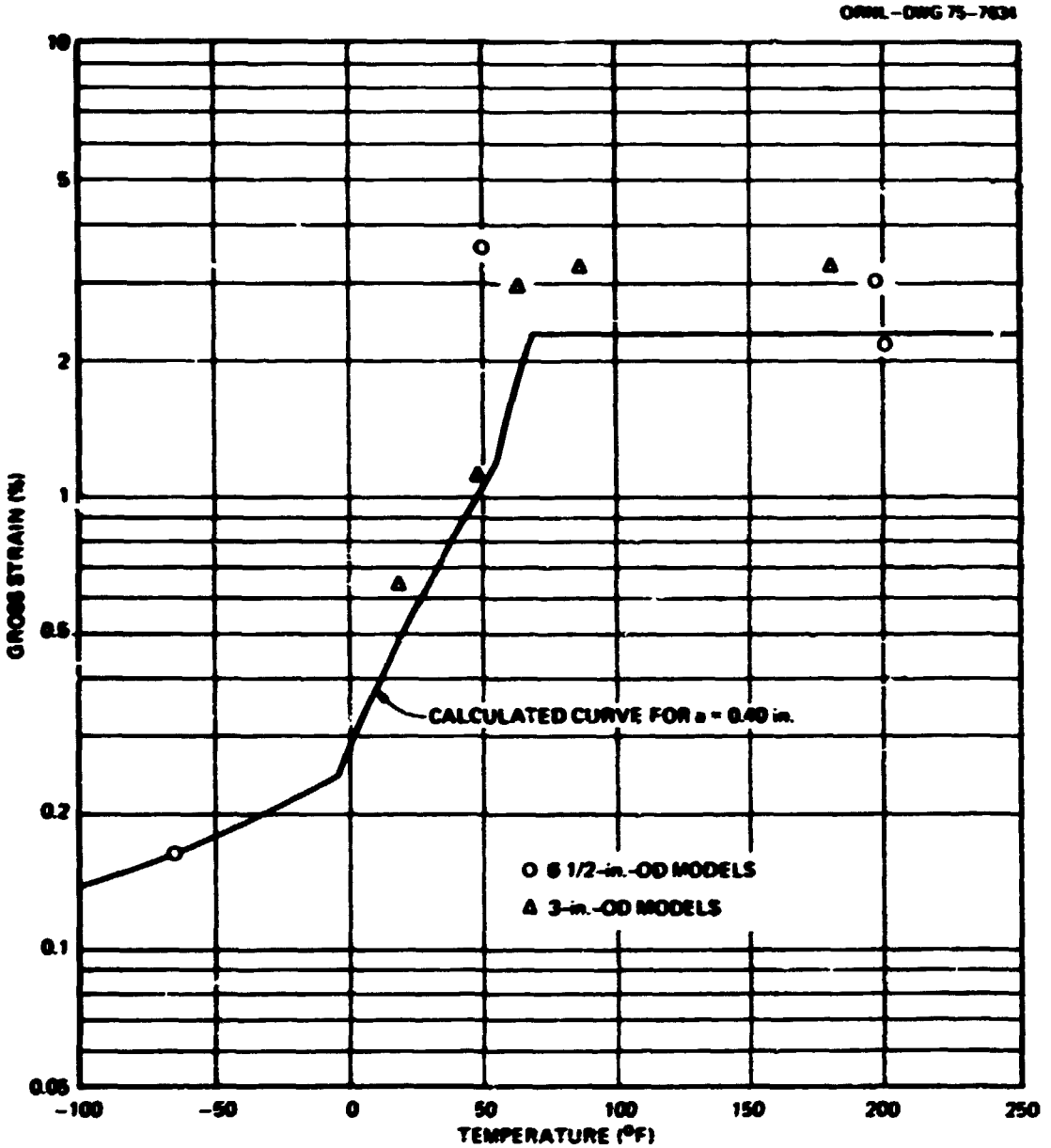

Fig. H.13. Experimental data and analytical results for 6.5- and 3-in.-OD model pressure vessels of A533, grade B, class 1 steel: temperatures of the 3-in.-diam models tested below 125°F have been adjusted to correspond to a flaw depth of 0.40 in.

gross and net section strain values for the specimen dimensions assumed were obtained from Eqs. (H.46), (H.49), and (H.52). From Eq. (H.46),

$$\lambda_1 = 0.216(1 - 0.10) = 0.195\% .$$

The value of λ_3 is 3.79%, as obtained previously from Eq. (H.49), for the intermediate tensile specimen

with $A_c/A = 0.10$. From Eq. (H.52),

$$\lambda_a = 12.00 \frac{(87)(0.1) \times 10^2}{3.15 \times 10^2} = 9.24\% .$$

The results of the temperature calculations are summarized in Table H.6, and the strain and temperature results are shown in Fig. H.14. The computed transition temperature, T_3, for a 0.25-in.-deep surface crack

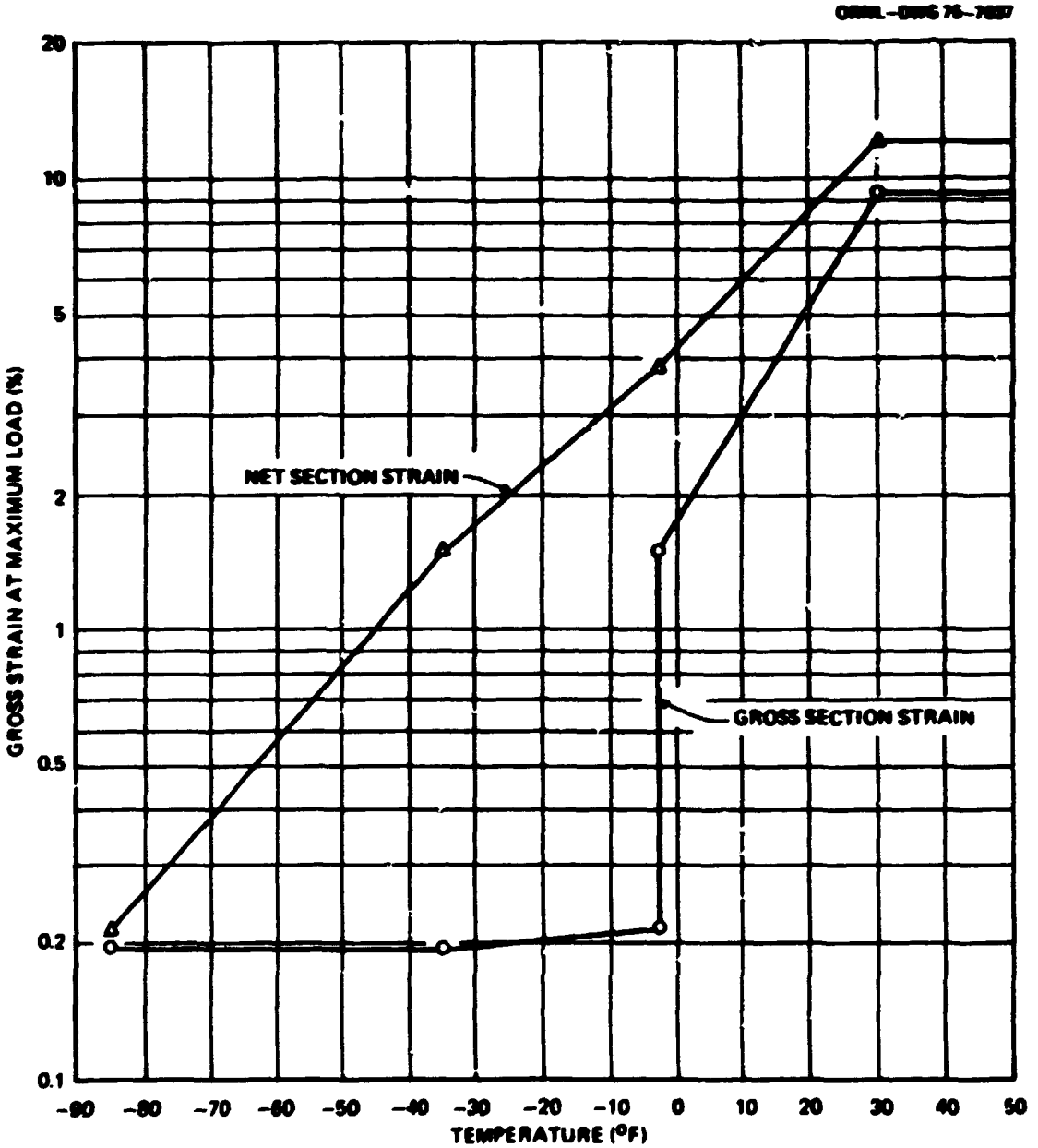

Fig. H.14. Calculated net and gross section fracture strain curves for gross strain tension specimens of A533, grade B, class 1 steel containing surface flaws 0.25 in. deep with $A_c/A = 0.10$.

Table H.6. Summary of temperature calculations by the tangent modulus method for gross strain tension specimens of A533, grade B, class 1 steel containing 0.25-in. deep surface cracks

$\frac{a}{W}$	$\frac{c}{a}$	$\frac{A_c}{A}$	Temp.	k_1	$\frac{\Delta S_p}{S}$	E_s (psi x 10^{-6})	$\sqrt{\frac{E_s}{E_t}}$	λ_f (%)	$\Delta\epsilon_f\sqrt{\rho}$ ($\sqrt{in.}$ x 10^3)	$\epsilon_f\sqrt{\rho}$ ($\sqrt{in.}$ x 10^3)	$\frac{K_c}{S_Y}$ ($\sqrt{in.}$)	$\frac{1}{\beta_c^2}$	$\frac{K_c}{K_{Ic}}$	$\frac{1}{(T-T_t)}$
0.25	0.90	0.10	T_1					0.316	1.94	1.94	0.798	0.785	1.34	85
			T_2	0.83	0.093	0.464	1.212	1.50	1.40	3.34	1.37	0.266	1.75	35
			T_3					3.79	3.89	5.83	2.40	0.0868	2.45	03
			T_4					12.00	7.40	13.23	5.45	0.0168	4.13	30

is 3 F, which appears quite reasonable in comparison with the experimental data shown in Figs. H.1 and H.3. In addition, noteworthy is the similarity in shape between the computed net and gross section fracture strain curves shown in Fig. H.14 and the experimental curves shown in Fig. H.3.

Discussion

The foregoing analyses indicate that reasonable predictions of fracture strain for surface cracks can be made by the tangent modulus method. In this method of analysis, the effects of strain gradients, transverse restraint, and the shape of the stress-strain curve are specifically considered. The fracture criterion is directly related to both the crack tip strain and to the value of K_{Ic} as conventionally measured. Furthermore, the linear elastic fracture mechanics shape factor C remains a constant for failure at all strain levels below the strain corresponding to the onset of plastic instability. Therefore, this quantity can be determined by elastic analysis or directly by experiment and then applied to the analysis of fracture conditions in the plastic range. In the equivalent-energy method, the experimentally determined shape factor appears to decrease with increasing failure strain (see Appendix G), whereas the shape factor C remains constant in the tangent modulus method while the effective tangent modulus E_g decreases with increasing failure strain.

Although the tangent modulus method as described above utilizes several simplifying approximations, it takes into account several aspects of physical behavior not specifically considered by most other methods of elastic-plastic fracture analysis, and the results agree well with experimental data. The fact that the analysis is in closed form and can be performed by hand constitutes a distinct advantage with respect to the time and expense required to obtain results and the ease of interpreting these results for engineering purposes. Finally, the analysis indicates that Randall's gross strain tests,[1-3] Derby's small steel model tests,[5] and Grigory's intermediate tension tests[6] have provided accurate and consistent experimental data that correctly describe the behavior of surface cracks in nuclear pressure vessel steels.

References

1. P. N. Randall, *Gross Strain Measure of Fracture Toughness of Steels*, HSSTP-TR-3, TRW Systems Group, Redondo Beach, Calif. (Nov. 1, 1969).
2. P. N. Randall, *Gross Strain Crack Tolerance of A533-B Steel*, HSSTP-TR-14, TRW Systems Group, Redondo Beach, Calif. (May 1, 1971).
3. P. N. Randall, *Effects of Strain Gradients on the Gross Strain Crack Tolerance of A533-B Steel*, HSSTP-TR-19, TRW Systems Group, Redondo Beach, Calif. (May 1, 1972).
4. P. N. Randall and J. G. Merkle, "Gross Strain Crack Tolerance of Steels," *Nucl. Eng. Des.* 17(1), 46–63 (August 1971).
5. R. W. Derby et al., *Test of 6-inch-thick Pressure Vessels, Series 1: Intermediate Test Vessels V-1 and V-2*, ORNL-4895 (February 1974).
6. P. N. Randall and J. G. Merkle, "Effects of Crack Size on the Gross-Strain Crack Tolerance of A533-B Steel," *J. Eng. Ind. ASME, Series B*, 94(3), 935–41 (August 1972).
7. J. G. Merkle, "Fracture Safety Analysis Concepts for Nuclear Pressure Vessels, Considering the Effects of Irradiation," *J. Basic Eng. ASME Series D*, 93(2), 265–73 (June 1971).

8. J. G. Merkle, "Stress-Intensity Factor Estimates for Part-Through Surface Cracks in Plates Under Combined Tension and Bending," *Quart. Prog. Rep. Reactor Safety Programs Sponsored by the Division of Reactor Safety Research for July–September 1974*, ORNL-TM-4729, Vol. II, pp. 3–32.

9. S. C. Gregory, *Tests of 6-in.-thick Flawed Tensile Specimens: First Technical Summary Report, Longitudinal Specimens Numbers 1 Through 7*, HSSTP-TR-18, Southwest Research Institute, San Antonio, Tex. (June 1972).

10. P. N. Randall and J. G. Merkle, "Effects of Strain Gradients on the Gross Strain Crack Tolerance of A533-B Steel," *Progress in Flaw Growth and Fracture Toughness Testing*, ASTM STP 536, pp. 404–30, American Society for Testing and Materials, 1973.

11. J. G. Merkle, *A Review of Some of the Existing Stress Intensity Factor Solutions for Part-Through Surface Cracks*, ORNL-TM-3983 (January 1973).

NOMENCLATURE

A	Gross section area, $in.^2$
A_c	Crack area, $in.^2$
A_1	Material parameter, $°F\sqrt{in.}$
a	Crack depth, in.
B	Thickness of a through-cracked test specimen, in.
b	Half surface length of a part-through surface crack, in.
C	Linear elastic fracture mechanics shape factor, dimensionless
d	Distance from the back surface to the area centroid of a part-through surface crack, in.
E	Modulus of elasticity, psi*
E_T	Effective tangent modulus corresponding to the gross strain λ, psi
E_n	Tangent modulus at the base of the notch, psi
E_t	Tangent modulus of the strain-hardening branch of the stress-strain curve, psi
E_{sec}	Secant modulus, psi
$f(\lambda)$	A function of the strain λ, dimensionless
g	Distance from the front surface to the area centroid of a part-through surface crack, in.
$g(\lambda)$	A function of the strain λ, dimensionless
H	Linear strain-hardening coefficient, dimensionless
K_I	Elastic crack tip stress intensity factor, ksi $\sqrt{in.}$
K_{Ic}	Critical value of K_I for fracture initiation under static plane strain conditions, ksi $\sqrt{in.}$
K_c	Critical value of K_I for fracture initiation under static but not necessarily plane strain conditions, ksi $\sqrt{in.}$
k_1	Ratio d/t, dimensionless
$M(\lambda)$	A function of the strain λ, $°F\sqrt{in.}$
M_1	Front face free-surface magnification factor, dimensionless
M_2	Back face free-surface magnification factor, dimensionless
p	Pressure, ksi
r_i	Inside radius, in.
r_o	Outside radius, in.
S	True stress, ksi
S'	Nominal stress, ksi
S_b	Total axial plus bending stress
S_f	True fracture stress, ksi

*Quantities having the dimensions of stress (psi) may be expressed in psi or ksi, as convenient.

S'_f	Nominal fracture stress, ksi
S_g	Gross section stress, ksi
S_{g1}	Gross section fracture stress at the temperature T_1, ksi
S_{g4}	Gross section fracture stress at the temperature T_4, ksi
S_n	Net section stress, ksi
S_{n3}	Net section fracture stress at the temperature T_3, ksi
S_o	Stress at the front surface, ksi
S_t	Stress at the back surface, ksi
S_{ult}	True ultimate tensile stress, ksi
S'_{ult}	Nominal ultimate tensile stress, ksi
S_Y	Yield stress, ksi
S'_Y	Effective yield stress for a linear strain-hardening approximation to the stress-strain curve (see Fig. H.12), ksi
T	Temperature, °F
T_1	Temperature at which the net section fracture strain equals the yield strain, °F
T_2	Temperature at which the net section fracture strain equals the strain at the onset of strain hardening, °F
T_3	Temperature at which fracture and gross section yielding coincide, °F
T_4	Lowest temperature at which the net section fracture strain equals the strain corresponding to the onset of plastic instability, °F
T_o	Characteristic temperature of a material, °F
t	Thickness, in.
x	Distance, in.
β_c	Plastic zone size parameter, dimensionless
β_{tc}	Plastic zone size parameter for plane strain conditions, dimensionless
ΔS_b	Stress difference between free surfaces due to bending, ksi
$\Delta S'_b$	Stress difference between the front surface and the centroidal depth of a part-through surface crack, ksi
ϵ	Notch root strain, in./in.*
ϵ_f	Notch root strain at fracture, in./in.
λ	Nominal strain, in./in.
λ_d	Strain parameter defined by Eq. (H.34), in./in.
λ_f	Fracture strain, in./in.
λ_i	Uniaxial tensile necking strain, in./in.

*Strain values may be expressed in percent, or in./in., as convenient.

λ_o Front surface strain, in./in.

λ_s Strain at the onset of strain hardening, in./in.

λ_t Back surface strain, in./in.

λ_y Yield strain, in./in.

λ_1 Gross section fracture strain at the temperature T_1, in./in.

λ_3 Net section fracture strain at the temperature T_3, in./in.

λ_4 Gross section fracture strain at the temperature T_4, in./in.

ρ Notch root radius, in.

Φ Elliptical integral, dimensionless